Transactions of the ASME® Journal of Heat Transfer

Published Quarterly by The American Society of Mechanical Engineers

VOLUME 119 • NUMBER 1 • FEBRUARY 1997

TECHNICAL PAPERS

1995 Max Jakob Lecture

Analytical And Experimental Methods

Heat Conduction

Forced Convection

Natural and Mixed Convection

Heat Exchangers

Radiation

(Contents continued on p. 1)

HEAT TRANSFER DIVISION
Chair, **S. M. CHO**
Vice Chair, **O. A. PLUMB**
Secretary, **R. A. NELSON, JR.**
Treasurer, **W. A. FIVELAND**
Technical Editor, **J. R. HOWELL (2000)**

Associate Technical Editors,
P. S. AYYASWAMY (2000)
T. L. BERGMAN (1998)
R. D. BOYD (1999)
S. H. CHAN (1997)
G. M. CHRYSLER (2000)
R. W. DOUGLASS (2000)
J.-C. HAN (2000)
M. KAVIANY (1999)
M. D. KELLEHER (1999)
A. S. LAVINE (1998)
M. P. MENGUC (2000)
R. A. NELSON, JR. (2000)
T. J. RABAS (1997)
S. RAMADHYANI (1998)
P. G. SIMPKINS (1998)
M. S. SOHAL (1998)
T. TONG (1999)
K. VAFAI (1997)
B. W. WEBB (1997)

BOARD ON COMMUNICATIONS
Chairman and Vice President
R. MATES

OFFICERS OF THE ASME
President, **R. J. GOLDSTEIN**
Executive Director,
D. L. BELDEN
Treasurer,
J. A. MASON

PUBLISHING STAFF
Managing Director, Engineering
CHARLES W. BEARDSLEY
Director, Technical Publishing
PHILIP DI VIETRO
Managing Editor, Technical Publishing
CYNTHIA B. CLARK
Managing Editor, Transactions
CORNELIA MONAHAN
Production Coordinator
COLIN MCATEER
Production Assistant
MARISOL ANDINO

Transactions of the ASME, Journal of Heat Transfer (ISSN 0022-1481) is published quarterly (Feb., May, Aug., Nov.) for $220.00 per year by The American Society of Mechanical Engineers, 345 East 47th Street, New York, NY 10017. Periodicals postage paid at New York, NY and additional mailing offices. POSTMASTER: Send address changes to Transactions of the ASME, Journal of Heat Transfer, c/o THE AMERICAN SOCIETY OF MECHANICAL ENGINEERS, 22 Law Drive, Box 2300, Fairfield, NJ 07007-2300. **CHANGES OF ADDRESS** must be received at Society headquarters seven weeks before they are to be effective. Please send old label and new address. **PRICES:** To members, $40.00, annually; to nonmembers, $220.00. Add $30.00 for postage to countries outside the United States and Canada.

STATEMENT from By-Laws. The Society shall not be responsible for statements or opinions advanced in papers or . . . printed in its publications (B7.1, Para. 3). **COPYRIGHT** © **1997** by The American Society of Mechanical Engineers. Authorization to photocopy material for internal or personal use under circumstances not falling within the fair use provisions of the Copyright Act is granted by ASME to libraries and other users registered with the Copyright Clearance Center (CCC) Transactional Reporting Service provided that the base fee of $3.00 per article is paid directly to CCC, 222 Rosewood Drive, Danvers, MA 01923. Request for special permission or bulk copying should be addressed to Reprints/Permission Department.

INDEXED by Applied Mechanics Reviews and Engineering Information, Inc. Canadian Goods & Services Tax Registration #126148048.

Downloaded 04 Feb 2011 to 194.85.80.107. Redistribution subject to ASME license or copyright; see http://www.asme.org/terms/Terms_Use.cfm

(Contents continued)

Boiling and Condensation

Phase Change and Multiphase Heat Transfer

Heat Transfer in Manufacturing

TECHNICAL BRIEFS

DISCUSSIONS AND CLOSURES

ANNOUNCEMENTS

Journal of
Heat Transfer

Letter From the Editor

The ASME Journal of Heat Transfer, along with all major journals, is facing a future of uncertainty. How will publication be done in a world of open electronic communication? Will archival journals survive when immediate dissemination of research results can be carried out through web-based publication? Have the technical journals become relics? Will CDs become the media of choice for future journal publication?

No one can answer these and similar questions with certainty. The ASME Journal of Heat Transfer continues to see, and will continue to see, its mission as providing an archival source of carefully reviewed technical information on research and applications in the field of heat transfer. To maintain this role we will continue to seek reviewers who will provide timely, careful, and frank reviews of work submitted to the journal. We will always have some delay between submission and publication of papers considered by the journal; this is the inevitable price that the community pays to insure that work that is published has passed careful scrutiny. Because I believe that the heat transfer community prizes care and diligence over immediacy, I believe that unreviewed web-based publication will not compete with archival journals in the long run.

We have, however, considered many avenues to speed transfer of information that is of interest to our readers. For example, the journal web page *http://hawkeye.me.utexas.edu:80/~heatran* now publishes the table of contents for upcoming issues as soon as they are prepared. This is usually about two months before the hard copy issue is mailed. If copyright problems and other details can be worked out, we will also publish abstracts of upcoming papers as they are accepted.

The integrity and viability of any archival journal is based on the competence and care of its reviewers. The heat transfer community is broad and deep, and most reviewers respond to requests for a review with a good deal of care. I would like to thank all of those who have reviewed for us over the period of the journal's existence. The reviewers for 1996 are listed elsewhere in this issue, as are last year's winners of the Outstanding Reviewer award, chosen by the associate editors of the journal based on the quality and frequency of their reviews.

Despite the good response by most reviewers, journal associate editors continue to note that the most difficult aspect of their job is obtaining timely and complete reviews. We recognize that reviews of technical papers are time consuming. The journal staff tracks the number of papers sent to individual reviewers, and this information is sent to the associate editors so that individual reviewers are not overloaded. However, some reviewers respond only after repeated requests by the associate editors, or do not respond at all. This may greatly delay publication, frustrating authors and associate editors (and yours truly). If you are requested to review a paper and find that it is outside of your area or you cannot review it in a timely way, then it would speed the process if you will simply return the review package to the associate editor at once so that another reviewer can be assigned.

Some authors of journal papers do not respond at all to requests for reviews of papers submitted to the journal by others. We require three complete reviews for every paper submitted to the journal, and so to maintain a viable review process, a journal author can expect to receive an average of three requests for review for each paper that you submit (whether to JHT or other archival journals). This should be viewed as a minimum commitment to the heat transfer community, which has provided this level of review to previously submitted papers. By not honoring this commitment, a heavier burden is placed on colleagues and the review process is degraded.

Again, I want to thank all of those who have contributed to the ongoing success of the ASME Journal of Heat Transfer through submission and review of quality archival papers.

Jack Howell, Technical Editor

Heat Transfer Enhancement—The Encouragement and Accommodation of High Heat Fluxes

A. E. Bergles
Heat Transfer Laboratory
Rensselaer Polytechnic Institute
Troy, NY 12180-3590
bergla@rpi.edu
Hon. Mem.

This review considers the many techniques that have been developed to enhance convective heat transfer. After introducing the techniques, the applications to most of the modes of heat transfer (single-phase forced convection, including compound techniques, pool boiling, convective boiling/evaporation, vapor-space condensation, and convective condensation) are described. Comments are offered regarding commercial introduction of this technology and the generations of heat transfer technology; advanced enhancement represents third-generation heat transfer technology.

Introduction

It is an honor and a privilege to join the many distinguished recipients of the Jakob Award, starting with the still-active Prof. Ernst Eckert who received the first Award in 1961. In addition, I am pleased to represent the many colleagues and students who have made it possible for me to contribute to enhanced heat transfer throughout much of my career.

I am fully aware that the Max Jakob Award has become the premier international award in heat transfer. This is appropriate, because Jakob (Fig. 1) was a towering figure in heat transfer research during the formative first half of this century (in heat transfer terms). His daughter summed it up well, ''My father's involvement in his work was extraordinarily intense and consumed a tremendous amount of time, but he managed to enjoy much else . . .'' (E. Jakob, 1988). Max Jakob has left a legacy of good heat transfer work that inspires us today, as well as great human qualities that are equally admirable. I was privileged to follow him as a student in the same institute at the Munich Technische Hochschule only 55 years later. Historically, it is appropriate to single out Jakob's paper of 1931 as presaging much of the current work on enhanced heat transfer. Jakob and Fritz (1931) presented data for nucleate boiling of water on a scored copper surface. As shown in Fig. 2, the boiling curves, recast in contemporary heat flux wall superheat, log-log coordinates, demonstrate an initial enhancement (boiling curve shifted to the left), but with time, the performance is diminished. This work was brought to the attention of the U S heat transfer community during Jakob's 1936 lecture tour (Jakob, 1936), an auspicous event of which we can celebrate the 60th anniversary this year. This characteristic of ''conventionally roughened'' surfaces, apparently due to outgassing of the nucleation sites, led to the search for stable pool boiling surfaces. This effort has been especially active during the past several decades.

The goals of enhanced heat transfer can be stated as the desire to encourage or accommodate high heat fluxes. Reference to Fig. 3 indicates that the heat flux can be increased by elevating the heat transfer coefficient for fixed temperature difference, for either constant heat transfer rate or constant area (two-fluid heat exchangers). Alternatively, enhancement permits the accommodation of high heat fluxes at a moderate temperature difference (systems with fixed heat generation). Another possibility for a two-fluid heat exchanger, is to use enhancement to reduce the temperature difference for a fixed heat flux. This reduces the entropy generation (Bejan, 1995), and increases the second-law efficiency.

The classification, listed in Table 1, of enhancement techniques has been suggested (Webb and Bergles, 1983).

The passive techniques do not require direct application of external power, whereas the active techniques require an external activator/power supply to bring about the enhancement. Two or more of the above techniques may be utilized simultaneously to produce an enhancement that is larger than the techniques operating separately. This is termed compound enhancement. A representative study is listed in Table 2 for each of the techniques.

A description of these techniques can be found in Bergles (1985, 1988). With 14 enhancement techniques (plus compound enhancement) and 6 modes of convection heat transfer (single-phase, boiling, and condensing—natural or forced flow), it is clear that there are a lot of opportunities for research in this field.

Figure 4 presents the results of the most recent bibliographic survey (Bergles et al., 1995), which indicates that the accumulated literature is extensive, and that the main publication has occurred since about 1955, when Jakob died. In fact, the final (posthumous) edition of Jakob's first textbook (Jakob and Hawkins, 1957) contains no mention of heat transfer enhancement.

It will be noticed that *Swirl Flow Devices* in Table 2 contains an old paper, in fact, the first major paper on heat transfer enhancement, by Joule, 135 years ago. The point here is that old literature may be very relevant to the current practice of enhanced heat transfer. In this field, especially, one should consider the past, or, in Santayana's words, ''Those who cannot remember the past are condemned to repeat it.''

This suggestion not withstanding, it is becoming very difficult for those entering the field of enhanced heat transfer to become familiar with the accumulated experience. Max Jakob himself offers the appropriate words for the information explosion, on a different thermal subject, ''I studied the colossal amount of material for at least a week and just got crushed by the weight'' (E. Jakob, 1988).

Contributed by the Heat Transfer Division for publication in the Journal of Heat Transfer. Manuscript received by the Heat Transfer Division August 14, 1996; revision received August 14, 1996; Keywords: Augmentation & Enhancement, Forced Convection, Heat Exchangers. Technical Editor: J. R. Howell.

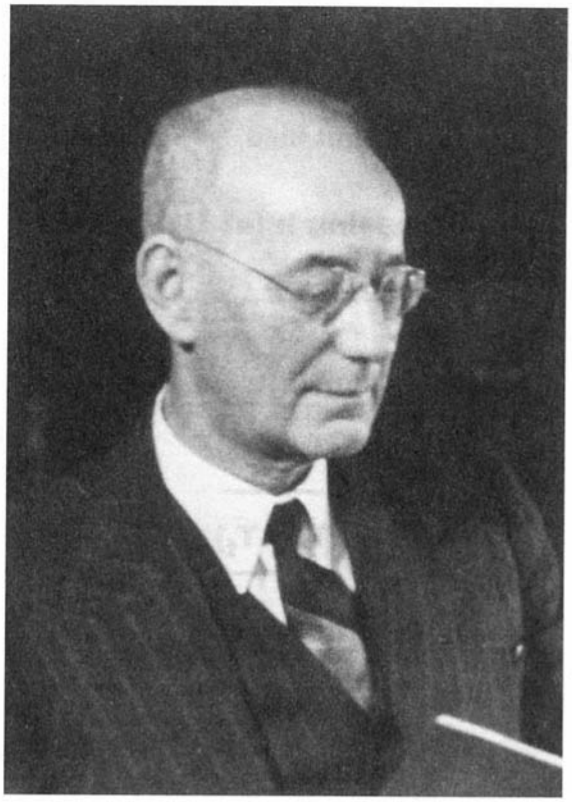

Fig. 1 Max Jakob, 1879–1955

A comment is in order regarding the apparent decline of literature generation in recent years. This is an illusion that is due simply to the delay in cataloging recent literature. The rate of literature generation has not decreased, but it has probably stabilized at about 400 papers and reports per year. The S-shaped curve of literature generation is indicative of the maturity of the field (Bergles, 1996).

Since it is clear that there is an overwhelming bibliography in the field, it is necessary to limit this discussion to a few developments, particularly those that have happened recently, and trends. This selectivity means that thousands of good papers are not referred to, and an apology is extended for not being able to be comprehensive. Basically, I will pick on subjects that I hope are interesting.

Developments in Single-Phase Enhancement

The enhancement of single-phase flow is important because that flow usually represents the dominant thermal resistance in a two-fluid heat exchanger, especially if it is a gas (as compared to a liquid). Interrupted fins are generally used to enhance gas flows; the idea is to elevate the heat transfer coefficient on the extended surface. The heat transfer and flow friction characteristics of louvered fins have recently been determined. Offset strip fins (Fig. 5(*a*)) are also popular for plate-fin heat exchangers.

The following correlations are recommended for calculating the *j* and *f* characteristics for gas flows (Manglik and Bergles, 1995):

$$j_h = 0.6522\,\mathrm{Re}_h^{-0.5403}\alpha^{-0.1541}\delta^{0.1499}\gamma^{-0.0678} \times [1 + 5.269 \times 10^{10^{-5}}\,\mathrm{Re}_h^{1.340}\alpha^{0.504}\delta^{0.456}\gamma^{-1.055}]^{0.1} \quad (1)$$

$$f_h = 9.6243\,\mathrm{Re}_h^{-0.7422}\alpha^{-0.1856}\delta^{0.3053}\gamma^{-0.2659} \times [1 + 7.669 \times 10^{-8}\,\mathrm{Re}_h^{4.429}a^{0.920}\delta^{3.767}\gamma^{0.236}]^{0.1} \quad (2)$$

where j_h, and f_h, and Re_h are based on the hydraulic diameter given by

$$D_h = 4shl/[2(sl + hl + th) + ts].$$

These equations are based on experimental data for 18 different offset strip fin geometries, and they represent the data continuously in the laminar, transition, and turbulent flow regions, as shown in Fig. 5(*b*). The development of accurate power-law correlations for a variety of enhancement configurations is possible when large data bases are available.

Nomenclature

A = heat transfer surface area, m^2
b = transverse dimension of vortex generator, m
c = constant pressure specific heat, J/kg K; longitudinal dimension of vortex generator, m
D, d = inner diameter of channel, m
D_h = hydraulic diameter, m
E = enhancement ratio h_a/h_s, -; electric field strength, V/m
f = Fanning friction factor, -
f_F = forced oscillating frequency, s^{-1}
G = mass flux, kg/m^2
g = gravitational acceleration, 9.8 m/s^2
h = heat transfer coefficient, W/m^{2}K; strip fin height, m; channel half height, m
j = Nu/Re Pr$^{1/3}$
k = thermal conductivity, W/mK
L = channel length, m
ℓ = length of strip-fin element, m
Nu = Nusselt number, hD/k, -
n = viscosity ratio exponent
P = pressure, Pa
Pr = Prandtl number, $c\mu/k$, -
q = heat transfer, W
q'' = heat flux, q/A, W/m^2 or Btu/hr ft^2
Ra = Rayleigh number, $g\beta\Delta TD^3c\rho/\nu k$, -
Re = Reynolds number, GD/μ, -
s = lateral spacing of strip fins, m
Sw = swirl flow parameter, $\mathrm{Re}/\sqrt{y}$, -
t = fin thickness at base, m; time, s; thickness of offset strip fin, m
T = temperature
ΔT_{sat}, ΔT_b = wall superheat, T_w-T_{sat}, °C or K
U = overall heat transfer coefficient, W/m^{2}K
$\bar{U}_c$ = equivalent flat channel centerline velocity, m/s
V = average flow velocity, m/s
y = tube diameters per 180° tape twist, -
α = aspect ratio for offset strip fins, s/h, -
β = bulk modulus of expansion, K^{-1}
γ = ratio t/s, -
δ = ratio t/ℓ, -; thickness of twisted tape, m
Λ = aspect ratio of vortex generator (Fig. 7)
μ = dynamic viscosity, Ns/m^2
ν = kinematic viscosity, m^2/s
ρ = density, kg/m^3
Ω_F = dimensionless frequency, $f_Fh/\bar{U}_c$
η = ratio of forcing velocity to main velocity

Subscripts

α = augmented or enhanced
ax = based on axial velocity in actual cross section
b, f = based on fluid temperature
h = based on hydraulic diameter
s = straight or plain; based on surface temperature, shell
sat = saturation condition
w = denotes wall condition
t = tubeside
∞ = refers to fully developed condition

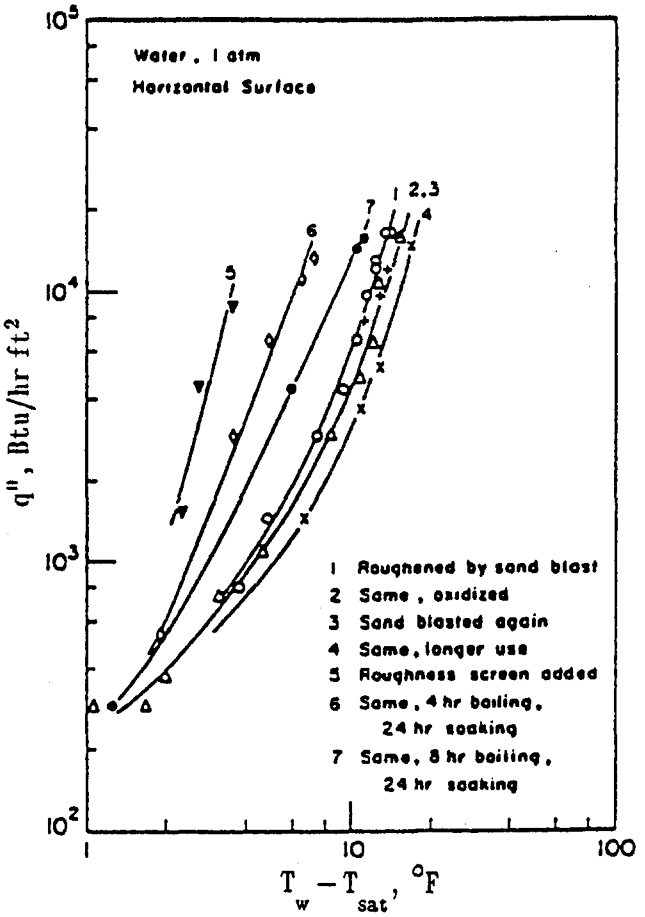

Fig. 2 Boiling curves for surfaces with various surface treatments and operating history (Jakob and Fritz, 1931)

A novel "aspirating" heat exchanger (Fujii et al., 1989) is shown in Fig. 6(*a*). Here, there is parallel flow or counter flow. The fluids are in either parallel flow or counter flow. The flow in a narrower portion of the channel has a higher velocity and a lower pressure than the flow in the plain channel. The opposite is true in the adjacent channel. Then, when the walls are perforated, there will then be an enhancing cross-flow of fluid. This disturbs the axial flow, elevating the heat transfer coefficient, as shown in Fig. 6(*b*). It is, of course, not easy to arrange the headers so that the necessary co-current or counter-current flow is present in adjacent channels.

$$\frac{q}{A} = h\,(T_{surface} - T_{fluid})$$

$$\frac{q}{A} = U\,(T_{hot\ fluid} - T_{cold\ fluid})$$

By increasing h (or U) we

Encourage High Heat Fluxes

or

Accommodate **High Heat Fluxes**

$q = Ah\,(T_s - T_f)$
↑ —↑ ———

$q = Ah\,(T_s - T_f)$
— ↓↑ ———

Encourage Low Temperature Differences

$q = Ah\,(T_s - T_f)$
— —↑ ↓

Fig. 3 The goals of heat transfer enhancement as related to the encouragement and accommodation of high heat fluxes

A particularly significant development is the use of vortex generators in plate-fin, tube-and-plate fin, or finned-tube heat exchangers. See Jacobi and Shah (1995) and Fiebig (1996) for recent summaries of this technique. The generators shown in Fig. 7(*a*) can be incorporated into heat transfer surfaces by punching, stamping, or embossing. They fall into the category of longitudinal three-dimensional vortex generators, as characterized by Fiebig (1996). The vortices disturb the flow and elevate the heat transfer coefficient, as shown in Fig. 7(*b*). Of course, the pressure drop is also increased for this case by about the same amount. With proper spacing of the vortex generators the entire heat transfer surface can be influenced. A recent paper that deals with the application of vortex generators to refrigerant coils is given by Gentry et al. (1996).

Table 1 Classification of Enhancement Techniques

- Passive Techniques
  - Treated surfaces
  - Rough surfaces
  - Extended surfaces
  - Displaced enhancement devices
  - Swirl flow devices
  - Coiled tubes
  - Surface tension devices
  - Additives for fluids
- Active Techniques
  - Mechanical aids
  - Surface vibration
  - Fluid vibration
  - Electrostatic fields
  - Suction or injection
  - Jet impingement
- Compound Enhancement
  - Rough surface with a twisted-tape swirl flow device, for example

A variety of new studies of in-tube enhancement have appeared. Consider the classical twisted-tape insert in a uniform temperature tube. Although most of the available data and correlations are for electrically heated tubes (constant heat flux) that are so convenient for laboratory studies, uniform wall temperature is the more appropriate boundary condition for shell-and-tube-heat exchangers.

The data for UWT were sparse, so we built a loop to study a wide range of internal and external flows for plain and enhanced tubes. The new data make possible a much better fully developed swirl flow correlation utilizing a new dimensionless parameter, $Sw = \mathrm{Re}_{sw}/\sqrt{y}$:. There is a strong evidence that there is an influence of free convection (horizontal tube) at low Reynolds number and low Sw. The final laminar flow design equation is involved because of this Rayleigh number effect, but the following equation correlates the data well (Manglik and Bergles, 1993a):

$$\mathrm{Nu}_m = 4.612(\{(1 + 0.0951 Gz^{0.894})^{2.5} + 6.413 \times 10^{-9}(Sw \cdot \mathrm{Pr}^{0.391})^{3.835}\}^{2.0} + 2.132 \times 10^{-14}(\mathrm{Re}_{ax} \cdot \mathrm{Ra})^{2.23})^{0.1}\left(\frac{\mu_b}{\mu_s}\right)^{0.14}. \quad (3)$$

Table 2 Representative Developments in Enhancement Techniques

Treated Surfaces	Painted surfaces to enhance pool boiling of "electronic liquids" O'Connor and You [1995]
Rough Surfaces	Numerical simulation of turbulent flow in rib-roughened channels. Ciofalo and Collins [1989]
Extended Surfaces	Evaporation and condensation of an alternate refrigerant and oil in a microfin-tube. Eckels et al. [1994 a,b]
Displaced Enhancement Devices	Winglet vortex generators applied to airflow in a tube-and-plate fin array. Fiebig and Sanchez [1992]
Swirl Flow Devices	Wires inserted in an annulus to cause spiralling flow of water. Joule [1861]
Coiled Tubes	Numerical investigation of flow in square ducts, helically formed. Eason et al. [1994]
Surface Tension Devices	Pool boiling of a refrigerant with beads on the surface. Fukusako et al. [1991]
Additives for Fluids	Small addition of alcohol to water increase the critical heat flux above that of pure water. McGillis and Carey [1996]
Mechanical Aids	Surface scraping used to improve heat transfer in food sterilization. Lee and Singh [1990]
Surface Vibration	Transverse vibration of a plate in forced flow to increase laminar heat transfer. Soria and Norton [1991]
Fluid Vibration	Enhancement of melting and solidification by application of ultrasound. Hong [1993]
Electrostatic Field	Corona discharge enhancement of heat transfer to air flowing in a tube. Ohadi et al. [1991]
Injection or Suction	Injection and suction enhancement of free convection heat transfer to air in natural convection over a vertical plate. Inagaki and Komori [1993]
Jet Impingement	Cooling of a moving hot plate with a water jet. Chen et al. [1991]
Compound Technique	Air jet impingement on rib-roughened walls. Gau and Lee [1992]

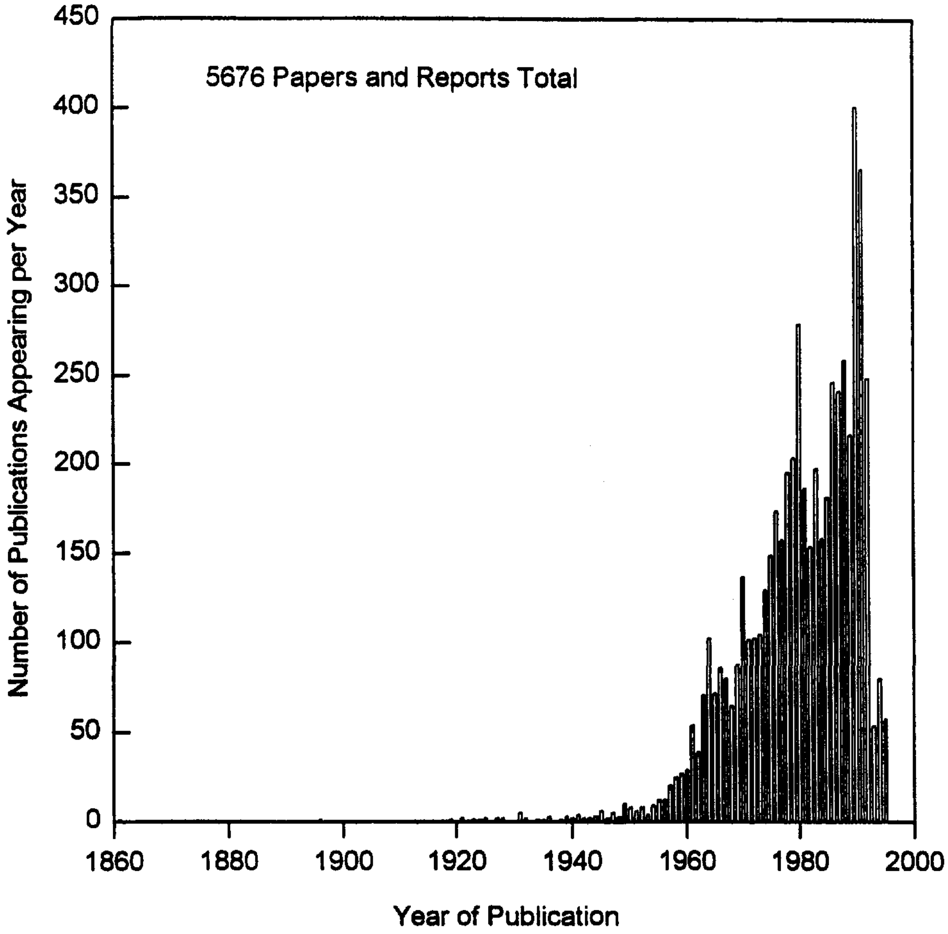

Fig. 4 Citations on heat transfer enhancement versus year of publication—computer file status as of August 1995 (Bergles et al., 1995)

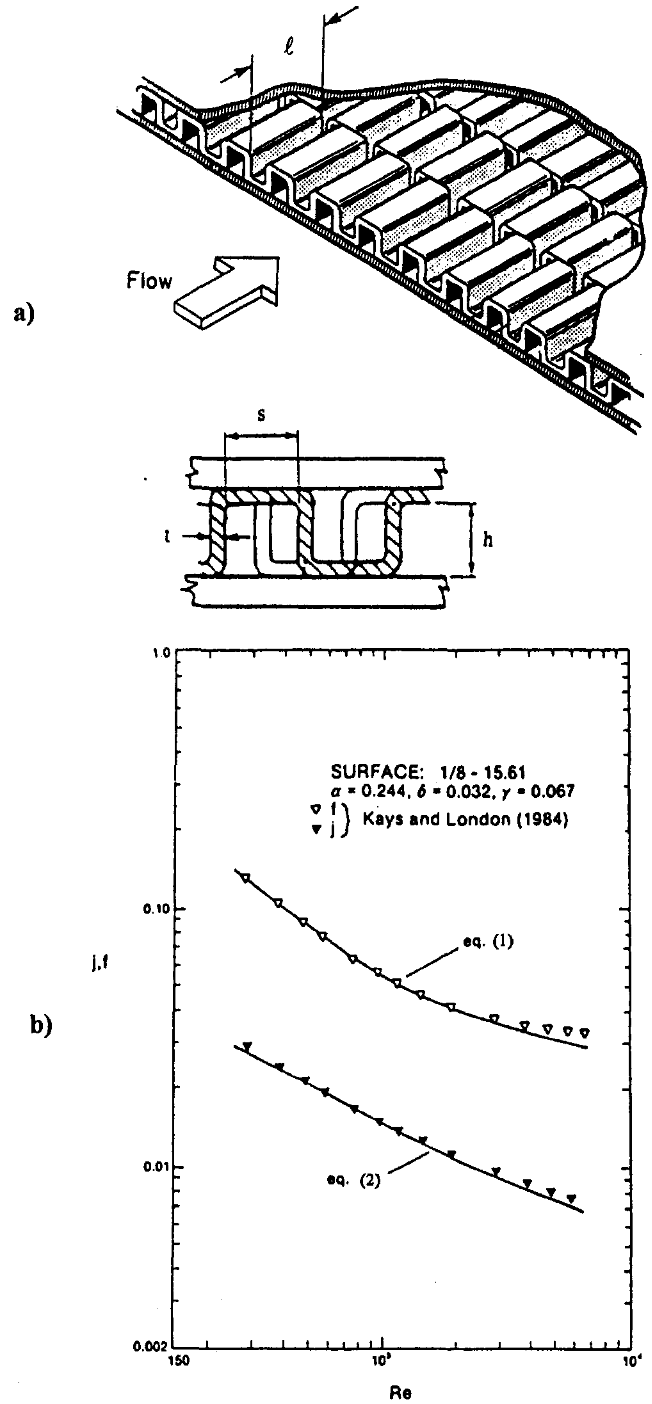

Fig. 5 (*a*) Geometry of the offset strip fin; (*b*) comparison of the predictions with data from Kays and London (1984), (Manglik and Bergles, 1995).

A turbulent flow correlation is also available (Manglik and Bergles, 1993b).

The challenge is how to get a "universal" correlation that encompasses both laminar and turbulent flow. Because of the complex laminar behavior, it is difficult to develop an equation that can go through the transition region. For convenience, we propose a graphical correlation where the laminar and turbulent behavior are simply connected by a straight line (Fig. 8). The basic swirl effect accounts for several hundred percent increase in average heat transfer coefficient in laminar flow; variable properties, radial temperature gradient and free convection (in the practical range of Re and Ra), are more like 10-percent effects.

The grooving of rectangular channels (Fig. 9(*a*)) might be considered to exploit instabilities, e.g., Greiner (1991), excited by oscillation of the main stream. In terms of Table 1, this is a variation of fluid vibration. The oscillation can be created by flow pulsation or transverse inserts that generate oscillating vortices. As noted by Fiebig (1996), the grooves are transverse, two-dimensional vortex generators. At resonance, the fluid in the grooves is periodically ejected, causing a substantial heat transfer enhancement for the entire surface.

Typical numerical data are shown in Fig. 9(*b*) and (*c*). The numerical predictions are compared with experimental data (for somewhat different geometrical characteristics); a sharply peaked enhancement is observed near the frequency of the natural or most unstable mode of the flow. Hydrodynamic resonance enhances the channel mixing and more than doubles the heat transfer coefficient. Much progress has been made in predicting this behavior through numerical simulation, e.g., Amon (1993). In general, it appears that this technique is best suited for low velocity laminar flows.

Under swirl-flow, in-tube enhancement, Fig. 10 depicts an insert that rotates under the action of the flowing gas (Yeh, 1989). While the hardware to accomplish this is rather involved, large improvements in heat transfer can be expected in the low-flow-velocity range.

Electrohydrodynamic (EHD) enhancement of heat transfer has been experiencing a resurgence, with major activities in England, Japan, and the U.S. The idea is to put electrodes in dielectric flow streams (gases or dielectric liquids) and create a high voltage ([0]10,000 v) *between the main flow and the* heat transfer surface. Electrophoretic or dielectrophoretic forces then create secondary flows which enhance the heat transfer, particularly for low-velocity main flows. A typical gas-gas heat exchanger rigged for EHD, on both the tube side and the shell side, is shown in Fig. 11(*a*); Fig. 11(*b*) shows that substantial

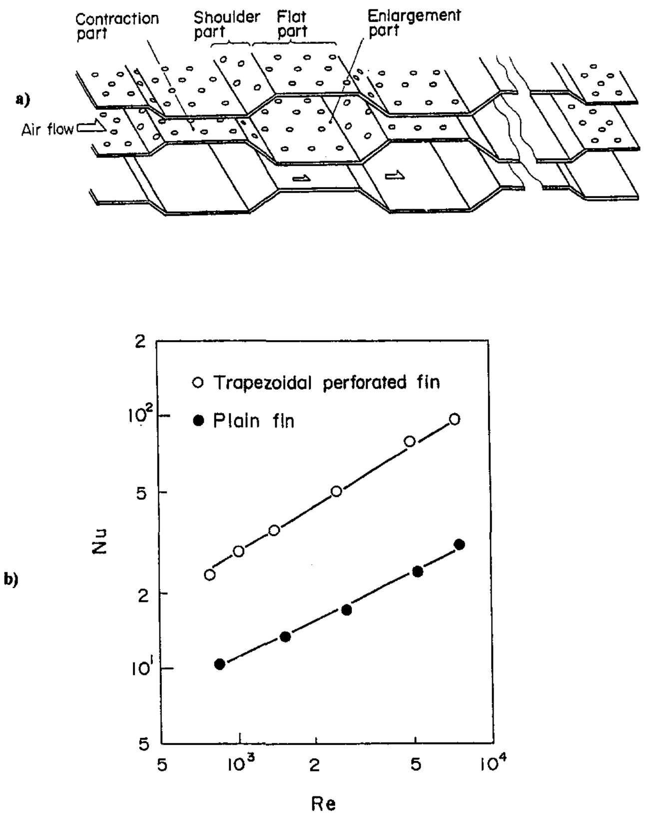

Fig. 6 (*a*) Plate-fin heat exchanger enhanced with breathing effect; (*b*) heat transfer characteristics of aspirating heat transfer surface (Fujii et al., 1989).

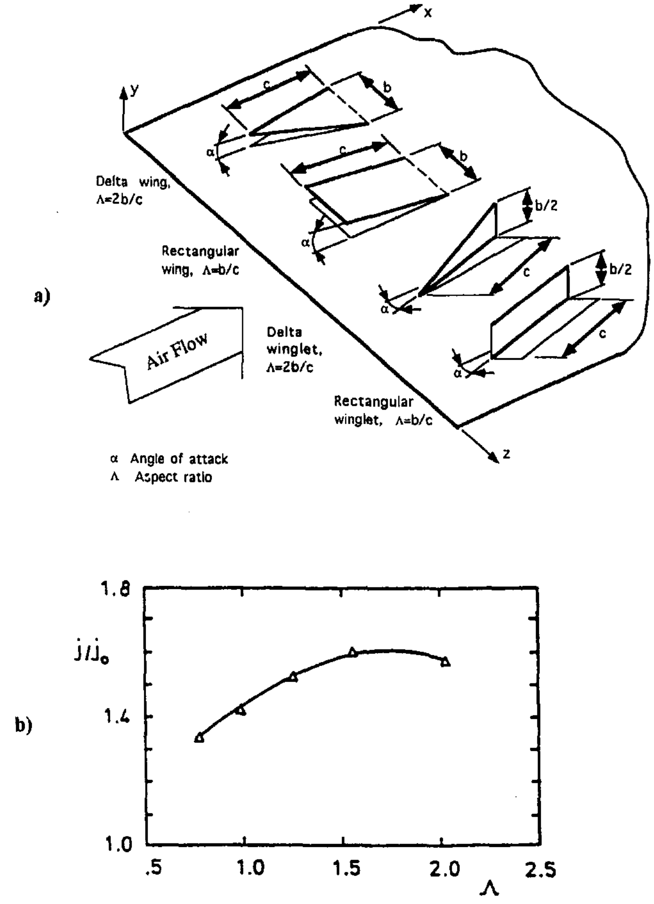

Fig. 7 **(a) Longitudinal vortex generators with geometrical definitions; (b) heat transfer enhancement as a function of aspect ratio for $\alpha = 30°$ and Re = 1815 (single delta winglet, area downstream of vortex generator, Jacobi and Shah, 1995).**

improvements in the overall heat transfer coefficient are possible. The power expenditure of the electrostatic generator is small, typically only several percent of the pumping power.

EHD has not yet been adopted commercially, largely because of concerns about installing the electrodes and using very high voltages during heat exchanger operation. It has a potential drawback, common to all active techniques, in that an extra system is required (in this case, the electrostatic generator); failure of that system means the enhancement is not obtained.

Compound Enhancement in Single-Phase Flow

Compound techniques are a slowly emerging area of enhancement that holds promise for practical applications since heat transfer coefficients can usually be increased above each of the several techniques acting alone. Some examples that have been studied are as follows: (1) rough tube wall with twisted-tape inserts, (2) rough cylinder with acoustic vibrations, (3) jet impingement on rough surfaces, (4) internally finned tube with twisted-tape insert, (5) finned tubes in fluidized beds, (6) externally finned tubes subjected to vibrations, (7) rib-roughened passage being rotated, (8) gas-solid suspension with an electrical field, (9) fluidized bed with pulsations of air, and (10) a rib-roughened channel with longitudinal vortex generation.

Enhancement of Boiling Heat Transfer

A great variety of surfaces have been studied in the laboratory to determine their potential to improve pool or shellside boiling. Some of these surfaces are shown in Fig. 12. They all work by having thin-film vaporization internally and bubbling through the openings to the pool. Nucleation must occur somewhere on the interior surface, and there must be an effective vapor-liquid exchange to continually supply liquid for vaporization. The process is fundamentally different from normal nucleate boiling from surface cavities. As mentioned earlier, the development of these surfaces was very much inspired by the early studies of Jakob and Fritz (1931). Patent protection is routinely sought for these surfaces because of the potential commercial benefits, particularly for the petrochemical and heating, ventilating, and air-conditioning (HVAC) industries. To give an idea as to the typical enhancement that can be achieved with these surfaces, refer to the data shown in Fig. 13.

It should be noted that many of these surfaces still have a large temperature overshoot/thermal excursion at the initiation of boiling with highly wetting liquids. The high temperature or heat flux required to initiate boiling can be a drawback, but there are systems that routinely have such a condition at start-up (e.g., air-conditioning evaporators). In any case, efforts have been made to develop surfaces that will both enhance the heat transfer and mitigate the thermal hysteresis. This includes a paint-type coating (O'Connor and You, 1995), carbon-fiber-matrix material (Wang et al., 1996), and bubbling—an active enhancement technique (Bergles and Kim, 1988).

It must be recognized that boiling (and condensing) are very efficient processes with high heat transfer coefficients. The "other side" of a two-fluid heat exchanger may offer the dominant thermal resistance, so it would be enhanced first. On the other hand, having done this, the boiling side may then represent the larger thermal resistance, and it should be enhanced (Thome, 1996).

Tube Bundles

Much attention has been directed toward two configurations: tube bundles and flow inside tubes. Within each category, a number of studies are possible, depending on the fluid. With the former, an additional variable is the mode of fluid supply, as seen in Table 3. Recent representative studies are listed in the table. It is emphasized that pool boiling from single tubes is of limited practical interest.

For horizontal bundles where spray evaporation is routinely used (absorption refrigeration, chemical processes), they allow

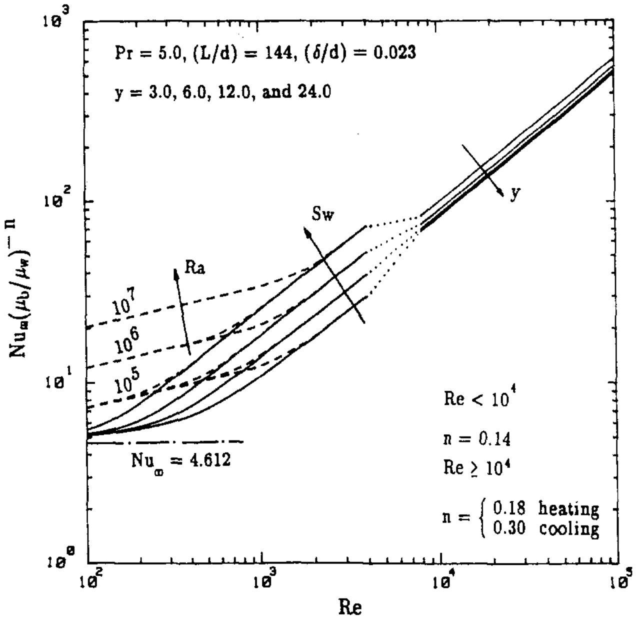

Fig. 8 **Heat transfer characteristics in laminar, transition, and turbulent flows in uniformly heated circular tubes with twisted-tape inserts (Manglik and Bergles, 1993b)**

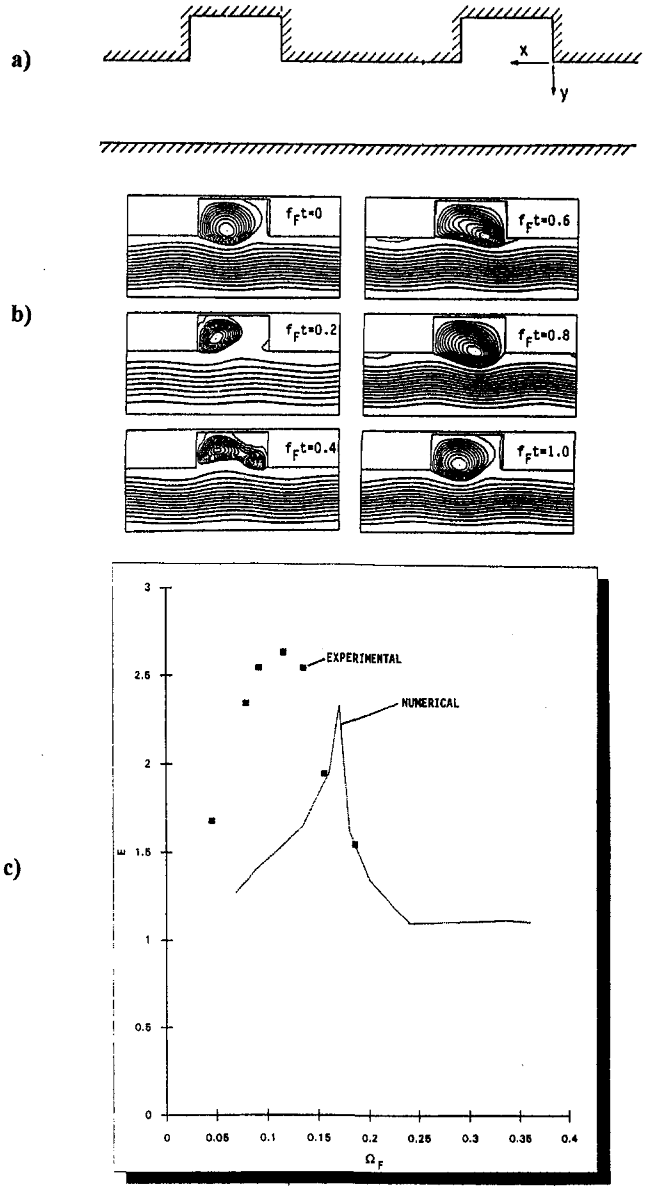

Fig. 9 (*a*) **The periodic, grooved-channel (steady-flow component from right to left); (*b*) numerically calculated instantaneous streamlines during the forced oscillating cycle; (*c*) numerically calculated and experimentally observed heat transfer enhancement. For (*b*) and (*c*): Re = 525, η = 0.2, Pr = 7 (Greiner et al., 1986).**

for the possibility of reducing refrigerant inventory (important for the expensive, ozone-friendly refrigerants) in large commercial and industrial chillers. Important variables are the nozzle geometry and the feed flow. Moeykens et al. (1996) reported tests of R-123 (with and without oil) with plain and several types of enhanced tubes in both square-pitch and triangular-pitch horizontal-tube bundles. The average heat transfer coefficients were dependent on the film-feed supply rate, oil concentration, and heat flux. The heat transfer coefficient increases with increasing feed rate; guidelines are given for the lower limit of feed rate below which film breakdown is likely to occur. Typical results are shown in Fig. 14, where the dramatic increase in heat transfer coefficient with the enhanced surface is evident. The data clearly indicate that the oil reduces the performance of the enhanced bundle.

The same behavior has been found for flooded horizontal tubes (e.g., Webb and McQuade, 1993). Flooded natural circulation, recirculation boilers (thermosyphon) reboilers may be of two types: vertical and horizontal (kettle reboilers). Enhanced tubes have been applied to both types; however, in the former, ID enhancement is used, while in the latter, OD enhancement is involved. The enhancement determines the vapor generation rate, which in turn, controls the circulation.

The behavior of vertical tubes in bundles can be studied with single tubes. Although many types of enhancement are possible, the main ones applied are sintered metallic matrix (Thome, 1990) and microfin tubes (Thome, 1996). Thome [1990] discusses the application of the former tubes, as a retrofit, indicating that the overall heat transfer coefficient was increased at least 80 percent.

The ID enhancement can be very effective because the reboilers usually are driven by condensing steam, and the in-tube fluid is typically a hydrocarbon with relatively low heat transfer coefficient. To get the circulation going, it is often necessary to "sparge" the flow. The artificial introduction of vapor thereby is equivalent to boiling at very low superheat, which is possible with enhanced tubes.

One of the issues with flooded horizontal evaporation is how well the single-tube tests describe the bundle performance. If the single-tube data were comparable to the bundle data, the more costly large-scale tests could be avoided. As shown in Fig. 15, the enhanced single-tube data are comparable to the bundle data (Yilmaz et al., 1981). However, the plain single-tube data are significantly to the right of the plain bundle data due to the convective boiling effect. The implication is that "convection-enhancing" surfaces will behave differently for the two geometries.

Enhanced horizontal flow-through bundles (usually used with refrigerants) with R-113 or R-11 were studied by Trewin et al. (1992). For a full bundle boiler, they found that the performance of the knurled enhanced tubes, or tubes coated with a sintered metallic matrix, could be predicted from the pool boiling results. This work was extended to mixtures of the two refrigerants. A model has been proposed to correlate/predict the data (Trewin et al., 1996), accounting for the degradation in boiling heat transfer coefficient (from that of R-113, when the more volatile R-11 is added).

Micro-Fin Tubes

Micro-fin tubes, circular tubes with numerous short intregal fins, are being widely used in air-conditioning and refrigeration, for both small and large units. The application of these enhanced tubes to vertical thermosyphon reboilers in the chemical process industry has been noted. The use of these tubes for pure conventional refrigerants (including oil effects) has been extensively discussed (e.g., Bergles, 1988). The current area of interest is alternate refrigerants.

Data for R-123 are reported by Kedzierski (1993), and tests of R-134a are described by Eckels et al. (1994a) (these being

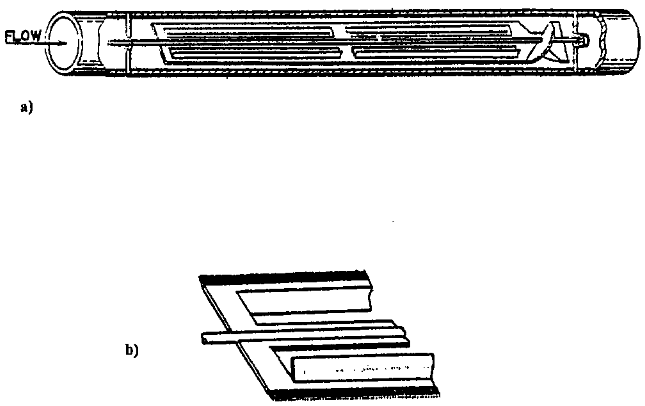

Fig. 10 (*a*) **Rotating element inserted in tube; (*b*) brushes attached to each edge of rotating element (Yeh, 1989).**

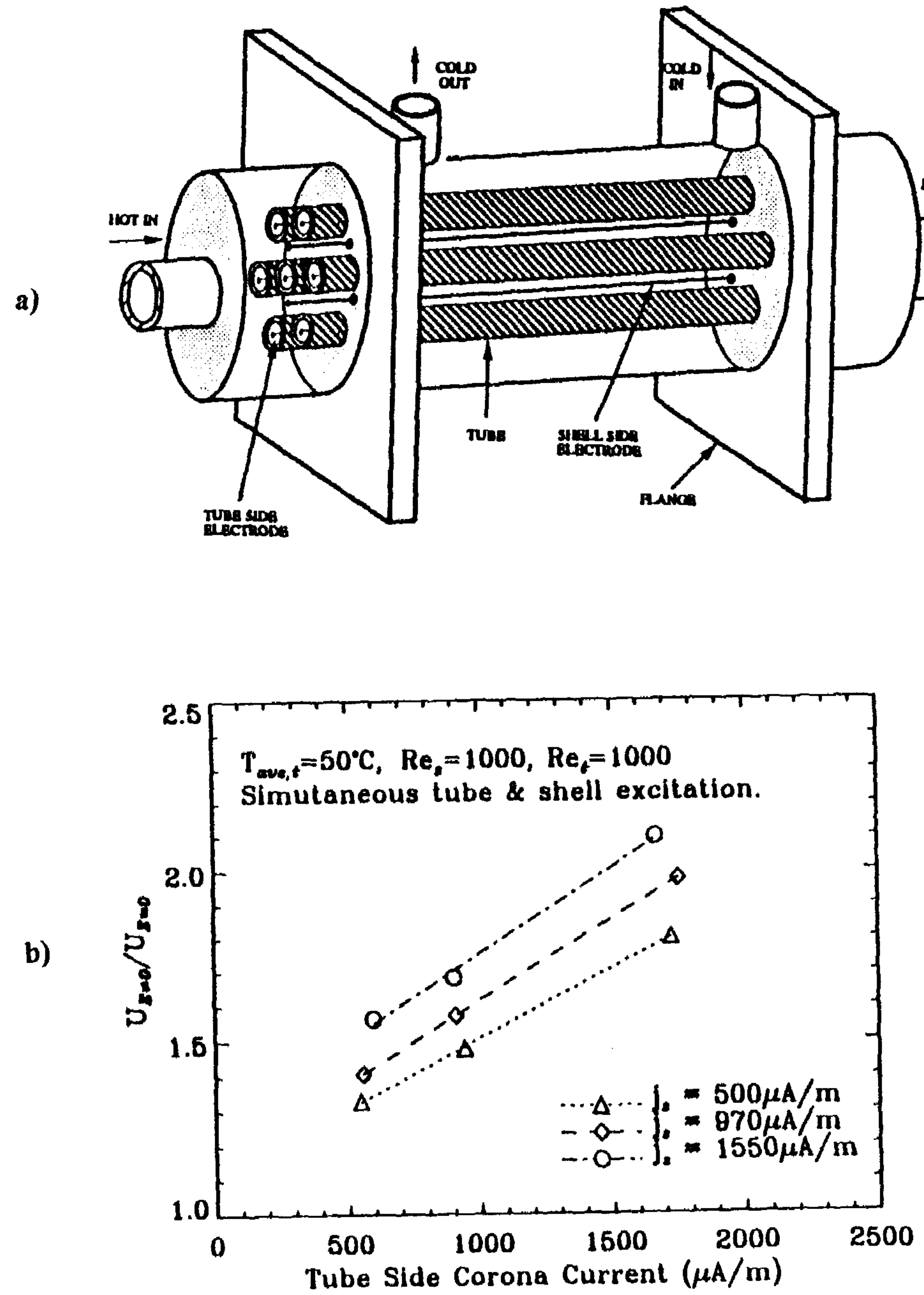

Fig. 11 (*a*) Schematic view of EHD-enhanced heat exchanger; (*b*) overall heat transfer coefficient improvement as a function of tube-side corona current (shell and tube excitation), Ohadi et al. (1994).

the generally accepted chlorine-free substitutes for R-11 and R-12, respectively). The general conclusion is that the enhancement is generally the same with the new refrigerants as for the traditional ones.

The oils are different with the new refrigerants, polyester or polyalkaline glycol, compared to mineral oil. One of the topics of much discussion is whether there is foaming with these new oils; of course, some of the old oil is still present in retrofit situations. The issue is not important for microfin tubes, as these tubes seem to inhibit foaming. With plain tubes the foaming, if it occurs, enhances heat transfer at several percent oil concentration. Recent work in our laboratory indicates that foaming does not occur in smooth tubes with R-134a and the recommended polyester oil. Since the replacement for R-22 is likely to be a mixture (e.g., Suva 9100: 50 weight percent R-32 and weight percent R-125; Anon, 1996) the behavior of micro-fin tubes with mixtures is important.

Vapor-Space Condensation

Condensation can be either filmwise or dropwise. In a sense, dropwise condensation is enhancement of the normally occurring film condensation by surface treatment. The only real application is for steam condensers because nonwetting coatings are not available for most other working fluids. Even after much study, little progress has been made in developing permanent hydrophobic coatings for practical steam condensers. The enhancement of dropwise condensation is pointless because the heat transfer-coefficients are already so high.

Surface extensions are widely employed for enhancement of condensation. The integral low fin tubing (Fig. 12) used for kettle boilers is also used for horizontal tube condensers. With proper spacing of the fins to provide adequate condensate drainage, the average coefficients can be several times those of a plain tube with the same base diameter. These fins are normally used with

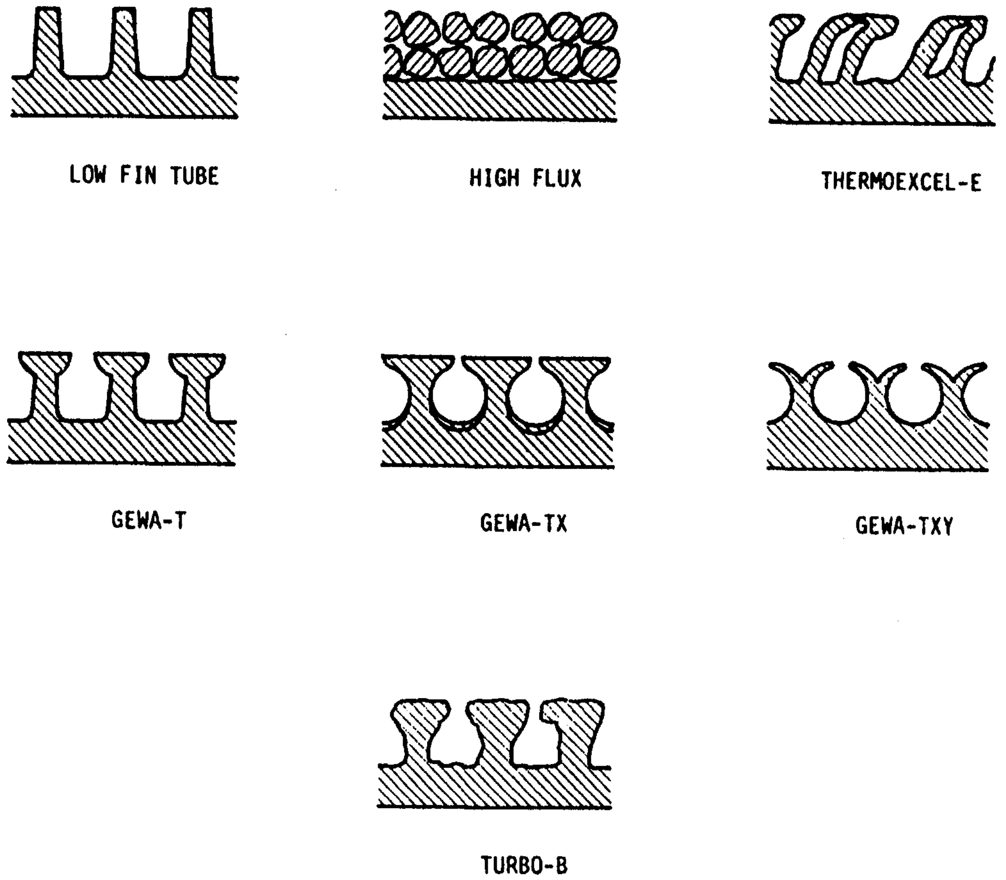

Fig. 12 Representative enhanced surfaces for shellside boiling (Pate et al., 1990)

refrigerants and other organic fluids that have low condensing coefficients, but which drain effectively because of low surface tension.

The fin profile can be altered according to mathematical analysis to take full advantage of the Gregorig effect, whereby, condensation occurs mainly at the tops of convex ridges. Surface-tension forces then pull the condensate into concave grooves where it runs off. The average heat transfer coefficient is greater than that for an axially uniform film thickness. The

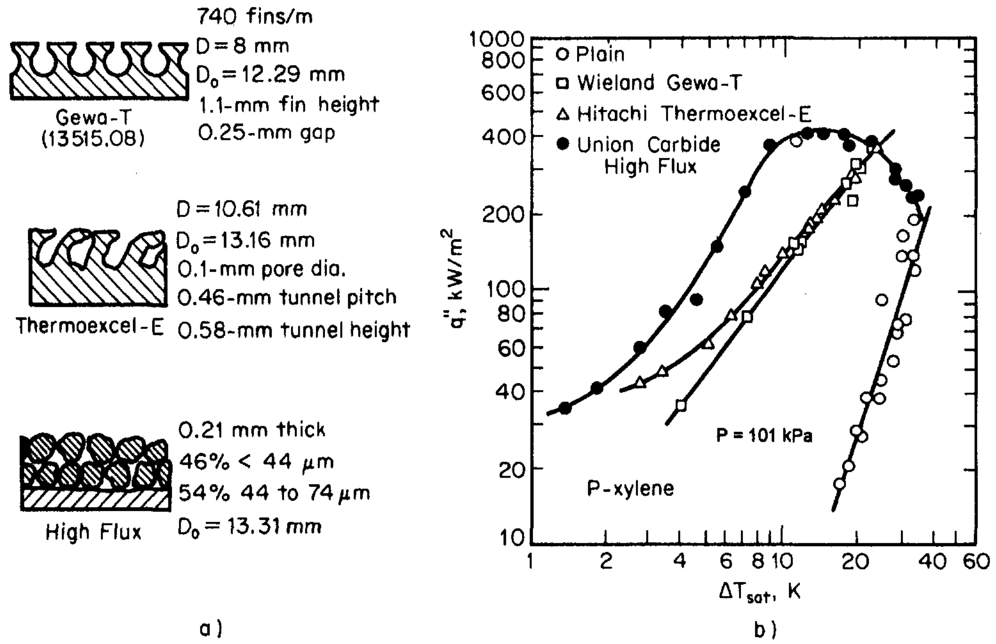

Fig. 13 Pool boiling from smooth and structured surfaces on the same apparatus: (*a*) sketch of cross sections of three enhanced heat transfer surfaces tested; (*b*) boiling curves for three enhanced tubes and smooth tube (Yilmaz et al., 1980).

Table 3 Representative Studies of Enhanced Boiling in Tube Bundles

Configuration	Pure Fluids	Pure Refrigerants Plus Oil	Pure Fluid Mixtures	Refrigerant Mixtures Plus Oil
Spray:				
horizontal	Moeykens et al. [1996]	Moeykens et al. [1996]		
vertical	Fagerholm et al. [1986]			
Flooded-Recirculation:				
horizontal	Yilmaz et al. [1981]	Memory et al. [1995a, 1995b]		
vertical	Thome [1990, 1996]	—		—
Flooded-Flow Through:				
horizontal	Trewin et al. [1992]		Trewin et al. [1996]	

initial application was for condensation of steam on vertical tubes used for reboilers and in desalination. According to numerical solutions, the optimum geometry is characterized by a sharp fin tip, gradually changing curvature of the fin surface from tip to root, wide grooves between fins to collect condensate, and periodic condensate strippers. Figure 16 schematically presents the configuration.

Recent interest has centered on three-dimensional surfaces for horizontal-tube condensers. The considerable improvement relative to low fins or other two-dimensional profiles is apparently due to multidimensional drainage at the fin tips. Other three-dimensional shapes include circular pin fins, square pins, and small metal particles that are bonded randomly to the surface.

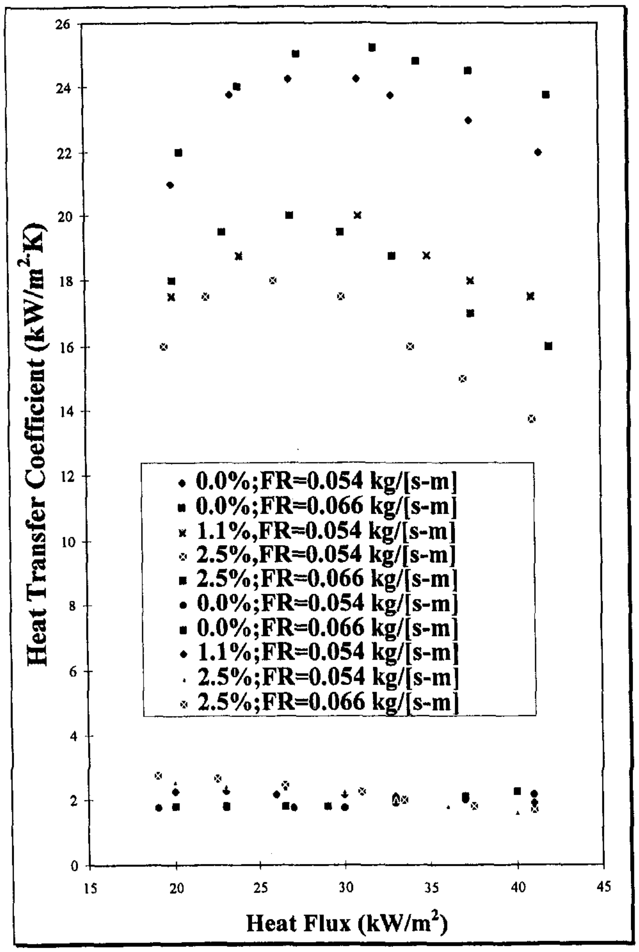

Fig. 14 Heat transfer results for R-123 boiling with spray films on a horizontal tube bundle. Oil percentages given and feed ratios specified (Moeykens et al., 1996).

Convective Condensation

This final section on enhancement of the various modes of heat transfer focuses on in-tube condensation. The applications include horizontal kettle-type reboilers, moisture separator reheaters for nuclear power plants, and air-conditioner condensers. It has been shown that internally grooved or knurled tubes, deep spirally fluted tubes, and random roughness, conventional inner-fin tubes are effective for condensation of steam and other fluids.

The micro-fin tubes mentioned earlier have also been applied successfully to in-tube condensing (Eckels et al., 1994b). As in the case of evaporation, the substantial heat transfer improvement is achieved at the expense of a lesser percentage increase in pressure drop. By testing a wide variety of tubes, it has been possible to suggest some guidelines for the geometry (e.g., more fins, longer fins, and sharper tips); however, general correlations are not yet available. Fortunately, for heat-pump operation, the tube that performs best for evaporation also performs best for condensation.

Twisted-tape inserts result in rather modest increases in the heat transfer coefficient for complete condensation of either steam or refrigerant. The pressure drop increases are large due to the large wetted surface. Coiled tubular condensers provide a modest improvement in average heat transfer coefficient.

Concluding Remarks

This review has given an overview of enhanced heat transfer technology, citing representative developments. The literature in enhanced heat transfer appears to be growing faster than that of the engineering-science literature as a whole. At least ten percent of the heat transfer literature is now directed toward enhancement.

An enormous amount of technology is available; what is needed is technology transfer. Many techniques, and variations thereof, have made the transition from the academic, or industrial research laboratory, to industrial practice. This development of enhancement technologies must be accelerated. In doing this, however, the "corporate memory" should be retained. The vast literature in the field should be pursued before starting expensive physical or numerical experiments. To facilitate this, bibliographic surveys, such as that of Bergles et al. (1995), should be continued.

Enhanced heat transfer will assume greater importance when energy prices rise again. With the current oil and gas "bubbles," there is little financial incentive to save energy. Usually, enhancement is now employed, not to save energy costs, but to save space. For example, process upgrading through the use of an enhanced heat exchanger that fits a given space is common (Ragi, 1995). It is expected that the field of enhanced heat transfer will experience another growth phase (refer to Fig. 1) when energy concerns are added to volume considerations.

Throughout this whole business, manufacturing methods and materials requirements may be overriding considerations. Can the enhancement be produced in the material that will survive

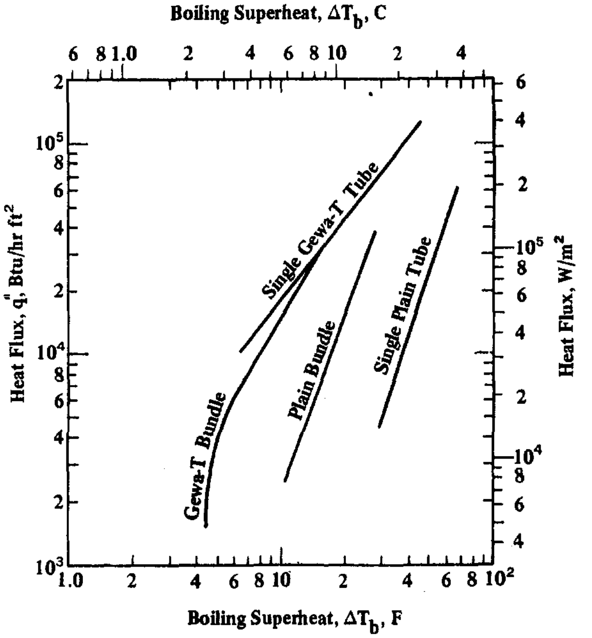

Fig. 15 Comparison of boiling curves for single horizontal tubes and bundles with and without enhancement; P-xylene at 103 kPa (Yilmaz et al., 1981).

any fouling and corrosion inherent in the environment? Much work needs to be done to define the fouling/corrosion characteristics of enhanced surfaces (Somerscales and Bergles, 1996). Particularly, "antifouling" surfaces need to be developed.

It should be noted that enhancement technology is still largely experimental, although great strides are being made in analytical/numerical descriptions of the various technologies (Webb, 1994). Accordingly, it is imperative that the craft of experimentation be kept viable. With the wholesale rush to "technology," laboratories everywhere are being decommissioned. Hands-on experiences in universities are being decreased or replaced by computer skills. Experimentation is still a vital art needed for direct resolution of transport phenomenon in complex enhanced geometries, as well as bench-marking of computer codes. As such, experimental skills should continue to be taught, and conventional laboratories should be maintained.

Finally, it is evident that heat transfer enhancement is well established and is used routinely in the power industry, process industry, and in HVAC. Many techniques are available for improvement of the various modes of heat transfer. Fundamental understanding of the transport mechanism is growing, but more importantly, design correlations are being established. Heat transfer enhancement has indeed become a second-generation heat transfer technology for encouraging or accommodating high heat fluxes, and is becoming widely used in industrial heat exchangers, particularly those that involve boiling. New journals (e.g., *Journal of Enhanced Heat Transfer* and *International Journal of Heating, Ventilating, Air-conditioning and Refrigerating Research*) feature this technology. What we want now is advanced enhancement or third-generation heat transfer technology. This is beginning to appear, as noted in Table 4. Max Jakob would indeed be proud of the way in which the field of enhanced heat transfer has developed.

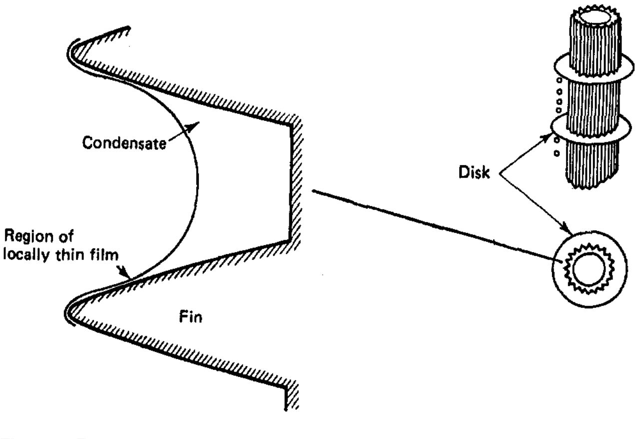

Fig. 16 Recommended flute profile and schematic of condensate strippers (Mori et al., 1981)

Table 4 The Generations of Heat Transfer Technology

Tube-and-Plate Fins, single-phase	
1st generation	bare tube
2nd generation	plain fins
3rd generation	longitudinal vortex generators on fins
In Channel, single-phase	
1st generation	smooth channel
2nd generation	2-D roughness
3rd generation	3-D roughness
Outside Tubes, boiling	
1st generation	smooth tube
2nd generation	2-D fins
3rd generation	3-D fins and metallic matrices
In-Tube, evaporation	
1st generation	smooth tube
2nd generation	massive fins and inserts
3rd generation	micro-fins
Outside Tubes, condensing	
1st generation	smooth tube
2nd generation	2-D fins
3rd generation	3-D fins and metallic matrices

References

Amon, C. H., 1993, "Spectral Element Fourier Method for Transitional Flows in Complex Geometries," *AIAA Journal*, Vol. 6, No. 1, pp. 42–48.

Anon, 1996, "A New Mix for 'SUVA'," *ASHRAE Journal*, July, p. 13.

Bejan, A., 1995, *Entropy Generation Minimization*, CRC Press, Boca Raton, FL.

Bergles, A. E., 1985, Techniques to Augment Heat Transfer, Chap. 3 in *Handbook of Heat Transfer Applications*, McGraw-Hill, New York, pp. 3-1, 3-80.

Bergles, A. E., 1988, "Some Perspectives on Enhanced Heat Transfer Second Generation Heat Transfer Technology," ASME JOURNAL OF HEAT TRANSFER, Vol. 110, pp. 1082–1096.

Bergles, A. E., 1996, "Heat Transfer Enhancement The Maturing of Second-Generation Heat Transfer Technology," Kern Award Lecture submitted to *Heat Transfer Engineering* for publication.

Bergles, A. E., Jensen, M. K., and Shome, B., 1995, "Bibliography on Enhancement of Convective Heat and Mass Transfer," Heat Transfer Laboratory Report HTL-23, Rensselaer Polytechnic Institute, Troy, NY. Introduction to appear in *Journal of Enhanced Heat Transfer*.

Bergles, A. E., and Kim, C. J., 1988, "A Method to Reduce Temperature Overshoots in Immersion Cooling of Electronic Devices," *Proceedings of the Inter Society Conference on Thermal Phenomena in the Fabrication and Operation of Electronic Components*, IEEE, New York, NY, pp. 100–105.

Chen, S. J., Lothavi, J., and Tseng, A. A., 1991, "Cooling of a Moving Plate with an Impinging Circular Water Jet," *Experimental Thermal and Fluid Science*, Vol. 4, pp. 343–353.

Ciofalo, M., and Collins, M. W., 1989, "Predictions of Heat Transfer for Turbulent Flow in Plane and Rib-Roughened Channels Using Large Eddy Simulation," *Proceedings of the Seventh National Congress on Heat Transfer*, Bologna, Italy, pp. 57–72.

Eason, R. M., Bayazitoglu, Y., and Miade, A., 1994, "Enhancement of Heat Transfer in Square Helical Ducts," *International Journal of Heat Mass Transfer*, Vol. 37, pp. 2077–2087.

Eckels, S. J., Doerr, T. M., and Pate, M. B., 1994a, "Heat Transfer and Pressure Drop of R-134a and Ester Lubricant Mixtures in a Smooth and a Micro-fin Tube: Part I-Evaporation" *ASHRAE Transactions*, Vol. 100, Part 2, pp. 265–281.

Eckels, S. J., Doerr, T. M., and Pate, M. G., 1994b, "In-Tube Heat Transfer and Pressure Drop of R-134a and Ester Lubricant Mixtures in a Smooth Tube and a Micro-Fin Tube: Part II-Condensation," *ASHRAE Transactions*, Vol. 100, Part 2, pp. 283–294.

Fagerholm, N. E., Kivoja, K., Ghazanfari, A. R., and Jarvinen, E., 1986, "Using Structured Surfaces to Enhance Heat Transfer in Falling Film Flow," Institute of Energy Engineering, Helsinki University of Technology, Helsinki, Finland, pp. 1–35.

Fiebig, M., 1996, "Vortices: Tools to Influence Heat Transfer. Recent Developments," *Proceedings of the 2nd European Thermal-Sciences and 14th UIT National Heat Transfer Conference*, Edizioni FTS, Pisa, Italy, Vol. 1, p. 41–56.

Fiebig, M., and Sanchez, M. A., 1992, "Enhancement of Heat Transfer and Pressure Loss by Winglet Vortex Generators in a Fin-Tube Element," *Compact Heat Exchangers for Power and Process Industries*, HTD-Vol. 201, ASME, New York, NY, pp. 7–14.

Fujii, M., Seshimo, Y., Veno, S., and Yamanaka, G., 1989, "Forced Air Heat Sink with New Enhanced Fins," *Heat Transfer-Japanese Research*, Vol. 18, No. 6, pp. 53–65.

Fukusako, S., Yamada, M., Kimoshita, K., and Kawake, H., 1991, "Boiling Heat Transfer in Liquid-Saturated Porous Bed," *Proceedings of the 1991 ASME-JSME Thermal Engineering Joint Conference*, Vol. 2, JSME, Tokyo, Japan and ASME, New York, NY, pp. 281–288.

Gau, C., and Lee, C. C., 1992, "Impingement Cooling Flow Structure and Heat Transfer Along Rib-Roughened Walls," *International Journal of Heat Mass Transfer*, Vol. 35, pp. 3009–3020.

Gentry, M. C., DeJong, N. C., and Jacobi, A. M., 1996, "Evaluating the Potential of Vortex-Enhanced Evaporator Performances for Refrigeration Applications," to be published in *ASHRAE Transactions*, Vol. 102.

Greiner, M., 1991, "An Experimental Investigation of Resonant Heat Transfer Enhancement in Grooved Channels," *International Journal of Heat and Mass Transfer*, Vol. 34, pp. 1383–1391.

Greiner, M., Ghaddar, N. K., Mikic, B. B., and Patera, A. T., 1986, "Resonant Convective Heat Transfer in Grooved Channels," *Heat Transfer 1986*, Proceedings of the Eighth International Heat Transfer Conference, Vol. 6, Hemisphere, Washington, D.C., pp. 2867–2872.

Hong, J. S., 1993, "The Study of Ultrasonic Enhancement in Phase-Change Process," ASME Paper No. 93-HT-2.

Inagaki, T., and Komori, K., 1993, "Experimental Study of Heat Transfer Enhancement in Turbulent Natural Convection Along a Vertical Flow Plate-Part 1: The Effect of Injection or Suction," *Heat Transfer Japanese Research*, Vol. 22, pp. 387–397.

Jacobi, A. M., and Shah, R. K., 1995, "Heat Transfer Surface Enhancement Through Use of Longitudinal Vortices: A Review of Recent Progress," *Experimental Thermal and Fluid Science*, Vol. 11, pp. 295–309.

Jakob, E., 1988, "Max Jakob, July 20, 1879-January 4, 1955, Fifty Years of His Work and Life," *History of Heat Transfer*, ASME, New York, NY, pp. 87–116.

Jakob, M., 1936, "Heat Transfer in Evaporation and Condensation–1 and 2," *Mechanical Engineering*, Vol. 58, pp. 643–660, 729–739.

Jakob, M., and Fritz, W., 1931, "Versuche Über den Verdampfungsvorgang," *Forschung auf dem Gebiete des Ingenieurwesens*, Vol. 2, pp. 435–437.

Jakob, M., and Hawkins, G. A., 1957, *Elements of Heat Transfer*, 3rd Edition, Wiley, New York, NY.

Kays, W. C., and London, A. L., 1984, *Compact Heat Exchangers*, 3rd Ed., McGraw Hill, New York.

Kedzierski, M. A., 1993, "Simultaneous Visual and Calorimetric Measurements of R-11, R-123, and R-123 Alkybenzene Nucleate Flow Boiling," *Heat Transfer with Alternate Refrigerants*, HTD-Vol. 243, ASME, New York, NY, pp. 27–33.

Lee, J. H., and Singh, R. K., 1990, "Mathematical Models of Scraped Surface Heat Exchangers in Relation to Food Sterilization," *Chemical Engineering Communications*, Vol. 87, pp. 21–52.

Manglik, R. M., and Bergles, A. E., 1993a, "Heat Transfer and Pressure Drop Correlation for Twisted-Tape Inserts in Isothermal Tubes: Part I, Laminar Flows," ASME Journal of Heat Transfer, Vol. 115, pp. 881–889.

Manglik, R. M., and Bergles, A. E., 1993b, "Heat Transfer and Pressure Drop Correlation for Twisted-Tape Inserts in Isothermal Tubes: Part II, Transition and Turbulent Flows," ASME Journal of Heat Transfer, Vol. 115, pp. 890–896.

Manglik, R. M., and Bergles, A. E., 1995, "Heat Transfer and Pressure Drop Correlations for the Rectangular Offset Strip Fin Compact Heat Exchanger," *Experimental Thermal and Fluid Science*, Vol. 10, pp. 171–180.

McGillis, W. R., and Carey, V. P., 1996, "On the Role of Marangoni Effects on the Critical Heat Flux for Pool Boiling of Binary Mixtures," ASME Journal of Heat Transfer, Vol. 118, pp. 103–109.

Memory, S. B., Sagiyama, D. C., and Marto, P. J., 1995a, "Nucleate Pool Boiling of R-114 and R-114-Oil Mixtures from Smooth and Enhanced Surfaces-I Single Tubes," *International Journal of Heat Mass Transfer*, Vol. 38, pp. 1347–1361.

Memory, S. B., Akcasayar, N., Eraydin, H., and Marto, P. J., 1995b, "Nucleate Pool Boiling of R-114 and R-114-Oil Mixtures from Smooth and Enhanced Surfaces-II Tube Bundles," *International Journal of Heat Mass Transfer*, Vol. 38, pp. 1363–1376.

Moeykens, S. A., Kelly, J. E., and Pate, M. B., 1996, "Spray Evaporation Heat Transfer Performance of R-123 in Tube Bundles," to be published in *ASHRAE Transactions*, Vol. 102, Part 2.

Mori, Y., Hijikata, K., Hirasawa, S., and Nakayama, W., 1981, "Optimized Performance of Condensers with Outside Condensing Surfaces," ASME Journal of Heat Transfer, Vol. 103, pp. 96–102.

O'Connor, J. P., and You, S. M., 1995, "A Painting Technique to Enhance Pool Boiling Heat Transfer in Saturated FC-72, ASME Journal of Heat Transfer, Vol. 117, pp. 387–393.

Ohadi, M. M., Li, S. S., and Dessiatoun, S., 1994, "Electrostatic Heat Transfer Enhancement in a Tube Bundle Gas-to-Gas Heat Exchanger," *Journal of Enhanced Heat Transfer*, Vol. 1, pp. 327–335.

Ohadi, M. M., Nelson, D. A., and Zia, S., 1991, "Heat Transfer Enhancement of Laminar and Turbulent Pipe Flow Via Corona Discharge," *International Journal of Heat Mass Transfer*, Vol. 34, pp. 1175–1187.

Pate, M. B., Ayub, Z. H., and Kohler, J., 1990, "Heat Exchangers for the Air-Conditioning and Refrigeration Industry: State-of-the-Art Design and Technology, *Compact Heat Exchangers*, Hemisphere, New York, NY, pp. 567–590.

Ragi, E. G., 1995, Praxair Corp., Tonawanda, NY, personal communication, Nov. 6.

Somerscales, E. F. C., and Bergles, A. E., 1996, "Enhancement of Heat Transfer and Fouling Mitigation," to be published in *Advances in Heat Transfer*.

Soria, J., and Norton, M. P., 1991, "The Effect of Transverse Plate Vibration on the Mean Laminar Convective Boundary Layer Heat Transfer Rate," *Experimental Thermal and Fluid Science*, Vol. 4, pp. 226–238.

Thome, J. R., 1990, *Enhanced Boiling Heat Transfer*, Hemisphere, New York, NY.

Thome, J. R., 1996, "Heat Transfer Augmentation of Shell-and-Tube Heat Exchangers for the Chemical Process Industry," *Proceedings of the 2nd European Thermal-Sciences and 14th UIT National Heat Transfer Conference*, Edizioni ETS, Pisa, Italy, Vol. 1, pp. 15–26.

Trewin, R. R., Jensen, M. K., and Bergles, A. E., 1992, "Crossflow Boiling in Enhanced Tube Bundles," *Two-Phase Flow in Energy Systems*, HTD-Vol. 220, ASME, New York, NY, pp. 11–17.

Trewin, R. R., Jensen, M. K., and Bergles, A. E., 1996, "Phenomenological Model of Pool Boiling from Enhanced Surfaces in Binary Mixtures," presented at special symposium in connection with ASME International Mechanical Engineering Congress and Exposition, Atlanta, GA, November 1996.

Wang, G. W., Liang, H. S., Yang, W. J., and Vrable, D., 1996, "Nucleate Pool Boiling on Micro Graphite-Copper Composite Surfaces," in press.

Webb, R. L., 1994, "Advances in Modeling Enhanced Heat Transfer Surfaces," *Proceedings of the Tenth International Heat Transfer Conference*, Institution of Chemical Engineers, Rugby, England, Vol. 1, pp. 445–459.

Webb, R. L., and Bergles, A. E., 1983, "Heat Transfer Enhancement: Second Generation Technology, *Mechanical Engineering*, Vol. 115, No. 6, pp. 60–67.

Webb, R. L., and McQuade, W. F., 1993, "Pool Boiling of R-11 and R-123 Oil-Refrigerant Mixtures on Plain and Enhanced Tube Geometries," *ASHRAE Transactions*, Vol. 99, Part 1, pp. 1225–1236.

Yeh, H.-C., 1989, "Device for Producing High Heat Transfer in Heat Exchanger Tubes," U.S. Patent 4,832,114, May 23.

Yilmaz, S., Hwalck, J. J., and Westwater, J. N., 1980, "Pool Boiling Heat Transfer Performance for Commercial Enhanced Tube Surfaces," ASME Paper No. 80-HT-41.

Yilmaz, S., Palen, J. W., and Taborek, J., 1981, "Enhanced Boiling Surfaces as Single Tubes and Tube Bundles," *Advances in Enhanced Heat Transfer 1981*, HTD-Vol. 18, ASME, New York, pp. 123–129.

C. Camci
Pennsylvania State University,
Department of Aerospace Engineering,
Turbomachinery Heat Transfer Laboratory,
153-E Hammond Building,
University Park, PA 16802
Mem.

B. Glezer
Head of Heat Transfer and
Turbine Cooling Design
Solar Turbines Inc.,
2200 Pacific Highway,
San Diego, CA 92101
Mem.

Liquid Crystal Thermography on the Fluid Solid Interface of Rotating Systems

Liquid crystal thermography is an effective method widely employed in transient and steady-state heat transfer experiments with excellent spatial resolution and good accuracy. Most of the past studies in liquid crystal thermography deal with stationary conditions. The present investigation deals with the influence of rotation on the color response of encapsulated liquid crystals attached to a flat rotating surface. A general methodology developed for the application of thermochromic liquid crystals in rotating systems is described for the first time. The investigation is performed for a rotational speed range from 0 to 7500 rpm using two different coatings displaying red at 30° and 45°C, under stationary conditions. Local liquid crystal color on the surface of a rotating disk is correlated with local temperature as measured by a non-intrusive infrared sensor at various rotational speeds. An immediate observation from the present study is that the color response (hue) of encapsulated liquid crystals is not altered by either the centrifugal acceleration of the rotating environment or the aerodynamic friction force at the rotating disk-air interface. Present investigation also shows that when a stroboscope light is introduced, the color response is not significantly altered due to additional periodic illumination. A complete and general experimental methodology including rotating surfaces with non-axisymmetric temperature distribution is presented. Results from the current liquid crystal technique agree well with the theoretical adiabatic temperature rise of a free rotating disk as predicted by an analytical method.

1.0 Introduction

Liquid crystal temperature indicators are widely used in convection heat transfer studies due to their excellent spatial resolution and accuracy. The heat transfer characteristics of liquid crystal coated rotating surfaces can be easily observed from a stationary frame of reference. Temperature/heat transfer measurement techniques based on the calibration of liquid crystal hue in function of local temperature have been developed in the past, Kim (1991), Camci et al. (1992), Camci et al. (1993), Wiedner and Camci (1993a,b), Wilson et al. (1993), Farina et al. (1994), Rizzo and Camci (1994). When the liquid crystal coated heat transfer surface is illuminated by white light, a selective reflection of a specific wavelength occurs in the helical structure of the liquid crystal. This can be explained by the "interference of light reflected from the helical layers so that the optical wavelength in the material actually equals the helical pitch," Jones et al. (1992), Collings (1990), Parsley (1987), de Gennes (1974). The pitch of the crystal helix is very sensitive to temperature, and hence, the selectively reflected color may be used to indicate temperature. Most of the past work in liquid crystal thermography is reported under stationary conditions. There are a limited number of measurements obtained from the rotating frame of thermal systems, mainly for rotating machinery applications. However, a quantitative investigation of hue response to temperature in the rotating environment does not exist.

Although the present study deals with encapsulated forms of liquid crystals that are temperature-sensitive/shear-stress-insensitive, there are many neat liquid crystal coatings that respond to both mechanical shear and temperature, Van Zante and Okiishi (1991), Bonnett et al. (1989). Shear sensitive crystals need direct exposure to their environment so they are always manufactured in the neat/unencapsulated form. In early studies dealing with shear sensitive crystals, the major problem was the difficulty in separating temperature effects and shear effects, Klein (1968), Klein and Margozzi (1969), Holmes and Obara (1987), Holmes (1986, 1987). Advances in liquid crystal formulations made since the late 60's allows the researcher to use shear sensitive crystals that have almost no sensitivity to temperature changes, Reda (1991, 1995a,b). During the manufacturing of thermochromic liquid crystals, microscopic droplets of liquid crystals can be enclosed in a polymer shell to reduce the shear sensitivity of the coating. Micro-encapsulation allows liquid crystals to respond with bright colors to only temperature, while having protection from the degrading effects of Oxygen and ultraviolet light, Cartmell (1993).

One of the first studies using liquid crystal temperature indicators in the rotating frame of reference is described in Metzger et al. (1991). In this study a disk rotating at speeds up to 10,000 rpm is sprayed directly by encapsulated liquid crystals. Although this study contains extremely detailed Nusselt number distributions with jet impingement onto a plane smooth disk, it is assumed that the rotation does not influence the color response of the liquid crystals. The centrifugal acceleration at the outer diameter of this disk (111,162 m/s^2) is close to the maximum value achieved in the present experiments, (89,968 m/s^2). These two centrifugal acceleration values fall into the same range as defined by actual rotating disk configurations used in gas turbines.

An experimental heat transfer investigation in a spanwise rotating channel with two opposite rib-roughened walls is reported by Taslim et al. (1991). Encapsulated liquid crystal coated polyester sheets are photographed in a rotating coolant passage. The absolute level of the maximum centrifugal acceleration is only about 392 m/s^2 which may be considered extremely low compared to the present study.

A mixture of 8 liquid crystal slurries, each having a 1°C color bandwidth has been used in a steady state heat transfer

---

Contributed by the Heat Transfer Division for publication in the Journal of Heat Transfer. Manuscript received by the Heat Transfer Division February 20, 1996; revision received August 29, 1996; Keywords: Forced Convection, Measurement Techniques, Rotating Flows. Associate Technical Editor: T. Bergman.

experiment performed in a large scale turbine rig by Blair et al. (1991). This paper contains the results of the first investigation claiming that there is a temperature measurement bias in liquid crystal thermography when encapsulated crystals are implemented in a rotational environment. It is reported that there is a +2°C temperature shift at 400 rpm when compared to stationary calibration of the liquid crystal. They attribute this deterministic rotational speed dependent shift to a combination of mechanical and aerodynamic stresses present in the liquid crystal/black paint coating, and mention its correction.

Another application of liquid crystal thermography in a rotating coolant passage is presented by Blair et al. (1991). They report a +3 to +4°C difference between the liquid crystal measurement and the thin foil thermocouple measurement at 525 rpm, in a rotor cooling channel attached to a rotating arm. The centrifugal acceleration experienced in this experiment (2768 m/s^2) can be considered as medium level. Blair et al. (1991) conclude that a more complete analysis of this phenomenon is necessary to permit the full implementation of liquid crystal thermography in the rotating frame.

Wilson et al. (1993) describe the recent efforts made in the use of an image processing based liquid crystal technique in rotating disk systems representing those found in gas turbine engines, without any information on the influence of rotation.

The current study has been initiated to address serious concerns about the accuracy of thermographic liquid crystal color calibrations in the rotating environment, Glezer (1992). The main objective of the present investigation is to quantify the influence of the strong centrifugal acceleration field and aerodynamic shear stress on the color calibration of encapsulated liquid crystals under rotation.

2.0 Apparatus and Experimental Procedures

2.1 Rotating Disk. The aluminum disk ($\rho_{Al} = 2707$ kg/m^3) has an outer diameter of $D = 0.3048$ m with a uniform axial thickness of $\delta_{Al} = 0.3175$ cm, Fig. 1(*a*). The disk rim is directly connected to an AC electric motor (115 V, 60 Hz) via an aluminum flange. The rotational speed of the disk is controlled between 0 and 7500 rpm in a steel protective cover. The thermocouple lead out wires are passed through a hollow flange and a flexible coupling that is connected to the rotor of the mercury slip-ring device. Although the setup initially included the slip-ring device for rotating thermocouple measurements, the current study uses a non-intrusive infrared point-sensor as local temperature reference. Figure 1(*b*) shows the disk geometry and typical forces acting on the disk surface.

2.2 Liquid Crystal Coating and Hue Capturing. The rotating disk has been coated with black paint and subsequently with an encapsulated liquid crystal material having a narrow color bandwidth of 1°C. Two different liquid crystals with different temperature color play zones are evaluated individually. The first coat R30C1W, manufactured by Hallcrest Inc., was sprayed in a 50 percent slurry and 50 percent distilled water mixture (volumetric), using an air brush after the application of an extremely thin black paint on the aluminum disk surface. The resulting approximate thickness of the black paint/liquid crystal layer is about 35–45 μm. After the completion of the tests with this crystal, R45C1W have been subsequently evaluated. The hue determination via a color image processing system at a reference point on the rotating disk is made simultaneously with the actual temperature measurement from the non-intrusive infrared point-sensor. The infrared sensor is positioned in the stationary frame. The temperature output from the infrared sensor is displayed in the video image containing the liquid crystal colors and continuously recorded on a video tape. The hardware which includes the 24 bit color image processor, the video decoder/encoder with an array processor to accelerate image intensive operations and the color model based on Hue, Saturation, and Intensity attributes is discussed in detail in Camci et al. (1992, 1993). The hue versus temperature calibrations are repeated at ten selected rotational speeds between 0 and 7500 rpm.

2.3 Infrared Point-Sensor. The current study uses an infrared point-sensor for non-intrusive local temperature measurements on the flat surface of the rotating disk. The infrared measurements, from a circular spot having a diameter of 2.54 mm, are used to construct hue versus temperature curves of the liquid crystal coating. The specific infrared sensor (Raytek/Thermalert/ET3LT) consists of a thin film thermopile detector along with a spectral filter. A lens system designed to transmit infrared energy is used to focus the energy onto the detector. Stray radiation from sources both inside and outside the sensor is eliminated using special baffling techniques. The output from the IR detector and an ambient temperature sensor are summed and then digitized to a 12 bit level. After linearization the 12 bit signal is fed into a digital-to-analog converter, followed by a sample and hold circuit and an output amplifier.

Figure 2 describes the orientation of the infrared point-sensor with respect to the reference calibration plate. The sensor head is required to be located at 76.2 mm (three inches) normal to the measurement surface. The spectral response of the infrared sensor is between 8 to 14 microns. This character makes

Nomenclature

b, D = disk outer diameter
C = specific heat of air
ds = differential circumferential distance = $r \cdot d\theta$
dr = differential radial length
IR = infrared
k = thermal conductivity
r = local radius on the disk surface
rpm = rotations per minute
R = disk outer radius, D/2
Re = Reynolds number = $\Omega \cdot r^2/\nu$
R30C1W = encapsulated thermochromic liquid crystal displaying red at 30°C under stationary conditions, color bandwidth is 1°C
Re = Reynolds number
T = temperature
TC = thermocouple
V = flow velocity
z = coordinate direction normal to the disk
θ = circumferential position, (positive in counter clockwise direction)
δ = shear layer thickness of disk boundary layer
φ = angle between aerodynamic shear stress and tangential direction
ρ = density
ν = kinematic viscosity = μ/ρ
σ = mechanical stress in solid material
τ = shear stress
λ = wavelength of the light selectively reflected from the liquid crystal surface
μ = absolute viscosity
Ω = angular speed

Subscripts

aw = adiabatic wall
Al = Aluminum
c = centrifugal
lc = liquid crystal
o = aerodynamic wall friction related
p = at constant pressure
tc = thermocouple
x, y, z = Cartesian coordinates
∞ = ambient quantity
θ, z = circumferential component at a given z position
r, z = radial component at a given z position

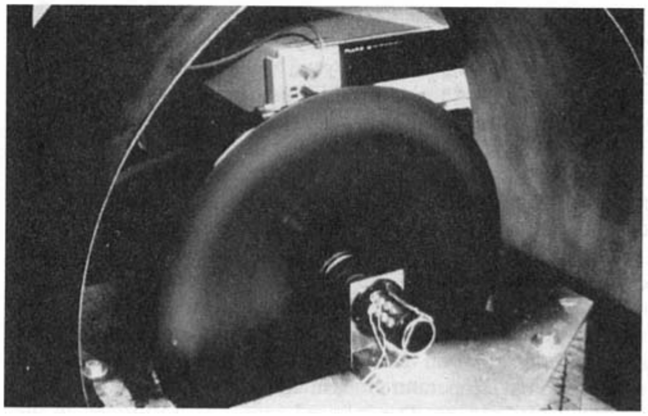

Fig. 1a Experimental setup: rotating disk assembly

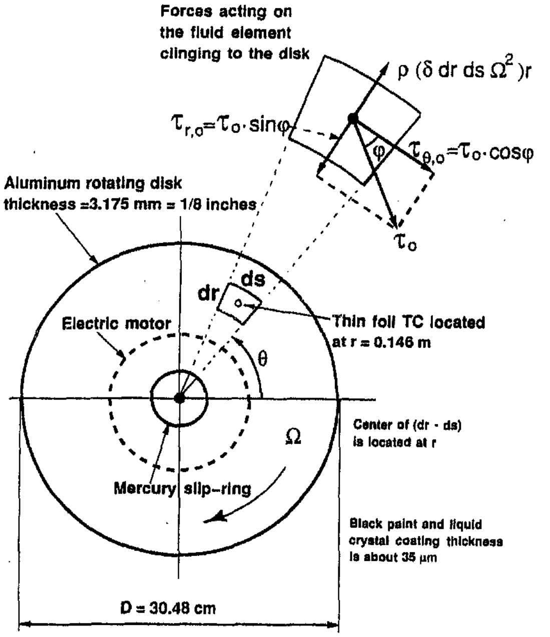

Fig. 1b Experimental setup: rotating disk geometry and forces near the disk surface

this sensor insensitive to the visible illumination used for liquid crystal hue determination. The plate has been illuminated by a 250 W incandescent light source located at a 1.5 m separation distance from the measurement spot. The light source has been oriented at 45 deg angle measured from the plane of the disk. Possible infrared emissions from incandescent bulbs have been filtered out in front of the light source. The emissivity of the liquid crystal covered surface has been determined using a calibrated thin foil thermocouple of K type. The thermocouple, as shown in Figure 2, is mounted in the black paint layer of the aluminum calibration plate that is identical to the rotating disk material. Although the current experimental procedure does not require an exact knowledge of the emissivity of the surface coated with liquid crystals, the emissivity has been determined ($\epsilon = 0.96$) using the calibrated thin foil thermocouple.

3.0 Experimental Results and Discussion

3.1 Experimental Strategy. The current strategy is based on constructing a non-intrusive measurement scheme in order to quantify the changes in the color response of the liquid crystal coating on a rotating disk surface. A thin foil thermocouple with an approximate thickness of 13 μm is imbedded in the surface coating before the liquid crystal layer is sprayed on the calibration plate, Fig. 2. The size of the reference spot containing the thermocouple is about 2.54 mm. A non-intrusive measurement scheme can be constructed by performing simultaneous temperature measurements on the calibration plate using liquid crystals, an infrared point sensor, and a thin foil thermocouple. The process described in this section provides the quantitative baseline calibrations for both the liquid crystal layer and the infrared sensor.

The reference plate is first heated up slowly to 60°C without causing damage to the black paint and the crystal layer. As soon as the heat gun is removed from the reference spot, a slow transient at an approximate cooling rate of 0.1°C/minute is generated. During the transient, a color video camera records the liquid crystal color image, the voltage output of the infrared sensor that is focussed on the reference spot, and the voltage output from the thin foil thermocouple that is imbedded in the reference spot location. Due to the extremely small thickness of the thermocouple junction and the crystal layer, and the large time scale of the thermal transient generated, one can reasonably assume that the local temperature, measured by the thin-foil thermocouple, is the same as the infrared sensor and the liquid crystal based temperature measurements.

Figure 3 provides the relationship between the local liquid crystal color (hue) and the local thermocouple based temperature measurement (T_{tc}) on the calibration plate. The linear portion of the hue versus temperature curve and the linear regression line fitted to measured data is given for the crystal designated as R30C1W. The hue versus temperature curve is highly repeatable on the stationary calibration plate as shown in Fig. 3. Different symbols show individual hue versus temperature curves from different cooling transients. It should be noticed that color data (hue) can only be recorded when the reference spot temperature is around 30°C because of the narrow band character of the liquid crystals selected.

Figure 4 shows the voltage output (V_{IR}) of the infrared point sensor plotted against the local thermocouple based measurement (T_{tc}) from the thin foil sensor on the reference calibration plate. The data presented in Figs. 3 and 4 are simultaneously obtained from the slow cooling transient described in the previous paragraph. The linear relationship shown in Fig. 4 is an accurate calibration of the infrared point sensor against a reference thermocouple, including the emissivity influence of the liquid crystal coated surface. Figure 4 provides data over the complete cooling transient because an infrared sensor output is continuously available during the complete transient. The plus signs clustered around 30°C (within ±0.5°C) show the high resolution data obtained during the appearance of the meaningful liquid crystal colors. In order to correlate liquid crystal color (hue) with another non-intrusively obtained temperature measure (V_{IR}), a cross plot of the information provided in Figs. 3 and 4 is presented in Fig. 5. This approach provides the possibility of using two independent non-intrusive temperature measurement techniques simultaneously. This style is very effective for the measurements to be performed in the rotating frame of reference in rotating thermal systems. For example, a locally obtained

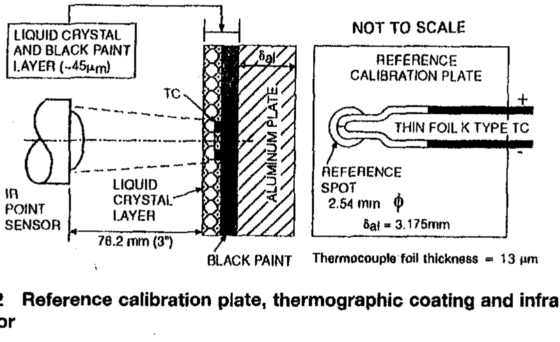

Fig. 2 Reference calibration plate, thermographic coating and infrared sensor

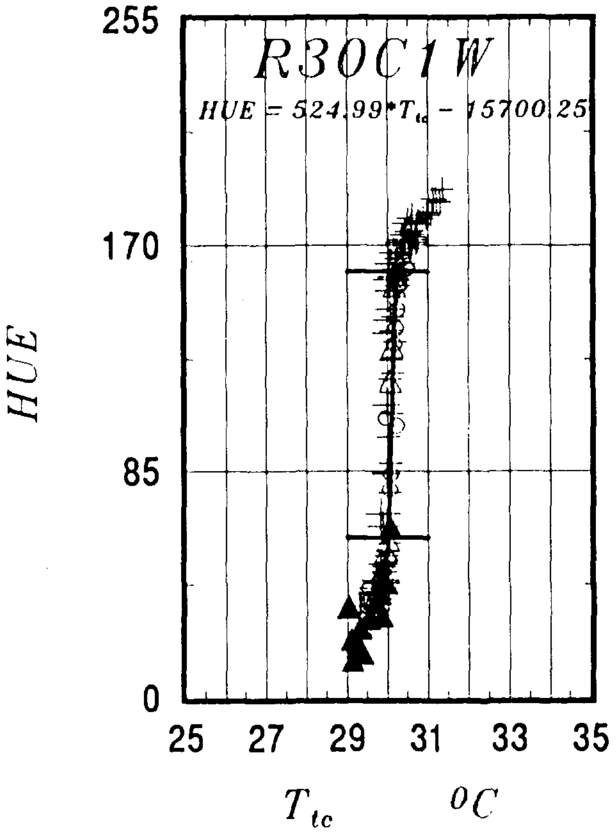

Fig. 3 Baseline calibration on the reference calibration plate, liquid crystal hue versus temperature measured by the thermocouple

liquid crystal hue can be quantified by using the infrared temperature measured at the same spot. In the present approach, the implementation of thermocouples, a slip-ring or telemetry, in the rotating frame is completely eliminated. Installation of thermocouples underneath a liquid crystal layer with a finite thickness becomes a significant error source in high speed rotating machinery applications. It is the authors' experience that thermocouple measurement errors in a rotating system, when combined with slip-ring related signal shifts, may become very significant. This is especially true at high rotational speeds where high local heat flux values on rotating surfaces may create large temperature differentials between the liquid crystal layer and the thermocouple location underneath the coating. This temperature bias may be amplified by other thermal boundary conditions existing near the reference thermocouple. Most of these adverse effects may accumulate as rotational speed dependent temperature bias errors. Since non-negligible bias errors have been observed during the initial phase of this investigation, the authors eliminated the use of a reference thermocouple sensor on the rotating disk surface in favor of an infrared temperature measurement system located in the stationary frame.

3.2 Implementation of Infrared Point-Sensor Measurements in the Rotating Frame. Although the liquid crystal calibration technique described in the previous paragraph shows excellent repeatability and good accuracy on the stationary calibration plate, its implementation on the rotating disk surface requires careful validation. Figure 5 shows hue versus infrared temperature results from four individual cooling transients obtained on the rotating disk surface in addition to calibration plate results. The rotating disk as shown in Fig. 1 is coated with an identical black paint/liquid crystal layer. The hue versus infrared temperature relationship obtained on the non-rotating disk surface is compared with that of the stationary calibration plate. The data from the disk surface, at 0 rpm, and the calibration plate show excellent agreement within the experimental uncertainty of hue capturing process and infrared measurement technique. This observation results in the conclusion that a nonintrusive liquid crystal technique and an infrared temperature measurement technique could be successfully used in a rotating frame of reference. However, an individual calibration of the infrared sensor and liquid crystal thermo-indicator on an equivalent stationary calibration plate as described in Fig. 2 is essential. The process described in this paragraph eliminates the need for a reference thermocouple sensor on the rotating disk surface.

Current temperature measurements using the infrared sensor are capable of generating one measurement every 80 milliseconds. During the experiments performed between 0 and 7500 rpm, the rotating disk is carefully heated at the disk centerline before a cooling transient. A heated impinging jet of air issued from a heat gun is the heating source for the rotating disk. The qualitative isothermal line visualization using liquid crystals shows that the isotherms on the disk surface are perfect circular lines, especially when the disk is cooled by forced convection due to the rotation. There are almost no temperature gradients in the circumferential direction in this axisymmetric free disk problem. The circumferential uniformity of the temperature profile is also checked by freezing the image by using a stroboscope light source. This feature makes the infrared point-sensor an ideal instrument for time averaged temperature measurements in the rotating frame. At 5000 rpm, an infrared spot located at 0.135 m is expected to time average the infrared emissions (from the 2.54 mm spot) over 6 rotations of the disk. The time response of the video image processing system collecting the liquid crystal color data is about 30 frames/second. Therefore, it is expected that liquid crystal data will be averaged over 2.7 rotations of the disk by the image processor. During the nonintrusive measurements, it is assumed that the emissivity of the liquid crystal/black paint layer does not change with rotational speed. It is a known fact that emissivity of an almost black

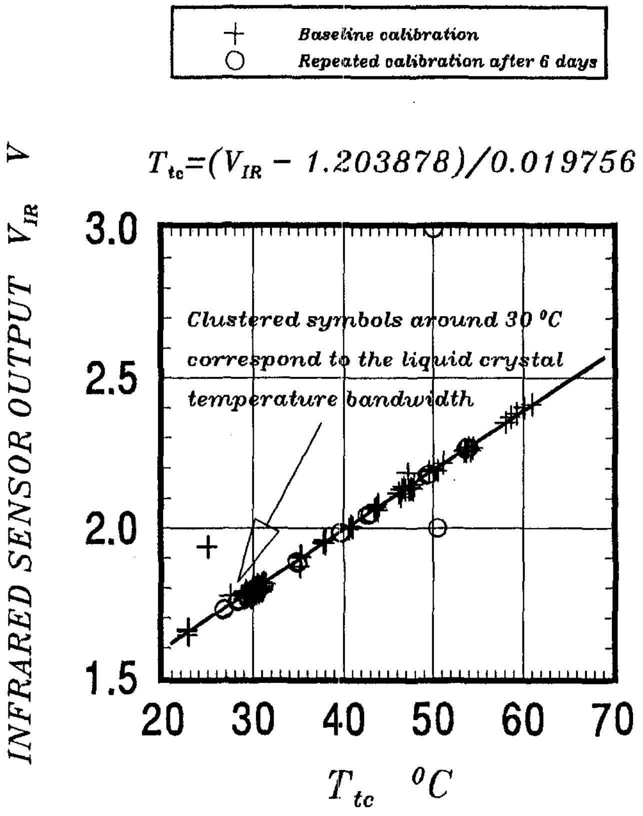

Fig. 4 Infrared sensor calibration using the reference thermocouple on the calibration plate

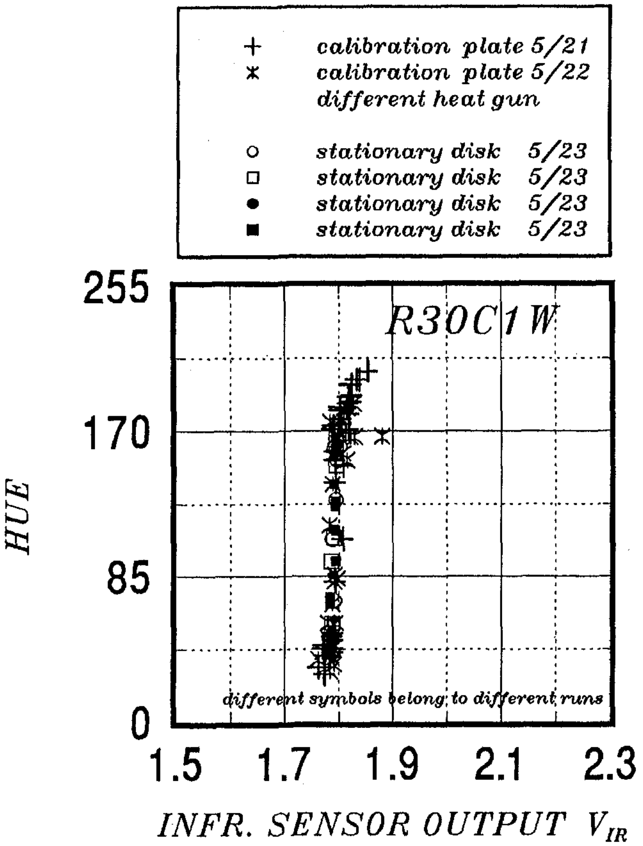

Fig. 5 Comparison of reference calibration plate and stationary disk hue calibrations using the infrared point sensor

surface is not influenced from how it moves with respect to a stationary reference frame. The emissivity is a strict function of the type of the surface material and its specific texture.

The non-intrusive infrared sensor described in the previous paragraph has been used to obtain temperature data in adiabatic disk experiments. The shear layer thickness at 7500 rpm has been estimated as 4.5 mm at the infrared sensor spot location (r = 0.135 m). Thicker shear layer thickness is predicted for lower rotational speeds. Since a wide rotational speed range is used in this experiment, it is important to document the status of the shear layer at the measurement location. Figure 6 shows the correlation for the prediction of the onset of transition and fully turbulent shear layer over the disk, Kobayashi et al. (1980). The correlation indicates that the disk boundary layer will always be fully turbulent when the rotational speed is over 2500 rpm at the spot location. In order to compare the infrared sensor measurements with existing analytical models, the surface temperature rise on an adiabatic disk is plotted against the rotational speed as shown in Fig. 7. Excellent agreement between the theory given by Owen (1971) and Chew (1985) and infrared point-sensor measurements above 2500 rpm is presented in Fig. 7. The infrared measurements on the present disk are underpredicted by the theory below 2500 rpm. This may be attributed to the fact that flow is expected to be transitional or laminar below 2500 rpm on a free disk at r = 0.135 m. The current non-intrusive infrared technique is in very good agreement with existing analytical models of temperature rise on an adiabatic disk in the fully turbulent flow zone.

3.3 Evaluation of Mechanical and Thermal Effects Influencing the Liquid Crystal Layer. There are three factors which could influence the liquid crystal color response under rotation: (1) the disk mechanical stresses associated with elastic deformations imposed by the rotation of the disk (the liquid crystal layer sprayed on the surface of the metallic disk may sense the stresses in the metallic disk as a surface force at the interaction surface); (2) aerodynamic friction forces on the flow side of the liquid crystal layer due to the rotation of the disk in air; (3) the mechanical stress (including the radial and circumferential components) induced by centrifugal forces in the relatively thin and low density black paint/liquid crystal layer.

3.3.1 Approximate Density of the Black Paint/Liquid Crystal Layer. An evaluation of mechanical stresses influencing the liquid crystal coating requires the knowledge of the density of a typical black paint/liquid crystal layer. For this purpose, an aluminum block in the form of a rectangular prism (0.125 m × 0.013 m × 0.03 m) has been machined to obtain square cross section fins on its external surface. This process helps to increase the effective area of the prism for further liquid crystal coats. Multiple coats of liquid crystal layers have been sprayed and left to drying repeatedly. The volume change with respect to the uncoated block has been measured. The accumulated liquid crystal mass has also been measured (0.408 gram mass) on an electronic scale accurate up to ±0.005 gram mass resolution. The resulting black paint/liquid crystal layer density was about $\rho_{lc} = \sim 81.6\ \mathrm{kg/m^3}$. In a second experiment, the density has also been obtained by filling the initially known volume of a cylindrical cavity carefully machined into an aluminum block. The cavity has been sprayed and dried repeatedly until the whole cavity is filled with liquid crystal material. The resulting density from this experiment was around $\rho_{lc} = \sim 84.7\ \mathrm{kg/m^3}$. Since the geometrical shape of the cavity open surface is difficult to control in multiple coating experiments, it is suggested that the approximate density value of $\rho_{lc} = \sim 81.6\ \mathrm{kg/m^3}$ from the previous experiment is adopted for the analysis presented in this paper. The uncertainty of the density measurement is estimated to be at least ±6%. The measured density of the dry liquid crystal layer is very close to the values typical to Balsa wood ($\rho = \sim 100\ \mathrm{kg/m^3}$). The measured $\rho_{lc} = \sim 81.6\ \mathrm{kg/m^3}$ value is about 33 times smaller than the aluminum disk density of $\rho_{Al} = \sim 2707\ \mathrm{kg/m^3}$.

3.3.2 Mechanical Stresses in the Rotating Disk. The approximate magnitude of disk mechanical stresses induced by rotation are much greater (about 33 times) than expected

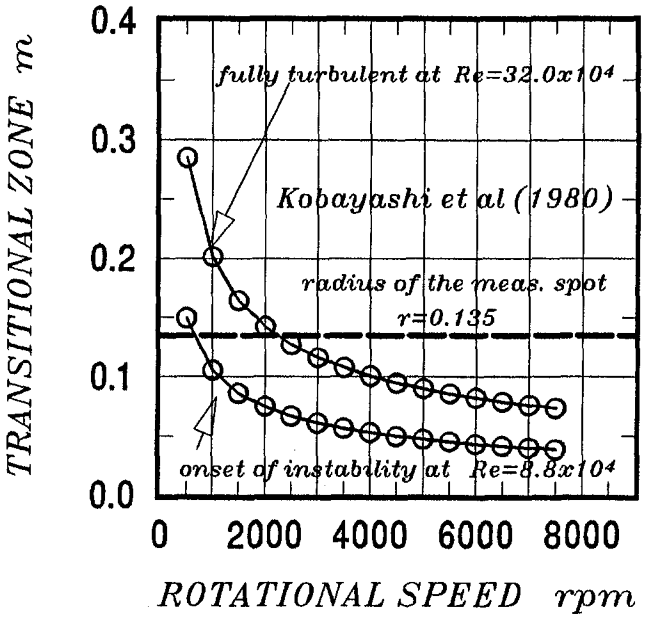

Fig. 6 Predicted onset of instability point and the transitional zone on the rotating free disk

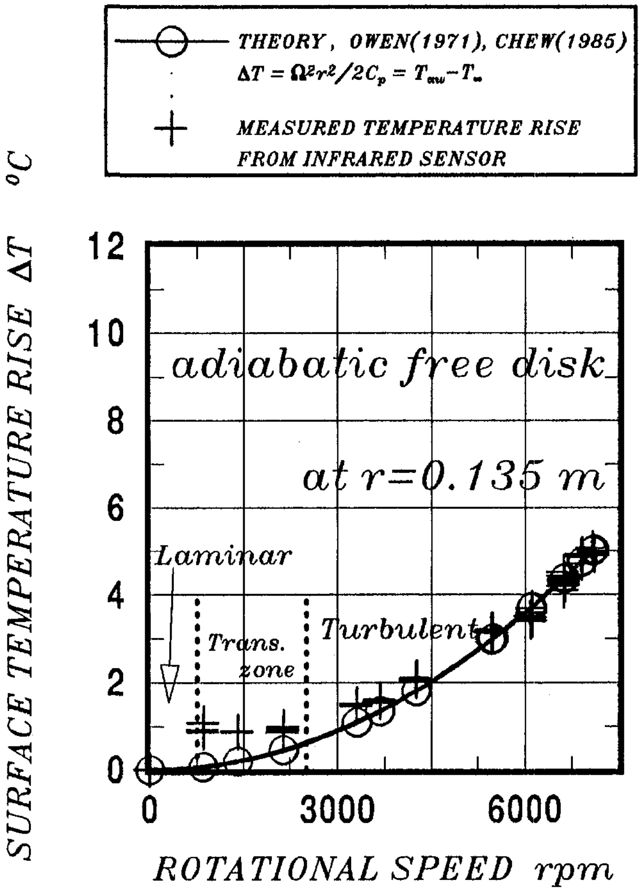

Fig. 7 Adiabatic disk temperature measurements using the infrared point sensor and comparison with theory

stresses in the liquid crystal layer due to the corresponding aluminum to liquid crystal density ratio. To verify the influence of the disk mechanical stress on the liquid crystal layer, a simple tension test using a liquid crystal painted test coupon has been performed. The coupon has been instrumented with a thermocouple which was installed flush to the surface underneath the liquid crystal. A wide range of tensile stresses (from zero to five times of total stresses corresponding to the disk rotating speed of 7500 rpm) have been applied. No liquid crystal color shift has been observed in these experiments when the coupon surface is kept at a prescribed temperature. This test clearly indicated that mechanical stresses in the substrate material alone cannot influence the color response of the liquid crystal coating.

3.3.3 Aerodynamic Wall Shear Stress. Another important force that may influence the liquid crystal layer is the aerodynamic wall friction force, $\tau_o \cdot ds \cdot dr$ acting on the flow side of the liquid crystal layer as described in Fig. 1. This force can be predicted from existing solutions of the turbulent viscous pump problem for a free disk. A detailed treatment of this classical problem starting from von Kármán's (1921) problem definition is given in Dorfman (1963) and Owen and Rogers (1989). In the radial direction, the balance of the turbulent shear force applied to the area $dr \cdot ds$ and the centrifugal force acting on the fluid volume results in,

$$\tau_{r,o} = \tau_o \cdot \operatorname{Sin} \varphi = \rho \cdot r \cdot \Omega^2 \cdot \delta. \tag{1}$$

According to Schlichting (1979), the shear stress component in the tangential direction ($\tau_{\theta,o} = \tau_o \cdot \operatorname{Cos} \varphi$) can be borrowed from a model developed for a flat plate boundary layer using the $\frac{1}{7}$th power velocity profile. One may show from Eq. 1 that the shear layer thickness for turbulent flow over the free disk can be estimated as,

$$\delta = \sim 0.5261 \cdot r^{3/5} \cdot (\nu/\Omega)^{1/5}. \tag{2}$$

This solution assumes that φ angle does not change with the radius. Equation 2 is also consistent with the experimental results of Schmidt (1921), Kempf (1924), Dorfman (1963) and Glezer (1969).

From a mechanical point of view, the liquid crystal layer sees the aerodynamic wall shear stress as a reaction to the fluid friction at the flow surface. The tangential component of the aerodynamic wall shear stress can be calculated from,

$$\begin{aligned} |\tau_{\theta,o}| &= 0.02668 \cdot \rho \cdot \Omega^2 \cdot b^2 \cdot (r/b)^{8/5} \cdot \mathrm{Re}_\theta^{-1/5} \\ &= 0.02668 \cdot \rho^{4/5} \cdot \Omega^{9/5} \cdot r^{8/5} \cdot \mu^{1/5}. \end{aligned} \tag{3}$$

The relationship between the radial and tangential component can be approximated as $|\tau_{r,o}|/|\tau_{\theta,o}| = 0.162$, Owen and Rogers (1989). The magnitude of the total aerodynamic shear stress vector is then,

$$\begin{aligned} |\tau_0| &= [\tau_{\theta,0}^2 + \tau_{r,0}^2]^{1/2} = [\tau_{\theta,0}^2 + (0.162)^2 \cdot \tau_{\theta,0}^2]^{1/2} \\ &= 1.013 \cdot |\tau_{\theta,o}| \end{aligned} \tag{4}$$

The predicted magnitude of aerodynamic shear stress from Eq. 4 has the same order of magnitude of the mechanical stress estimate inside the liquid crystal/black paint layer.

3.4 Liquid Crystal Hue Response at Different Rotational Speeds. In order to isolate the possible influence of rotation on the color response of liquid crystals, a series of tests have been performed in a wide rotational speed range (0–7500 rpm). The liquid crystal based temperature measurements, and infrared point-sensor, has been repeatedly used under almost identical conditions for many different rotational speeds at $r = 0.135$ m. Figure 8 presents hue versus infrared temperature measurements obtained from three different experimental arrangements. The narrow band liquid crystal designated as R30C1W has been tested on the stationary calibration plate, the non-rotating disk, and the rotating disk at many different speeds. An immediate observation from Fig. 8 is that rotation does not have any significant influence on the color response of liquid crystals used on a rotating disk surface. A few hundred data points, from many different rotational speeds, always follow the same curve defining the hue versus temperature relation. The figure also includes results from repeatability tests. Some minimal scatter existing in the present data is within the reported uncertainty band of the hue capturing system and infrared measurement system.

Similar hue versus infrared sensor based temperature measurements for a liquid crystal slurry designated as R45C1W are shown in Fig. 8. A well defined hue versus temperature relation has also been observed with very good repeatability for many rotational speed values between 0 and 7500 rpm. The data given in Fig. 8 supports the initial estimates made for the order of magnitude of the mechanical stresses inside the thermo-indicator coating and the aerodynamic shear stress at the fluid solid interface. Initial estimates of the mechanical stresses in the coating can be made with the density value provided in section 3.3.1. It seems that rotation induced aerodynamic shear stress when combined with internal mechanical stresses can not influence the physical process that causes specific color patterns appearing on the disk surface. The experimental observations made in this study, and simple analytical estimates of aerodynamic shear stress and mechanical stresses obtained under rotation, suggest that encapsulated liquid crystals are not influenced from rotational effects. The hue data clearly show that there is no significant color shift due to rotation of the disk tested under realistic gas turbine conditions. However, it is the authors' observation that systematic temperature shifts may be erroneously

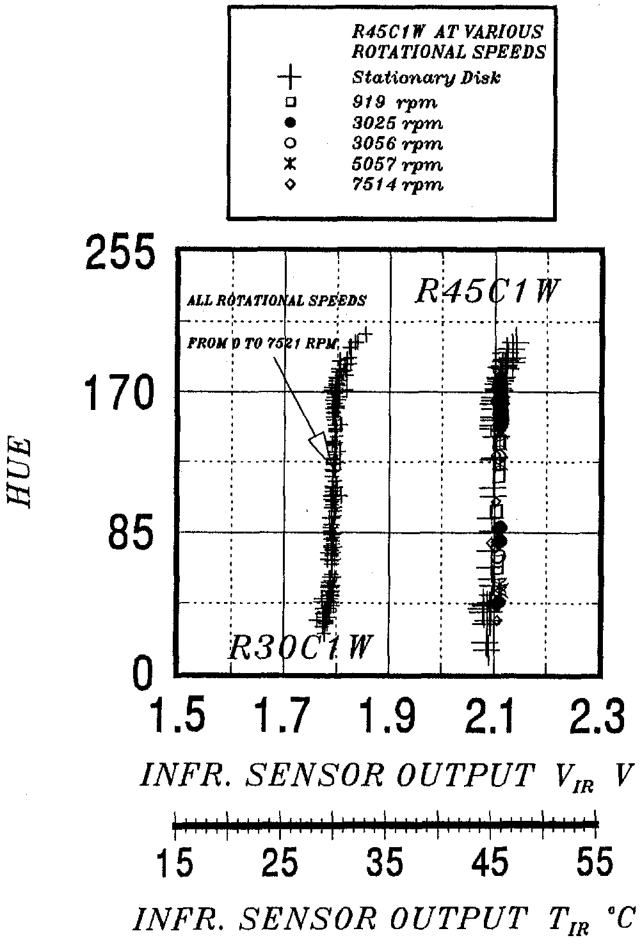

Fig. 8 Influence of rotation on color response of encapsulated Chiral-Nematic liquid crystals, hue versus infrared sensor raw output at various rotational speeds, R45C1W compared to R30C1W, calibration plate and stationary disk results included; Hue versus temperature data is also included.

recorded when surface thermocouples are utilized (underneath the liquid crystal coating) instead of a non-intrusive reference temperature measurement device such as the infrared point-sensor used in this study. Usually, these systematic temperature shifts (erroneously recorded bias errors) are rotational speed dependent and may easily be accounted for by a change in liquid crystal color calibration.

Past studies using thermochromic liquid crystals in the stationary frame wind tunnel experiments always assumed that encapsulated liquid crystals are not influenced by aerodynamic wall shear stress. However, there is not a single reference in open literature including quantitative information on this assumption. The present study quantitatively shows for the first time that liquid crystal hue cannot be altered by imposing different levels of aerodynamic shear stress from the flow side. At a given radial position, every rotational speed setting imposes a different aerodynamic wall shear stress value on the thermo-indicator layer as predicted by Eq. 4. Present results show no influence from aerodynamic wall shear stress on color response of liquid crystal layer in a wide range of aerodynamic shear stress magnitudes.

3.5 Adiabatic Disk Temperature Rise from Liquid Crystal Measurements. Further investigations on the use of liquid crystal thermo-indicators have been carried out by using liquid crystals in a free disk heat transfer experiment. When the ambient temperature is reasonably uniform around a rotating free disk, the convective heating of the disk from the neighboring viscous region creates a specific radial temperature distribution. The adiabatic temperature rise is known to be a function of the disk speed, radial position, and the specific heat of the fluid surrounding the disk. The liquid crystal based temperature measurements from the adiabatic disk experiments are shown in Fig. 9. The rotating disk is brought to an adiabatic condition by running the disk at 6648 rpm for about an hour. The liquid crystal colors falling into the linear range of the calibration shown in Fig. 3 have been observed to exist over a 6 cm radial band starting from $r = 0.03$ m. Four other adiabatic disk experiments have also been performed at 6545, 6345, 5932 and 5488 rpm. The liquid crystal color band containing the colors in the linear range of the calibration move radially outward by decreasing rotational speed. The ambient temperature slightly decreases with decreasing rotational speed as shown in Fig. 9. This slight change is because of the relatively small amount of heat dissipation to the still air at reduced rotational speeds. If one continues to reduce the rotational speed from 5488 rpm level, for an approximate still air temperature of $T_\infty = 27.5$°C, the liquid crystal color band will not continue to appear on the disk surface. In this relatively low rotational speed range, the actual disk temperatures are well below the meaningful color play zone of the thermoindicator (± 0.1°C) around 30°C. This observation shows the importance of the selection of the liquid crystal color play zone for a specific rotating disk heat transfer experiment. The specific location of the useful liquid crystal color band can be continuously adjusted by changing rotational speed or ambient temperature around the disk.

3.6 Comparison with Free Disk Heat Transfer Theory. Figure 10 shows the comparison of liquid crystal based adiabatic disk temperature measurement using the calibrations presented

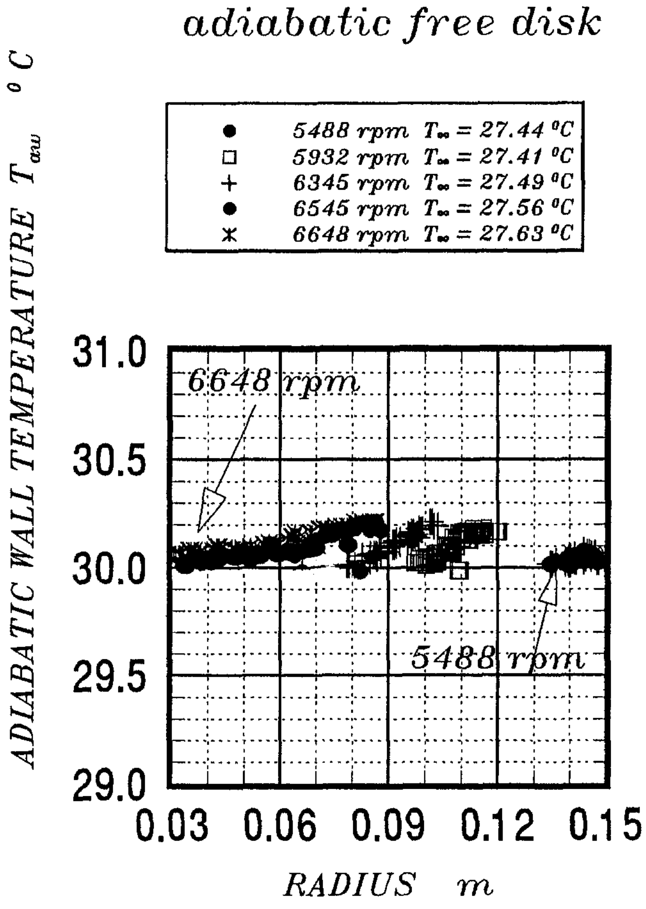

Fig. 9 Adiabatic wall temperature measurements on the rotating disk surface using the current liquid crystal technique, radial profiles for various rotational speeds

in Figs. 3, 4, 8 and the theoretical prediction from Owen (1971). The adiabatic disk temperature is predicted as $T_{aw} = T_\infty + \Omega^2 r^2 / 2C_p$ for 6345 rpm and 5488 rpm. Reasonably good agreement between the theory and the present liquid crystal measurements is shown in Fig. 10.

3.7 Influence of Added Stroboscope Illumination on Liquid Crystal Hue. The current experiments described in this paper have been performed by generating a completely axisymmetric flow and heat transfer situation on the rotating disk surface. Because of the infrared system's finite time response of 80 milliseconds, the measurement has been time averaged over 6 rotations of the disk at 0.135 m radius, at 5000 rpm. Time averaged character of infrared measurements is not an influencing factor as long as the flow and heat transfer parameters do not vary in a circumferential direction. Rotating disk problems may have variations in the axisymmetric direction in applications other than a perfect free disk problem. For example, the existence of a bolt head or a step may cause a strong temperature distribution in both the radial and circumferential directions. When thermal non-uniformities in the circumferential direction and radial direction are introduced, freezing the liquid crystal image by using a stroboscope light can be extremely beneficial.

Figure 11 compares the liquid crystal hue variation with respect to infrared sensor output with and without stroboscope light illumination at 3000 rpm. The stroboscope light has been used in these particular experiments in addition to the regular illumination lights as described in previous paragraphs. The information provided in Fig. 11 is from an axisymmetric free disk experiment, however, the conclusions drawn from this experiment are valid for any non-axisymmetric surface heat transfer problem making use of liquid crystal thermo-indicators. The experimental data presented clearly show that additional stroboscope light does not alter the hue versus temperature relationship in a rotating disk experiment. This observation can be explained with the insensitivity of hue measurements to small variations in the intensity of additional illumination from the stroboscope, Camci et al. (1992). The infrared sensor used in the specific experiment is also not sensitive to visible light emitted from the stroboscope and the illumination system because of its special spectral range in the infrared spectrum. Figure 11 provides the conclusion that a stroboscope device can be directly used over a liquid crystal coated surface for non-axisymmetric temperature mapping. It has also been observed that slight variations in camera angle (±15°) and slight camera zoom variations (±0.25 m) do not significantly influence the results presented in Fig. 11.

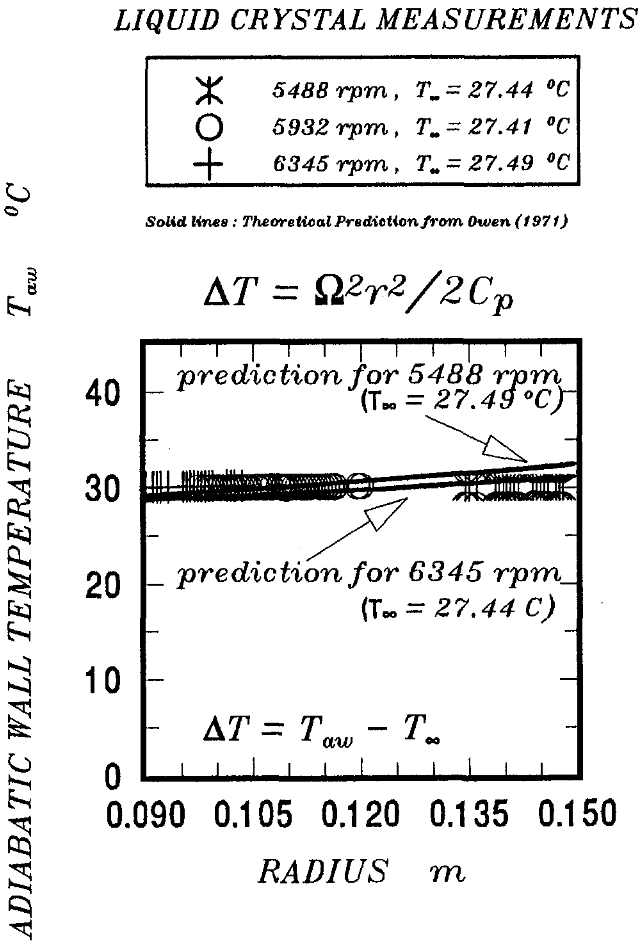

Fig. 10 Comparison of theoretical predictions of adiabatic wall temperature rise on a free rotating disk with the measured data from the current liquid crystal technique

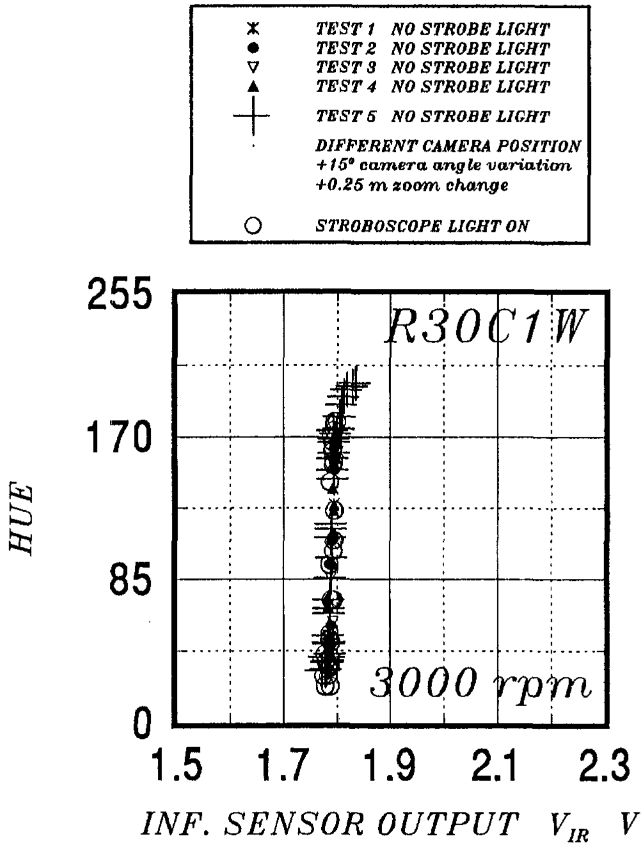

Fig. 11 Influence of stroboscope light intensity, camera position and zoom level on color response of liquid crystals on a rotating disk surface at 3000 rpm

4.0 Experimental Uncertainties

Stationary frame temperature measurements using the hue capturing method typically results in an overall uncertainty of less than ±0.1°C at about 30°C provided that the hue values between 30 and 140 are used for data reduction purposes. This specific error level requires a careful calibration of the reference thermocouple used in the construction of the hue versus temperature curve of liquid crystals. It is expected that the reference thermocouple is calibrated to an uncertainty of ±0.05°C around 30°C. Other individual uncertainty contributors such as the illumination angle, model to illumination source distance, spatial distribution of liquid crystal color response, and the repeatability of the hue capturing process should be taken into account, Camci et al. (1992).

In the hue versus temperature charts presented in this paper, the horizontal axis is infrared sensor output V_{IR} in Volts. A ±0.020 Volts uncertainty over a nominal output value of 1.7966 Volts (at 30°C) is estimated. This value corresponds to about ±0.10°C temperature measurement error on the infrared point-sensor. The repeatability of infrared based temperature measurements is estimated to be around ±0.05°C at 30°C.

An additional uncertainty contributor may be the determination of the rotational speed that is monitored constantly by an electronic rpm measuring device. This device uses the light reflections from a reflecting narrow strip on the disk surface. A ±5 rpm at a nominal speed of 2000 rpm is a standard estimate for this device.

Even with the most precise liquid crystal coating procedures, uncertainties may be introduced when different coats of liquid crystal layers deposited at different times are compared for their hue response. The final uncertainty of the temperature measurements in the rotating frame using liquid crystals is estimated as high as ±0.30°C around 30°C. This value is for all the experiments performed over a 4-month time period including both precision and bias errors.

5.0 Conclusions

1 A liquid crystal thermography system in the rotating environment of a disk has been developed. Although a mercury slip-ring and a thin foil reference thermocouple has been used in the initial phase of this study, the use of the slip-ring and the thermocouple sensor is not recommended due to the possible inclusion of rotational speed dependent thermocouple bias errors.

2 A new experimental strategy is described using two simultaneous non-intrusive temperature measurements on the rotating disk surface. Liquid crystal hue can be effectively correlated against a calibrated infrared-point-sensor indicating local temperature.

3 An estimate of the centrifugal forces acting in the liquid crystal layer requires the knowledge of the density of the liquid crystal coating. A new experiment has been designed for the first time for the approximate determination of the density of a typical dry liquid crystal coating.

4 Predictions show that centrifugal acceleration of the disk creates non-negligible mechanical stress in the metallic disk. However, present static tensile experiments show that the metallic disk stress alone does not influence the color response of the liquid crystal layer.

5 The predicted magnitude of the aerodynamic shear stress is approximately the same order of magnitude as the mechanical stress inside the liquid crystal/black paint layer.

6 The experimental observations made in this study, and the simple estimates of aerodynamic shear stress and mechanical stresses obtained under rotation, suggest that liquid crystal thermo-indicators are not influenced from rotational effects within the rotational speed range of the current experiments (0–7500 rpm, $r = 0.135$ m).

7 Although the current results are obtained from a circumferentially uniform free disk experiment, the specific method introduced is capable of performing well in situations where there are strong circumferential and radial temperature gradients. For this purpose, the use of a stroboscope is discussed. The current data shows that additional stroboscope light illumination does not influence the local liquid crystal based temperature measurements made on rotating disks.

8 Past studies using thermochromic liquid crystals in the stationary frame wind tunnel experiments always assumed that encapsulated liquid crystals are not influenced by aerodynamic wall shear stress. However, there is not a single source of quantitative information on this frequently made assumption. The present study quantitatively shows for the first time that hue values produced by encapsulated thermochromic liquid crystals can not be altered by imposing different levels of aerodynamic shear stress from the flow side, under present conditions.

9 Only a stationary frame calibration of the liquid crystal layer is sufficient for a temperature measurement to be performed on a rotating disk. An identical stationary calibration plate using a reference thermocouple is an effective tool in documenting the hue response of a liquid crystal thermo-indicator.

10 The present methodology describes a complete, high resolution, non-intrusive, and accurate temperature mapping technique on a rotating disk surface. The final uncertainty of the temperature measurements in the rotating frame using liquid crystal thermo-indicators is estimated as high as ±0.30°C around 30°C for all the experiments performed over a four month time period.

6.0 Acknowledgements

The authors wish to thank Dr. Michael Fox of Solar Turbines Inc., Heat Transfer Team, for the static coupon tension test and Mr. Harry Houtz of the Pennsylvania State University for the precision machining of the experimental setup. The authors also express their appreciation to Prof. J. M. Owen, University of Bath, U.K., for the productive interaction during the execution of this research program.

7.0 List of References

Blair, M. F., Wagner, J. H., Steuber, G. D., 1991, "New Applications of Liquid-Crystal Thermography in Rotating Turbomachinery Heat Transfer Research," ASME Paper 91-GT-354.

Bonnett, P., Jones, T. V., McDonnell, D. G., 1987, "Shear Stress Measurement in Aerodynamic Testing Using Cholesteric Liquid Crystals," *Liquid Crystals*, Vol. 6(3), pp. 271–280.

Camci, C., Kim, K., and Hippensteele, S. A., 1992, "A New Hue Capturing Technique for the Quantitative Interpretation of Liquid Crystal Images Used in Convective Heat Transfer Studies," ASME *Journal of Turbomachinery*, Vol. 114, No. 4, pp. 765–775.

Camci, C., Kim, K., Hippensteele, S. A., and Poinsatte, P. E., 1993, "Evaluation of a Hue Capturing Based Transient Liquid Crystal Method for High Resolution Mapping of Convective Heat Transfer on Curved Surfaces," ASME JOURNAL OF HEAT TRANSFER, Vol. 115, No. 2, pp. 311–318.

Cartmell, J. V., and Churchill, D., 1973, "Encapsulated Liquid Crystals," United States Patent 3,720,623.

Collings, P. J., 1990, *Liquid Crystals*, Princeton University, Princeton, NJ.

deGennes, P. G., 1974, *The Physics of Liquid Crystals*, Clarendon Press, Oxford, UK.

Dorfman, L. A., 1963, *Hydrodynamic Resistance and Heat Loss of Rotating Solids*, English translation, Oliver & Boyd, Edinburgh & London.

Farina, D. J., Hacker, J. M., Moffat, R. J., and Eaton, J., 1994, "Illuminant Invariant Calibration of Thermochromic Liquid Crystals," *Experimental Thermal and Fluid Science*, Vol. 9, pp. 1–12.

Glezer, B., 1969, "Investigation of a Flow Between Rotating Disk and Stator," *Energetica*, No. 3, University Press, Moscow.

Glezer, B., 1992, "Some Aspects of Industrial Gas Turbine Cooling Development," *Proceedings of the 1992 International Symposium on Heat Transfer in Turbomachinery*, R. J. Goldstein and D. E. Metzger, eds., organized by the Int. Center for Heat and Mass Transfer, Athens, Greece.

Holmes, B. J., 1986, "A New Method for Laminar Boundary Layer Transition Visualization In-Flight Color Changes in Liquid Crystal Coatings," NASA TM 87666, (Also see U.S. Patent 4,774,835).

Holmes, B. J., and Obara, C. J., 1987, "Advances in Flow Visualization Using Liquid Crystal Coatings," SAE Paper 871017.

Jones, T. V., Wang, Z., and Ireland, P. T., 1992, "Liquid Crystal Techniques," *Proceedings of the 1992 International Symposium on Heat Transfer in Turbomachinery*, R. J. Goldstein and D. E. Metzger, eds., organized by the Int. Center for Heat and Mass Transfer, Athens, Greece.

Kármán, T. von, 1921, "Über laminare und Turbulente Reibung," *Z. Agnew. Math. Mech.*, Vol. 1, pp. 233–252, (also English translation in NACA TM 1092).

Kempf, G., 1924, "Über Reibungswiderstand Rotierender Scheiben," *Vorträge auf dem Gebiet der Hydro- und Aerodynamik*, Innsbruck Congr., Berlin, p. 168.

Kim, K., 1991, "A New Hue Capturing Technique for the Quantitative Interpretation of Liquid Crystal Images Used in Convective Heat Transfer Studies," Ph.D. thesis, Pennsylvania State University.

Klein, E. J., 1968, "Application of Liquid Crystals to Boundary-Layer Flow Visualization," AIAA Paper 68-376.

Klein, E. J., and Margozzi, A. P., 1969, "Exploratory Investigation on the Measurement of Skin Friction by Means of Liquid Crystals," *Israel Journal of Technology*, Vol. 7, pp. 1–2.

Kobayashi, R., Kohama, Y., and Takamadate, C., 1980, "Spiral Vortices in Boundary Layer Transition Regime on a Rotating Disk," *Acta Mech.*, Vol. 35, pp. 71–82.

Metzger, D. E., Bunker, R. S., Bosch, G., 1991, "Transient Liquid Crystal Measurement of Local Heat Transfer on a Rotating Disk With Jet Impingement," ASME *Journal of Turbomachinery,* Vol. 113, No. 1, pp. 52–59.

Owen, J. M., and Rogers, R. H., 1989, "Flow and Heat Transfer in Rotating Disk Systems," *Rotor-Stator Systems,* Vol. 1, Research Studies Press, Taunton, Somerset, England and John Wiley and Sons.

Parsley, M., 1987, *An Introduction to Thermochromic Liquid Crystal Products,* Hallcrest Liquid Crystal Division.

Reda, D. C., 1991, "Observations of Dynamic Stall Phenomena Using Liquid Crystal Coatings," *AIAA Journal,* Vol. 29, No. 2, pp. 308–310.

Reda, D. C., 1995a, "Method for Determining Shear Direction Using Liquid Crystal Coatings," United States Patent 5,394,752.

Reda, D. C., 1995b, "Method for Measuring Shear Stress Magnitude and Direction Using Liquid Crystal Coatings," United States Patent 5,438,879.

Rizzo, D., and Camci, C., 1994, "The Effects of a Boundary Layer Fence on the Aerodynamic Flowfield and Endwall Heat Transfer in a 90° Turning Square Duct," 1994 ASME Winter Annual Meeting, Session: Heat Transfer in Gas Turbines, M. K. Chyu and N. Nirmalan, eds., Chicago.

Schlichting, H., 1979, *Boundary Layer Theory,* seventh edition, McGraw Hill, pp. 102–107.

Schmidt, W., 1921, "Ein einfaches Messverfahgren für Drehmomente," *Z.VDI,* Vol. 65, pp. 441–444.

Taslim, M. E., Rahman, A., and Spring, S. D., 1991, "An Experimental Investigation of Heat Transfer Coefficients in a Spanwise Rotating Channel with Two Opposite Rib-Roughened Walls," ASME *Journal of Turbomachinery,* Vol. 113, No. 1, pp. 75–82.

Van Zante, D..E., and Okiishi, T. H., 1991, "Visualization of Boundary Layer Development on Turbomachine Blades with Liquid Crystals," NASA Grant NAG 3-917, TCRL-36, ERI project 3067, Iowa State University.

Wiedner, B., Camci, C., 1993a, "Accurate Determination of Local Heat Flux on Steady State Heat Transfer Surfaces with Arbitrarily Specified External and Internal Boundaries," presented at the 1993 National Heat Transfer Congress, Atlanta, Georgia, ASME volume HTD-Vol. 242, pp. 21, 31, in press.

Wiedner, B., Camci, C., 1993b, "Passage Flow Structure and Its Influence on Endwall Heat Transfer in a 90° Turbulent Duct Flow: Mean Flow and High Resolution Heat Transfer Experiments," ASME Paper, ASME-93-WA/HT-52, presented at the 1993 ASME Winter Annual Meeting, in press.

Wilson, M., Syson, B. J., and Owen, J. M., 1993, "Image Processing Techniques Applied to Wide-band Thermochromic Liquid Crystals," *Proceedings of the Eurotherm 32, Heat Transfer in Single Phase Flows,* July 5–7, 1993, Oxford University.

The Effects of Forced Convection on the Power Dissipation of Constant-Temperature Thermal Conductivity Sensors

Y. Huang

H. H. Bau

Department of Mechanical Engineering and
Applied Mechanics,
University of Pennsylvania,
Philadelphia, PA 19104-6315

The effect of forced convection on the power dissipation of cylindrical and planar, constant temperature, thermal conductivity detectors (TCDs) is investigated theoretically. Such detectors can be used either for on-line continuous sensing of fluid thermal conductivity or for determining the sample concentrations in gas chromatography. A low Peclet number, asymptotic theory is constructed to correlate the TCD's power dissipation with the Peclet number and to explain experimental observations. Subsequently, the effect of convection on the TCD's power dissipation is calculated numerically for both time-independent and time-dependent flows. The theoretical predictions are compared with experimental observations.

1 Introduction

Thermal conductivity detectors (TCDs) are used to measure continuously the thermal conductivity of fluids in motion. In this paper, we consider a ''constant temperature'' TCD which consists of a hot, constant resistance, cylindrical or flat heater (a filament with an effective temperature, T_f^*) that is inserted in a narrow channel (Fig. 1) whose walls are maintained at a constant temperature (T_w^*, $T_w^* < T_f^*$). The filament's axis is parallel to the flow direction. Feedback controllers maintain the filament's resistance and the conduit's wall-temperature at fixed values. The electric power supplied to the filament is dissipated as heat through the gas to the conduit's (box) walls. The fluid's thermal conductivity is inferred from the measurement of the filament's power dissipation.

TCDs can be used for on-line, continuous monitoring of the thermal conductivity of process gases. TCDs were also introduced early on in gas chromatography to detect concentrations of trace gases (Littlewood, 1970, 339–381; Guiochou and Guillemin, 1988, chap. 10; and Messaros et al., 1984) and they facilitated major advances in this field. Although TCDs have lost their prominent role in chromatography in favor of more sensitive detectors such as the Flame Ionization Detector, they are still widely used in the analysis of gases which do not respond to other detectors; in industrial situations where safety considerations preclude the use of other detectors; in situations (such as separation) when sample destruction is undesirable; and in situations which do not require very high sensitivity. Moreover, when miniaturized, the TCD's sensitivity remains relatively high compared to that of other detectors (Jerman, 1981). Therefore, they have the potential of serving as ''detectors of choice'' in miniature gas chromatographs microfabricated on silicon wafers (Terry, 1975).

In gas chromatography, a sample (evaporated if necessary) of unknown composition is injected into a stream of carrier gas flowing through a long, narrow conduit (column) coated with a stationary phase (i.e., Giddings, 1991). As a result of adsorption and chemisorption differences in sample components and the carrier gas, the various components are separated. Towards the column's end one observes pockets of binary mixtures (effluent gas) each consisting of a nearly single unknown constituent mixed with the carrier gas, separated by pockets of pure carrier gas. The effluent gas enters the TCD which is located at the column's end. The effluent's thermal conductivity is different from that of the pure carrier. This, in turn, affects the filament's power dissipation. The chemical composition of the various components in the sample is determined by their arrival time at the detector. The difference between the power dissipation in the presence of the effluent, and in its absence, is used to compute the effluent's thermal conductivity and the concentration of the component.

TCDs may operate either in a constant temperature or constant current modes. In the non-constant temperature operation, as the gas' thermal conductivity changes so does the temperature field. This change in temperature causes undesirable changes in the gas' thermophysical properties such as thermal capacity, viscosity, and density and, in turn, affects the non-conductive power dissipation. These secondary effects are less significant in constant temperature TCDs. Constant temperature TCDs are, therefore, likely to have higher sensitivity than their non-constant temperature counterparts, and they are the TCD type we consider in this paper.

When used in chromatography, the TCD often operates in a differential mode. This is accomplished by either using two TCDs in parallel (flowing effluent through one TCD and pure carrier gas through the other) or by alternating effluent and pure carrier through a single TCD. The difference in the power dissipation in the presence of pure carrier and effluent is used to evaluate the mixture's composition. The differential measurement eliminates sensitivity to ambient factors such as fluctuations in atmospheric pressure. However, since the effluent and carrier follow separate hydraulic paths, the differential measurement cannot eliminate noise induced by flow fluctuations resulting from factors such as time-variations in the pressure source and flow instabilities. In order to improve TCD sensitivity, it will be necessary to reduce its noise level. As a first step in such a program, we embarked on studying the various transport mechanisms taking place in the TCD and their contribution to TCD noise.

Contributed by the Heat Transfer Division for publication in the JOURNAL OF HEAT TRANSFER. Manuscript received by the Heat Transfer Division August 11, 1995; revision received October 7, 1996; Keywords: Forced Convection, Instrumentation, Transient & Unsteady Heat Transfer. Associate Technical Editor: P. Simpkins.

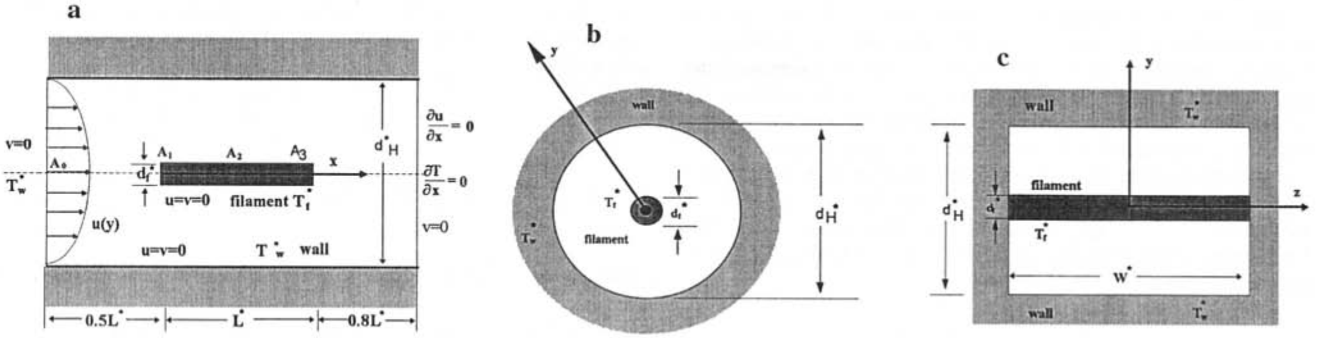

Fig. 1 Schematic description of the thermal conductivity detector's cross-sections: (*a*) a cross-section parallel to the flow direction; (*b*) A cross-section normal to the flow direction (circular TCD); and (*c*) a cross-section normal to the flow direction (planar TCD)

In this paper, in order to better understand the role of convection, we focus our attention only on the effect of time-independent and time-dependent pure-gas forced convection on the TCD's power dissipation. Surprisingly, until now, the role of convection in the TCD's operation has not been elucidated. Prior studies of the TCD either neglected convection all together (i.e., Jerman, 1981) or adopted a lumped parameter approach in which convection effects were described through the use of Newton's cooling law with an unknown heat transfer coefficient (i.e., Wells and Simon, 1983).

We start by deriving a simple asymptotic theory for a TCD operating at low Peclet numbers. Subsequently, we solve numerically, the time-independent and time-dependent flow equations for a gas with temperature-dependent thermophysical properties. The theoretical predictions are then compared with experimental observations.

2 The Mathematical Model

We consider both axisymmetric, cylindrical (Fig. 1*b*) and planar (Fig. 1*c*) TCDs. The planar conduit's aspect ratio (d^*_H/W^*) was assumed to be very small to allow its modeling as an infinite strip in the *z*-direction. We adopt here the convention that variables with/without a superscript star are dimensional/nondimensional.

The cross-section of the computational domain along the flow direction, together with the relevant geometric dimensions and kinematic and thermal boundary conditions used in our computations, are shown in Fig. 1*a*. For the cylindrical TCD, these dimensions correspond to those of the TCD used in our experiments (Huang, 1995). Briefly, for the cylindrical (planar) cross-sections, the channel's diameter (height) is d^*_H; the filament's diameter (thickness) is d^*_f; and its length is L^*. In our experiments and the numerical simulations described later in the paper, $d^*_f/d^*_H = 0.026$ and $L^*/d^*_f = 984$. The filament's leading edge is located at a distance of $0.5L^*$ downstream of the cell's entrance. The length of the TCD cell is $2.3L^*$. The coordinate x is aligned along the filament's length and the coordinate y is normal to the filament. The origin of the coordinate system is fixed at the filament's leading edge. In the analysis, we ignore the presence of supporting pins.

The filament and the conduit's walls are maintained at fixed temperatures T^*_f and T^*_w, respectively. Although the assumption of the filament's temperature uniformity is not strictly correct, we use it in order to gain simplicity and physical insight at the expense of precision. Non-slip velocity boundary conditions were applied at all solid boundaries.

We define the nondimensional temperature $\theta = (T^* - T^*_w)/(T^*_f - T^*_w)$, where T^* is the dimensional gas temperature. The filament's and conduit wall's nondimensional temperatures are, respectively, $\theta_f = 1$ and $\theta_w = 0$. The average entrance velocity, $\overline{u^*}$; the channel's diameter (height), d^*_H; $(\overline{\mu^*}\overline{u^*}/d^*_H)$, and the convective time $d^*_H/\overline{u^*}$ are, respectively, the velocity, distance, pressure, and time scales. The overbar denotes an average quantity, typically evaluated at the temperature $(T^*_f + T^*_w)/2$. α^* is the thermal diffusivity. $\overline{k^*}$ is the thermal conductivity. μ^* is the viscosity. $\mathrm{Pe} = \overline{u^*}d^*_H/\overline{\alpha^*}$ is the Peclet number.

The entrance conditions consist of isothermal gas at the conduit's nondimensional wall temperature, $\theta(-(L/2), y) = 0$, with a prescribed unidirectional velocity profile, $u(-(L/2), y, t)$. The variables u and v denote, respectively, the axial (x-direction) and transverse (y-direction) velocity components. The exit boundary conditions are $v(1.8L, y) = \partial u(1.8L, y)/\partial x = \partial\theta(1.8L, y)/\partial x = 0$. The sensitivity of the results to the location of the outlet was tested by varying that location. No significant variations were detected in the results when the exit's distance from the filament's trailing edge was larger than $0.8L$.

Nomenclature

d_f = filament's diameter
d_H = conduit's diameter (cylindrical TCD) or distance between cavity walls (planar TCD)
k = thermal conductivity (W/m-K)
L = filament's length
Pe = Peclet number, $\overline{u^*}d^*_H/\overline{\alpha^*}$
q = heat flux (W/m^2)
Q = filament's power dissipation (W)
Re = Reynolds number, $\overline{u^*}d^*_H/\overline{\nu^*}$
T = temperature (K)
u = axial velocity (m/s)
v = transverse velocity (m/s)
x, X = axial coordinate
y = transverse coordinate
W = width of planar TCD (m)
α = thermal diffusivity
δ = amplitude of filament's power dissipation oscillations
ϵ = amplitude of velocity oscillations
ϕ = amplitude of heat flux oscillations
ξ = leading/trailing edge coordinate
ν = kinematic viscosity
ρ = density
θ = non-dimensional temperature
ω = frequency
ΔT = the difference between the filament's and the conduit's wall temperatures

Subscripts

c = core variable
conv = convective effect
f = filament
w = TCD cavity's wall
0 = absence of convection

Superscripts

$*$ = dimensional quantity
$\overline{}$ = averaged quantity

Since the Mach number was very small (~ 0.01), the fluid was assumed to be incompressible. The gas was modeled as having temperature-dependent viscosity, thermal conductivity, and density. The specific heat was assumed to be temperature-independent. We neglected buoyancy effects, viscous dissipation, and pressure work. In the momentum equation, we dropped the dilatation term. This term is often dropped in fluid mechanical computations with a little effect on the results (Issa and Lockwood, 1977). The equations (i.e., Batchelor, 1967) in a form suitable for both planar ($n = 0$) and cylindrical ($n = 1$) geometries are:

$$\frac{\partial \rho}{\partial t} + \frac{\partial(\rho u)}{\partial x} + \frac{1}{y^n}\frac{\partial(y^n \rho v)}{\partial y} = 0, \tag{1}$$

$$\frac{\mathrm{Pe}}{\mathrm{Pr}}\rho\left(\frac{\partial u}{\partial t} + u\frac{\partial u}{\partial x} + v\frac{\partial u}{\partial y}\right)$$

$$= -\frac{\partial P}{\partial x} + \frac{\partial}{\partial x}\left(\mu\frac{\partial u}{\partial x}\right) + \frac{1}{y^n}\frac{\partial}{\partial y}\left(\mu y^n\frac{\partial u}{\partial y}\right), \tag{2}$$

$$\frac{\mathrm{Pe}}{\mathrm{Pr}}\rho\left(\frac{\partial v}{\partial t} + u\frac{\partial v}{\partial x} + v\frac{\partial v}{\partial y}\right)$$

$$= -\frac{\partial P}{\partial y} + \frac{\partial}{\partial x}\left(\mu\frac{\partial v}{\partial x}\right) + \frac{\partial}{\partial y}\left(\frac{1}{y^n}\mu\frac{\partial(y^n v)}{\partial y}\right), \tag{3}$$

$$\mathrm{Pe}\rho\left(\frac{\partial\theta}{\partial t} + u\frac{\partial\theta}{\partial x} + v\frac{\partial\theta}{\partial y}\right) = \frac{\partial}{\partial x}\left(k\frac{\partial\theta}{\partial x}\right) + \frac{1}{y^n}\frac{\partial}{\partial y}\left(y^n k\frac{\partial\theta}{\partial y}\right). \tag{4}$$

The nondimensional state equation for a constant pressure, ideal gas is:

$$\rho\left(1 + \theta\frac{T_f^* - T_w^*}{T_w^*}\right) = \frac{1}{2}\frac{T_f^* + T_w^*}{T_w^*}. \tag{5}$$

In the above, the density, thermal conductivity, and viscosity were normalized by their corresponding values, ρ^*, k^*, and μ^*, evaluated at the average temperature, $(T_f^* + T_w^*)/2$, i.e., $k(\theta) = k^*(T)/k^*$. The thermal conductivity and viscosity were approximated as linear functions of temperature. For example, for nitrogen, when $(T_f^* + T_w^*)/2 = 167.5°\mathrm{C}$, $k(\theta) = 0.252\theta + 0.873$, $\mu(\theta) = 0.212\theta + 0.894$, $k^* = 0.035 W/mK$, and $\mu^* = 2.26 \times 10^{-5}\ kg/ms$ (Kreith and Bohn, 1986).

3 Asymptotic Analysis

We derive a simple asymptotic theory which takes advantage of the fact that the filament is very long, $L \gg 1$. The objectives of this analysis are (i) to obtain a better understanding of the effect of convection on TCD operation, (ii) to explain the experimental observation (Huang, 1995) that $(dQ/dPe)_{Pe=0} = 0$, where Q denotes the filament's power dissipation, and (iii) to obtain a benchmark which can be used to verify the numerical code.

Since, for small Peclet numbers, the filament affects the gas' temperature and velocity fields only in its immediate vicinity, we can assume that the filament ($0 < x < L$) is in an infinitely long conduit ($-\infty < x < \infty$). We introduce a rescaled axial coordinate, $X = L^{-1}x$. In terms of X, the filament occupies the interval $0 < X < 1$. We rewrite Eqs. (1–4) in terms of the new variable, X. For example, Eq. (4) assumes the form:

$$\mathrm{Pe}\rho\left(\frac{\partial\theta}{\partial t} + L^{-1}u\frac{\partial\theta}{\partial X} + v\frac{\partial\theta}{\partial y}\right) = L^{-2}\frac{\partial}{\partial X}\left(k\frac{\partial\theta}{\partial X}\right)$$

$$+ \frac{1}{y^n}\frac{\partial}{\partial y}\left(y^n k\frac{\partial\theta}{\partial y}\right), \left(-\infty < X < \infty, 0 < y < \frac{1}{2}\right), \tag{6}$$

with the boundary conditions:

$$\theta(-\infty, y) = \theta(\infty, y) = 0 \quad \left(0 < y < \frac{1}{2}\right);$$

$$\theta\left(X, \frac{1}{2}\right) = 0 \quad (-\infty < X < \infty);$$

$$\theta\left(X, \frac{d_f}{2}\right) = 1 \quad (0 < X < L);$$

and

$$\frac{\partial\theta(X, 0)}{\partial y} = 0 \quad (-\infty < X < 0 \text{ or } L < X < \infty).$$

Next, we take advantage of the fact that $L \gg 1$ and that the Peclet number is relatively small (i.e., $\mathrm{Pe} \ll L$). In the limit $L \to \infty$, all the axial derivatives are eliminated from the conservation equations. The elimination of these terms prevents us, however, from satisfying the upstream and downstream boundary conditions. Thus, we divide the length of the filament into three regions: the inner (core) region of length $O(1)$ and the leading and trailing edge regions of length $O(L^{-1})$.

The Core Region. We denote the core variables with subscript c and construct a regular perturbation solution in terms of powers of L^{-1}:

$$\begin{pmatrix} u_c \\ v_c \\ \theta_c \\ \rho_c \\ P_c \end{pmatrix} = \begin{pmatrix} u_{c,0} \\ v_{c,0} \\ \theta_{c,0} \\ \rho_{c,0} \\ P_{c,0} \end{pmatrix} + L^{-1}\begin{pmatrix} u_{c,1} \\ v_{c,1} \\ \theta_{c,1} \\ \rho_{c,1} \\ P_{c,1} \end{pmatrix} + O(L^{-2}) \tag{7}$$

Upon substituting (7) into the Eqs. (1–4) and equating like powers in L^{-1}, we obtain

$$\frac{\partial u_c}{\partial X} = v_c = \frac{\partial\theta_c}{\partial X} = \frac{1}{y^n}\frac{\partial}{\partial y}\left(y^n k(\theta)\frac{\partial\theta_c}{\partial y}\right) = 0, \tag{8}$$

which is valid to all powers of L^{-1}. In other words, the core velocity and temperature fields are fully developed and independent of the X-coordinate. In the core, the isotherms are parallel to the filament, and convection (even when time-dependent) plays no role.

For a given $k(\theta)$, the energy, Eq. (8), can be integrated. For example, when the thermal conductivity is a linear function of temperature, $k(\theta) = 1 + k_\theta(\theta - (\frac{1}{2}))$, where $k(\frac{1}{2}) = 1$ and $k_\theta = (\partial k/\partial\theta)_{\theta=1/2}$, then

$$(2 - k_\theta + k_\theta\theta_c(y))\theta_c(y) = 2\begin{cases} \dfrac{1 - 2y}{1 - d_f} & (n = 0) \\[2ex] \dfrac{\ln(2y)}{\ln(d_f)} & (n = 1) \end{cases}. \tag{9}$$

The corresponding expression for a gas with temperature-independent thermal conductivity is obtained by setting $k_\theta = 0$ in (9).

The power (Q_c) dissipated in the core is

$$Q_c = \begin{cases} \dfrac{4L}{1 - d_f} & (n = 0) \\ -\dfrac{2\pi L}{\ln (d_f)} & (n = 1) \end{cases} , \tag{10}$$

where the power dissipation is normalized with $\overline{k^*}(T_f^* - T_w^*)(d_H^*)^n$. In the planar case, the power dissipation, Q_c^*, is computed per unit width of the filament.

Leading and Trailing Edge Regions. The core solution is not valid when $X \to 0$ and $X \to 1$. Equation (6) suggests the presence of boundary layers of length L^{-1} next to the leading and trailing edges. We introduce the stretched leading and trailing coordinates, $\xi^+ = x = LX$ and $\xi^- = L - x = L(1 - X)$, respectively. The superscripts (+/−) denote, respectively, the leading/trailing edge variables. For brevity's sake, we reproduce here only the boundary layer energy equation:

$$\mathrm{Pe}\rho^{\pm}\left(\frac{\partial\theta^{\pm}}{\partial t} \pm u^{\pm}\frac{\partial\theta^{\pm}}{\partial\xi^{\pm}} + v^{\pm}\frac{\partial\theta^{\pm}}{\partial y}\right)$$

$$= \frac{\partial}{\partial\zeta^{\pm}}\left(k^{\pm}\frac{\partial\theta^{\pm}}{\partial\xi^{\pm}}\right) + \frac{1}{y^n}\frac{\partial}{\partial y}\left(y^n k^{\pm}\frac{\partial\theta^{\pm}}{\partial y}\right). \tag{11}$$

The temperature boundary conditions are:

$$\frac{\partial\theta^{\pm}(\xi^{\pm}, 0)}{\partial y} = 0 \quad (-\infty < \xi^{\pm} < 0);$$

$$\theta^{\pm}\left(\xi^{\pm}, \frac{d_f}{2}\right) = 1 \quad (0 < \xi^{\pm} < +\infty);$$

$$\theta^{\pm}\left(\xi^{\pm}, \frac{1}{2}\right) = 0 \quad (-\infty < \xi^{\pm} < +\infty,);$$

and

$$\lim_{\xi^{\pm}\to+\infty} \theta^{\pm}(\xi^{\pm}, y) = \theta_c(y).$$

The boundary layer equations are similar to the original Eqs. (1–4), albeit with a simpler domain of definition. The boundary layer problems are independent of the filament's length L.

In order to solve the boundary layer energy Eq. (11), and the corresponding momentum equations (not shown here), we proceed with a regular perturbation expansion in powers of Pe:

$$\begin{pmatrix} \theta^{\pm} \\ \mathrm{Pe}u^{\pm} \\ \mathrm{Pe}v^{\pm} \\ \rho^{\pm} \\ \mu^{\pm} \\ k^{\pm} \\ P^{\pm} \end{pmatrix} = \begin{pmatrix} \theta_0^{\pm} \\ 0 \\ 0 \\ \rho(\theta_0^{\pm}) \\ \mu(\theta_0^{\pm}) \\ k(\theta_0^{\pm}) \\ P_0 \end{pmatrix} + \mathrm{Pe}\begin{pmatrix} \theta_1^{\pm} \\ u_1^{\pm} \\ v_1^{\pm} \\ \rho_\theta(\theta_0^{\pm})\theta_1^{\pm} \\ \mu_\theta(\theta_0^{\pm})\theta_1^{\pm} \\ k_\theta(\theta_0^{\pm})\theta_1^{\pm} \\ P_\theta(\theta_0^{\pm})\theta_1^{\pm} \end{pmatrix} + O(\mathrm{Pe}^2). \tag{12}$$

We substitute (12) into the boundary layer equations (such as 11) and equate the coefficients of like powers in Pe to obtain a set of equations for different orders of the Pe number (see Huang, 1995, for details). At zeroth order $O(\mathrm{Pe}^0)$, we obtain the conduction equation for θ_0. By inspection, we conclude that the temperature profiles in the trailing and leading edges are symmetric:

$$\theta_0^+(\xi^+, y) = \theta_0^-(\xi^-, y). \tag{13}$$

To the first order, $O(\mathrm{Pe}^1)$, we obtain creeping flow with

$$\{u_1^+(\xi^+, y, t), v_1^+(\xi^+, y, t), \theta_1^+(\xi^+, y, t)\}$$
$$= \{u_1^-(\xi^-, y, t), -v_1^-(\xi^-, y, t), -\theta_1^-(\xi^-, y, t)\}. \tag{14}$$

Composite Expansion. The uniformly valid, composite expansion for the temperature field is:

$$\theta(x, y, t) = \theta_0^+(x, y) + \theta_0^-(L - x, y) - \theta_c(x, y)$$
$$+ \mathrm{Pe}(\theta_1^+(x, y, t) - \theta_1^+(L - x, y, t)) + O(\mathrm{Pe}^2). \tag{15}$$

When one calculates the filament's power dissipation, the trailing and leading edges' first order, $O(\mathrm{Pe})$, contributions cancel each other and $Q_1 = 0$. Thus, the filament's total power dissipation is

$$Q = Q_0 + Q_2\mathrm{Pe}^2 + O(\mathrm{Pe}^3), \tag{16}$$

where Q_0 is the power dissipation in the absence of convection and Q_2 can be obtained by solving the second order, $O(\mathrm{Pe}^2)$ problem.

Since $Q_1 = 0$, the analysis presented above explains the experimental observation that $(dQ/d\mathrm{Pe})_{\mathrm{Pe}=0} = 0$. Note that the coefficients Q_i $(i > 0)$ in the series (16) are independent of L, and they can be obtained by solving the leading (or trailing) edge equations.

Example. In order to make these ideas more concrete, we proceed with a simple example. Consider plug flow ($u \equiv 1$) of a gas with temperature-independent thermophysical properties in a planar TCD with a zero thickness filament ($d_f = 0$). The core temperature distribution is

$$\theta_c(y) = 1 - 2y. \tag{17}$$

The leading (trailing) edge temperature satisfies

$$\mathrm{Pe}\frac{\partial\theta^{\pm}}{\partial\xi^{\pm}} = \frac{\partial^2\theta^{\pm}}{\partial\xi^{\pm 2}} + \frac{\partial^2\theta^{\pm}}{\partial y^2}, \tag{18}$$

with the boundary conditions,

$$\lim_{\xi^{\pm}\to-\infty} \theta^{\pm}(\xi^{\pm}, y) = 0 \quad \text{and} \quad \lim_{\xi^{\pm}\to\infty} \theta^{\pm}(\xi^{\pm}, y) = 1 - 2y,$$
$$\text{when} \quad (0 < y < \tfrac{1}{2});$$

$$\theta^{\pm}(\xi^{\pm}, 0) = 1 \quad \text{when} \quad (\xi^{\pm} > 0);$$

$$\frac{\partial\theta^{\pm}(\xi^{\pm}, 0)}{\partial y} = 0 \quad \text{when} \quad \xi^{\pm} < 0;$$

and

$$\theta^{\pm}(\xi^{\pm}, \tfrac{1}{2}) = 0 \quad (-\infty < \xi^{\pm} < \infty).$$

To solve Eq. (18), we use the conformal mapping (Moon & Spencer, 1971),

$$\xi_{\pm} + iy = \frac{1}{\pi}\mathrm{Ln}\,[\mathrm{Cosh}\,(s + iw)], \tag{19}$$

to transform the domain $(\xi_{\pm}, y)$ into a semi-infinite strip.

With the aid of Mathematica (Wolfram, 1991), we express Eq. (19) in terms of the $\{s, w\}$ coordinates,

$$\frac{\mathrm{Pe}}{\pi[\mathrm{Cosh}\,(2s) + \mathrm{Cos}\,(2w)]}\left[\frac{\partial\theta^{\pm}}{\partial s}\mathrm{Sinh}\,(2s) - \frac{\partial\theta^{\pm}}{\partial w}\mathrm{Sin}\,(2w)\right]$$
$$= \frac{\partial^2\theta^{\pm}}{\partial s^2} + \frac{\partial^2\theta^{\pm}}{\partial w^2}. \tag{20}$$

The boundary conditions are

$$\theta^{\pm}(s, 0) - 1 = \theta^{\pm}\left(s, \frac{\pi}{2}\right) = 0 \quad (0 < s < \infty)$$

and

$$\frac{\partial\theta^{\pm}(0, w)}{\partial s} = \lim_{s\to\infty}\left(\theta^{\pm}(s, w) - \left(1 - \frac{2w}{\pi}\right)\right) = 0$$

$$\left(0 < w < \frac{\pi}{2}\right).$$

We solve Eq. (20) using the regular perturbation expansion (12) in terms of Pe to obtain

$$\theta_0^{\pm}(s, w) = 1 - \frac{2w}{\pi}$$

and

$$\theta_1^{\pm}(s, w) = \left(\mp \frac{s}{\pi^2}\right) \mathrm{Tan}^{-1}\left[\frac{\mathrm{Sin}\,(2w)}{e^{2s} + \mathrm{Cos}\,(2w)}\right]$$

$$\pm \sum_{n=1}^{\infty} \frac{(-1)^n}{2n^2\pi^2} e^{-2ns}\,\mathrm{Sin}\,(2nw). \quad (21)$$

Note the sign difference between the leading and trailing edge solutions. $\theta_2^{\pm}$ was computed numerically using a central differences scheme. The uniformly valid temperature distribution ($\theta_{composite}$) is:

$$\theta_{composite}(x, y) = 1 - \frac{2}{\pi}[w(x, y) + w(L - x, y)] + 2y$$

$$+ \mathrm{Pe}(\theta_1^{+}(x, y) - \theta_1^{+}(L - x, y)) + O(\mathrm{Pe}^2), \quad (22)$$

where $w(\xi^{\pm}, y)$ is implicitly given by Eq. (19).

The heat flux along the filament is

$$q(x) = 2(g(x) + g(L - x) - 1) + \mathrm{Pe}(f(\mathrm{Cosh}^{-1}(e^{\pi x/2}))$$

$$- f(\mathrm{Cosh}^{-1}(e^{\pi(L-x)/2}))) + O(\mathrm{Pe}^2), \quad (23)$$

where

$$g(x) = \frac{1}{\sqrt{1 - e^{-\pi x}}}$$

and

$$f(\sigma) = \frac{1}{2\pi}\{\sigma - \tfrac{1}{2}\,\mathrm{Coth}\,(\sigma)\ln[2(1 + \mathrm{Cosh}\,(2\sigma))]\}.$$

Accounting for the fact that the filament loses heat from its two faces, the filament's power dissipation is

$$\frac{Q}{Q_0} = 1 + C_1\mathrm{Pe}^2 + O(\mathrm{Pe}^3), \quad (24)$$

where

$$Q_0 = -4L + \frac{8}{\pi}\ln\left(\frac{1 + \sqrt{1 - e^{-\pi L}}}{1 - \sqrt{1 - e^{-\pi L}}}\right)$$

$$\approx 4L + \frac{8}{\pi}\ln(4) \quad (\text{for } L \gg 1).$$

For example, for $L = 25$, $C_1 \sim 1.1 \times 10^{-3}$.

From this analysis, one may conclude the following: (i) since the end effects are confined to the boundary layers, they are independent of the filament's length. The longer the filament, the longer is the core region and the smaller are the end effects' relative contributions; (ii) convective effects, both time-dependent and time-independent, are confined to the leading and trailing edges. The core region's power dissipation is independent of convection; and (iii) at low Peclet numbers, the filament's power dissipation depends on Pe^2.

4 The Effect of Time-Independent Convection on the TCD's Power Dissipation

The time-independent versions of Eqs. (1–5) were solved using the SIMPLER algorithm (Patankar, 1980). The upstream and downstream velocity profiles far from the filament's edges (at $x = -L/2$ and $x = 1.8L$) were specified as fully developed, parabolic profiles. The code was verified for self-consistency by demonstrating that computational results were grid-size independent. The relative difference between the filament's power dissipation calculated using 60 × 50 and 300 × 100 grid points was smaller than 0.2 percent for nitrogen flow at Re = 60. In most of the calculations reported here, 60 × 50 grid points were used. Additionally, we solved a sequence of simple problems, including the one described in Section 3, for which analytical solutions could be obtained, and verified that the numerical and analytical results were in good agreement. For instance, Fig. 2 depicts the numerically computed Q_{conv} as a function of the Pe number for similar conditions as the example in Section 3. In Fig. 2, $L = 25$ and only one face of the flat filament dissipates heat (Q_0 is half of the value given in Eq. 24). The figure also depicts the small ($Q_{conv} \propto \mathrm{Pe}^2$, Section 3) and large Pe number asymptotes ($Q_{conv} \propto \sqrt{\mathrm{Pe}}$). Since we are interested only in small and moderate Pe number behavior, we did not include here the asymptotic analysis for large Pe numbers. Witness the good agreement between the asymptotic and the numerical predictions. Further details on code verification are given in Huang (1995).

Unless otherwise stated, results are presented for nitrogen gas with $T_f^* = 235$C, $T_w^* = 100$C, and $L^*/d_H^* = 25.6$. The specification of the gas and the temperatures is necessary because of the temperature-dependence of the gas' thermophysical properties. The results for the planar geometry are qualitatively similar to the ones presented here.

Figure 3 depicts the nondimensional temperature as a function of y at locations A_1 and A_2 for Re = 0, 5, 25, and 60. Differences between the temperature profiles for the different Reynolds numbers are visible only at the filament's leading edge. A short distance from the leading edge, the temperature profile assumes its fully developed, conductive shape.

For Re = 40, Fig. 4 depicts the temperature field (isotherms) in a cross-section that is parallel to the flow direction. In agreement with the asymptotic analysis (Section 3), the isotherms

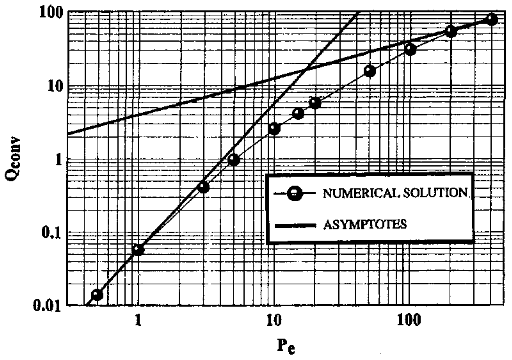

Fig. 2 For a flat filament dissipating heat from one face, Q_{conv} is depicted as a function of the Peclet number. The results of the numerical simulations are compared with analytically obtained asymptotes for small and large Peclet numbers, $L = 25$.

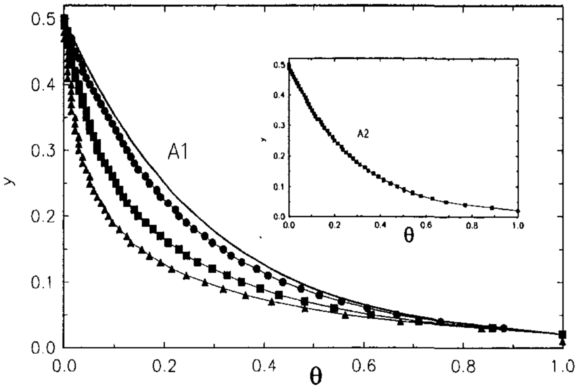

Fig. 3 **Numerically computed temperature profiles for various Reynolds numbers at the cylindrical filament's leading edge (A1) and the center of the filament (A2) for Re = 0 (solid line), 5 (circles), 25 (squares), and 60 (triangles)**

are parallel to the filament throughout most of its length. Parallel isotherms correspond to fully developed thermal conditions. Figure 4 indicates that along most of the filament's length, axial convection has no effect.

We define the hydrodynamic (l_H, circles) and thermal (l_T, squares) development lengths as the distance from the filament's leading (solid symbols) and trailing (hollow symbols) edges to points where the differences between the shear stress and the heat flux and their fully developed values are smaller than 1 percent. Figure 5 depicts these development lengths as functions of the Reynolds number. As the Reynolds number increases, the leading edge l_H and l_T increase, the trailing edge l_T decreases, and the trailing edge l_H initially increases from zero (at no flow) to a maximum and then decreases.

Next, we compare the filament's computed power dissipation with the measured one. For cylindrical and planar TCDs (with the same height as the cylinder's diameter), Fig. 6 depicts the normalized difference between the power consumption in the presence and absence of flow as a function of the Reynolds number. The lines and symbols denote, respectively, theoretical and experimental results. The solid circles and triangles correspond, respectively, to nitrogen and helium. The heavy and light dashed lines describe, respectively, theoretical predictions for nitrogen and helium flow in a cylindrical TCD. The dotted line describes the power dissipation in a planar TCD.

For nitrogen, the discrepancy between the computed and measured results is smaller than 15 percent and decreases as the flow rate increases. This discrepancy between the theoretical and experimental results can be attributed, in part, to (i) the difference between the TCD geometry used in the calculations (cylindrical) and the one employed in the experiments (rectangular), (ii) the fact that the theory ignores the presence of the supporting pins, and (iii) the fact that the filament's temperature is not strictly uniform.

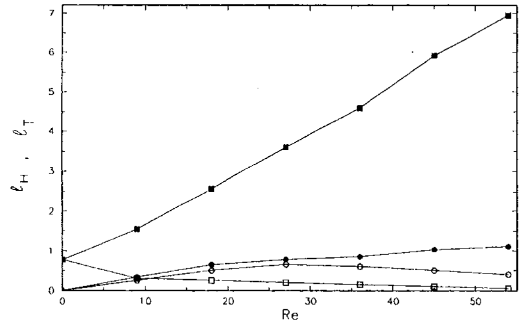

Fig. 5 **The leading (solid symbols) and trailing (hollow symbols), hydrodynamic (circles) and thermal (squares) development lengths are depicted as functions of the Reynolds number for a cylindrical TCD**

For helium, the discrepancy between the theoretical and experimental results is much larger than for nitrogen. We are not certain what the reason for this deviation might be. We suspect, however, that the deviation is caused by the presence of contaminants. Huang (1995) was able to eliminate the discrepancy between the experimental data and the theoretical results for helium by assuming that, at zero flow rate, the helium contained about 0.36 percent of air and that the air concentration declined as the flow rate increased.

Finally, Fig. 6 illustrates that convective power dissipation plays a more important role in a planar TCD than in a cylindrical one with the same diameter as the planar TCD's height. If one's objective is to minimize the relative contribution of convection to the total power dissipation, then the cylindrical TCD has a clear advantage over the planar one.

In agreement with the experimental data, the theoretical curves in Fig. 6 exhibit two regions. For Pe < Pe_1, Q_{conv} increases slowly with Pe. In this region, one can correlate the numerical data as $Q_{conv}/Q_0 = C_1 Pe^2$. For Pe > Pe_2, Q_{conv} increases nearly linearly as a function of Pe, $Q_{conv}/Q_0 = C_3 + C_2 Pe$. In the above, C_i and Pe_i are functions of the TCD geometry and the gases' thermophysical properties. For example, for nitrogen flow in a cylindrical TCD, $Pe_1 \sim 12$ and $Pe_2 \sim 25$.

In Section 3, we showed that the quadratic behavior for Pe < Pe_1 is a result of first order effects, $O(Pe)$, at the leading and trailing edges canceling each other. For moderate Pe numbers (Pe > Pe_2), the trailing edge boundary layer is pushed out

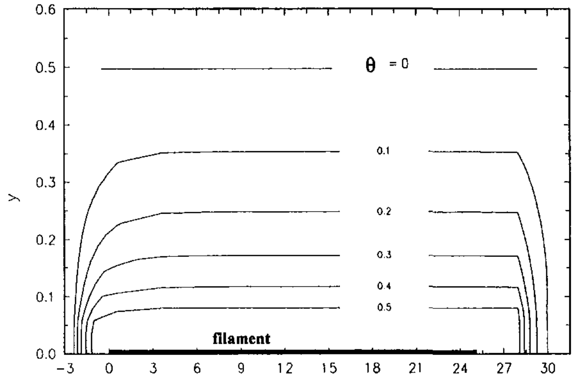

Fig. 4 **The temperature field (isotherms) in a cylindrical TCD's cross-section that is parallel to the direction of the flow, Re = 40**

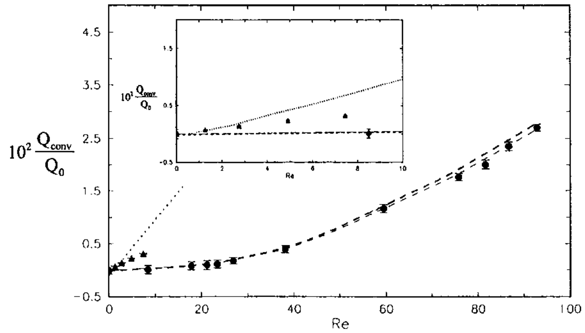

Fig. 6 **The relative contribution by convection to the power dissipation as a function of the Reynolds number for cylindrical and planar TCDs. The circles and triangles correspond, respectively, to experimental data for nitrogen and helium. The heavy and light dashed lines represent, respectively, numerical data for nitrogen and helium in a cylindrical TCD. The dotted line represents numerical data for nitrogen flow in a planar TCD.**

and it does not play a role in the heat transfer process. The convective heat transfer is affected only by the temperature distribution at the leading edge, which is a first order effect, and therefore the power dissipation is approximately a linear function of Pe.

5 The Effect of Time-Periodic Flow on the TCD'S Response

Oscillations in the flow rate cause fluctuations in the TCD's power dissipation. These oscillations are interpreted by the TCD operator as noise, and they compromise the TCD's accuracy. In this section, we quantify the effect of such oscillations on the TCD's response. All the results are given for nitrogen and a cylindrical TCD.

We solved the time-dependent, Eqs. (1–5), with the velocity boundary condition at $x = 0$:

$$\frac{u(y)}{u_{\max}} = (1 - 4y^2)(1 + \epsilon \operatorname{Sin}(\omega t)) \quad (0 \le y \le \tfrac{1}{2}), \qquad (25)$$

where ϵ is the velocity oscillations' amplitude. $\omega = \omega^* d_H^2/\alpha^*$ and ω^* are the nondimensional and dimensional angular frequencies, respectively.

Although the equations are not linear, the effect of the oscillations on the nonlinear terms is $O(\epsilon^2)$, where $\epsilon \ll 1$. Thus, the local heat flux $q(x, t)$ and the TCD's total power dissipation $Q(t)$ can be approximately expressed, respectively, as

$$q(x, t) \cong q_0(x) + q_{\text{conv}}(x) + \phi(x) \sin(\omega t + \varphi) \qquad (26)$$

and

$$Q \cong Q_0 + Q_{\text{conv}}(1 + \delta \sin(\omega t + \varphi)). \qquad (27)$$

In the above, $\phi(x)$ and δ are, respectively, the amplitudes of the heat flux and the power oscillations.

Figure 7 depicts the relative disturbance amplitude of the convective heat flux $\phi(x)/q0$ as a function of the normalized axial coordinate x for $\epsilon = 0.01$, $\omega = 0.044$, and Re = 3, 12, 15, 22, 38, and 61. $q0$ is the heat flux in the core region. The heat flux disturbance damps quickly as the distance from the leading edge increases. In other words, the effect of flow oscillations on the filament's power consumption is confined mostly to the leading edge region. Once the temperature profile becomes fully developed, the filament's power dissipation is independent of flow conditions.

The effect of the flow rate oscillations' frequency (ω) on the amplitude of the convective power oscillations ($\delta Q_{conv}/(\epsilon Q_0)$) is depicted in Fig. 8. For relatively low frequencies ($\omega < 1$), the amplitude of the convective power dissipation is a flat function of the frequency. There is a cut-off frequency at $\omega \sim 1$, beyond which the amplitude drops down sharply. One percent oscillations in the velocity caused about 0.0057 percent oscillations in the power dissipation, which is in good agreement with our experimental observations (Huang, 1995).

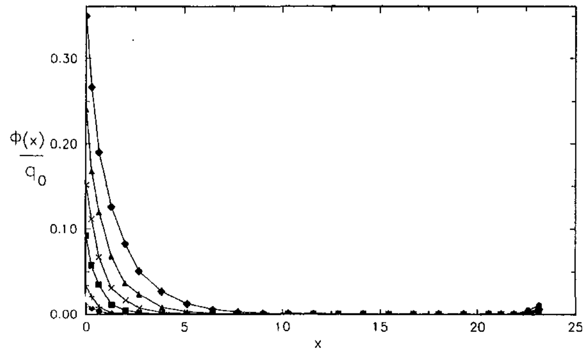

Fig. 7 The relative amplitude of the local heat flux at the cylindrical filament's surface as a function of the axial distance from the leading edge for Re = 3 (circles), Re = 12 (pluses), Re = 15 (squares), Re = 22 (crosses), Re = 38 (triangles), and Re = 61 (diamonds). The flow oscillations have an amplitude of ϵ = 1 percent, and an angular frequency ω = 0.044.

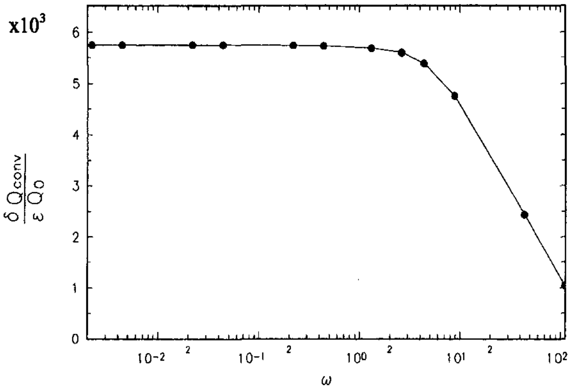

Fig. 8 The normalized amplitude of power oscillations as a function of the flow rate frequency: Re = 40; ϵ = 0.01

For Re = 40 and ω = 0.044, we examined the relationship between the amplitude of the convective power dissipation and the amplitude of the flow rate oscillations. We found that $\delta Q_{conv}/Q_0$ increases nearly as a linear function of ϵ. For the range of ϵ values considered here, Q's frequency was always the same as the frequency of the flow oscillations.

6 Conclusions

The effect of convection on the performance of the TCD was investigated theoretically. The length of the filament can be divided into three regions: leading edge, core, and trailing edge. The power dissipation in the leading and trailing edges is affected by convection. The power dissipation in the core is independent of both time-independent and time-dependent convection. If the leading and trailing edge regions were excluded from the area being sensed but were still maintained at the filament's temperature, then the dependence of the filament's power consumption on convection would be significantly reduced. Alternatively, the longer the filament is, the smaller the relative contribution of convection to the power dissipation will be. When the TCD is used in chromatography, however, the filament length cannot be increased without limit since increases in length may reduce, among other things, its sensitivity to the passage of short slugs of effluent. For small and moderate Peclet numbers, the convective power dissipation is, respectively, a quadratic and a linear function of the Peclet number.

Acknowledgments

This work was supported in part by a grant from the Hewlett-Packard, Little Falls Site, 2850 Centerville Rd, Wilmington, Delaware, 19808. We are grateful to HP's Dr. Leonid Blumberg for useful discussions and encouragement.

References

Batchelor, G., 1967, *An Introduction to Fluid Mechanics*, Cambridge.

Guiochou, G., and Guillemin, C. L., 1988, *Quantitative Gas Chromatography for Lab Analysis and On-Line Process Control*, Elsevier, Amsterdam.

Giddings, J. C., 1991, *Unified Separation Science*, Wiley, N.Y.

Huang, Y., 1995, *Transport Processes in Thermal Conductivity Detectors, Ph.D. dissertation*, University of Pennsylvania.

Issa, R. I., and Lockwood, F. C., 1977, "On the Prediction of Two-Dimensional Supersonic Viscous Interactions Near Walls," *AIAA J.*, Vol. 15, pp. 182–188.

Jerman, J. H., 1981, *A Miniature, Thin Film Thermal Conductivity Detector for an Integrated Gas Chromatograph,* Technical report G-109-2, Stanford University.

Kreith, F., and Bohn, M. S., 1986, *Principles of Heat Transfer,* Harper & Row.

Littlewood, A. B., 1970, *Gas Chromatography,* Academic Press.

Messaros, D. W., Law, C. E., Kolloff, R. H., Gearhart, R. C., and Freeman, R. R., 1984, *A New Low Volume, Single Filament-Single Column Thermal Conductivity Detector for Use with Open Tubular Columns, Gas Chromatography,* HP Technical Paper 104.

Moon, P., and Spencer, D. E., 1971, *Field Theory Handbook,* Springer-Verlag, Berlin.

Patankar, S. V., 1980, *Numerical Heat Transfer and Fluid Flow,* McGraw-Hill, New York.

Terry, S. C., 1975, *A Gas Chromatography System Fabricated on a Silicon Wafer Using Integrated Circuit Technology,* Technical report 4603-1, Stanford University.

Wells, G., and Simon, R., 1983, "Thermal Conductivity Detector: Theory and Numerical Model," *J. Chromatography,* Vol. 256, pp. 1–15.

Wolfram, S., 1991, *Mathematica,* Addison Wesley.

A. M. Osman[1]

K. J. Dowding

J. V. Beck

Heat Transfer Group
Department of Mechanical Engineering
Composite Materials and Structures Center
Michigan State University
East Lansing, MI 48824

Numerical Solution of the General Two-Dimensional Inverse Heat Conduction Problem (IHCP)

This paper presents a method for calculating the heat flux at the surface of a body from experimentally measured transient temperature data, which has been called the inverse heat conduction problem (IHCP). The analysis allows for two-dimensional heat flow in an arbitrarily shaped body and orthotropic temperature dependent thermal properties. A combined function specification and regularization method is used to solve the IHCP with a sequential-in-time concept used to improve the computational efficiency. To enhance the accuracy, the future information used in the sequential-in-time method and the regularization parameter are variable during the analysis. An example using numerically simulated data is presented to demonstrate the application of the method. Finally, a case using actual experimental data is presented. For this case, the boundary condition was experimentally measured and hence, it was known. A good comparison is demonstrated between the known and estimated boundary conditions for the analysis of the numerical, as well as the experimental data.

1 Introduction

In conventional heat conduction problems, interior temperature distributions of a solid body are calculated when the boundary/initial conditions are known. Conversely, in the inverse heat conduction problem (IHCP), the unknown surface heat flux is estimated by utilizing transient temperature measurements inside the solid. The conventional heat conduction problem is traditionally called the direct problem to distinguish it from the inverse problem.

Several schemes have been developed for the solution of the IHCP. In the exact matching method, proposed by Stolz (1960), the unknown heat flux components are estimated by exact matching between the measured temperatures and the corresponding calculated temperatures. Stolz's method is unstable in cases with small time steps and in the presence of measurement errors. Another solution technique is the sequential, function specification method, Beck et al. (1985). Publications employing this latter method include Bass et al. (1980) and Osman and Beck (1989a, 1990). Beck (1993) presented a comparison of this method with a whole domain method.

Another widely used technique is the "whole time domain" regularization method in which the unknown function is discretized into many components and these components are estimated simultaneously. Many authors have reported their studies on this approach including Tikhonov and Arsenin (1977), Hensel (1991), Jarny et al. (1991), Ozisik (1993), and Alifanov (1994). Another method used is the mollification method, Murio (1993).

The combined function specification and regularization (CFSR) method is used in this investigation for the solution of the IHCP. In addition, a sequential-in-time procedure is implemented for the solution. The sequential procedure allows the use of a quasi-linear approximation in the calculations of temperatures and sensitivity coefficients. This, conceptually, results in a substantial reduction of the computer time; memory requirements are also reduced. The reasons are: (1) it is not required to store data for the whole time domain; (2) considering additional time steps in the analysis increases computational requirements linearly; and (3) iteration is not required for non-linear problems.

The contents of this paper are briefly outlined below. First, the inverse problem and its mathematical model are presented in Section 2. Section 3 discusses the combined function specification and regularization method. Test cases, including numerical and experimental data, are presented in Section 4. The last section, Section 5, gives conclusions.

2 Problem Description

The mathematical description of a general two-dimensional, nonlinear inverse heat conduction problem is given in this section. In order to motivate the work, the physical geometry of a typical two-dimensional planar or axisymmetric cylindrical body with temperature-dependent thermal properties is considered. The spatial domain is Ω and the symbols Γ_i ($i = 1, 2, 3$, and 4) represent the domain boundaries. The boundaries Γ_1, Γ_2, and Γ_3 have known boundary condition of the first, second, and third kinds, respectively, while an unknown space-and-time dependent heat flux is to be estimated on boundary Γ_4. The vector $\hat{\mathbf{n}}$ denotes the outward pointing unit vector. Interior temperature histories are measured at several appropriate locations within the heat conducting body.

The inverse heat conduction problem is to find the "best" estimate of the unknown surface heat flux distribution around the boundary Γ_4 as a function of time and space. Data used are the interior transient temperature measurements at known locations in the body, which has a known physical description and known thermal conductivities and volumetric heat capacities.

Mathematical Model. The transient temperature distribution inside a two-dimensional region with orthotropic thermal properties is described by the two-dimensional heat conduction equation

---

[1] Present address: Mechanical and Industrial Engineering, Kuwait University, Safat, 13060, Kuwait.

Contributed by the Heat Transfer Division for publication in the Journal of Heat Transfer. Manuscript received by the Heat Transfer Division January 19, 1996; revision received September 13, 1996; Keywords: Conduction, Numerical Methods, Transient & Unsteady Heat Transfer. Associate Technical Editor: R. Boyd.

$$\frac{1}{x^n}\frac{\partial}{\partial x}\left(k_x(T)x^n\frac{\partial T(x,y,t)}{\partial x}\right)+\frac{\partial}{\partial y}\left(k_y(T)\frac{\partial T(x,y,t)}{\partial y}\right) = \rho c_p(T)\frac{\partial T(x,y,t)}{\partial t} \quad (x,y)\text{ in }\Omega,\quad (t_o<t\le t_M) \tag{1}$$

with the boundary conditions

$$-k_{x,i}(T)\frac{\partial T(x,y,t)}{\partial x}n_x - k_{y,i}(T)\frac{\partial T(x,y,t)}{\partial y}n_y + h_iT(x,y,t) = f_i(x,y,t) \quad (i=1,2,3)\quad (x,y)\text{ in }\Gamma_i,\quad (t_o<t\le t_M) \tag{2}$$

$$-k_x(T)\frac{\partial T(x,y,t)}{\partial x}n_x - k_y(T)\frac{\partial T(x,y,t)}{\partial y}n_y = q(x,y,t)\quad (x,y)\text{ in }\Gamma_4,\quad (t_o<t\le t_M) \tag{3}$$

and the initial condition

$$T(x,y,t_o) = T_o(x,y)\quad (x,y)\text{ in }(\Omega\cup\Gamma) \tag{4}$$

where $n = 0$ for cartesian coordinates and 1 for axisymmetric cylindrical coordinates, (x, y) represents cartesian or cylindrical coordinates system. The boundary conditions in Eq. (2) represent conditions of the first, second, and third kinds ($i = 1$, 2, and 3), respectively. The boundary coefficients $k_{x,i}$, $k_{y,i}$, and h_i are specified to form the correct boundary condition, e.g., $k_{y,3} = k_y(T)$, $k_{x,3} = k_x(T)$, and $h_3 = h(x, y, T)$ specify a convective boundary condition (third kind). The thermal properties (k_x, k_y, ρc_p), boundary conditions (f_i), and initial condition (T_o) are assumed to be completely known. The heat flux in Eq. (3), $q(x, y, t)$ is the unknown function to be estimated. The symbols n_x and n_y are the x- and y-components of the outward pointing unit vector $\hat{\mathbf{n}}$ which is perpendicular to the boundary surface. With this definition of $\hat{\mathbf{n}}$, the heat flux leaving a surface is positive.

To estimate the unknown function $q(x, y, t)$, discrete temperature measurements are available, $Y_{j,m} \equiv Y(x_j, y_j, t_m)$, at sensor j ($j = 1, 2, \ldots, J$) for times t_m, where $m = 1, 2, \ldots, M$. In this paper the commonly accepted definition of the IHCP is addressed. Specifically, all pertinent information about the conducting body, such as the thermal properties and geometry, are assumed to be known; boundary conditions other than $q(x, y, t)$ and the initial condition are also completely known. With the known information the goal is to estimate $q(x, y, t)$ from the internal measurements $Y_{j,m}$.

3 Combined Function Specification and Regularization

This section develops the combined function specification and regularization method (CFSR) used to solve the inverse problem. The inverse heat conduction problem is in a class of ill-posed problems in the sense that arbitrarily small errors in the temperature measurements can lead to arbitrarily large errors in the estimated values of the surface heat flux. Two well known methods for the solution of inverse heat conduction problems are the sequential function specification method, Beck et al. (1985) and the Tikhonov regularization method, Tikhonov and Arsenin (1977). A combined method, called CFSR, is used to stabilize and smooth the estimates of the surface heat flux distribution. A paper by Beck and Murio (1986) presents similar concepts. In their study, Tikhonov regularization was applied to the time variation of heat flux while in this study's formulation, the regularization is applied to the spatial variation of heat flux.

The solution method is based on the finite element technique for numerical solution of the direct heat conduction problem. The details of the CFSR method are given below.

3.1 Parameterization of the Surface Heat Flux Function. The numerical solution of the inverse problem is based on the finite element method for the numerical solution of the direct problem. The finite element method provides a technique for spatially discretizing the body and numerical integration of the resultant system of ordinary differential equations. The finite element code TOPAZ2D (version January 1986) was modified into a direct problem solver subroutine. TOPAZ2D uses linear four node quadrilateral elements.

The first step in the inverse problem solution procedure is to divide the domain into finite elements. The number of finite elements depends on the size of the problem and the distribution of the surface heat flux. More details regarding aspects of the finite element procedure are given in the TOPAZ user's manual (Shapiro, 1986). The next step is to approximate the time-and-space distribution of the continuous heat flux function $q(x, y, t)$ in Eq. (3).

Values of the heat flux are required at the spatial nodes on the surface of the body. In general, the number of surface nodes is very large, this can lead to a large number of unknown heat flux components to be estimated. To reduce the number of unknowns, a parameterization of the spatial distribution of the surface heat flux is used. The functional form used for the approximation of the heat flux is given below.

3.1.1 Spatial-Dependent Heat Flux Approximations. Boundary Γ_4, with the unknown heat flux, is divided into subintervals and a system of parameters are defined for each segment. For convenience, a surface coordinate "s" is used. In this case, the surface heat flux in Eq. (3) can be expressed as

$$q(x,y,t) = q(s,t) \tag{5}$$

where (x, y) is on Γ_4 and s is the surface coordinate along boundary Γ_4.

The parameterization of the arbitrary function $q(s, t)$ for a fixed instant of time is introduced along with a functional form

Nomenclature

c_p = specific heat (J/kgC)
$\mathbf{H}_o$ = zeroth order regularization matrix
$\mathbf{H}_1$ = first order regularization matrix
J = number of temperature sensors
k = thermal conductivity (W/mC)
M = number of discrete measurement times
$\hat{\mathbf{n}}$ = outward normal vector
p = number of spatial heat flux parameters
q = heat flux (W/m^2)
$\hat{q}$ = estimated heat flux (W/m^2)
r = number of future time steps
S_e = mean-squared error (W/m^2)
S_m^α = regularization sum-of-squares
S_m^r = function specification sum-of-squares
s = surface coordinate (m)
T = temperature (°C)
$\hat{T}$ = calculated temperature (°C)
t = time (sec)
W = weighting constant ((°C)$^{-2}$)
X = pulse sensitivity coefficients (°C/(W/m^2))
Y = measured temperature (°C)
α_0 = regularization parameter (zeroth order, (W/m^2)$^{-2}$)
α_1 = regularization parameter (first order, (W/m^2)$^{-2}$)
Δt_e = measurement time step (sec)
σ_T = standard deviation of temperature (°C)
ρ = density (kg/m^3)
ϕ_k = basis function

Subscripts

x = in direction of x-axis
y = in direction of y-axis

which interpolates the selected parameters at all the surface nodes. The function $q(s, t)$ is approximated by piecewise polynomials, of similar or different order, over each surface segment (between the surface parameter nodes),

$$q(s, t) = \sum_{k=1}^{p} \phi_k(s) q_k(t), \tag{6}$$

where p is the total number of spatial parameters, $\phi_k(s)$ is the basis function which can be constant, linear, or quadratic functions between s_k and s_{k+1}, and zero elsewhere. The time-dependent function $q_k(t) = q(s_k, t)$ in Eq. (6) represents the heat flux history at the kth parameter node. Equation (6) provides a spatial approximation of the surface heat flux distribution. The piecewise-polynomial function, which can be a combination of polynomials of different degrees, is used to approximate (parameterize) the spatial distribution of the unknown surface heat flux.

3.1.2 Time-Dependent Heat Flux Approximations. The time-dependent approximation of the surface heat flux is carried out by discretizing the continuous functions $q_k(t)$ in Eq. (6). For convenience, the time interval $t_o < t \le t_M$ is divided into uniform sub-intervals, each of length $\Delta t_e = (t_M - t_o)/M$ with the discrete coordinate $t_m = m\Delta t_e$, $(m = 1, 2, \ldots, M)$. The time steps at which the heat flux is estimated are arbitrary and for convenience are typically selected based on the measurement time step. If the heat flux is desired at intervals other than the measurement time step, interpolation could be used. The time-dependent function $q_k(t)$ at the spatial location s_k is approximated by stair-wise steps on time by

$$q_k(t) = (q_{k,1}, q_{k,2}, \ldots, q_{k,m}, \ldots, q_{k,M}) \tag{7}$$

where $q_{k,m} = q_k(t_m)$ is the value of q at the kth parameter location and at time index m. The choice of piecewise constant segments on time is consistent with the function specification method (FSM). In the FSM the heat flux is assumed constant over r-future time steps (discussed below). Since a typical problem has hundreds or thousands of measurements on time, assuming a more elaborate function on time will not significantly enhance the method (Beck et al., 1996). Therefore, the global approximation of the surface heat flux at time t_m is given by

$$q(s, t_m) = \sum_{k=1}^{p} \phi_k(s) q_{k,m}. \tag{8}$$

The flux components $q_{k,m}$ are the unknown surface heat flux parameters to be estimated. The parameters $q_{k,m}$ are estimated simultaneously in space, index k, and sequentially in time, index m. The approximating model for the surface heat flux $q(s, t)$, over time and space, involves the following parameters:

$$\mathbf{q}^T = [\mathbf{q}_1, \mathbf{q}_2, \ldots, \mathbf{q}_m, \ldots, \mathbf{q}_M] \tag{9a}$$

$$\mathbf{q}_m^T = [q_{1,m}, q_{2,m}, \ldots, q_{k,m}, \ldots, q_{p,m}]. \tag{9b}$$

The goal of the inverse problem is to estimate the components $q_{k,m}$, $k = 1, 2, \ldots, p$ and $m = 1, 2, \ldots, M$ from the interior temperature measurements.

3.2 Objective Function. A sequential-in-time procedure is used to estimate the surface heat flux parameters. The time domain $t_o \le t \le t_M$ is divided into analysis intervals each of length $t_{m-1} \le t \le t_{m+r-1}$ where r is the number of future time steps. The parameters $q_{k,m}$, for $k = 1, 2, \ldots, p$ are estimated simultaneously for each analysis interval.

It is assumed that the parameter vectors $\mathbf{q}_1, \mathbf{q}_2, \ldots, \mathbf{q}_{m-1}$ have been estimated and the task now is to estimate the unknown heat flux vector $\mathbf{q}_m$ for the next analysis interval (t_{m-1}, t_{m+r-1}). The combined function specification and regularization objective function for the analysis interval (t_{m-1}, t_{m+r-1}) is given by

$$S_m(\mathbf{q}) = S_m^r(\mathbf{q}) + S_m^\alpha(\mathbf{q}) \tag{10a}$$

where $S_m^r(\mathbf{q})$ is the function specification sum-of-squares function

$$S_m^r(\mathbf{q}) = \sum_{j=1}^{J} \sum_{i=1}^{r} W_{i,j} [Y_{j,m+i-1} - T_{j,m+i-1}(\mathbf{q})]^2 \tag{10b}$$

and $S_m^\alpha(\mathbf{q})$ is the Tikhonov regularization sum-of-squares function,

$$S_m^\alpha(\mathbf{q}) = \alpha_0 \sum_{k=1}^{p} (q_{k,m})^2 + \alpha_1 \sum_{k=2}^{p} (q_{k,m} - q_{k-1,m})^2. \tag{10c}$$

The objective function combines the function specification and regularization methods. The first part of the objective function (Eq. 10b) reduces the difference between the measured and calculated temperatures, in the least squares sense, over the analysis interval. The second part of the objective function (Eq. 10c) introduces a regularization effect in space and constrains variations in the estimated components.

The first term in the regularization part (Eq. 10c) is the zeroth order regularization, which has the effect of suppressing or eliminating the oscillations in the estimated values. The second term is the first order regularization, which reduces the first differences in the spatial variation of the estimated parameters. There are no explicit *time* regularizations of the zeroth and first order in Eq. (10c).

3.3 Minimization of the Objective Function $S_m(q)$. For the function specification method, a temporary assumption that $\mathbf{q}$ is constant over r future time steps is used

$$\mathbf{q}_m = \mathbf{q}_{m+1} = \ldots = \mathbf{q}_{m+r-1}. \tag{11}$$

Other assumptions on the functional form of q (linear, parabolic, or other approximation) are possible, see Beck et al. (1996). Beck's work showed that assuming higher order functions on time, over the r future time steps, did not significantly improve the estimated heat flux for the one-dimensional IHCP. Hence, the simplicity of the constant assumption over r future time steps is selected for the present method. The number of future time steps selected serves as regularization to stabilize the solution. Hence, for larger values of r, the solution is regularized more. Typical values of r range from 4 to 12, depending on the problem. The effect of r is discussed in Scott and Beck (1989).

In each analysis interval, linearization is introduced by evaluating the thermal properties at time t_{m-1}. With the assumption that $\mathbf{q}$ is constant over r future time steps, Eq. (11), the temperatures $T_{j,m+i-1}(\mathbf{q})$ can then be represented in a Taylor series as

$$T_{j,m+i-1}(\mathbf{q}) = T_{j,m+i-1}(\mathbf{q}^*) + \sum_{k=1}^{p} X_{j,i,k} \Delta q_{k,m} \tag{12a}$$

where $\mathbf{q}^*$ is an initial heat flux vector. The change in the heat flux and sensitivity coefficient are

$$\Delta q_{k,m} = q_{k,m} - q_{k,m}^* \tag{12b}$$

$$X_{j,i,k} = \frac{\partial T_{j,m+i-1}}{\partial q_{k,m}} \tag{12c}$$

where X is the pulse sensitivity coefficient. The difference, $\Delta q_{k,m}$, represents a correction in the heat flux. Since the thermal properties are temporarily held constant, the problem is temporarily linear. Consequently, Eq. (12) is exact and no iteration is required for the calculations of the correction $\Delta q_{k,m}$. This equation is used for the direct inverse problem as discussed below.

Substituting Eq. (12*a*) into (10*b*) and differentiating $S_m(\mathbf{q})$ with respect to the unknown parameters and setting the resulting equations to zero gives the following:

$$\frac{\partial S_m(\mathbf{q})}{\partial q_{l,m}} = 2 \sum_{j=1}^{J} \sum_{i=1}^{r} W_{i,j} \times \{[T_{j,m+i-1}(\mathbf{q}) - Y_{j,m+i-1} + \sum_{k=1}^{p} X_{j,i,k} \Delta q_{k,m}] X_{j,i,l}\} + 2[\alpha_0 q_{l,m} + \alpha_1(-q_{l-1,m} + 2q_{l,m} - q_{l+1,m})] = 0 \quad (13)$$

where $l = 1, 2, \ldots, p$. There are $(p \times 1)$ parameters to be estimated for each analysis interval.

After some algebraic manipulations, Eq. (13) is reduced to the following matrix equation which is a system of algebraic equations:

$$[\mathbf{X}^T\mathbf{W}\mathbf{X} + (\alpha_0 \mathbf{H}_0^T \mathbf{H}_0 + \alpha_1 \mathbf{H}_1^T \mathbf{H}_1)]\Delta\mathbf{q} = \mathbf{X}^T\mathbf{W}(\mathbf{Y} - \mathbf{T}^*) \quad (14a)$$

$$\Delta\mathbf{q} = (\mathbf{q} - \mathbf{q}^*), \quad \text{and} \quad \mathbf{T}^* = \mathbf{T}(\mathbf{q}^*) \quad (14b)$$

where $\mathbf{X}$ is the sensitivity matrix, $\mathbf{W}$ is a symmetric weighting matrix, and $\mathbf{H}_0$, and $\mathbf{H}_1$ are the zeroth, and first order regularization matrices. The regularization matrices are given in Beck et al. (Chapter 4, 1985).

Equation (14*a*) represents the normal equations for the estimation of the unknown parameters. In Eq. (14*a*), if the regularization parameters (α_0, α_1) are set equal to zero, the solution procedure is reduced to the sequential function specification method. On the other hand, the combined function specification and regularization method is appropriate for the following cases: (1) where there are large and sharp variations in the spatial distribution of the surface heat flux; (2) for a relatively large number of parameters compared to the number of sensors, i.e., estimating a number of parameters that is greater than the number of sensors.

The solution of Eq. (14*a*) marches forward in time by first solving for the heat flux correction vector $\Delta\mathbf{q}$ and then updating the heat flux distribution $\mathbf{q} = \Delta\mathbf{q} + \mathbf{q}^*$. The heat flux vector $\mathbf{q}^*$ can be any arbitrary vector. However, $\mathbf{q}^* = 0$ is a common choice. The estimated vector is retained only for the first time interval t_m. Then time index m is increased by one time step and the solution process is repeated by marching in time until the last unknown vector $\mathbf{q}_M$ is estimated. Retaining more than one component is possible, but has not been extensively studied.

3.4 Sensitivity Equations. To utilize the inverse heat transfer algorithm given in Eq. (14*a*), it is necessary to obtain values of the sensitivity coefficients. The sensitivity equation method is used for the calculations of the sensitivity coefficient in Eq. (12*c*). In the calculation of $\Delta\mathbf{q}$ using Eq. (14*a*), the sensitivity matrix $\mathbf{X}$ is found with the thermal properties fixed using the temperature at the previous time step $\hat{T}_{m-1}$. In the next time interval analysis for estimating $\Delta\mathbf{q}$ at the next time step, $\mathbf{X}$ is updated. For temperature-independent thermal properties, the sensitivity coefficients are the same for each analysis time interval (t_{m-1}, t_{m+r-1}), consequently, sensitivity coefficients are computed only for the first analysis interval.

The sensitivity equations are found using the mathematical model in Eqs. (1)—(4) with the following modifications introduced:

1 The analysis time interval is $(t_{m-1} < t \leq t_{m+r-1})$.
2 The initial condition $T_o(x, y)$ in Eq. (4) is replaced by the estimated temperature at time index $m - 1$. In case $m = 1$, the initial temperature distribution is used.
3 The heat flux function $q(x, y, t)$ in Eq. (3) is

$$q(x, y, t_m) = q(s, t_m) = \sum_{k=1}^{p} \phi_k(s) q_{k,m}. \quad (15)$$

4 The heat flux is assumed constant over the analysis time interval

$$\mathbf{q}_m = \mathbf{q}_{m+1} = \ldots = \mathbf{q}_{m+r-1}. \quad (16)$$

5 The thermal properties k and ρc_p are evaluated at the temperature at time $m - 1$ and held constant for the analysis interval (t_{m-1}, t_{m+r-1}). This means that the thermal properties are evaluated at the temperatures at the time t_{m-1} during the r future time steps, but it does not mean that the properties are the same at every location. This results in the problem being temporarily linear.

The sensitivity equations are obtained by differentiating Eqs. (1)–(4), with the above five modifications, with respect to $q_{k,m}$ and defining $X_k = (\partial T(x, y, t))/(\partial q_{k,m})$. After differentiating the following equations are obtained:

$$\frac{1}{x^n} \frac{\partial}{\partial x} \left(k_x(\hat{T}_{m-1}) x^n \frac{\partial X_k(x, y, t)}{\partial x} \right) + \frac{\partial}{\partial y} \left(k_y(\hat{T}_{m-1}) \frac{\partial X_k(x, y, t)}{\partial y} \right) = \rho c_p(\hat{T}_{m-1}) \frac{\partial X_k(x, y, t)}{\partial t}$$

$$(x, y) \text{ in } \Omega, \ (t_{m-1} < t \leq t_{m+r-1}) \quad (17)$$

with the boundary conditions

$$-k_{x,i} \frac{\partial X_k(x, y, t)}{\partial x} n_x - k_{y,i} \frac{\partial X_k(x, y, t)}{\partial y} n_y + h_i X_k(x, y, t) = 0 \quad (i = 1, 2, 3) \quad (x, y) \text{ in } \Gamma_i, \quad (t_{m-1} < t \leq t_{m+r-1}) \quad (18)$$

$$-k_x(\hat{T}_{m-1}) \frac{\partial X_k(x, y, t)}{\partial x} n_x - k_y(\hat{T}_{m-1}) \frac{\partial X_k(x, y, t)}{\partial y} n_y = \phi_k(s) \quad (x, y) \text{ in } \Gamma_4, \quad (t_{m-1} < t \leq t_{m+r-1}) \quad (19)$$

and the initial condition

$$X_k(x, y, t_{m-1}) = 0 \quad (x, y) \text{ in } \Omega \cup \Gamma \quad (20)$$

for $k = 1, 2, \ldots, p$. There are p sensitivity equations.

The kth sensitivity problem, Eqs. (17)–(20), is exactly the same as the direct problem in Eqs. (1)–(4) with three simplifications. First, the initial condition for all sensitivity equations is zero. Second, the heat flux distribution $q(x, y, t)$ in Eq. (3) is replaced by the kth basis function $\phi_k(s)$ in Eq. (19). Third, the known boundary conditions in Eq. (18) are homogeneous.

The numerical computations for the sensitivity coefficients are also simplified because (1) the sensitivity conductivity matrix and the capacitance matrix in the finite element formulation do not change over r future time steps and (2) these matrices are the same as for the temperature problem, therefore reducing the computations required.

Similarities between the temperatures and the sensitivity equations permit the use of the same direct problem solver for the solution of both problems after the required adjustments are made for the initial temperatures and boundary conditions for each problem. The sensitivity equation method is typically more accurate than the finite difference approximation of the sensitivity coefficients, Beck and Arnold (1977, Chapter 7). The sensitivity equation approach removes the dependence on the numerical step size of the finite difference approximation. In situations that require significant effort to solve the sensitivity equations the finite difference approximation may be adequate and much less work to implement. However, care must be used to guard against numerical errors when using a finite difference approximation.

3.5 Computer Program. The algorithm described herein is implemented in the computer program QUENCH2D written at Michigan State University, Osman and Beck (1989b). The finite element code TOPAZ2D (Shapiro, 1986) was modified into a direct problem solver subroutine for the calculation of temperatures and sensitivity coefficients. The direct problem solver was then linked with inverse algorithms to produce the powerful estimation program.

4 Test Cases

4.1 Simulated Data. A numerical experiment is presented to demonstrate the method. Figure 1 shows a schematic of the geometry considered, which models the axisymmetric cylinder wall of an internal combustion engine. The objective is to estimate the heat flux on the inside of the cylinder wall from temperature measurements on the backside. The surface heat flux generated by the combustion gases is modeled using three spatial components. All other surfaces are assumed to be insulated. Six sensors measure the simulated temperature along the back of the cylinder wall. The thermal conductivity is assumed to be temperature dependent and represented as follows:

$$k(T) = k_o + (k_1 - k_o)\left(\frac{T - T_o}{T_1 - T_o}\right) \qquad (21)$$

where $k_o = k(T_o = 0°\mathrm{C}) = 2(W/m - C)$ and $k_1 = k(T_1 = 1000°\mathrm{C}) = 22(W/m - C)$. The thermal conductivity varies nearly an order of magnitude during the simulated experiment, which has a maximum temperature change of 750°C. Although this variation is not typical of most materials, it provides a stringent test for the method and linearization procedure. The volumetric heat capacity was assumed constant $\rho c_P = 3.8 \times 10^6$ J/m^{3}C. A finite element program (TOPAZ2D) is used to generate the simulated temperature data for this nonlinear test case and the data are shown in Fig. 2.

Two analyses of the simulated data are discussed. In the first analysis the heat flux is estimated using "exact" data. The data for the second analysis is corrupted with additive, normally distributed, and zero mean random errors with a standard deviation of $\sigma_T = 5.0°\mathrm{C}$. The estimated heat flux computed using "exact" data is shown in Fig. 3(*a*) for $r = 3$ future steps and no spatial regularization ($\alpha_0 = \alpha_1 = 0$). Fig. 3(*b*) shows the estimates from the analysis with measurement errors. The number of future time steps is $r = 12$ for ($t < 5$ seconds), $r = 10$ for ($5 < t < 75$ seconds), and $r = 8$ for (75 seconds $< t$). Spatial regularization was used for this case, $\alpha_0 = 5.0 \times 10^{-7}$ and $\alpha_1 = 0$. The general effect of r and the spatial regularization are discussed in Scott and Beck (1989). Both of the analyses, with and without measurement errors, are briefly discussed next.

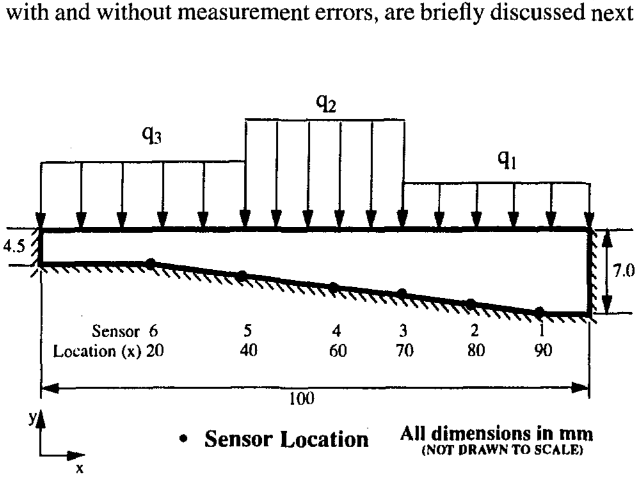

Fig. 1 Geometry and sensor locations for simulated experiment

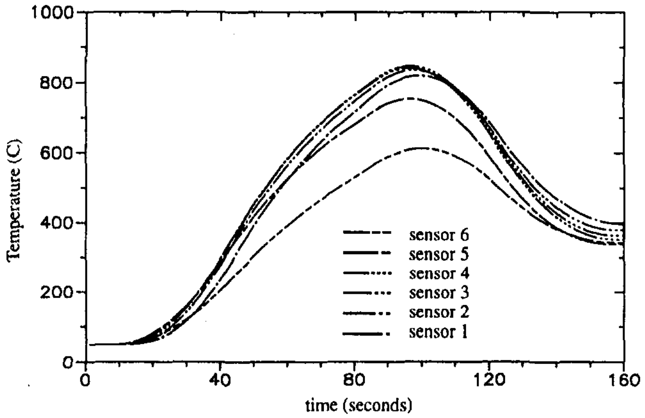

Fig. 2 Simulated experimental data for $\sigma_T = 0$

The surface heat flux is very accurately estimated with the exact data (Fig. 3(*a*)), including the areas of peaks or sudden changes in the heat flux. (The heat flux is positive in the direction of the outward pointing normal.) This accuracy is obtained even though the problem, which is highly non-linear, is temporarily linearizing during the sequential analysis (r-future time steps). Since the problem is linearized, iteration is not required. Consequently, the computational time is greatly reduced, without significantly affecting the accuracy. Notice also that the dimensionless time step (Fourier number) is small ($\alpha\Delta t/L^2 \approx 0.1$), which represents a difficult problem, Beck et al. (1985). Spatial regularization was not required for this case ($\alpha_0 = \alpha_1 = 0$) because the number of sensors was larger than the number of estimated heat flux components. Also, the data was expected to have small errors (actually "exact" for this case).

In the analysis with measurement errors (Fig. 3(*b*)) the heat flux is also accurately estimated. A measure of the accuracy, since the true value is known, is the mean-squared error

$$S_e^2 = \sum_{i=1}^{M} [\hat{q}(t_i) - q(t_i)]^2 \qquad (22)$$

where $\hat{q}(t_i)$ is the estimated component and $q(t_i)$ is the true value (Beck et al., 1985). This measure of the error represents the variance of the estimation and the bias of the estimation algorithm. The mean-squared error for each component is given in Fig. 3(*b*). These mean-squared errors are within four percent of the maximum heat flux for the respective components. The additional future time steps used, compared to the analysis of exact data, reduces the effect of the measurement errors. Using fewer future time steps produces oscillations in the estimates. The effect of using more future time steps (given above), compared to the analysis with exact data, is seen by comparing the estimates with the exact values at the peaks ($t = 40$ and $t = 120$ seconds). When more future time steps are used the estimation algorithm anticipates changes in the heat flux, which results in the smoothing of variations in the heat flux (Beck et al., 1985). Anticipation of the heat flux is a common effect seen when using FSM. The estimated component is computed assuming that the heat flux is constant over the analysis interval. Consequently, if the actual heat flux is increasing (or decreasing) the estimated component will reflect this by biasing slightly high (or low). Hence, the method anticipates changes in the heat flux. The larger the number of future time steps, the earlier the method anticipates the change in the heat flux. These issues are discussed in Scott and Beck (1989).

The errors seen in Fig. 3(*b*) are due to the nature of the inverse problem. It is not possible to replicate the exact flux. In fact, to obtain a solution, stability must be introduced due to the sensitivity of the inverse problem to measurement errors. Hence, to stabilize the problem and reproduce the general shape

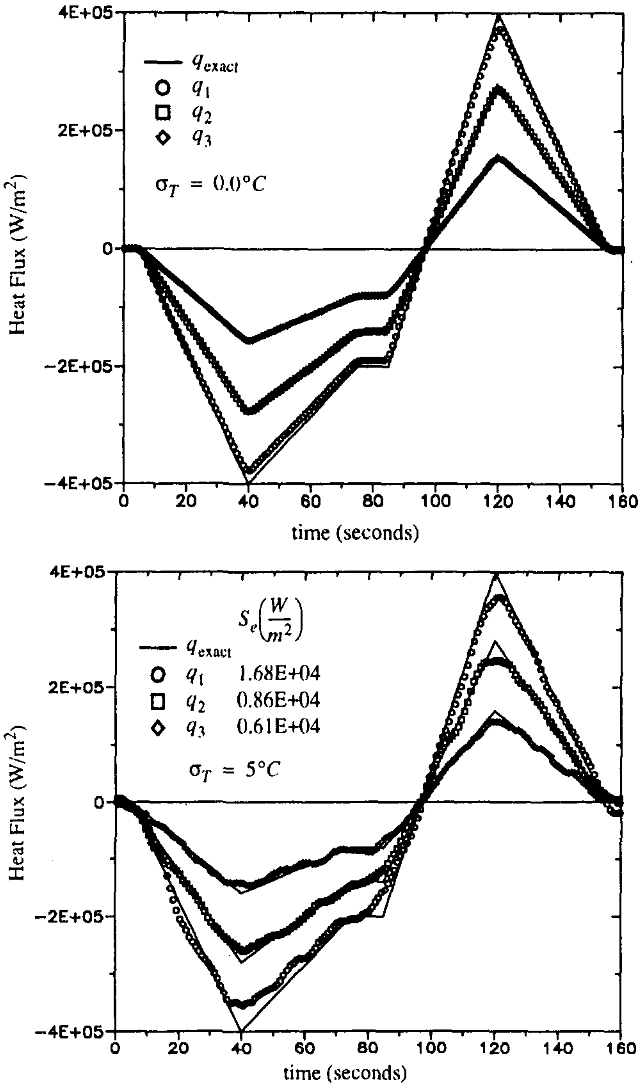

Fig. 3 Estimated heat flux for simulated experiment with $k(T)$: exact data ($\sigma_T = 0$ and $r = 3$); measurement errors ($\sigma_T = 5°C$ and $r = 12$ ($t < 5$ sec); 10 ($5 < t < 75$ sec) and 8 ($75 < t < 160$ sec)

of the heat flux, regularization is required. The use of regularization results in the smoothing of fluctuations and biasing in certain regions.

The previously discussed cases were analyzed on a Pentium P5-100 MHz computer. The finite element discretization used 250 elements and 160 time steps. The analysis required approximately five minutes of computational time.

4.2 Experimental Data. A schematic of an experimental set-up, which was used to estimate the thermal properties of the carbon-carbon composite material, is shown in Fig. 4. By measuring the transient temperatures and power supplied to the mica heater assembly, the thermal properties (orthotropic thermal conductivity and volumetric heat capacity) of a carbon-carbon composite were measured, Dowding et al. (1996). In this paper, using the same experimental data, the opposite problem is considered; the surface heat flux is recovered using the measured thermal properties and transient temperature measurements.

The thermal model of the experimental set-up is shown in Fig. 5. All outer surfaces are assumed to be insulated, except the surface where the energy is introduced by the heater. The energy to the heater is assumed to divide equally between the two symmetric halves and emanate from the middle of the heater assembly ($y = -0.042$ cm); see Fig. 4. The heater assembly contains three independently controlled heaters. Only one of the three heaters is energized (active heater in Fig. 4, the other two heaters are identified as inactive). The temperatures are averaged on opposite sides of the heater assembly to determine the temperature at each location. The sensor are located along $y = 0$ at $x = 0.89$, 1.91, 3.18, 4.45, and 6.73 cm and along $y = 0.91$ cm at $x = 1.27$ and 6.35 cm.

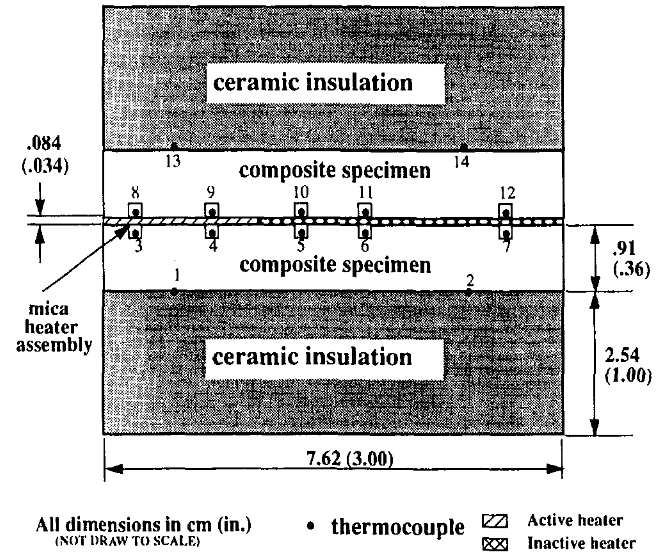

Fig. 4 Experimental set-up with measured surface heat flux

The unknown surface heat flux is parametrized. For this case, the heat flux is assumed to exist only on the $y = -0.042$ cm surface (at the midplane of the mica heat assembly) and all other surfaces are assumed insulated. Two cases are examined. The first has six spatial heat flux components defined for this surface, each 1.27 cm in length. The second case reduces the number of spatial components to four. The first two components are the same as the previous case, while the last four component are paired ($q_3 + q_4 \rightarrow q_3$, $q_5 + q_6 \rightarrow q_4$) to reduce four components to two. The heat flux is assumed to be constant over each spatial component, but varying with time.

The low thermal conductivity ($k = 0.1$ W/m − C) mica heat assembly significantly increases the difficulty of this problem. This makes the IHCP more difficult for two main reasons; the information used to determine the heat flux at the surface is damped and delayed. Because the sensors are above the plane of the active heater element, the effect that the heat flux has at the sensor location is lagged in time and the magnitude of the effect is damped (smaller). The farther away from the surface the sensor(s) is (are) moved, the more pronounced are the

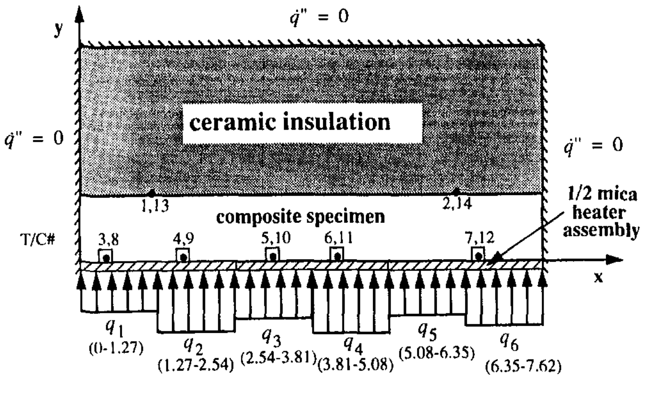

Fig. 5 Model of experimental set-up

lagging and damping effects. Consequently, the estimation problem is more difficult.

Figure 6(*a*) shows the six heat flux components estimated as a function of time and position. The measured heat flux applies for the components (q_1, q_2) in range $0 \le x \le 2.54$ cm, otherwise the heat flux is zero. This estimation problem with experimental data is unique, in that the values being estimated are accurately known. Hence, a comparison is possible between the estimated and known (measured) heat flux using real (experimental) data. The estimated component q_1, q_2 closely approximate the measured values, even where the heat flux has the step change in time. These components are within four percent, outside the region of the step change; errors are understandably larger at the step change. The other four components have a comparable error, relative to the maximum heat flux, with the exception of component q_5. The mean-squared error, Eq. (22), for each component is listed in Fig. 6(*a*). The inaccuracy in component q_5 is the result of a sensor not being located on the region of this component (see Fig. 5). Hence, less information is available for estimating this component and the results reflect this. In practice, the number of components that can be accurately estimated without spatial regularization is less than or equal the number of sensors, for this case five. Estimation of six spatial components was presented to illustrate this point. When the number of spatial components are reduced to four, the overall results are better, see Fig. 6(*b*). The estimated components q_1, q_2 are comparable to the previous estimation. The other two components closely approximate a zero flux.

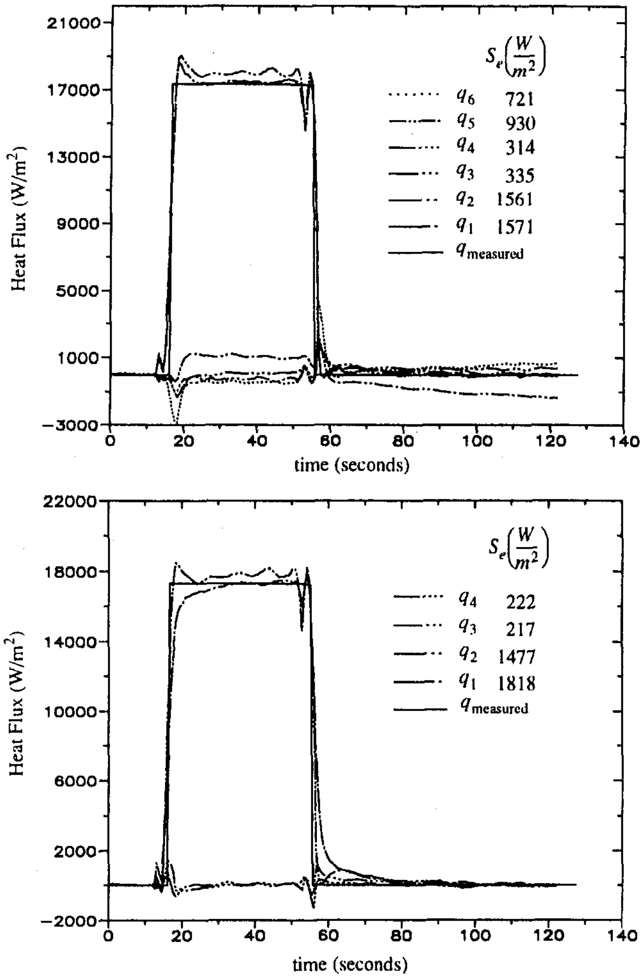

Fig. 6 Comparison of estimated and measured surface heat flux: *a*) six estimated components; *b*) four estimated components.

For the two-dimensional estimation, the number of future time steps is varied over the duration of the analysis. In general, the number is chosen to be small in regions of an abruptly changing heat flux and larger where the variation is more gradual. The number of future time steps, r, is $r = 6$ ($0 < t < 13.4$ sec), 3 ($13.4 < t < 17.9$ sec), 8 ($17.9 < t < 53.1$ sec), 3 ($53.1 < t < 56.3$ sec), and 8 ($t > 56.3$ sec). Selecting the number of future time steps and magnitude of the regularization parameter (α_0, α_1) is done by observing the residuals. The residuals are the difference between the measured and calculated temperatures. Using the residual principle (Alifanov, 1994), the number of future time steps and the regularization parameter were selected such that the sum-of-square, S^r_m, Eq. (10*b*) is reduced to the magnitude expected based on the measurement errors.

5 Summary and Conclusions

A method is presented for the solution of a general nonlinear, two-dimensional inverse heat transfer quenching and many other problems. The objective is to provide estimates of the surface heat flux distribution by using transient temperature measurements at appropriate interior locations inside the body. The method was implemented with a finite element program allowing for two-dimensional planar or cylindrical axisymmetric geometries with irregular boundaries that can be analyzed.

The combined function specification and regularization method is used for the solution of the inverse problem. A sequential-in-time estimation procedure is used for the solution of the inverse problem. A piecewise polynomial function, which can be any combination of the same or different degree polynomials, is used for the parameterization of the spatial distribution of the unknown surface heat flux. This has greatly improved the flexibility in the functional form for the heat flux that is specified.

The sequential-in-time procedure uses a quasi-linear approximation in the calculations of the temperatures and sensitivity coefficients, and formulation of the solution method. This conceptually results in substantial reduction of the computer time and storage requirements. The thermal properties were held constant during the calculations of temperatures and sensitivity coefficients in each analysis interval. This procedure eliminates iterations and reduces the extensive calculations necessary for the reformulation of the finite element conductivity and capacitance matrices.

Test cases presented verify the application and the accuracy of the methods. Using both numerically simulated data and experimental data for a case, where the boundary condition was measured, the surface heat flux was accurately reproduced.

Acknowledgment

The support of General Electric Aircraft Engine Business Group, Cincinnati, OH and Ladish Company, Cauchy, WI is acknowledged. Special thanks to Arthur B. Shapiro of Lawrence Livermore National Laboratory for his consultation during the modification of his program TOPAZ2D. The experimental work was supported by US Air Force contract FY1456-91-N0058 and performed at Michigan State University and Sandia National Laboratories. The input of Ben Blackwell is acknowledged.

References

Alifanov, O. M., 1994, *Inverse Heat Transfer Problems*, Springer-Verlag, New York.

Bass, B. R., Drake, J. B., and Ott, L. J., 1980, ORMDIN: "A Finite Element Program for Two-Dimensional Nonlinear Inverse Heat-Conduction Analysis," NUREG/CR-1709, ORNL/NUREG/CSD/TM-17, U.S. Nuclear Regulatory Commission, Washington, D.C.

Beck, J. V., 1993, "Comparison of the Iterative Regularization and Function Specification Algorithms for the Inverse Heat Conduction Problem," *Inverse*

Problems in Engineering: Theory and Practice, N. Zabaras, K. Woodbury and M. Raynaud, eds., ASME.

Beck, J. V., 1994, "Function Specification Method for Solution of the Inverse Heat Conduction Problem," *Inverse Problems in Diffusion Processes, Proceedings GAMM-SIAM Symposium,* H. Engl and W. Rundell, eds., Society of Industrial and Applied Mechanics, Philadelphia, PA, pp. 1–20.

Beck, J. V., and Arnold, K. J., 1977, *Parameter Estimation in Engineering and Science,* Wiley, New York.

Beck, J. V., and Murio, D., 1984, "Combined Function Specification Regularization Procedure for Solution of Inverse Heat Conduction Problem," AIAA Paper No. AIAA-84-0491.

Beck, J. V., Blackwell, B., and Haji-Sheikh, A., 1996, "Comparison of Some Inverse Heat Conduction Methods Using Experimental Data," *International Journal of Heat and Mass Transfer,* Vol. 39, No. 17, pp. 3649–3657.

Beck, J. V., Blackwell, B., and St. Clair, C. R., 1985, *Inverse Heat Conduction: Ill-Posed Problems,* Wiley, New York.

Dowding, K. J., Beck, J. V., and B. F. Blackwell, 1996, "Estimation of Directional-Dependent Thermal Properties in a Carbon-Carbon Composite," *International Journal of Heat and Mass Transfer,* Vol. 39, No. 15, pp. 3157–3164.

Dowding, K., Beck, J., Ulbrich, A., Blackwell, B., and Hayes, J., 1995, "Estimation of Thermal Properties and Surface Heat Flux in a Carbon-Carbon Composite Material," *Journal of Thermophysics and Heat Transfer,* Vol. 9, No. 2, pp. 345–351.

Hensel, E., 1991, *Inverse Theory and Applications for Engineers,* Prentice Hall, New Jersey.

Jarny, Y., Ozisik, M. N., and Bardon, J. P., 1991, "A General Optimization Method Using Adjoint Equation for Solving Multidimensional Inverse Heat Conduction," *International Journal of Heat and Mass Transfer,* Vol. 34, No. 11, pp. 2911–2919.

Murio, D. A., 1993, *The Mollification Method and Numerical Solution of Ill-Posed Problems,* Wiley, New York.

Osman, A. M., and Beck, J. V., 1989a, "Nonlinear Inverse Problem for the Estimation of Time-and-Space Dependent Heat Transfer Coefficients," *Journal of Thermophysics and Heat Transfer,* Vol. 3, No. 2, pp. 146–152.

Osman, A. M., and Beck, J. V., 1989b, "QUENCH2D: A General Computer Program for Two-Dimensional Inverse Heat Transfer Problems," Heat Transfer Group, Department of Mechanical Engineering, Michigan State University, Report MSU-ENGR-89-017, October 1, 1989.

Osman, A. M., and Beck, J. V., 1990, "Investigation of Transient Heat Transfer Coefficients in Quenching Experiments," ASME JOURNAL OF HEAT TRANSFER, Vol. 112, pp. 843–848.

Ozisik, N. M., 1993, *Heat Conduction,* 2nd ed., Wiley, New York, Chapter 14.

Scott, E. P., and Beck, J. V., 1989, "Analysis of Order of the Sequential Regularization Solutions of Inverse Heat Conduction Problems," ASME JOURNAL OF HEAT TRANSFER, Vol. 111, pp. 218–224.

Shapiro, A. B., 1986, "TOPAZ2D - A Two-Dimensional Finite Element Code for Heat Transfer Analysis, Electrostatic, and Magnetostatic Problems," Lawrence Livermore National Laboratory, Livermore, CA.

Stolz, G., 1960, "Numerical Solutions to an Inverse Problem of Heat Conduction for Simple Shapes," ASME JOURNAL OF HEAT TRANSFER, Vol. 82, pp. 20–26.

Tikhonov, A. N., and Arsenin, V. Y., 1977, *Solutions of Ill-Posed Problems,* V. H. Winston and Sons, Washington, D.C.

A Stochastic Lagrangian Model for Near-Wall Turbulent Heat Transfer

S. Mazumder

M. F. Modest

Department of Mechanical Engineering
The Pennsylvania State University
University Park, PA 16802

The modeling of near-wall turbulent heat transfer necessitates appropriate description of near-wall effects, namely, molecular transport, production of turbulence by inhomogeneities, and dissipation of the temperature fluctuations by viscosity. A stochastic Lagrangian model, based on the velocity-composition joint probability density function (PDF) method, has been proposed. The proposed model, when compared with experimental and direct numerical simulation (DNS) data, overdamps the dissipation of the temperature fluctuations in the inertial sublayer, but reaches the correct limit at the wall. The performance of the model has also been compared to the standard k-ε and the algebraic Reynolds stress model (ARSM) for both constant heat flux and constant temperature boundary conditions at large Reynolds numbers. The Lagrangian nature of the model helps eliminate numerical diffusion completely.

Introduction

The velocity-composition joint PDF method (Pope, 1985) is an important tool for the computation of turbulent reactive flows. Starting with the conservation equations for mass, momentum, energy, and concentrations of various species (for chemically reactive flows), a single transport equation can be derived for the joint probability density function of velocity and composition, $f_{u\phi}(\mathbf{V}, \boldsymbol{\psi}; \mathbf{x}, t)$, as described by Pope (1985). The quantity $f_{u\phi} d\mathbf{V}\, d\boldsymbol{\psi}$ represents the probability that $\mathbf{V} \le \mathbf{U} \le \mathbf{V} + d\mathbf{V}$ and $\boldsymbol{\psi} \le \boldsymbol{\Phi} \le \boldsymbol{\psi} + d\boldsymbol{\psi}$ occur simultaneously, where $\mathbf{U}$ is the velocity vector, $\boldsymbol{\Phi}$ is the set of all scalars (temperature or enthalpy, and concentrations), and $\mathbf{V}$ and $\boldsymbol{\psi}$ are independent sample-space variables corresponding to $\mathbf{U}$ and $\boldsymbol{\Phi}$, respectively. The transport equation for the joint PDF is a multidimensional partial differential equation, and cannot be solved efficiently by traditional finite-difference or finite-volume techniques, and the Monte-Carlo method is used instead. In this method, the fluid within the whole computational domain is discretized into representative "particles" (or samples). These particles then move with time and their motion is governed by their Lagrangian momentum equations which are recast in such a way that the forces acting on these representative particles are modeled after stochastic processes. The detailed equations for particle transport may be found in Pope (1985). The particles carry with them all passive scalars. Transport of energy will be discussed in this article.

During the last two decades, the velocity-composition joint PDF method has been used effectively to predict hydrodynamic and scalar fields in free-shear flow situations, namely, jet flames, mixing layers, and wakes (Janicka et al., 1978; Lockwood and Naguib, 1975; Anand and Pope, 1987; Haworth and Pope, 1987). Recently, the method has been applied to wall-bounded isothermal inert flows by Mazumder and Modest (1997) and by Dreeben and Pope (1995). The method has yet to be applied to scalar transport in near-wall regions of a turbulent flow. This article describes a methodology for incorporating scalar transport using the velocity-composition joint PDF method to wall-bounded turbulent flows.

Exact Lagrangian Description

In near-wall regions in a turbulent flow, two very important effects come into play. First, molecular transport starts to dominate as the wall is approached. Secondly, the turbulent fluctuations, which are primarily generated in the inertial sublayer due to nonlinear interactions, are completely damped out by viscosity in the viscous sublayer. The first of these two effects can be treated exactly by deriving the exact Lagrangian equation for a fluid particle. The second effect will be discussed in detail in a later section.

Consider a fluid particle moving through space with position $x_i^*(t)$, velocity $U_i^*(t)$, and temperature $T^*(t)$. This is the Lagrangian description of the fluid particle. The Lagrangian temperature, $T^*(t)$, is related to the Eulerian temperature field, $T(x_i, t)$, by the relationship

$$T_i^*(t) = T[x_i = x_i^*(t), t]. \tag{1}$$

The increment in temperature of a particle, ΔT^*, over a time Δt may be obtained by performing a Taylor series expansion,

$$\Delta T^* = \frac{\partial T}{\partial t}\Delta t + \frac{\partial T}{\partial x_i}\Delta x_i^* + \frac{1}{2}\frac{\partial^2 T}{\partial x_i \partial x_j}\Delta x_i^* \Delta x_j^* + \ldots, \tag{2}$$

where the second-order temporal term has been neglected because later on, only a first-order accurate time-marching scheme will be used to solve the final governing equations. If a particle is introduced into a fluid stream, it will be convected along the stream according to the Lagrangian equation

$$\Delta x_i^* = U_i^* \Delta t = U_i[x_i = x_i^*(t), t]\Delta t. \tag{3}$$

In the absence of convective transport, the particle could move by molecular mechanisms alone. At large Reynolds numbers, these molecular transport forces are very weak compared to the convective forces, and are typically neglected. In regions close to the wall, these forces become large, and need to be included. Einstein (1926), during his studies on Brownian motion, first suggested from a stochastic viewpoint that a particle in a stagnant fluid would move following the equation

$$\Delta x_i^* = \sqrt{2\nu}\, \Delta W_i, \tag{4}$$

where W_i is an isotropic Wiener process, and ν is the kinematic viscosity of the fluid. The Wiener process is a nondifferentiable function, which, when integrated over time, yields a random number drawn from a standardized Gaussian distribution with

---

Contributed by the Heat Transfer Division for publication in the Journal of Heat Transfer. Manuscript received by the Heat Transfer Division March 15, 1996; revision received September 5, 1996; Keywords: Enclosure Flows, Forced Convection, Modeling & Scaling, Numerical Methods, Turbulence. Associate Technical Editor: Y. Jaluria.

zero mean and a variance equal to the time interval over which the integration has been performed. For details pertaining to the Wiener process and other stochastic processes and terminology, the readers are referred to the two texts by Karlin and Taylor (1975, 1981). In the presence of both convection and molecular transport, the increment of a particle's position would be expressed as

$$\Delta x_i^* = U_i^* \Delta t + \sqrt{2\nu}\, \Delta W_i . \tag{5}$$

In addition to the aforestated properties, the Wiener process also has the following property (Einstein, 1926):

$$\overline{\Delta W_i \Delta W_j} = \delta_{ij} \Delta t, \tag{6}$$

where δ_{ij} is the Kronecker delta. Substituting Eq. (5) and (6) into Eq. (2), and retaining terms up to order Δt, we have

$$\Delta T^* = \frac{\partial T}{\partial t} \Delta t + \frac{\partial T}{\partial x_i} (U_i^* \Delta t + \sqrt{2\nu}\, \Delta W_i) + \nu \frac{\partial^2 T}{\partial x_i \partial x_i} \Delta t. \tag{7}$$

In the absence of chemical reaction, and neglecting viscous dissipation, radiation and pressure-work, for constant thermophysical properties, the instantaneous Eulerian energy transport equation is given by

$$\frac{\partial T}{\partial t} + U_i \frac{\partial T}{\partial x_i} = \alpha_H \frac{\partial^2 T}{\partial x_i \partial x_i} , \tag{8}$$

where α_H is the thermal diffusivity of the fluid, and is expressed as

$$\alpha_H = \lambda / \rho C_p, \tag{9}$$

where λ is the thermal conductivity, ρ is the density, and C_p is the specific heat capacity at constant pressure. Substitution of Eqs. (3) and (8) into Eq. (7) yields

$$\Delta T^* = (\alpha_H + \nu) \frac{\partial^2 T}{\partial x_i \partial x_i} \Delta t + \sqrt{2\nu} \Delta W_i \frac{\partial T}{\partial x_i} . \tag{10}$$

Equation (10) is the exact Lagrangian energy transport equation for a fluid particle, whose molecular motion has been modeled after a stochastic process. The instantaneous Eulerian temperature can be decomposed into its mean and fluctuating parts and used in Eq. (10) to yield

$$\Delta T^* = (\alpha_H + \nu) \frac{\partial^2 \overline{T}}{\partial x_i \partial x_i} \Delta t + \sqrt{2\nu}\, \Delta W_i \frac{\partial \overline{T}}{\partial x_i} + (\alpha_H + \nu) \frac{\partial^2 T'}{\partial x_i \partial x_i} \Delta t + \sqrt{2\nu}\, \Delta W_i \frac{\partial T'}{\partial x_i} , \tag{11}$$

where the overbars denote Eulerian mean quantities, and the primes denote fluctuations. The first two terms can be calculated exactly by averaging over Monte-Carlo cells and then by fitting splines as described by Mazumder and Modest (1997). The last two terms need to be modeled for complete closure.

Deterministic Model for Fluctuations

To model velocity fluctuations, the Langevin model can be used effectively. The same model, however, causes unboundedness of scalars such as temperature (Pope, 1985). The temperature space, unlike velocity space, is a bounded sample space, the bounds being provided by the Second Law of Thermodynamics. The Langevin model does not take this constraint into account and, therefore, cannot be used to model temperature fluctuations. In the seventies, Dopazo (1975) proposed a deterministic model for scalar fluctuations in homogeneous turbulence. His model is expressed as

$$\frac{d\phi^*}{dt} = -\frac{1}{2} \frac{1}{\tau_\phi} (\phi^* - \overline{\phi}), \tag{12}$$

where ϕ is any passive scalar and τ_ϕ is the time-scale for the dissipation of scalar fluctuations. In homogeneous turbulence, the first two terms on the right-hand-side of Eq. (11) are absent and consequently, Eq. (12) is actually a model for the last two terms on the right-hand-side of Eq. (11). Equation (12), upon multiplication by $\phi' = \phi^* - \overline{\phi}$, and some manipulation, yields

$$\frac{d\overline{\phi'^2}}{dt} = -\frac{1}{\tau_\phi} \overline{\phi'^2}. \tag{13}$$

The above model, when used for the temperature, suggests that the mean-square temperature fluctuations will decay exponentially with time in homogeneous turbulence. In regions close

Nomenclature

a_i, b_i, c_i = arbitrary constants in asymptotic expansion
A = constant in thermal wall-function
C_p = specific heat capacity at constant pressure
C_μ = constant in turbulence model
$f_{u\phi}$ = velocity-composition joint PDF
H = channel half-height
k = turbulent kinetic energy
n = time index
Pr = Prandtl number
Pr_t = turbulent Prandtl number
q_w = wall heat flux
$\overline{q}_w$ = nondimensional wall heat flux
R_i = standardized Gaussian random number
R_{vT} = notation for $\overline{u_2' T'}/u_* T_*$
Re_H = Reynolds number based on channel half-height
t = time
T = instantaneous Eulerian temperature
T_i = inlet bulk temperature
$\overline{T}$ = mean Eulerian temperature
T^* = Lagrangian temperature
T' = temperature fluctuations
T_w = wall temperature
T_* = wall conduction temperature
$\overline{U}_i$ = mean Eulerian velocity in the ith direction
u_i' = velocity fluctuation in the ith direction
U_i^* = Lagrangian velocity in the ith direction
$\mathbf{U}$ = instantaneous Eulerian velocity vector
u_* = friction velocity
W_i = isotropic Wiener process
x_i = space variable
x_i^* = position vector of a particle
x_{2+} = x_2 normalized by ν/u_*

Greek

α_H = thermal diffusivity
δ_{ij} = Kronecker delta
ϵ = rate of dissipation of k
κ = Von Karman constant
ν = kinematic viscosity
ϕ = arbitrary passive scalar
θ_T, θ_q = nondimensional temperature
θ_m = nondimensional bulk temperature
θ_w = nondimensional wall temperature
θ^+ = root-mean-square temperature fluctuation normalized by T_*
ρ = density
τ = turbulent time-scale
τ_ϕ = time scale for scalar dissipation

to the wall, the time-scale, as well as the mean temperatures, are strong functions of space, and need to be modified. This can be achieved by using thermal wall-functions and scaling arguments.

Consider a wall lying on the x_1-x_3 plane, and let x_2 be the normal distance from the wall. The predominant flow direction is x_1; x_3 is the azimuthal direction in which, gradient of all mean quantities are zero. For such a case, in the inertial sublayer, the mean temperature is given by the expression (White, 1991)

$$\bar{T} = T_w - \frac{q_w}{\rho C_p u_*}\left[\frac{\mathrm{Pr}_t}{\kappa}\ln\left(\frac{x_2 u_*}{\nu}\right) + A\right], \qquad (14)$$

where T_w is the wall temperature, q_w is the wall heat flux based on the thermodynamic sign convention, and Pr_t is the turbulent Prandtl number. κ, the Von Karman constant, is equal to 0.42, and u_* is the friction velocity given by (Launder et al., 1984).

$$u_* = C_\mu^{1/4} k^{1/2}, \qquad (15)$$

where k is the turbulent kinetic energy, and C_μ is equal to 0.09. The parameter A in Eq. (14) is a function of the Prandtl number of the fluid (Kader, 1981)

$$A = (3.85\ \mathrm{Pr}^{1/3} - 1.3)^2 + 2.12\ \ln(\mathrm{Pr}), \qquad (16)$$

where Pr is the Prandtl number. In the viscous sublayer, the mean temperature is given by

$$\bar{T} = T_w - \frac{q_w}{\rho c_p u_*}\left[\mathrm{Pr}\left(\frac{x_2 u_*}{\nu}\right)\right]. \qquad (17)$$

Several authors have suggested that the time-scale for scalar dissipation, τ_ϕ, is linearly proportional to the turbulent time-scale, τ. Beguier et al. (1978) suggested that the ratio of these two time-scales, $C_\phi = \tau/\tau_\phi$, assumes a value close to 2.0 for most shear flows. Experiments performed by Warhaft and Lumley (1978) suggest that C_ϕ is not a universal constant. Warhaft (1980) suggested values of C_ϕ in the range between 1.9 and 3.1. This is still a topic of turbulence research and will not be dwelt upon further in this article. For the current study a value of 2.0 was used. The turbulent time-scale, τ, is actually the time-scale for the dissipation of turbulent kinetic energy and is given by the ratio, k/ϵ, where ϵ is the rate of dissipation of the turbulent kinetic energy. In inhomogeneous turbulence the time-scale is a function of space and changes rapidly close to solid walls. In the near-wall layer, a good estimate of the dissipation rate is given by (Tennekes and Lumley, 1967)

$$\epsilon = u_*^3/\kappa x_2, \qquad (18)$$

which upon combination with Eq. (15) and the use of the definition of the turbulent time-scale yields

$$\frac{1}{\tau} = \frac{C_\mu^{3/4} k^{1/2}}{\kappa x_2}. \qquad (19)$$

It is useful at this point to investigate the modeled behavior of the temperature fluctuations as a function of the distance from the wall. In order to do that, we express velocity and temperature fluctuations as arbitrary functions of distance normal to the wall, x_2, yielding

$$u_i' = a_i + b_i x_2 + c_i x_2^2 + \ldots,$$

and

$$T' = a_T + b_T x_2 + c_T x_2^2 + \ldots, \qquad (20)$$

where a_i, b_i, c_i, a_T, b_T, and c_T are all arbitrary functions of x_1, x_3, and t. Application of no-slip, continuity, and zero temperature fluctuation at the walls yields

$$u_1' = b_1 x_2 + c_1 x_2^2 + \ldots,$$

$$u_2' = c_2 x_2^2 + \ldots,$$

$$u_3' = b_3 x_2 + c_3 x_2^2 + \ldots,$$

and

$$T' = b_T x_2 + c_T x_2^2 + \ldots. \qquad (21)$$

Equation (12), when written for temperature and using $C_\phi = \tau/\tau_\phi$, yields

$$\frac{dT^*}{dt} = -\frac{C_\phi}{2\tau}(T^* - \bar{T}). \qquad (22)$$

The wall functions, which we are using here (Eqs. (14) and (17)), suggest that the mean temperature, $\bar{T}$, is only a function of x_2 and, therefore, for the near-wall region, Eq. (22) may be written as

$$\frac{dT'}{dt} = \frac{dT'}{dx_2^*}\frac{dx_2^*}{dt} = U_2^* \frac{dT'}{dx_2^*} = -\frac{C_\phi T'}{2\tau}, \qquad (23)$$

where $T' = T^* - \bar{T}$ represents the deviation of the particle temperature from the mean, and U_2^* is the particle velocity in the direction normal to the wall. The particle velocity normal to the wall is a sum of the mean velocity and a fluctuation (both normal to the wall). Application of no-slip and continuity easily reveals that the mean normal velocity, $\bar{U}_2$, is zero, in the near-wall region. The use of Eq. (21) for the normal velocity fluctuation yields

$$U_2^* = c_2 x_2^{*2} + \mathcal{O}(x_2^{*3}). \qquad (24)$$

The coefficient, c_2, will be negative if a particle moves toward a wall and positive if it moves away from a wall. According to Eq. (24), if a particle travels toward the wall, its velocity (and consequently, the normal velocity fluctuation) will decrease monotonically until it reaches the wall, where its velocity will be zero. This, however, is not the correct picture, as shown earlier by Mazumder and Modest (1996). The particle's normal velocity actually reaches zero and changes sign even before the wall is reached. This can only be obtained by solving a system of ordinary differential equations for particle motion and taking all physical processes into account. For the current purposes, Eq. (24) gives a reasonable functional behavior of the normal velocity, especially since it does not violate any conservation laws or boundary conditions. Substituting Eqs. (19) and (24) into Eq. (23), and retaining terms up to leading order yields

$$\frac{dT'}{dx_2^*} = -\frac{C_\phi T' C_\mu^{3/4} k^{1/2}}{2 c_2 \kappa x_2^{*3}}. \qquad (25)$$

Using $k = \overline{u_i' u_i'}/2$, and Eq. (21), it can be shown that up to leading order,

$$k = \frac{(\overline{b_1^2} + \overline{b_3^2})}{2} x_2^2, \qquad (26)$$

which upon substitution into Eq. (25) yields

$$\frac{dT'}{dx_2^*} = -\frac{C_\phi C_\mu^{3/4}(\overline{b_1^2} + \overline{b_3^2})T'}{4 c_2 \kappa x_2^{*2}} = -C\frac{T'}{x_2^{*2}}, \qquad (27)$$

where the constant C has been introduced for brevity. Following the sign of c_2, the constant C will be negative for a particle moving towards the wall, and positive for a particle moving away from the wall. Integration of Eq. (27) from a given normal location $x_{2,0}^*$, where the fluctuation is T'_0, to an arbitrary location along a particle path, yields

$$T' = T'_0 \exp\left[C\left(\frac{1}{x_2^*} - \frac{1}{x_{2,0}^*} \right) \right] . \tag{28}$$

Obviously, the modeled behavior of the temperature fluctuations near the wall, shown in Eq. (28), is different from the modeled behavior shown by the asymptotic expansion in Eq. (21). The level of disparity will depend largely on the unknown coefficients. It should also be noted that the above analysis only accounted for dissipation of the fluctuations by viscosity. It did not account for transport or production of the fluctuations. In spite of all this, it reveals one very important characteristic of the proposed model: in the limiting case of $x_2^* \rightarrow 0$, the temperature fluctuations are zero. This simple observation may appear trivial; however, it is not in the context of Lagrangian schemes and models. The proposed model (Eq. (22)) is an initial value problem in time, and not a boundary value problem in space where spatial boundary conditions can be easily implemented. Therefore, in such Lagrangian formulations, it is not always easy to ensure that certain specific conditions will be satisfied at a certain point in space. In Eulerian schemes on the other hand, spatial boundary conditions are easily implemented, but instantaneous information pertaining to the fluctuations cannot be obtained. They can only be obtained in an averaged sense.

The problem of damping the turbulent fluctuations at the correct rate near walls has always been a challenge in the field of conventional turbulence modeling. In the past, ad hoc damping functions have been used to damp the Reynolds stresses in the viscous sublayer (Hanjalic and Launder, 1976; Launder et al., 1984). Current formulations, such as the one by Durbin (1993), uses an elliptic relaxation technique. For heat transfer, this issue is not usually encountered simply because of the use of the Reynolds analogy for turbulent transport, which essentially implies that the same damping functions that were used for the Reynolds stresses act to damp the turbulent fluxes as well. Nevertheless, in light of these problems in Eulerian turbulence models, it is not surprising that Lagrangian models will also be faced with similar problems.

The complete modeled Lagrangian energy transport equation is obtained by replacing the "unclosed" terms in Eq. (11) by the following proposed model:

$$\Delta T^* = (\alpha_H + \nu) \frac{\partial^2 \bar{T}}{\partial x_i \partial x_i} \Delta t + \sqrt{2\nu} \frac{\partial \bar{T}}{\partial x_i} \Delta W_i - \frac{1}{2} \frac{C_\phi}{\tau} (T^* - \bar{T}) \Delta t . \tag{29}$$

Euler-explicit integration of Eq. (29) yields

$$T^*|^{n+1} = T^*|^n + (\alpha_H + \nu) \frac{\partial^2 \bar{T}}{\partial x_i \partial x_i}\bigg|^n \Delta t + \sqrt{2\nu\Delta t} \frac{\partial \bar{T}}{\partial x_i}\bigg|^n R_i - \frac{1}{2} \frac{C_\phi}{\tau} (T^*|^n - \bar{T}|^n) \Delta t , \tag{30}$$

where R_i is a random number drawn from a standardized Gaussian distribution (with zero mean and variance equal to unity), n is the time-index, and Δt is the time-step. Equation (30) is unstable for large Δt. The stability characteristics can be improved by using T^* at $n + 1$ rather than at n in the last term in Eq. (30). Upon performing that step, we obtain

$$T^*|^{n+1} = \frac{1}{1 + C_\phi/2\tau} \left[T^*|^n + (\alpha_H + \nu) \frac{\partial^2 \bar{T}}{\partial x_i \partial x_i}\bigg|^n \Delta t + \sqrt{2\nu\Delta t} \frac{\partial \bar{T}}{\partial x_i}\bigg|^n R_i + \frac{1}{2} \frac{C_\phi}{\tau} \bar{T}|^n \Delta t \right] . \tag{31}$$

In the Monte-Carlo simulation, Eq. (31) is solved along with the hydrodynamic equations of transport. In the near-wall region, since the gradients change rapidly, the same equations after the aforestated modifications need to be solved using a higher order integration scheme. In the present context, a fourth-order Runge-Kutta method was used. The reader is referred to Mazumder and Modest (1996) for details of the solution algorithm.

Results and Discussion

Validation of Model. Although the primary interest of the authors lies in large Reynolds number flows, data of any reliable nature are not available for Re $> 10^4$. Therefore, validation of the model has been carried out for low Re flows for which both experimental and DNS data are available. Following this validation, the performance of the model will be compared with conventional turbulence models at high Re.

The test problem considered in this section is the same as the one for which Lyons et al. (1991) have provided direct numerical simulation (DNS) data, and Teitel and Antonia (1993) have provided experimental data. A hydrodynamically and thermally fully-developed flow is considered between two parallel plates. The lower plate is heated while the upper plate is cooled. The thermally fully developed state is attained by ensuring that the same heat flux that is supplied to the bottom plate is removed from the top one. The Reynolds number based on the channel half-height and the bulk-mean flow velocity was chosen as 2262, the same as the one that Lyons et al. used for their simulation. Using the properties of air at room temperature and a channel height of 21 mm (used by Teitel and Antonia) gives a bulk-mean velocity of 3.25 m/s. Lyons et al. used a Prandtl number of unity for their simulation, while Teitel and Antonia used the Prandtl number of air (0.712), which we have chosen to use. Since the results are eventually normalized by the Prandtl number, it is not expected to make a difference because the Prandtl number appears in a linear form in the governing equations.

The hydrodynamic entry length for the problem under consideration is in the order of a hundred times the channel height. To obtain the hydrodynamically fully developed solution, an isothermal case was run for a long channel of a length equal to hundred times the height, with an inlet plug velocity of 3.25 m/s. Such an approach guarantees a bulk-mean velocity of 3.25 m/s. An algebraic Reynolds stress model (ARSM) (Launder et al., 1984) was used as the turbulence model. The velocity profile at the outlet was then used as the inlet profile for an isothermal PDF Monte-Carlo simulation in a channel five times as long as its height. The process of taking the outlet profile and feeding it back as the inlet profile was repeated three times for this shorter channel. This approach was used to eliminate any differences in the fully developed velocity profiles arising due to the differences in the ARSM and the PDF model. Since the problem under consideration is incompressible, once a fully developed hydrodynamic field is reached it is not violated by any thermal gradients. Therefore, this preprocessed hydrodynamic field was used for the actual simulation, which was performed in a channel twice as long as its height. The thermal simulation was initiated by using the temperature profile provided by the ARSM as a first guess at all axial locations including the inlet. The simulation was repeated thrice after feeding the outlet temperature profile as the inlet in order to ensure that all effects of the initial guess was forgotten, and the turbulent statistics provided was indeed one that was simulated by the PDF model.

A 10 × 80 grid was used for the PDF simulation. Ten points were considered sufficient for the axial direction since both flow and temperature fields are fully developed. In the normal direction, a much larger number of sampling bins were used, primarily because the goal of this section is to investigate the performance of the proposed model in near-wall regions. The raw Monte-Carlo data were smoothed using two-dimensional least-square B-splines (DeBoor, 1978). The splines were also used to calculate all required spatial derivatives. The Monte-Carlo simulation was performed with 100,000 particles.

Figure 1 illustrates the behavior of the normalized root-mean-square temperature fluctuations near the wall. The notation θ^+ has been used for the quantity $\sqrt{\overline{T'^2}}/T_*$, where the wall conduction temperature, T_*, is expressed as

$$T_* = \frac{q_w}{\rho C_p u_*}, \tag{32}$$

where q_w is the supplied wall heat flux. The space variable normal to the wall, x_2, normalized by ν/u_*, has been denoted by x_{2+}. It is clear that the proposed model overdamps the fluctuations in regions away from the wall, i.e., in the inertial sublayer. However, very close to the wall, the correct behavior is replicated. This is consistent with the analytical observations made earlier.

The normalized correlation between the fluctuating normal velocity and the fluctuating temperature has been illustrated in Fig. 2 for the near-wall region. In this case, only DNS data of Lyons et al. (1991) have been shown since they match the experimental data of Teitel and Antonia (1993) almost exactly. The quantity $\overline{u_2' T'}/u_* T_*$ has been denoted by R_{vT}. In this case too, the damping rate is overpredicted, but to a smaller degree. This has two probable causes. First, the model used for the velocity fluctuations in the viscous sublayer (Mazumder and Modest, 1996) is quite accurate and accounts for the anisotropic dissipation of the Reynolds stresses. Secondly, since the velocity fluctuation of a particle could correlate positively or negatively with its temperature fluctuation, the error in the prediction of the decay rate of velocity-temperature fluctuations is not exactly proportional to the error in the prediction of the decay rate of the square of the temperature fluctuations.

Comparison with Existing Turbulence Models

The test problem considered for this purpose is that of a thermally developing, hydrodynamically fully developed, flow through a channel. The flow is assumed incompressible and two-dimensional in the mean. The channel is 1 meter wide and 10 meters long. The Reynolds number, based on the channel half-height, is $\mathrm{Re}_H = 5 \times 10^5$. For the sample calculations, a Prandtl number of 0.7, and a turbulent Prandtl number of 0.9, were used. The incoming plug temperature was set to 1000 K. The method was tested for two different boundary conditions; a constant wall temperature boundary condition (with the walls maintained at 300 K) and a constant flux boundary condition (with 1000 W/m^2 rejected at both walls).

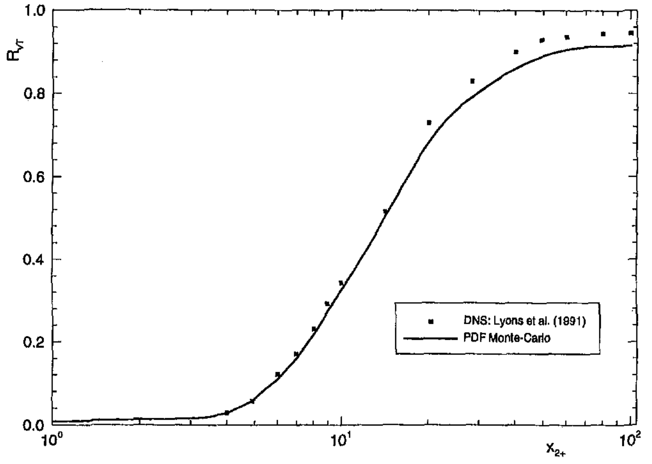

Fig. 2 Behavior of normal velocity-temperature correlation in the near-wall region

The Monte-Carlo calculations, in this case, were performed using 20 × 10 Monte-Carlo cells and with 100,000 particles. In addition, to account for strong gradients near the wall, the cells adjacent to the walls were broken up into subcells to obtain more samples for spline fitting. The finite-volume k-ϵ/algebraic Reynolds stress (ARSM) (Launder et al., 1984) calculations were performed using the commercial flow code Harwell-FLOW3D with 20 × 20 finite-volume cells. The thermal wall functions (Eqs. (14) and (17)) were employed to calculate the wall temperature for the constant wall heat flux case and to calculate the wall heat flux for the constant wall temperature case.

Figure 3 illustrates nondimensional wall heat fluxes, $\bar{q}_w$, and nondimensional bulk temperatures, θ_m, obtained using the three different models for the case of constant temperature boundary condition. Nondimensional temperatures for the constant temperature boundary condition and the constant heat flux boundary condition are denoted by θ_T and θ_q, respectively. They are defined as

$$\theta_T = \frac{\bar{T} - T_w}{T_i - T_w}; \quad \theta_q = \frac{\lambda(T_i - \bar{T})}{2 q_w H}. \tag{33}$$

In the above expressions, T_w is the wall temperature, T_i is the bulk temperature at the inlet, q_w is the wall heat flux, and

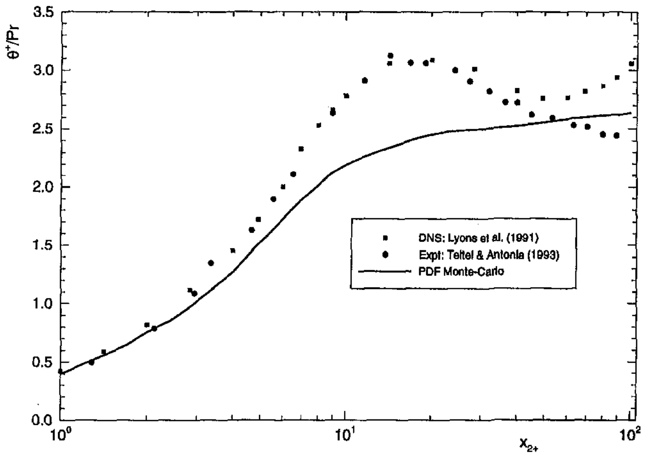

Fig. 1 Behavior of root-mean-square temperature fluctuations in near-wall region

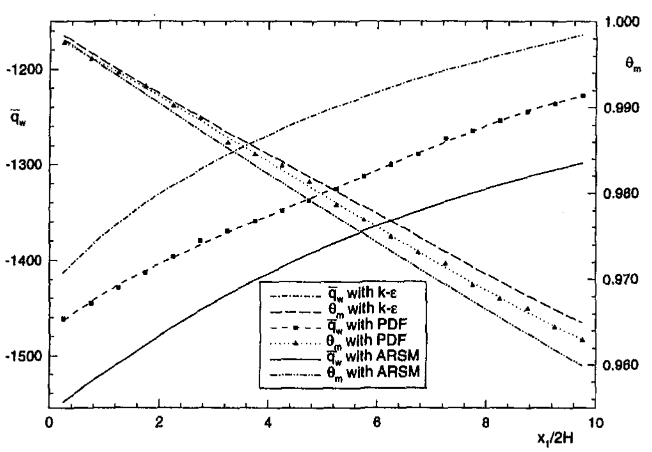

Fig. 3 Nondimensional wall heat flux and nondimensional bulk temperature for the case of isothermal walls

H is the channel half-height. For the isothermal wall case, the nondimensional heat flux, $\bar{q}_w$, is defined as

$$\bar{q}_w = \frac{2q_w H}{\lambda(T_i - T_w)}\,. \tag{34}$$

The differences in results, obtained by the three methods, is partly due to the use of different turbulent models in the three different cases, and partly due to different numerical techniques used (Lagrangian Monte-Carlo versus Eulerian finite-volume). In k-ϵ and ARSM calculations, the turbulent heat fluxes, $\rho u_i' T'$, are approximated by using a Gradient Diffusion Hypothesis (Tennekes and Lumley, 1967). However, the hydrodynamic moments are calculated more accurately in the ARSM than in k-ϵ, resulting in different flow fields. The difference in flow fields also led to different temperature fields.

In the PDF method, no approximations are made. However, in the PDF method, for purposes of simplicity, a simple algebraic model has been used to calculate ϵ (Mazumder and Modest, 1997), as opposed to the k-ϵ model and ARSM, where the modeled transport equation for ϵ was solved. Figure 4 illustrates the corresponding temperature profiles. The profile obtained by the PDF method was plotted after spline smoothing. Both k-ϵ and the ARSM profiles suffer a "smearing" effect due to numerical diffusion associated with the use of upwind differencing schemes (Raithby, 1976) at a certain point in space at large Re. The fact that this difference is indeed partly due to numerical diffusion has been demonstrated by using a quadratic upwind differencing scheme (Leshziner, 1980) with the same number of nodes. The effect of numerical diffusion is not observed at the cells adjacent to the inlet because a boundary condition of the first kind is imposed on the upstream face of these cells. The choice of a coarse grid for the PDF method was made to emphasize the point that in spite of the coarse nature of the grid, numerical diffusion problems do not arise in such treatments owing to its Lagrangian nature. For the constant heat flux boundary condition case, the nondimensional wall temperature, θ_w, has been illustrated in Fig. 5. The ARSM is observed to predict a somewhat larger wall temperature than the PDF or the k-ϵ model. The bulk temperatures were not plotted because they can simply be obtained from a global energy balance, resulting in the same linear decay in temperature for all three methods. The temperature profiles for this case look similar to the ones shown in Fig. 4, and have not been shown to save space.

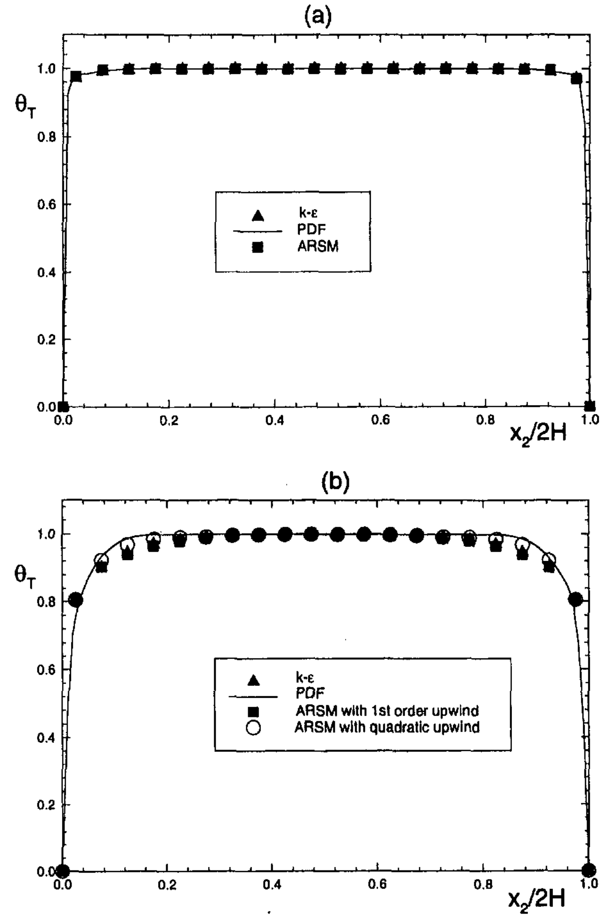

Fig. 4 Nondimensional mean temperature profiles for the case of constant wall temperature at (*a*) $x_1/2H = 0.25$, and at (*b*) $x_1/2H = 9.75$

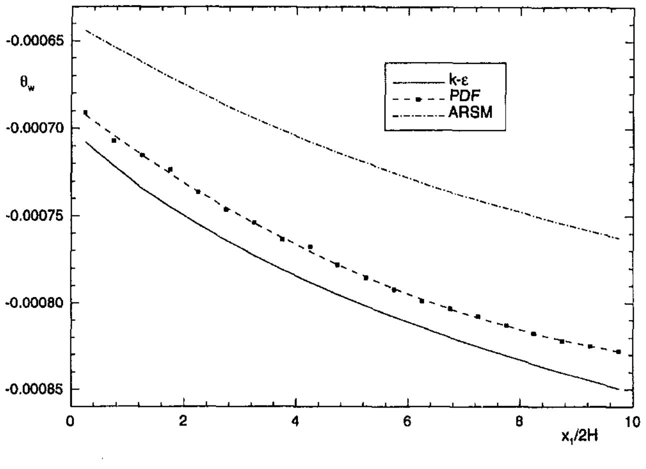

Fig. 5 Nondimensional wall temperature for the case of constant heat flux boundary condition

Conclusion

The velocity-composition joint PDF method has been extended to predict the temperature field in an incompressible channel flow. Exact Lagrangian transport equations were derived and solved for this purpose. The temperature fluctuations were modeled using a modified form of an existing model, which was originally developed for homogeneous turbulence. The proposed PDF model overdamps the temperature fluctuations close to the wall, but reaches the correct limiting behavior at the wall. This problem, as discussed, is a classical problem in turbulence modeling and needs further attention and research. The Lagrangian nature of the PDF model helped eliminate numerical diffusion completely. This is a particularly great advantage for high Re flows. The Gradient Diffusion Hypothesis was not used at any point, thereby eliminating the scope of any errors that are known to arise from the use of this hypothesis in reactive flows (Libby and Bray, 1980).

From the computational effort standpoint, the PDF calculations were about twice as slow as compared to the ARSM calculations and four times slower than the k-ϵ calculations. This information, although discouraging, needs further clarification. The advantage of stochastic methods really lie in the context of reactive flows or for situations where the accuracy of the flow problem requires use of the differential Reynolds stress model; in which six additional non-linear partial differential equations need to be solved. Researchers in finite-volume computations will note that it typically takes enormous amount of computational effort to get the scalar transport equations to converge in a reactive flow situation. This is not the case for stochastic calculations. In fact, reactive flow calculations using finite-volume techniques are severely intractable if one were to incorporate finite-rate kinetics and radiation. PDF methods can easily account for these additional complexities without significant increase in computational effort. Thus, the importance of the proposed model and method lies in the context of heat transfer in reactive flow situations. Under such circumstances, the advantage of using stochastic models and methods truly becomes apparent.

Acknowledgment

The authors are grateful to the Applied Research Laboratory at Penn State for partial funding of this research and for sharing their computer resources during the course of this work. The authors also wish to thank Prof. R. A. Antonia and Prof. T. J. Hanratty for providing the original data files used for comparison in some of the figures.

References

Anand, M. S., and Pope, S. B., 1987, "Calculations of Premixed Turbulent Flames by PDF Methods," *Combustion and Flame*, Vol. 67, pp. 127–142.

Beguier, C., Dekeyser, I., and Launder, B. E., 1978, "Ratio of Scalar and Velocity Dissipation Time-Scales in Shear Flow Turbulence," *Physics of Fluids*, Vol. 21, No. 3, pp. 307–310.

De Boor, C., 1978, *A Practical Guide to Splines*, Springer-Verlag.

Dopazo, C., 1975, "Probability Density Function Approach for a Turbulent Axisymmetric Heated Jet. Centerline Evolution," *Physics of Fluids*, Vol. 18, No. 4, pp. 397–404.

Dreeben, T. D., and Pope, S. B., 1995, "PDF and Reynolds Stress Modeling of Near-Wall Turbulent Flows," *Tenth Symposium on Turbulent Shear Flows*, The Pennsylvania State University, pp. 21.

Durbin, P. A., 1993, "A Reynolds Stress Model for Near-Wall Turbulence," *Journal of Fluid Mechanics*, Vol. 249, pp. 465–498.

Einstein, A., 1926, *Investigations on the Theory of Brownian Movement*, Methuen and Co. Ltd., London.

Hanjalic, K., and Launder, B. E., 1976, "Contribution Towards a Reynolds-Stress Closure for Low-Reynolds-Number Turbulence," *Journal of Fluid Mechanics*, Vol. 74, pp. 593–610.

Haworth, D. C., and Pope, S. B., 1987, "A PDF Modeling Study of Self-Similar Turbulent Free Shear Flows," *Physics of Fluids*, Vol. 30, pp. 1026–1044.

Janicka, J., Kolbe, W., and Kollmann, W., 1978, "The Solution of a PDF-Transport Equation for Turbulent Diffusion Flames," *Proc. Heat Trans. Fluid Mech. Inst.*, Stanford University Press.

Kader, B. A., 1981, "Temperature and Concentration Profiles in Fully Turbulent Boundary Layers," *Int. J. Heat Mass Transfer*, Vol. 24, No. 9, pp. 1541–1544.

Karlin, S. L., and Taylor, H. M., 1975, *A First Course in Stochastic Processes*, Academic Press, New York.

Karlin, S. L., and Taylor, H. M., 1981, *A Second Course in Stochastic Processes*, Academic Press, New York.

Launder, B. E., Reynolds, W. C., and Rodi, W., 1984, *Turbulence Models and their Applications*, Edition Eyrolles.

Leschziner, M. A., 1980, "Practical Evaluation of Three Finite Difference Schemes for the Computation of Steady-State Recirculating Flows," *Computer Methods in Applied Mechanics and Engineering*, Vol. 23, pp. 293–312.

Libby, P. A., and Bray, K. N. C., 1980, "Counter-Gradient Diffusion in Premixed Turbulent Flames," *AIAA*, Paper no. 80-0013.

Lockwood, F. C., and Naguib, A. S., 1975, "The Prediction of the Fluctuations in the Properties of Free, Round-Jet, Turbulent, Diffusion Flame," *Combustion and Flame*, Vol. 24, pp. 109–124.

Lyons, S. L., Hanratty, T. M., and McLaughlin, J. B., 1991, "Direct Numerical Simulation of Passive Heat Transfer in a Turbulent Channel Flow," *Int. J. Heat Mass Transfer*, Vol. 34, pp. 1149–1161.

Mazumder, S., and Modest, M. F., 1997, "Boundary Conditions and an Efficient Pressure Algorithm for Internal Turbulent Flows using the PDF Method," *Int. J. for Numerical Methods in Fluids*, Vol. 24, pp. 1–18.

Pope, S. B., 1985, "PDF Methods for Turbulent Reactive Flows," *Progress in Energy and Combustion Science*, Vol. 11, pp. 119–192.

Raithby, G. D., 1976, "A Critical Evaluation of Upstream Differencing Applied to Problems Involving Fluid Flow," *Computer Methods in Applied Mechanics and Engineering*, Vol. 9, pp. 75–103.

Teitel, M., and Antonia, R. A., 1993, "Heat Transfer in Fully Developed Turbulent Channel Flow: Comparison Between Experiment and Direct Numerical Simulations," *Int. J. Heat Mass Transfer*, Vol. 36, No. 6, pp. 1701–1706.

Tennekes, H., and Lumley, J., 1967, *A First Course in Turbulence*, MIT Press.

Warhaft, Z., and Lumley, J. L., 1978, "An Experimental Study of the Decay of Temperature Fluctuations in Grid-Generated Turbulence," *J. Fluid Mech.*, Vol. 88, pp. 659–684.

Warhaft, Z., 1980, "An Experimental Study of the Effect of Uniform Strain on Thermal Fluctuations in Grid-Generated Turbulence," *J. Fluid Mech.*, Vol. 99, pp. 545–573.

White, F. M., 1991, *Viscous Fluid Flow*, McGraw-Hill, Inc.

O. Iida[1]
iida@heat.mech.nitech.ac.jp

N. Kasagi
kasagi@thtlab.t.u-tokyo.ac.jp
Fellow, ASME

Department of Mechanical Engineering,
The University of Tokyo,
Hongo 7-3-1, Bunkyo-ku, Tokyo 113,
Japan

Direct Numerical Simulation of Unstably Stratified Turbulent Channel Flow

Direct numerical simulations of the fully developed horizontal channel flow under unstable density stratification were carried out to investigate interactive shear and buoyancy effects on the turbulent momentum and heat transport. As the Grashof number is increased, buoyant thermal plumes are generated. The large-scale thermal convection involving the thermal plumes diminishes the quasi-coherent streamwise vortices, which are known to play a major role in the transport mechanism of near-wall turbulence. The destruction of the streamwise vortices result in the increased bulk mean velocity and the decreased turbulent friction coefficient. The vertical fluid motion of thermal plumes drastically changes the transport mechanism of the Reynolds shear stress. The thermal plumes are spatially aligned in the streamwise direction, and the low-speed streaks and vortical structures are concentrated in the region where the thermal plume starts to rise. The Prandtl number effects on the turbulent kinetic energy are also studied when the thermal plumes emerge.

1 Introduction

In many important engineering and geophysical flows, turbulent heat transport occurs in the presence of thermal (or density) stratification. When the thermal stratification is dynamically unstable, large-scale thermal convection takes place (Turner, 1973; Tritton, 1977). The occurrence of thermal convection can also alter significantly the dynamics of turbulence near a wall and its transport mechanisms (Lumley et al., 1978; Domaradzki and Metcalfe, 1988). From theoretical and experimental studies, Lumley et al. (1978) found that in a convectively driven atmosphere, the turbulent diffusion should remove turbulent kinetic energy from the near-wall region and transport it vertically to the outer region. Through a direct numerical simulation, Domaradzki and Metcalffe (1988) found that the pressure diffusion should transfer the turbulent energy produced by the buoyancy in the convective layer toward the near-wall region. Both studies indicate that under unstable stratification, diffusion is more likely to transport kinetic turbulent energy between the near-wall and outer regions.

There has been continuous interest in the near-wall turbulence over the last three decades. From the studies of wall-bounded turbulent shear flows, the organized motion, i.e., the so-called bursting phenomenon, was identified as a primary turbulence mechanism for the production of the Reynolds stress and turbulence energy in the near-wall region (Kline et al., 1967; Kim et al., 1971). From this viewpoint, some experimental studies have also been carried out to reveal buoyancy effects on the bursting phenomena (Kasagi and Hirata, 1977; Mizushina et al., 1982; Fukui and Nakaijma, 1985; Fukui et al., 1991).

Kasagi and Hirata (1977) concluded that the unstable buoyant effects imposed on the near-wall region should cause mainly the decrease of the mean spacing of low-speed streaks with little influence on the mean bursting period. Mizushina et al. (1982) and Fukui and Nakajima (1985) found that with increasing buoyant instability the bursting period decreased and the outward movement of low-speed fluid, i.e., ejection, was intensified. Fukui and Nakajima (1985) also made clear the different dependence of the turbulent quantities and structure on unstable stratification in the near-wall region and outer region. On the other hand, Fukui et al. (1991) found that under a strongly unstable condition, the turbulent structure was essentially different from that under a neutral one, and the thermal plumes caused by the buoyancy force became the main contributor to the production of the Reynolds shear stress and turbulent heat flux. The intensified ejection (Mizushina et al., 1982; Fukui and Nakajima, 1985) should be associated with the generation of turbulent thermal plumes.

Recently, the quasi-coherent streamwise vortices have been found to dominate the turbulence mechanisms near a wall (Robinson, 1991; Kasagi et al., 1995). Thus, in order to understand buoyancy effects on the near-wall turbulence, it is necessary to learn how these streamwise vortices behave under such dynamical effects. However, with the complexity of the near-wall turbulence itself, the data obtained from an experimental study may be insufficient. For a more detailed investigation of the thermal stratification effects, a set of direct numerical simulations (DNS, hereafter) is suitable.

The objectives of this work are to perform a DNS study of a fully developed horizontal turbulent channel flow under unstable thermal stratification at several different Grashof numbers, and to investigate the unstable buoyancy effects on both the statistical and instantaneous near-wall turbulent structures. As a result of this study, it was found that the large-scale thermal convection involving the thermal plumes diminishes the quasi-coherent streamwise vortices. From DNS at different Prandtl numbers it was also found that this parameter strongly affects the structure of the large-scale thermal convection.

2 Numerical Procedure

The flow geometry and the coordinate system are shown in Fig. 1. The flow field is driven by a constant mean pressure gradient in the x-direction. The flow and thermal fields are assumed to be fully developed so that periodic boundary conditions are imposed in the x- and z-directions, respectively. The no-slip boundary condition is imposed on the velocity components on the two walls which are assumed to be at different but constant temperatures. As a result, there is a constant positive temperature difference $\Delta T \equiv (T_b - T_t)$ between the bottom

---

[1] Present address: Department of Mechanical Engineering, Nagoya Institute of Technology, Gokiso-cho, Showa-ku, Nagoya 466, Japan.

Contributed by the Heat Transfer Division for publication in the Journal of Heat Transfer. Manuscript received by the Heat Transfer Division January 16, 1996; revision received November 14, 1996; Keywords: Mixed Convection, Stratified Flows, Turbulence. Associate Technical Editor: M. Kaviany.

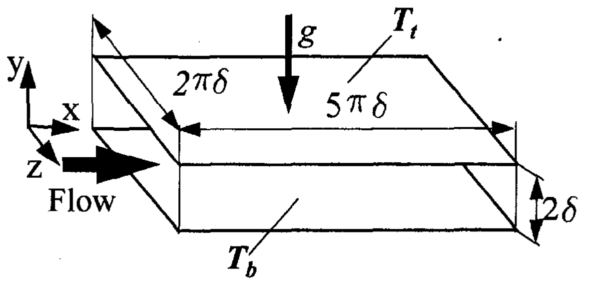

Fig. 1 Flow geometry and coordinate system

and top walls. The gravitational acceleration g is in the y-direction to cause an unstable buoyancy effect.

This physical problem of thermal convection can be described by the following standard set of hydrodynamic equations with the Boussinesq-Oberbeck approximation:

$$\rho_r \frac{D\mathbf{u}}{Dt} = -\nabla p - \rho_r \beta \theta \mathbf{g} + \mu \nabla^2 \mathbf{u}, \tag{1}$$

$$\frac{\partial u}{\partial x} + \frac{\partial v}{\partial y} + \frac{\partial w}{\partial z} = 0, \tag{2}$$

$$\rho_r C_p \frac{D\theta}{Dt} = \lambda \nabla^2 \theta, \tag{3}$$

where $\mathbf{u}(x, y, z, t) = (U + u, v, w)$ is the velocity vector. In these equations, the kinematic viscosity $\nu = \mu/\rho_r$, the coefficient of thermal diffusivity $\alpha = \lambda/(\rho_r C_p)$, the coefficient of thermal expansion β, and the gravitational acceleration $\mathbf{g}$ are assumed constant. The fluid density ρ is also set to be constant ρ_r in the above equations, although it becomes a function of temperature when coupled with the gravitational acceleration $\mathbf{g}$, i.e., $\rho = \rho_r(1 - \beta\theta)$.

All the variables and parameters in the equations are nondimensionalized by the channel half-width δ, the friction velocity u_τ and ΔT. The Reynolds number is fixed at $\mathrm{Re}_\tau = 150$ throughout the present study. The resultant bulk Reynolds number $\mathrm{Re}_m = 2U_m\delta/\nu$ is 4580 in the case without buoyancy (see Kasagi et al., 1992). The Grashof number $\mathrm{Gr} = g\beta\Delta T(2\delta)^3/\nu^2$ is varied from $\mathrm{Gr} = 0.0$ to 4.8×10^6 as shown in Table 1, while the Prandtl number $\mathrm{Pr} = \nu/\alpha$ is varied from 0.1 to 2.0 at $\mathrm{Gr} = 1.3 \times 10^6$.

Table 1 Flow conditions

Case	1	Kuroda et al. 1995	2	3	4	4 H	4 LLP	4 LP	4 HP	5
$Gr/10^6$	0.0		0.4	0.9	1.3					4.8
Re_τ	150									
Pr	0.71						0.01	0.1	2.0	0.71
U_b^+	14.50	15.26	14.47	14.81	14.68	15.57	14.80	15.00	14.47	13.55

Referring to the numerical procedure used by Kim et al. (1987), a fourth-order partial differential equation for v, a second-order partial differential equation for the wall-normal component of vorticity, and the continuity equation were used to solve the flow field.

In all cases, a spectral method is adopted with a Fourier series in the x- and z-directions and a Chebyshev polynomial expansion in the y-direction. The collocation grid used to compute the nonlinear terms in physical space has 1.5 times finer resolution in each direction to remove aliasing errors. For time-integration, the second-order Adams-Bashforth and Crank-Nicolson schemes are adopted for the nonlinear and viscous terms, respectively. A Crank-Nicolson scheme is also adopted for the buoyancy term in Eq. (1).

Initially, the computation is continued until both flow and thermal fields are judged to have reached their fully developed states. Then, in order to obtain various turbulent statistics and their budgets, ensemble averages are taken over time and the x–z plane.

Cases 1 to 5 at different Grashof numbers are calculated with a relatively coarse grid, i.e., $64 \times 49 \times 64$ in the x-, y-, and z-directions, respectively. Then, in order to assess the numerical accuracy, 128×128 Fourier modes and Chebyshev polynomials up to the 96th order in wavenumber space are used in the case of $\mathrm{Gr} = 1.3 \times 10^6$ (Case 4H). In all above cases, the spanwise period of the computational box is $2\pi\delta$, while the streamwise period is $5\pi\delta$. Since large-scale convection arises in the channel, simulations are repeated in Case 4 over computational domains of different sizes. In Case 4S, the streamwise and spanwise periods of the computational domain are reduced to $2.5\pi\delta$ and $\pi\delta$, respectively, while in Case 4L they are increased to $7.5\pi\delta$ and $3\pi\delta$, respectively. All three cases have the same grid resolution.

The flow conditions and the bulk mean velocity, U_b^+, in each case are summarized in Tables 1 and 2. The result of an isother-

Nomenclature

B_x, B_z = period of computational box in x- and z-directions
C_f = friction coefficient, $2\tau_w/\rho U_b^2$
C_p = specific heat at constant pressure
$E_{uu}(\kappa_z)$ = spanwise energy spectra of u^{+2}
F = flatness factor
Gr = Grashof number, $g\beta(T_b - T_t)(2\delta)^3/\nu^2$
Gr^+ = Grashof number, $g\beta\theta_\tau(\delta/\mathrm{Re}_\tau)^3/\nu^2$
g = gravitational acceleration
k = turbulent kinetic energy, $\overline{u_i u_i}/2$
Nu = Nusselt number, $2\delta q_w/\lambda\Delta T$
Pr = Prandtl number, ν/α
p = pressure
q_w = total heat flux at the wall, $-\lambda(dT/dy)_w$
Re_b = bulk mean Reynolds number, $2U_b\delta/\nu$
Re_τ = Reynolds number, $u_\tau\delta/\nu$
T = temperature
T_b, T_t = temperatures at bottom and top walls
t = time
U = mean velocity in x-direction
U_b = bulk mean velocity, $\int_{-\delta}^{\delta} U dy/2\delta$
u, v, w = fluctuating velocity components in x-, y-, and z-directions
u_τ = friction velocity, $\sqrt{\tau_w/\rho}$
x, y, z = streamwise, wall-normal and spanwise directions
α = thermal diffusivity, $\lambda/(\rho_r C_p)$
β = volumetric expansion coefficient
ΔT = temperature difference, $T_b - T_t$
δ = channel half width
θ = temperature difference, $T - T_t$
θ_τ = friction temperature, $q_w/(\rho C_p u_\tau)$
κ_z = wave number in z-direction, $2\pi j/B_z$ ($j = 0, 1, 2, \ldots$)
λ = thermal conductivity
μ = viscosity
τ_w = wall shear stress, $\mu(du/dy)_w$
ν = kinematic viscosity
ρ = density
ρ_r = reference density for Boussinesq approximation

Subscripts and Superscripts

rms = root-mean-square value
$_0$ = at Gr = 0 and Pr = 0.71
$\overline{}$ = ensemble average
+ = nondimensionalized by wall variables, u_τ and ν

Table 2 Flow conditions in supplemental calculations

	Case 4H	Case 4	Case 4S	Case 4L
Gr	1.3×10^6			
Re_τ	150			
Pr	0.71			
B_x/δ, B_z/δ	5π, 2π		2.5π, π	7.5π, 3π
Δx^+, Δz^+	18.4, 7.36	36.8, 14.72		

mal channel flow calculated by Kuroda et al. (1995) is also included for comparison. Their calculation was carried out with the same number of grid points as in Case 4H.

3 Results and Discussion

The effect of the size of the computational domain will be discussed first. Figure 2 shows the mean velocity distributions normalized by the friction velocity in Cases 4, 4S, and 4L. The result under the buoyancy free condition in Case 1 is also included for comparison. The mean velocity profiles in Cases 4, 4S, and 4L coincide well with each other, but they are markedly different from that of Case 1. This difference, i.e., the increase of the mean velocity under unstable stratification, is vitally important in this paper because it is closely associated with the most important stratification effect on the near-wall turbulent structure. It can be said that the stratification effects on the near-wall turbulent structure predicted by the different sizes of the computational box are almost the same, although the structure of the large-scale convection might be affected by the imposed periodic boundary conditions. This fact has also been confirmed from the observation of other turbulent statistics. Moreover, it should be noted that all the statistical changes observed in Case 4 are also clearly observed in Case 4L.

Figure 3 shows the mean velocity distributions normalized by the bulk mean velocity in Cases 1, 4, and 4H. The result of Kuroda et al. (1995) is also included. As shown in Table 1, the bulk mean velocities in Cases 1 and 4 are smaller than those obtained in Kuroda et al. (1995) and Case 4H, respectively. This indicates that the grid resolution is not sufficient to fully resolve the small-scale turbulent fluctuations in Cases 1 to 5. It is seen in Fig. 3, however, that the mean velocity profiles obtained on the two different grids are almost identical, once they are normalized by U_b. With the buoyancy effect, the central part of the velocity profile has leveled off, and this change is confirmed in the two sets of numerical results. Because of the heavy computational load of present DNS, most of the computations have been performed on the coarser grid, i.e., Cases 1 to 5. Thus, whereas these results may have slight grid dependence, their relative comparison should be valid, at least qualitatively, and deserves the in-depth discussion below.[2]

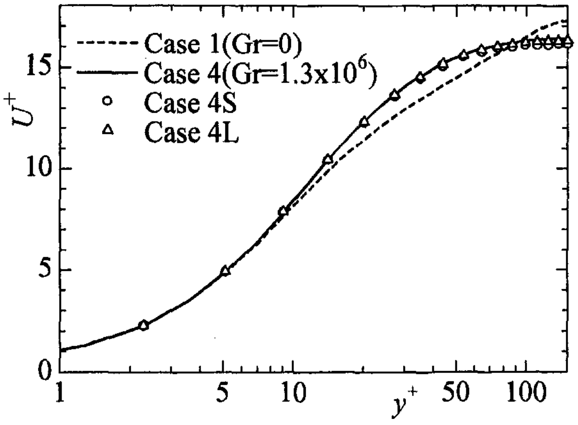

Fig. 2 Mean velocity profiles nondimensionalized by u_τ (Cases 1, 4, 4S, and 4L)

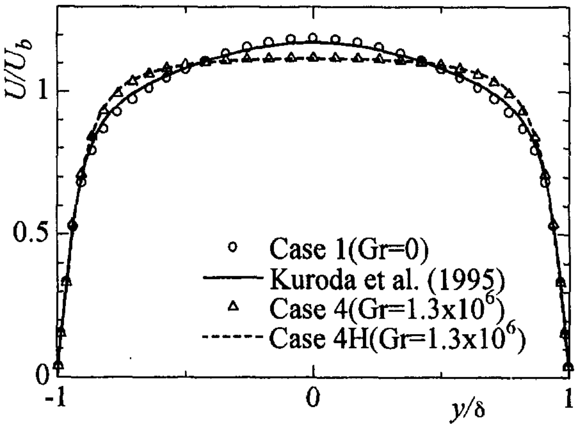

Fig. 3 Mean velocity profiles (Cases 1, 4, and 4H)

Figure 4 shows the changes in the normalized friction coefficient and Nusselt number, i.e., C_f/C_{f0} and $\mathrm{Nu}/\mathrm{Nu}_0$, versus the Grashof number. The friction coefficient first decreases when the Grashof number increases, and takes a minimum value of $\mathrm{Gr} = 9.0 \times 10^5$, to reach about 0.96. When the Grashof number further increases to 4.8×10^6, C_f increases because turbulence is much activated by buoyancy. On the other hand, $\mathrm{Nu}/\mathrm{Nu}_0$ simply increases with the Grashof number unlike the friction coefficient. Buoyancy generated eddies cause relatively little momentum transport although they are quite effective in transporting heat, as discussed in Tennekes and Lumley (1972).

The logarithmic plot of the mean velocity distribution in Cases 1 to 5 is shown in Fig. 5, while Fig. 6 shows the distribution of the Reynolds shear stress $-u^+v^+$. The mean velocity in the channel central region tends to decrease under unstable stratification. In the cases of $\mathrm{Gr} = 9.0 \times 10^5$ and 1.3×10^6, the mean velocity increases in the buffer as well as logarithmic regions. As shown in Fig. 6, this increase is mainly due to the decrease of $-u^+v^+$ in the buffer region and sublayer at $y^+ < 30$. The increased mean velocity under unstable stratification is an interesting phenomenon, which, to the authors' knowledge, has not been observed previously and should be associated with the decrease of the turbulent friction coefficient. When the Gras-

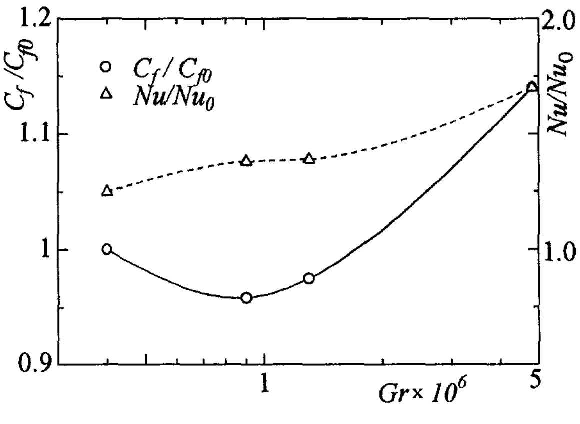

Fig. 4 Dependence of normalized friction coefficient and Nusselt number on Grashof number (Cases 2 to 5)

---

[2] The tabulated data of Case 4H are available from the DNS database site at the University of Tokyo (http://www.thtlab.t.u-tokyo.ac.jp/).

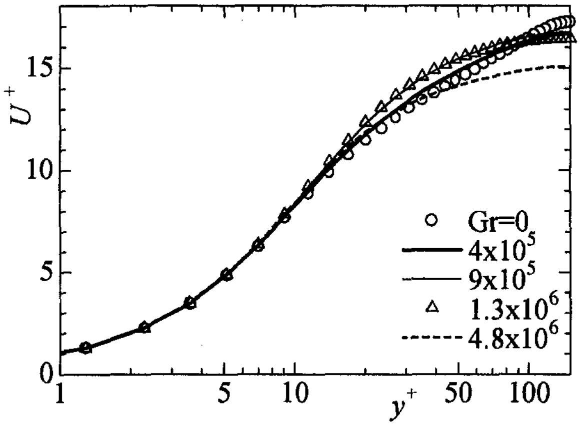

Fig. 5 Mean velocity profiles (Cases 1 to 5)

hof number is further increased to Gr = 4.8 × 10^6, the mean velocity decreases in almost all regions. This is because $-\overline{u^+v^+}$ increases considerably at $y^+ > 15$, although at $y^+ < 15$ it is still smaller than that at Gr = 0 (as shown in Fig. 6).

The distributions of the wall-normal turbulent heat flux $-\overline{v^+\theta^+}$ in Cases 1 to 5 are shown in Fig. 7. The effect of buoyancy on $-\overline{v^+\theta^+}$ is nearly the same as that on $-\overline{u^+v^+}$. Presently, the coupling between the flow and thermal fields is very tight in the near-wall region, so any change in the former is also observed in the latter in the same qualitative manner as when the temperature fluctuations are normalized by the friction temperature. Hence, the statistics of the velocity field are mainly discussed in the rest of the paper.

Here, the transport equation of u^+v^+ is examined in Cases 1 to 5. It has the form:

$$0 = \underbrace{\mathrm{Gr}^+\overline{u^+\theta^+}}_{G_{12}} - \underbrace{\overline{v^{+2}}\frac{dU^+}{dy^+}}_{P_{12}} - \underbrace{\frac{\partial}{\partial y^+}\overline{u^+v^{+2}}}_{T_{12}} + \underbrace{\frac{\partial}{\partial y^{+2}}\overline{u^+v^+}}_{V_{12}}$$
$$- \underbrace{\frac{\partial}{\partial y^+}\overline{p^+v^+}}_{\psi_{12}} + \underbrace{\overline{p^+\left(\frac{\partial u^+}{\partial y^+}+\frac{\partial v^+}{\partial x^+}\right)}}_{\phi_{12}} - \underbrace{2\overline{\frac{\partial u^+}{\partial x_i^+}\frac{\partial v^+}{\partial x_i^+}}}_{\epsilon_{12}}. \quad (4)$$

The primary terms in the above equation are shown in Figs. 8 and 9.

As shown in Fig. 8, the buoyant production G_{12} remains relatively small in the near-wall region where the Reynolds shear stress changes drastically with the increase of buoyancy.

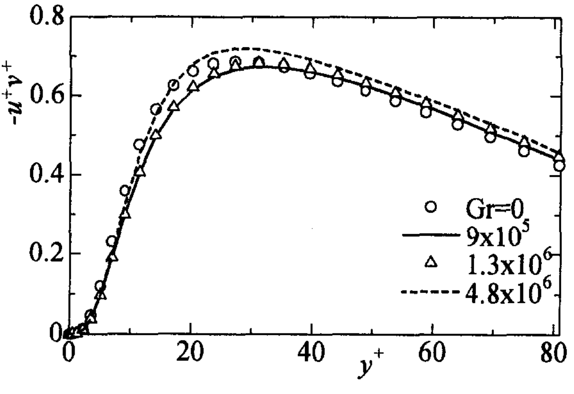

Fig. 6 Distribution of Reynolds shear stress $-\overline{u^+v^+}$ (Cases 1 to 5)

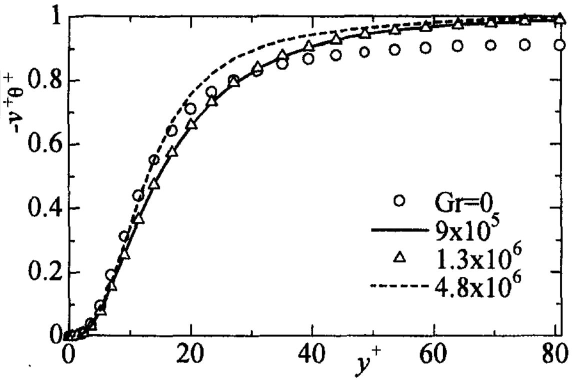

Fig. 7 Distribution of turbulent heat flux $-\overline{v^+\theta^+}$ (Cases 1 to 5)

Away from the wall, however, G_{12} becomes relatively important because the shear production P_{12} is much decreased by buoyancy. The pressure diffusion ψ_{12} and pressure-strain ϕ_{12} terms exhibit marked changes in the near-wall region as well as in the outer region. The role of the enhanced pressure diffusion term is to transfer u^+v^+ produced by the buoyancy and shear in the outer region toward the near-wall region; in the latter region the pressure-strain correlation which is the dominant sink term of u^+v^+ is also much enhanced. The turbulent diffusion T_{12} also increases in the near-wall region but transfers u^+v^+ toward the channel central regions.

Figure 9 shows the u^+v^+ budget at the largest Grashof number, i.e., Gr = 4.8 × 10^6. The buoyancy production term is still small at $y^+ < 10$ where the pressure-diffusion and pressure-strain correlation terms become dominant. Note that in this near-

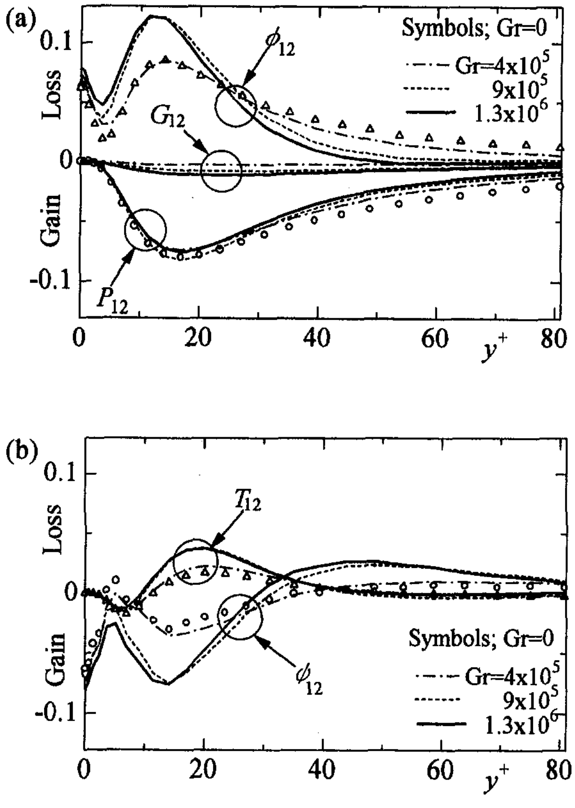

Fig. 8 Budget terms of $\overline{u^+v^+}$ in Cases 1 to 4: (a) P_{12}—shear production, G_{12}—buoyant production, ϕ_{12}—pressure strain; (b) ψ_{12}—pressure diffusion, T_{12}—turbulent diffusion

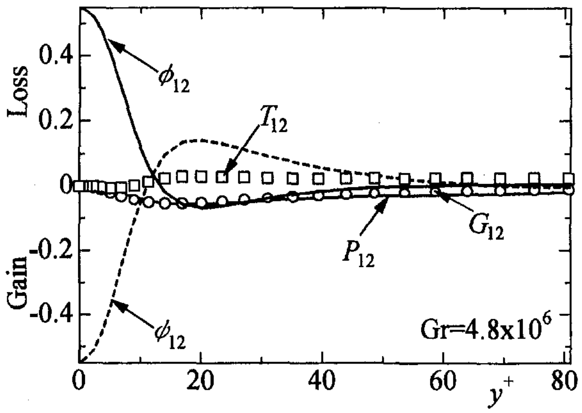

Fig. 9 Budget terms of $\overline{u^+v^+}$ in Case 5: P_{12}—shear production, G_{12}—buoyant production, ϕ_{12}—pressure strain, ψ_{12}—pressure diffusion, T_{12}—turbulent diffusion

wall region, the decrease of $-\overline{u^+v^+}$ is still observed as has been shown in Fig. 6. However, at $y^+ > 15$ the buoyancy production becomes large and almost equal to other terms. Both the minimum of ϕ_{12}, and the maximum of ψ_{12}, which are observed near the wall in Fig. 8, disappear, and their values monotonously increase toward the wall. It is of great interest that the pressure-strain correlation ϕ_{12} even becomes negative, acting as a source term of $\overline{u^+v^+}$ in the region of $y^+ > 20$, unlike in most turbulent shear flows. This suggests drastic changes of the structure of the near-wall turbulence.

The dimensionless root-mean-square velocity fluctuations are shown in Fig. 10. These quantities drastically change in the near-wall region as well as in the outer region under unstable stratification. The value of u^+_{rms} increases markedly with increasing buoyant instability, although $\overline{u^{+2}}$ itself does not have any buoyancy production process. The value of v^+_{rms} decreases in the near-wall region, while it increases in the outer region. In the cases of Gr = 1.3 × 10^6 and 4.8 × 10^6, the increase of w^+_{rms} is observed in almost all the regions of the channel. Especially at Gr = 4.8 × 10^6; it increases markedly and almost equals u^+_{rms}.

Figure 11 shows the spanwise energy spectra at $y^+ = 20$ in Cases 1, 4, and 5. These spectra are nondimensionalized by u_τ and δ. In this figure, the wave number $\kappa_z = 1$ corresponds to the wave length $\lambda^+ = 900$. It is seen at Gr = 1.3 × 10^6 that all components increase at the lower wave numbers, while they decrease at the medium wave numbers of $\kappa_z = 3$ to 10, which corresponds to $\lambda^+ = 300$ to 90. Since this medium wave number range includes the mean spanwise spacing of low-speed streaks ($\lambda^+ = 100$), the bursting phenomenon originated from the low-speed streaks should be suppressed. On the other hand, the increase at low wave numbers is a result from the large-scale thermal convection. Thus, there should be an interaction between the thermal convection and the bursting phenomenon in the near-wall region. In the case of Gr = 4.8 × 10^6, the energy spectrum decreases drastically at the medium to high wave numbers, while its increase at the low wave numbers becomes more remarkable.

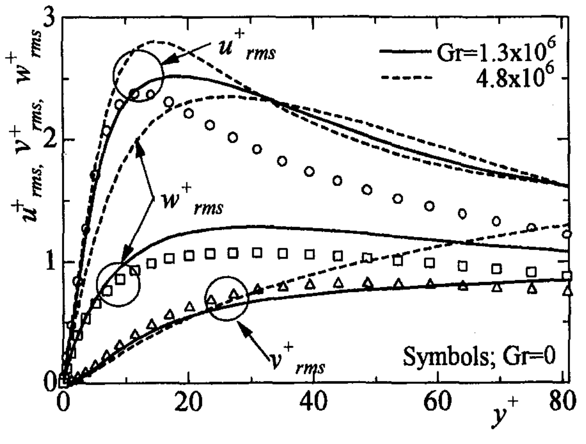

Fig. 10 Root-mean-square velocity fluctuations in Cases 1, 4, and 5

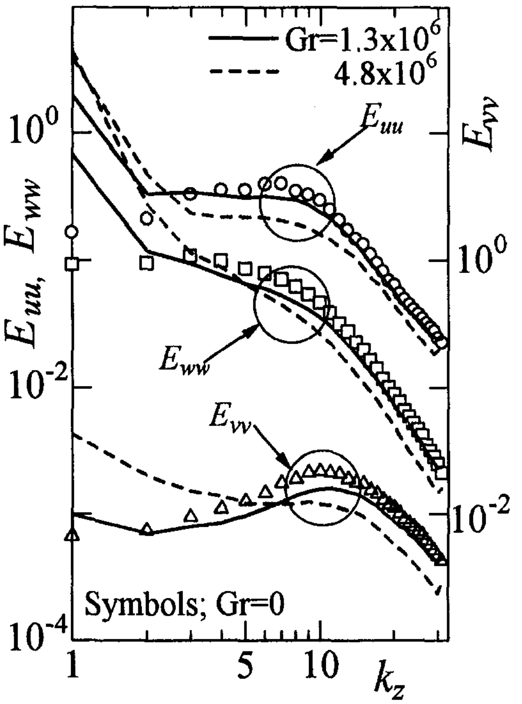

Fig. 11 One-dimensional spanwise energy spectra at $y^+ = 20$ in Cases 1, 4, and 5

From the statistical results in Figs. 6–11 it should be noted that the thermal convection associated with the unstable buoyancy imposes large effects on the Reynolds shear stress, its transport mechanisms, and its turbulent structure even in the near-wall region where the buoyancy production term is very small.

Finally, an instantaneous snapshot of the flow field is examined to show how the near-wall turbulence structures are affected by buoyancy. The distinctive features observed in the turbulent statistics are reconsidered in view of the turbulent structures. A typical example of the instantaneous distribution of velocity fluctuations in a cross-stream plane is shown in Figs. 12 and 13. In Case 4H, with Gr = 1.3 × 10^6, both the thermal plumes and the quasi-streamwise vortices exist simultaneously in the central channel region and in the near-wall region, respectively. In Fig. 12, the large-scale downward and upward plumes are seen at the center and at the sides in both Figs. 12 and 13. The thermal plumes, the height of which is as large as the width of the channel, emerge from the near-wall region and transport low-speed fluid toward the central channel region. Then, the high-speed fluid in the central channel region is pushed toward the opposite wall, where the spanwise flow is driven along the wall. The quasi-streamwise vortices seem to be swept out by this spanwise flow, induced by the plumes, and concentrated into the confined regions where the thermal plumes emerge. These figures clearly show the mechanism responsible for the fact suggested in Fig. 11 that the large-scale thermal convection

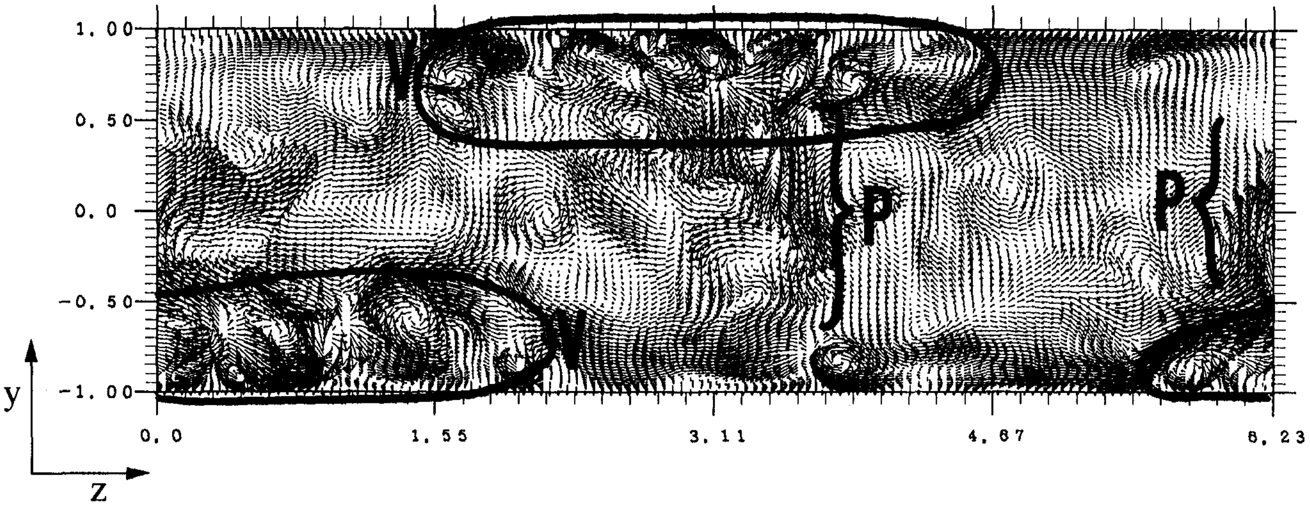

Fig. 12 **Instantaneous velocity vectors in the vertical (y–z) plane in Case 4H: P—thermal plume; V—streamwise vortices, $\Delta y^+ \times \Delta z^+ = 300 \times 943$**

breaks the quasi-streamwise vortices. At Gr $= 4.8 \times 10^6$, the thermal plumes become the only dominant turbulent structure and the near-wall streamwise vortices are rarely observed (not shown here).

Figure 14 shows iso-surfaces of instantaneous high and low u^+v^+ regions in the whole computational domain at the same instant as in Figs. 12 and 13. Note that on the top wall the ejection and sweep motions correspond to $u^+v^+ > 0$, while on the bottom wall they correspond to $u^+v^+ < 0$. It is seen that the strong ejection and sweep regions are concentrated at both sides on the bottom wall, while they are seen only at the center on the top wall. This indicates that both ejection and sweep motions disappear where the streamwise vortices are swept away, and this results in the decrease of the averaged shear stress $-u^+v^+$ in the near-wall region. Figure 14 also indicates that the thermal plumes are aligned in the streamwise direction when the mean shear is imposed.

Figures 15(a) and (b) show the iso-surfaces of instantaneous negative p^+ and u^+ regions in the cases of Gr $= 1.3 \times 10^6$ and 0, respectively. The visualized region is the bottom half of the computational domain. As indicated by Robinson (1990), the negative u^+ and p^+ regions correspond to the low-speed streaks and the vortical structures, respectively. In the case of Gr $= 1.3 \times 10^6$, both turbulent structures are concentrated only in the central part of channel where the thermal plume emerges. This feature is completely different from that of the neutral flow in Fig. 15(b). The concentration of these turbulent structures should increase the spatial intermittency and hence the flatness factors of turbulent quantities.

Figure 16 shows the flatness factors $F(u)$ and $F(v)$. At Gr $= 1.3 \times 10^6$, the formation of thermal plumes and the associated concentration of the low-speed streaks markedly increase the values of both $F(u)$ and $F(v)$. However, at Gr $= 4.8 \times 10^6$, where the streamwise near-wall vortices are rarely observed, both $F(u)$ and $F(v)$ decrease.

Finally, Prandtl number effects are investigated at Gr $= 1.3 \times 10^6$. Figure 17 shows the change in the distribution of k^+ with the Prandtl number, while Fig. 18 shows the buoyant pro-

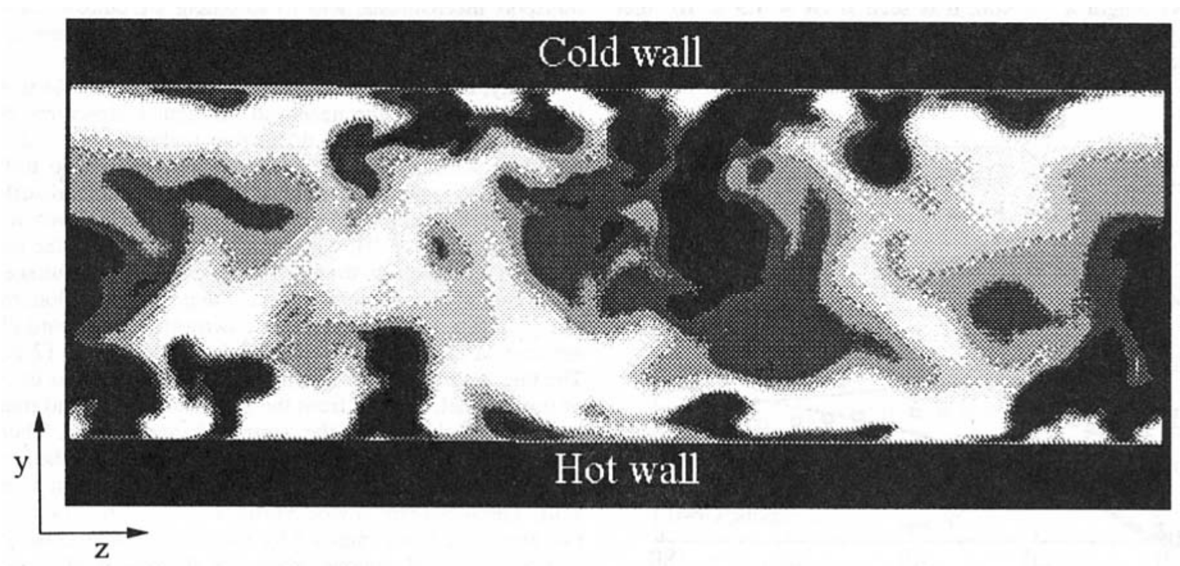

Fig. 13 **Instantaneous distribution of streamwise velocity fluctuation in the vertical (y–z) plane in Case 4H: black to white, $u^+ = -2$ to 2**

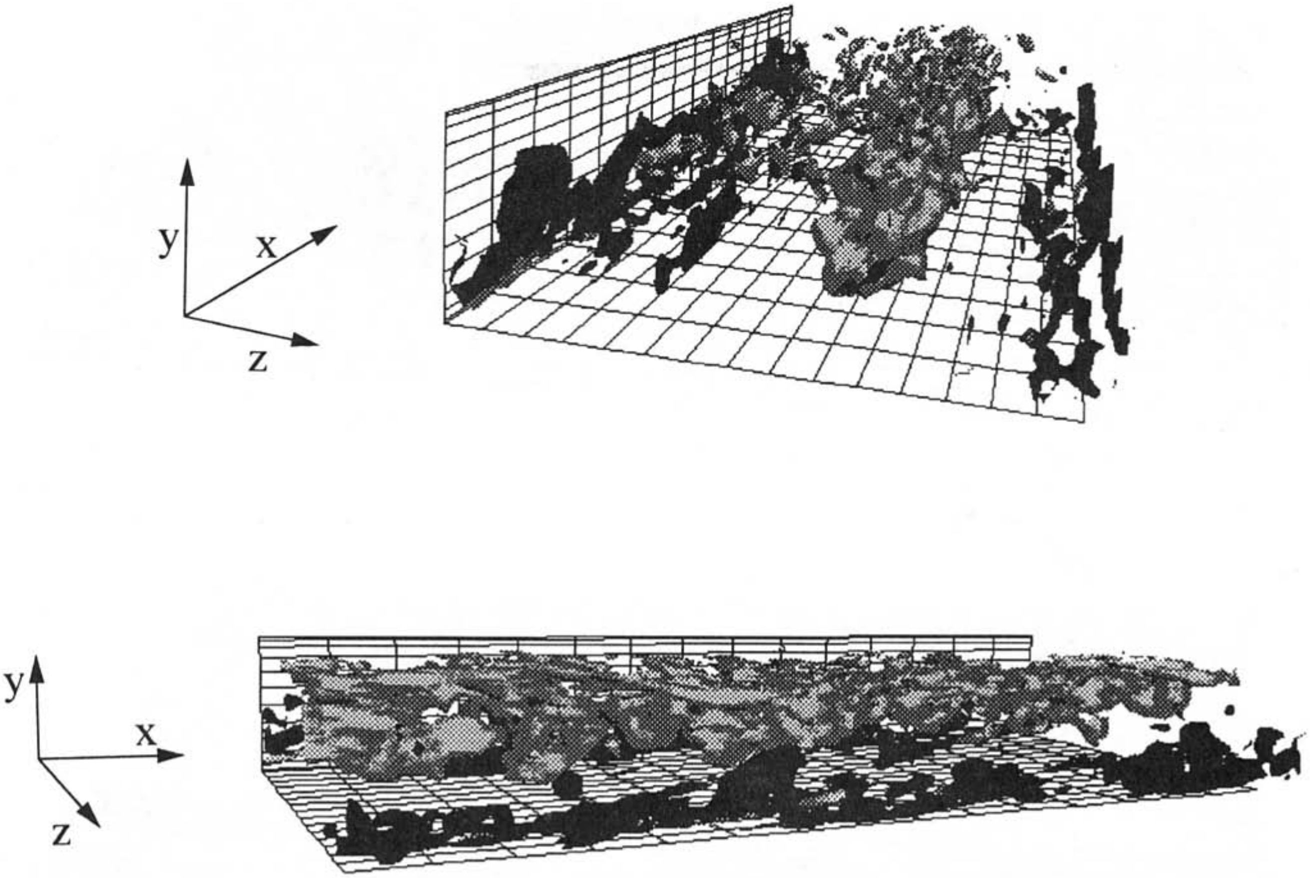

Fig. 14 Iso-surfaces of u^+v^+ in Case 4H: gray, $u^+v^+ = 3$; black, $u^+v^+ = -3$

duction term $\mathrm{Gr}^+\overline{v^+\theta^+}$ appearing in the k^+ budget. When Pr increases, k^+ first increases and takes the maximum value at Pr LY 0.1. However, as Pr increases further, k^+ decreases. This is owing to the change in $\mathrm{Gr}^+v^+\theta^+$. Thus, the nonlinear behavior of k^+, with the Prandtl number change, is associated with the effect of the buoyancy production.

The turbulent heat flux $v^+\theta^+$ included in the buoyancy production term should represent the ratio of the turbulent heat flux to the total flux. From the previous investigations (Kasagi and Ohtsubo, 1993; Iida and Kasagi; 1993), it is indicated that $v^+\theta^+$ decreases as the Prandtl number is decreased because in low Prandtl number fluids, heat is transported more vigorously by the thermal conduction rather than the turbulent heat flux. On the other hand, Gr^+ increases when Pr decreases because it represents the total flux transferred from the wall to the near-wall fluid through thermal conduction. Thus, the nonlinear behavior of the kinetic energy with the change in the Prandtl number should be due to these mixed effects.

As shown in Table 1, in Case 4LP where the large-scale thermal convection is most activated, the bulk mean velocity increases in comparison to Case 4, while it decreases in Case 4HP.

4 Conclusions

Direct numerical simulations of the fully developed horizontal turbulent channel flow under unstable density stratification were carried out to investigate the interactive shear and buoyancy effects on the turbulent structures. The following conclusions are obtained.

1 With the increasing of the Grashof number the buoyant thermal plumes emerge from the near-wall region. On the opposite wall the spanwise flow, driven by the thermal plumes, sweeps out the quasi-coherent streamwise vortices and concentrates them into a confined region near the wall. Thus, the region occupied by streamwise vortices is diminished. The velocity fluctuation components at the medium wave numbers associated with the low-speed streak and streamwise vortex clearly decrease, while those at the low wavenumbers caused by the thermal plumes are activated. The ejection and sweep motions associated with the streamwise vortices are also diminished, although the thermal plumes themselves should contribute to them. Thus, in the case where the thermal plumes are not so intensive, Reynolds shear stress decreases in the near-wall region, which results in the increase of the mean velocity profile and the decrease of the turbulent friction coefficient.

2 Thermal convection including the plumes is found to give large effects on the transport mechanisms even in the near-wall region where buoyancy production is relatively small. Through the pressure diffusion and turbulent diffusion terms, the Reynolds shear stress is more vigorously transported between the outer region and near-wall region; it is destroyed by the pressure-strain correlation in the near-wall region. When the Grashof number is very large, the pressure-strain correlation works even as a source term of the Reynolds shear stress.

3 The thermal plumes are spatially aligned in the streamwise direction. Low-speed streaks and streamwise vortices are concentrated in the region where the thermal plume emerges. The eruption of thermal plumes, and the associated concentration of the turbulent structures, increase the flatness factors of velocity components in the near-wall region.

4 The flow field is greatly affected by the Prandtl number. As the Prandtl number is decreased, heat is exchanged

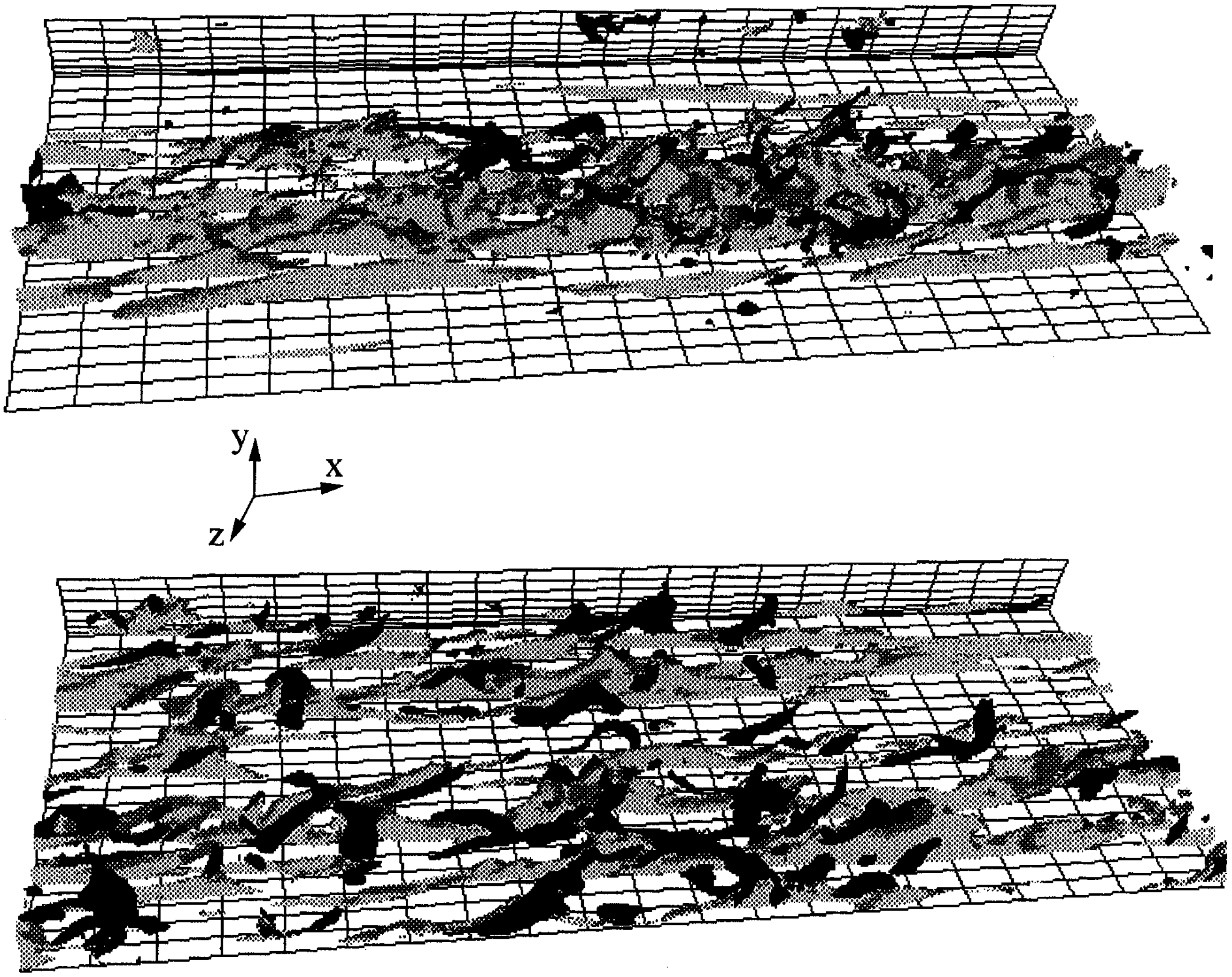

Fig. 15 Iso-surfaces of u^+ and p^+: (a) Case 4H, gray—$u^+ = -3$, black—$p^+ = -3$; (b) Gr = 0 (Kuroda et al., 1995), gray—$u^+ = -3$, black—$p^+ = -3$

more vigorously between the fluid and the wall; this increases the turbulent kinetic energy through the buoyancy effects. However, at the lowest Prandtl number studied, i.e., Pr = 0.01, heat is transported mainly by the molecular conduction rather than by the turbulent heat flux. In addition, the buoyancy effects become weaker, and the turbulent kinetic energy decreases. When the large-scale thermal convection is most activated at Pr = 0.1, the bulk mean velocity noticeably increases.

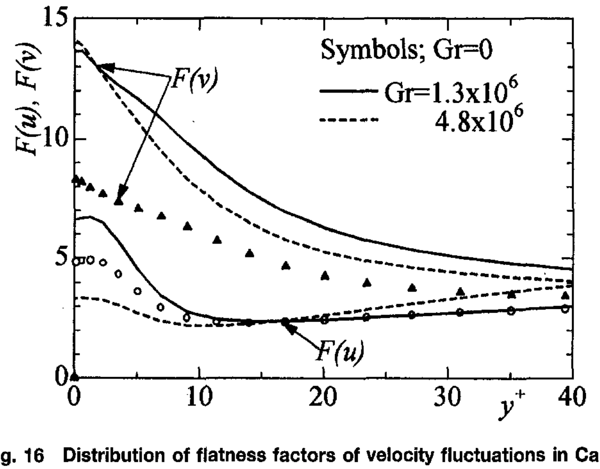

Fig. 16 Distribution of flatness factors of velocity fluctuations in Case 1, 4, and 5

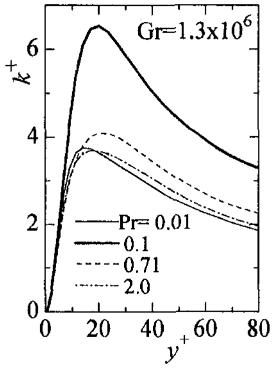

Fig. 17 Distribution of k^+ in Cases 4LLP, 4LP, 4, and 4HP

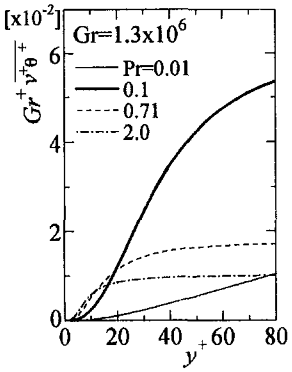

Fig. 18 Distribution of buoyant production of k^+ at different Prandtl numbers

Acknowledgments

This work was supported through the Grant-in-Aid for Scientific Research on Priority Areas (No. 05240103) by the Ministry of Education, Science, and Culture.

References

Domaradzki, J. A., and Metcalfe, R. W., 1988, "Direct Numerical Simulations of the Effects of Shear on Turbulent Rayleigh-Bénard Convection," *Journal of Fluid Mechanics,* Vol. 193, pp. 499–531.

Fukui, K., and Nakajima, M., 1985, "Unstable Stratification Effects on Turbulent Shear Flow in the Wall Region," *International Journal of Heat Mass Transfer,* Vol. 28, No. 12, pp. 2343–2352.

Fukui, K., Nakajima, M., and Ueda, H., 1991, "Coherent Structure of Turbulent Longitudinal Vortices in Unstably-Stratified Turbulent Flow," *International Journal of Heat Mass Transfer,* Vol. 34, No. 9, pp. 2373–2385.

Iida, O., and Kasagi, N., 1993, "Direct Numerical Simulation of Decaying Isotropic Turbulence With Scalar Transport," *Transactions JSME,* Vol. 59B, No. 567, pp. 3359–3364.

Kasagi, N., and Hirata, M., 1977, "Bursting Phenomena in Turbulent Boundary Layer on a Horizontal Flat Plate Heated From Below," *Heat Transfer and Turbulent Buoyant Convection,* D. B. Spalding and N. Afgan, eds., Hemishere, Washington, D. C., Vol. 1, pp. 27–38.

Kasagi, N., Tomita, Y., and Kuroda, A., 1992, "Direct Numerical Simulation of the Passive Scalar Field in a Turbulent Channel Flow," ASME JOURNAL OF HEAT TRANSFER, Vol. 114, pp. 598–606.

Kasagi, N., and Ohtsubo, Y., 1993, "Direct Numerical Simulation of Low Prandtl Number Thermal Field in a Turbulent Channel Flow," *Turbulent Shear Flows,* F. Durst, R. Friedrich, B. E. Launder, F. W., Schmit, U. Schuman, and J. H. Whitelaw, eds., Springer, Berlin, Vol. 8, pp. 97–119.

Kasagi, N., Sumitani, Y., Suzuki, Y., and Iida, O., 1995, "Kinematics of the Quasi-Coherent Vortical Structure in Near-Wall Turbulence," *International Journal of Heat and Fluid Flow,* Vol. 16, No. 1, pp. 2–10.

Kim, H. T., Kline, S. J., and Reynolds, W. C., 1971, "The Production of Turbulence Near a Smooth Wall in a Turbulent Boundary Layer," *Journal of Fluid Mechanics,* Vol. 50, pp. 133–160.

Kim, J., Moin, P., and Moser, R., 1987, "Turbulence Statistics in Fully Developed Channel Flow at Low Reynolds Number," *Journal of Fluid Mechanics,* Vol. 177, pp. 133–166.

Kline, S. J., Reynolds, W. C., Schraub, F. A., and Runstadler, P. W., 1967, "The Structure of Turbulent Boundary Layers," *Journal of Fluid Mechanics,* Vol. 30, pp. 741–773.

Kuroda, A., and Kasagi, N., and Hirata, M., 1995, "Direct Numerical Simulation of Turbulent Plane Couette-Poiseuille Flows: Effects of Mean Shear Rates on the Near Wall Turbulence Structures," *Turbulent Shear Flows,* F. Durst, N. Kasagi, B. E. Launder, F. W. Schmit, K. Suzuki, and J. H. Whitelaw, eds., Springer, Berlin, Vol. 9, pp. 241–257.

Lumley, J. L., Zeman, O., and Siess, J., 1978, "The Influence of Buoyancy on Turbulent Transport," *Journal of Fluid Mechanics,* Vol. 84, pp. 581–597.

Mizushina, T., Ogino, F., and Katada, N., 1982, "Ordered Motion of Turbulence in a Thermally Stratified Flow Under Unstable Conditions," *International Journal of Heat Mass Transfer,* Vol. 25, No. 9, pp. 1419–1425.

Robinson, S. K., 1991, "The Kinematics of Turbulent Boundary Layer Structure," NASA TM-103859.

Tennekes, H., and Lumley, J. L., 1972, *A First Course in Turbulence,* MIT Press, Cambridge.

Tritton, D. J., 1977, *Physical Fluid Dynamics,* Van Nostrand Reinhold, Wokingham.

Turner, J. S., 1973, *Buoyancy Effects in Fluids,* Cambridge University Press, Cambridge.

L. C. Yang

Y. Asako

Y. Yamaguchi

Department of Mechanical Engineering,
Tokyo Metropolitan University,
Tokyo, 192-03
Japan

M. Faghri
Department of Mechanical Engineering and
Applied Mechanics,
University of Rhode Island,
Kingston, RI 02881
faghrim@egr.uri.edu

Numerical Prediction of Transitional Characteristics of Flow and Heat Transfer in a Corrugated Duct

The numerical prediction of transitional characteristics of fluid flow and heat transfer in periodic fully developed corrugated duct is carried out by using a Lam-Bremhorst low Reynolds number turbulence model. Computations were performed for Prandtl number of 0.7, in the Reynolds number range of 100 to 2500, for corrugation angles of $\theta = 15$ and 30 deg, and for three interwall spacings. The predicted transitional Reynolds number is lower than the value for the parallel plate duct and it decreases with increasing corrugation angle. Experiments were also performed for pressure drop measurements and for flow visualization and the results were compared with the numerical predictions.

Introduction

Corrugated ducts are basic channel geometry in plate heat exchangers and plate-fin heat exchangers because of their efficient heat exchange capabilities. Such heat exchangers are employed in several engineering processes (e.g., food engineering, chemical engineering, etc.). Many studies for fluid flow and heat transfer in corrugated ducts have been presented in past including a series of experimental studies by O'Brien and Sparrow (1982) to measure the pressure drop and to visualize the flow field, by Sparrow and Comb (1983) to examine the effect of the inlet conditions on the heat transfer, and by Sparrow and Hossfeld (1984) to measure the pressure drop and heat transfer rates for corrugated ducts with rounded corners. Numerical solutions for the flow and heat transfer in a corrugated duct with right angle bends were reported by Izumi et al. (1983) and Amano (1984).

In the recent years, miniaturization has led to fabrication of mini and micro heat exchangers. Due to small characteristic lengths, the Reynolds numbers are low and the flow is usually laminar or in the transitional regime. This motivated the numerical study by Asako et al. (1987) for laminar flow and heat transfer in corrugated ducts with arbitrary bend angle by employing a coordinate transformation methodology. Also, experimental work was conducted by Nishimura et al. (1986) to measure the pressure drop and to visualize the flow field in a wavy channel with Reynolds number ranges from 100 to 4000. They reported the transition from laminar to turbulent flow occurs at about Re = 350, and the transitional Reynolds number is quite low compared with conventional ducts. A survey of the literature revealed a scarcity of numerical studies in the transitional regime with the exception of the work by Schmidt and Patankar (1987). They predicted the transitional Reynolds number for flow over a flat plate using a Lam-Bremhorst low-Reynolds number k-ϵ turbulence model and reported that this model is suitable for the prediction of the transition. This motivated the present work on the numerical prediction of transitional characteristics of flow and heat transfer in corrugated ducts with experimental confirmation.

The numerical computations were performed using the Lam-Bremhorst low-Reynolds number k-ϵ turbulence model to predict the transitional Reynolds number from laminar to turbulent flow in a corrugated duct with rounded corners. Furthermore, pressure drop measurements and flow visualizations were also performed. The numerical methodology utilizes an algebraic coordinate transformation developed by Faghri et al. (1984) which maps an irregular domain onto a rectangle. The numerical solutions are obtained for periodic fully developed flow under thermal boundary condition of uniform wall temperature. The calculations were carried out for corrugation angles θ of 15 deg and 30 deg, for three vertical spacings, H'/L, for Reynolds numbers in the range of 100 to 2500, and for Prandtl number of 0.7. Flow visualization and pressure drop measurements were also performed and the results were compared with the numerical predictions.

Formulation

Description of the Problem. The problem considered in the analysis is schematically shown in Fig. 1. As seen in this figure, the duct is infinitely long in the y-direction. When the flow becomes periodic fully developed, the velocity field repeats itself at corresponding axial stations in successive cycles. The solution domain is confined to a typical cycle shaded in Fig. 1.

The geometry of the duct is specified by the cycle length (L), the vertical spacing (H'), and the corrugation angle (θ). To get a converged solution, the sharpened edged corners are approximated by rounded corners using a sine curve with chord length, l. These rounded corners are shown by dashed lines in the figure. The ends of the duct at $y = 0$ and $y = L$ coincide with the x-axis. The deviation of the upper wall from the y-axis $\delta(y)$ to be used later for the coordinate transformation is expressed as follows:

$$0 < y < \frac{l}{2}: \quad \delta(y) = \frac{l}{2}\left[1 - \frac{2}{\pi}\cos\left(\frac{\pi y}{l}\right)\right] \times \tan\theta \tag{1}$$

$$\frac{l}{2} < y < \frac{L-l}{2}: \quad \delta(y) = y\tan\theta \tag{2}$$

$$\frac{L-l}{2} < y < \frac{L+l}{2}:$$

$$\delta(y) = \frac{L-l}{2}\tan\theta + \frac{l}{\pi}\cos\left[\frac{\pi}{l}\left(\frac{L}{2} - y\right)\right] \times \tan\theta \tag{3}$$

Contributed by the Heat Transfer Division for publication in the Journal of Heat Transfer. Manuscript received by the Heat Transfer Division December 4, 1995; revision received October 17, 1996; Keywords: Flow Transition, Numerical Methods, Turbulence. Associate Technical Editor: T. Rabas.

$$\frac{L+l}{2} < y < L - \frac{l}{2}: \quad \delta(y) = (L - y)\tan\theta \qquad (4)$$

$L - \frac{l}{2} < y < L$:

$$\delta(y) = \frac{l}{2}\left[1 - \frac{2}{\pi}\cos\left(\frac{\pi(L-y)}{l}\right)\right] \times \tan\theta. \qquad (5)$$

In the periodic fully developed region, the pressures of cyclically corresponding locations decrease linearly in the downstream direction such that

$$p(x, y) = -\dot{p}y + p'(x, y) \qquad (6)$$

where $\dot{p}$ is a per cycle pressure gradient and $p'(x, y)$ behaves in a periodic manner from module to module. The term $-\dot{p}y$ represents the nonperiodic pressure drop that takes place in the flow direction.

For the case of uniform wall temperature boundary condition, the fluid temperature approaches the wall temperature in the periodic fully developed region. Therefore, the dimensionless temperature will be defined as follows:

$$T(x, y) = [t(x, y) - t_w]/(t_b - t_w) \qquad (7)$$

where

$$t_b - t_w = \int (t - t_w)v\,dx \Big/ \int v\,dx. \qquad (8)$$

For a periodic thermally developed region, the dimensionless temperature satisfies the following relation

$$T(x, y) = T(x, y + L) = T(x, y + 2L) = \ldots. \qquad (9)$$

Therefore, the fully developed dimensionless temperature field repeats itself at corresponding axial station in successive cycles.

The Conservation Equation. The governing equations to be considered are the time-averaged continuity, momentum, and energy equations. The turbulence is modeled via the Lam-Bremhorst low-Reynolds number form of k-ϵ (1981). Constant thermophysical properties are assumed, and natural convection is excluded. The $(2/3)k\rho$ term is absorbed in the pressure gradient by redefining the pressure p^*. The governing equations are summarized in Table 1 and expressed in the following general form:

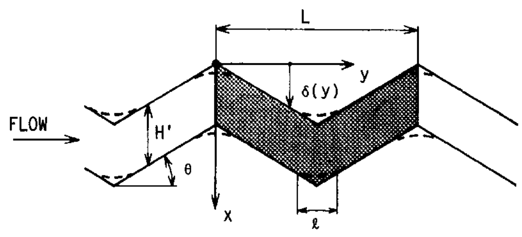

Fig. 1 Schematic diagram of a corrugated duct

$$\frac{\partial(\rho u\phi)}{\partial x} + \frac{\partial(\rho v\phi)}{\partial y} = \frac{\partial}{\partial x}\left(\Gamma\frac{\partial\phi}{\partial x}\right) + \frac{\partial}{\partial y}\left(\Gamma\frac{\partial\phi}{\partial y}\right) + b_\phi \qquad (10)$$

where ϕ stands for different dependent variables (u, v, T, k and ϵ). The term λ is a periodic parameter arising from the assumption of a constant wall temperature boundary condition. This value is determined as part of the solution process. The boundary conditions on the duct walls are

$$u = 0, \quad v = 0, \quad k = 0, \quad \epsilon_w = (\mu/\rho)\frac{\partial^2 k}{\partial n^2}, \quad T = 0 \qquad (11)$$

where n is a coordinate normal to the wall, and periodic boundary conditions are applied to the inlet and outlet boundaries.

Solution Methodology. The solution methodology based on the coordinate transformation is fully described by Asako and Faghri (1987). Specifically, the x, y-coordinates are transformed into η, ζ coordinates by the following relations:

$$\eta = x - \delta(y), \quad \zeta = y \qquad (12)$$

$$u_\eta = u - \beta v \qquad (13)$$

$$\left(\frac{\partial}{\partial x}\right)_y = \left(\frac{\partial}{\partial \eta}\right)_\zeta, \quad \left(\frac{\partial}{\partial y}\right)_x = \left(\frac{\partial}{\partial \zeta}\right)_\eta - \beta\left(\frac{\partial}{\partial \eta}\right)_\zeta \qquad (14)$$

Nomenclature

A_w = per-cycle heat transfer surface area per unit depth, m
b = source term
c_1, c_2 = turbulence model constants
D_H = hydraulic diameter = $2H'$, m
f = friction factor defined in Eq. (26)
f_1, f_2, f_μ = turbulence model functions
H' = vertical spacing between corrugated walls, m
h_m = fully developed heat transfer coefficient defined in Eq. (28), W/m^2 K
k = turbulence kinetic energy, m^2/s^2
L = axial length of a cycle, m
l = chord length, m
$\dot{m}$ = total mass flow rate per unit depth defined in Eq. (25), kg/(s m)
Nu$_m$ = average Nusselt number defined in Eq. (27)
n = coordinate normal to wall, m
Pr = Prandtl number
P = production term defined in Eq. (23)
p^* = redefined pressure, $=p' + (2/3)k\rho$, Pa
p' = periodic component of pressure defined in Eq. (6), Pa
$\dot{p}$ = per cycle pressure gradient, Pa/m
Q = per cycle wall heat transfer rate, W
Re = Reynolds number defined in Eq. (25)
T = dimensionless temperature defined in Eq. (7)
t_b = bulk temperature defined in Eq. (8), K
t_w = wall temperature, K
u, v = velocity components, m/s
x, y = coordinates, m

Greek symbols

α = geometric function defined in Eq. (17)
β = geometric function defined in Eq. (17)
Γ = diffusion coefficient
$\delta(y)$ = deviation from y-axis, m
ϵ = turbulence dissipation rate, m^2/s^3
ζ = transformed coordinate defined in Eq. (12), m
η = transformed coordinate defined in Eq. (12), m
θ = corrugation angle, deg
λ = bulk-temperature-gradient parameter
μ = viscosity, Pa s
μ_t = turbulent viscosity, Pa s
ρ = density, kg/m^3
ϕ = general dependent variable

utilizing coordinate transformation and integrating over a control volume, the governing equations take the following form:

$$\int_1 [\rho v\phi + \Gamma(\theta + \Psi)]d\eta - \int_3 [\rho v\phi + \Gamma(\theta + \Psi)]d\eta + \int_2 [\rho u_\eta\phi + \Gamma(\Omega + \Lambda)]d\zeta - \int_4 [\rho u_\eta\phi + \Gamma(\Omega + \Lambda)]d\zeta = \int_\forall b_\phi d\eta d\zeta \quad (15)$$

where

$$\Omega = -\alpha(\partial\phi/\partial\eta), \quad \theta = -(\partial\phi/\partial\zeta)$$
$$\Psi = \beta(\partial\phi/\partial\eta), \quad \Lambda = \beta(\partial\phi/\partial\zeta) \quad (16)$$

and

$$\beta = \partial\delta/\partial y, \quad \alpha = 1 + \beta^2. \quad (17)$$

Here, ϕ stands for different dependent variables (u_η, v, T, k and ϵ) and the source term b_ϕ for turbulent flow becomes more complex compared with laminar flow because the diffusion coefficients are not constant. The source terms for the conservation equations in the transformed domain are as follows:

$$\begin{aligned} b_{u_\eta} = {} & -\rho v^2 \frac{\partial\beta}{\partial\zeta} + \mu_{eff} v \frac{\partial^2\beta}{\partial\zeta^2} + 2\mu_{eff}\frac{\partial\beta}{\partial\zeta}\left(\frac{\partial v}{\partial\zeta} - \beta\frac{\partial v}{\partial\eta}\right) \\ & + v\frac{\partial\beta}{\partial\zeta}\left(\frac{\partial\mu_{eff}}{\partial\zeta} - \beta\frac{\partial\mu_{eff}}{\partial\eta}\right) + \frac{\partial v}{\partial\eta}\left(\frac{\partial\mu_{eff}}{\partial\zeta} - \beta\frac{\partial\mu_{eff}}{\partial\eta}\right) \\ & + \frac{\partial\mu_{eff}}{\partial\eta}\left(\frac{\partial u_\eta}{\partial\eta} + \beta\frac{\partial v}{\partial\eta}\right) - \beta\frac{\partial\mu_{eff}}{\partial\eta} \\ & \times\left[\left(\frac{\partial u_\eta}{\partial\zeta} - \beta\frac{\partial u_\eta}{\partial\eta}\right) + \beta\left(\frac{\partial v}{\partial\zeta} - \beta\frac{\partial v}{\partial\eta}\right) + v\frac{\partial\beta}{\partial\zeta}\right] \\ & - \beta\left(\frac{\partial\mu_{eff}}{\partial\zeta} - \beta\frac{\partial\mu_{eff}}{\partial\eta}\right)\left(\frac{\partial v}{\partial\zeta} - \beta\frac{\partial v}{\partial\eta}\right) \\ & - \left[\frac{\partial p^*}{\partial\eta} - \beta\left(\frac{\partial p^*}{\partial\zeta} - \dot{p}\right)\right] \end{aligned} \quad (18)$$

$$\begin{aligned} b_v = {} & \frac{\partial\mu_{eff}}{\partial\eta}\left[\left(\frac{\partial u_\eta}{\partial\zeta} - \beta\frac{\partial u_\eta}{\partial\eta}\right) + \beta\left(\frac{\partial v}{\partial\zeta} - \beta\frac{\partial v}{\partial\eta}\right) + v\frac{\partial\beta}{\partial\zeta}\right] \\ & + \left[\left(\frac{\partial\mu_{eff}}{\partial\zeta} - \beta\frac{\partial\mu_{eff}}{\partial\eta}\right)\left(\frac{\partial v}{\partial\zeta} - \beta\frac{\partial v}{\partial\eta}\right)\right] \\ & - \left(\frac{\partial p^*}{\partial\zeta} - \beta\frac{\partial p^*}{\partial\eta} - \dot{p}\right) \end{aligned} \quad (19)$$

$$b_k = P - \rho\epsilon \quad (20)$$

$$b_\epsilon = Pc_1 f_1 \frac{\epsilon}{k} - c_2 f_2 \rho\frac{\epsilon^2}{k} \quad (21)$$

$$\begin{aligned} b_T = {} & \left[2\Gamma\left(\frac{\partial T}{\partial\zeta} - \beta\frac{\partial T}{\partial\eta}\right) + T\left(\frac{\partial\Gamma}{\partial\zeta} - \beta\frac{\partial\Gamma}{\partial\eta}\right) - \rho vT\right]\lambda \\ & + \Gamma T\left(\lambda^2 + \frac{d\lambda}{d\zeta}\right) \end{aligned} \quad (22)$$

Table 1 Summary of equations solved

Equation	ϕ	Γ	b
Continuity	1	0	0
x momentum	u	μ_{eff}	$-\frac{\partial p^*}{\partial x} + \frac{\partial}{\partial x}\left(\mu_{eff}\frac{\partial u}{\partial x}\right) + \frac{\partial}{\partial y}\left(\mu_{eff}\frac{\partial v}{\partial x}\right)$
y momentum	v	μ_{eff}	$-\frac{\partial p^*}{\partial x} + \dot{p} + \frac{\partial}{\partial x}\left(\mu_{eff}\frac{\partial u}{\partial y}\right) + \frac{\partial}{\partial y}\left(\mu_{eff}\frac{\partial v}{\partial y}\right)$
		where $p^* = p' + 2/3k\rho$	
Energy	T	$\mu/Pr + \mu_t/Pr_T$	$\left[\Gamma\frac{\partial T}{\partial y} + \frac{\partial(\Gamma T)}{\partial y} - \rho vT\right]\lambda + \Gamma T\left(\lambda^2 + \frac{d\lambda}{dy}\right)$
Turbulence energy	k	$\mu + \mu_t/Pr_k$	$P - \rho\varepsilon$
Energy dissipation	ε	$\mu + \mu_t/Pr_\varepsilon$	$(c_1 f_1 P - c_2 f_2 \rho\varepsilon)\varepsilon/k$

where $P = \mu_t\left[2\times\left\{\left(\frac{\partial u}{\partial x}\right)^2 + \left(\frac{\partial v}{\partial y}\right)^2\right\} + \left(\frac{\partial u}{\partial y} + \frac{\partial v}{\partial x}\right)^2\right]$, and $\lambda = \frac{1}{(t_b - t_w)}\frac{d(t_b - t_w)}{dy}$

$\mu_{eff} = \mu + \mu_t$ $\qquad$ $\mu_t = c_\mu f_\mu \rho k^2/\varepsilon$

$f_1 = 1 + (0.05/f_\mu)^3$ $\qquad$ $f_2 = 1 - \exp(-R_T^2)$

$f_\mu = [1 - \exp(-0.0165R_y)]^2(1 + 20.5/R_T)$

$R_T = \rho k^2/\varepsilon\mu$ $\qquad$ $R_y = \rho k^{1/2}y/\mu$

$c_\mu = 0.09$ $\qquad$ $c_1 = 1.44$ $\qquad$ $c_2 = 1.92$

$Pr_k = 1.0$ $\qquad$ $Pr_\varepsilon = 1.3$ $\qquad$ $Pr_T = 0.9$

where

$$\begin{aligned} P = \mu_t \times \Bigg[& 2\left\{\left(\frac{\partial u_\eta}{\partial\eta} + \beta\frac{\partial v}{\partial\eta}\right)^2 + \left(\frac{\partial v}{\partial\zeta} - \beta\frac{\partial v}{\partial\eta}\right)^2\right\} \\ & + \left\{\left(\frac{\partial u_\eta}{\partial\zeta} - \beta\frac{\partial u_\eta}{\partial\eta}\right) + \beta\left(\frac{\partial v}{\partial\zeta} - \beta\frac{\partial v}{\partial\eta}\right)\right. \\ & \left. + v\frac{\partial\beta}{\partial\zeta} + \frac{\partial v}{\partial\eta}\right\}^2\Bigg] \end{aligned} \quad (23)$$

and where $b = 0$ for the continuity equation. The discretized procedure of the integrated equations is based on the power-law scheme of Patankar (1980). The details of the discretization for the source term are documented in a paper by Faghri et al. (1984). Therefore, the description for this will be omitted here. The power-law scheme used here has formally first order accuracy, and in general, the usage of the nonorthogonal grids which arise from the coordinate transformation may increase the false diffusion. However, the accuracy of the sample problems tested in the paper by Faghri et al. (1984) is very good. The pressure and velocities are linked by the SIMPLE algorithm of Patankar (1981), and the discretized equations are solved by using line-by-line method.

The numerical computations were performed for Prandtl number of 0.7 and for θ = 15 deg, 30 deg. If the peaks of both the top and bottom walls lie in the same plane, the vertical spacing H' can be expressed as a function of θ and L where

$$H' = (L/2)\tan\theta. \quad (24)$$

The selected values of H'/L are 0.25 tan θ (=0.0669), 0.5 tan θ (=0.1340), and 0.75 tan θ (=0.2010) for $\theta = 15°$ and 0.25 tan θ (=0.1443), 0.5 tan θ (=0.2886), and 0.725 tan θ (=0.4186) for $\theta = 30°$. These values are same as one in the previous work for the laminar flow. The numerical solutions do

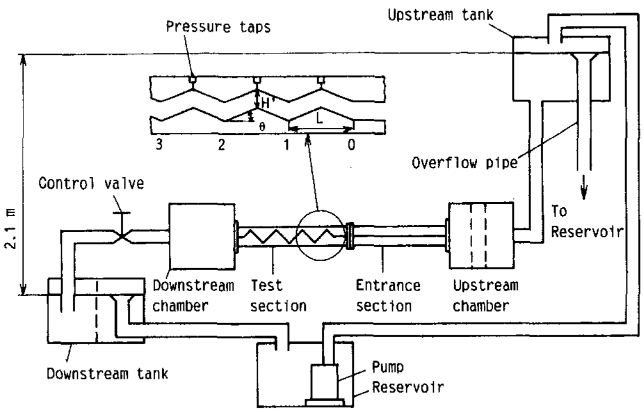

Fig. 2 Schematic diagram of experimental setup

not converge for ducts with sharp edged corners. For this reason, the corners are approximated with a sine curve with chord length, $l = L/10$.

Attention is now directed to the calculation of the Reynolds number defined as

$$\mathrm{Re} = 2\dot{m}/\mu \quad \text{where} \quad \dot{m} = \rho \int v dx. \tag{25}$$

Another quantity of interest is the calculation of the friction factor expressed in terms of the Darcy friction factor as follows:

$$f = -\dot{p}\,\frac{D_H}{\rho \bar{v}^2/2} \tag{26}$$

where $\bar{v} = \dot{m}/\rho H'$ and $D_H = 2H'$.

Finally, the cycle averaged heat transfer coefficient h_m and cycle averaged Nusselt number are defined as

$$\mathrm{Nu}_m = h_m \frac{2H'}{K} = \frac{2H'}{A_w}\left(-\int_0^L \lambda dy\right) \times \left\{\frac{\mathrm{Re\,Pr}}{2} - \int_0^{H'} \frac{K_{eff}}{K}\left(\lambda T + \frac{\partial T}{\partial y}\right)dx\right\} \tag{27}$$

where

$$K_{eff} = \frac{\mu}{\mathrm{Pr}} + \frac{\mu_t}{\mathrm{Pr}_T}, \quad h_m = \frac{Q}{A_w(\overline{t_w - t_b})} \tag{28}$$

and A_w is the per-cycle transfer surface area, approximately equal to $2L/\cos\theta$; Q is the rate of heat transfer from both walls to the fluid per cycle, and $\overline{t_w - t_b}$ is the average bulk-to-wall temperature difference. The log-mean temperature difference is expressed as

$$\overline{t_w - t_b} = (t_w - t_b)_{y=0}\,\frac{1 - e^{\int_0^L \lambda dy}}{-\int_0^L \lambda dy}. \tag{29}$$

The computations were performed with 24 × 46 grid points. These grid points were distributed nonuniformly, with a higher concentration of grids closer to the walls, by using the power formula (e.g., Patankar, 1991) with powers of 1.3 to 2 depending on the Reynolds number. The grid dependence test was performed for $\theta = 30$ deg and $H'/L = 0.2886$ with 20 × 38 and 28 × 54 grids and for an identical pressure gradient of $\dot{p} = -30$. The Reynolds number obtained with 24 × 46 grid points is 2728 for $\dot{p} = -30$. The change in the Reynolds number between the fine, 28 × 54, and medium, 24 × 46, grids was 0.2 percent and between the medium, 24 × 46, and coarse, 20 × 38, grids was 0.7 percent.

Table 2 Dimensions of corrugated duct

Duct angle (θ)	:	30°
Length of a cycle (L)	:	34.6 mm
Number of cycles	:	19.5
Inter-wall spacing (H')	:	10 mm
H'/L	:	0.2886

Experimental Setup

Pressure drop measurements and flow visualization were performed for a corrugated duct with sharp edge corners. A schematic representation of the experimental setup used in this study is shown in Fig. 2. A steady flow of water was supplied to the test section from an upstream tank. The flow rate was controlled by a valve and was measured by weighing the volume of water accumulated at the outlet reservoir over a period of 30 seconds. The weight of the water for the case of Re = 200 reached about 800 g. The test section consisted of a pair of corrugated plates of 19.5 cycles with an upstream entrance section of length 900 mm. As shown in the close-up view of the duct, the valleys of the bottom plate are numbered so that an exit corner of a cycle has the same number as the cycle. Two chambers (plenums) were placed at the entrance and at the exit of the test section, respectively. The detail of the test section is shown as an insert in Fig. 2 and the dimensions are tabulated in Table 2.

Axial pressure drops were measured by a diaphragm-type micro pressure difference sensor (Validyne DP103, maximum pressure difference 56 Pa, minimum pressure difference 0.14 Pa) connected to 0.6 mm holes drilled at the valleys of the top corrugated plate. The measurements were performed in the Reynolds number range of 200 to 3000.

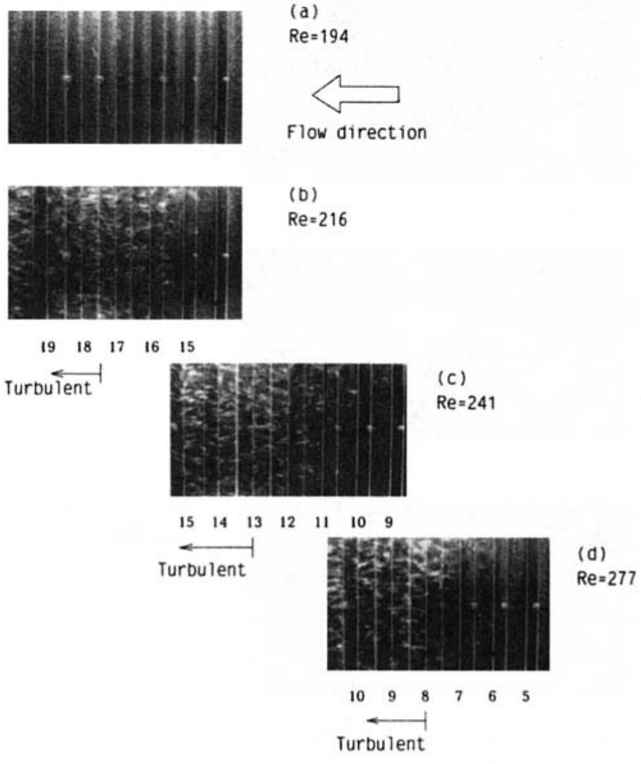

Fig. 3 Photographs of flow visualization

The respective uncertainties are: pressure drop, ±0.07 Pa, duct height H, ±0.1 mm, duct width, ±0.1 mm, interwall spacing, ±0.1 mm, location of pressure tap, ±0.1 mm, water temperature, ±0.1 K, weight, ±1 g and time, ±0.1 sec. The estimated uncertainty of the measured Reynolds number from these values ranges from 0.5 to 0.7 percent. And also from these values, the maximum uncertainty of the friction factor is estimated as ±13 percent at Re = 200 and the minimum uncertainty is estimated as ±3 percent at Re = 3000.

Results and Discussion

Results of Flow Visualization. The top view of the representative photographs of the flow are presented in Figs. 3(*a*) to (*d*) for Re = 194, 216, 241, and 277, respectively. The flow direction is shown by an arrow, and the vertical white lines in the photographs represent the corrugated duct corners. A pearl graze was used as a tracer. Since the pearl graze is flaky, disturbed trajectories (relatively large white dots in the pictures) can be observed clearly when the transition occurs. This is seen at the locations of the 16th to the 18th cycles from the entrance [Fig. 3(*b*)]. Note that the numbering scheme used here is that each exit corner of a cycle has same number as the cycle. The transition point marked in the figure is defined as the place where the disturbance spreads into entire places of the channel in the span direction. In the case of Fig. 3(*b*), the transition point locates at the middle of the 18th cycle from the entrance. The transition point moves upstream with an increase in the Reynolds number [Fig. 3(*c*) and (*d*)]. The disturbed trajectories are not seen in Fig. 3(*a*) when the flow is laminar. Note that the transition starts from near the side walls and flow is not symmetric. This trend is accentuated in Fig. 3(*d*).

The side view of the representative photographs of the flow in the 18th cycle is shown in Fig. 4, with an arrow indicating the direction of the flow. A separation bubble, which washes the entire rear face of the corrugated wall, can be seen at Re = 203 [Fig. 4(*a*)]. With an increase of the Reynolds number, these bubbles become larger [Fig. 4(*b*) and (*c*)]. With still further increase of the Reynolds number, the bubbles become smaller due to the high diffusion in the turbulent flow [Fig. 4(*d*) and (*e*)].

Figure 5 shows the location of the transition point as a function of Reynolds number obtained from the flow visualization experiments. As seen from this figure, the relation between the Reynolds number and the transition point asymptotes to a vertical line at about Re = 200. The transition to turbulent flow for conventional ducts behave in the same manner. Namely, the transition point moves upstream with an increase of Reynolds number. The transition Reynolds number from flow visualization is about 200. The experimental results for the friction factor will be presented later together with the numerical results.

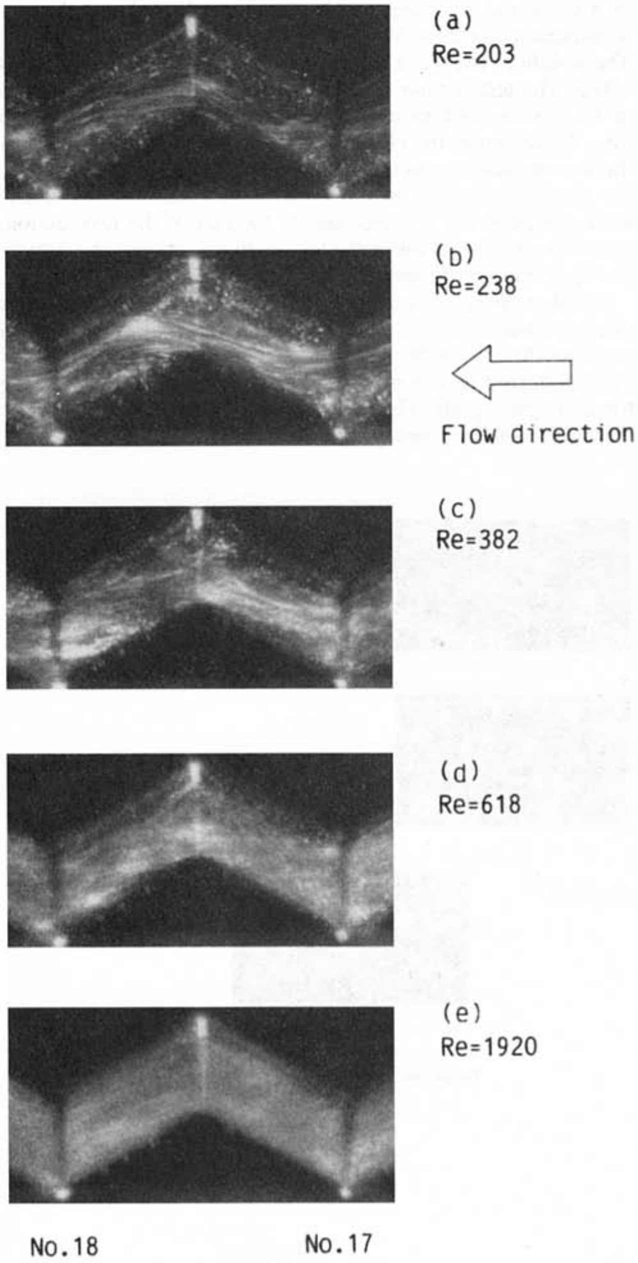

Fig. 4 Photographs of flow visualization

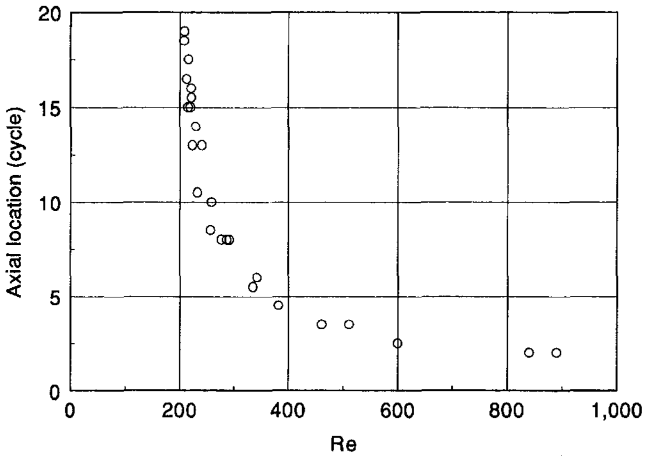

Fig. 5 Location of transition as a function of Re

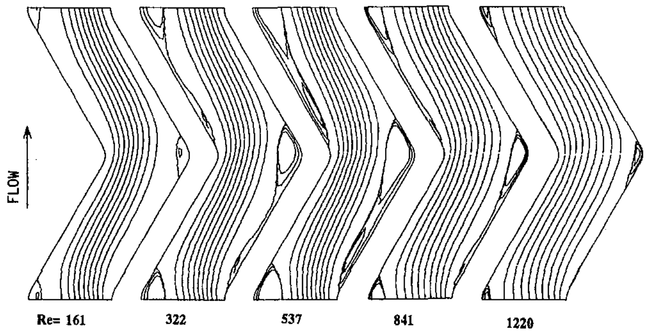

Fig. 6 Streamline diagram for θ = 30° and H'/L = 0.2886

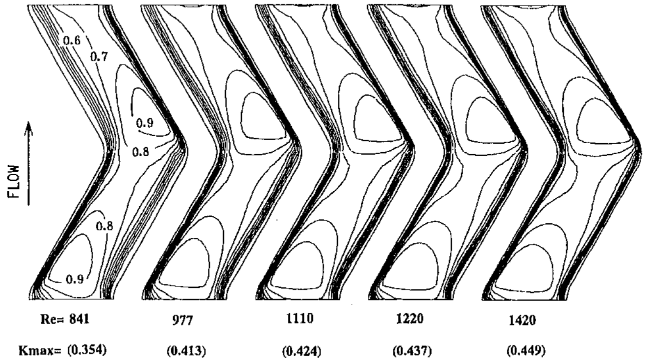

Fig. 7 Contours of turbulent kinetic energy for $\theta = 30°$ and $H'/L = 0.2886$

Flow Patterns and Turbulent Kinetic Energy Contours. The streamline contour maps for $H'/L = 0.2886$ and $\theta = 30$ deg, and for Reynolds numbers in the range of 161 to 1220 are presented in Fig. 6. As seen in this figure, separation bubbles which wash the entire rear face can be seen at Re = 161. As the Reynolds number increases, these bubbles grow bigger up to Re = 500. Then, at further increase of the Reynolds number, the bubbles become smaller because of high diffusion in turbulent flow. The same behavior is observed in experiments as seen in Fig. 4.

The turbulence kinetic energy contour maps are presented in Fig. 7 with the flow direction indicated by an arrow. The contours are plotted in intervals of 0.1 and are for $H'/L = 0.2886$ and $\theta = 30$ deg, and for the Reynolds numbers in the range of 841 to 1420. They are normalized by their maximum values, $k_{\max}$, as indicated in the figure. As seen from this figure, the turbulence kinetic energy is zero and the contour line spacings are very small near the walls. The maximum value of the turbulence kinetic energy occurs in the front face of the wall.

Maximum Value of Dimensionless Turbulence Kinetic Energy. The maximum value of the dimensionless turbulence kinetic energy, $(k/\bar{v}^2)_{\max}$, as a function of Reynolds number is plotted in Fig. 8 with the aspect ratio H'/L as the curve parameters. It can be seen from this figure that the turbulence kinetic energy is almost zero for laminar flow, and it greatly increases when the flow changes from laminar to turbulent. As shown in the figure, the value of the dimensionless turbulent kinetic energy in laminar flow ranges 4×10^{-4} to 2×10^{-3}, depending on the geometry. When the flow changes from laminar to turbulent, it greatly increases. Then, the Reynolds number, when the maximum value of the dimensionless turbulence kinetic energy changes suddenly, is defined as the transitional Reynolds number. The transitional Reynolds numbers evaluated from this figure are listed in Table 3. It will be useful if the transitional Reynolds number can be expressed by a simple correlation. A least squares fit of the transitional Reynolds number yields with

$$\mathrm{Re} = 360(H'/L)^{-0.56} \quad \text{for} \quad \theta = 15 \text{ deg} \quad \text{and}$$

$$\mathrm{Re} = 400(H'/L)^{-0.52} \quad \text{for} \quad \theta = 30 \text{ deg} \qquad (30)$$

with an extreme deviation of 9 percent. As stated earlier, the transitional Reynolds number obtained from the flow visualization for $H'/L = 0.2886$ and $\theta = 30$ deg is about 200. The predicted value is quite high compared with the value obtained from flow visualization experiments. This discrepancy will be discussed later.

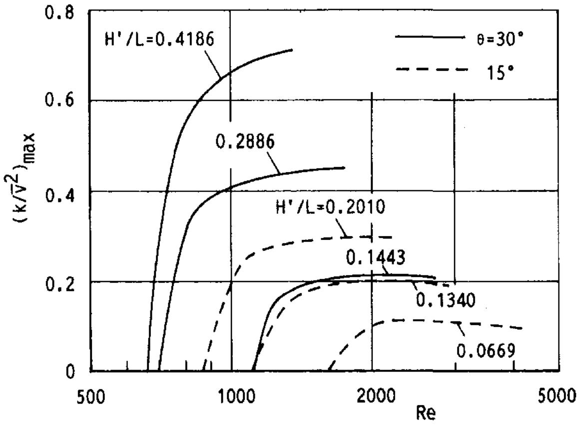

Fig. 8 Maximum value of turbulent kinetic energy, $(k/\bar{v}^2)_{\max}$, as a function of Re

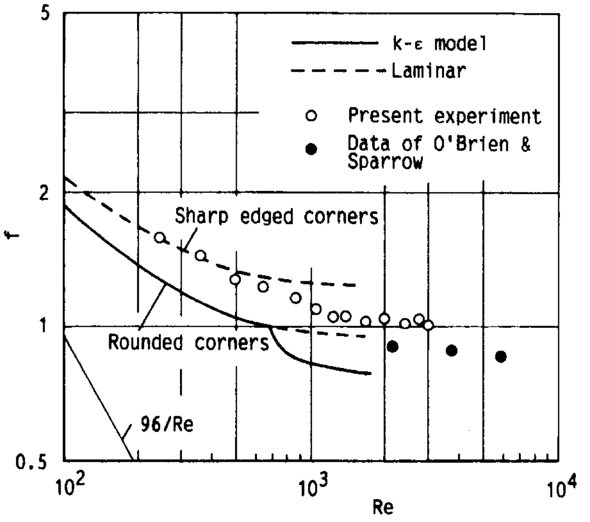

Fig. 9 Comparison of friction factor for $\theta = 30°$ and $H'/L = 0.2886$

Friction Factors. The numerical and experimental results for the friction factor for $H'/L = 0.2886$ and $\theta = 30$ deg are presented in Fig. 9. To obtain the friction factor in the fully developed region, the pressure drop of the cycle, which locates far from the transition region, should be measured. Then, the friction factor was evaluated from the pressure drop results between the 17th and 19th taps. In this figure, the data of O'Brien and Sparrow (1982) for $H'/L = 0.2886$ and $\theta = 30$ deg is also plotted. It is noteworthy that the experiments were performed for corrugated ducts with sharp edged corners and the numerical prediction were obtained for ducts with rounded corners. The only numerical prediction for the ducts with the sharp edged corners were obtained for laminar flow. The experimental results will be compared with laminar flow results of

Table 3 Transition Reynolds numbers

θ = 15°

H'/L	Re
0.0669	1610
0.1340	1110
0.2010	870

θ = 30°

H'/L	Re
0.1443	1130
0.2886	700
0.4168	670

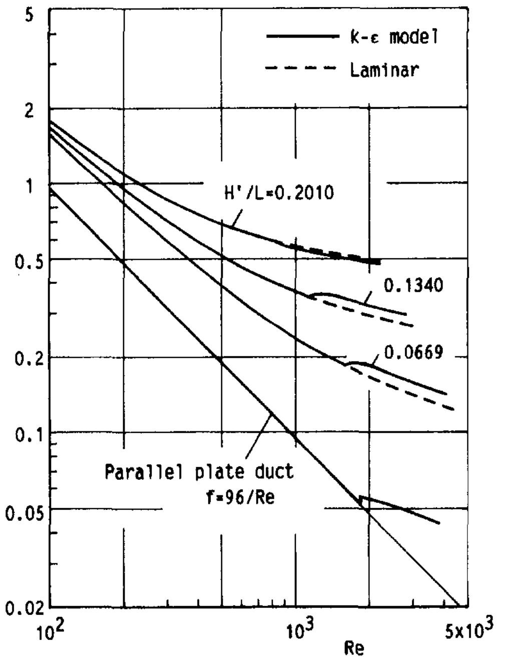

Fig. 10 Friction factor for θ = 15° as a function of Re

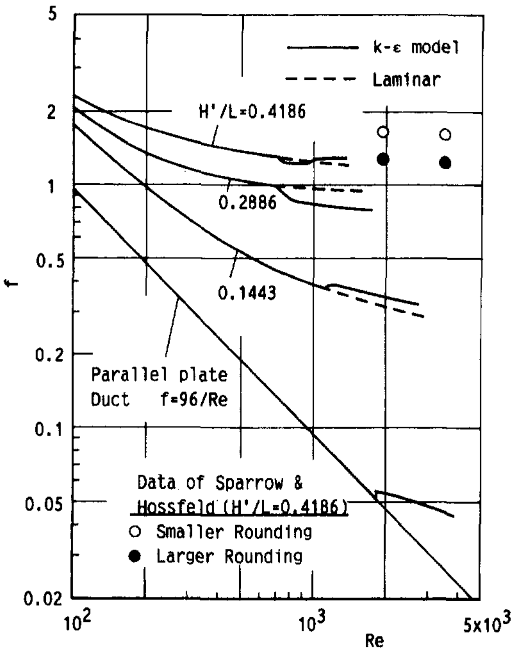

Fig. 11 Friction factor for θ = 30° as a function of Re

Asako and Faghri (1987), shown by dashed lines. In the range of Re < 400, both friction factors agree well but the experimental values become gradually lower in the range of Re > 500. The same trends can be seen for the numerical results for ducts with rounded corners. Since the onset of turbulence would strongly depend on external disturbances and the sharpness of the corners, discrepancies between the measured and predicted values are expected.

The transitional Reynolds number obtained from flow visualization is about 200. However, turbulence effects on the friction factor appeared at Reynolds of about 500 in the experiment. This fact indicates that the flow, in the range of 200 < Re < 500, has small turbulence, but time averaged quantities are identical to that of laminar flow. Since the numerical computation solves time averaged quantities, the predicted transitional Reynolds numbers are higher than those obtained from the flow visualization experiments.

The friction factors, as a function of the Reynolds number, are plotted in Figs. 10 and 11 with the aspect ratio H'/L as the curve parameters. Figures 10 and 11 are the results for $\theta = 15$ deg and 30 deg, respectively. The Lam-Bremhorst model used is quite stable for laminar flow region. Almost all of the calculated values of the friction factors in laminar flow region obtained by using the Lam-Bremhorst model perfectly coincide with the values obtained by assuming laminar flow. Some calculated values differ from the laminar friction factor. However, the maximum difference is less than 0.3 percent. The Reynolds number, when the friction factor curve undergoes a sudden change in slope, coincide with the transitional Reynolds number listed in Table 3.

For high Reynolds numbers, the friction factor obtained by using the k-ϵ model is higher than those obtained by assuming laminar flow, with the exception of the results for ducts with $\theta = 30°$ and $H'/L = 0.2886$. The experimental results for $\theta = 30$ deg and $H'/L = 0.4186$ and for the duct with rounded corners by Sparrow and Hossfeld (1984) are also plotted in Fig. 11. Two different degrees of roundness were examined. The cycle length, L, was 20.32 mm for both cases. The corners were removed 0.165 mm and 0.292 mm from the original peak for a smaller roundness and a larger roundness, respectively. The corresponding peak roundness of the numerical computation is 0.213 mm for the case of $L = 20.32$ mm. As seen from the figure, the experimental data lie on the extension line of the numerical results.

The friction factor for the plane Poiseuille flow is plotted in Fig. 10 and together with the laminar friction factors shown by dashed lines. Kao & Park (1970) and Patel & Head (1969) have shown by experiments that the plane Poiseuille flow is unstable to finite amplitude disturbances at Reynolds numbers as low as 2600. Also, Orszag & Kells (1980) has shown from the three-dimensional finite-amplitude disturbance analysis that the transitional Reynolds number for the plane Poiseuille flow is 2000. The transitional Reynolds number of the present analysis for the plane Poiseuille flow is 1840, and this value is slightly lower than the value predicted by Orszag & Kells.

Nusselt Numbers. The results for the periodically fully developed Nusselt number as a function of Reynolds number with the aspect ratio H'/L as the curve parameters are plotted in Figs. 12 and 13. Figures 12 and 13 are the results for $\theta = 15$ deg and 30 deg, respectively. The Nusselt number is based on

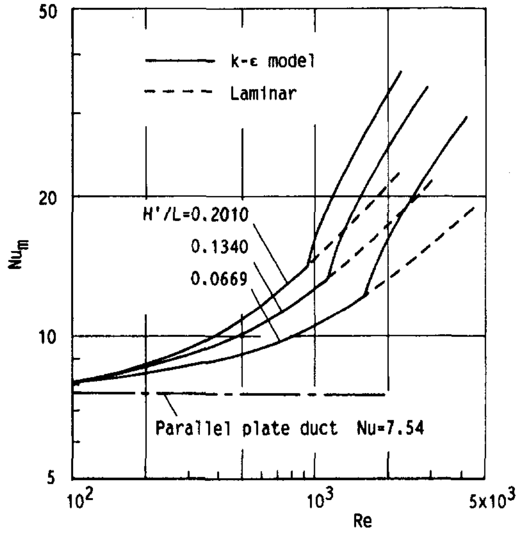

Fig. 12 Nusselt number for θ = 15° as a function of Re

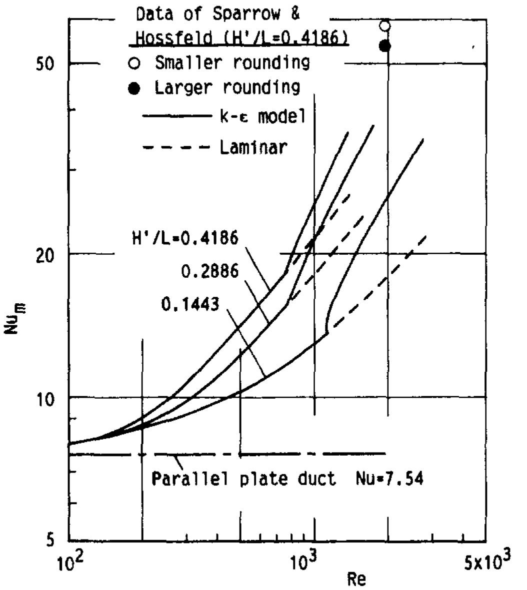

Fig. 13 Nusselt number for θ = 30° as a function of Re

the log-mean temperature difference defined by Eq. (29). It is noteworthy that the fully developed Nusselt number for straight duct for laminar flow is 7.54 and is independent of both Reynolds and Prandtl numbers. The Nusselt numbers obtained by assuming laminar flow are also plotted by dashed lines in these figures. For low Reynolds numbers, the Nusselt numbers obtained by using k-ϵ model are identical with those obtained by assuming laminar flow. The values of Nusselt number is higher than 7.54, and it increases gradually with an increase in the Reynolds number. For high Reynolds numbers, the Nusselt number obtained by using k-ϵ model is higher than laminar Nusselt numbers. There are no experimental data for the constant wall temperature condition. Therefore, the experimental data by Sparrow and Hossfeld (1984) for $\theta = 30$ deg and $H'/L = 0.4186$ and for the constant heat flux condition are plotted in Fig. 13 as references.

Concluding Remarks

The transitional characteristics of fluid flow and heat transfer in the periodic fully developed region of the corrugated duct were obtained by using the Lam-Bremhorst low-Reynolds number k-ϵ model and by using flow visualization and measurements of pressure drop. The main conclusions are:

1 In experiments, the transition Reynolds number obtained from the flow visualization for a corrugated duct with the sharp edged corners is about 200 for $\theta = 30$ deg and $H'/L = 0.2886$. However, the effect of the transition on the friction factor appears at Re > 500.

2 The predicted transitional Reynolds number is Re = 700 for the duct with small rounded corners of $\theta = 30$ deg and $H'/L = 0.2886$. Since the model is based on the time averaged quantities, the numerical computation by using the model gives higher transition Reynolds number.

3 Since the friction factor and the Nusselt number are the time averaged quantities, the numerical computation by using the model can predict these quantities.

References

Amano, R. S., 1984, "A Numerical Study of Laminar and Turbulent Heat Transfer in a Periodically Corrugated Wall Channel," ASME JOURNAL OF HEAT TRANSFER, Vol. 107, pp. 564–569.

Asako, Y., and Faghri, M., 1987, "Finite-Volume Solutions for Laminar Flow and Heat Transfer in a Corrugated Duct," ASME JOURNAL OF HEAT TRANSFER, Vol. 109, pp. 627–634.

Faghri, M., Sparrow, E. M., and Prata, A. T., 1984, "Finite Difference Solutions of Convection-Diffusion Problems in Irregular Domains Using a Non-Orthogonal Coordinate Transformation," *Numerical Heat Transfer*, Vol. 7, pp. 183–209.

Izumi, R., Yamashita, H., and Oyakawa, K., 1983, "Fluid Flow and Heat Transfer in Corrugated Wall Channels (4th Report, Analysis in the Case Where Channels are Bent Many Times)," *Bull. of J.S.M.E.*, Vol. 26, pp. 1146–1153.

Kao, T. W., and Park, C., 1970, "Experimental Investigations of the Stability of Channel Flows: Part 1—Flow of a Single Liquid in a Rectangular Channel," *Journal of Fluid Mechanics*, Vol. 43, pp. 145–164.

Lam, C. K. G., and Bremhorst, K., 1981, "A Modified Form of the k-ϵ Model for Predicting Wall Turbulence," *Journal of Fluid Engineering*, Vol. 113, No. 3, pp. 456–460.

Nishimura, T., Kajimoto, Y., and Kawamura, Y., 1986, "Mass Transfer Enhancement in Channels with a Wavy Wall," *Journal of Chemical Engineering of Japan*, Vol. 19, No. 2, pp. 142–144.

Orszag, S. A., and Kells, L. C., 1980, "Transition to Turbulence in Plane Poiseuille and Plane Couette Flow," *Journal of Fluid Mechanics*, Vol. 96, pp. 159–205.

O'Brien, J. E., and Sparrow, E. M., 1982, "Corrugated Duct Heat Transfer, Pressure Drop and Flow Visualization," ASME JOURNAL OF HEAT TRANSFER, Vol. 104, pp. 410–416.

Patankar, S. V., 1980, "Numerical Heat Transfer and Fluid Flow," MacGraw-Hill, New York.

Patankar, S. V., 1981, "A Calculation Procedure for Two-Dimensional Elliptic Situations," *Numerical Heat Transfer*, Vol. 4, pp. 409–425.

Patankar, S. V., 1991, "Computation of Conduction and Duct Flow Heat Transfer," Innovative Research, Minnesota.

Patel, V. C., and Head, M. R., 1969, "Some Observations on Skin Friction and Velocity Profiles in Fully Developed Pipe and Channel Flows," *Journal of Fluid Mechanics*, Vol. 38, pp. 181–201.

Schmidt, R. C., and Patankar, S. V., 1987, "Prediction of Transition on a Flat Plate Under the Influence of Free-Stream Turbulence Using Low-Reynolds Number Two-Equation Turbulence Models," ASME paper 87-HT-32, pp. 1–9.

Sparrow, E. M., and Comb, J. W., 1983, "Effect of Interwall Spacing and Fluid Flow Inlet Conditions on Corrugated-Wall Heat Exchanger," *International Journal of Heat and Mass Transfer*, Vol. 26, No. 7, pp. 993–1005.

Sparrow, E. M., and Hossfeld, L. M., 1984, "Effect of Rounding of Protruding Edges on Heat Transfer in a Corrugated Duct," ASME JOURNAL OF HEAT TRANSFER, Vol. 27, pp. 1715–1723.

Experimental Study of Forced Convection From Isothermal Circular and Square Cylinders and Toroids

G. Refai Ahmed[1]
Director
Advanced Thermal Engineering
R-Theta Inc.
2-130 Matheson Blvd. E.
Mississauga, Ontario, Canada, L4Z 1Y6
Mem. ASME

M. M. Yovanovich
Prof. and Director
Microelectronics Heat Transfer Laboratory
Department of Mechanical Engineering
University of Waterloo
Waterloo, Ontario, Canada, N2L 3G1
Fellow ASME

Experimental studies of forced convection heat transfer from different body shapes were conducted to determine the effects of Reynolds number and different characteristic body lengths on the area-averaged Nusselt number. Although the bodies differed significantly in their shapes, they had approximately the same total surface area, $A = 11{,}304\ \mathrm{mm}^2 \pm 5\%$. This ensured that for a given free stream velocity and total heat transfer rate all bodies had similar trends for the relationship of Nusselt and Reynolds numbers. The experimental program range was conducted in the Reynolds number range $10^4 \leq Re_{\sqrt{A}} \leq 10^5$ and Prandtl number 0.71. Finally, the empirical models for forced convection heat transfer were developed. These empirical models were valid for a wide range of Reynolds numbers $0 \leq Re_{\sqrt{A}} \leq 10^5$. The present experimental correlations were compared with available correlation equations and experimental data. These comparisons show very good agreement.

Introduction

Experimental forced convection heat transfer from circular and square cylinders, or toroids, is important in a number of fields, such as heat exchange, boiler design, gas turbine blades, hot wire anemometry and the rating of the electrical conductors. The present study has been initiated to resolve the issue of the effect of the geometric of the body on the area-averaged Nusselt number. Also, this work seeks to provide a simple procedure to predict forced convection heat transfer from bodies of different shapes, based on the characteristic length of the square root of total surface area, $\sqrt{A}$, which was first suggested by Yovanovich (1987a, 1987b). The experimental data obtained from the present study will provide the necessary empirical correlations needed.

A schematic diagram of the different body shapes, which will be investigated in the present study, is shown in Fig. 1. These different body shapes will be maintained at T_S and the ambient will be maintained at T_∞. These bodies will be subjected to a uniform crossflow of air.

Literature Survey

Circular Cylinder. Numerous studies have attempted to correlate the area-averaged heat transfer by forced convection from long circular cylinders in crossflow in the form: Nu = Nu(Re, Pr). However, all of them have failed to establish this goal in a general form, Nu = Nu(L/D, Re, Pr). Table 1 shows a summary of the important previous studies and their correlations. In addition, Table 1 reveals disagreement in the results. These results can be summarized as follows:

1 For three-dimensional flow, in general, each L/D has its own correlation.
2 For the same L/D, it is common to find disagreement in the value of Nu, e.g., between Ahmad and Qureshi (1992) and Galloway and Sage (1967) for $L/D = 8$, Burn et al. (1956)[2] and Krujilin (1938)[2] for $L/D = 50$ . . . etc.
3 The power of Reynolds number varied between 0.3 and 0.75.
4 A few studies considered the diffusive term and it was included in the correlations. However, these studies disagreed on how to estimate this term, for example, King (1914)[2] reported it to be equal to 0.315 ($1290 < L/D < 1520$) and Laurence and Landes (1952)[2] found it to be 0.19 ($400 < L/D < 2500$). Also, Hatton et al. (1970) estimated the diffusive term to be 0.384 ($96 < L/D < 1190$). However, Delleur (1964)[2] evaluated it as 1.148 ($L/D = 100$). On the other hand, most of the other studies neglected the diffusive term.
5 There are two-dimensional numerical studies that assumed $L \gg D$. However, it is not known when we can conclude that the circular cylinder is two-dimensional.

In addition, Churchill and Bernstein (1977) concluded many reasons for the above limitations. These limitations are: the lack of a comprehensive theory for the dependence on Pr, even for the boundary layer regime; competitive theories for low Re; the influence of natural convection at very low Re; discrete transitions in the boundary layer and the wake at high Re; the influence and the lack of specification of free stream turbulence; the use of different and undefined thermal boundary conditions; significant variation in physical properties between the surface and free stream around the surface; the incorporation of erroneous physical properties in older tabulated data, for example the work of Hilpert (1933); end effects, particularly at low Re; tunnel blockage; significant scatter in most of the data sets; and finally, unresolved discrepancies between the various sets of data. In addition, Morgan (1975) recognized many of these effects especially the blockage of the wind tunnel, turbulence intensity, and thermal properties. Based on that, Morgan (1975) also corrected and correlated many of the previous studies, in particular, the data of Hilpert (1933) as shown in Table 2.

Churchill and Bernstein (1977) developed a correlation for forced convection heat transfer from circular cylinders as follows:

---

[1] Present address: Nortel Technology, P.O. Box 3511, Station C, Ottawa, ON K1Y 4H7 Canada.

Contributed by the Heat Transfer Division for publication in the Journal of Heat Transfer. Manuscript received by the Heat Transfer Division November 8, 1995; revision received May 31, 1996; Keywords: Conduction, Forced Convection, Turbulence. Associate Technical Editor: Dr. T. Rabas.

[2] From Morgan (1975)

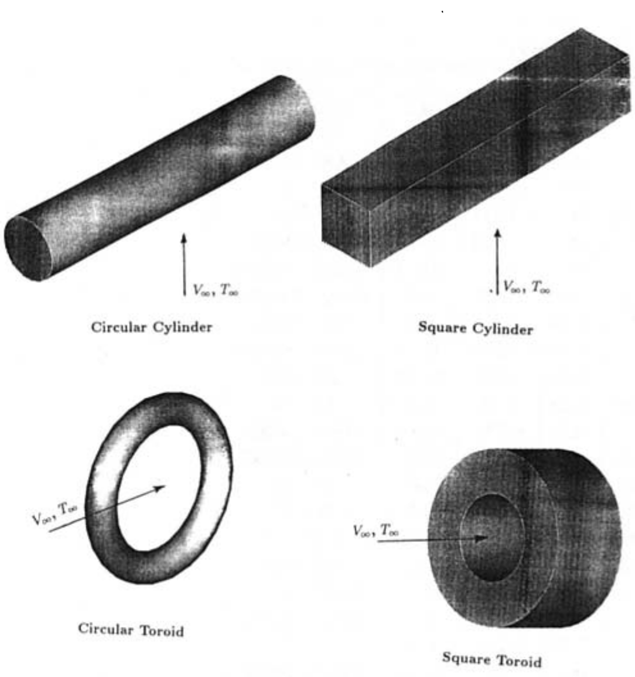

Fig. 1 Schematic diagram of body shapes

$$\mathrm{Nu}_D = 0.3 + 0.62\mathrm{Re}_D^{0.5}\frac{\mathrm{Pr}^{1/3}}{[1 + (0.4/\mathrm{Pr})^{2/3}]^{1/4}} \times [1 + (\mathrm{Re}_D/282000)^{5/8}]^{4/5} 10^2 \le \mathrm{Re}_D \le 10^7. \quad (1)$$

Equation (1) was developed for "infinite" circular cylinders, i.e., $L \gg D$, but they did not mention the ratio of L/D. However, they compared their correlation with experimental data for air of Hilpert (1933) ($0.95 \le L/D \le 5120$), Collis and Williams (1959)[2] ($2070 \le L/D \le 8860$) and Krall and Eckert (1973) ($L/D = 6.3$). These experimental studies have been done for different L/D. However, Churchill and Bernstein (1977) developed Eq. (1) by using the following procedure:

$$\mathrm{Nu}_D = a \cdot \mathrm{Re}_D^{0.5}\frac{\mathrm{Pr}^{1/3}}{[1 + (0.4/\mathrm{Pr})^{2/3}]^{1/4}} \quad (2)$$

where a has been obtained from the numerical studies of Masliyah and Epstein (1973) and Jain and Goel (1976) at $\mathrm{Re}_D = 1$. They found $a = 0.62$ in order to provide the best fit for their equation. The diffusive term has been estimated from the experimental and theoretical work of King (1914)[2].

Square Cylinder. A few previous studies investigated forced convection heat transfer from square cylinders. Table 3 shows the summary of the previous studies experimental correlations. Hilpert (1933) and Reiher (1926) examined this problem experimentally in different orientations using opposing flow and assisting flow. Igarashi (1985) also examined forced convection from square cylinders experimentally. He used three square cylinders, $L/W = 10$, 7.5, 5 and $L = 0.15$ m, and the turbulence level in the working section was 0.5% where $5.6 \times 10^3 \le \mathrm{Re}_W \le 5.6 \times 10^4$. Recently, Bishop (1987) and Oosthuizen and Bishop (1987) investigated mixed convection from square cylinders experimentally and numerically using opposing flow and assisting flow. Also, they examined this problem using the heat transfer transient technique. One can conclude the following limitations of the previous studies: the influence of free convection was ignored, especially at low Reynolds number; significant variations in physical properties between the surface and the free stream such as Oosthuizen and Bishop (1987), $\Delta T = 70$ K; the use of erroneous physical properties in older tabulated data, e.g., Hilpert (1933) and Reiher (1926); the effect of free stream turbulence on forced convection results; and finally, significant scatter in some of the data sets.

Nomenclature

A = surface area, m^2
a = constant in Eq. (2)
c = constants in Eq. (16)
$C_{\mathcal{L}}$ = constants in Eq. (21)
$C_{\sqrt{A}}$ = body shape parameter in Eq. (32)
C_1 = constants in Table 1
C_2 = constants in Tables 1, 2 and 3
C_p = specific heat transfer, kJ/kg K
CR = correction factor
D = cylinder diameter, m
D_{CS} = cross section diameter, m
D_I = inner diameter of toroids, m
D_O = outer diameter of toroids, m
F = view factor
$\mathcal{F} = F \times \epsilon$
$G_{\sqrt{A}}$ = gravity function
h = coefficient of convection heat transfer, W/m^2 K
I = electric current, A
k = thermal conductivity, W/m K
K = constant in Eq. (23)
L = length, m
$\mathcal{L}$ = arbitrary scale length, m
l = mixing length, $l = Ky$, m
m = exponent in Tables 1, 2 and 3
n = exponent in Eq. (9)
$\mathrm{Nu}_{\mathcal{L}}$ = area-averaged Nusselt number, $\mathrm{Nu}_{\mathcal{L}} = \mathcal{L}h/k$
$\mathrm{Nu}_{\mathcal{L}}^0$ = area-averaged diffusive Nusselt number, $\mathrm{Nu}_{\mathcal{L}} = \mathcal{L}h/k$
q = heat flux, W/m^2
Q_{FC} = forced convection heat transfer, W
Q_{NC} = natural convection heat transfer, W
Q_{Rad} = radiation heat transfer, W
Q_T = total heat transfer, W
Q_W = wire losses, W
P = perimeter, m
Pr = Prandtl number, $\mathrm{Pr} = \nu/\alpha$
$\mathrm{Re}_{\mathcal{L}}$ = Reynolds number, $\mathrm{Re}_{\mathcal{L}} = \mathcal{L}V_\infty/\nu$
T_S = surface temperature, K
T_∞ = ambient temperature, K
Tu = turbulence intensity
V = voltage, V
$\mathcal{V}$ = volume, m^3
V_∞ = free stream velocity, m/s
V'_∞ = measured free stream velocity, m/s
W = width of the square cylinder, m
x' = distance from the end of the contraction to the location of the object in the wind tunnel, m

Greek Letters

α = thermal diffusivity, $\alpha = k/C_p\rho$, m^2/s
α_t = turbulent thermal diffusivity, m^2/s
$\gamma_{\sqrt{A}}$ = constant in Eq. (27)
ϵ = emssivity
$\Delta T = T_S - T_\infty$
ν_t = turbulent kinematic viscosity, m^2/s
ρ = density, kg/m^3
σ = Stefan-Boltzmann constant, W/m^2 K^4
Υ = blockage correction

Abbreviations

Cond = conduction
Conv = convection
Diff = Difference
FC = forced convection
MHTL = Microelectronics Heat Transfer Laboratory
max = maximum
NC = natural convection
Rad = radiation
$T.S.$ = test section

Table 1 Forced convection Nusselt for circular cylinders in a crossflow for Pr = 0.71, $Nu_D = C_1 + C_2 Re_D^m$

Author	L/D	C_1	C_2	m	Re_D
King (1914)‡	1290 - 1520	0.32	0.48	0.5	0.06 - 50.0
King (1932)‡	–	0.0	0.764	0.41	3 - 300
	–	0.0	0.282	0.585	300 - 4000
Hilpert (1933)	5120	0.0	0.891	0.33	1 - 4
	1625 - 5120	0.0	0.821	0.385	4 - 40
	20 - 3170	0.0	0.615	0.466	40 - 40000
	5.6 - 20	0.0	0.174	0.618	40000 - 400000
Krujilin (1938)‡	2.7 - 42.4	0.0	0.27	0.6	6000 - 130000
Kramers (1946)	-	0.39	0.52	0.5	9.5 - 1420
Masil-Sherwood (1950)‡	4 - 2.5	0.0	0.322	0.57	6,000 - 30,000
Eckert-Soehngren (1952)‡	6 - 18	0.0	0.57	0.473	20 - 600
Laurence-Landes (1952)‡	400 - 2500	0.19	0.51	0.5	15 - 70
Snyder (1953)‡	12	0.0	0.278	0.55	8000 - 20000
Burn et al. (1956)‡	37.5 - 60.0	0.0	0.136	0.65	6000 - 15000
Van der Hegge (1956)‡	37.5 - 555	0.0	0.68	0.41	5 - 50
	37.5 - 555	0.35	0.43 *	0.5	20 - 80
Collis-Williams (1959)‡	2070 - 8660	0.24	0.56	0.45	0.02 - 44
	2070 - 8660	0.0	0.48	0.51	44 - 140
Kazabvetich (1959)‡	11.4	0.0	0.246	0.6	5000 - 35000
Van Mell (1962)‡	6.9	0.35	0.5	0.5	5000 - 37000
Delleur (1964)‡	100	1.15	0.726	0.5	1 - 3
Galloway-Sage (1967)	8.0	0.0	0.167	0.637	2700 - 38000
Hatton et al. (1970)	96 - 1190	0.38	0.581	0.439	0.6 - 45
	96 - 1190	0.0	0.95	0.3	0.6 - 4
	96 - 1190	0.0	0.81	0.38	4 - 40
	96 - 1190	0.0	0.786	0.392	16 - 45
Srenivasen-Ramachandram (1971)‡	17.5	0.0	0.226	0.6	2500 - 15000
Andrews (1972)‡	24 - 1300	0.34	0.65	0.45	0.015 - 20
Bradbury (1972)‡	270 - 2000	0.24	0.56	0.45	0.5 - 12
Krall-Eckert (1973)‡	6.3	0.0	0.93	0.37	5 - 50
	6.3	0.0	0.64	0.46	50 - 5000
Koch (1972)‡	230	0.72	0.8	0.45	1.2 - 4.1
Petrie-Simpson (1972)‡	5.7	0.0	0.042	0.75	4000 - 33000
Churchill-Bernstein (1977)	-	0.3	0.485	0.5	-
Zukauskas-Ziugzda (1985)	-	0.0	0.23	0.60	$1000 - 2 \times 10^5$
Ahmad-Qureshi (1991)	-	0.0	0.844	0.383	1 - 60
Ahmad-Qureshi (1992)	8.0	0.0	0.0675	0.733	6800 - 21300

‡ *from Morgan (1975)*

* $Nu_D = C_1 + C_2 Re_D^m + 0.001 Re_D$

The circular and square toroids were not considered in previous studies which were available to authors. The objectives of the present investigation can be summarized as follows:

1. use experimental techniques to study the forced convection heat transfer from different arbitrary body shapes such as spheres, circular horizontal cylinders, square horizontal cylinders, toroids and square toroid;
2. examine different scale lengths such as square root of the total heat transfer area, $\sqrt{A}$, diameter, D, the ratio of surface area to the perimeter length, A/p and the ratio of the volume to the surface area, $4\pi V/A$, etc. (The effect of the characteristic length, $\mathcal{L}$, will be taken into consideration in the present study.);
3. develop a general model based on the experimental results and the approximate analytical solution of Refai Ahmed and Yovanovich (1995) in order to explain the forced convection heat transfer from different body shapes;
4. develop design correlations of the experimental results in order to satisfy the needs of various engineering applications. In addition, the design correlations will also consider the conduction limit, $Re_{\mathcal{L}} = 0$, for the different body shapes which have been introduced by Jafarpur (1992) and Wang (1993).

Experimental Program

The purpose of the experimental program is to study the external forced convection heat transfer from isothermal bodies of different shapes. The experiments are necessary because of the analytical difficulties involved in finding a solution for any shape. These experiments can be a starting point in the development of empirical models of the bodies considered. The current experiments are designed to meet the following requirements: maintain the body at uniform temperature; minimize radiation heat transfer; accurately determine effective surface emissivity of the bodies in order to correct for radiation losses; and determine the effect of turbulence intensity.

The body geometries which were tested in the present study (see Fig. 1) are:

- horizontal circular cylinder with $L/D = 9$ and $D = 0.02$ m
- horizontal square cylinder with $L/W = 9.12$ and $W = 0.017$ m
- circular toroid with $D_O = 0.078$ m, $D_I = 0.039$ m and $D_{CS} = 0.039$ m
- square toroid, $D_O = 0.068$ m and $D_I = 0.034$ m and $L = 0.017$ m

These body shapes are manufactured from 6061-T6 aluminum with a thermal conductivity of 167 W/mK. The main reason to

Table 2 Recalculation of the Hilpert data (1933) by Morgan (1975), $Nu_D = C_2 Re_D^m$

Re_D	L/D	Hilpert (1933)		Morgan (1975)	
		C_2	m	C_2	m
1 - 4	5120	0.891	0.33	-	-
4 - 40	1625 - 5120	0.821	0.385	0.795	0.384
40 - 4000	20 - 3170	0.615	0.466	0.583	0.471
4000 - 40000	5.6 - 20	0.174	0.618	0.148	0.633
40000 - 400000	0.9 - 11.4	0.0239	0.805	0.0208	0.814

choose a high thermal conductivity material is to ensure that we maintain an isothermal boundary condition. Furthermore, the polished aluminum will minimize the radiative heat transfer between 5 percent to 2 percent of the total heat transfer rate. In addition, all body shapes have approximately the same surface area ($A = 11304$ mm^2 ± 5.5%).

Wind Tunnel. The present experiment was conducted in a low-speed open suction wind tunnel. Figure 2 shows a sketch of the wind tunnel. The cross section of the test section is 0.3 m by 0.3 m. The present investigation examined the flow quality in the X-direction and the Y-direction at three different fan speeds. It was observed that the maximum difference between the average velocity and the local velocity was approximately 3.8% (more details in Refai Ahmed, 1994). Furthermore, the velocity can be considered constant to within 30 mm of the side wall of the test section.

Blockage Effect. One of the main concerns for any forced convection heat transfer experiment inside the wind tunnel is the blockage effect, Υ, where the velocity of the stream is affected directly by the blockage as shown in the following equation:

$$V_\infty = (1 + \Upsilon) \cdot V'_\infty \tag{3}$$

Table 3 Forced convection Nusselt for square cylinders in crossflow for Pr = 0.71, $Nu_W = C_2 Re_W^m$†

Author	Orientation*	C_2	m	Re_W
Hilpert (1933)	0.0 $\pi/4$	0.085 0.201	0.675 0.588	3900 - 78500 3900 - 78500
Reiher (1926)	0.0 $\pi/4$	0.149 0.238	0.691 0.624	1960 - 6000 1960 - 6000
Igarashi (1985)	0.0 $\pi/4$	0.14 0.27	0.660 0.59	5600 - 56000 5600 - 56000
Oosthuizen - Bishop (1987)	0 $\pi/4$	0.281 0.414	0.57 0.537	300 - 5000 300 - 5000

† *Correlations were developed for both assisting and opposing flow*

* *0 means horizontal square cylinder*

$\pi/4$ means square horizontal with $\pi/4$ rotation about the longitudinal axis

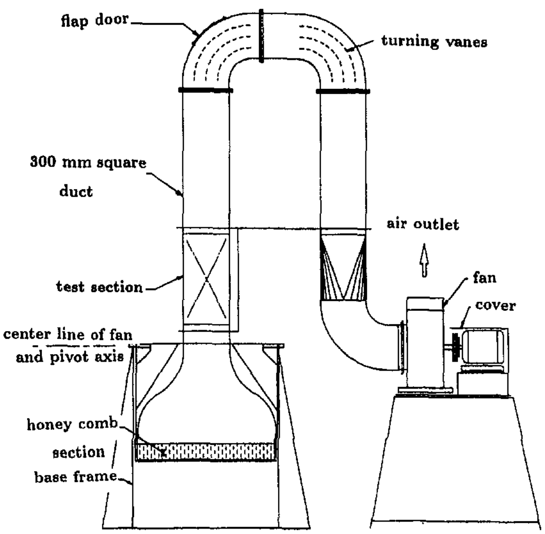

Fig. 2 Sketch of wind tunnel

where V'_∞ is the measured free stream velocity which does not account for the blockage effect. Rae and Pope (1984) suggested that the blockage equation, Υ, for a shape that needs to be tested in a tunnel is

$$\Upsilon = 0.25 \cdot \left[\frac{\text{Model Frontal Area}}{\text{Test Section Area}}\right]. \tag{4}$$

In the present study Υ will be fixed at a maximum value of 0.01. It is recommended to the reader to review Morgan (1975) for the extensive review of the blockage effect on the area-averaged Nusselt number.

Turbulence Intensity. One of the main concerns about the previous forced convection heat transfer studies is the turbulence intensity and its effect on the output results. Therefore, the present study determined the effect of the turbulence intensity. Figure 3 shows the experimental results for different velocities and the corresponding values of the turbulence intensity, Tu, at the inlet and outlet of the test section (more details in Refai Ahmed, 1994). Tu is calculated from the following equation:

$$Tu = 6.59 \times 10^{-6} \left(\frac{L}{x'}\right)^{1.15} \mathrm{Re}_{x'}^{0.575} \tag{5}$$

where $L = 2.17$ m and x' is the distance from the end of the contraction to the location of the object being tested.

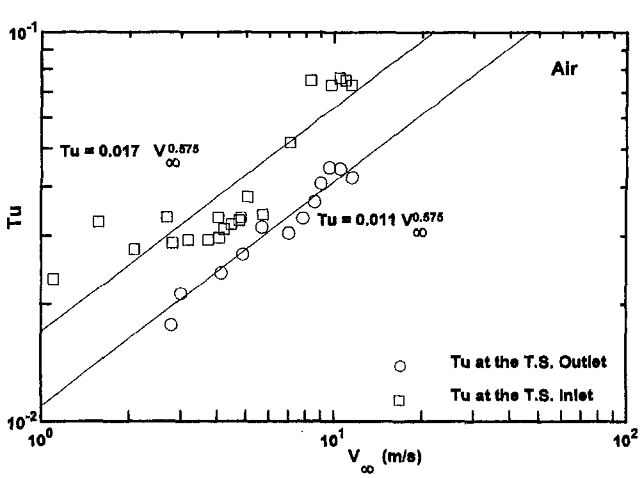

Fig. 3 Relationships between turbulence intensity and free stream velocity at inlet and outlet of MHTL wind tunnel test section

Emissivity Measurements. The general experimental method, which is used here, is similar to the approach used by Hassani (1987). The current study is designed to find the thermal emissivity at the steady state condition where

$$Q_T = Q_{Cond} + Q_{NC} + Q_{Rad} + Q_W. \tag{6}$$

Hassani (1987) has shown that the heat transfer due to convection and conduction can be ignored if the testing body is placed in a vacuum. However, Q_W, wire loss is determined by modeling the wire as an infinite circular fin.
Therefore,

$$\mathcal{F} = \frac{VI - Q_W}{\sigma A(T_S^4 - T_\infty^4)}. \tag{7}$$

The present study is conducted for different body shapes in a vacuum chamber in which the air pressure is approximately 10^{-5} Torr in order to measure the coefficient $\mathcal{F}$ (shape factor and emissivity constant). $\mathcal{F}$ was 0.15, 0.117, 0.125 and 0.115 for the circular cylinder, square cylinder, circular toroid, and square toroid, respectively.

Forced Convection Heat Transfer Calculation

The present experiments will give us the total heat transfer, Q_T, from the body (more details about the measurement of Q_T can be found in Refai Ahmed, 1994) where Q_T at the steady state is the sum of convection heat loss, Q_{Conv}, the radiation heat loss, Q_{Rad}, and the wire heat loss, Q_W.
Therefore,

$$Q_{Conv} = Q_T - Q_{Rad} - Q_W. \tag{8}$$

The effect of free convection on forced convection phenomena has been investigated under the subject of mixed or combined free and forced convection. Morgan (1975), Jaluria (1980), and Burmeister (1993) provide a detailed review of the many investigations on the subject of mixed convection from isothermal plates, cylinders, and spheres. Most of the previous studies such as Churchill (1977) and McAdams (1942) presented this phenomena in the following form:

$$\mathrm{Nu} = (\mathrm{Nu}_{FC}^n + \mathrm{Nu}_{NC}^n)^{1/n}. \tag{9}$$

Yovanovich and Vanoverbeke (1988) developed their mixed convection model based on the forced convection correlation of Yuge (1960) and the free convection correlation of Raithby and Hollands (1975) for sphere and $\Pr = 0.71$. These correlations are

$$\mathrm{Nu}_{D_{FC}} = 0.491\ \mathrm{Re}_D^{0.5} \tag{10}$$

and

$$\mathrm{Nu}_{D_{NC}} = 0.452\ \mathrm{Ra}_D^{0.25}. \tag{11}$$

Yovanovich and Vanoverbeke (1988) also proposed that for forced convection from a sphere, the dimensionless heat transfer rate by convection is the summation of the dimensionless heat transfer by conduction, free convection, forced convection, and a correction factor, CR, where CR is $0.86 - 2.86(\mathrm{Ra}_D/\mathrm{Re}_D^2)^{1/4}$. Furthermore, Steinberger and Treybal (1960) proposed a formula similar to Yovanovich and Vanoverbeke (1988) for assisted flow. Churchill (1977) used the same formula for either forced convection or free convection for air, but his constant for forced convection is 0.535 and for free convection is 0.511. For the mixed convection from spheres, this can create some differences in the limits of pure free convection and forced convection. These differences are carried to the mixed convection predication. Therefore, Eq. (9) can not predict Nu very accurately, unless Nu_{NC}, Nu_{FC}, and n are well known.

Other previous studies presented the mixed convection as a function of $(\mathrm{Gr}/\mathrm{Re}^2)$ such as Sparrow and Gregg (1959), Lloyd and Sparrow (1970), and Eshghy (1964) where at $\mathrm{Gr}/\mathrm{Re}^2 \simeq 1$, both free and forced convection are important. In contrast, free convection is dominant when $\mathrm{Gr}/\mathrm{Re}^2 \gg 1$ and forced convection is dominant when $\mathrm{Gr}/\mathrm{Re}^2 \ll 1$. Furthermore, Clift et al. (1978) stated that, "consideration of the available data for spheres indicates that forced flow correlations are accurate to about 10% for $\mathrm{Gr}/\mathrm{Re}^2 < 0.2$." Yovanovich and Vanoverbeke (1988) proved that Clift et al.'s statement is inaccurate for the Rowe et al. (1965) air data. Also, they found that free convection effects in cross flow were observed to be significant for $\mathrm{Gr}/\mathrm{Re}^2$ as low as 10^{-4}. In addition, Clift et al. (1978) examined Yuge (1960) sphere's experimental data for mixed convection of aiding flow and cross flow in the ranges of $3 < \mathrm{Re}_D < 300$, $180 < \mathrm{Gr}_D < 1800$ and $\Pr = 0.71$. They concluded that aiding flow data lay slightly above those for crossflow. Similar behavior occurs for cylinders as observed by Hatton et al. (1970) and Oosthuizen and Madan (1971).

The present study will use the Yovanovich and Vanoverbeke (1988) concept to remove the effect of free convection from the data of different body shapes. However, in the experimental range of the present study CR is negligible. Therefore, Q_{FC} can be approximated as

$$Q_{FC} = Q_{Conv} - Q_{NC} \tag{12}$$

for assisted flow conditions.

Radiation Heat Loss. After the method of how to obtain $\mathcal{F}$ is described, the radiation heat loss can be determined as follows:

$$Q_{Rad} = \mathcal{F}\sigma A(T_S^4 - T_\infty^4). \tag{13}$$

It is estimated from the preliminary experiments that the maximum Q_{Rad} is approximately 6 percent of the input power when $\mathcal{F} = 0.115$ and $T_S = 310$ K.

Wire Loss. The wire loss by heat conduction from the thermocouple wires and the power leads is taken into account by treating them as infinite fins. Mack (1991) reported that the conduction losses were of the order of 0.5% of the total input power which is an order of magnitude less than the radiation loss. However, in the experimental procedure for radiation tests the wire loss is considered.

Free Convection Heat Loss

The free convection heat loss for the different body shapes will be calculated based on the proposed model of Jafarpur (1992).

$$Q_{NC} = \sqrt{A}\cdot\Delta T\cdot k\cdot F(\Pr)\cdot G_{\sqrt{A}}\cdot \mathrm{Ra}_{\sqrt{A}}^{1/4} \tag{14}$$

where $F(\Pr)$ is the Prandtl number function, which was proposed by Churchill (1983)

$$F(\Pr) = \frac{0.67}{[1 + (0.5/\Pr)^{9/16}]^{4/9}} \tag{15}$$

and $G_{\sqrt{A}}$ is the body gravity function defined as

$$G_{\sqrt{A}} = c\left(\frac{P_{\max}}{\sqrt{A}}\right)^{1/4} \tag{16}$$

where $P_{\max}$ is the maximum perimeter and $\sqrt{A}$ is the surface area, i.e., c depends on the body shape and it lies in the range of 0.8 to 1.

Error Analysis. The overall uncertainties for $\mathrm{Re}_{\mathcal{L}}$, $\mathrm{Ra}_{\mathcal{L}}$, ϵ, and $\mathrm{Nu}_{\mathcal{L}}$ are investigated, and it is found that the uncertainty of $\mathrm{Re}_{\mathcal{L}}$ is ±7.2 percent which occurs at low values of the Reynolds

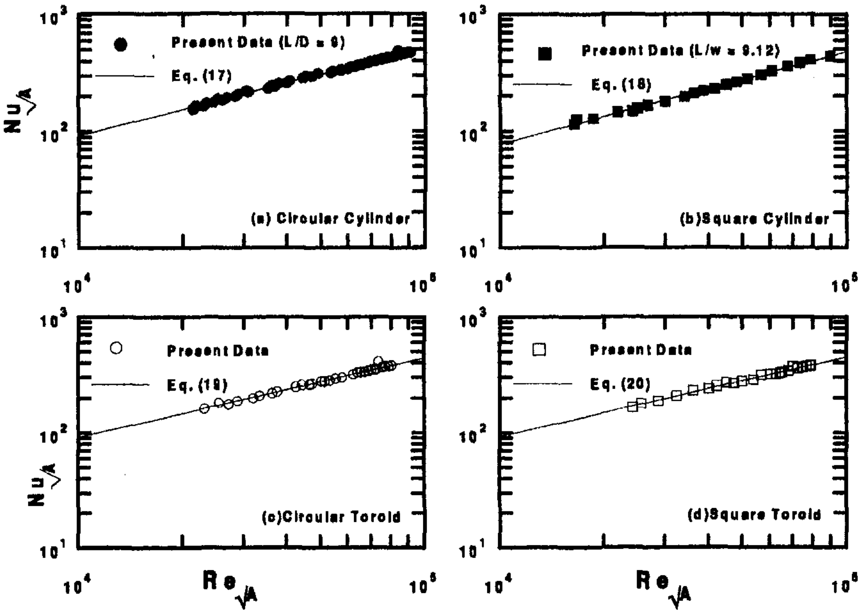

Fig. 4 Relationships between Nusselt and Reynolds number for different body shapes (air)

number. In addition, it is found that the uncertainty in $\text{Nu}_{\mathcal{L}}$ is approximately ±5.4 percent (more details in Refai Ahmed, 1994).

Data Analysis

Figure 4 shows the present experimental results of forced convection heat transfer from the isothermal circular cylinder, square cylinder, circular toroid, and square toroid in the Reynolds number range, $10^4 \leq \text{Re}_{\sqrt{A}} \leq 10^5$ and $0.012 \leq \text{Tu} \leq 0.049$. These data have been reduced by removing radiation and free convection heat transfer effects. However, the effect of the turbulence intensity has not been removed. The dimensionless parameters, $\text{Nu}_{\mathcal{L}}$ and $\text{Re}_{\mathcal{L}}$, have been defined with respect to $\mathcal{L} = \sqrt{A}$.

Two procedures were used to generate the experimental results. The first technique involved fixing the electric power input of the heater at five and ten W and varying the flow velocity. In contrast, the second technique was to fix the temperature difference, ΔT, by varying the flow velocity and the electric power simultaneously. Both methods produced similar experimental results.

Figure 4(a) shows the present data of Nusselt and Reynolds numbers for forced convection heat transfer ($\text{Pr} = 0.71$) from the isothermal circular cylinder in cross flow with $L/D = 9$ and $D = 0.02$ m. The effect of natural convection in the experimental data was between 10 percent and 3.5 percent for the range of Reynolds numbers between 21,000 and 92,000. However, the radiation effect in the same range of Reynolds number was 2 percent to 0.8 percent.

Figure 4(b) presents the present data of Nusselt and Reynolds numbers for forced convection ($\text{Pr} = 0.71$) from a horizontal square cylinder with $L/W = 9.12$ and $W = 0.017$ m. The maximum effect of radiation in the range of Reynolds number from 24,000 to 9×10^4 was 2 percent at $\text{Re}_{\sqrt{A}} \simeq 24{,}000$. However, the free convection effect was 20 percent at $\text{Re}_{\sqrt{A}} \simeq 24{,}000$ and the minimum effect was 5 percent at $\text{Re}_{\sqrt{A}} \simeq 90{,}000$.

Figures 4(c) and 4(d) show the present data of the Nusselt and Reynolds numbers for forced convection heat transfer ($\text{Pr} = 0.71$) from both the isothermal horizontal circular toroid with $D_O = 0.078$ m, $D_I = 0.039$ m, and $D_{CS} = 0.039$ m and the square toroid with $D_O = 0.068$ m, $D_I = 0.034$ m, and $L = 0.017$ m (see Fig. 1). The effect of free convection was found to be a maximum of 13.4 percent at $\text{Re}_{\sqrt{A}} = 23153$ and a maximum of 1.6 percent for radiation at $\text{Re}_{\sqrt{A}} = 23153$. Table 4 shows the relationships between $\text{Nu}_{\sqrt{A}}$ and $\text{Re}_{\sqrt{A}}$ and the maximum and RMS percent differences for the different body shapes.

Effect of Characteristic Length on Nu − Re Relationship

One of the important issues in a study dealing with different body shapes is how to present the relationships between the Nusselt and Reynolds numbers. Therefore, the choice of an appropriate scale length is a very important step in the development of the final results for this type of study. Yovanovich (1987b) examined a number of different scale lengths, such as the diameter for the sphere and the horizontal circular cylinder, the height of a vertical cylinder and flat plate, and the minor and major axes of oblate spheroids. Yovanovich (1987b) concluded that these scale lengths are not general when they approach zero as the thickness of the body goes to zero. Other scale lengths have also been used in the literature, such as the diameter of a sphere having the same volume as the body, $\mathcal{L} = (6\mathcal{V}/\pi)^{1/3}$, $\mathcal{L} = 2\mathcal{V}/A$ was used by Tsubouchi and Sato (1960). In addition, Churchill and Churchill (1975) used $\mathcal{L} = 4\pi\mathcal{V}/A$. Jafarpur (1991) examined these scale lengths and found that as the thickness goes to zero, the characteristic lengths becomes zero. Therefore, none of these characteristic lengths can be considered as a general scale length. Pasternak and Gauvin (1960) proposed a characteristic length of A/P. Furthermore, other studies have also used this scale length such as, Goldstein

Table 4 Experimental correlation of forced convection

Body Shape	Correlation Equation of $Nu_{\sqrt{A}}$	RMS Diff. %	Maximum Diff. %	Eq.
Circular Cylinder	$0.508\ Tu^{0.174}\ Re_{\sqrt{A}}^{0.647}$	2.15	6.03	(17)
Square Cylinder	$0.303\ Tu^{0.174}\ Re_{\sqrt{A}}^{0.685}$	1.53	4.73	(18)
Circular Toroid	$0.899\ Tu^{0.174}\ Re_{\sqrt{A}}^{0.584}$	1.41	7.80	(19)
Square Toroid	$0.901\ Tu^{0.174}\ Re_{\sqrt{A}}^{0.585}$	1.98	4.97	(20)

et al. (1973), Weber et al. (1984), and Sahraoui et al. (1990). Jafarpur (1991) stated some criteria for choosing an appropriate characteristic body length. These criteria can be summarized as follows: the characteristic length should be well defined, applicable to all bodies, possible to calculate or measure easily, intrinsic, physically interpretable, related to the orientation of the body, able to collapse all data into a single curve. Jafarpur examined both $\mathcal{L} = \sqrt{A}$ and $\mathcal{L} = A/P$ and based on these criteria he found that $\sqrt{A}$ is the most appropriate scale length. In addition, the scale length of $\sqrt{A}$ has also been used by Yovanovich (1987b), (1988) and Yovanovich and Vanoverbeke (1989).

The present study has examined the relationships between $Nu_{\mathcal{L}}$ and $Re_{\mathcal{L}}$ based on different characteristic lengths such as $\sqrt{A}$, A/P, $(6\mathcal{V}/\pi)^{1/3}$ and $4\pi\mathcal{V}/A$ (for the circular cylinder, square cylinder, circular toroid, and square toroid). The present investigation concluded that all of the relationships have the same trend and approximately the same slope ($m \simeq 0.7$). Therefore, $Nu_{\mathcal{L}}$ verses $Re_{\mathcal{L}}$ relationships may be expressed in the following form:

$$Nu_{\mathcal{L}} = Nu^0_{\mathcal{L}} + C_{\mathcal{L}}\, Re^{0.7}_{\mathcal{L}}. \tag{21}$$

$Nu^0_{\mathcal{L}}$ is the diffusive Nusselt number and $C_{\mathcal{L}}$ is constant which is dependent on body shape. The maximum percent differences, using various scale lengths such as $\sqrt{A}$, A/P, $(6\mathcal{V}/\pi)^{1/3}$, and $4\pi\mathcal{V}/A$, between the coefficients of $C_{\mathcal{L}}$ for different body shapes are 30 percent, 18 percent, 25 percent and 23 percent and the maximum percent differences between the value of $Nu^0_{\mathcal{L}}$ for different body shapes are 19 percent, 51 percent, 28 percent and 59 percent, respectively. One can also observe that the characteristic length of A/P, $(6\mathcal{V}/\pi)^{1/3}$, and $4\pi\mathcal{V}/A$ are better than $\sqrt{A}$ at high Reynolds number (where the diffusive limit is negligible). However, these scale lengths $[(6\mathcal{V}/\pi)^{1/3}$ and $(4\pi\mathcal{V}/A)]$ can not be used if the body thickness goes to zero. In contrast, at low Reynolds number (where the diffusive limit is more pronounced) the scale length of $\sqrt{A}$ is better than the other characteristic body lengths. Therefore, the choice of the characteristic length is limited to either A/P or $\sqrt{A}$. In the present study the scale length of $\sqrt{A}$ has been selected where this characteristic body length is the appropriate scale length, all over the wide range of Reynolds number, to collapse the experimental data. Also, all the present body shapes have the same surface area.

Empirical Models

In this section empirical models are developed based on:

- the experimental results for the circular cylinder, the square cylinder, the circular toroid and the square toroid;
- the characteristic body length, $\sqrt{A}$, which was shown to have certain advantages in the above section;
- the removal of the effect of the free stream turbulence from $C_{\sqrt{A}}$ by using Refai Ahmed et al. (1996) method; and
- the separation of $F(Pr, \gamma_{\sqrt{A}})$ (which was derived in Refai Ahmed and Yovanovich, 1995) from $C_{\sqrt{A}}$.

Recently Refai Ahmed et al. (1996) investigated analytically and experimentally the effect of the turbulence intensity on forced convection heat transfer from isothermal spheres. In addition, they developed an approximate analytical solution in the following form based on the linearization of the thermal energy equation:

$$Nu_{\sqrt{A}} = \left(1 + Pr\,\frac{\alpha_t}{\nu}\right) \cdot \left[3.545 + \frac{1.032\, Re^{0.5}_{\sqrt{A}} \left[\dfrac{(1/Pr) + (\alpha_t/\nu)}{1 + (\nu_t/\nu)}\right]^{1/6}}{\sqrt{(2\gamma_{\sqrt{A}} + 1)\left(\dfrac{1}{Pr} + \dfrac{\nu_t}{\nu}\right)} \left(1 + \left[\dfrac{(1/Pr) + (\alpha_t/\nu)}{(2\gamma_{\sqrt{A}} + 1)^3 (1 + (\nu_t/\nu))}\right]\right)^{1/6}}\right] \tag{22}$$

where

$$\frac{\nu_t}{\nu} = [(1.253 K Tu \sqrt{Re_{\sqrt{A}}})^3 + (0.928 K^2 Tu^2 Re_{\sqrt{A}})^3]^{1/3} \tag{23}$$

and

$$K = 0.05 \quad \text{and} \quad \alpha_t = \nu_t. \tag{24}$$

The variable $\gamma_{\sqrt{A}}$ was defined in Refai Ahmed and Yovanovich (1995). The solution of Refai Ahmed et al. (1996) was found to be in very good agreement with their experimental data and the data of Raithby (1967).

The present study applies the Refai Ahmed et al. (1996) solution to remove the effect of the turbulence intensity from the heat transfer results of the sphere. This solution is now applied to remove the turbulence intensity effect from the circular cylinder, square cylinder, circular toroid, and square toroid results. The relationships between Nusselt and Reynolds numbers based on the square root of the area have the same trend for each of these bodies, as mentioned before ($m \simeq 0.7$), after removing the radiation effect and the free convection effect. Therefore, the only effects left are the turbulence intensity and Prandtl number. Furthermore, the magnitude of the turbulence intensity is the same for all body shapes at the same Reynolds number, e.g., at $Re_{\sqrt{A}} = 22000$, $Tu = 0.022$ and $Re_{\sqrt{A}} = 80000$, $Tu = 0.046$.

The present experimental results can be presented in the general form

$$Nu_{\sqrt{A}} = Nu^0_{\sqrt{A}} + C_{\sqrt{A}}\, Re^{0.5}_{\sqrt{A}} F(Pr, \gamma_{\sqrt{A}}) \qquad 0 \le Re_{\sqrt{A}} \le 6 \times 10^6. \tag{25}$$

This general form has been developed through the approximate analytical approach given in Refai Ahmed and Yovanovich (1995). Also, it was shown that $F(Pr, \gamma_{\sqrt{A}})$ for different body shapes can be defined as follows:

$$F(Pr, \gamma_{\sqrt{A}}) = \frac{Pr^{1/3}}{\left[(2\gamma_{\sqrt{A}} + 1)^3 + \dfrac{1}{Pr}\right]^{1/6}} \qquad 0 < Pr < \infty \tag{26}$$

where, for the circular cylinder:

$$\gamma_{\sqrt{A}} = \frac{1}{[1 + 0.49\, Re^{1.25}_{\gamma\sqrt{A}}]^{1/5}}. \tag{27}$$

The empirical expression for $\gamma_{\sqrt{A}}$ for the circular cylinder will be used for the square cylinder, circular toroid, and square toroid. The reduced experimental data from the turbulence intensity effect (using Refai Ahmed et al., 1996) can be correlated for the different body shapes as shown in Table 5.

Table 5 Proposed correlations of forced convection

Body Shape	Correlation Equation of $Nu_{\sqrt{A}}$	RMS Diff. %	Maximum Diff. %	Eq.
Circular Cylinder	$4.15 + 1.71\ Re_{\sqrt{A}}^{0.5}\ F(Pr, \gamma_{\sqrt{A}})$	4.47	9.9	(28a)
	$0.76 + 0.73\ Re_D^{0.5}\ F(Pr, \gamma_D)$	4.47	9.9	(28b)
Square Cylinder	$4.01 + 1.37\ Re_{\sqrt{A}}^{0.5}\ F(Pr, \gamma_{\sqrt{A}})$	1.09	3.69	(29a)
	$0.65 + 0.55\ Re_W^{0.5}\ F(Pr, \gamma_W)$	1.09	3.69	(29b)
Circular Toroid	$3.41 + 1.58\ Re_{\sqrt{A}}^{0.5}\ F(Pr, \gamma_{\sqrt{A}})$	0.92	3.58	(30)
Square Toroid	$3.37 + 1.60\ Re_{\sqrt{A}}^{0.5}\ F(Pr, \gamma_{\sqrt{A}})$	0.87	3.34	(31)

One observes from the correlations in Table 5 that the body shape parameter, $C_{\sqrt{A}}$, can be correlated in the general form

$$C_{\sqrt{A}} = 0.84\left(\frac{P_{\max}}{\sqrt{A}}\right)^{0.5}. \tag{32}$$

This semi-empirical form can predict $C_{\sqrt{A}}$ within ±9 percent.

Comparison of Present Results and Previous Work

This section compares the present experimental model with the available data and correlations from previous studies. These comparisons will be done based on the characteristic length D for the circular cylinder, and W for the square cylinder. The main reason is that most previous works were reported based on these scale lengths and there is insufficient information to calculate the surface area.

Figure 5 shows the relationship between $\mathrm{Re}_{\sqrt{A}}$ and $\mathrm{Nu}_{\sqrt{A}} - \mathrm{Nu}_{\sqrt{A}}^0/[0.84(P_{\max}/\sqrt{A})^{0.5}]$ for the reducing experimental data of circular and square toroids and cylinders. Figure 5 also shows that the experimental data have the same trend and all of them lie together. This relationship concluded that the function $0.84(P_{\max}/\sqrt{A})^{0.5}$ can estimate the parameter $C_{\sqrt{A}}$.

Circular Cylinder. Figure 6 shows comparisons between the empirical model, Eq. (28*b*), the approximate solution of Refai Ahmed and Yovanovich (1995), and the correlations of the previous works in a wide range of Reynolds number, $1 \leq \mathrm{Re}_D \leq 10^5$. One observes from Fig. 6 at low Re_D ($\mathrm{Re}_D < 5$) that there are significant differences between most of the previous works and the empirical model. This is due to the effect of L/D, where the correlation equations of the approximate solution, Van der Hegge (1956), Morgan (1975), and Ahmed and Qureshi (1991) are based on $L/D \gg 1$, i.e., their Nusselt numbers at the diffusive limit go to zero. At high Reynolds number range, $\mathrm{Re}_D \geq 10^4$, most of the correlation equations of previous works are slightly higher than the empirical model. This is also due to the effect of L/D, the free stream turbulence and the free convection. Other correlation such as Ahmed and Qureshi (1992) was higher than the present work due to their boundary condition (isoflux boundary). In contrast, the correlation equation of Churchill and Bernstein (1977) was found lower than both the empirical model and the previous works.

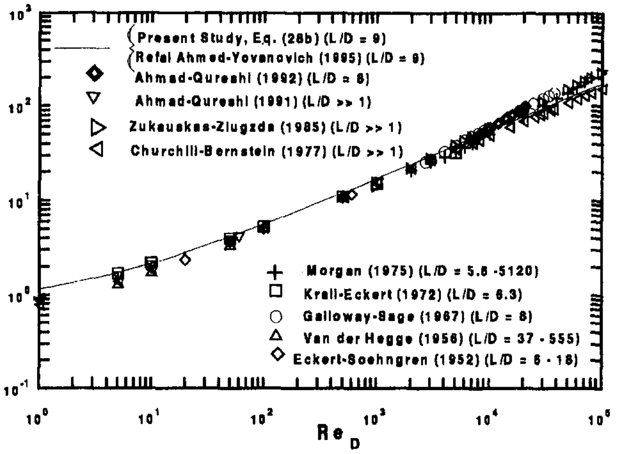

Fig. 6 Comparison between present study and previous works for circular cylinders (air)

Figure 6 also shows comparisons between the recent forced convection correlations for circular cylinder from Churchill and Bernstein (1977), Morgan (1975), and Zukauskas and Ziugzda (1985) and the present study. Figure 6 shows very good agreement, within three percent, between the present study and Morgan (1975) and the maximum difference is 14 percent. In addition, the present study is higher than the Churchill and Bernstein correlation by 6.8 percent. In contrast, the experimental correlation of Zukauskas and Ziugzda (1985) is higher than the present study, Eq. (28*b*), by 13 percent. These comparisons show that the present study, Eq. (28*b*), is in good agreement with most of the previous studies.

Square Cylinder. Figure 7 shows comparisons between the experimental model, Eq. (29*b*), with other available experimental correlations in the literature[3] such as Rieher (1926),

---

[3] The correlation equations are available in Table 3

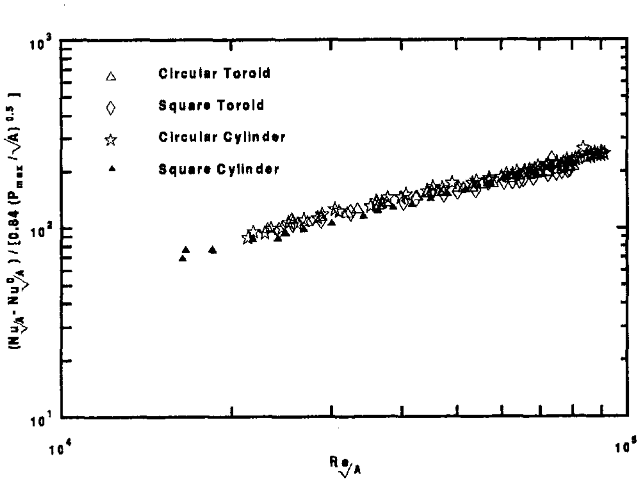

Fig. 5 Relationships between Reynolds number and body shape parameter for different body shapes (air)

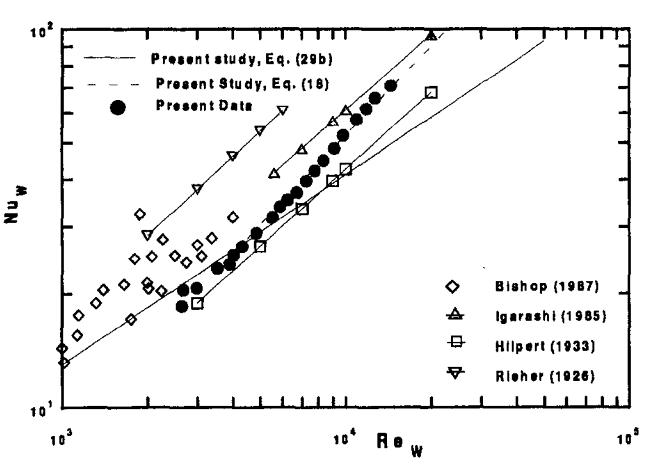

Fig. 7 Comparison between present study and previous works for square cylinders (air)

Helpert (1933), Igarashi (1985), and data of Bishop (1987). Bishop (1987) and Oosthuizen and Bishop (1987) examined this problem and developed an experimental correlation for assisted flow and opposing flow,

$$\mathrm{Nu}_W = 0.281\ \mathrm{Re}_W^{0.57} \quad 7 \leq L/W \leq 12.5$$

The average difference between this correlation and their measurements was ±22 percent, which is reflected in the scatter as shown in Fig. 7. Furthermore, the range of Grashof number in the experiments of Bishop was $74{,}000 \leq \mathrm{Gr}_W \leq 450{,}000$ which can influence the forced convection results. In addition, the effect of turbulence intensity can be another reason for the scatter in the data. The high temperature difference between the surface temperature and the ambient temperature, $\Delta T = 75$ K, can also influence the heat transfer results as observed by Hilpert (1933) and Churchill and Brier (1956) in their experimental work. Hilpert (1933) and Churchill and Brier (1956) found that the temperature effect can influence the heat transfer result by $(T_S/T_\infty)^{0.124}$ and $(T_S/T_\infty)^{0.12}$, respectively. In addition, Fig. 7 shows that the Igarashi (1985) correlation is also above the experimental correlation, Eq. (18), by 30 percent. However, he did not discuss the influence of radiation, free convection, and free stream turbulence on his experimental measurements. Furthermore, the experimental error was not reported. Therefore, it is difficult to justify the difference between Eq. (18) and the correlation of Igarashi.

In contrast, Hilpert's (1933) correlation is in good agreement with Eq. (29*b*). However, concerns about Hilpert's circular cylinder work were reported by Fand and Keswani (1973), Morgan (1975), and Churchill and Bernstein (1977). These concerns include the calculation of the thermal properties, the turbulence intensity effect, and the blockage effect. It is difficult to examine these concerns for the square cylinder since there is insufficient information. Figure 6 also shows the experimental correlation of Reiher (1926) is higher than other previous studies including the present study, Eq. (18). One concludes that there is insufficient information to examine the previous studies and the only available data, Bishop (1987), had a lot of scatter.

Summary

A series of experiments were conducted for the area mean Nusselt number for forced convection from different body shapes such as isothermal circular cylinders, square cylinders, circular toroids, and square toroids in the range of Reynolds number, $10^4 \leq \mathrm{Re}_{\sqrt{A}} \leq 10^5$. The present experiments have been reduced to remove the effects of free convection, radiation, and free stream turbulence. Furthermore, experimental models for heat transfer by forced convection from different body shapes were developed. In addition the present study found that $C_{\sqrt{A}}$ depends on the geometric of the body shape as shown in Eq. (32). The model, Eq. (28*b*), of the circular cylinder is compared against approximate solution of Refai Ahmed and Yovanovich (1995), and other available correlations. These comparisons show good agreement between the model and most of the previous studies. However, the present study could not compare the circular toroid and square toroid results because there is insufficient, well documented, data available in the literature.

Acknowledgements

The authors wish to acknowledge the financial support of the Natural Sciences and Engineering Research Council of Canada under grant No. A7455. The first author also wishes to acknowledge the financial support of R-Theta Inc., Ontario, Canada.

References

Ahmad, R. A., and Qureshi, Z. H., 1991, "Laminar Mixed Convection from a Uniform Heat Flux Cylinder," *AIAA-91-0383, AIAA 29th Aerospace Sciences Meeting and Exhibit.*

Ahmad, R. A., and Qureshi, Z. H., 1992, "Buoyancy Effects on Forced Convection From a Uniform Heat Flux Horizontal Cylinder in a Cross Flow," *AIAA-92-0711, AIAA 30th Aerospace Sciences Meeting and Exhibit.*

Boulos, M., 1972, "Dynamics of Heat Transfer from Cylinders in a Turbulent Air Stream," *Ph. D. thesis, Department of Chemical Engineering,* University of Waterloo, Waterloo, Ontario, Canada.

Boulos, M., and Pei, D., 1974, "Dynamics of Heat Transfer from Cylinders in a Turbulent Air Stream," *Int. J. Heat Mass Transfer,* Vol. 17, pp. 767–783.

Bishop, M. R., 1987, "Combined Convection Heat Transfer From Horizontal Square Cylinders," *M. Sc., Department of Mechanical Engineering, Queen's University,* Kingston, Ontario, Canada.

Burmeister, L. C., 1993, *Convective Heat Transfer,* John Wiley & Sons, New York.

Churchill, S. W., and Brier, J. C., 1956, "Convective Heat Transfer from a Gas Stream at High Temperature to a Circular Cylinder Normal to the Flow," *Chem. Eng. Progr.,* Vol. 52, pp. 57–66.

Churchill, S. W., and Churchill, R. V., 1975, "A Comprehensive Correlating Equation for Heat and Component Transfer by Free Convection," *AIChE J.,* Vol. 21, No. 4, pp. 604–606.

Churchill, S. W., 1977, "A Comprehensive Correlating Equation for Laminar, Assisting, Forced and Free Convection," *AIChE J.,* Vol. 23, No. 1, pp. 10–16.

Churchill, S. W., and Bernstein, M., 1977, "A Correlating Equation for Forced Convection from Gases and Liquids to a Circular Cylinder in Crossflow," ASME JOURNAL OF HEAT TRANSFER, Vol. 99, No. 2, pp. 300–306.

Churchill, S. W., 1983, "Comprehensive Theoretically Based, Correlating Equations for Free Convection from Isothermal Spheres," *Chem. Eng. Commun.,* Vol. 24, pp. 339–352.

Clift, R., Grace, J. R., and Weber, M. E., 1978, *Bubbles, Drops and Particles,* Academic Press, New York.

Eshghy, S., 1964, "Forced Flow Effects on Free Convection Flow and Heat Transfer," ASME JOURNAL OF HEAT TRANSFER, Vol. 86, No. 2, pp. 290–291.

Fand, R. M., and Keswani, K. K., 1973, "Recalculation of Hilpert's's Constants," ASME JOURNAL OF HEAT TRANSFER, Vol. 16, No. 2, pp. 224–226.

Galloway, T. R., and Sage, B. H., 1967, "Local and Macroscopic Transport from a 1.5-In. Cylinder in a Turbulent Air Stream," *AIChE J.,* Vol. 13, No. 4, pp. 563–570.

Goldstein, R. J., Sparrow, E. M., and James, D. C., 1973, "Natural Convection to Horizontal Plates," *Int. J. Heat and Mass Transfer,* Vol. 16, pp. 1025–1035.

Hatton, A. P., James, D. D., and Swire, H. W., 1970, "Combined Forced Convection and Natural Convection with Low-Speed Air Flow Over Horizontal Cylinders," *J. Fluid Mechanics,* Vol. 42, pp. 17–31.

Hassani, A. V., 1987, "An Investigation of Free Convection Heat Transfer From Bodies of Arbitrary Shapes," *Ph. D. thesis, Mechanical Engineering Department, University of Waterloo,* Waterloo, Ontario, Canada.

Hilpert, R., 1933, *see Morgan (1975).*

Igarashi, T., 1985, "Heat Transfer from a Square Prism to an Air Stream," *Int. J. Heat and Mass Transfer,* Vol. 28, No. 2, pp. 175–181.

Jafarpur, K., 1992, "Analytical and Experimental Study of Laminar Free Convection Heat Transfer from Isothermal Convex Bodies of Arbitrary Shapes," *Ph.D. thesis, Mechanical Engineering Department, University of Waterloo,* Waterloo, Ontario, Canada.

Jain, P. C., and Goel, B. S., 1976, "A Numerical Study of Unsteady Laminar Forced Convection from a Circular Cylinder," JOURNAL OF HEAT TRANSFER, Vol. 98, No. 2, pp. 303–307.

Jaluria, Y., 1980, *Natural Convective Heat and Mass Transfer,* Pergamon Press, New York.

Krall, K. M., and Eckert, E. R., 1973, "Local Heat Transfer Around a Cylinder at Low Reynolds Number," JOURNAL OF HEAT TRANSFER, Vol. 95, No. 2, pp. 273–275.

Kramers, H., 1946, "Heat Transfer from Spheres to Flowing Media," *Physica,* Vol. 12, No. 2-3, pp. 61–81.

Laws, E. M., and Livesey, J. L., 1978, "Flow Through Screens," *Ann. Rev. Fluid Mech.,* Vol. 10, pp. 247–266.

Lloyd, J. R., and Sparrow, E. M., 1970, "Combined Forced and Free Convection Flow on Vertical Surface," *Int. J. Heat and Mass Transfer,* Vol. 13, No. 3, pp. 434–442.

Mack, B., 1991, "Natural Convection from an Isothermal Cube on a Vertical Plate," *M. A. Sc. thesis, Mechanical Engineering Department, University of Waterloo,* Waterloo, Ontario, Canada.

McAdams, W. H., 1954, *Heat Transmission,* 3rd Ed., McGraw-Hill Book Company, New York.

Masliyah, J. H., and Epstein, N., 1973, "Heat and Mass Transfer from Elliptical Cylinders in Steady Symmetric Flow," *Ind. and Engng. Chem. Funda.,* Vol. 12, pp. 317–323.

Morgan, V. T., 1975, "The Overall Convection Heat Transfer from Smooth Circular Cylinders," *Advances in Heat Transfer,* Vol. 11, Academic Press, New York, pp. 199–264.

Oosthuizen, P. H., and Madan, S., 1971, "The Effect of Flow Direction on Combined Convective Heat Transfer from Cylinders to Air," JOURNAL OF HEAT TRANSFER, Vol. 14, No. 2, pp. 240–242.

Oosthuizen, P. H., and Bishop, M., 1987, "An Experimental Study of Mixed Convection Heat Transfer from Square Cylinders," *AIAA-87-1592, AIAA 22nd Thermophysics Conference,* Honolulu, Hawaii.

Rae, W. H., and Pope, A., 1984, *Low-Speed Wind Tunnel Testing,* 2nd Ed., John Wiley & Sons, Inc.

Raithby, G., 1967, "The Effect of Turbulence and Support Position on the Heat Transfer From, and Flow Around, Spheres," *Ph. D. thesis*, University of Minnesota, U. S. A.

Raithby, G. D., and Eckert, E. R. G., 1968, "The Effect of Turbulence Parameters and Support Position on the Heat Transfer from Spheres," *Int. J. Heat Mass Transfer*, Vol. 11, pp. 1233–52.

Raithby, G. D., and Hollands, K. G. T., 1975, "A General Method of Obtaining Approximate Solutions to Laminar and Turbulent Free Convection Problems," *Advances in Heat Transfer*, Vol. 11, Academic Press, New York, pp. 266–315.

Refai Ahmed, G., 1994, "Experimental and Approximate Analaytical Study of Forced Convection Heat Transfer from Isothermal Body Shapes," *Ph. D. thesis, Mechanical Engineering Department, University of Waterloo*, Waterloo, Ontario, Canada.

Refai Ahmed, G., and Yovanovich, M. M., 1994, "Approximate Analytical Solution of Forced Convection Heat Transfer from Isothermal Spheres for All Prandtl Numbers," JOURNAL OF HEAT TRANSFER, Vol. 116, No. 4, pp. 838–843.

Refai Ahmed, G., and Yovanovich, M. M., 1995, "Approximate Analytical Solutions of Forced Convection Heat Transfer From Isothermal Simple Body Shapes for All Prandtl Numbers," *J. Thermophysics and Heat Transfer*, Vol. 9, No. 3, pp. 515–523 *and AIAA 94-1971, AIAA-ASME 6th Joint Thermophysics and Heat Transfer Conference.*

Refai Ahmed, G., Yovanovich, M. M., and Culham, R., 1996, "Experimental and Approximate Analytical Study of Forced Convection with the Effect of Turbulence Intensity From Isothermal Spheres," *AIAA 96-0366, 34th Aerospace Sciences Meeting & Exhibit*, Reno, Nevada, and *Journal of Thermophysics and Heat Transfer*, Vol. 11, No. 2, 1997.

Reiher, H., 1926, "Wärmeübergang Von Strömender Luft an Rohre," *VDI Froschungsheft*, Z. 70, pp. 47–52.

Rowe, P. N., Claxton, K. T., and Lewis, J. B., 1965, "Heat and Mass Transfer From a Single Sphere in an Extensive Fluid," *Trans. Inst. Chem. Engrs.*, Vol. 43, pp. T14–T31.

Pasternak, I. S., and Gauvin, W. H., 1960, "Turbulent Heat and Mass Transfer from Stationary Particles," *Can. J. Chem. Engr.*, Vol. 38, pp. 35–42.

Sahraoui, M., Kaviany, M., and Marshall, H., 1990, "Natural Convection from Horizontal Disks and Rings," JOURNAL OF HEAT TRANSFER, Vol. 112, No. 1, pp. 110–116.

Sparrow, E. M., and Gregg, J. L., 1959, "Buoyancy Effects in Forced Convection Flow and Heat Transfer," *J. Applied Mechanics*, Vol. 26, pp. 133–134.

Tsubouchi, T., and Sato, S., 1960, "Heat Transfer From Fine Wires and Particles by Natural Convection," *Chem Eng. Progr. Symp., Series No. 30*, Vol. 56, pp. 269–284.

Steinberger, L., and Treybal, R., 1960, "Mass Transfer From a Solid Sphere to a Flowing Liquid Stream," *AIChE Journal*, Vol. 6, No. 2, pp. 227–232.

Wang, C., 1993, "Surface Element Methods Based on Ring Sources and Line Sources for Accurate Calculations of Shape Factors for Arbitrary Isothermal Axisymmetric Surfaces and Some Two Dimensional Problems," *M. A. Sc. thesis, Mechanical Engineering Department, University of Waterloo*, Waterloo, Ontario, Canada.

Weber, M. E., Astrauskas, P., and Pestsalis, S., 1984, "Natural Convection Mass Transfer to Non-Spherical Objects at High Rayleigh Number," *Can. J. Chem. Eng.*, Vol. 62, pp. 68–72.

Yovanovich, M. M., 1987a, "Natural Convection From Isothermal Spheroids in the Conductive to Laminar Flow Regimes," *AIAA-87-1587, AIAA 22nd Thermophysics Conference.*

Yovanovich, M. M., 1987b, "New Nusselt and Sherwood Numbers for Arbitrary Isopotential Bodies at Near Zero Peclet and Rayleigh Numbers," *AIAA-87-1643, AIAA 22nd Thermophysics Conference.*

Yovanovich, M. M., 1988, "General Expression for Forced Convection Heat and Mass Transfer from Isopotential Spheroids," *AIAA-88-0743, AIAA 26th Thermophysics Conference.*

Yovanovich, M. M., and Vanoverbeke, C. A., 1988, "Combined Natural and Forced Convection Heat Transfer From Isothermal Spheres," *AIAA-88-2618, AIAA Thermophysics, Plasmadynamics and Laser Conference.*

Yuge, T., 1960, "Experiments on Heat Transfer From Spheres including Combined Natural Convection," JOURNAL OF HEAT TRANSFER, Vol. 82, No. 2, pp. 214–20.

Zukauskas, A., and Ziugzda, J., 1985, *Heat Transfer of a Cylinder in Crossflow*, Hemisphere Publishing Corporation.

Experimental Investigation of Thermal and Hydrodynamic Development Regions for Drag-Reducing Surfactant Solutions

K. Gasljevic

E. F. Matthys

Department of Mechanical and
Environmental Engineering,
University of California,
Santa Barbara, CA 93106

The reductions in friction and heat transfer exhibited by a surfactant solution in the entry region of a circular pipe were measured and analyzed, with special attention paid to the relationship between the local heat transfer and friction. Two entrance configurations were used, a cone contraction and wire mesh plugs used as a device for velocity profile flattening. Both the simultaneous development of temperature and velocity profiles and the development of temperature profile with hydrodynamically predeveloped flow were studied. Interestingly, the local heat transfer measurements for surfactant solutions matched very well a correlation developed for polymer solutions, but for surfactants the development of the heat transfer and velocity profiles appear coupled, unlike what is thought to happen for polymer solutions. The development patterns appear to be independent of velocity and entrance type at low disturbance levels. At high disturbance levels, however, some striking changes in the fluid itself, likely due to temporary micellar structure degradation by high local shear stress in the inlet region, were observed as well, and quantified.

1 Introduction and Literature Review

Much more is known about fully developed drag and heat transfer reductions for drag-reducing solutions, both polymers and surfactants, than about phenomena in the hydrodynamic and thermal developing regions. Studies of the latter regions may, however, shed more light on the fundamental nature of drag reduction than results obtained under developed conditions. Besides such theoretical considerations, there are also practical reasons why this entrance region is of importance. Indeed, entry lengths for viscoelastic fluids are usually significantly longer than for Newtonian fluids, and the entry effects may well contribute significantly to the overall heat transfer and pressure drop in short pipes (e.g., for L/D up to 1000).

Of special interest is the thermal development region. Reduced heat transfer in flows with drag-reducing additives may be an issue in some possible applications like hydronic cooling and heating systems. As some tube heat exchangers used in these systems may be of a length comparable to the usual thermal entry length for viscoelastic fluids (which was thought to be up to about 1000 diameters), the total heat transfer in these heat exchangers may perhaps be significantly higher than one would expect based on fully developed conditions. Measurements of heat transfer in the entry region may therefore help us predict the heat transfer levels to be encountered in practical applications, especially if inserts or obstructions are present.

Not much information is available for turbulent flow of non-Newtonian fluids in general, and fewer still are the studies dealing with turbulent flow of drag-reducing fluids. Most of these investigations were conducted for polymer solutions, and, not surprisingly, were mostly experimental with results expressed numerically by curve-fitting. The experimental conditions studied pertain to two main groups.

The first one can be idealized as flow development after plug flow, usually achieved through a conical contraction with high contraction ratio. It is commonly believed that the velocity profile becomes fully developed after about 100 diameters for polymer solutions (Cho and Hartnett 1982). On the heat transfer side, measurements by Kwack et al. (1981) showed a thermal entry length for polyacrylamide solution of up to 430 diameters for simultaneous development of temperature and velocity fields. Others measured even longer entrance lengths (e.g., Matthys 1991). Toh and Ghajar (1988) studied the thermal entry length for a Separan solution after hydrodynamically-developed flow was already achieved. They observed thermally developing flow still after 600 diameters, with an effect of the Reynolds number (i.e., the flow develops faster at lower Reynolds numbers). Yoo et al. (1993) proposed a correlation for heat transfer of viscoelastic polymer solutions based on their experimental data corresponding to asymptotic drag reduction in the developing and developed regions, as a function of Reynolds and Graetz numbers. In general, the experimental data on developed heat transfer and friction for asymptotic polymer solutions are consistent with the measurements of entry lengths, as well as velocity and temperature profiles. Cho and Hartnett (1982) did indeed review calculations of eddy diffusivities for heat, momentum, and mass transfer, based on data from different authors. They suggested that large differences in eddy diffusivities for mass, momentum, and heat (decreasing in that order) would result in corresponding variations in the mass, momentum, and heat transfer entry lengths (35 D, 100 D, and 500 D, respectively). The effect of degradation on heat transfer and friction for drag-reducing polymer solutions is also affected by this apparent uncoupling of heat transfer and friction. It is indeed generally believed (e.g., Ng et al. 1980; Matthys 1991) that heat transfer is affected earlier by degradation than is friction.

The second class of flow development problems for drag-reducing polymer solutions are those after an abrupt expansion in a pipe. In this case, the hydrodynamic changes in the flow are less severe than in the case of flow development after a plug velocity profile, but the same basic principles of flow readjustment to the new conditions are to be expected. Pak et al. (1991a, 1991b) measured the pressure drop and heat transfer for polyacrylamide solution after a sudden expansion. After

---

Contributed by the Heat Transfer Division for publication in the Journal of Heat Transfer. Manuscript received by the Heat Transfer Division April 24, 1996; revision received October 18, 1996; Keywords: Flow Nonuniformity, Forced Convection, Non-Newtonian Flows & Systems. Associate Technical Editor: S. Ramadhyani.

an expansion ratio of $d/D = 1.899$, the Nusselt number they calculated returned to its original value after about 200 diameters without visible effect of variations over a ratio of about 2 in Reynolds number. On the other hand, it took only 25 to 50 diameters for the pressure drop per unit length to achieve again the fully developed value. The reattachment length was also found to increase relative to the water flow.

For surfactant solutions, we are not aware of detailed data in the thermal entry region. Weber et al. (1991) did, however, propose an expression for the thermal entry length as a function of Reynolds number and tube diameter. An interesting finding by Brunn (1987), achieved by LDV velocity measurements in a rectangular channel for surfactant solutions, contrasts with the common belief that the flow of polymeric solutions is fully developed hydrodynamically after about 100 diameters. He found that the velocity profile was still developing after a length of 300 channel heights. Similarly, Gasljevic and Matthys (1992) measured the variations in friction factor for a surfactant solution downstream of both a centrifugal pump and a pressurized fluid reservoir, and the friction factor still showed evidence of development after 150 diameters in both cases.

Even though there is comparatively little data on surfactant solutions, it appears that there may be interesting differences between polymer and surfactant solutions as far as entrance regions go, and the present study was intended to examine further this issue. There is, of course, no analytical solution available for friction, nor heat transfer of drag-reducing fluids in pipe flow, that would be based on fluid properties and first principles since a general understanding of the drag reduction phenomenon is still lacking. Parameter nondimensionalization is therefore also tentative. We can, however, conduct experiments to clarify particular aspects of the general problem, especially by fixing the fluid properties. The main objective of this study was, therefore, to develop a phenomenological understanding of the flow and heat transfer of drag-reducing surfactant solutions in the entry region through new experiments with high spatial resolution and accuracy.

2 Experimental Setup and Procedure

The setup used for these experiments consisted of a 0.15 m^3 tank, a three-stage centrifugal pump with variable-speed control (providing a pressure rise of up to 10 bars) an instrumented test tube, and an air-cooled heat exchanger for fluid cooling. The heat transfer was measured under constant heat flux heating conditions. The test tube was heated by direct current through the test tube wall, the power being provided by two 20 kW DC power supplies. The stainless steel test tube is half inch pipe (15.3 mm inner diameter), schedule 40. The centrifugal pump did not cause any noticeable degradation effects to the surfactant solution. This was shown by measuring the friction coefficient in the pipe flow immediately downstream of the pump discharge and comparing it with the flow in the same tube driven by compressed air. No significant difference was indeed noticed (Gasljevic and Matthys 1992).

Variations in heat transfer were reported up to $L/D = 1000$ for polymer solutions, but for most practical purposes the variations at the end of the entry length are not very large. Accordingly, we decided to focus here on the thermal development for up to about 130 diameters, (and in some cases 330), which enabled us to get a much finer spatial resolution. We also varied the entry conditions. To make this possible, the test tube was made of several segments which were connected by brass unions specially designed for this purpose. These unions aimed at providing smooth transitions and uniform heating, and indeed, no abrupt changes in friction coefficient and temperature profiles were detected at these joints.

Flow measurements were achieved by continuous monitoring of the volume of discharged fluid from the open loop. The height of accumulated fluid in a calibrated discharge vessel was measured by a pressure transducer, and differentiated with respect to time. The accuracy of this measurement of flow rate was proven to be better than 1 percent. Although somewhat cumbersome, this flow measurement technique is probably the most reliable and the easiest to calibrate with a high level of confidence for complex viscoelastic fluids which may affect the performance of most common flow meters.

The pressure drop was measured every 6.5 diameters over the length of the test tube with Validyne pressure transducers. These interchangeable diaphragm transducers can reach, with proper calibration, a total accuracy of 0.5 percent of the full range chosen. To improve further the repeatability and accuracy, the same pressure transducer was used for all pressure drop measurements and was switched from one pair of pressure taps to another by means of a pressure scanner (Scanivalve). Four holes were drilled in a symmetric pattern at each axial location on the test tube where a pressure measurement was taken. These holes were reamed and the inside of the test tube was honed to minimize the pressure hole error induced by the fluid viscoelasticity. Tests with water showed deviations in differential pressure measurements of less than 2 percent even when measuring pressure differences of a few millimeters of water column under absolute pressures up to 50 times higher. For measurements of a pressure difference the viscoelastic pressure hole error cancels out, in principle, if both pressure tap holes are perfectly identical, but this is difficult to achieve in practice because of the presence of burrs at the hole edge. In particular, if the flow velocity is high, and the measured pressure difference is small, the viscoelastic pressure hole error in a given pressure drop measurement may be significant. When consecutive pressure drop measurements are taken, however, curve fitting through the

Nomenclature

$Cf = \tau_w/(1/2\rho v^2)$ = Friction coefficient

$Cf_{rel} = Cf/Cf_{x/D=***}$ = Relative frict. coef. with respect to Cf at location $x/D = ***$

$DR = (Cf_w - Cf_s/Cf_w)$ = Drag reduction

D = Tube diameter (m)

h = Convective heat transfer coefficient (W/m^2 K)

$HTR = (Nu_w - Nu_s)/Nu_w$ = Heat transfer reduction

k = Thermal conductivity (W/m K)

$Nu = (hD)/k$ = Nusselt number

$Nu_{rel} = Nu/Nu_{x/D=***}$ = Relative Nusselt # with respect to Nu at location $x/D = ***$

$Pr = \eta Cp/k$ = Prandtl number

η = Dynamic viscosity at the wall temperature (Ns/m^2)

Subscripts

w = water

s = surfactant solution

data points ''eliminates'' the error because a pressure difference error at any given location affects the pressure drop in the two adjacent tube segments by an equal amount, but with opposite signs. Calibration runs were conducted to evaluate these errors and generate correction factors.

The estimated uncertainty for our measurements of friction coefficient and drag reduction is estimated to be about 2 percent to 3 percent, disregarding the uncertainty on the test tube diameter. This uncertainty is eliminated by calibration with water tests and is irrelevant for the drag reduction calculations, or for any comparison purposes, because the same test tube was used for all tests.

The temperature measurements needed for the heat transfer calculations (i.e., the fluid bulk temperature and the tube's outer wall temperature) were measured with two types of miniature RTDs (1 × 2 × 2 mm and 1 × 2 × 10 mm, respectively). Indeed, although much effort was spent to achieve good temperature measurements by use of thermocouples through shielding, filtering, etc., it was concluded that thermocouple measurements suffered from too much electrical noise and poor repeatability. On the other hand, and providing that self-heating problems and the heat transfer from RTD sensors and connecting cables are taken care of, the RTDs provided us with a ten times higher signal to noise ratio than for thermocouples, and much better stability with time. An accuracy level of better than 0.05° C was proven and consistently achieved with our RTDs. Both heat transfer and friction data shown hereafter are averages obtained over several tens of seconds.

Most of these tests were conducted under a narrow range of temperatures. The fluid inlet temperature varied between 22 and 25° C. The increase in the bulk temperature of the fluid due to heating was kept below 3° C, and the difference between fluid bulk temperature and inner wall temperature was kept below 10° C. This allowed the uncertainty margin to be maintained under 2 percent for the relative heat transfer reduction data and under 4 percent to 5 percent for absolute Nusselt numbers. Because our goal was not so much to provide correlations of broad validity (e.g., for a wide range of Prandtl numbers) but to investigate phenomena happening at different entry conditions, a narrow range of temperature also allowed easier comparison of different runs. For this reason, Nusselt numbers rather than Colburn factors are used here to present our heat transfer data. The low temperature also eliminated the risk of thermal degradation effects.

Two basic entry conditions were studied. In the first one, the fluid discharged from the pump was slowed down in a 75 mm diameter and 300 mm long tube, and after, a light screen to further flatten the velocity profile was introduced in the test tube through a cone (D_1 = 75 mm, D_2 = 15.3 mm; L = 60 mm). A schematic of the configuration is shown in Fig. 1. This makes the setup a reasonable simulation of flow development from rest. Two different heating conditions were used: (1) simultaneous development of velocity and temperature fields; and (2) the development of a temperature field after the velocity field is already developed. However, some deviations from that ideal could not be avoided. Although the velocity at the entrance to the cone is very small, and there were no signs of recirculation regions, there is of course some flow development taking place in the cone itself which is four tube diameters long. Also, because of the width of the electrical clamp, the heating starts 3 diameters downstream of the end of the cone (the end of which is the beginning of the straight measurement tube), i.e., approximately 7 diameters after the start of the hydrodynamic development of the flow in the cone. Fortunately, this is much less a concern in the flow of drag-reducing fluids than it is in the flow of Newtonian fluids because of the much longer entry lengths in the former case, and we can still consider this case to be a good approximation of ''simultaneous'' development.

In the second heating configuration with the cone entry, the heating would start 190 diameters downstream of the cone end, at which point the flow is close to being hydrodynamically fully developed.

The second type of entry was created by placing a plug made of a number of wire mesh discs sandwiched in a special union fitting. This eliminated any other disturbance to the flow and allowed uniform heating. The plug was intended to provide a flat velocity profile at the entrance of the second tube section, and imposed a relatively high resistance to the flow in uniform fashion over the cross section of the tube (this is a realistic expectation given a pressure drop of the order of 1 bar on the mesh). This setup alleviates some of the problems of cone entry in that the location of the beginning of flow development downstream of the plug is precisely defined and that it is possible to start the heating at about the same location. Although it is realistic to expect a very flat velocity profile after the plug, there will also be strong turbulence from the very start of the flow development; this is not the case with flow development from rest. None of these two entry conditions is ideal, but we hoped to achieve some information on the flow development by comparing the results of these two different experiments. We also wanted to see if the wire mesh would affect the micellar structure of the surfactant solution. Various plugs were tested to provide different levels of obstruction to the flow. In the plug setup, we have only investigated combined thermal and hydrodynamic development conditions with the heating starting 3 tube diameters downstream of the plug. Details on the experimental setup can be found in Gasljevic (1995).

The fluid used in all these tests was a solution of surfactant Ethoquad T13, a tris (2-hydroxyethyl) tallowalkyl ammonium acetate (TTAA) by AKZO Chemicals, and sodium salicylate (NaSal) in deionized water. The concentration used was 2300 ppm of surfactant plus 2000 ppm of NaSal as counterion. This combination was shown to give good drag reduction over the temperature range of 10° C–40° C. The concentration is above the CMC for rod-like micelles formation, and at this high salt ratio it results in formation of supermicelles or structures at rest, and more so under shear (Hu and Matthys 1996). More chemistry details on similar surfactant counterion systems can also be found in Chou et al. (1989).

3 Results and Discussions

Drag reduction (DR) and heat transfer reduction (HTR) are defined as the difference between the values for friction coefficient, Cf, or Nusselt number, Nu, for water and the surfactant solution at the same Reynolds number, divided by the value for water. This is usually expressed as a percentage:

$$\mathrm{DR} = \frac{\mathrm{Cf}_w - \mathrm{Cf}_s}{\mathrm{Cf}_w} 100 \qquad \mathrm{HTR} = \frac{\mathrm{Nu}_w - \mathrm{Nu}_s}{\mathrm{Nu}_w} 100,$$

with Cf being the ratio of wall shear stress and dynamic pressure, and the Nusselt number being hD/k, where h is the convective heat transfer coefficient on the solution side and k is the solution thermal conductivity. In this article we are using the viscosity of water in all calculations, see below.

For practical purposes it may be convenient to present the results using the fully developed friction coefficient and Nusselt number of water under the same conditions as a reference. From a theoretical point of view, however, the use of fully developed values for the surfactant solution may be more appropriate as a reference to show the changes in the entry region, but two issues should be kept in mind, and especially so in this case. First, a ''fully developed value'' for the surfactant solution will always be an approximation because of setup length limitations. Second, if the fluid changes significantly after its discharge from the pump or under heavy shear, the water values may constitute a more reliable reference for comparison purposes than values associated with a changing surfactant solution. In this article, we used both kinds of nondimensionalization, depending on the purpose.

The viscosity, thermal conductivity, and specific heat used here in the Reynolds and Prandtl numbers calculations are those

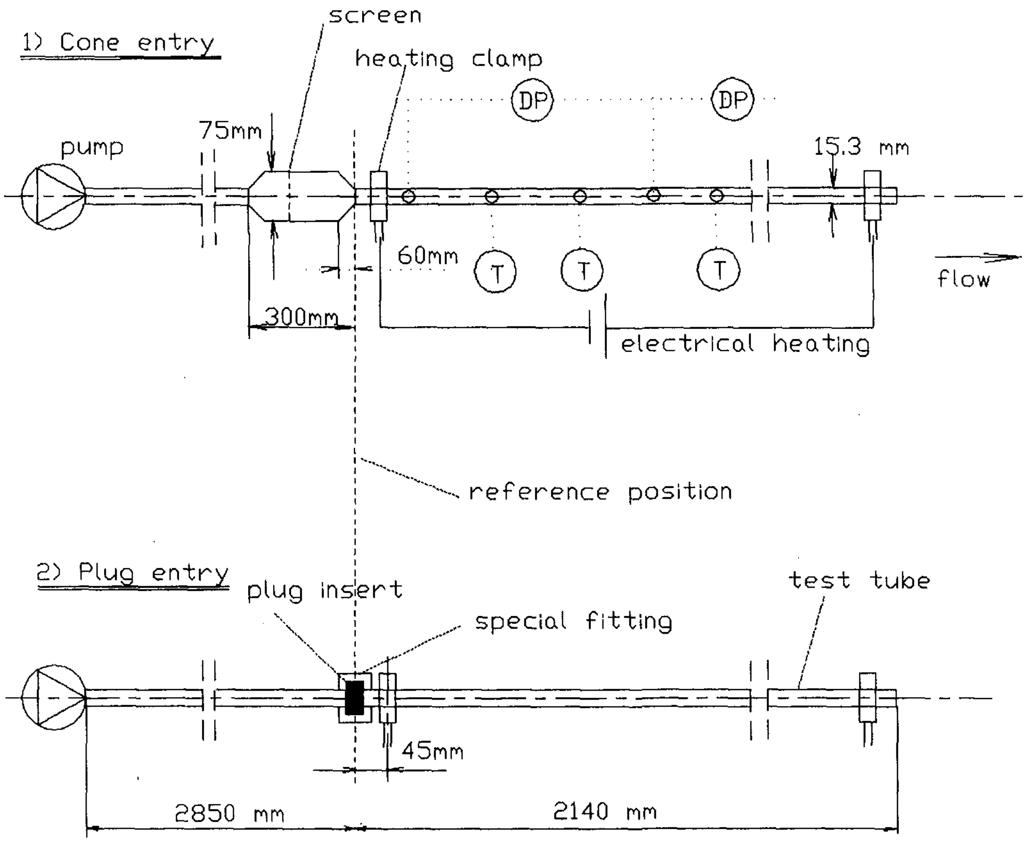

Fig. 1 Schematic of the setups for the cone and plug entry experiments. The actual test tube and its pressure drop and temperature sensors are the same for both (only a few sensors are shown for the cone entry setup and none for the plug entry schematic, for clarity).

of the solvent (water) at the wall temperature. The use of water viscosity is convenient because in this application oriented study we are more interested in the drag reduction with respect to water at a constant flow rate. Of course, surfactant solutions may show a much higher viscosity than water at low shear rates; if this is not taken in account, the difference could cause large errors in the analysis. The solution used for the tests described here was about 3 months old, however, and was used for other tests in the meantime. Even though the fresh solution showed a viscosity higher than that of water by a factor of 15 at shear rates of about 30 s^{-1}, the 3 month old fluid used in these tests showed the same viscosity as water at all shear rates measured while still retaining its full drag reducing ability. We used this fluid rather than a fresh fluid for this work because it would otherwise be very difficult to quantify the appropriate local fluid viscosity for the changing conditions of the entry region.

3.1 Conical Entry and Simultaneous Development. Some friction and heat transfer development results for a cone shaped inlet over a wide range of velocity are shown in Fig. 2. The friction coefficient and Nusselt number are normalized by their values at $x/D = 117$ and $x/D = 130$, respectively, and are designated here as relative friction coefficient "Cf_{rel}" and relative Nusselt number "Nu_{rel}". It was seen that the friction and the heat transfer do not change much after 100 diameters when compared to the very large variations seen for the first 50 diameters. Therefore, in this paper we are focusing on the first 130 diameters, but it should be kept in mind that the flow changes some more downstream, as discussed below, although by much less. Interestingly, the data indicated a very similar development of velocity and temperature profiles. The relative friction coefficient appeared slightly smaller for $x/D < 30$, but this is likely due to the fact that the electrical connector clamp is located 3 diameters downstream of the test tube entry, i.e., the heating begins at $x/D = 3$. In addition, as discussed above, some lesser level of hydrodynamic development already took place in the conical entry itself, which is about 4 diameters long and located immediately before the beginning of the test tube.

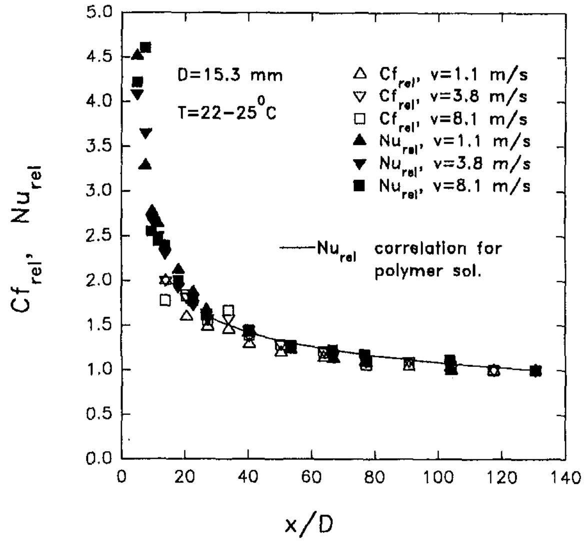

Fig. 2 Friction coefficient and Nusselt number downstream of a cone entry, relative to the corresponding values at location $x/D = 117$ and $x/D = 130$, respectively. Matthys (1991) results for polymer solution shown for comparison. Cone diameter ratio: 75 mm/15.3 mm; cone length 60 mm. Simultaneous hydrodynamic and thermal development of the flow; tube entry at $x/D = 0$, heating starts at $x/D = 3$ (Solution: 2300 ppm Ethoquad T13 plus NaSal 2000 ppm).

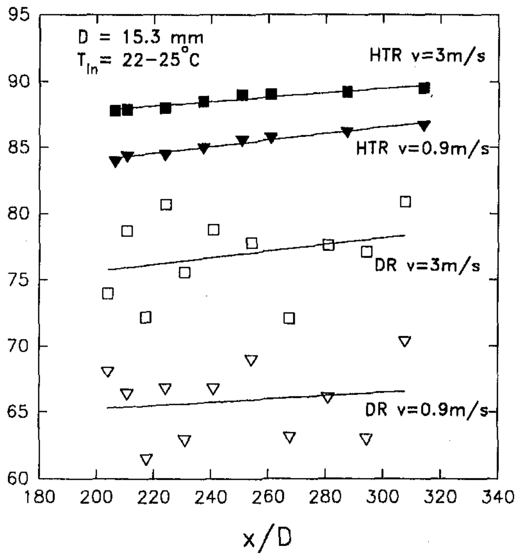

Fig. 3 Drag reduction and heat transfer reduction for two fluid velocities between $x/D = 210$ and 310 downstream of the cone entry (Note enlarged vertical scale). Reference: water values at the same Reynolds number (Solution: 2300 ppm Ethoquad T13 plus NaSal 2000 ppm; Same conditions as Figure 2).

With the inlet fluid temperature being kept constant, the velocity was the only independent variable. A correlation of thermal measurements in the thermal entrance region for polymer solutions obtained in a different setup is also shown here as reference. This correlation is generated from results obtained in a 7.9 mm inner diameter tube for $6000 < \mathrm{Re}_a < 90000$ and $35 < x/D < 560$, assuming fully developed conditions at $x/D = 560$:

$$\frac{C_h \,\mathrm{Pr}_a^{2/3}[@x/D]}{C_h \,\mathrm{Pr}_a^{2/3}[@560]} = 6.32(x/D)^{-0.293}$$

(Matthys, 1991). Even though the two setups, fluids, and experimental conditions were significantly different, the agreement is very good between the surfactant data and the polymer solutions results. Interestingly, the hydrodynamic and thermal developments for the surfactant solutions also appear to be coupled; this is generally not believed to be the case for polymer solutions. Our data for heat transfer for the surfactant solutions (which cover the range $5 < x/D < 125$ and $1 < V < 8$ m/s) are very well correlated (with a maximal deviation of ±5 percent) in this case by the double exponential equation:

$$\mathrm{Nu}_{rel} = 1.56e^{-0.0035(x/D)} + 5.31e^{-0.133(x/D)}$$

which may be an indication of superposed formation mechanisms. For simplicity, they may also be represented by the simpler power law expression:

$$\mathrm{Nu}_{rel} = 8.66(x/D)^{-0.47}$$

although the fit is not as good (max. deviation ±10 percent). However, this expression is easier to use for engineering calculations. The correlations are not shown on Fig. 2 for clarity.

Some measurements of friction coefficient and Nusselt number were also obtained further downstream, and some results are shown in Fig. 3 in terms of drag and heat transfer reductions with respect to fully developed water values at the same Reynolds number. As can be seen, both parameters are changing at about the same rate, on average, over the distance covered, which suggests that the corresponding radial temperature and velocity profiles are still changing in a similar manner. It is important to stress that the effect of the changing temperature along the tube is already taken into account in evaluating the fluid viscosity. It should also be noted here that the use of "reductions" with respect to water may mask somewhat the absolute changes. For example, a change in heat transfer reduction from 87.5 percent to 89.5 percent, as in the case of 3 m/s flow velocity, appears at first glance rather small. In reality, however, this corresponds to a change in Nusselt number from 12.5 percent to 10.5 percent of that of water, or about 20 percent in relative change over the distance between $x/D = 200$ and $x/D = 300$. This is still a significant change and implies that fully developed conditions are still not fully achieved after 300 diameters. This 20 percent change is also very similar to results obtained for heat transfer with polymer solutions over the same range of x/D in a different setup (Matthys 1991). The larger scatter of differential pressure measurements used for calculation of the friction coefficients is due to the viscoelastic pressure hole errors; to illustrate their magnitude they have not been eliminated here through the use of calibrated correction factors as in other graphs. It is worth mentioning that measuring pressure drops with the same accuracy as temperature differences is also a much more challenging task in this type of situation because of the hole pressure errors and the very low pressure drops involved. It may well be that some of the smaller variations may not have been observed for polymer solutions for this reason, especially if more than one transducer is used for the measurements along the pipe. Naturally, caution should also be exercised when considering the present data as well. As in the case of results obtained with polymer solutions, we see that the heat transfer is reduced proportionally more than the friction. Again, it appears in the case of surfactants that the entrance regions are of the same order of magnitude for friction and heat transfer, unlike in the case of polymer solutions. The difference in behavior between the polymer and surfactant solutions may be due to the difference in their molecular structure although it is not clear yet why this might be so. Further work may provide additional information for this purpose.

3.2 Conical Entry, Hydrodynamically Predeveloped Flow. To measure developments in the thermal entry region with an already predeveloped velocity profile, we moved the upstream heating clamp further downstream (in effect, starting the tube heating at $x/D = 190$ from the conical tube inlet). The

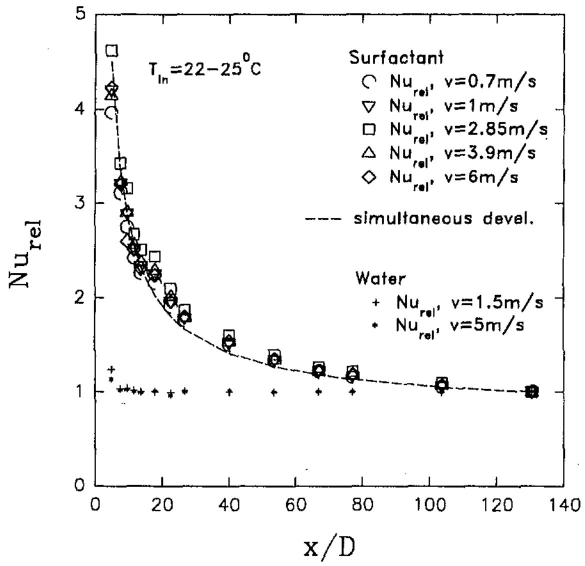

Fig. 4 Nusselt number in the tube relative to the value at $x/D = 130$ as a function of distance. Hydrodynamically predeveloped flow. Conical tube entry 200 diameters upstream ($x/D = -200$). Heating starts at $x/D = 3$. The best curve fit for simultaneously-developed flow (Fig. 2) is shown for comparison in the same relative presentation (Solution: 2300 ppm Ethoquad T13 plus NaSal 2000 ppm).

corresponding results are shown in Fig. 4. For better comparison, the length reference is adjusted to show heating starting at $x/D = 3$. Here again, the relative results for all velocities collapse on the same curve and do not differ noticeably from the curve for simultaneous development of hydrodynamic and thermal fields (shown as a dashed line). However, note that in the case of simultaneous hydrodynamic and thermal development, we saw about 90 percent heat transfer reduction at $x/D = 130$ (the reference value) for velocities between 2.8 m/s and 6 m/s, but we already have about 93 percent heat transfer reduction (i.e., about asymptotic reduction) at the same location in the case of this hydrodynamically predeveloped flow. Note also that if we had used the fully developed values for both cases as reference, the relative values for the simultaneous development case would be 30 to 40 percent higher and still developing somewhat, whereas the relative Nusselt number for hydrodynamically predeveloped flow would be close to developed conditions at $x/D = 130$. In terms of relative values with respect to $x/D = 130$, however, it appears that the predeveloped and simultaneously developing cases are very similar.

3.3 Plug Entry. Entry flow with wire mesh plugs, instead of the cone, was studied with several plugs generating various levels of obstruction to the flow. The plug is expected to flatten the velocity profile, ideally providing a flat velocity profile downstream of the plug by generating a relatively high resistance to the flow. The pressure drop over the plug can be used as a measure of the energy loss at that location and, in a certain sense, as a measure of the work done on the fluid that may change the micellar structure of the surfactant and, therefore, the fluid properties. In this case, it is more appropriate to use developed values of friction coefficient and Nusselt number for water as references because the possible changes to the fluid could extend the entry length and make developed values for surfactant solution harder to define. In all these runs we had simultaneous development of velocity and temperature profiles. Results for two wire mesh plugs are given here. For reference, it should be mentioned that no sign of temporary degradation (i.e., departure from asymptotic behavior) was seen under fully developed conditions for velocities up to 10 m/s in the tube without obstructions. In Figs. 5 and 6 the drag and heat transfer reductions are shown for a plug with relatively small flow resistance. The plug consisted of 16 juxtaposed discs made of square wire mesh with 14 wires per cm and a wire diameter of 0.125 mm positioned at random angular orientation. Up to velocities of 3.7 m/s, the drag and heat transfer reductions increase (or stay the same if asymptotic) with increasing velocity immediately downstream of the plug, as expected. The fully developed levels of drag and heat transfer reductions achieved are also consistent with those at fully developed conditions with no plug. For flow velocities of 5 m/s and higher, however, a qualitative difference which may be linked to a temporary degradation of the fluid becomes apparent. There is a dramatic decrease in drag and heat transfer reductions for 5 and 6.9 m/s immediately downstream of the plug, but both drag and heat transfer reductions recover to the normal levels within the region of x/D shown. For 9.1 m/s, however, the heat transfer reduction showed a large decrease over the entire length of the measurements, and no recovery was yet achieved at $x/D = 130$ (the 9.1 m/s pressure data were not obtained because of transducer range limitation at the time).

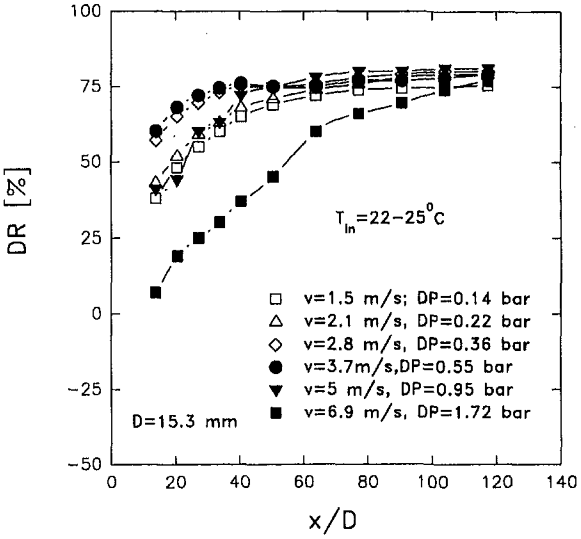

Fig. 5 Drag reduction downstream of the wire mesh plug No. 1 (16 discs; 14 wires per cm mesh; 0.125 mm wire) as a function of distance for various velocities and pressure drop over the plug. Plug at $x/D = 0$. Simultaneous development. Reference: fully-developed water values at the same Reynolds number (Solution: 2300 ppm Ethoquad T13 plus NaSal 2000 ppm).

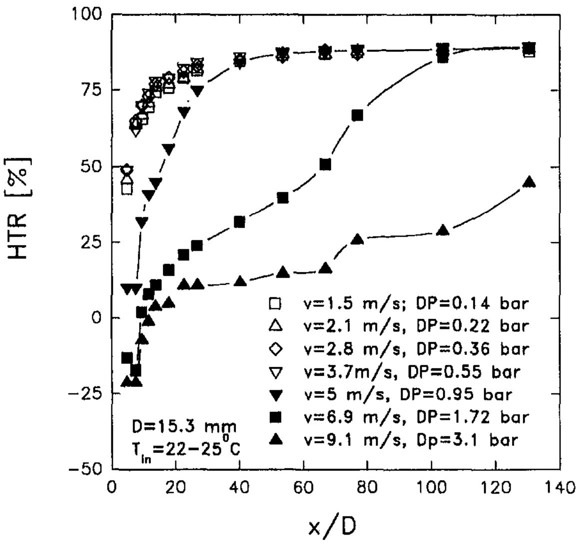

Fig. 6 Heat transfer reduction downstream of the wire mesh plug No. 1 (16 discs; 14 wires per cm mesh; 0.125 mm wire). Heating starts at $x/D = 3$. Simultaneous development. Reference: fully-developed water values at same Reynolds number (Solution 2300 ppm Ethoquad T13 plus NaSal 2000 ppm).

This sudden change in behavior (a slower flow development) can be attributed to changes in the fluid itself. As more energy is dissipated at the plug location, the effect is longer lasting. It should be noted, however, that this apparent effect on the fluid takes place at a pressure drop over the plug of 1 bar, equivalent to the pressure drop over about 2000 diameters of this pipe which is a rather large loss. Even in these runs, it is still seen that the friction and heat transfer developments occur in parallel and over similar distances.

Results for another wire mesh plug with greater flow obstruction (10 discs of 50 wires per cm mesh, with a wire thickness of 0.1 mm) are shown in Figs. 7 and 8. Here, as expected, degradation effects are more noticeable. It is seen that at 1.5 m/s the drag and heat transfer reductions still show "normal" behavior. At higher velocities (and higher pressure drop over the plug) we see a rapid decrease of both drag and heat transfer reductions. Interestingly, the drag and heat transfer reductions decrease only up to a point at small distances, as if the degradation effect reaches a maximum, where the fluid is not further affected. However, the length over which the effect is felt is clearly increasing with increasing velocity. Note that zero drag and heat transfer reductions correspond to fully developed values of friction coefficient or Nusselt number for water, and not surprisingly, that the heat transfer at high velocity near the plug

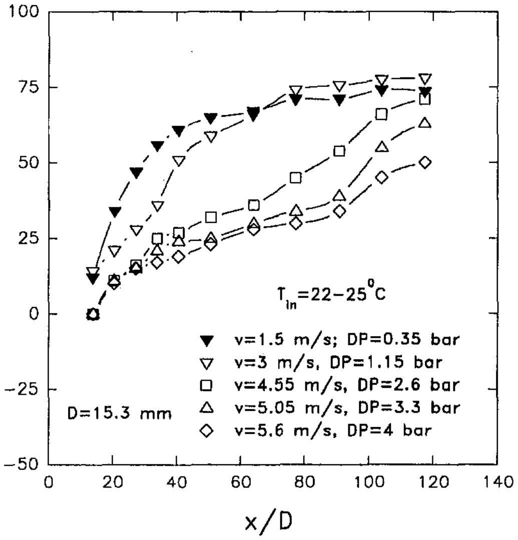

Fig. 7 Drag reduction downstream of the wire mesh plug No. 2 (10 discs; 50 wires per cm mesh; 0.1 mm wire) as a function of distance. Simultaneous development. Reference: fully-developed water values at the same Reynolds number (Solution 2300 ppm Ethoquad T13 plus NaSal 2000 ppm).

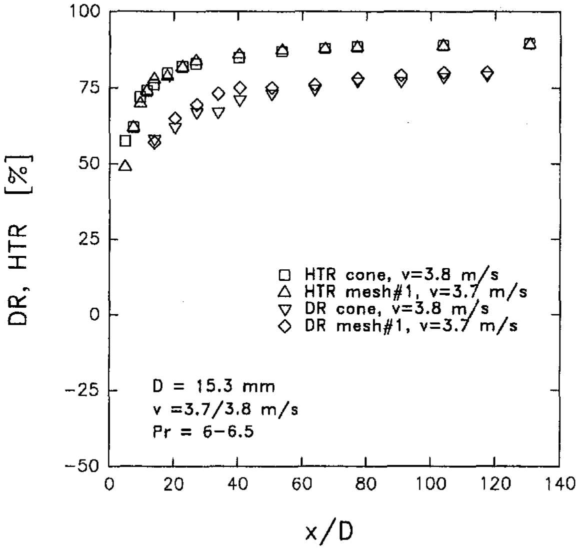

Fig. 9 Comparison of flow development after the conical entry and plug entry No. 1. Simultaneous thermal and hydrodynamic development. Reference: fully-developed water values at the same Reynolds number (Surfactant solution: 2300 ppm Ethoquad T13 plus NaSal 2000 ppm).

may reach values higher than that for water under developed conditions.

Again, in the case of this plug, the temporary degradation effects are only becoming significant for high pressure drops over the plug (1.15 bar at 3 m/s). Although more measurements at the onset of apparent degradation are necessary, it seems that this onset can be related to a pressure drop over the plug of about 1 bar for both plugs. This pressure drop is the flow energy loss over the plug per unit of volumetric flow rate, and is, therefore, a measure of the energy dissipated in the fluid either thermally or through changes in micellar structure. Estimates of equivalent average stresses in the plug suggest that the fluid stresses generated by the plug are indeed much larger, in that case, than the critical shear stress, beyond which the fluid loses its drag reduction ability in an unobstructed circular pipe.

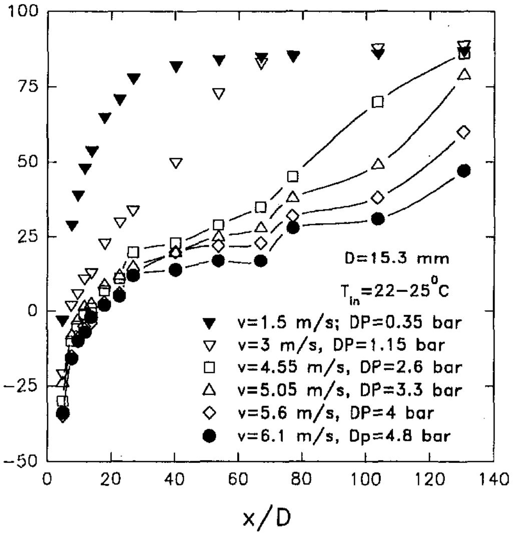

Fig. 8 Heat transfer reduction downstream of the wire mesh plug No. 2 (10 discs, 50 wires per cm mesh, 0.1 mm wire). Heating starts at location $x/D = 3$. Simultaneous development (Solution: 2300 ppm Ethoquad T13 plus NaSal 2000 ppm).

3.4 Entry Comparisons. Figure 9 shows a comparison of friction and heat transfer results for the cone entry and mesh plug #1 for a fluid velocity of 3.7 m/s for the mesh and 3.8 m/s for the cone. This small difference in velocity can be considered negligible given the presentation of the results in terms of drag reduction and heat transfer reduction. At that velocity, there was no apparent sign of temporary fluid degradation, and the difference between results corresponding to the two types of entrance is very small and can be considered to be within the limits of experimental error. Both entries vary from the ideal case of flow development from rest, but these variations are of very different nature. The effects on the flow disappear so fast, however, that we were not able to detect a difference between the two entrance types as close to the beginning of flow development as 5 diameters. This means that we can expect developing entry flows of surfactant solutions to behave in very similar ways despite differences in entrance type and geometry, if the fluid itself is not affected by the entrance stresses.

Figure 10 shows a comparison of friction and heat transfer results between the cone entry and both mesh plugs, with a higher fluid velocity of 5 m/s. The pressure drop over the cone is 0.12 bar including the difference in dynamic pressure, and for the mesh plugs #1 and #2 it is 1 bar and 3.3 bars, respectively. The difference between the cone entry and mesh plug #1 is significant only up to $x/D = 50$. This is the same 50 diameters seen in Fig. 5 and is the only region affected by degradation at that velocity for plug #1. For plug #2, the effect of temporary degradation of the fluid is much greater and extends over a larger region, but the fluid eventually recovers completely some distance downstream (not shown). The 3.3 bars pressure drop over plug 2 is a very high singular pressure drop compared to normal pressure drops in fittings in hydronic loops. It is likely that in normal situations in such systems, we would not be concerned with apparent changes in the fluid itself for this particular solution. Again, even when the mesh plug had a large effect on the fluid structure, the development of drag and heat reductions took place at the same rate and both were affected to a similar degree. In addition, we have shown that other changes, such as permanent chemical degradation of the surfactant solutions, affect both heat transfer and drag reductions in the same proportion (Gasljevic 1995). Note that the coupling between heat transfer and friction seen in the entry region for these surfactant solutions is in contradiction with the

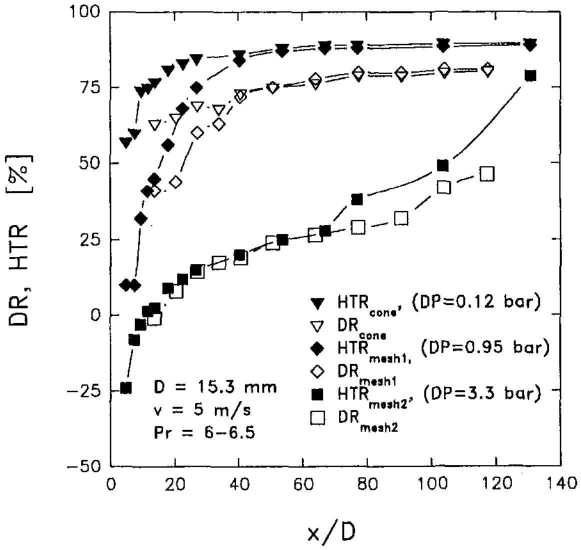

Fig. 10 Heat transfer reduction and drag reduction downstream of several types of tube entrance: a cone and two wire mesh plugs imposing different levels of obstruction to the flow (different pressure drops over the plug). Heating starts at $x/D = 3$. Simultaneous development. Reference: fully-developed water values at the same Reynolds number (Solution: 2300 ppm Ethoquad T13 plus NaSal 2000 ppm).

common belief that the hydrodynamic entrance length is much shorter than the thermal entrance length for drag reducing polymer solutions.

The apparent coupling between the hydrodynamic and thermal development has an important practical consequence; it is unlikely that the heat transfer can be augmented locally by some disturbance for these surfactant solutions without seeing the friction increase proportionally as well. It had been thought previously, based on the uncoupling of these two aspects for polymer solutions, that a longer thermal entrance region might also exist for surfactant solutions and that a local flow disturbance would benefit more the heat transfer than the friction. This is probably not the case generally, as the two vary together with distance. As in the case of Newtonian fluids, any increase of heat transfer due to a disturbance in the flow will probably be accompanied by a proportional increase of friction in addition to the local pressure drop caused by normal stresses (shape drag). It is also apparent from these results that temporary degradation of the fluid induced by intensive local energy dissipation (as in the case of plug #2) may not be for this solution a viable means of heat transfer augmentation in heat exchangers because of the very high pressure drop necessary. It is important to note, however, that recent results we obtained at different concentrations and counterion ratios suggest that variations in the fluid nature may lead to a much higher susceptibility to temporary degradation.

4 Summary and Conclusions

A number of experiments were conducted on flow and heat transfer development for drag reducing surfactant solutions. Whereas the hydrodynamic entry length is commonly thought to be up to ten times shorter than the thermal entry length for polymer solutions, we found that for our surfactant solution the friction coefficient and the Nusselt number are still changing at the same rate 300 diameters after a conical entry. Furthermore, results for the relative friction coefficient and Nusselt number (referenced to their values at $x/D = 117$ and 130, respectively) coincide after the entry, indicating that the velocity and temperature profiles developments are coupled. These data also show that the entry lengths and the relative flow development do not depend on the fluid bulk velocity over a large range of velocity. The variations of heat transfer in the thermal entrance region appeared to match very well those found for polymer solutions up to $x/D = 300$. The thermal development up to $x/D = 130$, in terms of Nusselt number relative to its value at $x/D = 130$, did not show any significant difference between the case of simultaneous development of velocity and temperature profiles on the one hand, and that of hydrodynamically predeveloped flow on the other. However, all absolute values of the Nusselt number up to $x/D = 130$ were found to be about 30 percent to 40 percent higher at the same x/D in the case of simultaneous development.

Tests were also conducted with two wire mesh plugs located at the flow entry to flatten the velocity profile as an alternative to the conical entry. No significant differences were found in flow development between these two very different entry conditions (cone and mesh plug) in the runs with low energy dissipation at the plug. However, if high stresses are imposed at the entrance (e.g., a pressure drop greater than 1 bar over the plug) a striking difference in fluid behavior appears. Both heat transfer and friction are increased dramatically over a long distance, which is thought to be due to the fluid undergoing temporary degradation of its micellar structure. It may then take several hundred diameters or more for the fluid to recover. In our recent tests with heavy throttling by a valve (e.g., a pressure drop above 5 bar) the same surfactant solution did not recover for 1000 diameters downstream of the valve in some cases (Gasljevic, 1995). The appearance of this temporary degradation is gradual, but the onset seems to be related to a singular pressure drop over the plug of about 1 bar in this case which can also be understood as energy dissipated at that singular location per unit volumetric flow rate. This threshold appears to be dependent on the type of solution used. In less extreme situations, the surfactant solution itself did not appear to be affected in the developing regions. From a phenomenological perspective, one could then think of two successive regimes as the level of disturbance increases: one where only the flow field is affected, and one when we must also consider changes in the fluid itself. This temporary degradation for this fluid results from a singular pressure loss that is very large by engineering standards for hydronic cooling and heating recirculation systems. A solution of this concentration would therefore not be affected much by pipe fittings and other hydraulic components, but would also not be readily degraded intentionally for heat transfer control purposes. The latter may, however, be possible with other solutions.

Very interestingly, perhaps, for the general study of the drag reduction phenomenon, we saw that, in contrast to drag reducing polymer solutions, the friction and heat transfer developments in the entrance region appear fully coupled for this drag reducing surfactant solution. On the other hand, the development of heat transfer appeared identical for the surfactant and polymer solutions. This contrast between the solutions behaviors may be related to the difference in fluid structure between them. It may also imply that it might be useful to revisit the measurements in the development regions for polymer solutions to ascertain their generality.

Acknowledgments

The authors acknowledge gratefully the financial support of the California Institute for Energy Efficiency (Contract No. 4902610 to EFM) and AKZO-Nobel Chemicals for providing us with samples of Ethoquad T13-50 and information on this product. Some of the results shown here were originally presented at the 1994 IMECE in Chicago.

References

Brunn, P. O., 1987, "Some Modern Developments in the Flow of Dilute Polymer and Surfactant Solutions," *PhysicoChemical Hydrodynamics*, Vol. 8, No. 4, pp. 449–459.

Cho, Y. I., Hartnett, J. P., 1982, "Non-Newtonian Fluids in Circular Pipe Flow," *Advances in Heat Transfer,* Vol 15, pp. 59–141.

Chou, L. C., Christensen, R. N., and Zakin, J. L., 1989, "The Influence of Chemical Composition of Quaternary Ammonium Salt Cationic Surfactants on Their Drag-Reducing Effectiveness," *In Drag Reduction in Fluid Flows,* R. H. J. Sellin and R. T. Moses, eds., Ellis Horwood Pubs., Chichester, England, pp. 141–148.

Gasljevic, K., Matthys, E. F., 1992, "Effect of Drag-Reducing Surfactant Solutions on Centrifugal Pumps Performance," *Recent advances in Non-Newtonian Flows,* Vol. AMD-153, ASME New York, pp. 49–56.

Gasljevic, K., Matthys, E. F., 1993, "Effect of Drag-Reducing Additives on Heat Exchangers," *Developments in Non-Newtonian Flows,* Vol. AMD-175, ASME New York, pp. 101–108.

Gasljevic, K., 1995, "An Investigation of Drag-Reducing Surfactant Solutions and Their Implementation in Hydronic Systems," Ph.D. thesis, University of California, Santa Barbara, CA.

Gasljevic, K., Matthys, E. F., 1995, "On the Diameter Effect for Turbulent Flow of Drag-Reducing Surfactant Solutions," *Developments and Applications of Non-Newtonian Flows,* FED-Vol. 231, ASME, New York, pp. 237–244.

Hu, Y., and Matthys, E. F., 1996, "The Effects of Salts on the Rheological Characteristics of a Drag-Reducing Cationic Surfactant Solution With Shear-Induced Micellar Structures," *Rheol. Acta,* Vol. 35, No. 5, pp. 470–480.

Kwack, E. Y., Cho, Y. I., and Hartnett, J. P., 1981, "Heat Transfer to Polyacrylamide Solutions in Turbulent Pipe Flow: The Once-Through Mode," *AIChE Symposium Series,* No. 208, Vol. 77, pp. 123–130.

Matthys, E. F., 1991, "Heat Transfer, Drag Reduction, and Fluid Characterization for Turbulent Flow of Polymer Solutions: Recent Results and Research Needs," *J. of Non-Newtonian Fluid Mechanics,* Vol. 38, pp. 313–342.

Ng, K. S., Cho, Y. I., and Hartnett, J. P., 1980, "Heat Transfer Performance of Concentrated Polyethylene Oxide and Polyacrylamide Solutions," *AIChE Symposium Series,* No. 199, Vol. 76, pp. 250–256.

Pak, B., Cho, Y. I., and Choi, S. U. S., 1991a, "Turbulent Hydrodynamic Behavior of Drag-Reducing Viscoelastic Fluids in a Sudden-Expansion Pipe," *J. Non-Newtonian Fluid Mechanics,* Vol. 39, pp. 353–373.

Pak, B., Cho, Y. I., and Choi, S. U. S., 1991b, "A Study of Turbulent Heat Transfer in a Sudden-Expansion Pipe With Drag-Reducing Viscoelastic Fluid," *Int. J. Heat Mass Transfer,* Vol. 34, No. 4/5, pp. 1195–1208.

Toh, K. H., and Ghajar, A. J., 1988, "Heat Transfer in the Thermal Entrance Region for Viscoelastic Fluids in Turbulent Pipe Flow," *Int. J. Heat Mass Transfer,* Vol. 31, pp. 1261–1267.

Weber, M., Steiff, A., and Weinspach, P.-M., 1991, "Waermeuebergang und druckverlust waesseriger tensidloesungen in rohren," *Forschung im ingenieurwesen,* Bd. 57, Nr1, pp. 1–7.

Yoo, S. S., Hwang, T. S., Eum, C. S., and Bae, S. C., 1993, "Turbulent Heat Transfer of Polyacrylamide Solutions in the Thermal Entrance Region of Circular Tube Flows," *Int. J. Heat Mass Transfer,* Vol. 31, No. 2, pp. 365–370.

Solar Radiation Assisted Natural Convection in Uniform Porous Medium Supported by a Vertical Flat Plate

A. J. Chamkha
Department of Mechanical
and Industrial Engineering,
Kuwait University,
P.O. Box 5969,
Safat, 13060
Kuwait

Natural convection flow of an absorbing fluid up a uniform porous medium supported by a semi-infinite, ideally transparent, vertical flat plate due to solar radiation is considered. Boundary-layer equations are derived using the usual Boussinesq approximation and accounting for applied incident radiation flux. A convection type boundary condition is used at the plate surface. These equations exhibit no similarity solution. However, the local similarity method is employed for the solution of the present problem so as to allow comparisons with previously published work. The resulting approximate nonlinear ordinary differential equations are solved numerically by a standard implicit iterative finite-difference method. Graphical results for the velocity and temperature fields as well as the boundary friction and Nusselt number are presented and discussed.

Introduction

Natural convection flow in porous media supported by surfaces has application in a broad spectrum of engineering systems. Some of these include geothermal reservoirs, building thermal insulation, direct-contact heat exchangers, solar heating systems, packed-bed catalytic reactors, nuclear waste disposal systems, and enhanced recovery of petroleum resources. Most studies of natural convection in porous media have been based on Darcy's law which is applicable for slow flows and does not account for non-Darcian inertial effects. These effects represent the additional pressure drop across the porous media resulting from interpore mixing for fast flows. In this case, the total pressure drop across the porous medium is a quadratic function of the velocity of the fluid flowing in it. In the presence of a heated boundary, heat transfer to the porous medium can be accounted for by employing the conservation of energy law and Brinkman's extension of Darcy's law modified to include the thermal buoyancy effect. The boundary and inertia effects on convective flow and heat transfer were analyzed and discussed by Vafai and Tien (1981).

In natural convection, flows combine with solar radiation effects and the radiative heat transfer often becomes substantial, even at relatively low temperatures. This is because the rates of natural convection heat transfer are often small, as is the case in gases. Depending on the surface properties and geometry, radiative transport is often comparable to, or larger than, the convective heat transfer in many practical applications. It is, therefore, of great significance and interest to investigate its effects on the flow and heat transfer aspects. The book by Gebhart et al. (1988) provides more discussions on the various convection-radiation situations and summarizes some of the work done in that area. The problem discussed in the present work is that of steady, laminar, two-dimensional, free convection flow of an absorbing fluid up a vertical heated flat plate embedded in a uniform porosity transparent medium. Heating to the plate is supplied by the absorbing working fluid which receives incident rays of solar radiation. This type of flow has direct applications in furnaces, natural water bodies, flames and fires, crystal growth, environmental heat transfer, glass technology, solar ponds, nuclear accident containment, and solar energy collectors with direct solar collection using an absorbing fluid. Typical absorbing and emitting fluids are ammonia, carbon dioxide, and water. The book by Siegal and Howell (1981) discusses combined convection-radiation effects of nonabsorbing and nonemitting fluids such as air, inert gases, and nitrogen. Vafai and Ettefagh (1988) analyzed the radiative and conductive heat transfer characteristics of a waste package canister in the absence of natural convection. Natural convection from a heated plate has been studied by many investigators (see, for instance, Kierkus, 1968; Hassan and Mohamed, 1970; Sparrow and Gregg, 1956; Elsayed and Fathalah, 1979; and Fathalah and Elsayed, 1980). Cheng and Minkowycz (1977) considered boundary-layer free convection in the presence of a Darcian porous medium and were able to obtain similarity solution for the case of a constant wall temperature. Non-Darcian inertia effects on heat transfer were considered by Plumb and Huenfeld (1981), Evans and Plumb (1978), Vafai and Tien (1982), and Hong et al. (1987). Kim and Vafai (1989) studied, in detail, buoyancy-driven fluid flow and heat transfer about a vertical flat plate embedded in a porous medium for the cases of constant wall temperature and constant wall heat flux using the Brinkman-extended Darcy flow model. In addition, Evans and Plumb (1978) reported on the influence of medium inertia on natural convection from a vertical isothermal surface adjacent to a fluid-saturated porous medium. Other related works can be found in the papers by Singh and Tewari (1993), Nakayama et al. (1990), Chen et al. (1989) and Chen and Lin (1995). The present work represents a generalization of the problem discussed by Fathalah and Elsayed (1980) to include a uniform porous medium with Darcian and Forchheimer (non-Darcian) effects. The semi-infinite vertical flat plate is assumed to be nonreflecting, nonabsorbing, and ideally transparent. In addition, the transparent plate has no other thermal effects such as the axial thermal diffusion or thermal capacity. It is also assumed that the plate receives solar incident radiation flux which penetrates the plate and is absorbed by the fluid-saturated porous medium and that both the plate and the porous medium are in perfect thermal contact and are in local thermal equilibrium. By interaction with the absorbing fluid and the porous medium,

---

Contributed by the Heat Transfer Division for publication in the Journal of Heat Transfer. Manuscript received by the Heat Transfer Division December 4, 1995; revision received September 13, 1996; Keywords: Natural Convection, Porous Media, Radiation Interactions. Associate Technical Editor: K. Vafai.

both heat transfer from the fluid to the plate and heat loss from the plate to the surroundings take place. The fluid is assumed Newtonian, absorbing, and isotropic.

Mathematical Formulation

Consider steady, laminar, two-dimensional, free convection flow up a solar radiation-heated vertical semi-infinite flat plate immersed in a fluid-saturated porous medium. The coordinate system is such that x measures the distance along the plate and y measures the distance normally outward. The schematic of the problem under consideration is shown in Fig. 1. Both the surrounding and the absorbing fluid far away from the plate are maintained at a constant temperature T_∞. Due to the heating of the absorbing fluid and thus, the plate by radiation, heat is transferred from the plate to the surroundings. As mentioned before, the working fluid is assumed to be an absorbing one. In fact, one may have a nonabsorbing fluid. In this situation, the solid porous medium absorbs the incident solar radiation and transmits it to the working fluid by convection. Upon treating the fluid-saturated porous medium as a continuum (see Vafai and Tien, 1981), including the non-Darcian inertia effects, and assuming that the Boussinesq approximation is valid, the boundary-layer form of the governing equations can be written as (see Vafai and Tien, 1981; Gebhart et al., 1988)

$$\frac{\partial u}{\partial x} + \frac{\partial v}{\partial y} = 0 \qquad (1)$$

$$u\frac{\partial u}{\partial x} + v\frac{\partial u}{\partial y} = \nu\frac{\partial^2 u}{\partial y^2} - \frac{\nu}{K}u - Cu^2 + g\beta(T - T_\infty) \qquad (2)$$

$$u\frac{\partial T}{\partial x} + v\frac{\partial T}{\partial y} = \frac{k_e}{\rho c}\frac{\partial^2 T}{\partial y^2} + \frac{1}{\rho c}\frac{\partial q''_{\text{rad}}}{\partial y} \qquad (3)$$

where u, v, and T are the fluid velocity components in the x and y direction, and the fluid temperature, respectively. ρ, ν, c, and k_e are the fluid density, kinematic viscosity, specific heat, and effective thermal conductivity, respectively. K and C are the porous medium permeability and inertia coefficient, respectively. g and β are the gravitational acceleration and coefficient of volumetric thermal expansion, respectively. q''_{rad} is the applied absorption radiation heat transfer per unit area. It should be noted that viscous dissipation is neglected and all properties are assumed constant except the density in the buoyancy term. In addition, the effect of porosity variation near the plate, and the dispersion effect, are negligible.

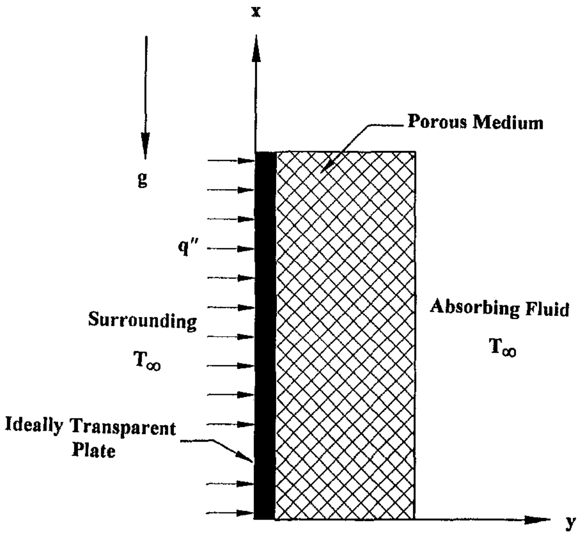

Fig. 1 Schematic of the problem

The appropriate boundary and matching conditions for the problem under consideration can be written as

$$u(x, 0) = 0, \quad v(x, 0) = 0,$$

$$k_e\frac{\partial T}{\partial y}(x, 0) = U(T(x, 0) - T_\infty) \quad u(x, \infty) = 0,$$

$$T(x, \infty) = T_\infty, \quad T(0, y) = T_\infty, \quad u(0, y) = 0 \qquad (4a\text{–}g)$$

where U is the heat transfer coefficient for the heat lost from the plate to the surroundings; that is, the heat transfer coefficient between the inner surface of the plate and the ambient conditions. Equations ($4a$, b) indicate that there is no slip condition and no suction or injection at the plate surface, respectively. Equation ($4c$) indicates that the heat conduction at the plate is convected away to the surroundings. Equations ($4d$, e) indicate that, far away from the plate, the fluid is undisturbed and is at the ambient or surrounding temperature. Equations ($4f$, g)

Nomenclature

a = absorption or extinction coefficient of fluid, m^{-1}
B_f = boundary friction, defined by Eq. ($14a$)
c = specific heat of fluid, J/kg K
C = porous medium inertia coefficient, m^{-1}
Da = Darcy number (Ka^2)
F = dimensionless stream function, defined by Eq. ($6g$)
g = gravitational acceleration, m/s^2
G = dimensionless normal velocity ($\partial F/\partial \xi$)
G_a = Grashof number based on absorption coefficient a, defined by Eq. ($6f$)
G_x = local Grashof number, defined by Eq. ($6e$)
h = heat transfer coefficient to the fluid, W/m^{2}K
H = dimensionless temperature gradient with ξ ($\partial\theta/\partial\xi$)
k_e = effective thermal conductivity of porous medium, W/mK
K = porous medium permeability, m^2
Nu_a = Nusselt number based on absorption coefficient a, defined by Eq. ($14b$)
Pr = effective Prandtl number, ($\mu c/k_e$)
q'' = incident radiation flux, W/m^2
q''_{rad} = radiation flux distribution in fluid, W/m^2, defined by Eq. (5)
T = dimensional fluid temperature, K
$T_{\max}$ = maximum local fluid temperature, K
T_w = wall or plate temperature, K
T_∞ = ambient temperature, K
u = dimensional tangential velocity, m/s
U = heat transfer loss coefficient to surroundings, W/m^{2}K
v = dimensional normal velocity, m/s
x, y = Cartesian coordinates along and normal to the plate, respectively, m
α = dimensionless heat transfer loss coefficient to surroundings ($U/(k_e a)$)
β = volumetric expansion coefficient, K^{-1}
η = dimensionless normal distance defined by Eq. ($6d$)
Γ = dimensionless porous medium inertia coefficient ($C\text{G}_a^5/a$)
μ = dynamic viscosity of fluid, kg/ms
ν = kinematic viscosity of fluid, m^2/s
ρ = density of fluid, kg/m^3
ψ = stream function, m^2/s
θ = dimensionless temperature defined by Eq. ($6h$)
ξ = dimensionless tangential distance defined by Eq. ($6b$)

mean that the conditions at the plate's leading edge are such that the fluid is at a uniform temperature and stagnant.

Following Beer's law of radiation absorption as quoted by Cooper (1972) and Fathalah and Elsayed (1980), it will be assumed that

$$q''_{\mathrm{rad}} = q''(1 - \exp(-ay)) \quad (5)$$

where q'' and a are the incident radiation flux (a constant) and the fluid's absorption or extinction coefficient (a constant), respectively. This law was applied to Dorsey's data for the absorption of radiation in water layers of different thicknesses. The estimated value of a ranges from 6 m^{-1} to 151.5 m^{-1} for distilled water of thickness 10 cm to 1 mm, respectively. The large variation in the values of a may be attributed to either inaccuracy of Dorsey's measurements, as stated by Cooper (1972), or to the reflectance and spectral dependence of the absorption coefficient of distilled water, which is not considered by Beer's law as stated by Fathalah and Elsayed (1980). In the present study, an absorption coefficient ranging between 200 m^{-1} and 2000 m^{-1} is assumed for a blackened grey water. The average value of radiation flux intensity q'' in Saudi Arabia and Kuwait is 900 $\mathrm{w/m}^2$. It should be mentioned that it is assumed herein that the absorption of solar radiation and its distribution in the porous medium, which is made up of transparent solid material such as glass, occurs in the same manner as in a fluid. This may not be totally true since it is known that normally solid materials respond to radiation differently than a fluid, and that the mechanism of travel of its rays in solids is different than in a fluid. However, in general, it seems reasonable to assume that the form of Beer's law may be the same for a transparent solid-fluid system, but the values of the absorption coefficient will be different. In the presence of a porous solid material, the values of a will be higher than that of the fluid alone since the system will have higher energy capacity. This assumption is employed herein due to the absence of an experimentally based, proper form of solar energy distribution in a fluid-saturated porous medium, which is a solid-fluid combination, and as a first approximation. Numerical results for various values of a are reported subsequently. Therefore, the results of this work may be applied to such fluid-saturated transparent porous media that closely exhibit the behavior of Eq. (5). This highlights the need of extensive experimental effort in this area.

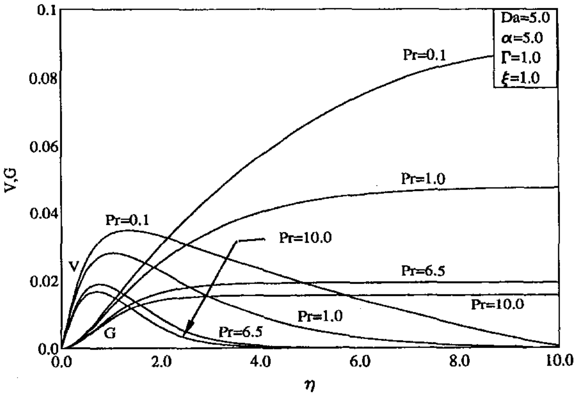

Fig. 2 Effects of Pr on tangential and normal velocity profiles

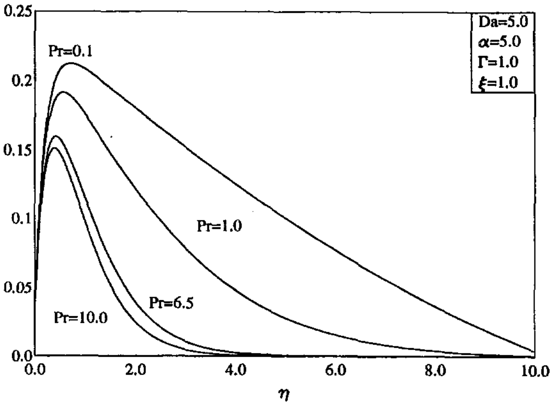

Fig. 3 Effects of Pr on temperature profiles

Equations (1) through (5) do not possess a similarity solution. However, the local nonsimilar technique employed by Sparrow and Yu (1971), and later by Fathalah and Elsayed (1980), appears to be suitable for this problem. This technique will be employed in this work. It is convenient to work with the stream function ψ and to nondimensionalize the governing equations by using the following transformations:

$$u = \frac{\partial \psi}{\partial y}, \quad v = -\frac{\partial \psi}{\partial x}, \quad \xi = \frac{\mathrm{G}_x}{\mathrm{G}_a^5}, \quad \eta = \frac{y\mathrm{G}_x}{5x}$$

$$\mathrm{G}_x = 5\left(\frac{g\beta q'' x^4}{5k_e\nu^2}\right)^{1/5}, \quad \mathrm{G}_a = 5\left(\frac{g\beta q''}{5k_e\nu^2 a^4}\right)^{1/5}$$

$$\psi = \nu \mathrm{G}_x F(\xi, \eta), \quad T = T_\infty - \frac{5xq''}{k_e\mathrm{G}_x}\theta(\xi, \eta) \quad (6a\text{–}h)$$

where G_x is the local Grashof number based on the distance along the plate x, and G_a is the Grashof number based on the fluid's absorption coefficient a.

Substituting Eqs. (5) and (6) into Eqs. (1) through (4), and performing the necessary mathematical operations, results in the following equations:

$$F''' + 4FF'' - 3F'^2 - \theta + 4\xi(GF'' - F'G') - 25\xi^{1/2}\,\mathrm{Da}^{-1}\,F' - 5\xi^{5/4}\Gamma F'^2 = 0 \quad (7)$$

$$\theta'' + \mathrm{Pr}(4F\theta' - F'\theta) - 4\xi\,\mathrm{Pr}(F'H - \theta'G) - 5\xi^{1/4}\exp(-5\xi^{1/4}\eta) = 0 \quad (8)$$

where $\mathrm{Da}^{-1} = 1/(Ka^2)$, $\Gamma = C\mathrm{G}_a^5/a$, and $\mathrm{Pr} = \rho\nu c/k_e$ are the inverse Darcy number, the dimensionless porous medium inertia coefficient, and the effective Prandtl number, respectively. In the quasi-similar Eqs. (7) and (8), a prime denotes ordinary differentiation with respect to η, and G and H are the first derivatives of F and θ with respect to ξ, respectively.

The transformed boundary and matching conditions can be shown to be

$$F(\xi, 0) = 0, \quad F'(\xi, 0) = 0, \quad \theta'(\xi, 0) = 5\alpha\xi^{1/4}\theta(\xi, 0)$$

$$F'(\xi, \infty) = 0, \quad \theta(\xi, \infty) = 0,$$

$$\theta(0, \eta) = 0, \quad F(0, \eta) = 0 \quad (9a\text{–}g)$$

where $\alpha = U/(k_e a)$ is the heat transfer loss coefficient. A typical value of α is 0.2 (corresponding to an absorbing fluid with a = 200 m^{-1} and a surrounding air moving at a speed of 5 m/s). Larger values of α can also be used for higher wind velocities and/or lower values of the absorption coefficient a.

Additional equations governing G and H are needed to render the problem complete, as is done by the local nonsimilarity technique (Sparrow and Yu, 1971). These are obtained by dif-

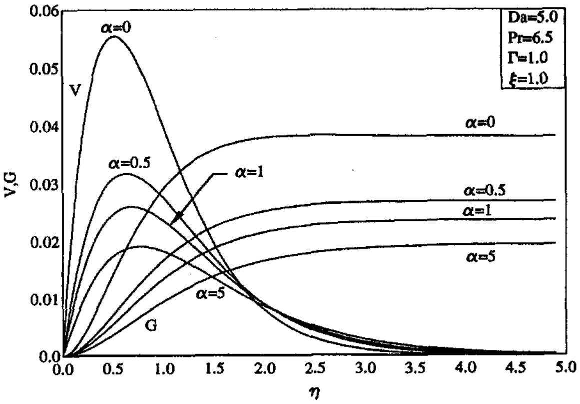

Fig. 4 Effects of α on tangential and normal velocity profiles

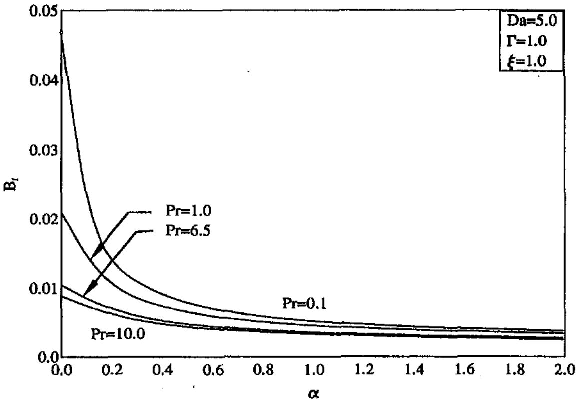

Fig. 6 Effects of Pr and α on boundary friction coefficient

ferentiating both Eqs. (7) and (8) with respect to ξ to respectively give

$$G''' + 4FG'' + 8GF'' - 10F'G' - H - 4\xi(G'^2 - GG'') - 25\xi^{1/2}\,\mathrm{Da}^{-1}G' - \tfrac{25}{2}\,\xi^{-1/2}\,\mathrm{Da}^{-1}F' - 10\xi^{5/4}\Gamma F'G' + \tfrac{25}{4}\,\xi^{1/4}\Gamma F'^2 = 0 \quad (10)$$

$$H'' + \mathrm{Pr}(8G\theta' + 4FH' - G'\theta - 5F'H) - 4\xi\,\mathrm{Pr}(G'H - GH') + \tfrac{5}{4}\,\xi^{-3/4}(1 - 5\xi^{1/4}\eta)\exp(-5\xi^{1/4}\eta) = 0. \quad (11)$$

Similarly, differentiating Eqs. (9) with respect to ξ yields the boundary and matching conditions for G and H as follows:

$$G(\xi, 0) = 0, \quad G'(\xi, 0) = 0,$$
$$H'(\xi, 0) - \tfrac{5}{4}\,\alpha\xi^{-3/4}\theta(\xi, 0) - 5\alpha\xi^{1/4}H(\xi, 0) = 0$$
$$G'(\xi, \infty) = 0, \quad H(\xi, \infty) = 0,$$
$$H(0, \eta) = 0, \quad G(0, \eta) = 0. \quad (12)$$

Equations (7) through (12) represent the governing equations for the problem under consideration. It should be mentioned that these ordinary differential equations are approximate since higher order ξ derivative terms are neglected, as required by the local similarity method. However, the exact equations are partial differential equations and can be easily solved numerically by a marching finite-difference technique, but the local similarity method herein is chosen so as to allow comparisons with the previously published work of Fathalah and Elsayed (1980). Also, note that setting $\Gamma = 0$ and letting $\mathrm{Da} \to \infty$, the equations reported by Fathalah and Elsayed (1980) are recovered.

Of special significance in free convection problems are the local boundary-friction coefficient and the Nusselt number. These physical parameters can be defined in dimensional form as

$$B_f^* = \frac{-\mu\partial^2\psi(x, 0)}{\partial y^2}, \quad \mathrm{Nu}_a = \frac{h}{k_e a},$$
$$h = \frac{q'' - U(T_w - T_\infty)}{T_{\max} - T_\infty} \quad (13a\text{–}c)$$

where μ is the fluid dynamic viscosity, T_w is the plate or wall temperature, $T_{\max}$ is the maximum local temperature, and h is the local heat transfer coefficient. Upon using Eqs. (6a–h), it can be shown that

$$B_f = \frac{B_f^*}{\rho\nu^2 G_x a^2} = -\frac{F''(0)}{25\xi^{1/2}},$$
$$\mathrm{Nu}_a = -\left(\frac{1}{5\xi^{1/4}\theta_{\max}} + \alpha\,\frac{\theta_w}{\theta_{\max}}\right). \quad (14a, b)$$

Results and Discussion

Equations (7) through (12) are nonlinear coupled ordinary differential equations and conditions that must be solved numerically since they exhibit no analytical solution. An implicit, iterative, tridiagonal finite-difference numerical method similar to that discussed by Blottner (1970) is devised for this purpose.

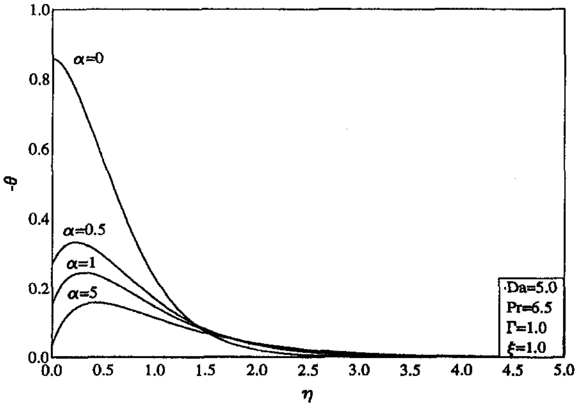

Fig. 5 Effects of α on temperature profiles

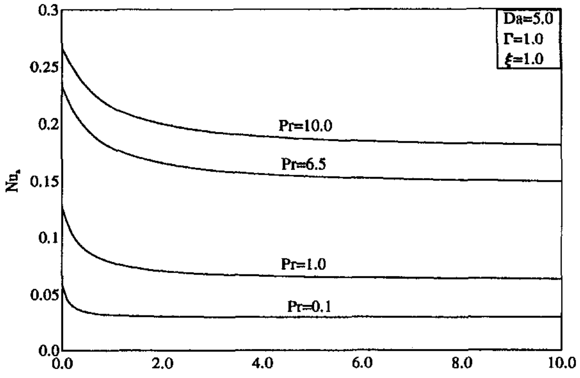

Fig. 7 Effects of Pr and α on Nusselt number

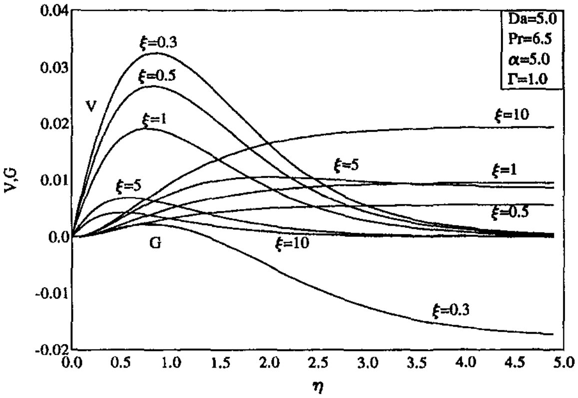

Fig. 8 Effects of ξ on tangential and normal velocity profiles

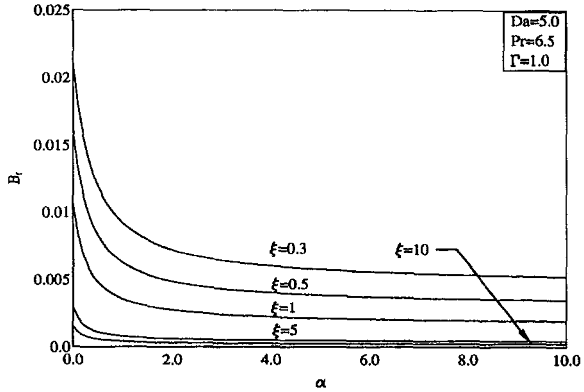

Fig. 10 Effects of ξ and α on boundary friction coefficient

The third-order differential equations are converted into second-order differential equations by making variable changes. Then, all second-order equations in η are discretized using three-point central difference quotients while first-order equations are discretized using the trapezoidal rule. With this, the differential equations are converted into a set of algebraic equations which are solved with iteration (to deal with the nonlinearities of the governing equations) by the Thomas' algorithm (see Blottner, 1970). Most changes in the dependent variables are expected to occur in the vicinity of the wall where viscous effects dominate. Far away from the wall the fluid adjusts to the ambient conditions and changes in the dependent variables are expected to be small. For this reason, variable step sizes in η are employed in the present work. The initial step size $\Delta\eta_1$ was set to 10^{-3} and the growth factor was set to 1.03. These values were arrived at after many numerical experimentations were performed to assess grid independence. A convergence criterion based on the relative difference between two successive iterations (set to 10^{-4} in the present work) was employed.

More details of the numerical solution and the procedure followed can be explained as follows:

Consider Eq. (7) governing the dimensionless stream function F. By defining

$$V = F' \qquad (15)$$

Eq. (7) may be written (before the central-difference formulas are used) as

$$\pi_1 V'' + \pi_2 V' + \pi_3 V + \pi_4 = 0 \qquad (16)$$

where

$$\pi_1 = 1, \quad \pi_2 = 4F + 4\xi G - (3 + 5\xi^{5/4}\Gamma)V$$

$$\pi_3 = -4\xi G' - 25\xi^{1/2}\,\mathrm{Da}^{-1}, \quad \pi_4 = -\theta. \qquad (17a\text{–}d)$$

The boundary conditions for V are

$$V(0) = 0, \quad V(\eta_{\max}) = 0 \qquad (18a, b)$$

where infinity is replaced by $\eta_{\max}$, which is set to a maximum value of ten in the present work.

The coefficients π_1, π_2, π_3, and π_4 in the inner iteration step are evaluated using the solution from the previous iteration step. Equation (16) is then converted into tridiagonal finite-difference algebraic equations which can be solved by the Thomas' algorithm.

Equation (15) can be integrated to give

$$F_{n+1} = F_n + \frac{(V_{n+1} + V_n)\Delta\eta_n}{2} \qquad (19)$$

where n corresponds to the nth point along the η direction.

The boundary condition for F is

$$F(0) = 0. \qquad (20)$$

The same procedure can be applied to solve Eqs. (8), (10), and (11). Many numerical results were obtained throughout the course of this work. A representative set is reported below in Figs. (2) through (19).

Figures 2 and 3 show typical profiles for the fluid tangential velocity V, normal velocity G, and temperature θ along the vertical plate for various values of the Prandtl number Pr. Increases in the Prandtl number have a tendency to decrease both the tangential velocity and temperature and to confine them to

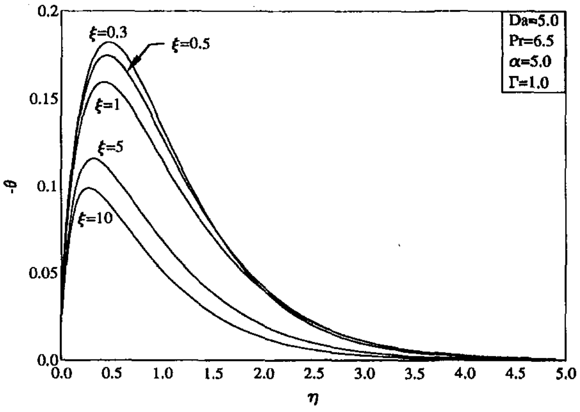

Fig. 9 Effects of ξ on temperature profiles

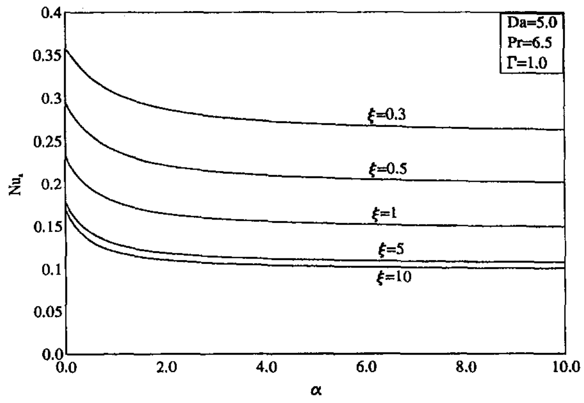

Fig. 11 Effects of ξ and α on Nusselt number

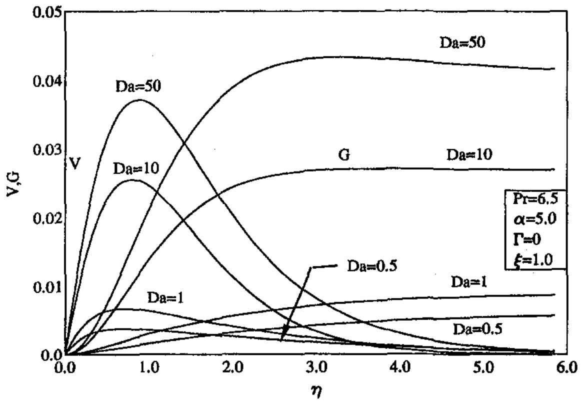

Fig. 12 Effects of Da on tangential and normal velocity profiles

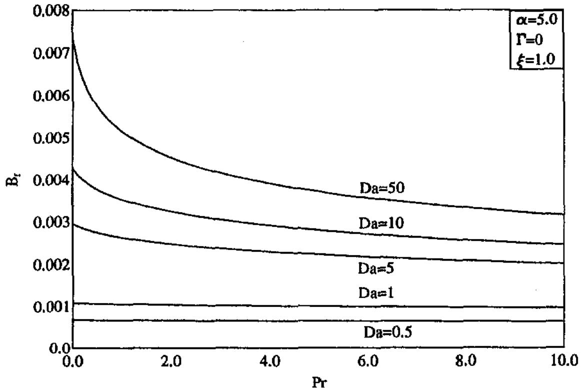

Fig. 14 Effects of Da and Pr on boundary friction coefficient

an increasingly smaller region closer to the vertical plate. In addition, the normal velocity of the fluid decreases as a result of increasing Pr. These behaviors are clearly depicted in Figs. 2 and 3. It is also seen from Fig. 3 that the maximum temperature occurs in the fluid away from the plate surface. This is because the incident solar radiations are absorbed by the absorbing fluid which in turn heats up the ideally transparent plate. This operation is believed to enhance solar collection by direct absorption in which heat losses are reduced as a result of lower plate temperatures.

Figures 4 and 5 show the influence of the heat transfer loss coefficient to the surrounding α on the tangential and normal velocity and temperature profiles, respectively. As the heat transfer loss to the surroundings increases, the absorbing fluid in the porous medium tends to slow down and its temperature tends to decrease. This is evident from the decreases in V, G, and θ as α increases (shown in Figs. 4 and 5). It can be seen from Fig. 5 that for $\alpha = 0$ (no heat loss to the surroundings) the maximum temperature occurs at the plate surface, which is consistent with results obtained for nonconvective boundary conditions.

Figures 6 and 7 present the boundary friction, B_f, and the Nusselt number, Nu_a, for various values of the effective Prandtl number, Pr, and the heat transfer loss coefficient to the surrounding α, respectively. It is observed from these figures that B_f and Nu_a decrease and increase for fixed values of α as Pr increases. The lower values of B_f are due to the lower tangential velocities predicted by increasing Pr. However, the increase in the Nu_a value is due to the reductions of the maximum temperature (occurring for higher values of Pr) since it is inversely proportional to it (see definition of Nu_a). Increases in the loss coefficient α have the same effect on the tangential velocity and temperature as that of Pr. Namely, it causes V and θ to decrease. This results in reductions in the values of both B_f and Nu_a as α increases. These behaviors are evident from Figs. 6 and 7, respectively.

Figures 8 through 11 illustrate the influence of the axial or tangential distance ξ on the flow and heat transfer parameters of the problem under consideration. Figures 8 and 9 present the profiles of the fluid tangential and normal velocity components, and the temperature profiles at different values of ξ (for Pr = 6.5 and $\alpha = 5$, corresponding to water at high wind velocities), respectively. Higher peaks in the values of the tangential velocity of the absorbing fluid V are observed at small values of ξ. This is related to the thickness of the fluid layer adjacent to the plate which is larger at lower values of ξ. It is also observed that a back-flow condition exists in the fluid's normal velocity component G for $\xi = 0.3$. This type of flow reversal behavior has been reported and discussed by Gebhart et al. (1988, p. 174). As ξ increases, the tangential velocity decreases while the normal velocity increases causing a slower net motion up the porous medium adjacent to the plate. The temperature distribution of the absorbing fluid also shows that higher peaks in the temperature occur for small values of ξ and these peak values decrease as ξ increases. Again, the maximum temperature does not occur at the plate surface as is the case of nonabsorbing fluids.

Figures 10 and 11 depict the changes of the boundary friction coefficient, B_f, and the Nusselt number, Nu_a, as a result of changing both α and ξ, respectively. As expected, higher tangential velocities at small values of ξ lead to higher boundary frictions, and as ξ increases, V decreases which results in increased reductions in B_f. This is evident from Fig. 10. Looking at the definition of Nu_a, it can be seen that Nu_a is inversely proportional to ξ for fixed values of α. Thus, an increase in the

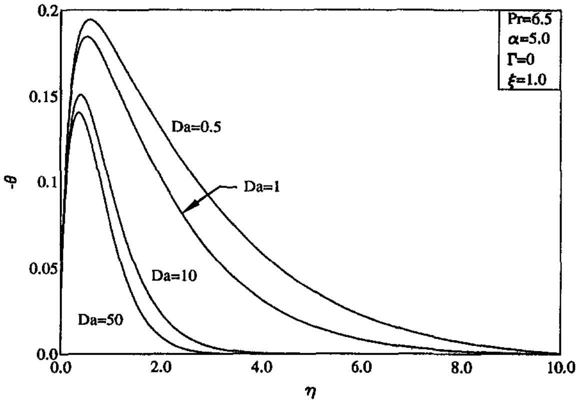

Fig. 13 Effects of Da on temperature profiles

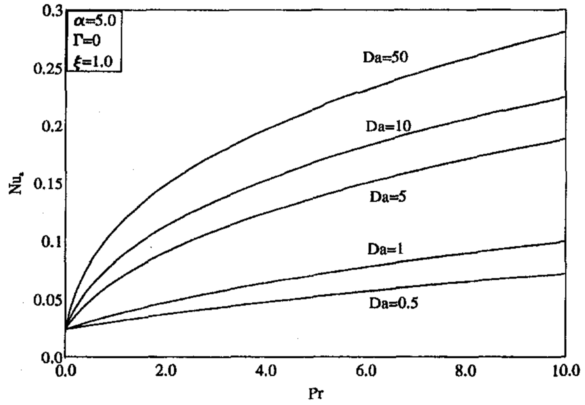

Fig. 15 Effects of Da and Pr on Nusselt number

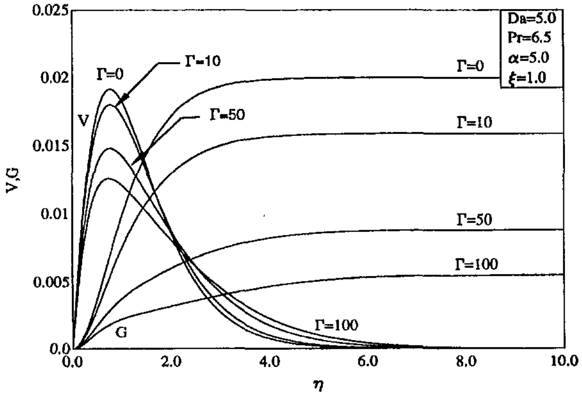

Fig. 16 Effects of Γ on tangential and normal velocity profiles

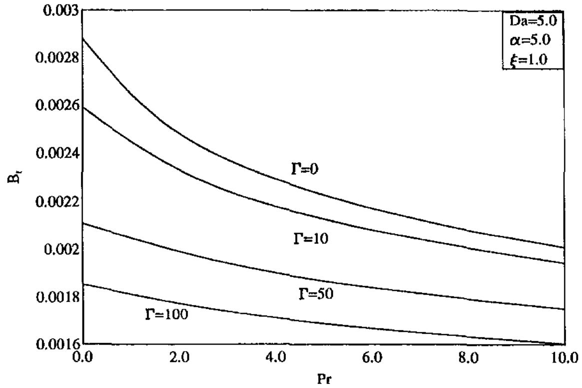

Fig. 18 Effects of Γ and Pr on boundary friction coefficient

values of ξ has the effect of reducing the Nusselt number. This behavior is clearly seen in Fig. 11.

Figures 12 through 15 elucidate the influence of the presence of the uniform porous medium on the flow and heat transfer through the Darcy number Da. The results in these figures are obtained for slow flow ($\Gamma = 0$) in order to evaluate the relative effect of Da alone. Figures 12 and 13 present the profiles for V, G, and θ for various values of Da. It should be noted that large values of Da correspond to high porosity porous medium, and the limit Da $\rightarrow \infty$ corresponds to the case of no porous medium present. Obviously, a high porosity porous medium exerts less resistance to flow. This causes higher tangential and normal fluid velocities, and these velocities decrease as the porous medium gets tighter (as Da decreases). This is clearly shown in Fig. 12. However, the presence of the porous medium (smaller values of Da) has the tendency to increase the fluid temperature. This is due to the increased fluid restriction resulting from decreasing the porosity of the porous medium. This behavior is evident from Fig. 13.

Figures 14 and 15 show the influence of both Da and Pr on B_f and Nu_a, respectively. As mentioned before, increases in Pr cause decreases in B_f and increases in Nu_a, for a relatively open porous medium. The slowing of the absorbing fluid as a result of decreasing the Darcy number, Da, has the direct effect on decreasing the wall or boundary friction as shown in Fig. 14. It is also seen that for small porosity medium, specifically for Da = 0.5 and Da = 1.0, B_f is constant for any value of Pr. It is also evident from Fig. 15 that increases in the values of Da (that is, increases in the porosity of the medium) cause increases in the Nusselt number at any fixed value of Pr. This is because Nu_a is inversely proportional to $\theta_{\max}$ which decreases as Da increases.

The influence of the porous medium inertia coefficient Γ on the flow and heat transfer parameters is the same as that of the inverse Darcy number Da^{-1} since it also represents resistance to flow. Namely, as Γ increases, V, G, and B_f decrease while θ and Nu_a increase and decrease, respectively. These behaviors are depicted in Figs. 16 through 19.

It should be mentioned that for $\Gamma = 0$ and as Da $\rightarrow \infty$, the results reported by Fathalah and Elsayed (1980) are recovered. This comparison serves as a check on the numerical procedure. No comparisons with experimental data were performed due to lack of such data at present.

Conclusion

Natural convection flow of an absorbing fluid up a uniform porous medium supported by a semi-infinite, ideally transparent, vertical flat plate due to solar radiation is considered. Boundary-layer equations are derived using the usual Boussinesq approximation and accounting for applied incident radiation flux. A convection type boundary condition is used at the plate surface. These equations exhibit no similarity solution. However, the local similarity method is employed for the solution of the present problem so as to allow comparisons with previously published work. The resulting approximate nonlinear ordinary differential equations are solved numerically by a standard implicit iterative finite-difference method. Graphical results for the velocity and temperature fields, as well as the boundary friction and Nusselt number, are presented and discussed. It was found that increases in any of the following: effective Prandtl number, heat transfer loss coefficient, tangential distance along the plate, inverse Darcy number, and the porous medium inertia coefficient caused reductions in the boundary friction coefficient. However, the Nusselt number based on the absorbing fluid coefficient was increased as the Prandtl number

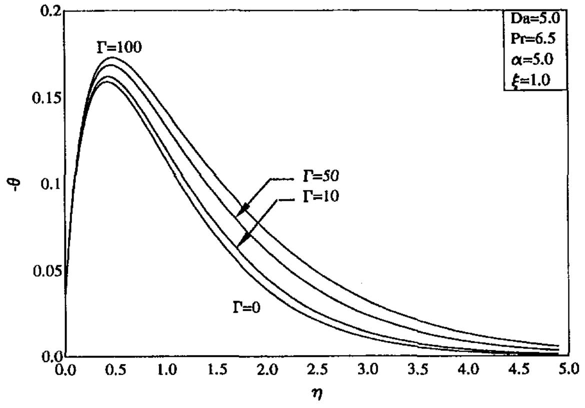

Fig. 17 Effects of Γ on temperature profiles

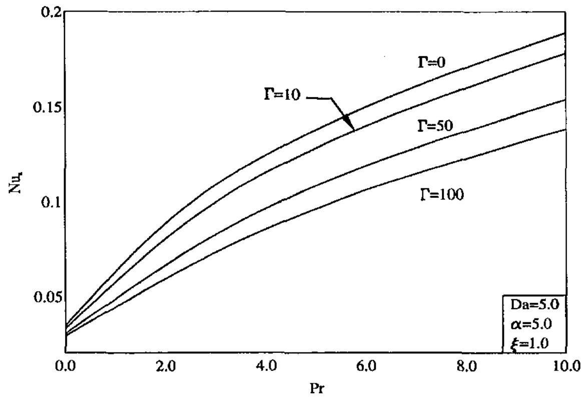

Fig. 19 Effects of Γ and Pr on Nusselt number

increased, and reductions were observed as a result of increasing any of the following: heat transfer loss coefficient, tangential distance, inverse Darcy number, and the medium inertia coefficient. In addition, a flow reversal condition was predicted for water with high heat transfer loss coefficient in the presence of a porous medium. Comparison with previously published work was performed and the results were found to be in excellent agreement. It is hoped that the present work will serve as a stimulus for experimental work which appears to be lacking at present.

References

Blottner, F., 1970, "Finite Difference Methods of Solutions of the Boundary-Layer Equations," *AIAA Journal*, Vol. 8, 193–205.

Chen, C., and Lin, C., 1995, "Natural Convection From an Isothermal Vertical Surface Embedded in a Thermally Stratified High-Porosity Medium," *International Journal of Engineering Science*, Vol. 33, 131–138.

Chen, C. K., Hung, C. I., and Horng, H. C., 1989, "Transient Natural Convection on a Vertical Flat Plate Embedded in a High-Porosity Medium," ASME JOURNAL OF HEAT TRANSFER, Vol. 109, 112–118.

Cheng, P., and Minkowycz, W. J., 1977, "Free Convection About a Vertical Flat Plate Embedded in a Porous Medium with Application to Heat Transfer From a Dike," *Journal of Geophysical Research*, Vol. 82, 2040–2044.

Cooper, P. I., 1972, "Some Factors Affecting the Absorption of Solar Radiation in Solar Stills," *Solar Energy*, Vol. 13, 373–381.

Elsayed, M. M., and Fathalah, K. A., 1979, "Temperature Distribution in a Direct Solar Heater," presented at the 72nd Annual Meeting of AIChE, Paper No. P–7d.

Evans, G. H., and Plumb, O. A., 1978, "Natural Convection From a Vertical Isothermal Surface Embedded in a Saturated Porous Medium," ASME Paper No. 78-HT-55.

Fathalah, K. A., and Elsayed, M. M., 1980, "Natural Convection Due to Solar Radiation Over a Non-Absorbing Plate With and Without Heat Losses," *International Journal of Heat & Fluid Flow*, Vol. 2, 41–45.

Gebhart, B., Jaluria, Y., Mahajan, R. L., and Sammakia, B., 1988, *Buoyancy-Induced Flows and Transport*, Hemisphere Publishing Corporation, New York, p. 914.

Hassan, K., and Mohamed, S., 1970, "Natural Convection From Isothermal Flat Surfaces," *International Journal of Heat and Mass Transfer*, Vol. 13, 1873–1886.

Hong, J., Yamada, Y., and Tien, C. L., 1987, "Effect of Non-Darcian and Nonuniform Porosity on Vertical-Plate Natural Convection in Porous Media," ASME JOURNAL OF HEAT TRANSFER, 109, 356–362.

Kierkus, W. T., 1968, "An Analysis of Laminar Free Convection Flow and Heat Transfer About an Inclined Isothermal Flat Plates," *International Journal of Heat and Mass Transfer*, Vol. 11, 241–253.

Kim, S. J., and Vafai, K., 1989, "Analysis of Natural Convection About a Vertical Plate Embedded in a Porous Medium," *International Journal of Heat Mass Transfer*, Vol. 32, 665–677.

Nakayama, A., Kokudai, T., and Koyama, H., 1990, "Non-Darcy Boundary Layer Flow and Forced Convective Heat Transfer Over a Flat Plate in a Fluid-Saturated Porous Medium," ASME JOURNAL OF HEAT TRANSFER, Vol. 112, 157–162.

Plumb, O. A., and Huenefeld, J. C., 1981, "Non-Darcy Natural Convection from Heated Surfaces in Saturated Porous Media," *International Journal of Heat Mass Transfer*, Vol. 24, 765–768.

Siegel, R., and Howell, J. R., 1981, *Thermal Radiation Heat Transfer*, Hemisphere Publishing Corporation, Washington, D.C.

Singh, P., and Tewari, K., 1993, "Non-Darcy Free Convection from Vertical Surfaces in Thermally Stratified Porous Media," *International Journal of Engineering Science*, Vol. 31, 1233–1242.

Sparrow, E. M., and Gregg, J. L., 1956, "Laminar Free Convection from a Vertical Plate With Uniform Surface Heat Flux," *Transfer ASME*, Vol. 78, p. 435.

Sparrow, E. M., and Yu, H. S., 1971, "Local Non-Similarity Thermal Boundary-Layer Solutions," ASME JOURNAL OF HEAT TRANSFER, Vol. 93, No. 4, 328–334.

Vafai, K., Ettefagh, J., 1988, "Analysis of the Radiative and Conductive Heat Transfer Characteristics of a Waste Package Canister," ASME JOURNAL OF HEAT TRANSFER, Vol. 110, 1011–1014.

Vafai, K., and Tien, C. L., 1982, "Boundary and Inertia Effects on Convective Mass Transfer in Porous Media," *International Journal of Heat Mass Transfer*, Vol. 25, 1183–1190.

Vafai, K., and Tien, C. L., 1981, "Boundary and Inertia Effects on Flow and Heat Transfer in Porous Media," *International Journal of Heat Mass Transfer*, Vol. 24, 195–203.

S. Wakitani
Department of Mechanical Engineering
College of Industrial Technology
1-27-1 Nishikoya, Amagasaki 661
JAPAN

Development of Multicellular Solutions in Natural Convection in an Air-Filled Vertical Cavity

Consideration is given to the multiple solutions of two-dimensional natural convection in a vertical air-filled tall cavity with differentially heated sidewalls. Numerical simulations are carried out for a wide range of Rayleigh numbers from the onset of the steady multicellular flow, through the reverse transition to the unicellular pattern, to the unsteady multicellular flow. The dependence of the flow structure on the initial condition is clarified from the simulations by means of starting from a motionless and isothermal state, and gradually increasing or decreasing the Rayleigh number.

Introduction

Considerable attention has been given to the problem of natural convection in a tall cavity, with differentially heated sidewalls, because of its importance in many engineering applications. Typical applications include thermal insulation using double-grazed windows, nuclear reactors, solar energy collectors, electronic components in enclosure, and others. Some studies of this type of convection have still been continued and new features have been found for large Prandtl number fluids, experimentally and numerically (Wakitani, 1996). There, flow becomes substantially unsteady at a Rayleigh number slightly higher than a critical value and the number of secondary cells increases as the Rayleigh number is increased. As the Rayleigh number is further increased, the flow becomes quasi-steady at the Rayleigh numbers in some regions. Then the flow becomes unsteady again and is a unicellular one formed by a single secondary cell.

In an air-filled cavity (the Prandtl number, $\mathrm{Pr} = 0.71$) of aspect ratio A larger than a value between 11 and 12, steady multicellular flow has been observed numerically for the Rayleigh number $\mathrm{Ra} \approx 10^4$ by Roux et al. (1980) and Lauriat (1980). Lee and Korpela (1983) have expected the critical value of A between 10 and 12.5. Their computational result for $\mathrm{Pr} = 0$ demonstrates that the number of secondary cells depends on an initial condition. For an air-filled cavity, some discrepancies are indicated among analytical, experimental, and numerical results (e.g., Le Quéré, 1990).

Furthermore, at a high Rayleigh number, a reverse transition from multicellular to unicellular structure has been shown by Roux et al. (1980). By gradually increasing or decreasing Ra for $\mathrm{Pr} = 0.71$ and $A = 16$, Le Quéré (1990) has confirmed the reverse transition and found the existence of several branches of solutions characterized by different numbers of cells. The simulation for large Pr number fluids does not show such a reverse transition as in an air-filled cavity (Wakitani, 1994; Wakitani, 1996). Unsteady calculation of Le Quéré (1990) has shown that as Ra is gradually increased, the return to the unicellular pattern from the multicellular structure occurs through a gradual decrease in the number of cells. His diagram showing the different branches of solutions is reproduced in Fig. 1. He has also found the existence of unsteady two-cell solutions in some Ra ranges less than 4×10^4 (Fig. 1), in contrast to the other numerical results (e.g., Lee and Korpela, 1983; Chait and Korpela, 1989). However, Le Quéré (1990) does not clarify the dependence of the multiple solutions on initial conditions. His computation was conducted only by gradually varying Ra. Most experiments will start from a motionless and isothermal condition.

In this paper, we perform a two-dimensional numerical simulation of natural convection in an air-filled cavity. To find out the dependence of the flow structure on the initial condition, the numerical calculations are conducted by starting from a motionless and isothermal state, or impulsive run, and by gradually increasing or decreasing Ra, or gradual run. In the gradual run, after a steady or an asymptotic solution has been reached, the next calculation is continued by slightly varying Ra. The calculations are conducted until a high Ra where unsteady solutions occur after establishment of the return to the unicellular pattern.

Numerical Simulations

Governing Equations. We consider two-dimensional natural convection in an air-filled vertical cavity of height H and width W (aspect ratio $A = H/W$). The left and right sidewalls are held at constant uniform temperatures, T_1 and T_2 ($T_1 > T_2$), respectively. The top and bottom of the cavity are thermally insulated. We define the coordinate system so that the x-axis is in the horizontal direction and z-axis is in the vertical direction (positive upward) with the origin at the bottom corner on the left sidewall of the cavity. We consider the flow of a Newtonian fluid and assume that the fluid satisfies the Boussinesq approximation. According to Ostrach's suggestion (Ostrach, 1988) for natural convection of $(\mathrm{Ra}/\mathrm{Pr})^{1/2} \geq 1$ and $\mathrm{Pr} \leq 1$, we introduce $V_r = (g\beta\Delta TW)^{1/2}$ as reference velocity, where Ra is the Rayleigh number, Pr the Prandtl number, g the acceleration due to gravity, β the coefficient of thermal expansion, and ΔT the temperature difference $(T_1 - T_2)$.

The equations that govern the velocity, pressure, and temperature fields are the continuity equation, Navier-Stokes equations, and energy equation. These equations can be put into dimensionless forms by scaling length with the width W, velocity with V_r, pressure with ρV_r^2, temperature with ΔT, and time with $W/V_r = (\mathrm{Pr}/\mathrm{Ra})^{1/2} W^2/\nu$, where ρ is density. The dimensionless temperature is defined as $T = (T^* - T_r)/\Delta T$ with $T_r = (T_1 + T_2)/2$, where T^* is fluid temperature.

The governing equations can be written in the following dimensionless forms:

$$\frac{\partial u}{\partial x} + \frac{\partial w}{\partial z} = 0, \tag{1}$$

$$\frac{\partial u}{\partial t} + u\frac{\partial u}{\partial x} + w\frac{\partial u}{\partial z} = -\frac{\partial p}{\partial x} + \left(\frac{\mathrm{Pr}}{\mathrm{Ra}}\right)^{1/2} \nabla^2 u, \tag{2}$$

Contributed by the Heat Transfer Division for publication in the JOURNAL OF HEAT TRANSFER. Manuscript received by the Heat Transfer Division April 29, 1996; revision received September 13, 1996; Keywords: Enclosure Flows, Natural Convection. Associate Technical Editor: P. Simpkins.

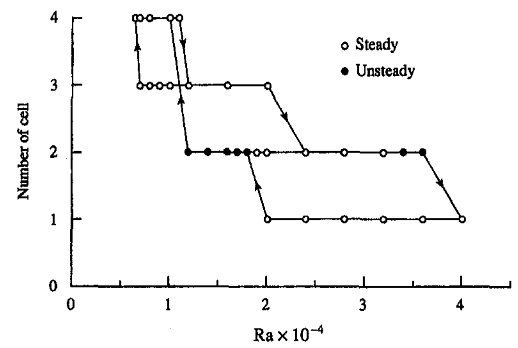

Fig. 1 Diagram showing the different branches of solutions calculated by Le Quéré (1990)

$$\frac{\partial w}{\partial t} + u\frac{\partial w}{\partial x} + w\frac{\partial w}{\partial z} = -\frac{\partial p}{\partial z} + T + \left(\frac{\mathrm{Pr}}{\mathrm{Ra}}\right)^{1/2}\nabla^2 w, \quad (3)$$

$$\frac{\partial T}{\partial t} + u\frac{\partial T}{\partial x} + w\frac{\partial T}{\partial z} = \frac{1}{(\mathrm{Pr\,Ra})^{1/2}}\nabla^2 T, \quad (4)$$

where t is the time, u and w are the velocity components in the x- and z-directions, respectively, p is the deviation from the hydrostatic pressure and ∇^2 is the Laplacian operator.

The boundary conditions are

$$u = w = 0 \quad \text{on} \quad x = 0, 1; \quad z = 0, A, \quad (5)$$

$$T = 0.5 \quad \text{on} \quad x = 0 \quad \text{and} \quad T = -0.5 \text{ on } x = 1, \quad (6)$$

$$\frac{\partial T}{\partial z} = 0 \quad \text{on} \quad z = 0, A. \quad (7)$$

As the initial condition for impulsive run, a motionless and isothermal state is taken where

$$u = w = T = p = 0 \; (0 < x < 1, 0 < z < A) \quad \text{at} \quad t = 0, \quad (8)$$

unless otherwise described.

Numerical Algorithm. The numerical technique used in the present study is the same as that of Wakitani (1996) based on the finite difference method of Kawamura and Kuwahara (1984). First, the Poisson equation for the pressure, which is derived from Eqs. (2) and (3), is solved, subject to the appropriate boundary conditions. The equation of continuity (1) is satisfied at each time step. Then, the velocity and temperature at the next time step are computed from discretized ones of Eqs. (2), (3) and (4) using the Euler implicit scheme. The nonlinear terms in their equations are linearized and approximated by means of a third-order upwind scheme (Kawamura and Kuwahara 1984; Kawamura et al. 1986). The spatial derivatives in the remaining terms are expressed in terms of the second-order central differences. These finite difference equations are solved by using the SOR method.

An orthogonal, nonuniform, and nonstaggered grid system is used. The effects of the grid size and the time increment on the flow characteristics have been examined. Finally, the grid with 25 × 121 points and the time increment of $\Delta t = 0.002$ are generally used in the present computations. The finest grid size near the walls is about three times smaller than the one corresponding to a uniform grid. All computations are performed on a workstation (Sun SPARC station 20 SX8 M502).

Table 1 Comparison of the solutions with those of Chenoweth and Paolucci (1986), and de Vahl Davis (1983)

		Ra = 10^5		
grids	41 × 41	61 × 61	81 × 81	—
Nu	4.566 (4.567)	4.548 (4.540)	4.541 (4.531)	[4.519]
$u_{\max}$	0.1306 (0.1285)	0.1303 (0.1295)	0.1303 (0.1299)	[0.1303]
z	0.8553 (0.8551)	0.8548 (0.8549)	0.8549 (0.8548)	[0.855]
$w_{\max}$	0.2573 (0.2541)	0.2572 (0.2559)	0.2572 (0.2566)	[0.2574]
x	0.0656 (0.0653)	0.0656 (0.0657)	0.0658 (0.0658)	[0.066]
		Ra = 10^6		
grids	61 × 61	81 × 81	101 × 101	—
Nu	8.917 (8.988)	8.885 (8.907)	8.871 (8.874)	[8.800]
$u_{\max}$	0.07680 (0.07567)	0.07690 (0.07617)	0.07695 (0.07645)	[0.07670]
z	0.8513 (0.8547)	0.8506 (0.8528)	0.8501 (0.8518)	[0.850]
$w_{\max}$	0.2619 (0.2565)	0.2610 (0.2585)	0.2610 (0.2597)	[0.2603]
x	0.0367 (0.0372)	0.0377 (0.0374)	0.0377 (0.0376)	[0.0379]

Accuracy Assessment. The computation based on the above algorithm was tested for a square cavity ($A = 1$, $\mathrm{Pr} = 0.71$) at $\mathrm{Ra} = 10^5$ and 10^6. The results were compared with the results of Chenoweth and Paolucci (1986) and the benchmark solutions of de Vahl Davis (1983). They used uniform, square grids. Table 1 gives our steady results obtained for some grids. In the table we give the averaged Nusselt number Nu, the maximum horizontal and vertical velocities $u_{\max}$ and $w_{\max}$ at the midwidth and midheight, respectively, and their z and x locations. The Nusselt number is obtained by averaging the heat flux over the hot and cold wall. The results from the hot and cold wall agree within the accuracy in the table. The values of the maximum velocities and their locations are obtained using polynomial interpolations.

The values in parentheses represent the results of Chenoweth and Paolucci (1986) and the values in brackets represent the benchmark solutions obtained by de Vahl Davis (1983) using Richardson's extrapolations. Their velocity data are multiplied by $(\mathrm{Pr\,Ra})^{-1/2}$ to fit with our notation.

The present results are in excellent agreement with those of Chenoweth and Paolucci (1986), and the results for the finest grid at each Ra are in good agreement with the benchmark solutions obtained by de Vahl Davis (1983).

Results and Discussion

Computations are made for $\mathrm{Pr} = 0.71$ and $A = 16$. A numerical simulation is conducted by gradually increasing or decreasing Ra, or gradual run, in the same manner as Le Quéré (1990). Another simulation is conducted by starting from a motionless and isothermal state as initial conditions, or impulsive run.

Nomenclature

A = aspect ratio = H/W
g = acceleration due to gravity
H = height of cavity
Nu = averaged Nusselt number
Nu_z = local Nusselt number
p = dimensionless pressure
Pr = Prandtl number = ν/κ
Ra = Rayleigh number = $g\beta W^3\Delta T/\nu\kappa$
t = dimensionless time
T = dimensionless temperature
u, w = dimensionless velocity components
W = width of cavity
x, z = Cartesian coordinates
β = volumetric expansion coefficient
Δt = time increment
ΔT = temperature difference
κ = thermal diffusivity
ν = kinematic viscosity
ρ = density

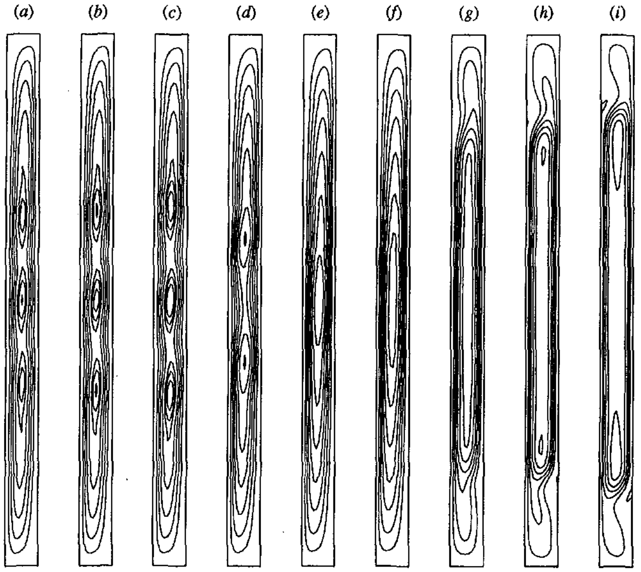

Fig. 2 Streamlines at dimensionless time $t = 500$ for gradually increasing Ra: (a) Ra = 9×10^3; (b) 1×10^4; (c) 1.2×10^4; (d) 1.8×10^4; (e) 3.3×10^4; (f) 5×10^4; (g) 1×10^5; (h) 2×10^5; (i) 3×10^5; constant values of the stream function are −0.05, −0.1, −0.15, −0.20, −0.25, −0.27, −0.29 for (a)–(c), −0.05, −0.10, −0.15, −0.20, −0.25, −0.30, −0.35 for (d)–(f), −0.05, −0.10, −0.15, −0.20, −0.25, −0.30 for (g), (h), and 0.0, −0.05, −0.10, −0.15, −0.20, −0.25 for (i).

Gradual Run. Figure 2 shows the streamlines at a dimensionless time $t = 500$ for various values of Ra obtained from gradually increasing Ra (typically, increments of about 0.1–0.2 Ra). The hot wall is on the left side in every figure. These flow patterns are in a steady state. The first computation starts from a steady unicellular solution at Ra = 5×10^3 obtained from impulsive run. Figure 2(*a*) shows a three-cell pattern characterized by a middle cell and two weaker outer cells. This pattern first appears at Ra = 8×10^3, where two outer cells are very weak. The three-cell pattern continues to Ra = 1.7×10^4 with increasing its amplitude (Figs. 2*b*, *c*). Lee and Korpela (1983) found the transition from a unicellular to a multicellular flow in the range $7.1 \times 10^3 < \text{Ra} < 7.81 \times 10^3$ for $A = 20$. At Ra = 7.1×10^3, Roux et al., (1980) and Chenoweth and Paolucci (1986) confirmed the existence of a multicellular flow for $A = 20$. Our result is different from that of Le Quéré (1990), in which a four-cell pattern has appeared at Ra = 7×10^3. We have not obtained any four-cell pattern from the simulations by gradually increasing Ra. Lee and Korpela (1983) obtained a three-cell pattern for $A = 15$ and a four-cell pattern for $A = 17.5$ at Ra = 1.065×10^4. Their results may be in agreement with our results rather than Le Quéré (1990).

At Ra = 1.8×10^4, the transition to a two-cell pattern occurs (Fig. 2*d*). Further, at Ra = 3.3×10^4, the reverse transition to a unicellular structure occurs (Fig. 2*e*). Le Quéré (1990) obtained their transitions at Ra = 2.4×10^4 and 4×10^4, respectively. He indicated that the two-cell solutions at Ra = 3.4×10^4 and 3.6×10^4 were time-periodic asymptotic ones. However, we have not obtained such time-periodic asymptotic solutions at any Ra until the reverse transition occurs. At present, we cannot give decisive reasons for the difference between the present predictions and Le Quéré's results.

Table 2 Comparison of typical quantities for the two-cell solutions in the case *A = 16, Pr = 0.71 and Ra = 2.4 × 10⁴ with those of Le Quéré (1990)*, and Jin and Chen (1996)

Authors	grids	$\lvert\psi\rvert$	ω	Nu	α
Present study	25 × 121	0.2545	9.560	1.913	1.63
	31 × 131	0.2514	9.496	1.910	1.64
Le Quéré (1990)	16 × 90	0.2414	9.330	1.901	1.59
	24 × 120	0.2419	9.337	1.901	—
Jin and Chen (1996)	33 × 129	0.2456	9.627	1.901	1.60

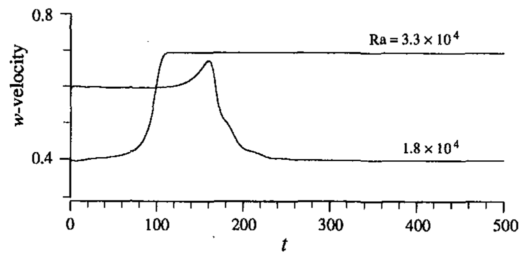

Fig. 3 Time evolution of the *w*-velocities at point $x = 0.053$, $z = 8$ for gradually increasing Ra

Some quantities, for the two-cell solutions in the case where $A = 16$, Pr = 0.71 and Ra = 2.4×10^4, can be compared with those of Le Quéré (1990), and Jin and Chen (1996). Table 2 shows comparisons of the value of the stream function ψ at a center of the slot, the vorticity ω at the midheight on the hot wall, the averaged Nusselt number Nu, and the wavenumber α based on the distance between two cells. The maximum difference appears in ψ with about 5 percent, but others are within 3 percent of the results of Le Quéré, and Jin and Chen.

At Ra ≈ 1×10^5, a unicellular structure characterized by the streamlines around the lower and upper portions of the cavity appears (Fig. 2*g*). Then, a two-cell pattern appears with its cores in the lower and upper portions (Figs. 2*h*, *i*).

Figure 3 shows the time evolution of the *w*-velocities at the midheight near the hot wall ($x = 0.053$, $z = 8$). Steady states are reached in a dimensionless time (t = 300 and 120) for Ra = 1.8×10^4 and 3.3×10^4, respectively. The abrupt change in the velocity shows that the transition in cellular patterns has occurred there. The streamlines corresponding to these Rayleigh numbers are shown in Fig. 4 for some dimensionless times.

Figure 5(*a*) shows the streamlines for Ra = 1.4×10^4 at some times and Fig. 5(*b–d*) ($t = 500$) are obtained from gradually decreasing Ra. At Ra = 1.4×10^4, the transition from unicellular to two-cell pattern occurs, and a steady solution is reached. Le Quéré (1990) found the same transition at Ra =

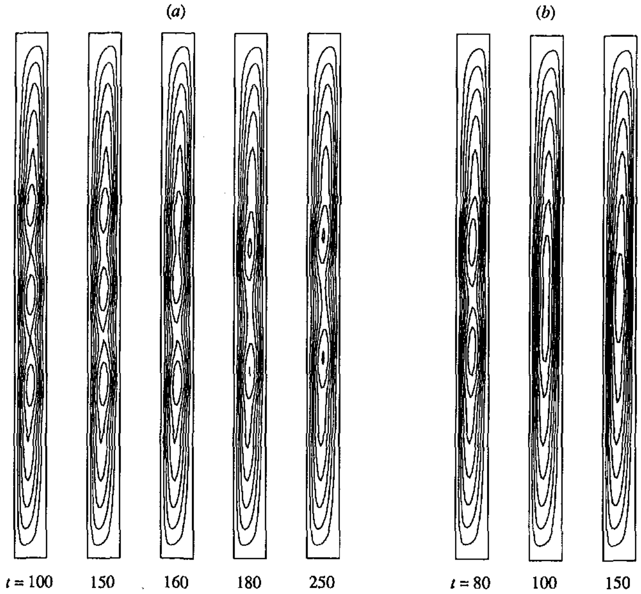

Fig. 4 Streamlines at some different dimensionless times for gradually increasing Ra: (a) Ra = 1.8×10^4; (b) 3.3×10^4; constant values of the stream function are −0.05, −0.1, −0.15, −0.20, −0.25, −0.30, −0.35.

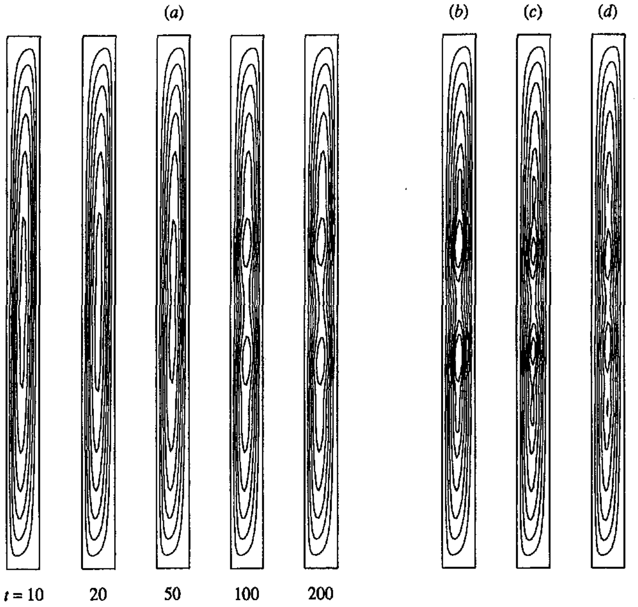

Fig. 5 Streamlines at some different dimensionless times for gradually decreasing Ra: (a) Ra = 1.4×10^4, and streamlines at dimensionless time $t = 500$; (b) Ra = 1.2×10^4; (c) 1×10^4; (d) 9×10^3; constant values of the stream function are −0.05, −0.1, −0.15, −0.20, −0.25, −0.30 for (a), and −0.05, −0.1, −0.15, −0.20, −0.25, −0.27, −0.29 for (b)–(d).

1.8×10^4 but the solution was time-periodic. When the Rayleigh number is further decreased, a four-cell pattern appears at Ra = 1.1×10^4 with two weak outer cells. This four-cell pattern continues to Ra = 8.6×10^3 and the transition to a three-cell pattern occurs at Ra = 8×10^3. Then, a unicellular pattern appears at Ra = 7×10^3. The transition from a three-cell to a four-cell pattern has not been found in the process with gradually decreasing Ra, in contrast to the result of Le Quéré (1990).

Impulsive Run. Figure 6 shows the streamlines at $t = 500$ for various values of Ra obtained from starting from a motionless and isothermal state as initial conditions. The solutions for Ra $\leq 9 \times 10^3$ coincide with those by gradually increasing Ra. However, a four-cell pattern appears in the short range Ra = 1×10^4 – 1.1×10^4 (Fig. 6b). A two-cell pattern appears at Ra = 1.2×10^4 (Fig. 6c) and the reverse transition to a unicellular structure occurs at Ra = 1.5×10^4 (Fig. 6d), the streamlines for which agree with those by gradually decreasing Ra. The reverse transition largely depends on the initial condition, whether gradually increasing Ra or impulsive run. On the other hand, the streamlines for Ra $\geq 5 \times 10^4$ agree with those by gradually increasing Ra (Figs. 6f–i).

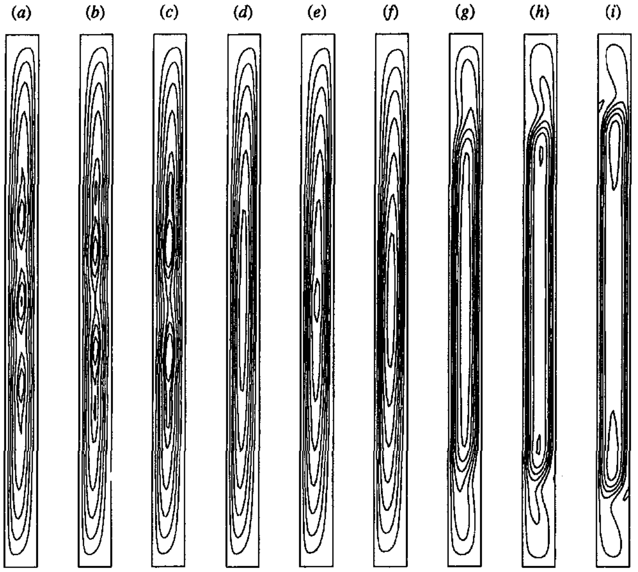

Fig. 6 Streamlines at dimensionless time $t = 500$ for impulsive run: (a) Ra = 9×10^3; (b) 1×10^4; (c) 1.2×10^4; (d) 1.5×10^4; (e) 2×10^4; (f) 5×10^4; (g) 1×10^5; (h) 2×10^5; (i) 3×10^5; constant values of the stream function are same as Fig. 2.

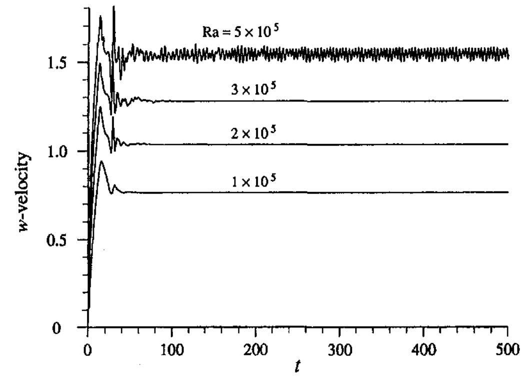

Fig. 7 Time evolution of the w-velocities at point $x = 0.053$, $z = 8$ for impulsive run

Figure 7 shows the time evolution of the w-velocities at the midheight near the hot wall ($x = 0.053$, $z = 8$) for high Rayleigh numbers. Steady solutions are reached for Ra $\leq 3 \times 10^5$. A time-periodic unsteady solution first appears at Ra = 4×10^5 and the amplitude of fluctuation grows as Ra is increased.

The transition of the cell pattern based on the number of cells is summarized in Fig. 8. Figure 8(a) shows the result for gradual run, together with the result of Le Quéré (1990), and Fig. 8(b) that for impulsive run. A hysteresis, which is characteristic in bifurcation phenomena, is found in the transition between the two-cell and the unicellular pattern in the range Ra = 1.4×10^4 – 3.3×10^4 (Fig. 8a). However, such a hysteresis

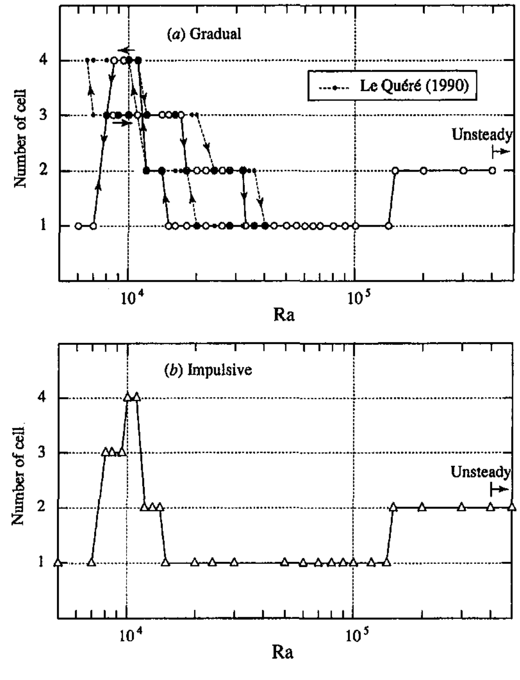

Fig. 8 Diagram showing the various cell patterns: (a) for gradually increasing or decreasing Ra; (b) for impulsive run.

cannot be found at Rayleigh numbers higher than 5×10^4 and the solutions there coincide with those of impulsive run as shown in Fig. 8(*b*). Thus the dependence of the multiple solutions on initial conditions does not appear in such high Rayleigh numbers.

Heat Transfer. Heat transfer across the cavity depends on the flow structure. The multiple solutions corresponding to the different cell patterns are considered to possess the different heat transfer coefficients. Figure 9 shows an example of the local Nusselt numbers Nu_z along the hot wall at some Rayleigh numbers for gradually increasing Ra. These Nusselt numbers correspond to those for a subcritical state, two-cell pattern, unicellular pattern after reverse transition, and two-cell pattern at high Rayleigh number. These values are calculated from steady solutions at a dimensionless time $t = 500$. The profile at $Ra = 2 \times 10^5$ exhibits the minima around the lower and upper portions of the cavity.

The averaged Nusselt numbers obtained from different initial conditions are shown in Fig. 10. Small differences are found at $Ra \leq 3 \times 10^4$, corresponding to the multiple solutions. However, these averaged values do not show the substantial differences among the initial conditions. This is because most of the heat is transferred across the cavity in the bottom and the top end region, as indicated by Le Quéré (1990).

Conclusion

In this paper numerical investigations have been described on natural convection in a vertical air-filled cavity of an aspect ratio $A = 16$. A multicellular flow with a three-cell pattern first appears at the Rayleigh number $Ra = 8 \times 10^3$ for the initial condition of a motionless and isothermal state and for the condition by gradually increasing Ra. At the range $1 \times 10^4 \leq Ra < 5 \times 10^4$, the differences are found in the cell patterns obtained from their conditions. The solutions for $Ra \geq 5 \times 10^4$ do not depend on the initial conditions. A distinguished hysteresis is found in the transition between two-cell and unicellular pattern involving the reverse transition. A time-periodic unsteady solution first appears at $Ra = 4 \times 10^5$ after the reverse transition has occurred.

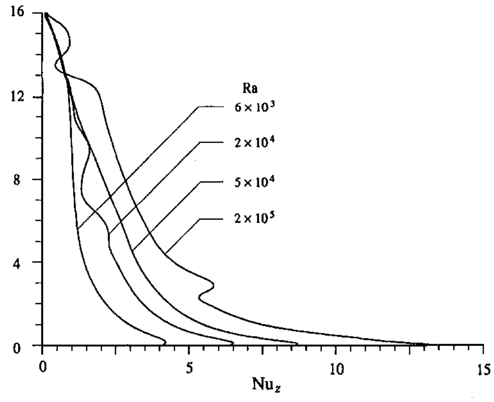

Fig. 9 Local Nusselt numbers along the hot wall for gradually increasing Ra

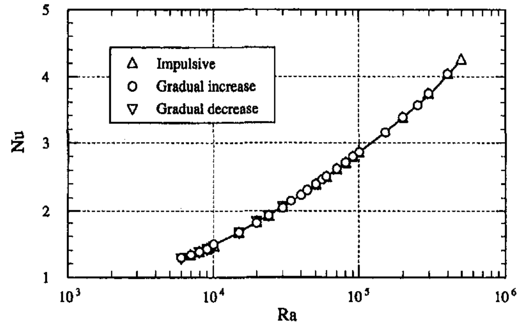

Fig. 10 Averaged Nusselt numbers obtained from different initial conditions

References

Chait, A., and Korpela, S. A., 1989, "The Secondary Flow and its Stability for Natural Convection in a Tall Vertical Enclosure," *Journal of Fluid Mechanics*, Vol. 200, pp. 189–216.

Chenoweth, D. R., and Paolucci, S., 1986, "Natural Convection in an Enclosed Vertical Air Layer with Large Horizontal Temperature Differences," *Journal of Fluid Mechanics*, Vol. 169, pp. 173–210.

de Vahl Davis, G., 1983, "Natural Convection of Air in a Square Cavity: a Bench Mark Numerical Solution," *International Journal for Numerical Methods in Fluids*, Vol. 3, pp. 249–264.

Jin, Y. Y., and Chen, C. F., 1996, "Instability of Convection and Heat Transfer of High Prandtl Number Fluids in a Vertical Slot," ASME JOURNAL OF HEAT TRANSFER, Vol. 118, pp. 359–365.

Kawamura, T., and Kuwahara, K., 1984, "Computations of High Reynolds Number Flow around a Circular Cylinder with Surface Roughness," AIAA Paper No. 84-0340.

Kawamura, T., Takami, H., and Kuwahara, K., 1986, "Computation of High Reynolds Number Flow around a Circular Cylinder With Surface Roughness," *Fluid Dynamics Research*, Vol. 1, pp. 145–162.

Lauriat, G., 1980, "Numerical Study of Natural Convection in a Narrow Cavity: an Examination of High Order Accurate Schemes," ASME Paper No. 80-HT-90.

Le Quéré, P., 1990, "A Note on Multiple and Unsteady Solutions in Two-Dimensional Convection in a Tall Cavity," ASME JOURNAL OF HEAT TRANSFER, Vol. 112, pp. 965–974.

Lee, Y., and Korpela, S. A., 1983, "Multicellular Natural Convection in a Vertical Slot," *Journal of Fluid Mechanics*, Vol. 126, pp. 91–121.

Ostrach, S., 1988, "Natural Convection in Enclosures," ASME JOURNAL OF HEAT TRANSFER, Vol. 110, pp. 1175–1190.

Roux, B., Grondin, J., Bontoux, P., and de Vahl Davis, G., 1980, "Reverse Transition From Multicellular to Monocellular Motion in Vertical Fluid Layer," *Phys. Chem. Hydro.*, Vol. 3F, pp. 292–297.

Wakitani, S., 1994, "Experiments on Convective Instability of Large Prandtl Number Fluids in a Vertical Slot," ASME JOURNAL OF HEAT TRANSFER, Vol. 116, pp. 120–126.

Wakitani, S., 1996, "Formation of Cells in Natural Convection in a Vertical Slot at Large Prandtl Number," *Journal of Fluid Mechanics*, Vol. 314, pp. 299–314.

A Numerical Study of Local and Average Natural Convection Nusselt Numbers for Simultaneous Convection Above and Below a Uniformly Heated Horizontal Thin Plate

B. Chambers

Tien-Yu T. Lee

Simulation and Design Center
Motorola Inc.
2100 East Elliot Road
M.D. EL615
Tempe, AZ 85284
R10893@email.sps.mot.com

Numerical simulations were conducted to determine local and average natural convection Nusselt numbers for uniformly heated horizontal plates with convection occurring simultaneously from upper and lower surfaces. Plate width and heating rate were used to vary the modified Rayleigh number over the range of 86 to 1.9×10^8. *Upper surface Nusselt numbers were found to be smaller than corresponding lower surface Nusselt numbers. The local Nusselt number was largest at the plate edge and decreased towards the plate center for both surfaces. This variation followed approximately a minus* $\frac{1}{3}$*-power law variation with the non-dimensionalized* x *coordinate on the upper surface for modified Rayleigh numbers greater than* 10^4, *and a minus* $\frac{1}{9}$*-power law variation on the lower surface for all modified Rayleigh numbers. Comparative simulations were also performed for upward and downward facing uniformly heated plates (single sided convection). For these cases, Nusselt numbers on the upward facing plates were larger than for downward facing plates.*

Introduction

Of the basic configurations typically addressed in natural convection heat transfer, the heated horizontal plate has been problematic due to the intractability of solving the governing differential equations for this orientation and to the difficulty of obtaining experimental results except for the simplest of boundary conditions. Experimental data are limited to several commonly cited references with uniform wall temperature boundary conditions and a single reference for a uniform heat flux boundary condition. These include McAdams (1954) (heat transfer—upward and downward facing isothermal surfaces), Goldstein, et al. (1973) (naphthalene sublimation—upward facing "isothermal" surface), Lloyd and Moran (1974) (electrochemical mass transfer—upward facing "isothermal" surface), and Sparrow and Carlson (1986) (heat transfer—upward facing uniform heat flux surface).

One consideration not addressed in the literature is the effect of concurrent heat transfer from both upper and lower surfaces. For this configuration, Nusselt numbers are difficult to obtain experimentally due to the necessity of having to locally measure the percentage of the total heat being convected from each surface. Conversely, a numerical study allows easy determination of local heat fluxes and surface temperatures allowing local Nusselt numbers to be readily calculated. Numerical integration further allows average Nusselt numbers to be determined.

Numerical Model

CFD Model and Boundary Conditions. Numerical work for this study was performed using the FLOTHERM® finite-volume computational fluid dynamics (CFD) code developed specifically for thermal analysis of electronic enclosures. The software utilizes a Cartesian coordinate system and can model two- and three-dimensional problems. The program contains a number of modeling features, but only those utilized in this study are discussed. Additional details of modeling features, and the computational method, can be obtained from the FLOTHERM Reference Manual (1994).

All analyses for this study were performed using two-dimensional models. The fluid was modeled using constant property values and the Boussinesq model to account for buoyancy effects. The software solves for the variables p, u, v, and T using the well known SIMPLE algorithm (Patankar, 1980).

The simulation model consisted of a thin horizontally oriented plate, heated by a uniform source. The plate was placed at the center of a "solution domain" which defined the extent of the flow field. The sides of the solution domain were defined by exterior wall elements, the bottom surface was bounded by an inlet vent, while the top surface was bounded by an outlet vent. The solution domain width was set at three times the plate width to allow adequate area for fluid flow around the plate edges without causing significant acceleration due to flow area constriction. Solution domain height was set at approximately two-thirds its width to provide sufficient area for boundary layer development above and below the plate. The plate and solution domain are shown in Fig. 1.

The heated plate was modeled using a cuboid block element. Several plate widths (W) were used in spanning the range of modified Rayleigh numbers investigated. Plate widths of 5.1, 10.2, 20.4, 40.8, and 102 mm were used in the modeling. Each plate was discretized into 51 nodes along its width. An odd number of nodes was used to provide a node of symmetry at the center of the plate's width. The plate thickness, t, was set at $\frac{1}{51}$st of its width giving values of 0.1, 0.2, 0.4, 0.8, and 2.0 mm respectively. The plate's thickness was discretized by only

---

Contributed by the Heat Transfer Division for publication in the JOURNAL OF HEAT TRANSFER. Manuscript received by the Heat Transfer Division February 6, 1996; revision received September 30, 1996; Keywords: Conjugate Heat Transfer, Natural Convection, Numerical Methods. Associate Technical Editor: P. Simpkins.

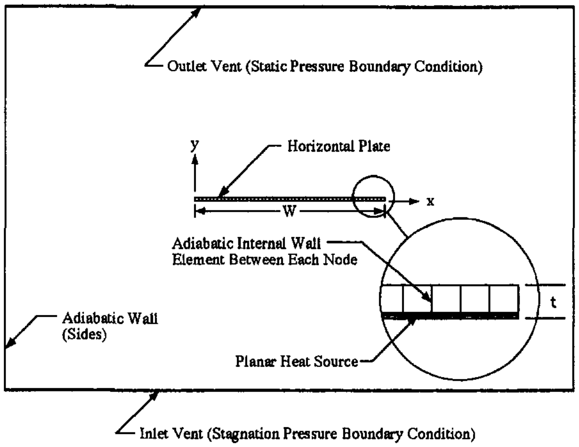

Fig. 1 CFD simulation model including the horizontal flat plate, heat source, and solution domain

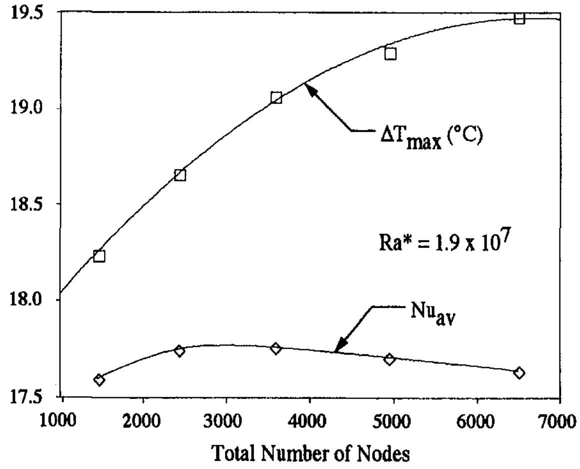

Fig. 2 Effects of grid refinement within the fluid on simulated temperature rise and average Nusselt number

one node. The plate was given a thermal conductivity of 30 *W/m*°C, approximately 1000 times larger than the thermal conductivity of the fluid which was nominally modeled as air. This resulted in the temperature drop within the plate (node to surface) being less than one percent of the total temperature drop between the plate node and the adjacent fluid node. This allowed the plate surface temperature needed in calculating the film coefficient to be well approximated by the plate node temperature. To prevent unwanted lateral conduction within the plate, adiabatic internal wall elements were centered between successive pairs of plate nodes (Fig. 1). Similar adiabatic wall elements were placed at each end of the plate to prevent convection from the plate ends. For cases where either an upward or downward facing heated plate were simulated, an adiabatic internal wall element was used to block convection from the opposite surface of the plate. Finally, the plate was heated by embedding a uniform heat source (heat per unit area) within it. This heat flux was the other parameter used to vary the value of the modified Rayleigh number. Typical values used for this parameter were 50, 100, 200, and 500 W/m^2.

Governing Equations. Assuming steady, laminar flow the governing equations for the fluid region of the model are:

Conservation of mass

$$\frac{\partial u}{\partial x} + \frac{\partial v}{\partial y} = 0 \tag{1}$$

Conservation of momentum

$$u\frac{\partial u}{\partial x} + v\frac{\partial u}{\partial y} = -\frac{1}{\rho}\frac{\partial p}{\partial x} + \nu\left(\frac{\partial^2 u}{\partial x^2} + \frac{\partial^2 u}{\partial y^2}\right) \tag{2}$$

$$u\frac{\partial v}{\partial x} + v\frac{\partial v}{\partial y} = g\beta(T - T_\infty) + \nu\left(\frac{\partial^2 v}{\partial x^2} + \frac{\partial^2 v}{\partial y^2}\right) \tag{3}$$

Conservation of energy

$$u\frac{\partial T}{\partial x} + v\frac{\partial T}{\partial y} = \alpha\left(\frac{\partial^2 T}{\partial x^2} + \frac{\partial^2 T}{\partial y^2}\right) \tag{4}$$

The governing equation within the solid plate is:

$$\frac{\partial^2 T}{\partial x^2} + \frac{\partial^2 T}{\partial y^2} + \frac{q^*/t}{k} = 0 \tag{5}$$

Boundary Conditions. A stagnation pressure and a uniform (ambient) temperature were imposed at the inlet vent, while a static pressure was applied to the outlet vent. No slip conditions were imposed at all solid boundaries. The exterior wall elements defining the edges of the solution domain were adiabatic.

Nomenclature

g = acceleration of gravity (m/s^2)
h = heat transfer coefficient (W/m^2-K)
k = thermal conductivity (W/m-K)
Nu = Nusselt number, hW/k
Pr = Prandtl Number
p = pressure (N/m^2)
q = uniform surface heat flux (W/m^2)
q^* = uniform heat generation rate per unit area (W/m^2)
q_x = local natural convection heat flux (W/m^2)
Ra* = modified Rayleigh number based on a uniform surface heat flux, Eq. (10)
Ra** = modified Rayleigh number based on uniform heat generation, Eq. (11)
T = temperature (°C)
T_∞ = bulk (ambient) fluid temperature (°C)
t = plate thickness (m)
W = plate width (m)
u = fluid velocity in x direction (m/s)
v = fluid velocity in y direction (m/s)
x = coordinate along the plate width, $x = 0$ at the plate's edge (m)
y = coordinate perpendicular to the plate width (m)

Greek Symbols

α = thermal diffusivity (m^2/s)
β = coefficient of thermal expansion (K^{-1})
ν = kinematic viscosity (m^2/s)
ρ = fluid density (kg/m^3)

Subscripts

av = average parameter value
down = lower plate surface
up = upper plate surface
x = local parameter value

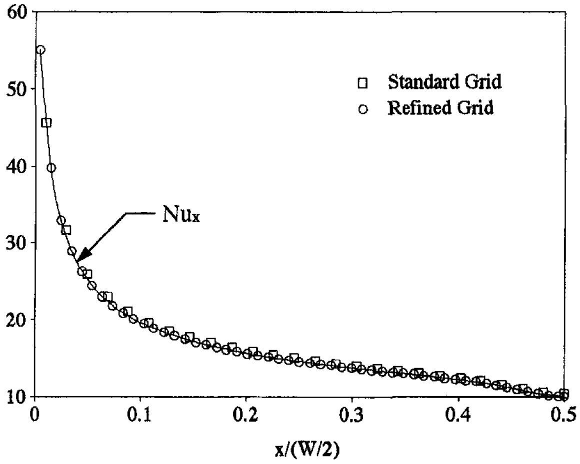

Fig. 3 Effect of grid refinement across the plate width on the simulated local Nusselt number

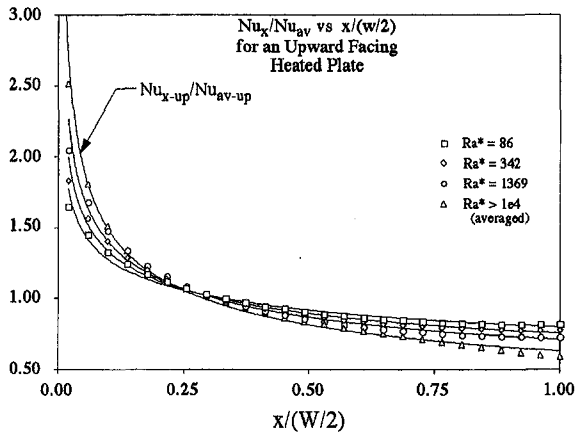

Fig. 5 Normalized local Nusselt number distribution across the plate width for a uniformly heated upward facing plate (uniform surface heat flux)

Discretization. An 83 × 43 node grid (3569 nodes) was utilized for the simulation work reported here. The grid was non-uniform, decreasing geometrically toward the ends and surfaces of the plate, resulting in an increasingly fine grid where large thermal and velocity gradients existed. At the plate surface the fluid grid thickness was approximately one-half the plate thickness, while at the plate ends the grid width was approximately equal to the plate thickness. Within the solid, however, the grid was uniform. A grid sensitivity study was performed by varying the grid within the fluid, with the results shown in Fig. 2. Comparisons were made with grids of 63 × 23 (1449 total nodes), 73 × 33 (2409), 93 × 53 (4929), and 103 × 63 (6489) nodes at a modified Rayleigh number, Ra* (defined below), of 1.9×10^7. Maximum temperature rise and average Nusselt number (also defined below) for each test case were compared to the results obtained from the finest grid. The coarsest grid yielded a temperature rise result 6.4 percent smaller and a Nusselt number result 0.22 percent smaller than the finest grid. The 83 × 43 grid yielded values 2.1 percent smaller and 0.7 percent larger, respectively, compared to the finest grid. Since this latter grid required approximately seven times less computational effort than the 103 × 63 grid, it was chosen as a good tradeoff between accuracy and computational time.

The effect of refining the grid within the solid was also investigated by doubling the number of grids laterally across the plate width. These results are shown in Fig. 3, with no significant change in local Nusselt numbers occurring from this refinement. Since no significant increase in accuracy was gained, the "standard" grid (51 lateral nodes) was utilized.

Data Reduction

For each simulation, temperature, and heat flux were recorded at each node along the plate width. Using this data, a local heat transfer coefficient and Nusselt number were calculated for each node as

$$h_x = q_x/(T_x - T_\infty) \tag{6}$$

and

$$\mathrm{Nu}_x = h_x W/k \tag{7}$$

For the cases where heat transfer occurred simultaneously from both plate surfaces, q_x in Eq. (6) became $q_{x\text{-up}}$ for the upper plate surface and $q_{x\text{-down}}$ for the lower surface. Similarly, h_x became $h_{x\text{-up}}$ and $h_{x\text{-down}}$ in Eq. (7). Use of the plate width, W, as the characteristic length instead of the local coordinate, x, was adopted by Sparrow and Carlson (1986) allowing the x-dependence of the Nusselt number to exhibit the same x-dependence as the local heat transfer coefficient. It will be used here to allow straightforward comparison with their data.

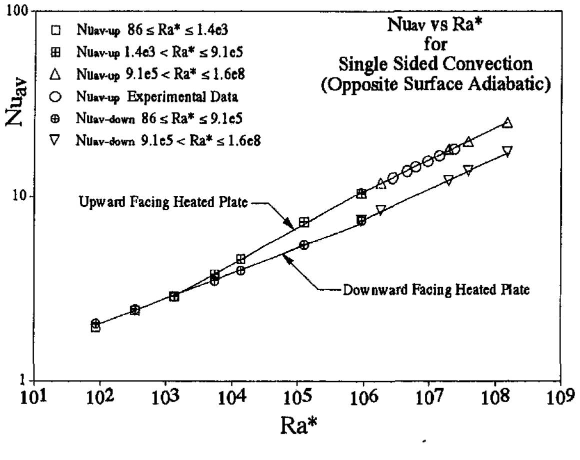

Fig. 4 Comparison of simulated and experimental Nusselt numbers for an upward facing uniformly heated plate and simulated results for a downward facing uniformly heated plate (uniform surface heat flux)

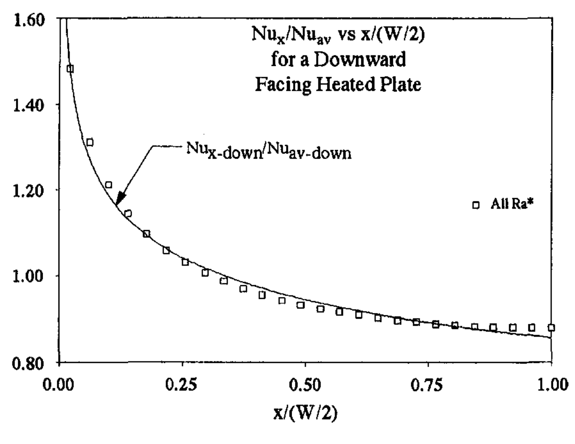

Fig. 6 Normalized local Nusselt number distribution across the plate width for a uniformly heated downward facing plate (uniform surface heat flux)

Table 1 Average Nusselt number correlation parameters for an upward facing heated plate (single sided convection)

Ra* Range	$Nu_{av\text{-}up} = C(Ra^*)^n$ Least Squares Fit		$Nu_{av\text{-}up} = C(Ra^*)^n$ Forced Slope	
	C	n	C	n
86 to $1.4x10^3$	1.060	0.138	1.030	1/7
$1.4x10^3$ to $9.1x10^5$	0.677	0.200	0.677	1/5
$9.1x10^5$ to $1.6x10^8$	1.013	0.170	1.076	1/6

Table 2 Local Nusselt number correlation parameters for an upward facing heated plate (single sided convection)

Ra*	$Nu_{x\text{-}up}/Nu_{av\text{-}up} = C[x/(W/2)]^n$	
	C	n
86	0.799	-0.203
342	0.755	-0.247
1369	0.709	-0.296
10^4 to $1.6x10^8$	0.630	-0.373

Table 3 Average Nusselt number correlation parameters for a downward facing heated plate (single sided convection)

Ra* Range	$Nu_{av\text{-}down} = C(Ra^*)^n$ Least Squares Fit		$Nu_{av\text{-}down} = C(Ra^*)^n$ Forced Slope	
	C	n	C	n
86 to $9.1x10^5$	1.060	0.140	1.033	1/7
$9.1x10^5$ to $1.6x10^8$	0.786	0.164	0.747	1/6

Table 4 Local Nusselt number correlation parameters for a downward facing heated plate (single sided convection)

Ra* Range	$Nu_{x\text{-}down}/Nu_{av\text{-}down} = C[x/(W/2)]^n$	
	C	n
86 to $1.6x10^8$	0.857	-0.142

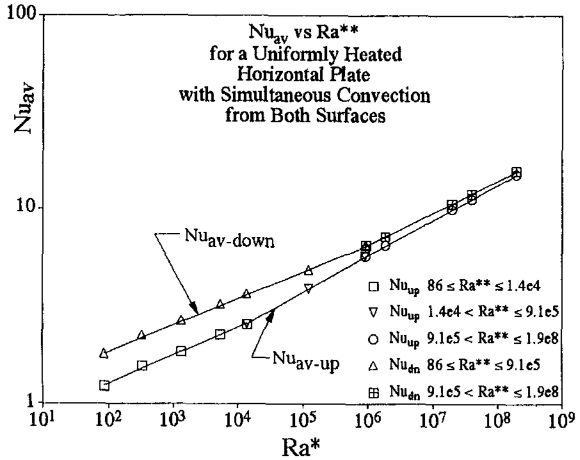

Fig. 7 Average Nusselt numbers for simultaneous convection from both surfaces of a uniformly heated horizontal flat plate

Average heat transfer coefficients and Nusselt numbers were then calculated from these local quantities as follows.

$$h_{av} = \frac{1}{W}\int_0^W h_x dx \qquad (8)$$

and

$$Nu_{av} = h_{av}W/k \qquad (9)$$

The Nusselt number will be parameterized in terms of a modified Rayleigh number, since a heat flux or heat generation rate was prescribed instead of a surface temperature. Two definitions of the modified Rayleigh number will be used in presenting these results. The first definition is given by:

$$Ra^* = \frac{g\beta q W^4}{\nu^2 k} Pr \qquad (10)$$

and is used where convection occurs from only one surface of the plate. The parameter q is a uniform surface heat flux.

For the simulations where convection occurs simultaneously from both upper and lower plate surfaces, the modified Rayleigh number will be redefined as

$$Ra^{**} = \frac{g\beta q^* W^4}{\nu^2 k} Pr \qquad (11)$$

where q^* is the uniform heat generation rate per unit area within the plate. For this case, summation of both surface heat fluxes at a location x is equal to q^*. Equation (10) is actually a special case of Eq. (11) since a uniform heat generation rate results in a uniform surface heat flux when convection occurs from only one plate surface.

Results and Discussion

Convection from a Single Plate Surface. The first task performed in this study was a comparison of simulation results to the experimental data obtained by Sparrow and Carlson (1986) for an upward facing uniformly heated horizontal plate. Here, the modified Rayleigh number, Ra*, is utilized. Sparrow and Carlson's data resulted in the correlation

$$Nu_{av} = 1.07(Ra^*)^{1/6} \quad \text{for}$$

$$2.7 \times 10^6 \le Ra^* \le 2.3 \times 10^7 \qquad (12)$$

Their results are shown along with the CFD results in Fig. 4. Excellent agreement was obtained between simulated and

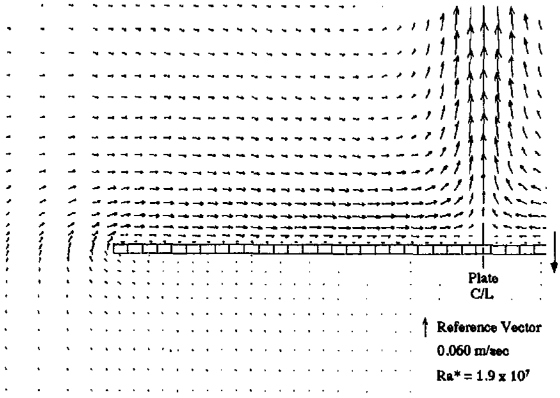

Fig. 8 Velocity vectors for an upward facing uniformly heated plate (adiabatic lower surface)

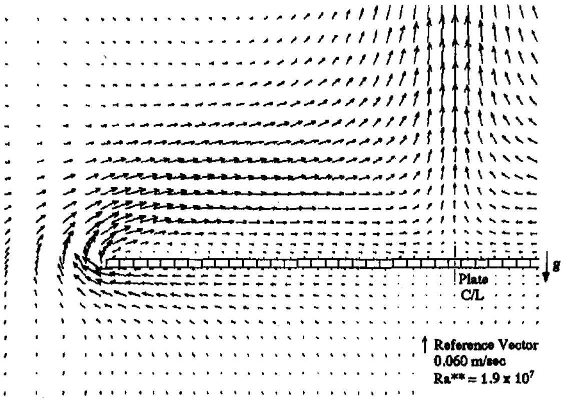

Fig. 9 Velocity vectors for simultaneous convection from both upper and lower surfaces of a uniformly heated horizontal plate

experimental results, with the CFD code giving a least squares fit correlation of

$$\mathrm{Nu}_{av} = 1.013(\mathrm{Ra}^*)^{0.170} \quad \text{for} \quad 9.1 \times 10^5 \leq \mathrm{Ra}^* \leq 1.6 \times 10^8 \quad (13)$$

Forcing a slope of $\frac{1}{6}$ to match the experimental data gives

$$\mathrm{Nu}_{av} = 1.076(\mathrm{Ra}^*)^{1/6} \quad \text{for} \quad 9.1 \times 10^5 \leq \mathrm{Ra}^* \leq 1.6 \times 10^8 \quad (14)$$

Simulated results are within one percent of the experimental data. While limited in range, the CFD code is seen to make excellent predictions with available experimental data. Unfortunately, no experimental data exists (to the authors' knowledge) for a downward facing isoflux plate to confirm the CFD code's ability to correctly simulate this orientation.

Simulation results for single sided convection were extended downward to a modified Rayleigh number of 86 as shown in Fig. 4. The Nusselt numbers exhibit interesting behavior below a modified Rayleigh number of approximately 10^6. The slopes of the curves change below this value, with the upward facing plate increasing from approximately a $\frac{1}{6}$ to a $\frac{1}{5}$-power dependence on the modified Rayleigh number; while the downward facing plate decreases from a $\frac{1}{6}$ to a $\frac{1}{7}$-power dependence. These curves intersect at a modified Rayleigh number of about 1400, and remain nearly coincident below this value with both curves exhibiting a $\frac{1}{7}$ power dependence. These results suggest that a conduction limit has been reached where upward/downward orientation is no longer important.

Behavior of local Nusselt numbers for upward and downward facing plates are shown in Figs. 5 and 6 respectively. Local Nusselt numbers have been normalized by their corresponding average Nusselt number, giving the ratio $\mathrm{Nu}_x/\mathrm{Nu}_{av}$, which is plotted against the dimensionless plate coordinate $x/(W/2)$, where x is measured from the edge of the plate towards the plate centerline. For modified Rayleigh numbers greater than approximately 10^4 on the upward facing plate, $\mathrm{Nu}_x/\mathrm{Nu}_{av}$ is nearly independent of Ra^*, with $\mathrm{Nu}_x/\mathrm{Nu}_{av}$ exhibiting approximately a minus $\frac{1}{3}$-power dependence (-0.373) on $x/(W/2)$. This closely agrees with the findings of Sparrow and Carlson (1986). For modified Rayleigh numbers less than 10^4, the normalized local Nusselt number shows dependence on Ra^*. At $\mathrm{Ra}^* = 86$, $\mathrm{Nu}_x/\mathrm{Nu}_{av}$ varies with approximately a minus $\frac{1}{5}$-power dependence on $x/(W/2)$. For the downward facing plate (Fig. 7), $\mathrm{Nu}_x/\mathrm{Nu}_{av}$ was independent of Ra^*, exhibiting a minus $\frac{1}{7}$-power dependence (-0.142) with $x/(W/2)$ for all cases simulated.

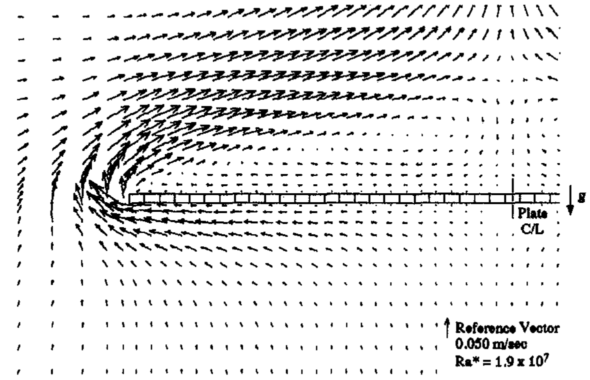

Fig. 10 Velocity vectors for a downward facing uniformly heated plate (adiabatic upper surface)

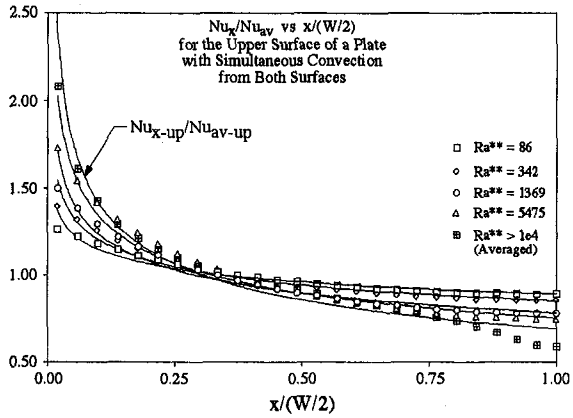

Fig. 11 Normalized local Nusselt number distribution across the upper surface of a uniformly heated horizontal plate with simultaneous convection from both upper and lower surfaces

Tables 1–4 list correlation parameters (coefficients and exponents) for single sided convection. For average Nusselt numbers (Tables 1 and 3) both least square fit and forced slope (fractional exponent) parameters are listed.

Simultaneous Convection from Both Plate Surfaces. Figure 7 shows average Nusselt numbers versus modified Rayleigh numbers, Ra**, for simultaneous convection from both surfaces. The average Nusselt number on the lower surface is now larger than the corresponding Nusselt number on the upper surface, with the ratio of lower to upper Nusselt numbers varying from approximately 1.45 at a modified Rayleigh number of

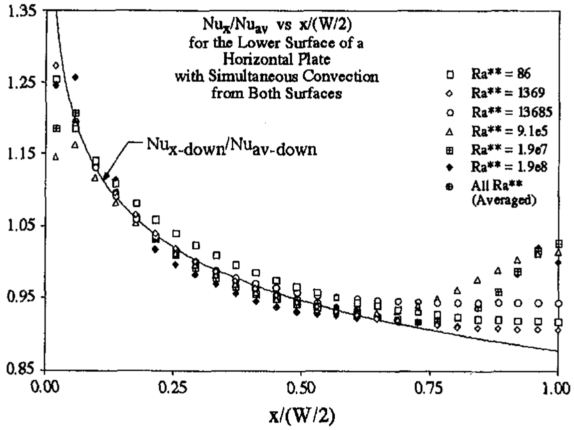

Fig. 12 Normalized local Nusselt number distribution across the lower surface of a uniformly heated horizontal plate with simultaneous convection from both upper and lower surfaces

Table 5 Average Nusselt number correlation parameters for the upper surface of a heated plate with simultaneous convection from both surfaces (double sided convection)

Ra* Range	$Nu_{av\text{-}up} = C(Ra^*)^n$ Least Squares Fit		$Nu_{av\text{-}up} = C(Ra^*)^n$ Forced Slope	
	C	n	C	n
86 to $1.4\text{x}10^4$	0.653	0.143	0.653	1/7
$1.4\text{x}10^4$ to $9.1\text{x}10^5$	0.418	0.189	0.367	1/5
$9.1\text{x}10^5$ to $1.9\text{x}10^8$	0.470	0.181	0.608	1/6

86 to 1.05 for the largest modified Rayleigh number simulated. This large decrease in upper surface Nusselt numbers results from the fluid being preheated as it flows along the bottom surface increasing its buoyancy which in turn causes a thickening of the upper surface boundary layer. Qualitatively this can be seen by comparing Figs. 8 and 9 which show vector plot outputs from the CFD software for an upward facing heated plate and a heated plate with simultaneous convection respectively. A similar plot for a downward facing heated plate is also presented in Fig. 10 to show the flow field for this orientation. For the upper surface, Nu_{av} decreases by an average of about 42 percent when convection is allowed to occur from both surfaces, while for the lower surface, Nu_{av} decreases by an average of about 15 percent.

Normalized local Nusselt numbers for upper and lower surfaces are shown in Figs. 11 and 12 respectively. At increasingly high values of Ra** where the flow rates become larger, a localized decrease in the upper surface Nusselt number along with a complementary increase in the lower surface Nusselt number becomes increasingly noticeable near the plate centerline. This occurs due to a thickening of the boundary layer on the upper surface where the inward flows collide forming the plume along with a thinning of the lower surface boundary layer where the outward flows divide. For the upper surface, the normalized Nusselt numbers are relatively independent of Ra** values greater than approximately 10^4. Above this value of Ra**, Nu_x/Nu_{av} varies with approximately a minus $\frac{1}{3}$-power dependence (-0.312) on $x/(W/2)$. For modified Rayleigh numbers below 10^4, the local Nusselt number again shows dependency on Ra**. For the lower surface, local Nusselt numbers show a decreased x dependence compared to the data for the downward facing heated plate. Ignoring the rise in the Nusselt number at the plate's center at large modified Rayleigh numbers, Nu_x/Nu_{av} can be reasonably well characterized by a single curve for all values of Ra** with a minus $\frac{1}{9}$-power dependence (-0.110) on $x/(W/2)$.

Tables 5 through 8 list correlation parameters for simultaneous convection from both surfaces.

Temperature Distribution Across The Plate Surface. Figure 13 shows temperature rise across the plate width for both single and double sided convection at a modified Rayleigh number of 1.9×10^7. Here, ΔT follows approximately a $\frac{1}{3}$ power law with $x/(W/2)$ for the upward facing heated plate, a $\frac{1}{7}$ power law for the downward facing heated plate, and a $\frac{1}{5}$ power law for both sides convecting. These slopes hold for $Ra^* > \sim 10^3$ for the upward facing heated plate, all Ra* for the downward facing heated plate, and $Ra^{**} \geq \sim 10^5$ for double sided convection, with the slopes decreasing below these values.

Table 6 Local Nusselt number correlation parameters for the upper surface of a heated plate with simultaneous convection from both surfaces (double sided convection)

Ra*	$Nu_{x\text{-}up}/Nu_{av\text{-}up} = C[x/(W/2)]^n$	
	C	n
86	0.891	-0.110
342	0.850	-0.152
1369	0.782	-0.199
5475	0.753	-0.252
10^4 to $1.9\text{x}10^8$	0.690	-0.312

Table 7 Average Nusselt number correlation parameters for the lower surface of a heated plate with simultaneous convection from both surfaces (double sided convection)

Ra* Range	$Nu_{av\text{-}down} = C(Ra^*)^n$ Least Squares Fit		$Nu_{av\text{-}down} = C(Ra^*)^n$ Forced Slope	
	C	n	C	n
86 to $9.1\text{x}10^5$	0.979	0.137	0.922	1/7
$9.1\text{x}10^5$ to $1.9\text{x}10^8$	0.654	0.166	0.654	1/6

Extending the Results—Additional Work. These results are of limited value since they were derived for two-dimensional models. It may be possible to extend these results by reformulating them using a characteristic length, Lc, applicable to three-dimensional geometry. A likely choice would be the ratio of plate area to perimeter suggested by Lloyd and Moran (1974). For an infinitely long plate this definition yields $W/2$ (in lieu of W used in this paper). Assuming the correlation slope (exponent), n, is unaffected by the transformation, the correlation coefficient, C, for average Nusselt numbers is transformed from W to $W/2$ by the following equation.

$$C_{Lc=W/2=A/P} = 2^{4n-1} \cdot C_{Lc=W} \tag{15}$$

Equation 15 is specific for the transformation from W to $W/2$ and does not represent a generalized equation. Also, remember that both Rayleigh and Nusselt numbers are affected by the change in characteristic length. The authors would caution against applying the local correlations to three-dimensional problems since the local flow conditions will have added complexities.

Perhaps the real importance of this present work is not in the presentation of these limited two-dimensional correlations, but instead is in showing that the current practice of simultaneously applying upward facing and downward facing single sided correlations is incorrect, and that additional (three-dimensional) double sided convection correlations need to be developed. The authors would also like to encourage the academic community to undertake the difficult task of verifying such results experimentally.

Conclusions

Numerical simulations of natural convection heat transfer simultaneously occurring from both upper and lower surfaces of a uniformly heated horizontal plate were conducted. Results were obtained for local and average Nusselt numbers over a range of modified Rayleigh numbers of 86 to 1.9×10^8. Plate width and heat generation rate were varied in these simulations.

Table 8 Local Nusselt number correlation parameters for the lower surface of a heated plate with simultaneous convection from both surfaces (double sided convection)

Ra* Range	$Nu_{x\text{-}down}/Nu_{av\text{-}down} = C[x/(W/2)]^n$	
	C	n
86 to $1.9\text{x}10^8$	0.877	-0.110

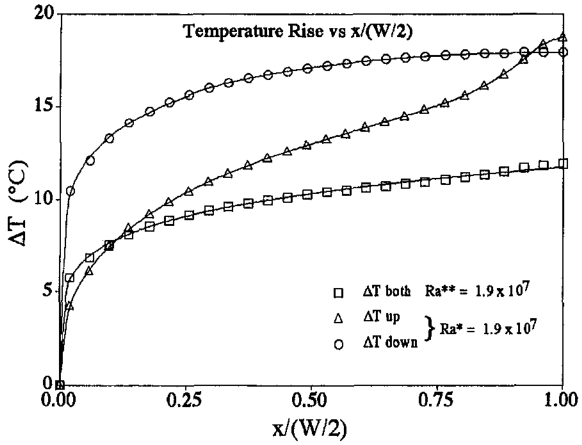

Fig. 13 Temperature rise distribution across the plate surface for both single and double sided convection

Results were also obtained for a uniformly heated upward facing horizontal plate primarily as a means of calibrating the software to experimental data, and secondarily to extend the results to lower modified Rayleigh numbers. A third set of results was gathered on a uniformly heated downward facing plate for comparative purposes with the above results.

This work shows, perhaps for the first time, that strong coupling effects exist between upper and lower surfaces of thin horizontally oriented plates experiencing concurrent heat transfer from both surfaces. Simultaneous convection from both plate surfaces had a major effect on upper surface Nusselt numbers compared to convection from only the heated upper surface.

$Nu_{av\text{-up}}$ decreased by an average of 42 percent for convection from both surfaces compared to convection occurring from only the heated upper surface. $Nu_{av\text{-down}}$ was also depressed by an average of 15 percent on the lower surface for simultaneous convection compared to convection from just the heated lower surface.

The local Nusselt number, Nu_x, was observed to decrease by power law variations from the edge to the center of the plate. For the upper surface, Nu_x/Nu_{av} decreased by approximately $x/(W/2)$ to the minus $\frac{1}{3}$-power for modified Rayleigh numbers, Ra**, greater than 10^4. For smaller values of Ra**, the power dependence decreased with decreasing modified Rayleigh number. For the lower surface, Nu_x/Nu_{av} decreased by approximately $x/(W/2)$ to the minus $\frac{1}{9}$-power for all modified Rayleigh numbers simulated.

References

''FLOTHERM Reference Manual,'' 1994, Flomerics Limited, Kingston-Upon-Thames, Surrey, England.

Goldstein, R. J., Sparrow, E. M., and Jones, D. C., 1973, ''Natural Convection Mass Transfer Adjacent to Horizontal Plates,'' *Int. J. Heat Mass Transfer,* Vol. 16, pp. 1025–1035.

Lloyd, J. R., and Moran, W. R., 1974, ''Natural Convection Adjacent to Horizontal Surface of Various Planforms,'' JOURNAL OF HEAT TRANSFER, Vol. 96, pp. 443–447.

McAdams, W. H., 1954, *Heat Transmission,* 3rd ed., McGraw-Hill, New York.

Patankar, S. V., 1980, *Numerical Heat Transfer and Fluid Flow,* Hemisphere Publishing Corporation, New York.

Sparrow, E. M., and Carlson, C. K., 1986, ''Local and Average Natural Convection Nusselt Numbers for a Uniformly Heated, Shrouded or Unshrouded Horizontal Plate,'' *Int. J. Heat Mass Transfer,* Vol. 29, No. 3, pp. 369–379.

Chi-chuan Wang
Energy & Resources Laboratories,
Industrial Technology Research Institute,
D200 ERL/ITRI,
Bldg. 64. 195-6 Section 4,
Chung Hsing Road,
Chutung, 310, Hsinchu, Taiwan
f781058@erlb.erl.itri.org.tw

Yi-chung Hsieh

Yur-tsai Lin

Yuan-Ze Institute of Technology
Chungli, Taiwan

Performance of Plate Finned Tube Heat Exchangers Under Dehumidifying Conditions

Systematic studies of continuous fin-and-tube tube heat exchangers under dehumidifying conditions are reported in the present study. The heat exchangers consist of nine fin-and-tube heat exchangers having plane fins. The effects of fin spacing, the number of tube row, and inlet conditions are investigated. Data are presented in terms of j *factors and friction factors* f. *It is found that the inconsistencies in the open literature may be associated with the wet fin efficiency. A correlation is proposed for the present plate fin configuration; this correlation can describe 92 percent of* j, *and 91 percent of the* f *data within ±10 percent.*

Introduction

In the evaporators of air-conditioning equipment, which typically use aluminum fins, the surface temperature of the fins is generally below the dew point temperature. As a result, moisture is condensed on the fins. Since the water condensate has a high contact angle on the aluminum fins, the water may adhere as droplets causing bridging between the fins, and increasing air pressure drop. In general, the complexity of the air flow pattern across the dehumidifying coils makes the theoretical simulations very difficult. Accordingly, it is necessary to resort to experimentation.

Many experimental studies have been carried out to study the heat and mass transfer characteristics of the dehumidifying heat exchangers. For instance, McQuiston (1978a, 1978b) presents experimental data for five plate fin-and-tube heat exchangers, and presents a well-known heat transfer and friction correlation for both dry and wet surfaces. Mirth and Ramadhyani (1993, 1994) investigated the heat and mass characteristics of wavy fin heat exchangers. Their results showed that the Nusselt numbers were very sensitive to change of inlet dew point temperatures, and the Nusselt number decreases with an increase of dew point temperatures. Similar results were reported by Fu et al. (1995) in dehumidifying heat exchangers having a louver fin configuration. They reported a pronounced decrease of the wet sensible heat transfer coefficients with increases of inlet relative humidity. On the contrary, the experimental data of Seshimo et al. (1988) indicated that the Nusselt number was relatively independent of inlet conditions.

Even though many efforts have been devoted to the study of the wet-coils, the available literature on the dehumidifying heat exchangers still offers limited information to assist the designer in sizing and rating a fin-and-tube heat exchanger. It appears that the design process for such coils is based on proprietary heat transfer and pressure drop for a specified coil configuration. In addition, systematic investigations of the effect of fin spacing, the number of tube row, and the inlet conditions of the heat transfer characteristics under dehumidification are rare. Therefore, the objective of the present study is to provide systematic experimental information on the air-side performance of fin-and-tube heat exchangers under dehumidifying conditions. The effects of inlet conditions, fin spacing, and the number of tube rows on the heat transfer characteristics are examined in this study. The experimental data are obtained using the plain fin-and-tube heat exchangers described in Table 1. The test fin-and-tube heat exchangers are tension wrapped, having a "*L*" type fin collar. The test conditions of the inlet air are as follows:

Dry-bulb temperatures of the air:	27 ± 0.5°C
Inlet relative humidity for the incoming air:	50 and 90%
Inlet air velocity:	From 0.3 to 4.5 m/s
Inlet water temperature:	7 ± 0.5°C
Water velocity inside the tube:	1.5~1.7 m/s

The test conditions approximate those encountered with typical fan-coils and evaporators of air-conditioning applications.

Experimental Apparatus

The schematic diagram of the experimental air circuit assembly is shown in Fig. 1. It consists of a closed-loop wind tunnel in which air is circulated by a variable speed centrifugal fan (7.46 kW, 10 HP). The air duct is made of galvanized sheet steel and has an 850 mm × 550 mm cross-section. The dry-bulb and wet-bulb temperatures of the inlet air are controlled by an air-ventilator that can provide a cooling capacity up to 21.12 kW (6RT). The air flow-rate measurement station is an outlet chamber set up with multiple nozzles. This setup is based on the ASHRAE 41.2 standard (1987). A differential pressure transducer is used to measure the pressure difference across the nozzles. The air temperatures at the inlet and exit zones across the sample heat exchangers are measured by two psychometric boxes based on the ASHRAE 41.1 standard (1986).

The working medium on the tube side is cold water. A thermostatically controlled reservoir provides the cold water at selected temperatures. The temperature differences on the water side are measured by two precalibrated RTDs. The water volumetric flow rate is measured by a magnetic flow meter with a ±0.001 L/s precision. All the temperature measuring probes are resistance temperature devices (Pt100), with a calibrated accuracy of ±0.05°C. In the experiments, only the data that satisfy the ASHRAE 33-78 (1978) requirements, (namely, the energy balance condition, $|\dot{Q}_w - \dot{Q}_{avg}|/\dot{Q}_{avg}$, is less than 0.05, where $\dot{Q}_w$ is the water-side heat transfer rate and $\dot{Q}_{avg}$ is the mathematical average heat transfer rate for $\dot{Q}_w$ and air-side heat transfer rate $\dot{Q}_a$), are considered in the final analysis. Uncertainties reported in the present investigation, following the single-sample analysis proposed by Moffat (1989), are tabulated in Table 2.

Analysis

Basically, the present reduction method is the Threlkeld (1970) method. Details of the reduction process can be de-

---

Contributed by the Heat Transfer Division for publication in the JOURNAL OF HEAT TRANSFER. Manuscript received by the Heat Transfer Division May 16, 1996; revision received October 30, 1996; Keywords: Augmentation & Enhancement, Finned Surfaces, Heat Exchangers. Associate Technical Editor: T. Rabas.

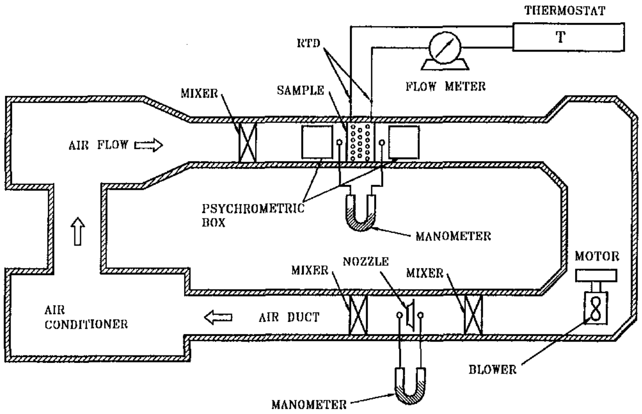

Fig. 1 Schematic of experimental setup

scribed as follows: the total heat transfer rate used in the calculation is the mathematical average of $\dot{Q}_a$ and $\dot{Q}_w$, namely,

$$\dot{Q}_a = \dot{m}_a(i_{a,\text{in}} - i_{a,\text{out}}) \tag{1}$$

$$\dot{Q}_w = \dot{m}_w C_{pw}(T_{w,\text{out}} - T_{w,\text{in}}) \tag{2}$$

$$\dot{Q}_{\text{avg}} = (\dot{Q}_a + \dot{Q}_w)/2 \tag{3}$$

The overall heat transfer coefficient, $U_{o,w}$, is based on the enthalpy potential and is given as follows:

$$\dot{Q}_{\text{avg}} = U_{o,w} A_o F \Delta i_m \tag{4}$$

where Δi_m is the mean enthalpy difference for counter flow coil, according to Bump (1963) and Myers (1967), and is defined as

$$\Delta i_m = i_{a,\text{in}} + \frac{(i_{a,\text{in}} - i_{a,\text{out}})}{\ln\left(\dfrac{i_{a,\text{in}} - i_{r,\text{out}}}{i_{a,\text{out}} - i_{r,\text{in}}}\right)} - \frac{(i_{a,\text{in}} - i_{a,\text{out}})(i_{a,\text{in}} - i_{r,\text{out}})}{(i_{a,\text{in}} - i_{r,\text{out}}) - (i_{a,\text{out}} - i_{r,\text{in}})}. \tag{5}$$

F is the correction factor accounting for the present cross-flow unmixed/unmixed configuration. The overall heat transfer coefficient is related to the individual heat transfer resistance (Myers, 1967) as follows:

$$\frac{1}{U_{o,w}} = \frac{b'_r A_o}{h_i A_{p,i}} + \frac{b'_p x_p A_o}{k_p A_{p,m}} + \frac{1}{h_{o,w}\left(\dfrac{A_{p,o}}{b'_{w,p} A_o} + \dfrac{A_f \eta_{f,\text{wet}}}{b'_{w,m} A_o}\right)} \tag{6}$$

where

$$h_{o,w} = \frac{1}{\dfrac{C_{p,a}}{b'_{w,m} h_{c,o}} + \dfrac{y_w}{k_w}} \tag{7}$$

and y_w in Eq. (7) is the thickness of the water film. A constant of 0.005 inch was proposed by Myers (1967). In practice, (y_w/k_w) accounts for only 0.5 ~ 5 percent compared to $(C_{p,a}/b'_{w,m} h_{c,o})$, and has often been neglected by previous investigators. As a result, this term is not included in the final analy-

Nomenclature

$A_{\min}$ = minimum free flow area
A_o = total surface area
$A_{p,i}$ = inside surface area of tubes
$A_{p,m}$ = mean heat transfer area of tubes
$A_{p,o}$ = outer surface area of tubes
b'_p = slope of a straight line between the outside and inside tube wall temperatures
b'_r = slope of the air saturation curved at the mean coolant temperature
$b'_{w,m}$ = slope of the air saturation curve at the mean water film temperature of the external surface
$b'_{w,p}$ = slope of the air saturation curve at the mean water film temperature of the primary surface
C = parameter
$C_{p,a}$ = moist air specific heat at constant pressure
$C_{p,w}$ = water specific heat at constant pressure
D_c = tube outside diameter, include collar
D_i = tube inside diameter
f = friction factor
f_i = in-tube friction factors of water
F = correction factor
F_p = fin pitch
$G_{\max}$ = maximum mass velocity based on minimum flow area
$h_{c,o}$ = sensible heat transfer coefficient for wet coils
h_i = inside heat transfer coefficient
$h_{o,w}$ = total heat transfer coefficient for wet external fin
I_0 = modified Bessel function solution of the first kind, order 0
I_1 = modified Bessel function solution of the first kind, order 1
i = air enthalpy
$i_{a,\text{in}}$ = inlet air enthalpy
$i_{a,\text{out}}$ = outlet air enthalpy
i_{fg} = latent heat of water vapor
$i_{r,m}$ = saturated air enthalpy at the mean refrigerant temperature
$i_{r,\text{in}}$ = saturated air enthalpy at the inlet of refrigerant temperature
$i_{r,\text{out}}$ = saturated air enthalpy at the outlet of refrigerant temperature
$i_{s,fm}$ = saturated air enthalpy at the fin mean temperature
$i_{s,fb}$ = saturated air enthalpy at the fin base temperature
$i_{s,p,i,m}$ = saturated air enthalpy at the mean inside tube wall temperature
$i_{s,p,o,m}$ = saturated air enthalpy at the mean outside tube wall temperature
$i_{s,w,m}$ = saturated air enthalpy at the mean water film temperature of the external surface
Δi = mean enthalpy difference
j = the Colburn factor
j_4 = the Colburn factor for four-row coil
j_N = the Colburn factor for a coil does not have four row
K_0 = modified Bessel function solution of the second kind, order 0
K_1 = modified Bessel function solution of the second kind, order 1
K_c = abrupt contraction pressure-loss coefficient
K_e = abrupt expansion pressure-loss coefficient
k_f = thermal conductivity of fin
k_p = thermal conductivity of tube
k_w = thermal conductivity of water
l = fin length
m = parameter
$\dot{m}_a$ = air mass flow rate
$\dot{m}_w$ = water mass flow rate
N = the number of tube row
P = circumference of the fin
ΔP = pressure drop
P_l = longitudinal tube pitch
Pr = Prandtl number
P_t = transverse tube pitch
$\dot{Q}_{\text{avg}}$ = mathematical average heat transfer rate for $\dot{Q}_w$ and air side heat transfer rate $\dot{Q}_a$
$\dot{Q}_a$ = air side heat transfer rate
$\dot{Q}_w$ = water side heat transfer rate
r_i = distance from the center of the tube to the fin base
r_o = distance from the center of the tube to the fin tip

Table 1 Geometric dimensions of the sample plate fin-and-tube heat exchangers

No.	Fin Thickness (mm)	Fp (mm)	Dc (mm)	P_t(mm)	P_l(mm)	Row No
1	0.13	1.82	10.23	25.4	22	2
2	0.13	2.24	10.23	25.4	22	2
3	0.13	3.20	10.23	25.4	22	2
4	0.13	2.03	10.23	25.4	22	4
5	0.13	2.23	10.23	25.4	22	4
6	0.13	3.00	10.23	25.4	22	4
7	0.13	1.85	10.23	25.4	22	6
8	0.13	2.21	10.23	25.4	22	6
9	0.13	3.16	10.23	25.4	22	6

Note: Tube wall thickness after expansion: 0.336 mm.
The test samples are all staggered layout.
Contact resistance provided by the manufacturer is always less than 3% of the total resistance throughout the test range, and is neglected in the reduction.

Table 2 Summary of estimated uncertainties

Primary Measurements		Derived Quantities		
Parameter	Uncertainty	Parameter	Uncertainty Re_{Dc} =400	Uncertainty Re_{Dc}=5000
$\dot{m}_{air}$	0.3-1%	Re_{Dc}	±1.0%	±0.57%
$\dot{m}_w$	0.5%	Re_{Di}	±0.73%	±0.73%
ΔP	0.5%	f	±15.7%	±2.2%
T_w	0.05°C	$\dot{Q}_w$	±3.95%	±1.22%
T_a	0.1°C	$\dot{Q}_a$	±5.5%	±2.4%
T	0.1 °C	j	±11.4%	±5.9%

sis. The tube-side heat transfer coefficient, h_i, is evaluated with the Gnielinski correlation (Gnielinski, 1976) where

$$h_i = \frac{(f_i/2)(\mathrm{Re}_{Di} - 1000)\,\mathrm{Pr}}{1.07 + 12.7\sqrt{f_i/2}\,(\mathrm{Pr}^{2/3} - 1)} \cdot \frac{k_i}{D_i} \tag{8}$$

and the friction factor, f_i, is obtained with

$$f_i = \frac{1}{(1.58 \ln \mathrm{Re}_{D_i} - 3.28)^2}. \tag{9}$$

The Reynolds number used in Eq. (8) is based on the inside diameter of the tube and $\mathrm{Re}_i = \rho V D_i/\mu$. In all cases, the water side resistance is less than ten percent of the overall resistance.

In Eq. (7) there are four quantities ($b'_{w,m}$, $b'_{w,p}$, b'_p, and b'_r) involving enthalpy-temperature ratios that must be evaluated. The quantities of b'_p and b'_r can be calculated as

$$b'_r = \frac{i_{s,p,i,m} - i_{r,m}}{T_{p,i,m} - T_{r,m}} \tag{10}$$

$$b'_p = \frac{i_{s,p,o,m} - i_{s,p,i,m}}{T_{p,o,m} - T_{p,i,m}}. \tag{11}$$

The values of $b'_{w,p}$ and $b'_{w,m}$ are the slope of saturated enthalpy curve evaluated at the outer mean water film temperature at the base surface and at the fin surface. Without loss of generality, $b'_{w,p}$ can be approximated by the slope of saturated enthalpy curve evaluated at the base surface temperature. Unfortunately, there is no explicit way to evaluate $b'_{w,m}$ and it must be determined by trial and error procedures. The evaluation procedure is as follows:

1 Assume a value of $T_{w,m}$, and determine its corresponding value of $b'_{w,m}$.
2 Obtain the overall heat transfer coefficient, $h_{o,w}$, from Eq. (6).
3 Calculate the $i_{s,w,m}$ using the following equation:

$$i_{s,w,m} = i - \frac{C_{p,a} h_{o,w} \eta_{f,\mathrm{wet}}}{b'_{w,m} h_{c,o}} \times \left(1 - U_{o,w} A_o \left[\frac{b'_r}{h_i A_{p,i}} + \frac{x_p b'_p}{k_p A_{p,m}}\right]\right)(i - i_{r,m}). \tag{12}$$

4 Determine $T_{w,m}$ at $i_{s,w,m}$. If it is not equal to the assumed value, assume a new value and repeat the procedure.

Determination of Wet Fin Efficiency η_{wet}

The determination of wet fin efficiency is quite ambiguous based on information presented from previous publications. McQuiston (1975) developed an approximation for wet fin efficiency for the case of a plane fin (Fig. 2(*a*)). McQuiston and Parker (1994) extended the analysis to circular fins (Fig. 2(*b*)) using the approximation proposed by Schmidt (1949). The fin efficiency is given as

$$\eta_f = \frac{\tanh M_m r_i \theta}{M_m r_i \theta} \tag{13}$$

where

$$M_m^2 = \frac{h_{c,o} P}{kA}\left(1 + \frac{C i_{fg}}{C_p}\right) \tag{14}$$

$$\theta = \left(\frac{r_o}{r_i} - 1\right)\left[1 + 0.35 \ln\left(\frac{r_o}{r_i}\right)\right] \tag{15}$$

and the constant C in Eq. (14) is given by

$$C = \frac{W_a - W_{\mathrm{wall}}}{T_a - T_{\mathrm{wall}}}. \tag{16}$$

Following the approximation (Eq. 16) proposed by McQuiston (1975), Hong and Webb (1996) derived the analytical formulation of wet surface for circular fins as (Fig. 2(*b*))

Nomenclature (cont.)

Re_{Di} = Reynolds number based on inside diameter
Re_{Dc} = Reynolds number based on D_c
RT = refrigeration tons
S = number of sectors
T = temperature
$T_{w,m}$ = mean temperature of the water film
$T_{w,\mathrm{in}}$ = water temperature of at the tube inlet
$T_{w,\mathrm{out}}$ = water temperature of at the tube outlet
$T_{p,i,m}$ = mean temperature of the inner tube wall
$T_{p,o,m}$ = mean temperature of the outer tube wall
$T_{r,m}$ = mean temperature of refrigerant coolant
$U_{o,w}$ = overall heat transfer coefficient
W = humidity ratio
x_p = thickness of tube wall
y_w = thickness of condensate water film
ϵ = fining factor
δ = fin thickness
η_{circular} = fin efficiency of a dry circular fin
$\eta_{\mathrm{circular,wet}}$ = fin efficiency of a wet circular fin
η_f = fin efficiency
$\eta_{f,\mathrm{wet}}$ = wet fin efficiency
η_i = fin efficiency of a sector
μ = dynamic viscosity of water
ϕ = relative humidity
ρ_i = mass density of inlet air
ρ_o = mass density of outlet air
ρ_m = mean mass density of air
σ = contraction ratio

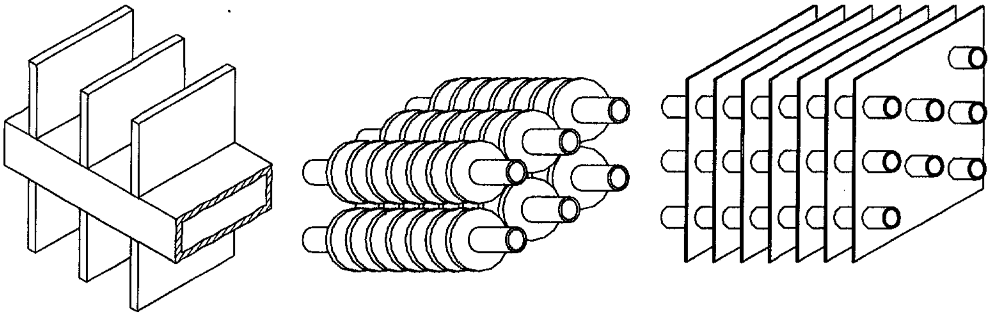
(a) Straight fin (b) Circular fin (c) Continuous plate fin

Fig. 2 Type of fin configuration

$$\eta_{\text{circular}} = \frac{2r_i}{M_m(r_o^2 - r_i^2)} \times \left[\frac{K_1(M_m r_i)I_1(M_m r_o) - K_1(M_m r_o)I_1(M_m r_i)}{K_1(M_m r_o)I_0(M_m r_i) + K_0(M_m r_i)I_1(M_m r_o)}\right] \quad (17)$$

where

$$M_m = \sqrt{\frac{2h_{c,o}}{k_f\delta}\left(1 + \frac{i_{fg}}{C_{p,a}}C\right)} = m\sqrt{\left(1 + \frac{i_{fg}}{C_{p,a}}C\right)} \quad (18)$$

and

$$m = \sqrt{\frac{2h_{c,o}}{k_f\delta}}. \quad (19)$$

In their calculations, Hong and Webb (1996) concluded that the empirical approximation of Schmidt (1949) for a circular fin might give errors over ten percent.

The present study adopts the basic formulation proposed by Threlkeld (1970). However, the original formulation of the wet fin efficiency by Threlkeld (1970) was for straight fin configuration (Fig. 2(*a*)). For a circular fin (Fig. 2(*b*)), we have derived its corresponding wet fin efficiency formula

$$\eta_{\text{circular,wet}} = \frac{2r_i}{M_T(r_o^2 - r_i^2)} \times \left[\frac{K_1(M_T r_i)I_1(M_T r_o) - K_1(M_T r_o)I_1(M_T r_i)}{K_1(M_T r_o)I_0(M_T r_i) + K_0(M_T r_i)I_1(M_T r_o)}\right] \quad (20)$$

where

$$M_T = \sqrt{\frac{2h_{o,w}}{k_f\delta}} = \sqrt{\frac{2h_{c,o}}{k_f\delta}}\sqrt{\frac{b'_w}{C_{p,a}}} = m\sqrt{\frac{b'_w}{C_{p,a}}}. \quad (21)$$

Note that the wet fin efficiency is defined as

$$\eta_{f,\text{wet}} = \frac{i - i_{s,fm}}{i - i_{s,fb}} \quad (22)$$

where $i_{s,fm}$ is the saturated air enthalpy at the fin mean temperature and $i_{s,fb}$ is saturated air enthalpy at the fin base temperature. The use of the enthalpy potential equation, Eq. (4), greatly simplifies the fin efficiency calculation as illustrated by Kandlikar (1990). The test heat exchangers are of Fig. 2(*c*) configuration. The evaluation of fin efficiency for the present geometry is calculated by the equivalent circular area and the sector method as depicted in Fig. 3. The sector method is depicted by Shah (1988), and is given by

$$\eta_{f,\text{wet}} = \frac{\sum_{i=1}^{s} \eta_i A_i}{\sum_{i=1}^{s} A_i} \quad (23)$$

where the fin efficiency for each small sector is obtained from the angular fin with constant fin thickness. In the scope of the study, we found that the difference between the sector method and equivalent circular area method is less than two percent. This result is analogous to the findings of Hong and Webb (1996). Due to the calculation difficulties associated with the sector method in engineering application, the equivalent circular area method is adopted in the final reduction.

With Eqs. (6, 7, 10, 11, 12, and 20), an iterative procedure is needed to obtain the air-side heat transfer coefficient, $h_{c,o}$, and the fin efficiency $\eta_{f,\text{wet}}$. The heat transfer characteristics of

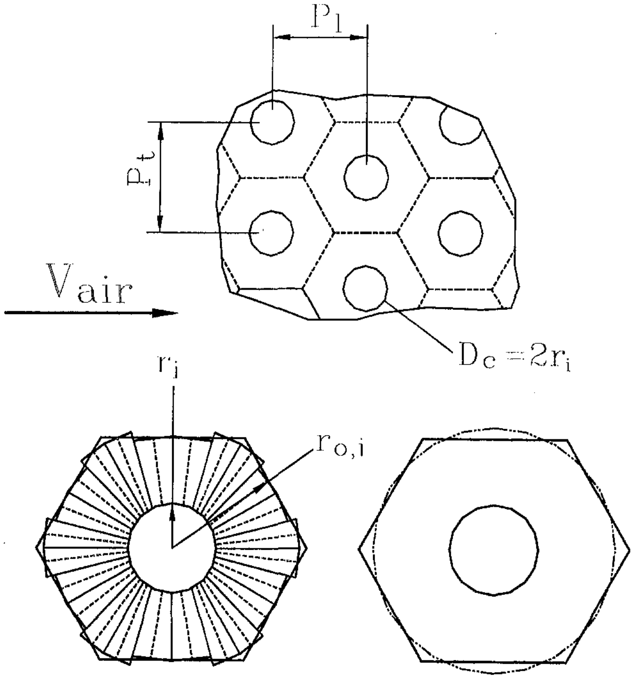

(a) Sector Method (b) Equivalent Circular Area Method

Fig. 3 Approximation method for treating a plate fin of uniform thickness in terms of (*a*) sector method, and (*b*) equivalent circular area method

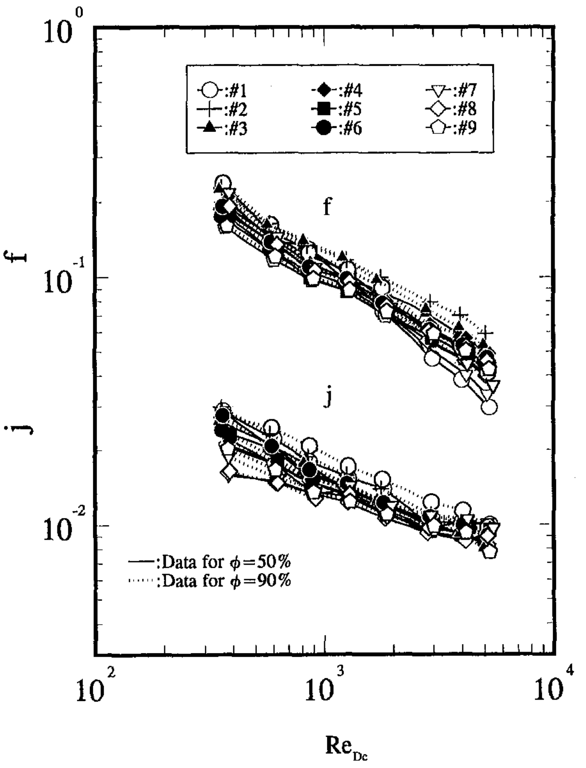

Fig. 4 *j* **and** *f* **for the tested samples**

the heat exchanger is presented by the following nondimensional group:

$$j = \frac{h_{c,o}}{G_{\max} C_{p,a}} \mathrm{Pr}^{2/3}. \tag{24}$$

The friction factor of the heat exchanger is evaluated from the pressure drop equation proposed by Kays and London (1984) as

$$f = \frac{A_{\min}}{A_o} \frac{\rho_m}{\rho_i} \left[\frac{2\rho_i \Delta P}{G_{\max}^2} - (K_c + 1 - \sigma^2) - 2\left(\frac{\rho_i}{\rho_o} - 1\right) + (1 - \sigma^2 - K_e) \frac{\rho_i}{\rho_o} \right] \tag{25}$$

where entrance and exit losses of the core were included. The entrance and exit loss coefficients, K_c and K_e, are adapted from Figs. 14–26 from McQuiston and Parker (1994).

Results and Discussions

The heat transfer and friction characteristics for the tested heat exchangers for relative humidity ϕ = 50 percent and ϕ = 90 percent are shown in Fig. 4. As expected, the friction factors and the sensible *j* factors decrease with an increase of the Reynolds number.

Figure 5 shows the effect of relative humidity on the sensible *j* factors and friction factors for Sample #4. The test results under completely dry conditions are also seen in the figure. As shown in the figure, the experimental data indicate a significant increase of friction factors under dehumidifying conditions. In fact, the friction factors are approximately 60–120 percent higher than those of a dry surface. In addition, the friction factors are insensitive to the change of relative humidity.

Apparently, the sensible heat transfer *j*-factor shown in Fig. 5 during dehumidifying is lower than that for a dry surface for a Reynolds number less than 2000. When the Reynolds number was larger than 2000, the wet surface sensible heat transfer *j* factor is nearly the same, or slightly higher, than that for completely dry conditions. For a fin-and-tube heat exchanger having continuous plain fins, an enhancement of sensible heat transfer coefficient was reported by Myers (1967), Elmahdy (1975), and Eckels and Rabas (1987). Their results showed that the sensible wet surface heat transfer coefficients were considerably higher than those of the completely dry surface. Eckels and Rabas (1987) suggested that the augmentation was due to the suction velocity effect during dehumidifying. Kandlikar (1990) reexamined the effect of the suction velocity based on a detailed mathematical analysis, and concluded that the augmentation due to suction velocity is relatively small (less than one percent). Despite the fact that most of the data from Eckels and Rabas (1987) indicated an enhancement of wet sensible heat transfer coefficient, some of their experimental data showed a trend similar to the present test data (their sample #B had a similar fin geometry as the present sample #5). A close examination of the test data for the sensible heat transfer coefficient, $h_{c,o}$, and pressure drop, ΔP, between these two samples are within ±20 percent.

There are no general agreements about the enhancement of sensible heat transfer coefficients during dehumidification for plain fins. McQuiston (1978a, 1978b) found that the sensible heat transfer coefficients were higher when the fin density was less than ten fins per inch, and that they decreased with more than ten fins per inch. The experimental data of Bryan (1961, 1962) seemed to agree favorably with these results. He reported an increase of sensible heat transfer coefficient for bare-tube heat exchangers, and a decrease of sensible heat transfer coefficient for finned-tube heat exchangers. Nevertheless, the wet sensible heat transfer coefficients for wavy fin geometry reported by Mirth and Ramadhyani (1993) were 17–50 percent lower than the dry-surface values.

The present test results are similar to the experimental data reported by Jacobi and Goldschmidt (1990). They found that the enhancement of sensible heat transfer coefficient to be dependent upon the Reynolds number. A degradation was ob-

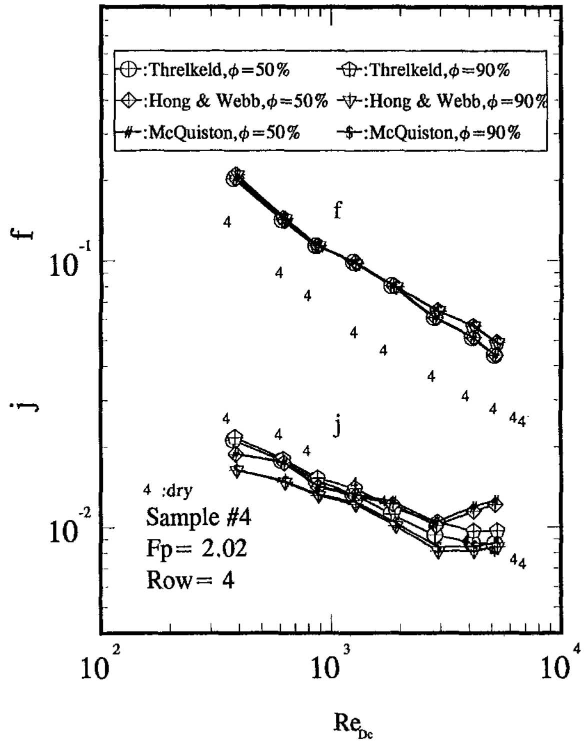

Fig. 5 Effect of inlet relative humidity on the heat transfer and friction characteristics

served at low Reynolds numbers, and an enhancement was seen at a higher Reynolds number range. Jacobi and Goldschmidt (1990) attributed their findings to the condensate retention. At lower Reynolds numbers, condensate retention occurs with a deleterious effect of heat transfer; at higher Reynolds numbers, vapor shear removes the condensate and leads to enhanced heat transfer due to the surface roughness. This explanation was recently supported by the work of Uv and Sonju (1992).

The results of analysis, using the methods of McQuiston and Parker (1994) and Hong and Webb (1996), are also shown in Fig. 5. As shown in the figure, the effect of relative humidity on the sensible *j*-factor is negligible by the present method (Threlkeld, 1970). On the contrary, the sensible *j*-factors are strongly related to the inlet relative humidity when using the fin efficiencies proposed by McQuiston and Parker (1994) and Hong and Webb (1996) approaches. The effect of relative humidity on wet fin efficiency for a circular fin with constant thickness is shown in Fig. 6. As seen, the wet fin efficiency calculated by the method of McQuiston and Parker (1994) and Hong and Webb (1996) shows a significant influence of the relative humidity, while the calculation results of wet fin efficiency for Threlkeld (1970) is only slightly affected by the air relative humidity. There are also controversies about the effect of the inlet air conditions on the wet fin efficiency. Elmahdy and Biggs (1983) derived the wet fin efficiency for circular fins under dehumidifying operation. Their numerical results indicated a pronounced effect of relative humidity on the wet fin efficiency. The conclusion that the wet fin efficiency is strongly related to the wet bulb temperature is also obtained using the approach of McQuiston (1975) and Hong and Webb (1996). Converse to the results, Kandlikar (1990) reexamined the differential equation for the temperature distribution derived by Elmahdy and Biggs (1983). He had provided a complete mathematical proof showing that the wet fin efficiency derived from the differential equations is independent of the relative humidity, and claimed an erroneous numerical solution of Elmahdy and Biggs (1983). Wu and Bong (1994) had carried out an analysis on the overall fin efficiency of a straight fin (Fig. 2(*a*) using a linear approximation between the humidity ratio and surface temperature. Their calculations showed that the wet fin efficiency is relatively independent of the relative humidity (less than two percent for a fin parameter, *ml*, up to 1.2). They had also evaluated several variants from McQuiston (1975) and Threlkeld (1970). Wu and Bong (1994) found that their results were in excellent agreement with those of Threlkeld (1970).

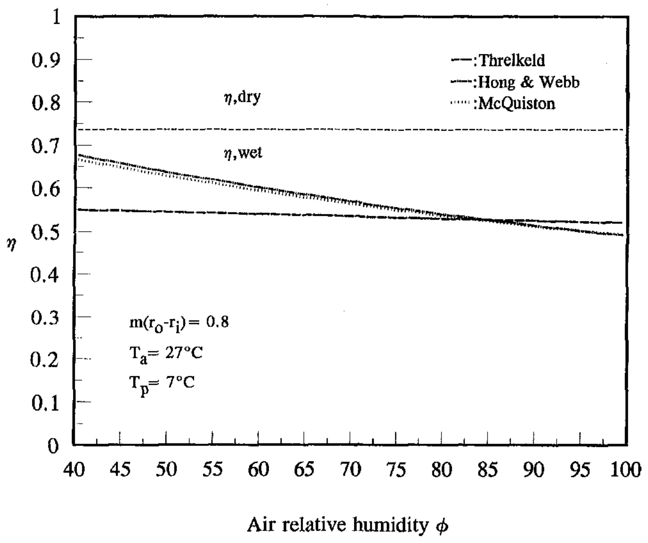

Fig. 6 Fin efficiency of a circular fin as a function of inlet air relative humidity

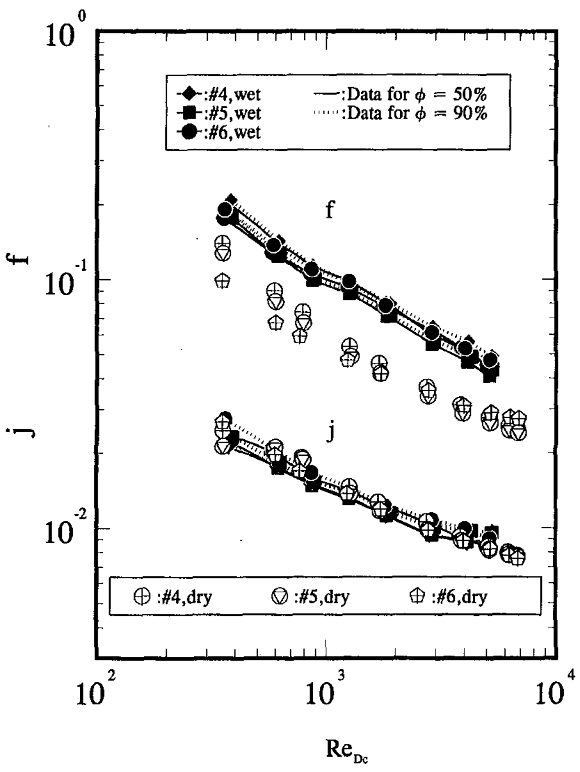

Fig. 7 Effect of fin pitch on heat transfer and friction characteristics

However, the calculation of the fin efficiency proposed by McQuiston (1975) showed a pronounced dependence of relative humidity. Wu and Bong (1994) argued that the basic formulation of McQuiston (Eq. 16) is not physically appropriate. This is because whatever value of *C* is chosen (a given constant) for a fixed incoming air condition, the assumption only allows one possible value for the surface temperature. However, the surface temperature should relate to the saturated humidity and varies along the fin. Therefore, the approximation suggested by McQuiston (1975) may fix a constant temperature for the whole fin but this is not the physical problem in practice. This may explain why the test results of Mirth and Ramadhyani (1993) and Fu et al. (1995) are strongly related to the inlet air condition; they all used the fin efficiency equations proposed by McQuiston (1975). Kandlikar (1990) also reviewed different approaches to the calculation of wet fin efficiency. He recommended the use of the method proposed by Threlkeld (1970). In summary, the approach of Threlkeld (1970) may be more appropriate.

For heat exchangers under completely dry operation, Rich (1973) concluded that the heat transfer coefficients were essentially independent of fin spacing for continuous plain fin geometry. The experimental data of Wang et al. (1996a) also supports this result. This phenomenon is also seen in other fin patterns. Wang et al. (1996b), Chang et al. (1995), and Wang et al. (1996c) report similar results for wavy fin, louver fin, and convex-louver fin geometry, respectively. For heat exchangers under dehumidification, Fig. 7 shows that the effect of fin spacing on the heat transfer and friction factors is also very small. Note that the friction factors for dry surface show a cross-over phenomenon as fin spacing changes. This does not occur for the wet surface.

Figure 8 illustrates the effect of the number of tube rows on the heat transfer and friction characteristics. The number of tube rows are 2, 4, and 6, respectively. The fin spacing is approximately 1.57 mm. As can be seen, the Colburn *j*-factors decrease with an increase of the number of tube rows. This phenomenon is especially pronounced in the low Reynolds number region.

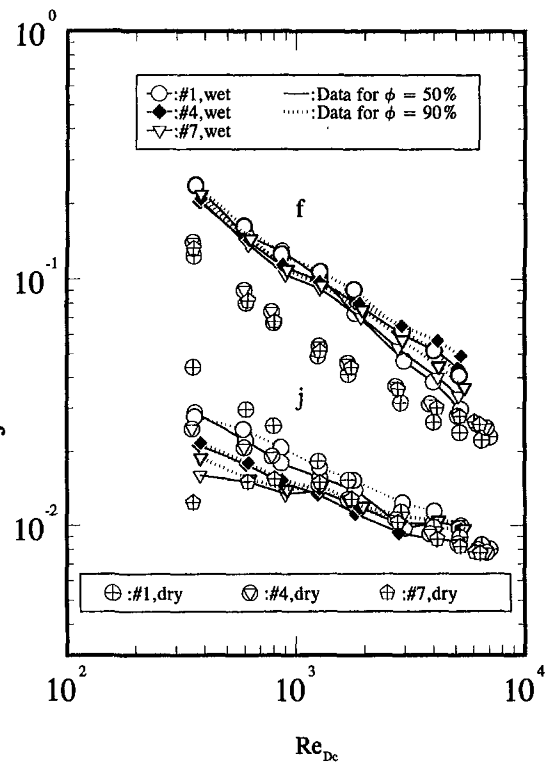

Fig. 8 Effect of the number of tube row on the heat transfer and friction characteristics

Explanation of this phenomenon is two-fold. Namely, the condensate retention, and the deterioration of the downstream turbulence by the vortices formed behind the tube row. A close examination of the dry and wet data reveals that the decreases of sensible *j*-factors under dehumidification are not so significant compared to dry surface. In fact, a maximum (level off) phenomenon is seen for the dry surface for the high fin densities of a six row coil. This phenomenon had been explained by Wang et al. (1996a). With the experimental evidence of Chen and Ren (1988), they explained that this phenomenon may be due to the downstream turbulence tending to diminish; and expected the vortices behind the tube to form as the Reynolds number decreases. Eventually, the number of tube rows cause a significant reduction to the heat transfer characteristics during dry conditions. However, the sensible *j*-factors under dehumidification do not show this kind of maximum behavior and are higher than those of the dry surface. An explanation of this result is that the condensate drainage may disturb or even break up the vortices causing higher sensible heat transfer coefficients. Figure 8 also indicates that the friction factors are independent of the number of tube rows. Again, this phenomenon is very similar to other plain fin-and-tube heat exchangers under dry conditions as shown by Rich (1975) and Wang et al. (1996a), louver fin geometry for Chang et al. (1995), wavy fin configuration of Wang et al. (1996b), and convex-louver fin geometry of Wang et al. (1996c).

Figure 9 compares the present experimental data with the correlation proposed by McQuiston (1978b). Although, McQuiston (1978a) claimed applicability of the correlation to the configuration of the present heat exchangers. However, as seen in the figure, both the sensible *j*-factors and friction factors were considerably underpredicted by the McQuiston correlation (1978a). Note that the original experimental heat exchangers for McQuiston (1978b) were all four row coils. The major discrepancy between the present data and the McQuiston (1978a) data may be summarized as: (1) the difference in fin efficiency calculation; (2) the original test data for McQuiston (1978b) were all four-row configuration which could not take into account the effect of tube row accurately; and (3) the uncertainty of the McQuiston correlation reported to be ±35 percent. Inconsistency exists between the present reduced data and the McQuiston correlation (1978b). Therefore, we re-reduced the original raw data tabulated in the McQuiston paper (1978a) using the Threlkeld method (1970). The original heat exchangers of McQuiston (1978a) were all four-row coil with 4, 8, 10, 12, and 14 fins per inch. Figure 10 shows the reduced results for an almost identical heat exchanger (the present sample #5 and the sample having 12 fins per inch, which has the same number of tube rows, tube diameter, longitudinal pitch, transverse pitch, and a very close of fin pitch). As expected, the reduced results of the *j* or *f*-factors of McQuiston (1978b) fall along the same line regardless of the inlet air conditions. The original reduced data of McQuiston (1978*b*) showed scattering for different inlet conditions. McQuiston (1978b) had clarified the difference of the test data to be dropwise and filmwise condensation. He (1978a) had proposed two different equations set for these two conditions. Basically, it is hard to tell the difference between these two modes during the experiments. It would be more appropriate to identify the coils as "all wet", "all dry", and "partially wet" as suggested by ARI-410 (1991). Therefore, with the present fin efficiency definition, the

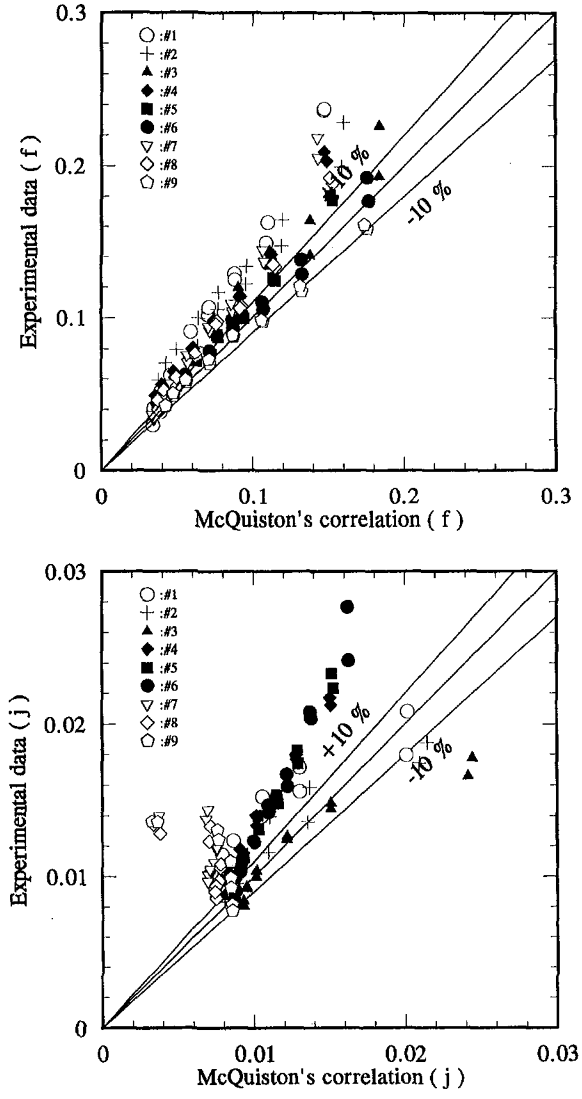

Fig. 9 Comparison of the experimental data and the McQuiston correlations: (*a*) *f*; and (*b*) *j*

sensible heat transfer j-factors would be independent of inlet conditions. This suggested that a better correlation may be achieved. The wet sensible heat transfer coefficients for McQuiston were about 10–20 percent less than the present results. The experimental friction factors for McQuiston are considerably higher than the present data for $Re < 2000$. It is not clear about the difference between these test results.

It is obvious from the curves shown in Fig. 4 that no single curve can be expected to describe the complex behaviors for both j and f-factors. As a result, using a multiple linear regression technique in a practical range of experimental data ($300 < Re_{Dc} < 5500$), the appropriate correlation form of j and f for the present data are

$$j = \begin{cases} j_4 = 0.29773\, Re_{Dc}^{-0.364} \epsilon^{-0.168} \\ j_N = 0.4\, Re_{Dc}^{-0.468+0.04076N} \epsilon^{0.159} N^{-1.261} \end{cases} \tag{26}$$

$$f = 28.209\, Re_{Dc}^{-0.5653} N^{-0.1026} \left(\frac{F_p}{D_c}\right)^{-1.3405} \epsilon^{-1.3343} \tag{27}$$

where

$$\epsilon = \frac{A_o}{A_{p,o}} . \tag{28}$$

As shown in Fig. 11, Eq. (26) can describe 92 percent of the j-factors within 10 percent and Eq. (27) can correlate 91 percent of the friction factors within 10 percent.

Conclusions

On the basis of previous discussions, the following conclusions are made:

- The sensible j-factors under dehumidifying conditions are not dependent on the inlet air conditions.
- The friction factor is very sensitive to surface conditions. For fully wet surface conditions, the friction factors do not change with the inlet air conditions and is also insensitive to the fin spacing and the number of tube row.
- The friction factors of wet-coils are found to be much greater than those of dry-coils, and a degradation of sensible heat transfer coefficients under dehumidification was observed at low Reynolds number; a small enhancement was seen at higher Reynolds number. However, this phenomenon becomes less intense as the number of tube row increases.
- A correlation is proposed for the present plate fin configuration; this correlation can describe 92 percent of j and approximately 91 percent of the f data within 10 percent.

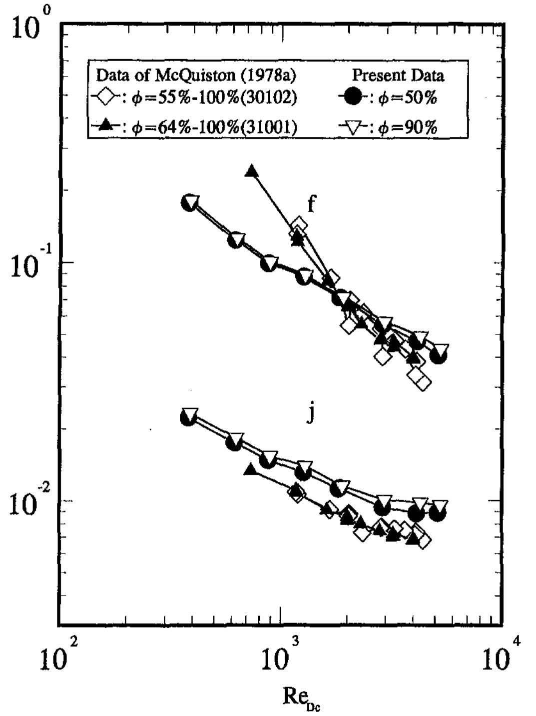

Fig. 10 Comparison of j and f values between test samples with McQuiston (1978a) and the present experimental data with identical number of tube row, longitudinal tube pitch, and transverse tube pitch, as well as a very close fin pitch ($Fp \approx 2.12$–2.23 mm)

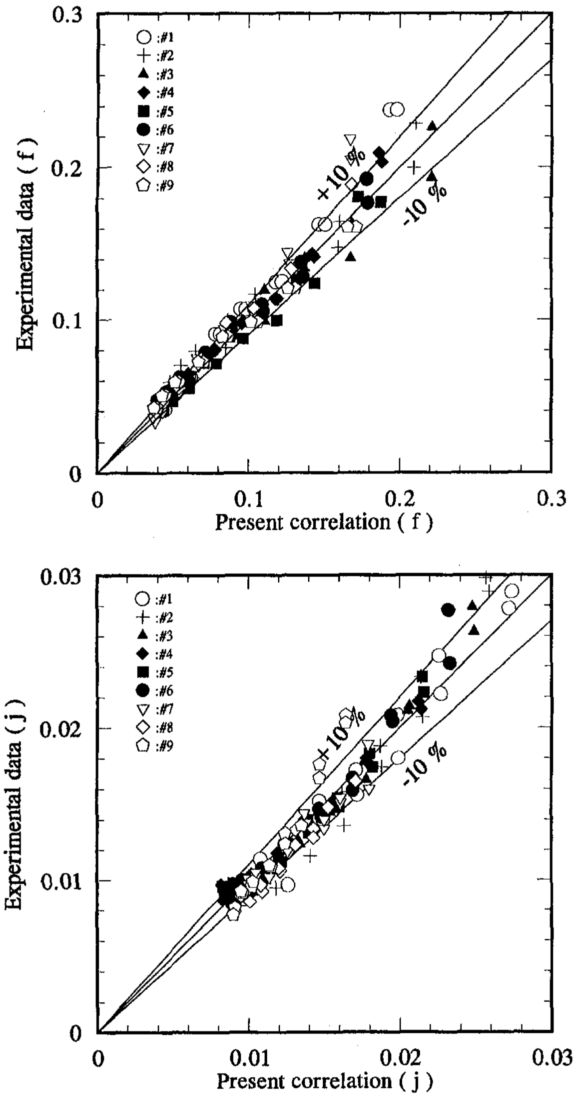

Fig. 11 Comparison of the experimental data and the present correlations: (a) f; and (b) j

Acknowledgments

The authors are indebted to the Energy R&D foundation funding from the Energy Commission of the Ministry of Economic Affairs, Taiwan for supporting this study. The valuable suggestions from Prof. Ralph Webb are very much appreciated.

References

ARI Standard 410-91, 1991, Forced-Circulation Air-Cooling and Air-Heating Coils, Air-Conditioning & Refrigeration Institute, Arlington, VA.

ASHRAE Standard 33-78, 1978, Method of Testing Forced Circulation Air Cooling and Air Heating Coils, American Society of Heating, Refrigerating and Air-Conditioning Engineers, Inc., Atlanta, GA.

ASHRAE Standard 41.1-1986, 1986, Standard Method for Temperature Measurement, American Society of Heating, Refrigerating and Air-Conditioning Engineers, Inc., Atlanta, GA.

ASHRAE Standard 41.2-1987, 1987, Standard Methods for Laboratory Air-Flow Measurement, American Society of Heating, Refrigerating and Air-Conditioning Engineers, Inc., Atlanta, GA.

Bryan, W. L., 1961, "Heat and Mass Transfer in Dehumidifying Surface Coils," *ASHRAE Transactions,* Vol. 67, pp. 393–405.

Bryan, W. L., 1962, "Heat and Mass Transfer in Dehumidifying Extended Surface Coils," *ASHRAE Transactions,* Vol. 68, pp. 237–247.

Bump, T. R., 1963, "Average Temperatures in Simple Heat Exchangers," ASME Journal of Heat Transfer, Vol. 85, No. 2, pp. 182–183.

Chang, W. R., Wang, C. C., Tsi, W. C., and Shyu, R. J., 1995, "Air-Side Performance of Louver Fin Heat Exchanger," *4th ASME/JSME Thermal Engineering Joint Conference,* Vol. 4, pp. 467–372.

Chen, Z. Q., and Ren, J., 1988, "Effect of Fin Spacing on the Heat Transfer and Pressure Drop of a Two-Row Plate Fin and Tube Heat Exchanger," *International Journal of Refrigeration,* Vol. 11, pp. 456–360.

Eckels, P. W., and T. J. Rabas, 1987, "Dehumidification: On the Correlation of Wet and Dry Transport Process in Plate Finned-Tube Heat Exchangers," ASME Journal of Heat Transfer, Vol. 109, pp. 575–582.

Elmahdy, A. H., 1975, "Analytical and Experimental Multi-Row, Finned-Tube Heat Exchanger Performance During Cooling and Dehumidification Process," Ph.D. thesis, Carleton University, Ottawa, Canada.

Elmahdy, A. H., and Biggs, R. C., 1983, "Efficiency of Extended Surfaces With Simultaneous Heat Transfer and Mass Transfer," *ASHRAE Transactions,* Vol. 89, Part 1A, pp. 135–143.

Fu, W. L., Wang, C. C., and Chang, C. T., 1995, "Effect of Anti-Corrosion Coating on the Thermal Characteristics of a Louvered Finned Heat Exchanger Under Dehumidifying Condition," *Advances in Enhanced Heat/Mass Transfer and Energy Efficiency,* ASME HTD-Vol. 320/PID-Vol. 1, pp. 75–81.

Gnielinski, V., 1976, "New Equation for Heat and Mass Transfer in Turbulent Pipe and Channel Flow," *International Chemical Engineering,* Vol. 16, pp. 359–368.

Hong, T. K., and Webb, R. L., 1996, "Calculation of Fin Efficiency for Wet and Dry Fins," *International Journal of HVAC & R Research,* Vol. 2, No. 1, pp. 27–41.

Jacobi, A. M., and Goldschmidt, V. W., 1990, "Low Reynolds Number Heat and Mass Transfer Measurements of an Overall Counterflow, Baffled, Finned-Tube, Condensing Heat Exchanger," *International Journal of Heat and Mass Transfer,* Vol. 33, pp. 755–765.

Kandlikar, S. G., 1990, "Thermal Design Theory for Compact Evaporators," *Compact Heat Exchangers,* R. K. Kraus et al., eds., Hemisphere Publishing Corp., New York, NY, pp. 245–286.

Kays, W. M., and London, A. L., 1984, *Compact Heat Exchanger,* 3rd edition, McGraw-Hill, New York, NY.

McQuiston, F. C., 1975, "Fin Efficiency With Combined Heat and Mass Transfer," *ASHRAE Transactions,* Part 1, Vol. 81, pp. 350–355.

McQuiston, F. C., 1978a, "Heat Mass and Momentum Transfer Data for Five Plate-Fin Tube Transfer Surface," *ASHRAE Transactions,* Part 1, Vol. 84, pp. 266–293.

McQuiston, F. C., 1978b, "Correlation of Heat, Mass, and Momentum Transport Coefficients for Plate-Fin-Tube Heat Transfer Surfaces With Staggered Tubes," *ASHRAE Transactions,* Part 1, Vol. 84, pp. 294–309.

McQuiston, F. C., and Parker, J. D., 1994, *Heating, Ventilating, and Air Conditioning,* 4th edition, John Wiley & Sons, Inc., New York, NY, p. 594.

Mirth, D. R., and Ramadhyani, S., 1993, "Prediction of Cooling-Coils Performance Under Condensing Conditions," *International Journal Heat and Fluid Flow,* Vol. 14, No. 4, pp. 391–400.

Mirth, D. R., and Ramadhyani, S., 1994, "Correlations for Predicting the Air-Side Nusselt Numbers and Friction Factors in Chilled-Water Cooling Coils," *Experimental Heat Transfer,* Vol. 7, pp. 143–162.

Moffat, R. J., 1988, "Describing the Uncertainties in Experimental Results," *Experimental Thermal and Fluid Science,* Vol. 1, pp. 3–17.

Myers, R. J., 1967, "The Effect of Dehumidification on the Air-Side Heat Transfer Coefficient for a Finned-Tube Coil," M. S. Thesis, University of Minnesota, Minneapolis.

Moffat, R. J., 1988, "Describing the Uncertainties in Experimental Results," *Experimental Thermal and Fluid Science,* Vol. 1, pp. 3–17.

Rich, D. G., 1973, "The Effect of Fin Spacing on the Heat Transfer and Friction Performance of Multi-Row, Plate Fin-and-Tube Heat Exchangers," *ASHRAE Transactions,* Part 2, Vol. 79, pp. 137–145.

Rich, D. G., 1975, "The Effect of the Number of Tube Rows on Heat Transfer Performance of Smooth Plate Fin-and-Tube Heat Exchanger," *ASHRAE Transactions,* Part 1, Vol. 81, pp. 307–317.

Schmidt, Th. E., 1949, "Heat Transfer Calculations for Extended Surfaces," *Refrigerating Engineering,* Vol. 49, pp. 351–357.

Senshu, T., Hatada, T., and Ishibane K., 1981, "Heat and Mass Transfer Performance of Air Coolers Under Wet Conditions," *ASHRAE Transactions,* Part 2, Vol. 87, pp. 109–115.

Seshimo, Y., Ogawa, K., Marumoto, K., and Fujii, M., 1988, "Heat and Mass Transfer Performances on Plate Fin and Tube Heat Exchangers With Dehumidification," *Transactions JSME,* Vol. 54, No. 499, pp. 716–721.

Shah, R. K., 1988, "Plate-Fin and Tube-Fin Heat Exchanger Design Procedures," *Heat Transfer Equipment Design,* R. K. Shah et al., eds., Hemisphere Publishing Corp., Washington, DC, pp. 255–266.

Threlkeld, J. L., 1970, *Thermal Environmental Engineering,* Prentice-Hall, Inc., New York, NY.

Wang, C. C., Hsieh, Y. C., Chang, Y. J., and Lin, Y. T., 1996a, "Sensible Heat and Friction Characteristics of Plate Fin-and-Tube Heat Exchangers Having Plane Fins," *International Journal of Refrigeration,* Vol. 19, No. 4, pp. 223–230.

Wang, C. C., W. L., Fu, Chang, C. T., 1996b, "Heat Transfer and Friction Characteristics of Typical Wavy Fin-and-Tube Heat Exchangers," *Experimental Thermal and Fluid Science,* in press.

Wang, C. C., Chen, P. Y., Jang, J. Y., 1996c, "Heat Transfer and Friction Characteristics of Convex-Louver Fin-and-Tube Heat Exchangers," *Experimental Heat Transfer,* Vol. 9, No. 1, pp. 61–78.

Wu, G., and Bong, T. Y., 1994, "Overall Efficiency of a Straight Fin With Combined Heat and Mass Transfer," *ASHRAE Transactions,* Part 1, Vol. 100, pp. 367–374.

Uv, E. H., and Sonju, O. K., 1992, "Heat Transfer Measurements of Circular Finned Tubes With and Without Partial Condensation," *Institute of Chemical Engineers Symposium Series,* Vol. 1, No. 129, pp. 295–302.

P. J. Coelho
Assistant Professor

M. G. Carvalho
Professor,

Mechanical Engineering Department,
Instituto Superior Técnico
Technical University of Lisbon,
Av. Rovisco Pais,
1096 Lisboa Codex,
Portugal

A Conservative Formulation of the Discrete Transfer Method

The discrete transfer method, often employed to calculate radiative heat transfer in combustion chambers, is not conservative. The reason for this behavior is examined and a conservative formulation is proposed and evaluated. A simple treatment of isotropic scattering media is also presented. The original and the conservative formulation of the method are applied to two-dimensional and three-dimensional enclosures containing a participating medium. It is shown that the accuracy of the original and the conservative formulation is very similar, but the proposed formulation has the advantage of ensuring energy conservation.

Introduction

Radiative heat transfer plays an important role in many engineering problems, especially in aeronautics, astronautics, and mechanics, and it is the dominant heat transfer mechanism in many industrial combustion equipments, including boilers and furnaces. Hence, the accurate prediction of the heat transferred by radiation is a key issue in the design and operation of combustion chambers. In this case, the calculation of radiative heat transfer is part of a more complex problem which involves the numerical simulation of a turbulent reactive flow.

Although many radiation models have been developed for emitting, absorbing, and scattering media (e.g., Viskanta and Mengüç, 1987), generally based on the solution of the radiative heat transfer equation (RTE), most of them are not recommended for coupled fluid flow/heat transfer problems. Despite their recognized accuracy, some methods, such as the zonal (Hottel and Sarofim, 1967) and the Monte Carlo (Howell, 1968) methods, require long computing times and involve numerical algorithms very different from those employed in fluid flow calculations. Others, such as the flux method of Schuster-Schwarzchild and its generalization for two- and three-dimensional domains (Selçuk 1983), have low accuracy. The spherical harmonics method (e.g., Mengüç and Viskanta, 1985) is not accurate for low order approximations, except in optically thick media, and the increase of accuracy achievable using high order approximations is mathematically involved (Modest, 1993). Three of the most attractive methods, as far as accuracy and computational requirements are concerned, are the discrete transfer (Shah, 1979; Lockwood and Shah, 1981), the discrete ordinates (Carlson and Lathrop, 1968; Fiveland, 1984), and the finite volume method (Raithby and Chui, 1990; Chai et al., 1994). They are easily incorporated in reactive fluid flow codes and a comparative study of their performance for several benchmark problems has recently been published (Coelho et al., 1995).

Lockwood and Shah (1981) claim that the discrete transfer method (DTM) is economical, straightforwardly applicable to complex geometries, easy to apply, and able to return any desired degree of precision. These features justify its popularity and wide application in calculations in combustion chambers (e.g., Gosman et al., 1982; Boyd and Kent, 1986; Carvalho and Coelho, 1989), as well as its incorporation in commercial computational fluid dynamics codes, such as FLUENT and FLOW3D. However, since the method was proposed by Lockwood and Shah, only a few fundamental studies or extensions have been reported. Murthy and Choudhury (1992) applied the method to two-dimensional domains of arbitrary shape and Carvalho et al. (1993) studied two- and three-dimensional enclosures containing a scattering medium. Recently, Bressloff et al. (1995) proposed a new set of weighting coefficients for the radiation intensity along each ray tracing direction. The new weighting set is based on the discretization of the hemispherical solid angle using quasi-equal solid angles in an attempt to provide a more even distribution of ray directions and to mitigate the ray effect. More accurate quadrature formulae for the calculation of the incident heat flux have been developed by Cumber (1995). In the proposed formulae, the incident intensity is assumed to vary within each solid angle resultant from the discretization of the hemisphere, rather than being constant, as in the original method. Similarly, when integrating the RTE, the temperature is assumed to vary linearly in each control volume.

A major shortcoming of the DTM, which has not been addressed in the literature, is that, in general, the method is not conservative if the boundary temperature is prescribed, i.e., the numerical solution calculated by the DTM does not satisfy the principle of conservation of energy. This is in contrast with other competitive methods, namely the discrete ordinates and the finite volume method, which are conservative. The present work explains why, in general, the DTM is not conservative and proposes a simple correction to overcome this problem. In addition, it employs a treatment of isotropic scattering simpler and more accurate than that proposed by Lockwood and Shah (1981) and used in Carvalho et al. (1993).

A brief description of the method is given in the next section. Then, the conservation problem is addressed and two different modifications are proposed. These are evaluated by means of the application of the different formulations to benchmark problems. The results obtained are presented and discussed, and the paper ends with a summary of the main conclusions.

The Discrete Transfer Method

Original Formulation. The main features of the DTM are described below in order to facilitate the discussion of the conservation problem. A complete description of the method is given by Lockwood and Shah (1981).

The DTM is based on the numerical solution of the RTE along specified directions. For a gray medium, as considered in this paper, the RTE may be written as follows (e.g., Modest, 1993):

$$\frac{dI}{ds} = -\beta I + \kappa I_b + \frac{\sigma_s}{4\pi}\int_0^{4\pi} I(\vec{s}\,')\phi(\vec{s}\,', \vec{s})d\Omega\,' \qquad (1)$$

The ratio $\phi(\vec{s}\,', \vec{s})/4\pi$ represents the probability that radiation propagating in the direction $\vec{s}\,'$ and confined within the solid

---

Contributed by the Heat Transfer Division for publication in the Journal of Heat Transfer. Manuscript received by the Heat Transfer Division October 2, 1995; revision received September 25, 1996; Keywords: Conjugate Heat Transfer, Numerical Methods, Radiation. Associate Technical Editor: M. Modest.

angle $d\Omega'$ is scattered through the angle $(\vec{s}', \vec{s})$ into the direction $\vec{s}$ confined within the solid angle $d\Omega$. The absorption, scattering, and extinction coefficients are related to the single scattering albedo as follows:

$$\omega = \sigma_s/(\kappa + \sigma_s) = \sigma_s/\beta \tag{2}$$

Equation (1) is a statement of the principle of conservation of energy applied to a pencil of radiation traveling along direction $\vec{s}$.

In the DTM the physical domain is divided into control volumes (CV). The temperature and the radiative properties of the medium are taken as constant in each one of them. For all the CV adjacent to the boundary, the central points of the faces of the CV coincident to the boundary are determined. Let P_j be one of such points. The hemisphere centered at P_j is discretized into a prescribed number of solid angles. Each solid angle defines a direction along which the RTE is solved.

Hence, given a point P_j at the center of a cell face on the boundary, a radiation beam is fired from P_j for each one of the directions specified above (Fig. 1). The path of a radiation beam is followed until it hits another boundary. Let Q_i be the impingement point. Although, in general, Q_i is not the central point of a boundary cell, it is assumed that the radiation intensity at Q_i and at the central point of the boundary cell which contains Q_i are equal. Then, starting from Q_i, the path of the beam is followed back to the origin (point P_j) and the RTE is integrated analytically along this path. Henceforth, the radiation beam traveling from P_j to Q_i will be referred to as a radiosity ray, and the radiation beam traveling back from Q_i to P_j will be referred to as an irradiation ray. The starting point of a radiosity ray and the ending point of an irradiation ray are always the center of a cell face on the boundary. On the contrary, the ending point of a radiosity ray and the starting point of an irradiation ray do not usually coincide with the center of a boundary cell face.

The integration of the RTE yields (Lockwood and Shah, 1981):

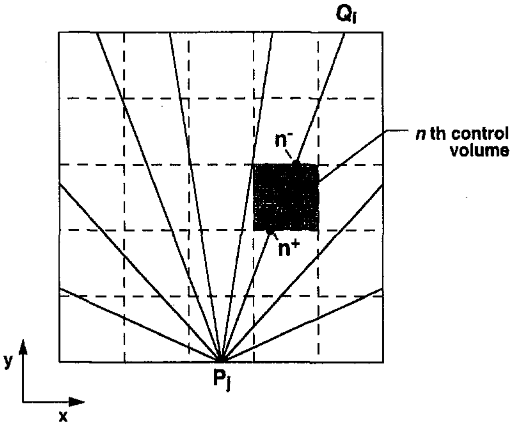

Fig. 1 ***Projection onto the x-y plane of the radiation beams resultant from the discretization of the hemisphere centered at the boundary point P_j***

$$I_{n^+,i\to j} = I_{n^-,i\to j}e^{-\beta\delta s} + \left[(1-\omega)I_b + (\omega/4\pi)\int_0^{4\pi} I(\vec{s}')\phi(\vec{s}', \vec{s})d\Omega'\right](1 - e^{-\beta\delta s}) \tag{3}$$

where the subscript $i \to j$ identifies the direction of the irradiation ray traveling from Q_i to P_j, and the subscripts n^- and n^+ denote the points where that ray enters and leaves the nth CV, respectively (Fig. 1). In the CV where the irradiation ray originates, n^- coincides with Q_i; in the control volume where the irradiation ray hits the boundary, n^+ coincides with P_j.

The incident radiative heat flux at point P_j, i.e., the irradiation, is calculated by adding the contributions due to all the irradiation rays that reach point P_j (one for each solid angle

Nomenclature

A = Area
C = Correction factor
$D_{j,i}$ = Integral of cos $\theta_{j,i}$ over a solid angle element associated with the direction $j \to i$
E = Absolute error
E_1, E_2, E_3 = Unsteady, conductive and radiative terms of the energy equation integrated in space and time
G = Incident radiation
H = Irradiation onto a surface
I = Radiation intensity
$I_{k,i\to j}$ = Radiation intensity at point k of an irradiation ray traveling in direction $i \to j$
J = Radiosity
k = Thermal conductivity
$\hat{n}$ = Unit surface normal
N = Conduction-to-radiation parameter
NI = Number of control volumes along x direction
NJ = Number of control volumes along y direction
N_θ = Number of θ angles per octant
N_φ = Number of φ angles per octant
q = Radiative heat flux
Q = Dimensionless heat flux
$\dot{Q}$ = Volumetric heat source
s = Geometric path length
$\vec{s}$ = Unit vector into a given direction
S = Radiative source term of the energy conservation equation
t = Time
T = Temperature
α = Thermal diffusivity
β = Extinction coefficient
δs = Optical length within a control volume
Δt^* = Time step
ΔV = Volume
$\Delta\theta$ = Discrete polar angle
$\Delta\varphi$ = Discrete azimuthal angle
$\Delta\Omega_{j,i}$ = Discrete solid angle associated with the direction $j \to i$
ϵ = Emissivity
η = Relative error
θ = Polar angle; dimensionless temperature
$\theta_{j,i}$ = Angle between the surface normal at P_j and the direction $j \to i$
κ = Absorption coefficient
σ = Stefan-Boltzmann constant
σ_s = Scattering coefficient
τ = Optical coordinate
ϕ = Scattering phase function
φ = Azimuthal angle
ψ = Dimensionless radiation intensity
ω = Single scattering albedo
Ω = Solid angle

Subscripts

avg = Averaged value over a control volume
b = Blackbody value
g = Gas
$j \to i$ = Direction from point P_j to point Q_i
n = Control volume
n^-, n^+ = Entry (n^-) into or exit (n^+) from a control volume
o = Reference value
P = Point P
x, y = Cartesian coordinates
w = Wall

Superscripts

$*$ = Dimensionless quantity
$-$ = Mean value

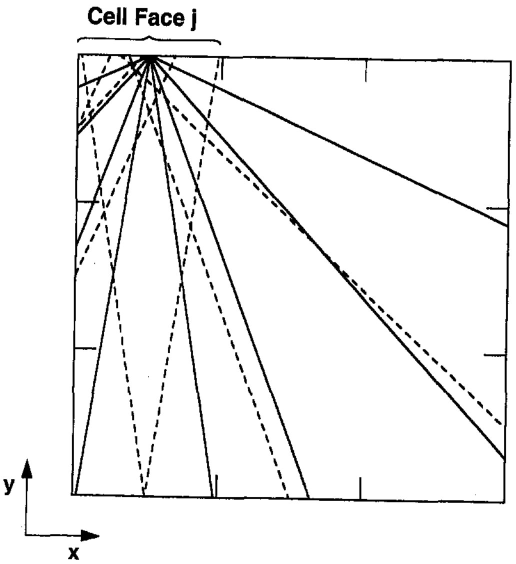

Fig. 2 Projection onto the x-y plane of all the irradiation rays that arrive (solid lines) or start (dashed lines) at the boundary cell face centered at P_j, for $NI = NJ = 3$ and $N_\theta = N_\varphi = 2$

resultant from the discretization of the hemisphere centered at P_j):

$$H_j = \int_0^{2\pi} I(\mathbf{\hat{s}})\mathbf{\hat{n}}.\mathbf{\hat{s}}d\Omega \approx \sum_i I_{j,i\rightarrow j} D_{j,i} . \quad (4)$$

$I_{j,i\rightarrow j}$ is the radiation intensity at point P_j of the irradiation ray traveling from Q_i to P_j. It is important to point out that only the radiation intensity of irradiation rays is involved in DTM calculations. $D_{j,i}$ is the integral of the cosine of the angle $\theta_{j,i}$ between the surface normal at P_j and the direction $j \rightarrow i$ over a solid angle element $\Delta\Omega_{j,i}$:

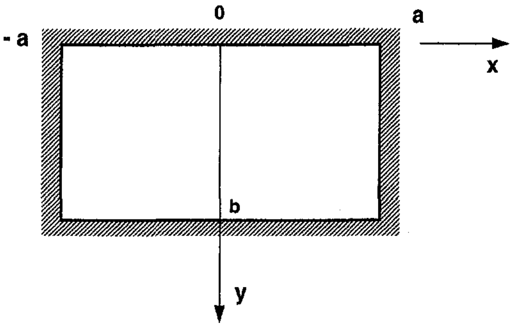

Fig. 3 Geometry of test case 1

$$D_{j,i} = \int_{\Delta\Omega_{j,i}} \cos\theta_{j,i}\, d\Omega$$

$$= \cos\theta_{j,i} \sin\theta_{j,i} \sin(\Delta\theta_{j,i})\Delta\varphi_{j,i} . \quad (5)$$

Since the solid angles ($\Delta\Omega_{j,i}$) are defined from the discretization of a hemisphere centered at P_j, the following identity holds: $\sum_i D_{j,i} = \pi$.

The solution of the RTE requires the specification of the boundary conditions. If the wall temperature is prescribed, the boundary condition for a gray diffuse boundary surface may be written as follows:

$$J_j = \epsilon_w \sigma T_w^4 + (1 - \epsilon_w) H_j . \quad (6)$$

The calculation procedure is iterative, unless $\epsilon_w = 1$, because the radiation intensities of the irradiation rays at the points Q_i are not known a priori. Other boundary conditions may be treated as described by Lockwood and Shah (1981).

The radiation source (or sink) for each CV, which appears in the energy conservation equation, may be defined as

Table 1 Ratio between the heat rate received and the heat rate leaving the boundary of the enclosure of test case 1 calculated using DTM-0, mean absolute errors of the normalized incident heat flux on the boundary, and normalized emissive power at $x = 0$

a/b	NI x NJ	N_θ x N_φ	$\frac{\sum_j A_j H_j}{\sum_j A_j J_j}$	$\bar{E}(q/\sigma T_w^4) \times 10^2$			$\bar{E}(T_g^4/T_w^4) \times 10^2$		
				DTM-0	DTM-1	DTM-2	DTM-0	DTM-1	DTM-2
0.2	10 x 20	2 x 2	0.8750	1.38	1.41	—	3.04	3.22	—
	10 x 20	5 x 5	0.9984	0.38	0.38	0.41	0.85	0.85	0.80
	20 x 40	2 x 2	1.0000	1.30	1.30	1.36	2.78	2.78	2.88
	20 x 40	5 x 5	1.0426	0.44	0.43	0.46	0.74	0.72	0.77
	40 x80	2 x 2	0.9063	1.39	1.37	1.53	2.84	2.81	3.26
	40 x80	5 x 5	1.0267	0.43	0.43	0.52	0.74	0.72	1.05
	40 x80	10 x 10	1.0262	0.15	0.14	0.14	0.59	0.46	0.51
5	20 x 10	2 x 2	1.0125	3.09	2.71	2.89	0.81	0.83	2.02
	20 x 10	5 x 5	1.0002	1.12	1.11	1.06	0.23	0.23	0.52
	40 x 20	2 x 2	1.0000	3.19	3.19	3.01	0.81	0.81	1.75
	40 x 20	5 x 5	0.9957	1.35	1.19	1.30	0.25	0.32	0.67
	80 x 40	2 x 2	1. 0094	3.06	2.88	3.15	0.81	0.81	1.67
	80 x 40	5 x 5	0.9973	1.25	1.18	1.30	0.26	0.29	0.67
	80 x 40	10 x 10	0.9974	0.94	0.84	0.77	0.17	0.19	0.19

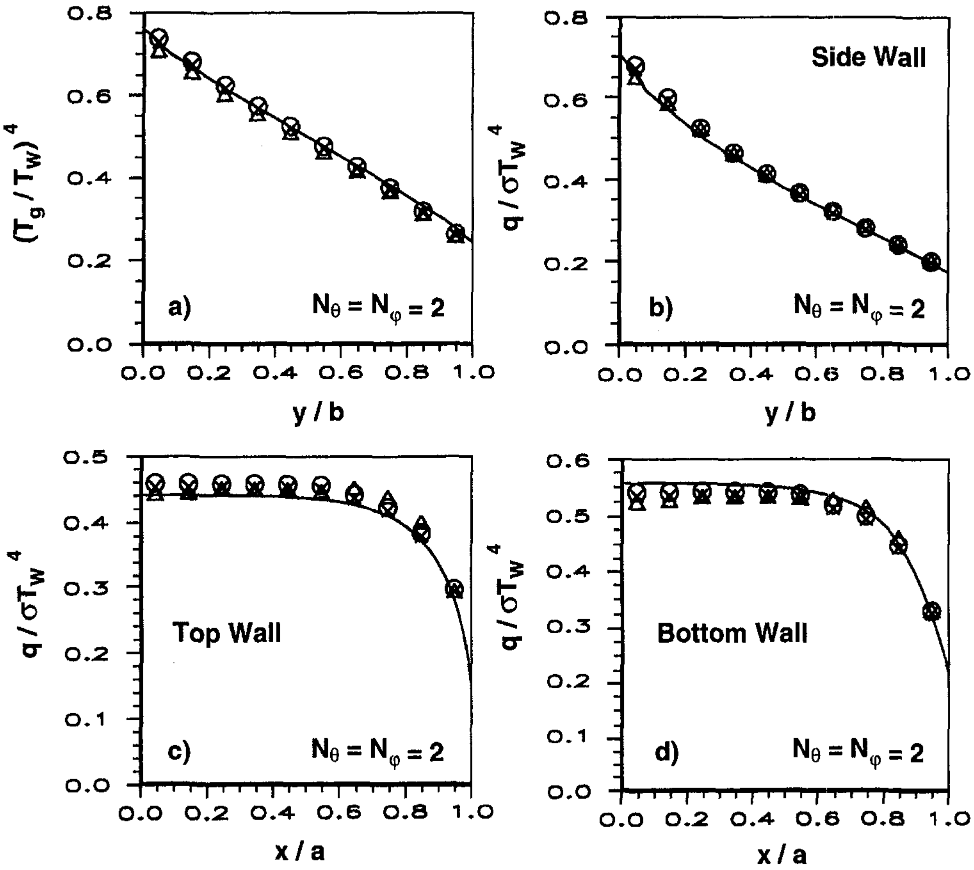

Fig. 4 Predictions for test case 1 with $a/b = 5$ and $N_\theta = N_\varphi = 2$ (solid line: Crosbie and Schrenker; O-DTM-0, X-DTM-1; Δ-DTM-2): (*a*) normalized emissive power at $x = 0$; (*b*) normalized incident heat flux on side wall; (*c*) normalized incident heat flux on top wall; and (*d*) normalized incident heat flux on bottom wall.

$$S = \int_{CS} \vec{q} . \vec{n} dA = \int_{CS} \int_0^{4\pi} I(\vec{s}) \vec{n} . \vec{s} d\Omega dA \tag{7}$$

where $\vec{q}$ is the radiative heat flux vector and the integration is carried out over the surface area, CS, of the CV. However, the DTM does not perform a discretization of the RTE over a CV. Therefore, the source term S is not evaluated from the discretization of Eq. (7). Instead, the source term for a CV is obtained from the sum of the contributions of all the irradiation rays which cross that CV. It is assumed that the contribution of each irradiation ray is proportional to the change of the radiation intensity leaving and entering that CV. This yields the following equation:

$$S_n = \sum_j \sum_i (I_{n^+, i \to j} - I_{n^-, i \to j}) D_{j,i} A_j \tag{8}$$

In this equation, index j runs over all the boundary cell faces and index i extends over all the irradiation rays hitting cell face j. If an irradiation ray traveling from Q_i to P_j does not cross the nth CV then $I_{n^+, i \to j} = I_{n^-, i \to j} = 0$.

Consideration of Scattering. The calculation of radiative heat transfer in scattering media requires the computation of the integral which appears in the in-scattering term (Eq. 3). Lockwood and Shah (1981) have approximated this integral as

$$\int_0^{4\pi} I(\vec{s}\,')\phi(\vec{s}\,', \vec{s}) d\Omega' \approx \sum (I(\vec{s}\,'))_{\text{avg}} \phi(\vec{s}\,', \vec{s}) \Delta\Omega' \tag{9}$$

where the averaged intensity is taken as the arithmetic mean of the radiation intensity at the inlet and outlet of the CV. The summation extends over all the irradiation rays that cross the CV. This approximation was successfully used by Carvalho et al. (1993) for isotropic scattering media, and we are not aware of any attempt to apply it for anisotropic scattering media.

In the case of isotropic scattering, however, the approximation used in Eq. (9) can be avoided. In fact, in this case the scattering phase function is equal to one. Therefore, the integral in the in-scattering term is equal to the incident radiation

$$\int_0^{4\pi} I(\vec{s}\,')\phi(\vec{s}\,', \vec{s}) d\Omega' = G. \tag{10}$$

If the equation for the conservation of radiative energy (e.g., Modest, 1993)

$$\nabla . q = \kappa(4\sigma T^4 - G) \tag{11}$$

is integrated over the CV, the left hand side yields the radiation source (or sink) of the energy conservation equation, S. Therefore, Eq. (11) can be used to compute G as

$$G = 4\sigma T^4 - \frac{S}{\kappa \Delta V}. \tag{12}$$

In this way, the in-scattering term is easily obtained without the approximation embodied in Eq. (9). In the case of pure scattering ($\kappa = 0$), Eq. (12) is not applicable. However, the case of pure scattering is mathematically equivalent to an absorbing-emitting medium in radiative equilibrium (Modest, 1993). Therefore, in such a case the incident radiation is given by $G = 4\sigma T^4$.

Conservative and Non-Conservative Formulations. A desirable feature of any solution method for the RTE is that the numerical solution satisfies conservation of energy. However, in general, the numerical solution obtained using the DTM does

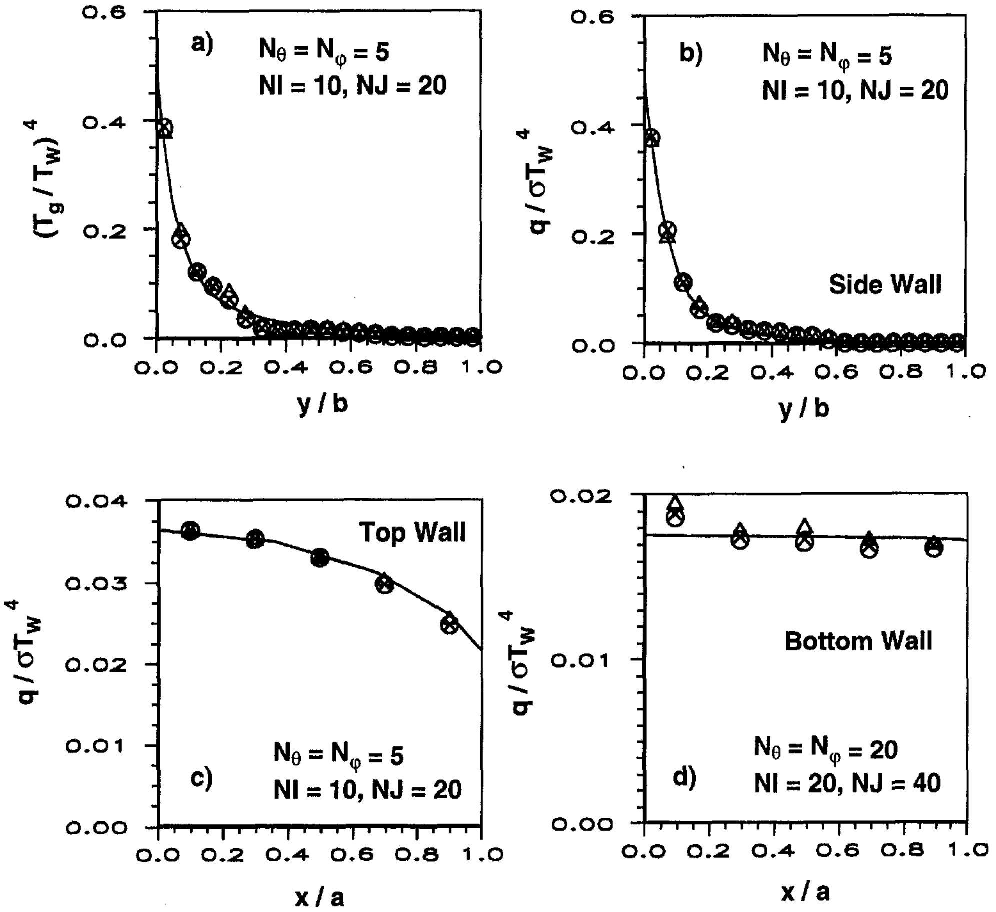

Fig. 5 Predictions for test case 1 with *b/a* = 5 (solid line: Crosbie and Schrenker; O-DTM-0; X-DTM-1; Δ-DTM-2): (*a*) normalized emissive power at *x* = 0; (*b*) normalized incident heat flux on side wall; (*c*) normalized incident heat flux on top wall; and (*d*) normalized incident heat flux on bottom wall.

not satisfy this principle. The reason why this happens is examined below and alternative conservation formulations are proposed.

If thermal radiation is the only mechanism of heat transfer present, the principle of conservation of energy applied to an enclosure states that the net heat rate leaving the enclosure through its boundary is equal to the difference between the radiative energy generated (emitted) and destroyed (absorbed) within the enclosure per unit time. Mathematically, this means that

$$\sum_j A_j(H_j - J_j) = \sum_n S_n \tag{13}$$

where the summation on the left hand side runs over all the cell faces on the boundary and that on the right hand side extends over all the control volumes. This equation is also valid for a scattering medium since scattering only redirects radiation beams and does not change the energy balance.

From Eq. (8), the radiative heat source in the enclosure may be expressed, using the commutative law of addition, as

$$\sum_n S_n = \sum_j \sum_i \Big[\sum_n (I_{n^+,i\to j} - I_{n^-,i\to j})\Big] D_{j,i} A_j. \tag{14}$$

The term in the square brackets represents the change of the radiation intensity of an irradiation ray along its path from Q_i to P_j. Therefore, Eq. (14) may be written as

$$\sum_n S_n = \sum_j \sum_i (I_{j,i\to j} - I_{i,i\to j}) D_{j,i} A_j. \tag{15}$$

Inserting Eqs. (4) and (15) into Eq. (13) and simplifying, results in

$$\sum_j A_j J_j = \sum_j \sum_i I_{i,i\to j} D_{j,i} A_j. \tag{16}$$

Interchanging indices i and j on the right hand side of this equation, and applying the commutative law of addition, yields the following:

$$\sum_j A_j J_j = \sum_j \sum_i I_{j,j\to i} D_{i,j} A_i. \tag{17}$$

In this equation, index j runs over all the cell faces on the boundary, and index i extends over all the irradiation rays traveling in direction $j \to i$.

In the DTM, the irradiation rays that start at cell face j and travel in direction $j \to i$ are not associated with the discretization of a hemisphere centered at a point on the boundary cell face j. Hence, the number of these irradiation rays may change from cell to cell and, in general, for a given cell j, it will be $\sum_i D_{i,j} \neq \pi$ (in contrast to $\sum_i D_{j,i} = \pi$), as illustrated below using a simple example. Therefore, setting $I_{j,j\to i} = J_j/\pi$ for diffusely emitting-reflecting boundaries, Eq. (17) is not generally satisfied, even if the areas are all equal.

As an example, consider a two-dimensional square enclosure discretized using a uniform grid with 3 × 3 control volumes and four solid angles per octant ($N_\theta = N_\varphi = 2$). Although these spatial and angular discretizations may be too coarse if an accurate solution is sought, they are adequate for the present purpose. Figure 2 shows the projection onto the x-y plane of all the irradiation rays that hit cell face j. The solid angles associated with these rays have resulted from the discretization of a hemisphere and, therefore, $\sum_i D_{j,i} = \pi$. Figure 2 also shows the projection onto the x-y plane of all the irradiation rays starting at cell face j which strike different boundary cells. It can be seen that there are 14 irradiation rays leaving cell face j. Each dashed line plotted in Fig. 2 corresponds to a pair of rays, one fired in the positive z direction and the other in the negative z direction. The solid angles associated with these irradiation rays do not add up to 2π, and it is not difficult to verify that $\sum_i D_{i,j} = 7\pi/8$ for the cell face j in Fig. 2 (notice that $\Delta\theta = \Delta\varphi = \pi/4$, and $\theta = \pi/8$ or $\theta = 3\pi/8$, yielding $D_{i,j}$ = constant = $\pi/16$ and $\sum_i D_{i,j} = 7\pi/8$). Hence, in general, Eq. (17) is not satisfied.

A solution method is conservative if and only if the numerical solution satisfies Eq. (13). However, it was shown that, in general, the DTM does not satisfy Eq. (17) and, therefore, Eq. (13) is not satisfied either, i.e., the original formulation is not conservative. It is important to emphasize that no assumptions about the radiative properties of the medium have been made in the derivation of Eq. (17) or in the example described above. The original formulation is nonconservative regardless of the radiative properties of the medium, including the especial case of a transparent medium.

To achieve a conservative formulation, two different methods are proposed based on a modification of the heat rate associated with the irradiation rays leaving the boundary cells. In one of them, hereafter referred to as DTM-1, the right hand side of Eqs. (14) to (17) is multiplied by a global correction factor, C, to ensure that the heat rate leaving the boundary of the enclosure is correctly evaluated as $\sum_j A_j J_j$. This global correction factor may be obtained from Eq. (17) after replacing $I_{i,j\rightarrow i}$ with J_j/π,

$$\sum_j A_j J_j = \sum_j \sum_i \frac{J_j}{\pi} C D_{i,j} A_i \qquad (18)$$

yielding

$$C = \frac{\sum_j A_j J_j}{\sum_j J_j \left(\sum_i D_{i,j} A_i/\pi\right)} . \qquad (19)$$

This is mathematically equivalent to set $I_{i,i\rightarrow j} = C J_i/\pi$ when applying Eq. (3) to the irradiation ray starting at cell face i.

In the other modification, which will be referred to as DTM-2, a local correction factor, C_j, is applied to each boundary cell, such that

$$A_j J_j = \sum_i \frac{J_j}{\pi} C_j D_{i,j} A_i \qquad (20)$$

yielding

$$C_j = \frac{A_j}{\sum_i D_{i,j} A_i/\pi} . \qquad (21)$$

The DTM-2 can be applied only if there is at least one irradiation ray leaving every boundary cell. Otherwise, the denominator in Eq. (21) will be zero. However, this situation is likely to occur only if coarse angular discretizations are used.

Both DTM-1 and DTM-2 are conservative, i.e., the numerical solution satisfies Eq. (13); they are evaluated below and compared with the original method (DTM-0).

Evaluation of the Conservative Formulations

Test Case 1—Two-Dimensional Rectangular Enclosure With an Emitting-Absorbing Medium. Evaluation of the conservative formulations for an emitting-absorbing medium was undertaken by comparison of the predictions of the DTM for a two-dimensional rectangular enclosure with the solutions reported by Crosbie and Schrenker (1984). The method of Crosbie and Schrenker is based on the numerical solution of the integral equation for radiative transfer (removing the singularity) and yields accurate results except at very large optical thicknesses. Figure 3 shows the geometry for this problem. The walls of the enclosure are black and at zero temperature, except the top wall which has an emissive power of unity. The optical thickness of the enclosed medium along the y direction is equal to one, i.e., $\beta b = 1$, and the medium is assumed to be in radiative equilibrium. Two different configurations were studied: $a/b = 5$ and $b/a = 5$.

Since, in this problem, a volumetric heat source, $\dot{Q}$, is prescribed ($\dot{Q} = 0$), an iterative procedure is required. Starting from an initial guess for the temperature field, an iteration of the DTM is carried out allowing the calculation of the radiative source term S. Then, the temperature field is updated for each CV as follows:

$$(T^4)^{\text{new}} = (T^4)^{\text{old}} + \left(\dot{Q} - \frac{S}{\Delta V}\right)\frac{1}{4\kappa\sigma} . \qquad (22)$$

The iterative procedure continues until the difference between the new and the old temperature fields decreases below a prescribed tolerance.

Table 1 shows the ratio between the heat rate received and the heat rate leaving the boundary of the enclosure calculated using DTM-0 for the two studied configurations and for several

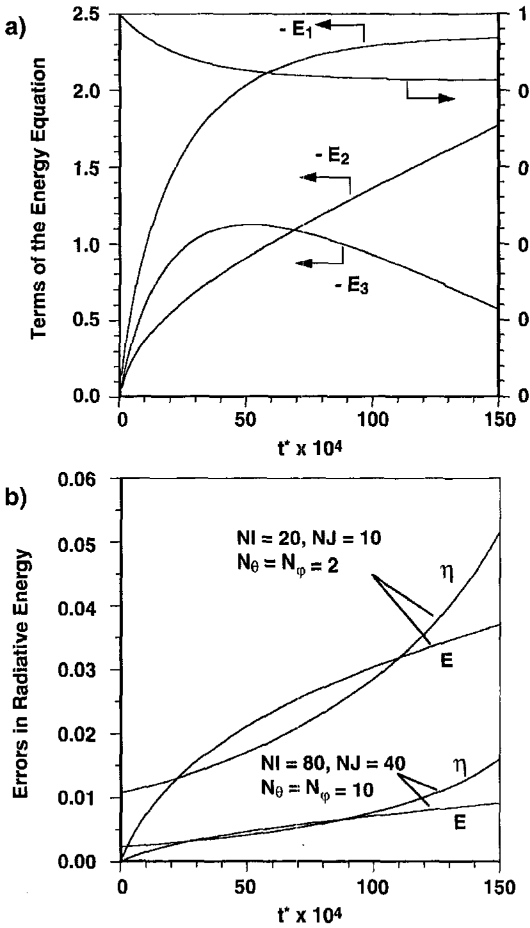

Fig. 6 Transient combined conduction-radiation problem in a two-dimensional enclosure: (*a*) terms of the energy conservation equation integrated in time and over the whole enclosure (Eq. 28), and dimensionless temperature at the center of the enclosure; (*b*) absolute and relative errors of the radiative energy E_3.

Table 2 Terms of the global energy balance for the three-dimensional rectangular furnace of test case 3 calculated using the original formulation of the DTM

Run	κ (m^{-1})	σ_s (m^{-1})	NIxNJxNK	$N_\theta \times N_\varphi$	$\sum_j A_j H_j$ (kW)	$\sum_j A_j J_j$ (kW)	$\sum_n S_n$ (kW)	$\sum_j A_j (H_j - J_j) - \sum_n S_n$ (kW)
1	0.25	0	9 x 9 x 15	2 x 2	1844.3	1760.7	80.0	3.6
2			9 x 9 x 15	5 x 5	1840.5	1759.7	80.0	0.8
3			27 x 27 x 45	5 x 5	1839.4	1759.2	80.0	0.2
4			27 x 27 x 45	10 x 10	1838.6	1759.0	80.0	0.4
5	0.5	0	9 x 9 x 15	2 x 2	1840.4	1756.8	80.0	3.6
6			9 x 9 x 15	5 x5	1836.6	1755.7	80.0	0.9
7	1.0	0	9 x 9 x 15	2 x 2	1834.8	1751.0	80.0	3.8
8			9 x 9 x 15	5 x 5	1830.9	1750.0	80.0	0.9
9	0.15	0.35	9 x 9 x 15	2 x2	1840.4	1756.8	80.0	3.6
10			9 x 9 x 15	5 x 5	1836.6	1755.7	80.0	0.9

spatial and angular discretizations. This ratio should be equal to one because there are no radiative sources or sinks in the medium. The results show that as the spatial and the angular discretizations become finer, the predicted ratio approaches one, but not monotonically. If $a/b = 0.2$, an imbalance of 2.6 percent occurs for fine spatial and angular discretizations, which increases for coarser discretizations, while if $a/b = 5$, the imbalance is smaller. The DTM-0 is not conservative, except in two of the cases. On the contrary, the proposed conservative formulations always yield a ratio of unity. This does not mean that they are more accurate, but simply that they are conservative. Indeed, both DTM-1 and DTM-2 always yield a unity ratio regardless of the solution accuracy.

The mean absolute errors of the normalized incident heat flux on the boundary and the normalized emissive power at $x = 0$ are also listed in Table 1. These errors are defined as the absolute value of the difference between the numerical solution and the reference solution of Crosbie and Schrenker, averaged over all the cell faces on the boundary, for the incident heat fluxes, or over all the CV crossing the line $x = 0$, for the emissive power. The results show that the solution accuracy is only marginally influenced by the spatial grid refinement, regardless of the method employed. On the contrary, a finer angular discretization yields improved accuracy.

In the case $a/b = 0.2$, the results obtained using DTM-1 are slightly more accurate than those calculated by means of DTM-0, except for the coarser discretization. The DTM-2 is less accurate than the others, except for the finer discretization. Moreover, it cannot be applied to the coarser discretization because no irradiation rays leave the cell faces on the top and bottom boundaries which are adjacent to the vertices. In the case $a/b = 5$, the accuracy of DTM-0 and DTM-1 is similar, but the mean absolute error of the normalized heat flux is lower using DTM-1, while the corresponding error of the normalized emissive power is lower employing DTM-0. The DTM-2 is much worse regarding the prediction of the emissive power of the medium, except for the finer discretization, but performs similarly to the others as far as the heat flux calculation is concerned.

Additional insight into the predictions is provided in Figs. 4 and 5. Figure 4 shows the predicted results obtained for a rectangular slab with $a/b = 5$ using a grid with 20 × 10 CV and $N_\theta = N_\varphi = 2$; they closely follow the solution of Crosbie and Schrenker. As expected from the ratio $\sum_i A_i H_i / \sum_i A_i J_i = 1.0125$ and from the mean absolute errors (Table 3), the results computed using DTM-0 and DTM-1 are almost identical.

The columnar shaped geometry with $b/a = 5$ was studied using a grid with 10 × 20 CV and $N_\theta = N_\varphi = 5$. The predictions

Table 3 Mean relative errors of temperature and net heat fluxes for test case 3; the runs are characterized in Table 2

Run	$\bar{\eta}(T) \times 10^2$			$\bar{\eta}(q) \times 10^2$		
	DTM-0	DTM-1	DTM-2	DTM-0	DTM-1	DTM-2
1	1.03	1.01	1.37	2.78	2.77	6.00
2	0.33	0.33	0.38	0.84	0.86	1.03
3	0.31	0.31	0.41	0.79	0.80	1.00
4	0.27	0.27	0.26	0.81	0.80	0.88
5	0.90	0.88	1.14	1.12	1.12	5.58
6	0.30	0.29	0.33	1.18	1.20	1.45
7	0.73	0.71	0.99	1.00	0.90	4.34
8	0.23	0.22	0.32	1.39	1.39	1.04
9	0.73	0.72	0.98	1.12	1.18	5.58
10	0.25	0.25	0.32	1.18	1.20	1.45

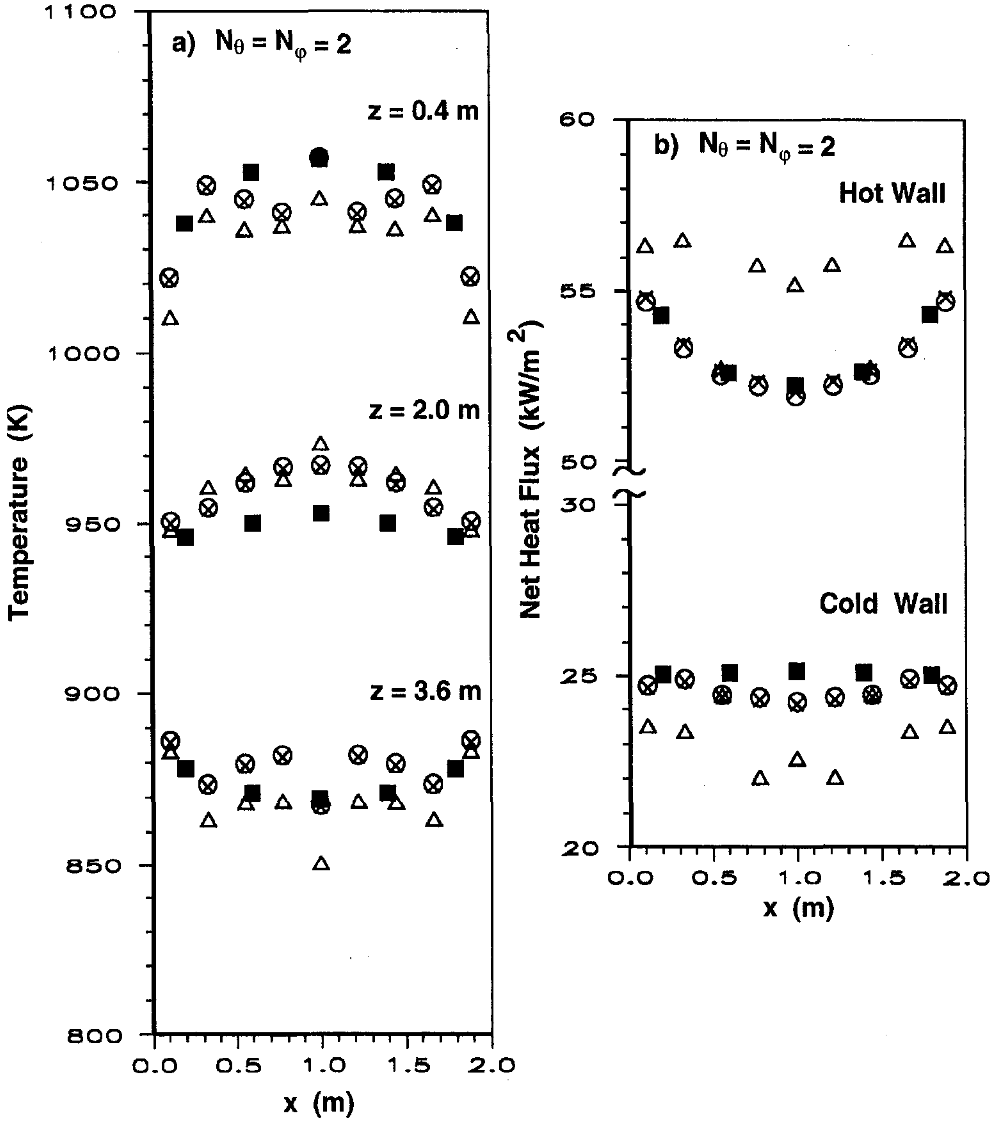

Fig. 7 Predictions for test case 3 using $N_\theta = N_\varphi = 2$ (■—zonal method; O-DTM-0; X-DTM-1; Δ-DTM-2): (*a*) temperature (K) profiles; (*b*) net heat fluxes (kWm^{-2}).

of the three methods are similar and close to the solution of Crosbie and Schrenker, as shown in Fig. 5. However, even this discretization is unable to reproduce the incident heat flux on the bottom wall, not shown here. This is explained by the shape of the enclosure and the boundary conditions. Only the top wall is hot, and the gas temperature is only significant close to this wall, up to $y/b \approx 0.2$ (Fig. 5*a*). Therefore, radiosity rays fired from the bottom wall must reach the top region of the enclosure to contribute to the incident heat flux at the bottom wall. Since b/a is large, only a few radiosity rays actually reach the top region, especially if they are fired from x close to zero. This is the so-called ray effect (Lathrop, 1968; Chai et al., 1993) which is also responsible for the nonmonotonic convergence and the lack of accuracy at coarse resolution. It explains the need to use a very fine angular discretization ($N_\theta = N_\varphi = 20$) to satisfactorily predict the incident heat flux on the bottom wall (Fig. 5*d*).

Test Case 2—Two-Dimensional Transient Combined Conduction-Radiation Problem. A two-dimensional rectangular black enclosure with $a/b = 5$ is considered again in this test case. A transient coupled conductive and radiative heat transfer problem is analyzed to show the accumulation of errors in the energy balance along the time. The mathematical formulation of the problem for an anisotropic scattering medium in dimensionless form is given by the following equations:

$$\frac{\partial\theta}{\partial t^*} = \frac{\partial^2\theta}{\partial\tau_x^2} + \frac{\partial^2\theta}{\partial\tau_y^2} - \frac{1}{N}\nabla\cdot Q$$

$$-\beta a < \tau_x < \beta a, \quad 0 < \tau_y < \beta b, \quad t^* > 0 \qquad (23)$$

where

$$\nabla\cdot Q = (1-\omega)\left(4\theta^4 - \int_{4\pi}\psi d\Omega\right) \qquad (24)$$

and

$$\frac{d\psi}{d\tau_s} = -\psi + \frac{(1-\omega)}{\pi}\theta^4 + \frac{\omega}{4\pi}\int_{4\pi}\psi d\Omega. \qquad (25)$$

The dimensionless quantities are defined as

$$\tau_x = \beta x, \quad \tau_y = \beta y, \quad \tau_s = \beta s, \quad t^* = \alpha\beta^2 t,$$

$$\theta = T/T_o, \quad N = k\beta T_o/(\sigma T_o^4),$$

$$Q = q/(\sigma T_o^4), \quad \psi = I/(\sigma T_o^4). \qquad (26)$$

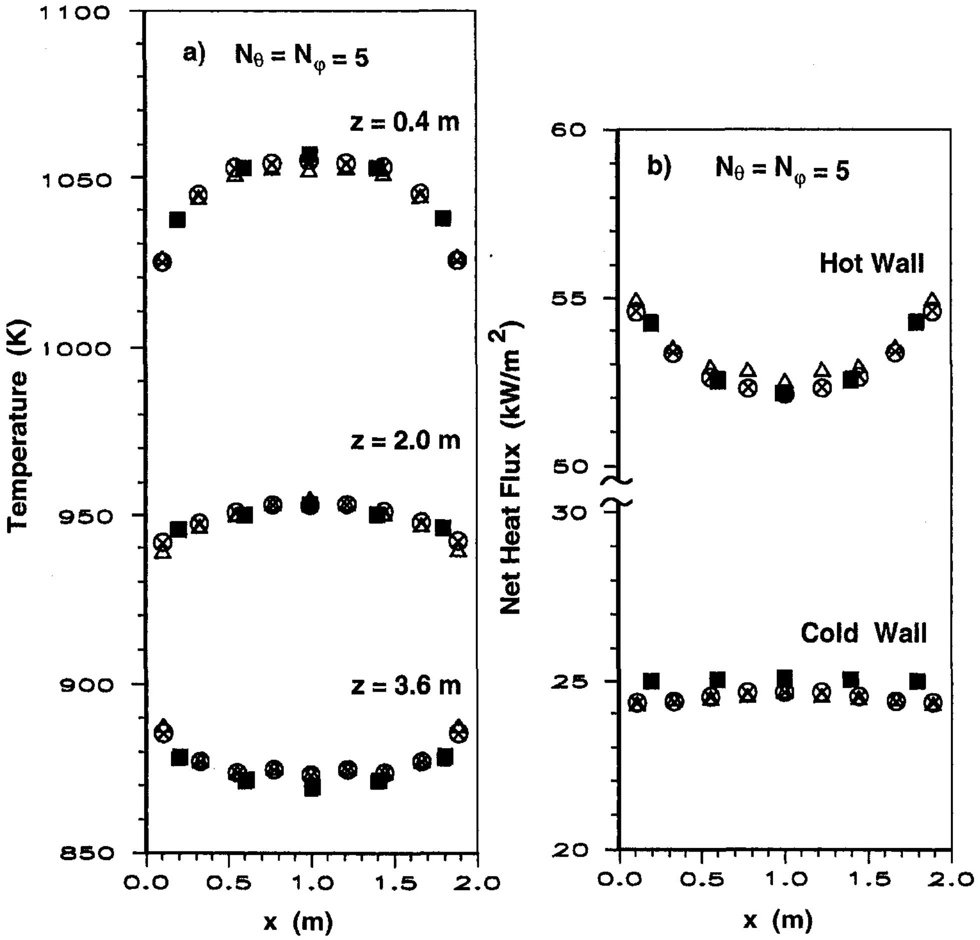

Fig. 8 Predictions for test case 3 using $N_\theta = N_\varphi = 5$ (■—zonal method; O-DTM-0; X-DTM-1; Δ-DTM-2): (*a*) temperature (K) profiles; (*b*) net heat fluxes (kWm^{-2}).

At $t^* = 0$, the temperature of the medium and top wall is T_o, and the temperature of the remaining walls is zero. The temperature of the boundaries is kept constant along the time. Therefore, the initial and boundary conditions of Eq. (23) become

$$\theta(\pm\beta a, \tau_y, t^*) = \theta(\tau_x, \beta b, t^*) = 0,$$

$$\theta(\tau_x, 0, t^*) = 1, \quad \text{for} \quad t^* > 0$$

$$\theta(\tau_x, \tau_y, 0) = 1,$$

$$\text{for} \quad -\beta a < \tau_x < \beta a, \quad 0 < \tau_y < \beta b. \quad (27)$$

Notice that if the conduction to radiation parameter, N, were equal to zero, the present problem would be simplified, becoming precisely the purely radiative heat transfer problem studied in test case 1.

The energy conservation Eq. (23) was solved using a finite volume/finite difference method, and the fully implicit method was employed for time discretization (Gosman et al., 1985). Calculations were performed for $\omega = 0$, $\beta = \kappa = 1$, $\sigma T_o^4 = 1$, and $N = 1$. A discretization with 80×40 control volumes, $N_\theta = N_\varphi = 10$ and $\Delta t^* = 10^{-4}$ was selected. The accuracy of the time discretization was checked by repeating the calculations using a time step equal to 0.5×10^{-4}. It was found that the numerical solution is independent of Δt^* for the two reported values.

Figure 6*a* shows the symmetric of the unsteady, conductive, and radiative terms of Eq. (23) integrated over the whole domain from 0 to t^*, with $t^* \le 1.5 \times 10^{-2}$:

$$E_1 = \int_{-\beta a}^{\beta a} \int_0^{\beta b} \int_0^{t^*} \frac{\partial \theta}{\partial t}\, dt d\tau_y d\tau_x \quad (28a)$$

$$E_2 = \int_{-\beta a}^{\beta a} \int_0^{\beta b} \int_0^{t^*} \left(\frac{\partial^2 \theta}{\partial \tau_x^2} + \frac{\partial^2 \theta}{\partial \tau_y^2} \right) dt d\tau_y d\tau_x \quad (28b)$$

$$E_3 = \int_{-\beta a}^{\beta a} \int_0^{\beta b} \int_0^{t^*} \left(-\frac{\nabla \cdot Q}{N} \right) dt d\tau_y d\tau_x . \quad (28c)$$

The temporal evolution of the dimensionless temperature at the center of the enclosure ($\tau_x = 0$, $\tau_y = \beta b/2$) is also plotted. These results were computed using DTM-1 to solve the RTE. Since the temperature of the boundaries is fixed, the medium receives energy from the top wall and looses energy to the remaining walls by conduction and radiation. Globally, energy is released from the medium to the surroundings by radiation and conduction, up to $t^* \approx 50 \times 10^{-4}$, while the temperature of the medium decreases. For larger values of t^*, the medium still looses energy by conduction but its temperature is already small enough such that $\nabla \cdot Q$ becomes negative. The conductive and the radiative terms of Eq. (23) tend to compensate each other such that the temperature of the medium and the total energy release level off as steady state is approached for large values of t^*.

The numerical method used to solve Eq. (23) is conservative and, therefore, the numerical solution satisfies the global energy balance $E_1 = E_2 + E_3$, regardless of the method used to solve the RTE. However, if DTM-0 is used, the dimensionless form of Eq. (13) is not satisfied. Hence, the value of $\nabla \cdot Q$ fed into Eq.

(23), integrated over the whole domain, does not correspond to the net radiative heat rate on the boundary of the enclosure. This does not happen if DTM-1 or DTM-2 are used.

The present problem has no analytical solution which prevents the calculation of the numerical errors. However, it is easy to compute the absolute value of the difference between the radiative energy term E_3, calculated using DTM-0 and DTM-1, as well as the ratio of this difference to the result of DTM-1. These quantities are a measure of the absolute and relative errors of the radiative energy term E3 calculated by means of DTM-0, taking the results of a conservative method as a reference. They quantify the imbalance in the dimensionless form of Eq. (13) and represent the extent over which the nonconservative formulation departs from a conservative one. These errors are shown in Fig. 6*b* for coarse and fine discretizations. It can be seen that both the absolute and the relative errors accumulate along the time. This increase is larger for the relative errors as a result of the decrease of $|E_3|$ for $t^* > 50 \times 10^{-4}$.

Test Case 3—Three-Dimensional Rectangular Furnace with an Emitting-Absorbing-Scattering Medium. The rectangular furnace idealized by Mengüç and Viskanta (1985), and also examined by others (Jamaluddin and Smith, 1988; Truelove, 1988; Carvalho et al., 1993), was selected for evaluation of the methods in a three-dimensional gray enclosure. The dimensions of the furnace are $2 \times 2 \times 4$ m^3 in x, y, and z directions, respectively. The emissivity of the walls is 0.7, except at $z = 0$ m, where $\epsilon_w = 0.85$. The temperature of the walls is 900 K, except at $z = 0$ m, where $T_w = 1200$ K, and at $z = 4$ m, where $T_w = 400$ K. There is a prescribed volumetric heat source equal to 5 kW/m^3. Standard calculations were performed using a grid with $9 \times 9 \times 15$ CV, uniform in each direction. Several angular discretizations and radiative properties of the medium were considered, as described below. Additional calculations were carried out using much finer spatial and angular discretizations ($27 \times 27 \times 45$ CV, $N_\theta = N_\varphi = 10$).

The computed heat rate received and leaving the boundary of the enclosure, the radiative heat source, and the imbalance of the energy equation are listed in Table 2 for the different studied cases. The imbalance is about 0.2 percent for $N_\theta = N_\varphi = 2$, and 0.05 percent for $N_\theta = N_\varphi = 5$, regardless of the absorption and scattering coefficients. If the proposed conservative formulations are used the numerical solution satisfies the energy equation.

The mean relative errors of temperature and net heat fluxes, taking the zonal method solution reported by Truelove (1988) as a reference, are given in Table 3. DTM-2 generally yields larger errors than the others. Since the predictions of DTM-2 were also worse than the others in test case 1 and, in addition, it cannot be always applied, DTM-2 is not recommended for practical applications. The accuracy of DTM-0 and DTM-1 is similar, with slightly lower errors for the temperature if DTM-1 is used.

The predicted gas temperature distribution along the centerline of three different planes and the net heat flux along the centerline of the hot ($z = 0$ m) and cold ($z = 4$ m) walls are displayed in Fig. 7 ($N_\theta = N_\varphi = 2$) and 8 ($N_\theta = N_\varphi = 5$), for $\kappa = 0.5$ m^{-1} and $\sigma_s = 0$ m^{-1}. The zonal method solution (Truelove, 1988) is also shown for comparison purposes. As in the previous test cases, the solution computed using DTM-1 is very close to that of DTM-0. The DTM-2 yields rather poor predictions of the net heat fluxes for $N_\theta = N_\varphi = 2$ and exhibits larger oscillations than both DTM-1 and DTM-0. A possible explanation for this behavior is that the ray effects are enhanced by the local correction of the radiation intensity leaving a boundary, yielding larger oscillations and worse predictions.

The predicted temperatures exhibit unrealistic oscillations at $z = 0.4$ m and $z = 3.6$ m for the coarser angular discretization. These wiggles are attributed to the ray effects. Nevertheless, the DTM predictions are within 20 K of the zonal method solution. Small oscillations are also observed for the net heat flux at the cold wall. If a finer angular discretization is used, the results become closer to the zonal method solution, as shown in Fig. 8. Although not shown here, similar results were obtained for nonscattering media with $\kappa = 0.25$ m^{-1} and $\kappa = 1$ m^{-1}.

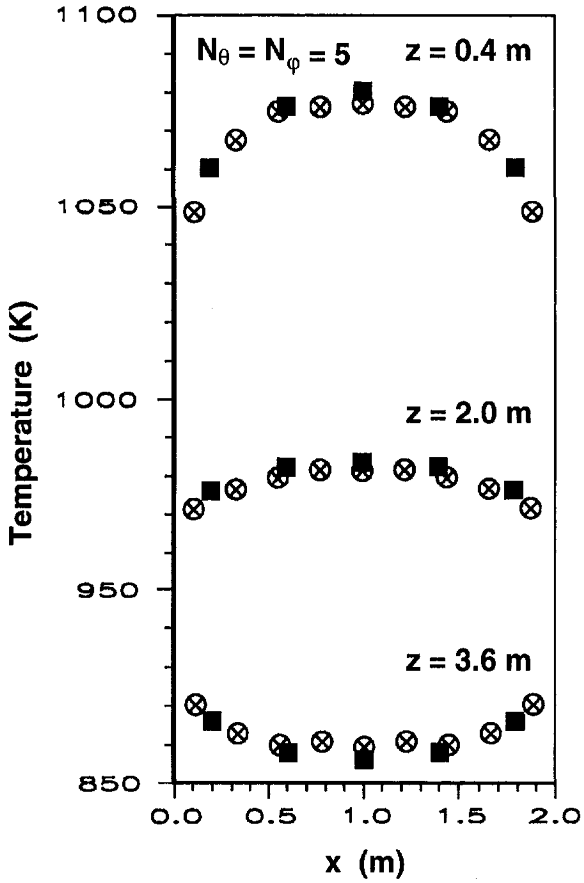

Fig. 9 Predicted temperature (K) profiles for test case 3 with an emitting-absorbing-scattering medium (■—zonal method; O-DTM-0; X-DTM-1)

Finally, an emitting-absorbing-scattering medium with $\omega = 0.7$ and $\beta = 0.5$ m^{-1} was considered, using $N_\theta = N_\varphi = 5$. The net heat fluxes are equal to those calculated for a nonscattering medium with $\kappa = 0.5$ m^{-1}. In fact, the radiative heat flux distribution is independent of ω for isotropic scattering with specified heat generation in the medium (Truelove, 1988). However, the emissive power of the medium increases, as shown in Fig. 9. The results obtained using DTM-0 and DTM-1 closely follow the zonal method solution. The accuracy of the results, taking the zonal method solution as the reference, is comparable to that observed for the nonscattering medium.

Conclusions

The original formulation of the DTM was examined and new conservative formulations applicable to enclosures with diffusely emitting-reflecting boundaries were proposed and evaluated. A simple treatment for isotropic scattering media was described and validated. From the analysis carried out the following conclusions may be drawn:

1 The original formulation of the DTM is not conservative. Imbalance of the energy equation applied to an enclosure may be large if coarse spatial and angular discretizations are used. The imbalance decreases with spatial and angular refinement, but not monotonically.

2 The original formulation of the DTM is not conservative because the solid angles associated with the irradiation rays leaving a cell face on the boundary do not add up to 2π, in general. Therefore, if the radiation intensity leaving the wall, taken as J/π, is integrated over all those solid angles, it does not yield the radiosity J.

3 A local correction of the energy per unit time of the irradiation rays leaving the boundary (DTM-2) was evaluated. However, the results obtained were not satisfactory in terms of accuracy and, therefore, this method should not be used.

4 The conservative formulation based on a global correction of the energy per unit time of the irradiation rays leaving the boundary (DTM-1) is recommended for future applications of the DTM. The solution accuracy obtained using this formulation is very close to the accuracy of the original one for all the test cases examined, but the proposed formulation satisfies energy conservation.

5 A simple treatment of isotropic scattering was demonstrated. The proposed method calculates the integral appearing in the in-scattering term using the incident radiation derived from the equation for the conservation of radiative energy. No additional approximations are needed to deal with isotropic scattering media besides those embodied in the treatment of nonscattering media.

References

Boyd, R. K., and Kent, J. H., 1986, "Three-dimensional Furnace Computer Modelling," *21st Symposium (Int.) on Combustion,* The Combustion Institute, Pittsburgh, PA, pp. 265–274.

Bressloff, N. W., Moss, J. B., and Rubini, P. A., 1995, "Application of a New Weighting Set for the Discrete Transfer Radiation Model," *Proceedings, 3rd European Conference on Industrial Furnaces and Boilers,* Lisbon, Portugal.

Carlson, B. G., and Lathrop, K. D., 1968, "Transport Theory—The Method of Discrete Ordinates," *Computing Methods in Reactor Physics,* H. Greenspan, C. N. Kelber, and D. Okrent, eds., Gordon & Breach, New York.

Carvalho, M. G., and Coelho, P. J., 1989, "Heat Transfer in Gas Turbine Combustors," *Journal of Thermophysics and Heat Transfer,* Vol. 3, No. 2, pp. 123–131.

Carvalho, M. G., Farias, T., and Fontes, P., 1993, "Multidimensional Modeling of Radiative Heat Transfer in Scattering Media," ASME JOURNAL OF HEAT TRANSFER, Vol. 115, pp. 486–489.

Chai, J. C., Lee, H. S., and Patankar, S., 1993, "Ray Effect and False Scattering in the Discrete Ordinates Method," *Numerical Heat Transfer,* Part B, Vol. 24, pp. 373–389.

Chai, J. C., Lee, H. S., and Patankar, S. V., 1994, "Finite Volume Method for Radiation Heat Transfer," *Journal of Thermophysics and Heat Transfer,* Vol. 8, pp. 419–425.

Coelho, M. G., Gonçalves, J. M., and Carvalho, M. G., 1995, "A Comparative Study of Radiation Models for Coupled Fluid Flow/Heat Transfer Problems," *Proceedings, 9th International Conference for Numerical Methods in Thermal Problems,* Vol. IX, Part 1, R. W. Lewis and P. Dubertaki, eds., Pineridge Press, Swansea, pp. 378–389.

Crosbie, A. L., and Schrenker, R. G., 1984, "Radiative Heat Transfer in a Two-Dimensional Rectangular Medium Exposed to Diffuse Radiation," *Journal of Quantitative Spectroscopy and Radiative Transfer,* Vol. 31, No. 4, pp. 339–372.

Cumber, P. S., 1995, "Improvements to the Discrete Transfer Method of Calculating Radiative Heat Transfer," *International Journal of Heat and Mass Transfer,* Vol. 38, No. 12, pp. 2251–2258.

Fiveland, W. A., 1984, "Discrete-Ordinates Solutions of the Radiative Transport Equation for Rectangular Enclosures," ASME JOURNAL OF HEAT TRANSFER, Vol. 106, pp. 699–706.

Gosman, A. D., Launder, B. E., and Reece, G. J., 1985, *Computer-Aided Engineering, Heat Transfer and Fluid Flow,* John Wiley & Sons, New York.

Gosman, A. D., Lockwood, F. C., Megahed, I. E. A., and Shah, N. G., 1982, "Prediction of the Flow, Reaction and Heat Transfer in a Glass Furnace," *Journal of Energy,* Vol. 6, No. 6, pp. 353–360.

Hottel, H. C., and Sarofim, A. F., 1967, *Radiative Transfer,* McGraw-Hill, New York.

Howell, J. R., 1968, "Application of Monte Carlo to Heat Transfer Problems," *Advances in Heat Transfer,* J. P. Hartnett and T. F. Irvine, eds., Vol. 5, Academic Press, New York.

Jamaluddin, A. S., and Smith, P. J., 1988, "Predicting Radiative Transfer in Rectangular Enclosures Using the Discrete Ordinates Method," *Combustion Science and Technology,* Vol. 59, pp. 321–340.

Lathrop, K. D., 1968, "Ray Effects in Discrete Ordinates Equations," *Nuclear Science and Engineering,* Vol. 32, pp. 357–369.

Lockwood, F. C., and Shah, N. G., 1981, "A New Radiation Solution Method for Incorporation in General Combustion Prediction Procedures," *18th Symposium (Int.) on Combustion,* The Combustion Institute, Pittsburgh, PA, pp. 1405–1414.

Mengüç, M. P., and Viskanta, R., 1985, "Radiative Transfer in Three-Dimensional Rectangular Enclosures Containing Inhomogeneous Anisotropically Scattering Media," *Journal of Quantitative Sprectroscopy and Radiative Transfer,* Vol. 33, pp. 533–549.

Modest, M. F., 1993, *Radiative Heat Transfer,* McGraw-Hill, New York.

Murthy, J. Y., and Choudhury, D., 1992, "Computation of Participating Radiation in Complex Geometries," HTD-Vol. 203, *Developments in Radiative Heat Transfer,* ASME, New York, pp. 153–160.

Raithby, G. D., and Chui, E. H., 1990, "A Finite Volume Method for Predicting Radiant Heat Transfer in Enclosures with Participating Media," ASME JOURNAL OF HEAT TRANSFER, Vol. 112, pp. 415–423.

Selçuk, N., 1983, "Evaluation of Multi-Dimensional Flux Models for Radiative Transfer in Combustion Chambers: A Review," AGARD CP-353, Paper No. 28.

Shah, N. G., 1979, "New Method of Computation of Radiation Heat Transfer in Combustion Chambers," Ph. D. Thesis, Imperial College of Science and Technology, London.

Truelove, J. S., 1988, "Three-dimensional Radiation in Absorbing-Emitting-Scattering Media using the Discrete-Ordinates Approximation," *Journal of Quantitative Spectroscopy and Radiative Transfer,* Vol. 39, No. 1, pp. 27–31.

Viskanta, R., and Mengüç, M. P., 1987, "Radiation Heat Transfer in Combustion Systems," *Progress in Energy and Combustion Science,* Vol. 13, pp. 97–160.

Radiation Heat Transfer of Arbitrary Three-Dimensional Absorbing, Emitting and Scattering Media and Specular and Diffuse Surfaces

S. Maruyama

T. Aihara

Institute of Fluid Science
Tohoku University
2-1-1 Katahira, Aoba-Ku
Sendai 980
Japan

Analysis of radiation heat transfer using the Radiation Element Method by Ray Emission Model, REM^2, is described. The REM^2 is a generalized numerical method for calculating radiation heat transfer between absorbing, emitting and scattering media and specular surfaces with arbitrary three-dimensional configurations. The ray emission model for various radiation elements is expressed by polyhedrons and polygons. Arbitrary thermal conditions can be specified for each radiation element, and generalized radiation transfer can be achieved for both of surface and volume elements by introducing a new definition of view factors. The accuracy of the present method is verified using simple configurations. A cubic participating medium with a spherical cavity covered with specular and diffuse surfaces is analyzed as an example of an arbitrary configuration. The temperature distribution shows good accuracy with a small number (45) of rays emitted from each element compared with the Monte Carlo method.

Introduction

Recent advances in computer technology have accelerated the development of computer simulations of engineering systems. There are a number of simulation tools for analyzing structure, thermal conduction, convective heat transfer, and fluid dynamic problems which can be applied to arbitrary configurations of machine elements or to total systems.

Radiation transfer of participating media is important for the design of furnaces, precision heat-transfer control of semiconductor processes, and prediction of the effect of dust and CO_2 on the global environment. Many methods have been developed for the problem such as the Monte Carlo method by Siegel and Howell (1992) and Kudo et al. (1993), the discrete ordinate method by Fiveland (1984), the discrete transfer method by Lockwood and Shah (1981), the boundary element method by Bialecki (1993) and other methods such as that of Tan and Howell (1990). However, it is difficult to apply these methods to a complicated three-dimensional configuration such as the one used in finite element analysis.

Maruyama and Aihara (1987) proposed a simple numerical method for analyzing radiation transfer of three-dimensional arbitrary configurations, and the effective radiation area. Maruyama (1993a) introduced a new definition of view factors and proposed a numerical method for three-dimensional arbitrary surfaces with diffuse and specular reflections. This method was applied to an axisymmetric system of a Czochralski furnace by Maruyama and Aihara (1994a). Radiation transfer in a participating medium in a plane parallel configuration was solved using the concept of the view factors proposed by Maruyama and Aihara (1994b).

In the present study, the Radiation Element Method by the Ray Emission Model, REM^2, is proposed. The REM^2 is a generalized numerical method for radiation transfer in participating media which is descretized using numerous polyhedrons and specular and diffuse surfaces which are descretized using polygons. The present method is verified by radiation transfer of a simple configuration. An example of an arbitrary configuration composed of a cubic participating medium with a spherical cavity is demonstrated.

Basic Equations

We consider the participating medium contained in a polyhedron, as shown in Fig. 1. The radiation intensity at $\vec{r}$ in the direction $\hat{s}$ can be expressed from radiation energy balance as

$$\frac{dI_\lambda(\vec{r},\hat{s})}{dS} = -(\kappa_\lambda+\sigma_{s,\lambda})I_\lambda(\vec{r},\hat{s})+\kappa_\lambda I_{b,\lambda}(T) + \frac{\sigma_{s,\lambda}}{4\pi}\int_{4\pi} I_\lambda(\vec{r},\hat{s}')P_\lambda(\hat{s}'\to\hat{s})d\omega \quad (1)$$

where κ_λ and $\sigma_{s,\lambda}$ are spectral absorption and scattering coefficients, respectively. $P_\lambda(\hat{s}'\to\hat{s})$ is a phase function from the direction $\hat{s}'$ to $\hat{s}$.

In order to simplify the problem, the following assumptions are introduced.

1 Each element is at a constant uniform temperature. The refractive index and heat generation rate per unit volume are also constant and are uniform over the polyhedral radiation element.
2 Scattering in the participating medium is isotropic.
3 The scattered radiation distributes uniformly over the element.

Referring to Fig. 1, the ray passing through the radiation element attenuates and a part of the ray is scattered. The ray is separated into absorbed, scattered, and transmitted fractions. The scattered ray is isotropic according to assumption (2) and is distributed uniformly over the element according to assump-

---

Contributed by the Heat Transfer Division and based on a paper presented at the 1995 ASME/JSME Thermal Engr. Joint Conference, Maui, Hawaii. Manuscript received by the HEAT TRANSFER DIVISION October 9, 1995; revision received August 27, 1996; Keywords: Furnaces & Combustors, Numerical Methods, Radiation. Associate Technical Editor: M. Modest.

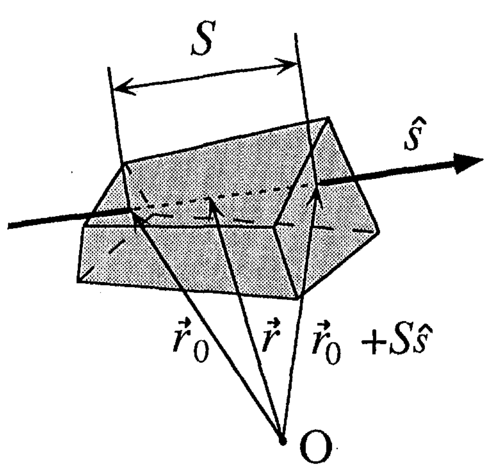

Fig. 1 Attenuation of radiation ray along the direction $\hat{s}$

tion (3). The third term of the right hand side of Eq. (1) is approximated as

$$\frac{\sigma_{s,\lambda}}{4\pi}\int_{4\pi} I_\lambda(\vec{r}, \hat{s}')P_\lambda(\hat{s}' \to \hat{s})d\omega$$

$$= \frac{\sigma_{s,\lambda}}{4\pi}\int_{4\pi} I_\lambda(\vec{r}, \hat{s}')d\omega = \sigma_{s,\lambda} I^D_\lambda \quad (2)$$

where I^D_λ is the average diffuse radiant intensity, i.e., the sum of emitted and scattered radiant intensities. It should be noted that I^D_λ is similar to diffuse radiosity that was used for radiation transfer of arbitrary diffuse and specular surfaces (Maruyama, 1993a; Maruyama and Aihara, 1994a).

Introducing the extinction coefficient $\beta_\lambda \equiv \kappa_\lambda + \sigma_{s,\lambda}$ and albedo Ω, Eq. (1) is rewritten as

$$\frac{dI_\lambda(\vec{r}, \hat{s})}{dS} = \beta_\lambda[-I_\lambda(\vec{r}, \hat{s}) + (1 - \Omega)I_{b,\lambda}(T) + \Omega I^D_\lambda]. \quad (3)$$

Referring to Fig. 1, the solution of Eq. (3) along $\hat{s}$ becomes

$$I_\lambda(\vec{r}_0 + S\hat{s}, \hat{s}) = I_\lambda(\vec{r}_0, \hat{s}) \exp(-\beta_\lambda S)$$

$$+ [(1 - \Omega)I_{b,\lambda}(T) + \Omega I^D_\lambda][1 - \exp(-\beta_\lambda S)]. \quad (4)$$

When there is no incident radiation in direction $\hat{s}$, Eq. (4) expresses radiation intensity that is emitted from the element itself. By integrating Eq. (4) over all cross-sections with $I_\lambda(\vec{r}_0, \hat{s}) = 0$, one can obtain the radiation energy emitted in direction $\hat{s}$. However, this procedure is tedious when we apply the integration of Eq. (4) to an arbitrary polyhedron. We introduce the following average thickness $\bar{S}$ of the radiation element in direction $\hat{s}$ to simplify the integration:

$$\bar{S} \equiv V/A(\hat{s}) \quad (5)$$

where V and $A(\hat{s})$ are the volume and area projected onto the surface normal to $\hat{s}$, respectively. Then the radiant energy emitted from the element can be approximated as

$$dQ_{J,\lambda}(\hat{s})$$

$$= A(\hat{s})[(1 - \Omega)I_{b,\lambda} + \Omega I^D_\lambda][1 - \exp(-\beta_\lambda \bar{S})]d\omega. \quad (6)$$

As previously mentioned, I^D_λ in Eq. (6) is the diffuse part of radiation intensity, and the transmitted fraction of the ray along direction $\hat{s}$ is not included in I^D_λ. The relation between the transmitted and diffusely scattered rays is the same as that between specular and diffuse reflections (Maruyama, 1993a; Maruyama and Aihara, 1994a). The analogy between isotropic scattering and diffuse reflection is shown in Fig. 2(*b*). In order to describe surfaces and participating media generally, the diffuse reflectivity of the surfaces and the albedo of the participating media in Eq. (6) are redefined as Ω^D. The specular reflectivity Ω^S is also introduced to describe the specular reflectivity of the surfaces.

Consider a radiation element i, which may be either a volume element or a surface element. A generalized expression of Eq. (6) is

$$dQ_{J,i,\lambda}(\hat{s}) = A_i(\hat{s})[(1 - \Omega^D - \Omega^S)I_{b,\lambda} + \Omega^D I^D_\lambda]$$

$$\times [1 - \exp(-\beta_\lambda \bar{S}_i)]d\omega \quad (7)$$

where $\beta_\lambda \bar{S}_i \gg 1$ for a surface element and $\Omega^S = 0$ for a volume element.

Integrating over all solid angles, the spectral radiation energy from the radiation element i is given by

$$Q_{J,i,\lambda} = [(1 - \Omega^D - \Omega^S)I_{b,\lambda} + \Omega^D I^D_\lambda]$$

$$\times \int_{4\pi} A_i(\hat{s})[1 - \exp(-\beta_\lambda \bar{S}_i)]d\omega. \quad (8)$$

We consider the case of a participating medium with $\beta_\lambda \bar{S}_i \gg$

Nomenclature

A = Area
A^R = Effective radiation area (Eq. (10))
F^A_{ij}, F^D_{ij} = Absorption and diffuse scattering view factors from element i to j, respectively (Eq. (14))
F^E_{ij} = Extinction view factor from element i to j (Eq. (13))
$f^j_i(\hat{s})$ = Fraction of radiation energy leaving radiation element i that is absorbed or isotropically scattered or diffusely reflected by radiation element j
$I(\vec{r}, \hat{s})$ = Radiation intensity
$I_b(T)$ = Blackbody radiation intensity
I^D_λ = Diffuse radiant intensity (Eq. (2))
l = Reference length
N = Number of elements
N_{tr} = Number of rays emitted from each element
Q_G = Heat transfer rate of irradiation, (Eq. (18))
Q_T = Heat transfer rate of emissive power, (Eq. (18))
Q_J = Heat transfer rate of diffuse raiosity (Eq. (16))
Q_X = Net heat transfer rate of heat generation (Eq. (17))
q_X = Net rate of heat generation per unit volume or unit surface area
$\vec{r}$ = Position vector, Fig. 1
$\bar{S}$ = Average thickness of element in the direction $\hat{s}$ (Eq. (5))
S = Pass length though element, Fig. 1
$\hat{s}$ = Unit direction vector, Fig. 1
T = Temperature
V = Volume of a volume element or surface area of a surface element
β = Extinction coefficient
$\Delta\tau$ = Optical thickness of a radiation element in Fig. 6
ϵ = Emissivity $\equiv 1 - \Omega^D - \Omega^S$
κ = Absorption coefficient
Φ = Dimensionless temperature (Eq. (25))
Ω^D = Albedo of a volume element or diffuse of a surface element, reflectivity, Fig. 2
Ω^S = Specular reflectivity, Fig. 2
ω = Solid angle
σ = Stefan–Boltzmann constant
σ_s = Scattering coefficient
τ = Optical thickness $\equiv \beta l$

Subscripts

i = Element i
j = Element j
λ = Spectral value

1 to verify the present model. If there are no concave surfaces on the radiation element, the average projection area becomes one-quarter of the total surface area A_t (Van de Hulst, 1981). The value of $[1 - \exp(-\beta_\lambda \bar{S}_i)]$ approaches to unity for $\beta_\lambda \bar{S}_i \gg 1$. Then, the integration in Eq. (8) becomes

$$\int_{4\pi} A(\hat{s})[1 - \exp(-\beta_\lambda \bar{S}_i)] d\omega \rightarrow \int_{4\pi} \frac{A_t}{4} d\omega = \pi A_t. \quad (9)$$

Consequently, the following effective radiation area A_i^R (Maruyama and Aihara, 1987) is introduced:

$$A_i^R \equiv \frac{1}{\pi} \int_{4\pi} A_i(\hat{s})[1 - \exp(-\beta_\lambda \bar{S}_i)] d\omega \quad (10)$$

where A_i^R is identical to the surface area for a surface element in which the reverse side is not considered. For the case of $\beta_\lambda \bar{S}_i \ll 1$, the value of $[1 - \exp(-\beta_\lambda \bar{S}_i)]$ approaches to $\beta_\lambda \bar{S}_i$. Then, using the relation in Eq. (5), A_i^R is expressed as

$$A_i^R \rightarrow \frac{1}{\pi} \int_{4\pi} A(\hat{s}) \beta_\lambda \bar{S}_i d\omega = 4\beta_\lambda V_i. \quad (11)$$

The model shows a consistency with the analytical solutions for the optically thick limit and optically thin limit. For the case of moderate $\beta_\lambda \bar{S}_i$, A_i^R becomes a value between A_t and $4\beta_\lambda V$ due to the definition, Eq. (10).

Finally, the rate of radiation energy emitted and isotropically scattered by the radiation element can be expressed in generalized form as

$$Q_{J,i,\lambda} = \pi(\epsilon_i I_{b,\lambda} + \Omega^D I_\lambda^D) A_i^R \quad (12)$$

where $\epsilon_i = 1 - \Omega_i^D - \Omega_i^S$, and $Q_{J,i\lambda}$ is the diffuse radiation transfer rate that was introduced in the previous reports (Maruyama, 1993a; Maruyama and Aihara, 1994a) for arbitrary diffuse and specular surfaces.

In the present radiation element method, both the surface and volume elements are accounted for by introducing the generalized form of radiation energy Eq. (7) and (8), and it is not necessary to distinguish between the different types of elements. Numerical integration of Eq. (4) is simplified by introducing the effective radiation area A^R, and average thickness $\bar{S}$.

The proposed method needs the assumption of isotropic scattering for the volume elements and isotropic reflection for the diffuse fraction of reflection for the surface elements. Also, the assumption of isotropic emission is required as shown in Fig. 2. The scattering by particles is generally anisotropic. Maruyama et al. (1995) compared radiation transfer of nongray participating gas with anisotropic and isotropic scattering particles. The nongray radiation transfer was carried out with the isotropic scaling, taking into account the δ-M approximation (Wiscombe, 1977) for the anisotropic scattering. The result with the isotropic assumption showed reasonably good agreement with the Monte Carlo simulation with anisotropic scattering (Farmer and Howell, 1994).

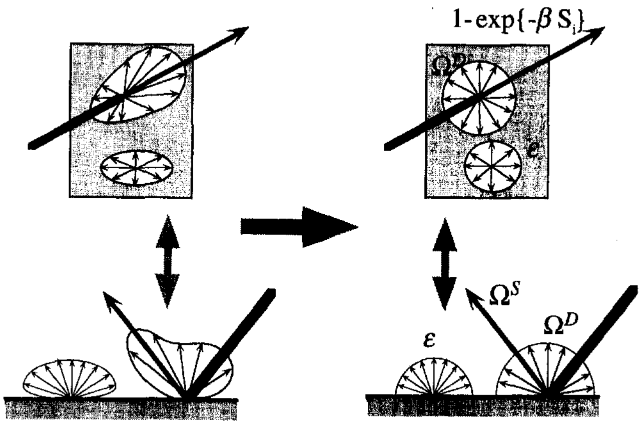

(a)

(b)

Fig. 2 Isotropic models of volume and surface elements form analogy of anisotropic emission and scattering or reflection

Some numerical methods such as the discrete ordinate method and the P_N method can take into account the anisotropic scattering. When one applies the discrete ordinate method to a complicated three-dimensional engineering model, the ray effect (Chai et al., 1993) is unavoidable unless the number of discrete ordinates treated is very large. The number of unknown radiant intensities increases rapidly with increasing the number of discrete ordinates because the unknowns are functions of position and direction. It should also be noted that the discrete ordinate method and the P_N method are difficult to solve for complex three-dimensional systems with unstructured mesh elements which contain specular surfaces. Also, these methods are not suitable for solving for the equilibrium temperature with a given heat transfer rate of the radiation element.

The proposed method REM^2 can be easily applied to the above mentioned complicated system. When one analyzes a radiation transfer with anisotropic scattering particles, there will be a trade off between accuracy and complexity in geometry and thermal conditions.

Extinction, Absorption and Diffuse Scattering View Factors

The authors have introduced absorption and diffuse scattering view factors for radiation transfer of diffuse and specular surfaces, in which specular reflection is not included in those view factors (Maruyama and Aihara, 1994). If one considers Eq. (7) and Fig. 2, it can be found that the isotropically scattered ray and transmitted ray through the radiation element can be treated in the same manner as those of diffuse reflection and specular reflection, respectively. Considering the radiation element i and j, as shown in Fig. 3, an extinction view factor $F_{i,j}^E$ is defined as: the fraction of radiation energy leaving radiation element i that is absorbed or isotropically scattered or diffusely reflected by the radiation element j.

Considering Fig. 3 and Eq. (1), $F_{i,j}^E$ can be written as

$$F_{i,j}^E = \int_{4\pi} f_i^j(\hat{s}) A_i(\hat{s}) [1 - \exp(-\beta_{\lambda,i} \bar{S}_i)] \times [1 - \exp(-\beta_{\lambda,j} S_j)] d\omega / (\pi A_i^R) \quad (13)$$

where S_j is the path length of a ray attenuated in the volume element j, and $f_i^j(\hat{s})$ is the fraction of the energy emitted from the element i in the direction of $\hat{s}$ which reaches the element j. The value of $\beta_\lambda S_j$ is much larger than unity for a surface element. Then, the absorption view factor $F_{i,j}^A$ and diffuse scattering view factors $F_{i,j}^D$ can be written as,

$$F_{i,j}^A = \frac{\epsilon_j F_{i,j}^E}{(1 - \Omega_j^S)}, \quad F_{i,j}^D = \frac{\Omega_j^D F_{i,j}^E}{(1 - \Omega_j^S)}. \quad (14)$$

By introducing $F_{i,j}^A$ and $F_{i,j}^D$, radiation transfer under arbitrary thermal conditions can be carried out as was shown in a previous report (Maruyama, 1993a). As shown in the following section, the present method can solve the radiation transfer equation including specular surfaces without difficulty by introducing the above mentioned view factors.

For the calculation of view factors, surface elements and volume elements are treated separately in the zone method. It should be noted that the proposed method does not distinguish surface and volume elements by introducing Eqs. (7), (10) and

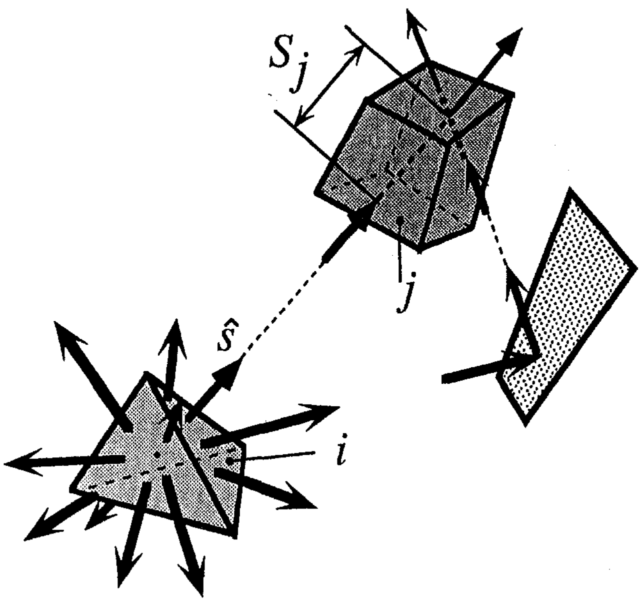

Fig. 3 Extinction of radiation ray between elements *i* and *j*

the above mentioned view factors, and generalized treatment can be achieved for both surface and volume elements.

Radiation Transfer

The above mentioned relations can be applied to radiation transfer at each wavelength. However, in order to simplify the problem, gray assumption is introduced in the following sections. An analogy from the previous work on radiation transfer between surfaces deduces the following relation of diffuse radiant intensity:

$$I_i^D = \epsilon_i I_{b,i} + \Omega_i^D G_i / \pi \tag{15}$$

where G_i is the irradiance on radiation element i. The diffuse radiosity heat transfer rate $Q_{J,i}$ is expressed as

$$Q_{J,i} \equiv A_i^R \pi I_i^D = A_i^R(\epsilon_i n^2 \sigma T_i^4 + \Omega_i^D G_i) \tag{16}$$

where n is the refractive index of element i. The net rate of heat generation $Q_{X,i}$ can be derived from the heat balance on the radiation element as

$$Q_{X,i} = A_i^R \epsilon_i (n^2 \sigma T_i^4 - G_i). \tag{17}$$

Consider the case that the system is constructed of N volume and surface elements. Introducing the following heat transfer rates of irradiation energy $Q_{G,i}$ and emissive power $Q_{T,i}$ of the radiation element,

$$Q_{G,i} \equiv A_i^R G_i, \quad Q_{T,i} \equiv A_i^R \epsilon_i n^2 \sigma T_i^4, \tag{18}$$

then, Eqs. (16) and (17) can be rewritten as

$$Q_{J,i} = Q_{T,i} + \sum_{j=1}^{N} F_{j,i}^D Q_{J,j}, \quad Q_{X,i} = Q_{T,i} - \sum_{j=1}^{N} F_{j,i}^A Q_{J,j}. \tag{19}$$

The heat transfer rate of emissive power $Q_{T,i}$ or net rate of heat generation $Q_{X,i}$ for each radiation element is given arbitrarily as a boundary condition. The unknown $Q_{X,i}$ or $Q_{T,i}$ can be obtained, respectively, by solving Eq. (19) using the method described by Maruyama (1993a). The relation between T_i, $q_{X,i}$, and $Q_{T,i}$, $Q_{X,i}$ are deduced from the following equations, respectively.

$$I_{b,i} = \frac{n^2 \sigma T_i^4}{\pi} = \frac{Q_{T,i}}{\epsilon_i \pi A_i^R}, \quad q_{X,i} = \frac{Q_{X,i}}{V_i} \tag{20}$$

When a system is composed of N radiation elements, $N \times N$ view factors are required. Hence, memory area and calculation time increase rapidly with increasing the element number N. Reduction of the number of radiation elements by excluding transparent spaces and perfect mirror surfaces was taken into account to reduce the number of view factors by Maruyama and Aihara (1996).

Too fine radiation elements do not guarantee accurate solutions by the Monte Carlo method, the discrete ordinate method, and the proposed method because a very large number of ray emissions is required to obtain view factors. Hence, these methods need to give reasonably accurate solutions with rather coarse radiation elements for a complicated three-dimensional configuration in engineering use. The proposed method gives reasonably accurate solutions with a small number of elements as will be discussed in the following section. When one combines the proposed method REM^2 with a finite difference analysis for convection heat transfer etc., re-definition of calculation meshes may be necessary with a proper interpolation between meshes or element values.

Ray Emission Model

Practical engineering elements can be described by numerous polygons and polyhedrons by applying general-purpose pre and post-processor packages for the finite element method. In order to utilize these tools, radiation elements are numerically modeled by arbitrary triangles, quadrilaterals, tetrahedrons, wedges, and hexahedrons, as shown in Fig. 4. Let the surface areas of a polyhedron i be $A_{i,k}$, and its normal unit vectors be $\hat{n}_{i,k}$; the projected area of the polyhedron is

$$A_i(\hat{s}) = \sum_{k=1}^{K} A_{i,k} \operatorname{sgn}(\hat{n}_{i,k} \cdot \hat{s})$$

$$\operatorname{sgn}(x) = x \quad \text{for} \quad x > 0, \quad \operatorname{sgn}(x) = 0 \quad \text{for} \quad x \le 0 \tag{21}$$

where K is the number of surfaces on a polyhedron (i.e., six for a hexahedron and one for a surface element).

Then, A^R is obtained by numerical integration of Eq. (10). The discrete directions of $\hat{s}(\theta_i, \phi_j)$ were distributed uniformly over the entire solid sphere, or the weights of the discretized direction were set uniform. The following relation was adopted in the proposed method:

$$\theta_i = \pi(i-1)/(N_\theta + 1), \quad (i = 1 \ldots N_\theta + 2)$$
$$\phi_j = 2\pi R_i + j\Delta\phi_i, \quad (j = 1 \ldots N_i)$$
$$\Delta\phi_i = 2\pi/N_i, \quad N_i = 2(N_\theta + 1)\sin(\theta_i)/i,$$
$$(i = 2 \ldots N_\theta + 1) \tag{22}$$

where $N_\theta + 2$ is the partition number of the polar angle θ, N_i is an integer rounded to the nearest whole number, and R_i is a random number in the range of $0 \le R_i \le 1$ for a given θ_i. Once Eq. (22) is determined, the relation is used for all radiation elements, so, the calculation time for the random numbers is minimized. The total number of emitted rays N_{tr} and discrete solid angle $\Delta\omega$ are

$$N_{tr} = 2 + \sum_{i=2}^{N_\theta + 1} N_i, \quad \Delta\omega = 4\pi/N_{tr}. \tag{23}$$

Figure 4 shows ray emission from various radiation elements when $N_\theta = 4$ and $N_{tr} = 33$. Each ray starts at the intersection of $\vec{r}_G + t\hat{s}$ and the surface, where $\vec{r}_G$ is a position vector of the centroid of the radiation element.

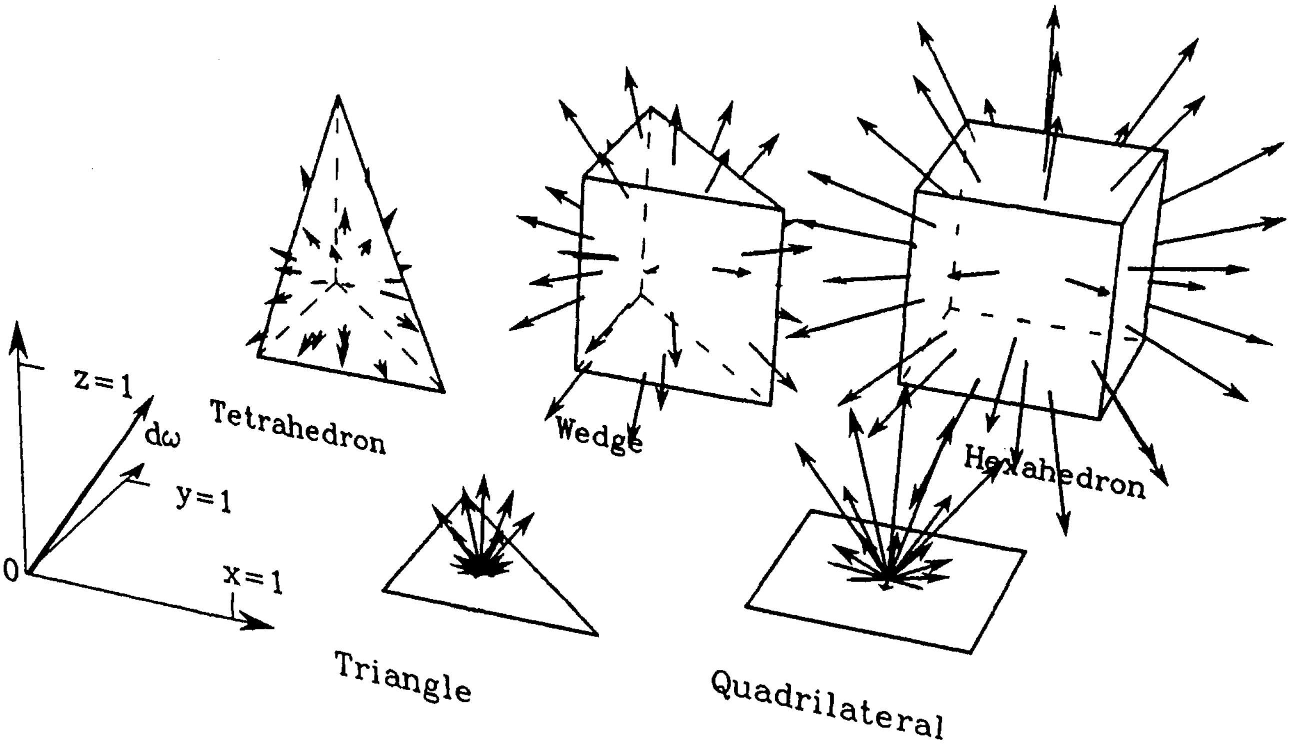

Fig. 4 Ray emission model of various shapes

The length of the arrows expresses the intensity defined as

$$\Delta A^R \equiv A(\bar{s})[1 - \exp(-\beta\bar{S})]\Delta\omega. \quad (24)$$

Each element is covered by equilateral triangles and squares with edges of unit length, and β is set at unity. The larger the surface element or volume element is, the greater the value of ΔA^R, as shown in Fig. 4.

As shown in Eqs. (9) and (10), A^R is equal to A_t for the case of $\beta\bar{S}_i \gg 1$. Calculated A^R and geometrical A_t for various shapes are compared for the optically thick case. The shapes in Fig. 4 are examined, and the deviation of A^R from A_t against the number of emitted rays is plotted in Fig. 5. The relation between N_θ and N_{tr} is also plotted in Fig. 5. Upon increasing the number of emitted rays, the difference between A^R and A_t decreases rapidly. A^R can be calculated accurately with a number of emitted rays as small as $N_\theta = 5$ ($N_{tr} = 45$).

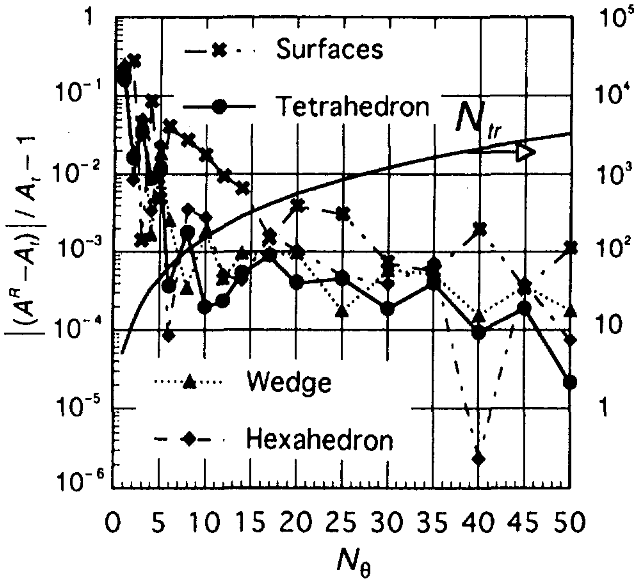

Fig. 5 Accuracy of effective radiation areas with number of emitted rays

Once ΔA^R in Eq. (24) is specified for each element and direction, the ray is traced numerically according to a method similar to that reported in previous work (Maruyama and Aihara, 1994a), and view factors mentioned in the previous section are calculated. The radiation ray tracing method was used for directional control of radiation transfer by Maruyama (1993b), and can result in substantial savings in calculation time compared with the Monte Carlo method, as has been reported by Hayasaka et al., (1986).

This procedure is similar to the one used in the discrete transfer method (Lockwood and Shah, 1981). However, the ray starts from the surface of a volume element, as shown in Fig. 4, according to Eq. (24) in the proposed method. This fact allows the generalized treatment of the surface and volume elements, and contributes to the accuracy of the ray emission model.

Radiation Transfer of Simple Configurations

The present method, REM^2, was applied to a simple configuration, as shown in Fig. 6. The participating medium is a rectangular solid with τ_0 and τ_a edge lengths. The medium does not generate heat, i.e., $q_X = 0$. Two surfaces of the rectangular solid are covered with isothermal black plates at T_1 and T_2. Four surfaces are covered with totally reflecting specular surfaces in order to express a one-dimensional plane parallel configuration. The body elements are divided into N_m elements whose optical thicknesses are $\Delta\tau$.

The dimensionless temperature distributions in the participating media are calculated, and are shown in Fig. 7 to verify the accuracy and the effect of element size. The aspect ratio and number of emitted rays are set at $\tau_a/\tau_0 = 1$ and $N_{tr} = 45$, respectively. The present numerical results are compared with analytical solutions by Heaslet and Warming (1965). The present results show good accordance with the analytical solutions even though the elements are optically as thick as $\Delta\tau = 2$.

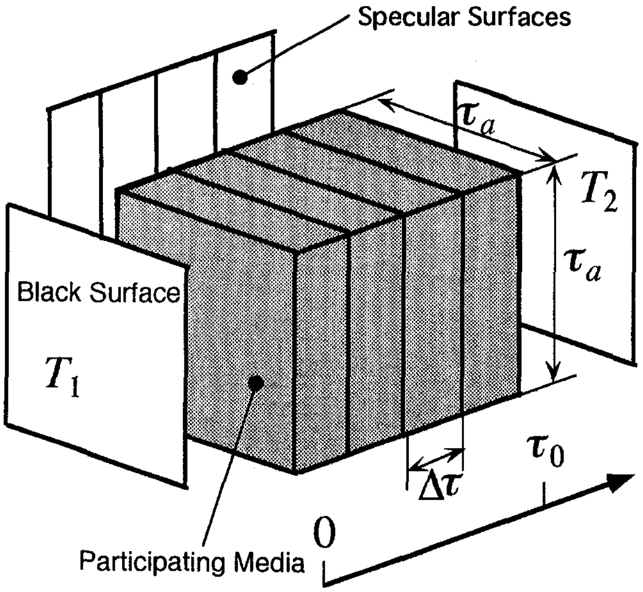

Fig. 6 Calculation model of a rectangular solid participating medium covered with surfaces

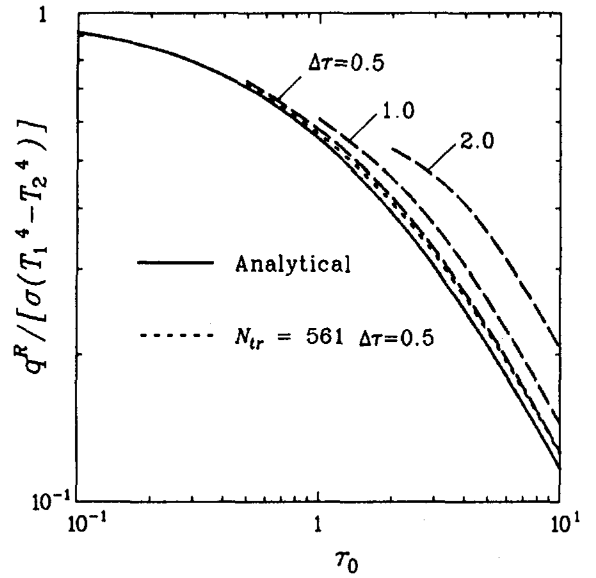

Fig. 8 Comparison of dimensionless heat flux through plane parallel participating media

As has been discussed in the previous report (Maruyama, 1993a), the view factors obtained may not satisfy the reciprocity rule. In order to improve the accuracy of numerical solutions, the extinction view factors $F_{i,j}^E$ and $F_{j,i}^E$ are corrected to satisfy the reciprocity rule using a method similar to that of Omori et al. (1992). The number of ray emissions in the present method is usually much larger than that used in the discrete ordinate method.

The calculation in Fig. 7 is carried out for very large aspect ratio $\tau_a/\tau_0 = 100$ to examine the effect of specular surfaces. The obtained results are almost identical with those for $\tau_a/\tau_0 = 1$. The radiant heat flux q^R is compared with analytical solutions by Heaslet and Warming (1965) in Fig. 8. The same configuration of Fig. 6 is applied to the numerical results. Figure 8 shows good accordance with the analytical solution when $\Delta\tau$ is less than 0.5. However, large $\Delta\tau$ results in poor accordance for q^R whose temperature distribution shows better accordance as shown in Fig. 7.

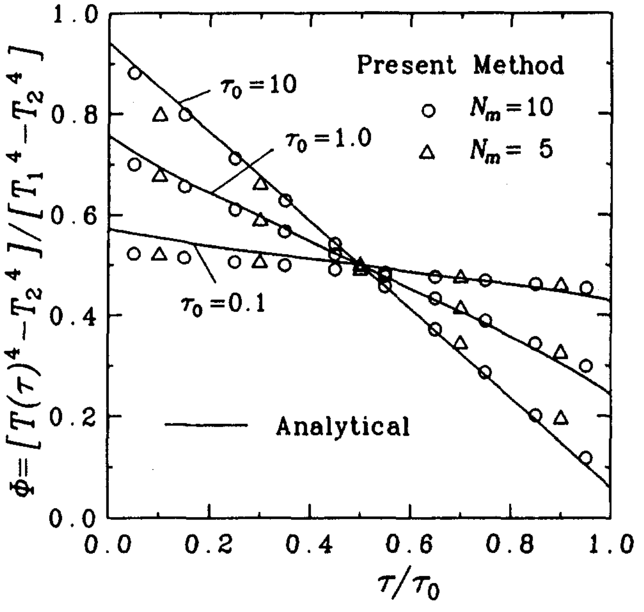

Fig. 7 Comparison of dimensionless temperature distribution between analytical solution and the present numerical method

The same calculation is carried out for a large number of ray emissions, $N_{tr} = 561$, for $\Delta\tau = 0.5$. As shown in Fig. 8, the results for $N_{tr} = 45$ and $N_{tr} = 561$ are almost the same. Consequently, the small number of ray emissions gives a more accurate solution than the Monte Carlo method. The number of ray emissions is usually much larger than that used in the discrete ordinate method. The ray effect (Chai et al., 1993), which causes errors in analysis of a complicated geometry by the discrete ordinate method, is minimized in the present method due to the large number of ray emission and the correction of view factors.

The present method, REM^2, has been applied to two-dimensional square and three-dimensional cubic configurations. The obtained results were compared with the semi-analytical solution by Crosbie and Schrenker (1984) and the zonal analysis by Larsen and Howell (1985), respectively, and the results were presented elsewhere (Maruyama and Aihara, 1996). The numerical results by REM^2 showed good agreement with the existing solutions.

Radiation Transfer of an Arbitrary Configuration

As an example of radiation heat transfer of an arbitrary configuration, a cubic participating medium with a spherical cavity is considered. The cubic participating medium has edges of optical length $2\tau_0$ (= 2), and has a spherical cavity of diameter τ_0 (= 1). The surface of the spherical cavity is isothermal at the temperature of T_1 = 1000 K. Four of the outer surfaces are kept at T_2 = 0 K. The other two surfaces are adiabatic. The albedo of the medium and diffuse reflectivity of the surfaces are set at 0.5. The heat generation rate of the participating medium is set at zero.

Figure 9 shows a one-eighths symmetrical analysis model of the participating medium covered with opaque surfaces. The medium in Fig. 9 is divided into 136 polyhedrons. The opaque and diffuse surfaces are placed on the surface of the medium. Three totally reflecting specular surfaces of $\Omega^S = 1$ are placed to achieve the symmetry. The number of surface elements is 140.

Numerical analysis is carried out for the 276 radiation elements, and the number of ray emissions for each radiation element is set at N_{tr} = 45. The calculation time for the present case is 4.7 s (with one CPU) by a Cray YMP.

A general-purpose three-dimensional CAE package for finite element analysis is used for mesh generation of the radiation elements. There are almost no restrictions for modeling the radiation elements, and the surface and volume elements are not distinguished in the program. Hence, the present method, REM^2, can be combined easily with conduction and convection heat transfer analyses.

The dimensionless temperature distribution of the participating medium is shown in Fig. 10, where the contributions by the surface elements are omitted. Hence, temperatures on the surfaces of the medium are not equal to those of boundary conditions. The dimensionless temperature in Fig. 10 is defined as follows:

$$\Phi = T^4/(T_1^4 - T_2^4). \quad (25)$$

The temperature of the media is the lowest near the edge where the low temperature surfaces intersect. On the surface of the spherical cavity, the temperature is the highest on the surfaces facing the adiabatic surface. However, it should be noted that, on the surface of the spherical cavity, the temperature is the lowest not on surfaces facing low temperature surfaces but on those facing the corner.

The same analysis was conducted for the number of ray emissions $N_{tr} = 561$, and a result almost identical to those for $N_{tr} = 45$ is obtained. The Monte Carlo method usually needs an enormous number of ray emissions, more than 10^4, for each element. The proposed method can be applied to various problems. Furthermore, the method can be efficiently vectorized, and efficient calculation can be carried out using computers with vector processors.

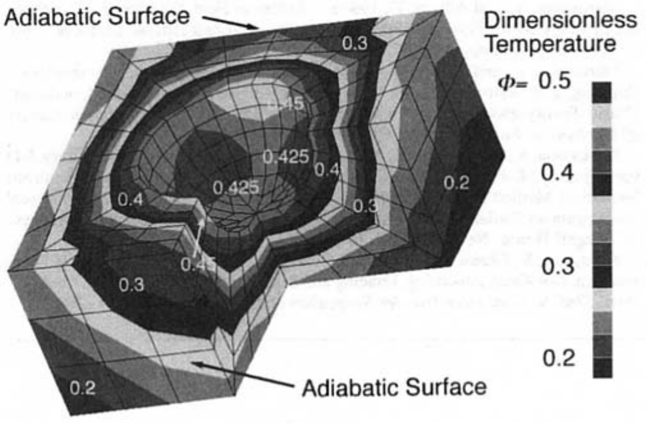

Fig. 10 Dimensionless temperature distribution of a participating cube with a spherical cavity

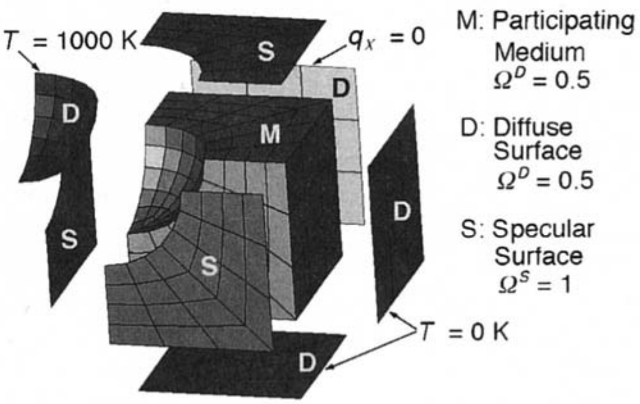

Fig. 9 One-eighths symmetric model of a participating cube with a spherical cavity covered with opaque surfaces

Conclusions

The Radiation Element Method by Ray Emission Model, REM^2, is proposed. This is a generalized method for participating media comprised of arbitrary polyhedrons and surfaces comprised of arbitrary polygons. Arbitrary thermal conditions can be specified for each radiation element by introducing extinction, diffuse scattering and absorption view factors, and effective radiation areas.

The ray emission model shows a consistency with the analytical solutions for the optically thick limit and optically thin limit. The model can describe various radiation elements with a small number of emitted rays. The volume and surface elements can be treated in the same manner by introducing the generalized form of radiation energy and the effective radiation area.

The present method is applied to a participating medium of rectangular solid covered with opaque surfaces, and the results are compared with analytical solutions of plane parallel configuration. The temperature distributions show good agreement with analytical solutions. The heat flux through the media shows good accordance if the optical thickness of a radiation element $\Delta\tau < 0.5$. However, the heat flux shows poor accuracy for large $\Delta\tau$.

Radiation heat transfer of a cubic participating medium with a spherical cavity covered with opaque surfaces is analyzed. A general purpose 3-D CAE package is used for mesh generation of the radiation elements. Hence, REM^2 can be combined easily with conduction and convection heat transfer analyses.

The temperature distribution of the participating medium shows good accuracy with a small number, i.e., 45, of rays emitted from each radiation element. This number is extremely small compared with that required by the Monte Carlo method. The REM^2 can also be efficiently vectorized, and efficient calculation is expected using computers with vector processors.

References

Bialecki, R. A., 1993, "Solving Heat Radiation Problems Using the Boundary Element Method," *Topics in Engineering,* Computational Mechanics Publications, Southampton U.K., Vol. 15, pp. 67–89.

Chai, J. C., Lee, H. S., and Patankar, S. V., 1993, "Ray Effect and False Scattering in the Discrete Ordinates Method," *Numerical Heat Transfer, Part B,* Vol. 24, pp. 373–389.

Crosbie, A. L., and Schrenker, R. G., 1984, "Radiative Transfer in a Two-Dimensional Rectangular Medium Exposed to Diffuse Radiation," *J. Quant. Spectrosc. Radiant. Transfer,* Vol. 31, pp. 339–372.

Farmer, J. T., and Howell, J. R., 1994, "Monte Carlo Prediction of Radiative Heat Transfer in Inhomogeneous, Anisotropic, Nongray Media," *J. Thermophsics and Heat Transfer,* Vol. 8, pp. 133–139.

Fiveland, W. A., 1984, "Discrete Ordinates Solutions of the Radiative Transport Equation for Rectangular Enclosures," ASME JOURNAL OF HEAT TRANSFER, Vol. 106, pp. 699–706.

Hayasaka, H., Kudo, K., Taniguchi, H., Nakamachi, I., Omori, T., and Katayama, T., 1986, "Radiative Heat Transfer Analysis by the Radiative Heat Ray Method," *Trans. Japan Society of Mechanical Engineers,* Vol. 52, pp. 1734–1740.

Heaslet, M. A., and Warming, R. F., 1965, "Radiative Transport and Wall Temperature Slip in an Absorbing Planar Medium," *Int. J. Heat and Mass Transfer,* Vol. 8, pp. 979–994.

Kudo, K., Taniguchi, H., Kuroda, A., and Eid, A., 1993, "Development of Analytical Method on Combined Radiative–Convective Heat Transfer in Arbitrary Shaped Domain," *Proceedings of the 30th National Heat Transfer Sympo., Japan,* Vol. 1, pp. 265–267.

Larsen, M. E., and Howell, J. R., 1985, "The Exchange Factor Method: An Alternative Basis for Zonal Analysis of Radiating Enclosures," ASME JOURNAL OF HEAT TRANSFER, Vol. 107, pp. 936–942.

Lockwood, F. C., and Shah, N. G., 1981, "A New Radiation Solution Method for Incorporation in General Combustion Prediction Procedures," *Eighteenth Symposium (International) on Combustion,* The Combustion Institute, pp. 1405–1414.

Maruyama, S., 1993a, "Radiation Heat Transfer Between Arbitrary Three-Dimensional Bodies with Specular and Diffuse Surfaces," *Numerical Heat Transfer, Part A,* Vol. 24, pp. 181–196.

Maruyama, S., 1993b, "Uniform Isotropic Emission from an Involute Reflector," ASME JOURNAL OF HEAT TRANSFER, Vol. 115, pp. 492–495.

Maruyama, S., and Aihara, T., 1987, "Numerical Analysis of Radiative Heat Transfer from Three–Dimensional Bodies of Arbitrary Configurations," *JSME International Journal,* Vol. 30, pp. 1982–1987.

Maruyama, S., and Aihara, T., 1994a, "Radiation Heat Transfer of a Czochralski Crystal Growth Furnace With Arbitrary Specular and Diffuse Surfaces," *Int. J. Heat Mass Transfer,* Vol. 37, pp. 1723–1731.

Maruyama, S., and Aihara, T., 1994b, "Radiation Heat Transfer in Absorbing, Emitting, and Scattering Media With Arbitrary Shapes and Thermal Conditions (Basic Theory and Accuracy in Plane Parallel System)," *Trans. Japan Society of Mechanical Engineers,* Vol. 60, pp. 3138–3144.

Maruyama, S., and Aihara, T., 1996, "Radiative Heat Transfer of Arbitrary 3-D Participating Media and Surfaces With Non-Participating Media by a Generalized Numerical Method REM^2," *Radiative Transfer–I Proc., The First International Symposium on Radiative Heat Transfer,* August, Kusadasi, Turkey, M. P. Menguc, ed., Begell House, New York, pp. 153–167.

Maruyama, S., Ukaku, M., and Aihara, T., 1995, "Radiative Heat Transfer of Non-Uniform, Non-Gray, Absorbing, Emitting and Scattering Media Using Band Models," *Proc. 32nd National Heat Transfer Symposium of Japan,* Vol. 2, pp. 591–592.

Omori, T., Murakami, S., Katoh, S., Choi, C. K., and Kobayashi, H., 1992, "Coupled Simulation of Convective and Radiative Heat Transfer in Enclosed Space: Accuracy of Shape Factors Obtained by Monte Carlo Method," *Proc. Air-Con. Sanit. Eng. Japan,* pp. 653–656.

Siegel, R., and Howell, J. R., 1992, *Thermal Radiation Heat Transfer,* 3rd Ed., Hemisphere, Washington DC., pp. 795–804.

Tan, Z., and Howell, J. R., 1990, "New Numerical Method for Radiation Heat Transfer in Non–Homogeneous Participating Media," *J. Thermophsics and Heat Transfer,* Vol. 4, pp. 419–424.

Van de Hulst, H. C., 1981, *Light Scattering by Small Particles,* Dover, New York, pp. 110–111.

Wiscombe, W. J., 1977, "The Delta–M Method: Rapid Yet Accurate Radiative Flux Calculations for Strongly Symmetric Phase Functions," *J. the Atmospheric Sciences,* Vol. 34, pp. 1408–1422.

M. Epstein

J. P. Burelbach

M. G. Plys

Fauske & Associates, Inc.,
16W070 West 83rd Street,
Burr Ridge, IL 60521

Surface Temperature Profiles Due to Radiant Heating in a Thermocapillary Channel Flow

Experiments were conducted to determine the temperature distribution at the surface of a thermocapillary channel flow generated by heating a shallow liquid layer locally from above with a radiant energy source. The measured temperature profiles are explained by an available nonlinear conduction model that incorporates the combined effects of thermocapillary and thermogravitational convection in shallow liquid layers.

Introduction

Problems related to the ignition of floating organic layers in waste tanks have stimulated the present interest in the heat-transfer characteristics of surface-tension induced flows in a liquid layer heated from above by a sharply focused source. A recent comprehensive review by Ross (1994) documents very well the research on thermocapillary flow in shallow liquid layers heated from above by a stationary concentrated source or by a moving source (flame). Experimental and theoretical work have shown that the convective motion in the liquid layer is complex and involves a single eddy or multiple eddies within the vicinity of the heat source (Burgoyne et al., 1968; Glassman and Hansel, 1968; Sirignano and Glassman, 1970; Mackinven et al., 1970; Akita, 1973; Torrance and Mahajan, 1975; Di Blasi et al., 1990; and Fukano et al., 1990). Despite the complexity of the flow, it has been well established that the local rise in liquid temperature beneath the heat source results in a reduction in the surface tension and the surface flow of liquid away from the source. The liquid which flows from the heat source is replenished by a submerged, oppositely directed current of cooler liquid. Moreover, for sufficiently shallow liquid layers, thermogravitational forces play a relatively minor role in the liquid motion.

Recently, Burelbach et al. (1996) reported a theory for the heat transported radially away from a circular heat source through a shallow liquid layer by thermocapillary and thermogravitational convection. By first considering a radial segment of the axisymmetric flow field with the assumed characteristics of adiabatic horizontal boundaries (substrate and liquid surface) and a known surface temperature gradient, they derived a nonlinear Fourier-type heat-conduction equation having an effective thermal conductivity which incorporates the effects of both thermocapillary and thermogravitational flow. This heat flux "law" was then combined with a global energy balance, that accounts for heat losses off the surface of the liquid, to obtain an expression for the liquid-surface temperature rise beneath the heat source as a function of the physical properties of the liquid, the liquid-surface heat-transfer coefficient, and the strength of the source. The temperature rise experiments performed by Burelbach et al. (1996) generally verify this expression.

The effective thermal conductivity theory developed by Burelbach et al. (1996) is not only capable of predicting the temperature rise beneath the heat source but can be used to estimate the liquid surface temperature as a function of distance from the heat source. The latter capability, however, has not yet been tested by experiment. The objective of this paper is to report experimental results obtained on one-dimensional thermocapillary channel flow in which the liquid surface temperature profile is revealed and compared with the above referenced effective thermal conductivity theory. In the development of the theory the heat-source spatial distribution is regarded as a step function involving a finite uniformly heated zone adjacent to a semi-infinite unheated zone.

Effective Thermal Conductivity Theory for Heat Transport Via Thermocapillary and Thermogravitational Convection in an Open Channel Heated at its Closed End

The previous analysis of cylindrically symmetric, combined thermocapillary and thermogravitational convection in a liquid layer subject to a local radiant heat source (Burelbach et al., 1996) is extended here to x directional flow in a channel formed by two parallel walls at a distance W apart (see Fig. 1). The depth of the layer is denoted by the symbol δ. We focus our attention on sufficiently shallow layers ($\delta \ll W$) such that the velocity profile does not depend on the z coordinate (see Fig. 1). The channel is regarded as semi-infinite in length and the axial distance x is measured from the closed end of the channel. The surface of the liquid is exposed to a heat flux q_o over the finite distance interval $0 < x < x_o$. The walls and base of the channel are assumed to be adiabatic surfaces. The heat gained by the liquid is given up to the overlying atmosphere by surface cooling within the finite interval $x_o < x < x_\infty$ at a rate given by Newton's law of cooling, $h(T - T_\infty)$, where T is the local temperature of the surface of the liquid, T_∞ is the temperature of the atmosphere, and h is an effective, constant heat transfer coefficient which accounts for both free convection and radiation heat transport off the surface of the liquid. The location $x = x_\infty$ (not shown in Fig. 1) is where the surface temperature T is reduced to the ambient temperature T_∞ (see below).

The choice of a constant heat transfer coefficient over the free surface outside the heated zone could be regarded as an oversimplification considering the complex flow pattern created in the gas space by the outward thermocapillary flow of the liquid surface and the inward buoyancy induced flow established by the heat source. Nevertheless, this "type" of oversimplification has been used successfully in numerous applications involving complex flow patterns over heat-transfer surfaces. Consider, for example, the now-classical fin problem. The justifications for a constant h are: (i) it is standard engineering practice when confronted with complex geometries; (ii) it is in line with our objectives of developing a practical model for fire

---

Contributed by the Heat Transfer Division for publication in the JOURNAL OF HEAT TRANSFER. Manuscript received by the Heat Transfer Division February 22, 1996; revision received October 17, 1996; Keywords: Fire/Flames, Natural Convection, Thermocapillary Flows. Associate Technical Editor: T. Tong.

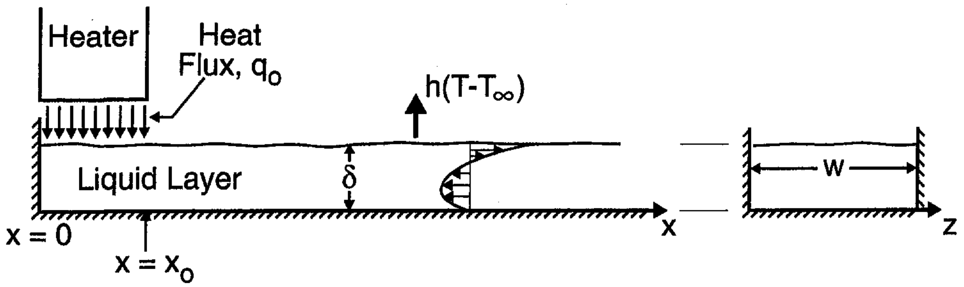

Fig. 1 Schematic diagram of semi-infinite liquid layer in a channel subject to a surface heat flux at the closed end. The countercurrent, horizontal velocity profile is produced by combined thermocapillary and thermogravitational convection.

safety engineers; and (iii) it results in good agreement with the temperature rise measurements.

Much like the case of the cylindrically symmetric liquid layer (Burelbach et al., 1996), the horizontal heat flow q away from the heat source due to both thermocapillary and thermogravitational convection is assumed to be given by

$$q = -k_e\left(\frac{dT}{dx}\right)^3 \qquad (1)$$

where k_e is the effective thermal conductivity given by

$$k_e = \frac{\rho c_p(\sigma')^2\delta^4}{1680\alpha\mu^2}\left(1 + \frac{7}{24}Bo + \frac{19}{864}Bo^2\right). \qquad (2)$$

The symbols are defined in the nomenclature section. The reader should consult Burelbach et al. (1996) for the derivation of Eq. (1) and a discussion of its validity when applied to macro-scale thermocapillary and thermogravitational flow fields. Suffice it to say here that for typical liquid fuels, Eq. (1) is valid as long as the layer thickness δ is less than about 6 mm.

We can now solve for the variation of surface temperature with distance x along the length of the channel shown in Fig. 1 by assuming that the axial heat flow in the positive x direction follows Eq. (1). A thermal energy balance on a segment dx of the liquid layer beneath the heat source results in

$$\frac{d}{dx}\left[\left(\frac{dT_1}{dx}\right)^3\right] = -\frac{q_o}{\delta k_e} \quad 0 < x < x_o. \qquad (3)$$

Similarly, an energy balance for a segment of the layer in the surface cooling (unheated) region is

$$\frac{d}{dx}\left[\left(\frac{dT_2}{dx}\right)^3\right] = \frac{h}{\delta k_e}(T_2 - T_\infty) \quad x_o < x < x_\infty. \qquad (4)$$

In the above differential equations, $T_1(x)$ is the surface temperature distribution at the surface of the liquid layer under the heater, and $T_2(x)$ is the surface temperature distribution at the surface of the liquid layer outside the heated zone. At the intersection of these two zones we have the boundary conditions

$$T_1 = T_2, \quad \frac{dT_1}{dx} = \frac{dT_2}{dx} \quad \text{at} \quad x = x_o. \qquad (5)$$

At the closed end of the channel ($x = 0$) there is no heat flow in the horizontal direction, and the liquid surface temperature achieves its maximum value $T_{\max}$. At this location the boundary conditions are

$$T_1 = T_{\max}, \quad \frac{dT_1}{dx} = 0 \quad \text{at} \quad x = 0. \qquad (6)$$

Note that $T_{\max}$ is an unknown quantity that we seek to determine as part of the solution. Far from the heat source at $x = x_\infty$, we have the boundary conditions

$$T_2 = T_\infty, \quad \frac{dT_2}{dx} = 0 \quad \text{at} \quad x = x_\infty. \qquad (7)$$

It is known that surface tension effects are generally of finite extent so that the liquid surface temperature T will be reduced to the ambient value T_∞ at the location $x = x_\infty$. This location is unknown and must be determined as part of the solution.

Unlike the axisymmetric flow case treated previously (Burelbach et al., 1996), Eqs. (3) and (4) for one-dimensional channel

Nomenclature

Bo = bond number ($g\rho\beta\delta^2/\sigma'$)
c_p = specific heat of the liquid
$c_{p,g}$ = specific heat of air
D = binary diffusion coefficient for dodecane vapor in air
g = gravitational acceleration
h = heat transfer coefficient for surface cooling
h_{fg} = latent heat of evaporation of dodecane
k_e = effective conductivity transport coefficient
q = heat flux transmitted horizontally through the liquid layer
q_o = heat flux transmitted from heater to the liquid layer
R_1 = ratio of evaporative to radiant fluxes defined in Eq. (14)
R_2 = ratio of evaporative to convective fluxes defined in Eq. (15)
T = surface temperature
$T_{\max}$ = maximum liquid temperature
T_∞ = ambient temperature
W = width of channel
x = horizontal coordinate in the direction of flow
x_o = length of heated zone
x_∞ = location far from heater at which $T = T_\infty$
Y_{eq} = dodecane vapor mass fraction in equilibrium with its liquid
z = coordinate perpendicular to flow direction

Greek Letters

α = thermal diffusivity of liquid
α_g = thermal diffusivity of air
β = liquid volumetric expansion coefficient
δ = layer thickness (depth)
μ = absolute viscosity of liquid
ρ = density of liquid
σ = surface tension
σ' = absolute variation of σ with temperature, $|d\sigma/dT|$

Subscripts

1 = under the heater
2 = outside the heated zone

flow can be integrated analytically, and the resulting closed form expressions for the liquid surface temperature versus distance from the closed end of the channel are

$$T_1 = T_{\max} - \frac{3}{4}\left(\frac{q_o}{\delta k_e}\right)^{1/3} x^{4/3} \qquad (8)$$

for the temperature profile in the heated zone and

$$T_2 - T_\infty = \left[\left(\frac{q_o x_o}{\delta k_e}\right)^{1/3}\left(\frac{3\delta k_e}{2h}\right)^{1/4} - \frac{1}{2}\left(\frac{2h}{3\delta k_e}\right)^{1/4}(x - x_o)\right]^2 \qquad (9)$$

for the temperature profile in the unheated zone. The expressions for $T_{\max}$ and x_∞ are

$$\frac{h(T_{\max} - T_\infty)}{q_o} = \frac{3}{4}\left(\frac{x_o^4 h^3}{k_e \delta q_o^2}\right)^{1/3} + \sqrt{\frac{3}{2}}\left(\frac{x_o^4 h^3}{k_e \delta q_o^2}\right)^{1/6} \qquad (10)$$

$$\frac{x_\infty}{x_o} = 1.0 + 2\sqrt{\frac{3}{2}}\left(\frac{k_e \delta q_o^2}{x_o^4 h^3}\right)^{1/6}. \qquad (11)$$

The first term on the right-hand-side of Eq. (10) represents the dimensionless temperature decrease in the heated zone ($0 < x < x_o$), while the second term is the dimensionless temperature decrease in the unheated zone ($x_o < x < x_\infty$). In most practical applications, the temperature decrease in the heated zone is small compared with that in the unheated zone. Equation (11) yields the distance x_∞ beyond which the thermal effects of the heater are no longer felt by the liquid.

Experimental Apparatus and Procedure

Figure 2 illustrates the experimental apparatus. The channel was constructed from a flat plastic strip measuring 1 cm thick × 5 cm wide × 50 cm long. A 6.4 mm deep flat-bottomed channel was cut along the centerline on the upper face. This channel measured 1.3 cm wide and 42 cm long. A small hole was drilled through the channel bottom at one end to allow a thermocouple (TC1) to pass through from below. Five other thermocouples (TC2 through 6) were placed in the channel from above. Of these five, only TC6 was not fastened in place; this thermocouple was manually translated to measure temperatures along the channel. The plastic substrate was encased in rigid foam insulation so that only the channel cut out was exposed. Two thermocouples (TC7 and TC8, not shown in Fig. 2) were embedded in the bottom insulation layer directly below TC2. These thermocouples were used to estimate downward heat losses.

The channel assembly was fastened to a wood block which in turn was attached to a metal support plate. Positioning screws in the support plate were used to level the channel. Dodecane was then added to the channel until the layer depth was about 2.5 mm. The six surface thermocouples were then adjusted so that their tips just contacted the liquid surface midway between the channel walls.

The small, calibrated radiant heater previously used by Burelbach et al. (1996) was used as the heat source for the channel tests. A small aluminum foil screen was placed between the heater coil and the target liquid to restrict the effective radiant heat transfer area. A rectangular cut out in the foil screen provided for a 5 mm long heated zone which extended across the 1.3 cm wide channel and which was centered above thermocouple TC1. Note that the 42 cm long channel used in the experiments may be regarded as semi-infinite in the sense that this length exceeds x_∞ for all the test conditions investigated. Uncertainty in the effective heater power is estimated at ±ten percent based on scatter in the calibration data. The degree of uniformity of the source heat flux was not determined, as such measurements are difficult and would have required a separate laboratory program. Since the size of the heated zone is so small compared with the length of the unheated thermocapillary flow zone, the degree of uniformity of the source is not an important factor in terms of predicting the liquid surface temperature profile.

Four tests were performed by first setting the electric heater to the desired power level and then waiting for the system to approach steady state, as determined from the surface temperature histories. Up to 7000 seconds were typically required for the measured temperatures to "level out" to steady conditions, and some temperatures were still increasing gradually at the time of our subjective steady-state determination (see below). Concern over layer thinning (due to evaporation or capillary losses via wicking up the channel walls) precluded a more prolonged test duration. Steady surface temperature profiles were recorded using TC6 by traversing the length of the channel and measuring temperatures at 2.5 cm intervals.

In some cases, the temperatures measured during the traverse with TC6 were observed to be several degrees lower than temperatures measured with the fixed thermocouples at the same axial location, particularly at locations near the heated region. This bias error was within ten percent of the local surface temperature rise as determined from the fixed thermocouples, which were generally considered to be more accurate due to their better positioning at the liquid surface. Where possible, fixed thermocouple readings were used in reporting measured temperature profiles. Precision error in the measured surface temperature rise is estimated to be as much as ±1.5°C, or generally within ±ten percent, due to residual system unsteadiness and fluid instabilities.

Downward heat losses were estimated using temperature readings from TC7 and TC8 which were embedded in the insulating layer beneath the channel and were vertically separated from each other by 3 mm of ceramic wool. Both thermocouples were located 2.5 cm from the center of the heated zone, directly beneath TC2. The surface (upward) temperature difference, $\Delta T_{\rm up} = \mathrm{TC2}-T_\infty$, and the downward temperature drop, $\Delta T_{\rm dn} = \mathrm{TC7}-\mathrm{TC8}$, were recorded near steady state for each run. In general, $\Delta T_{\rm dn}$ was about ten percent of $\Delta T_{\rm up}$. Assuming that the thermal conductivity of the insulation is close to that for air, say 0.03 W $\mathrm{m^{-1}\,K^{-1}}$, and taking the upward facing natural convection heat transfer coefficient to be $h = 25$ W $\mathrm{m^{-2}\,K^{-1}}$ (see below), this leads to estimates of the upward and downward heat fluxes. In all cases, the downward heat losses are a small fraction (about four percent) of the natural convection heat losses off the liquid surface. It is therefore inferred that steady state heat losses across the channel insulation are negligible—consistent with the boundary conditions assumed in the effective thermal conductivity theory.

The layer thickness, δ, was measured both before and shortly after each test with a vertically translating temperature probe (namely TC1). This technique was used previously by Burelbach et al. (1996). The maximum error in measuring the layer thickness is estimated to be ±0.05 mm, this accounts for the uncertainty in both the substrate and the free surface positions. It was observed that the layer thickness decreased during each test. This is believed to be due to evaporation and capillary wicking of fluid up the channel walls, particularly near the heater. Residual surface temperature variations after each test may also have contributed to local thinning via thermocapillary forces. Layer thicknesses reported in Table 1 represent arithmetic averages of the measurements taken before and after each test. The decrease in δ amounted to about 0.1 mm in each case, or roughly four percent. The theory suggests that measured temperatures are not particularly sensitive to this level of uncertainty in δ.

Knowledge of the effective heat transfer coefficient for combined natural convection and thermal radiation off the liquid

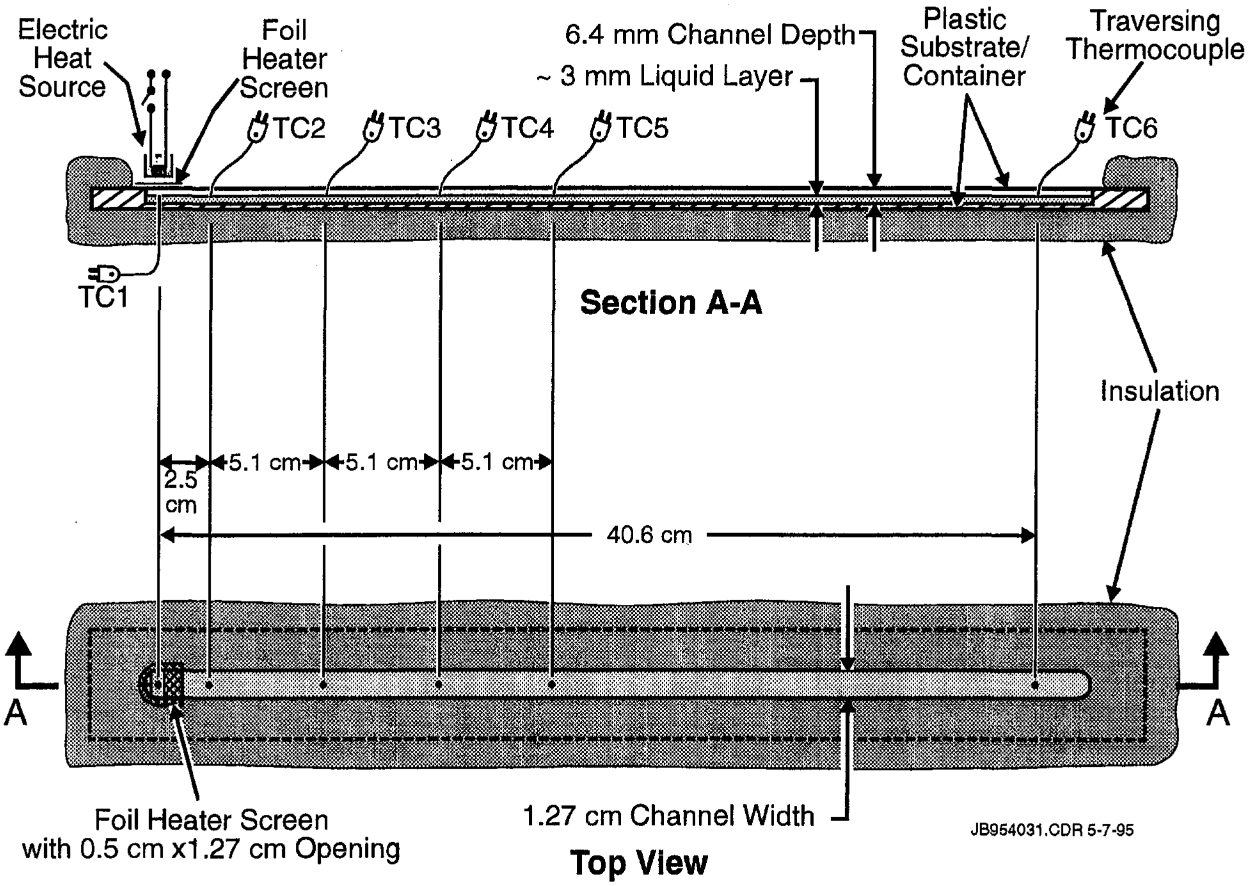

Fig. 2 Channel convection apparatus; distance measured from center of heated zone

surface is required in order to test the theory against the experimental data. The source heat emission rate must equal the rate at which the liquid loses heat to the overlying gaseous ambient outside the heat impingement zone, or

$$x_o q_o = \int_{x_o}^{x_\infty} h[T - T_\infty]dx. \tag{12}$$

An effective mean value of h can be estimated by removing h from the integrand to obtain

$$h = \frac{x_o q_o}{\int_{x_o}^{x_\infty} (T - T_\infty)dx}. \tag{13}$$

The integral was evaluated from the measured liquid surface temperature versus distance profiles, and the heat transfer coefficient was determined to be in the range 23–28 W m^{-2} K^{-1}.

The root-sum-square method (Kline and McClintock, 1953) was used to perform an uncertainty analysis of the experimental measurements. Expressing the results in the dimensionless form suggested by Eq. (10) leads to an uncertainty of up to 18 percent in the quantity $h(T_{\max} - T_\infty)/q_o$ and up to 28 percent in the quantity $x_o^4 h^3/(k_e \delta q_o^2)$ for fixed h as defined above.

Table 1 Summary of channel convection experiments

Test ID#	1	2	3	4
q_o (kW m^{-2})	8	16	18	31
δ (mm)	2.6	2.6	2.5	2.5
h (W m^{-2} K^{-1})	23	25	28	28
T_∞ (°C)	20	19	20	20
T_{max} - T_∞ (°C)				
experiment	18	28	30	42
theory	22	33	35	50

Experimental Results and Discussion

Table 1 summarizes experimental conditions for four tests using dodecane layers of about 2.5 or 2.6 mm thickness and source heat fluxes ranging from 8 to 31 kW m^{-2}. Also shown are measured peak surface temperature differences and temperature differences predicted by Eq. (10) using dodecane properties at 30°C, and the heat transfer coefficients inferred from the data. The theory overpredicts the maximum temperature rise data by about 20 percent. Thus, the theory provides a conservative but reasonably accurate equation for estimating the potential for liquid fuel layer ignition (by comparing $T_{\max}$ with the fuel's flash point temperature).

Figure 3 compares measured and predicted surface temperature profiles using Eqs. (8) and (9) for each test. The typical uncertainty in the temperature rise measurements (about ± 1°C) is shown as a single error bar. The nearly identical results for tests 2 and 3, which had similar layer thicknesses and imposed heat fluxes, illustrate good experimental reproducibility. Figure 3 indicates good agreement between theory and experiment in the region away from the heater. However, the theory consistently overestimates the measured temperature in the vicinity of the heated zone by about 11 percent.

At first glance, one may opine that evaporation cooling is responsible for this discrepancy in the vicinity of the heater. This idea may be tested by comparing the heat flux ''absorbed'' by surface evaporation with the heat flux q_o from the radiant energy source. The ratio of these heat fluxes is

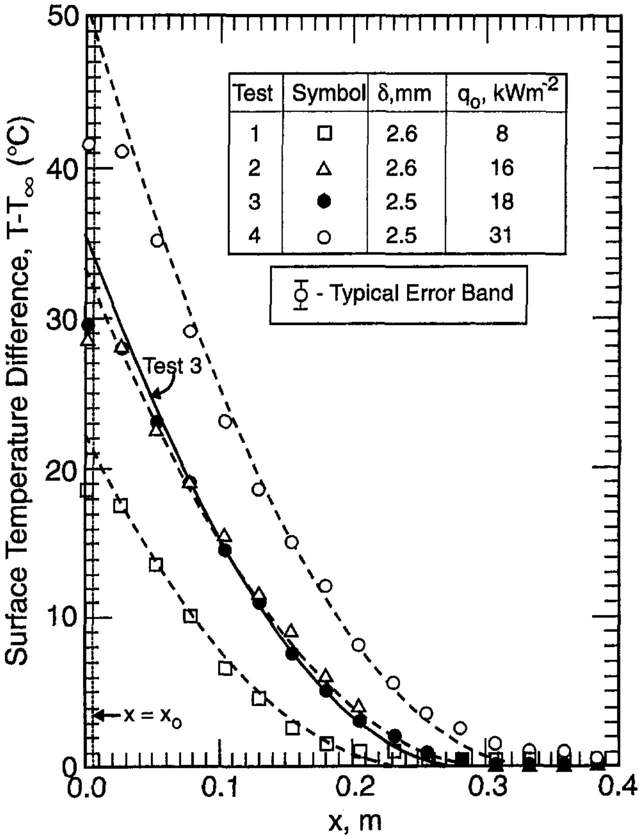

Fig. 3 Comparison of measured temperature profiles with effective conductivity model. The dashed and solid curves represent model predictions.

$$R_1 = \frac{h_{fg} Y_{eq} h (D/\alpha_g)^{2/3}}{c_{p,g} q_o} \tag{14}$$

where h_{fg} is the latent heat of evaporation of dodecane (3.4×10^5 J kg^{-1}), D is the binary diffusion coefficient for the dodecane vapor/air pair (5.5×10^{-6} m^2 s^{-1}), $c_{p,g}$ is the heat capacity of air (10^3 J kg^{-1} K^{-1}), α_g is the thermal diffusivity of air (2.2×10^{-5} m^2 s^{-1}), Y_{eq} is the dodecane vapor mass fraction in equilibrium with its liquid (0.013 at 60°C), h is the heat transfer coefficient for surface cooling ($\simeq 25$ W m^{-2} K^{-1}), and q_o is the radiant energy source ($\simeq 2 \times 10^4$ W m^{-2}). Equation (14) for R_1 was derived by using the Chilton-Colburn heat-mass transfer analogy to eliminate the mass transfer coefficient in favor of the heat-transfer coefficient h. R_1 is of the order 10^{-3}. Indeed, surface evaporation effects beneath the heater are negligible. The region outside the heated zone may be similarly evaluated by comparing the heat flux absorbed by surface evaporation with the convection heat flux, $h(T - T_\infty)$, off the surface of the film. The ratio of these fluxes is

$$R_2 = \frac{h_{fg} Y_{eq}}{c_{p,g}(T - T_\infty)} \left(\frac{D}{\alpha_g}\right)^{2/3}. \tag{15}$$

R_2 is at most 0.05 (at 60°C). Thus, temperature reductions due to surface evaporation are acceptably small outside the heated zone.

The flattening of the temperature profile in the vicinity of the heater is likely due to the cold return flow of liquid rising up in this region. This recirculation phenomenon is not included in the effective thermal conductivity model and is probably responsible for the discrepancy in $T_{\max}$ between the model and the experimental data. Also, according to the theory, the layer thickness δ in the experiments was small enough to neglect thermogravitational effects; that is, Bo in Eq. (2) is small compared with unity. The maximum increases in surface temperature measured or predicted by Eq. (10) are one order of magnitude less than those predicted by considering only molecular conduction through the liquid layer. This indicates the vital role played by thermocapillary convection in preventing the heating of a shallow fuel layer to its ignition point.

Conclusions

We have experimentally determined the surface temperature distributions in locally top-heated thin liquid layers. The configuration investigated was that of a one-dimensional channel with large lateral extension relative to the thickness of the layer and with thermally insulated bottom and side walls. Thus, the heat gained by the liquid at one end of the channel via a concentrated heat source was lost to the ambient through the free liquid interface. This situation is of interest for its relevance to the ignitability of a pool or channel of liquid fuel. The measured surface temperature distributions are in good agreement with an effective conductivity theory of thermocapillary flow in shallow liquid layers.

References

Akita, K., 1973, "Some Problems of Flame Spread Along a Liquid Surface," *Proceedings of the 14th Symposium on Combustion,* The Combustion Institute, pp. 1075–1083.

Burelbach, J. P., Epstein, M., and Plys, M. G., 1996, "The Temperature Rise at the Surface of a Liquid Layer Subject to a Concentrated Heat Source Placed Above the Layer," ASME JOURNAL OF HEAT TRANSFER, Vol. 118, pp. 374–380.

Burgoyne, J. H., Roberts, A. F., and Quinton, P. G., 1968, "The Spread of Flame Across a Liquid Surface I. The Induction Period," *Proc. Roy. Soc.,* Vol. A308, pp. 39–54.

Di Blasi, C., Crescitelli, S., and Russo, G., 1990, "Model of Pulsating Flame Spread Across Liquid Fuels," *Proceedings of the 23rd Symposium on Combustion,* The Combustion Institute, pp. 1669–1675.

Fukano, T., Choudhury, S. K., and Ito, A., 1990, "Thermocapillary Flow in Thin Liquid Layers," *Mem. Fac. Eng. Kyushu Univ.,* Vol. 50, pp. 75–88.

Glassman, I., and Hansel, J. G., 1968, "Some Thoughts and Experiments on Liquid Fuel Spreading, Steady Burning and Ignitability in Quiescent Atmospheres," *Fire Research Abstracts and Reviews,* Vol. 10, pp. 217–321.

Kline, S. J., and McClintock, F. A., 1953, Describing Uncertainties in Single-Sample Experiments, ASME *Journal of Mechanical Engineering,* January, pp. 3–8.

Mackinven, R., Hansel, J. G., and Glassman, I., 1970, "Influence of Laboratory Parameters on Flame Spread Across Liquid Fuels," *Combustion Science and Technology,* Vol. 1, pp. 293–306.

Ross, H. D., 1994, "Ignition of and Flame Spread Over Laboratory-Scale Pools of Pure Liquid Fuels," *Prog. Energy Combust. Sci.,* Vol. 20, pp. 17–63.

Sirignano, W. A., and Glassman, I., 1970, "Flame Spreading Above Liquid Fuels: Surface Tension-Driven Flows," *Combustion Sci. and Tech.,* Vol. 1, pp. 307–312.

Torrance, K. E., and Mahajan, R. L., 1975, "Surface Tension Flows Induced by a Moving Thermal Source," *Combustion Sci. and Tech.,* Vol. 10, pp. 125–136.

Nucleate Pool Boiling Heat Transfer Coefficients of Distilled Water (H_2O) and R-134a/Oil Mixtures From Rib-Roughened Surfaces

Shou-Shing Hsieh
Professor of Mechanical Engineering.
Dean of Engineering.
Fellow ASME

Chun-Jen Weng
Graduate Student,
Department of Mechanical Engineering,
National Sun Yat-Sen University,
Kaohsiung, Taiwan 80424
Republic of China

Measurements of pool-boiling heat transfer coefficients in distilled water and R-134a/oil mixtures with up to 10 percent (by weight) miscible EMKARATE RL refrigeration lubricant oil are extensively studied for a smooth tube and four rib-roughened tubes (rib pitch 39.4 mm, rib height 4 mm, rib width 15 mm, number of rib element 8, rib angle 30 deg–90 deg). Boiling data of pure refrigerants and oil mixtures, as well as the influences of heat flux level on heat transfer coefficient, are presented and discussed. A correlation is developed for predicting the heat transfer coefficient for both pure refrigerants and refrigerant-oil mixtures. Moreover, boiling visualizations were made to broaden our fundamental understanding of the pool boiling heat transfer mechanism for rib roughened surfaces with pure refrigerants and refrigerant-oil mixtures.

1 Introduction

Many water chillers of the centrifugal type have evaporators utilizing a flood type of operation whereby the water is circulated through the tubes and refrigerant is evaporated on the shellside of the tubes. While designing the evaporator of such a system, one must be able to accurately predict the boiling heat transfer coefficients of the refrigerants used. However, the fluids being circulated in these refrigeration systems generally are not pure refrigerants, but are refrigerant-oil mixtures. Even with pure liquids the prediction of the boiling heat transfer coefficient is difficult because the boiling phenomenon is rather complex. The addition of a miscible liquid to the pure fluid further complicates the problem by producing an extremely complex process when compared to those with the pure fluid. Today, the design of compact evaporators almost always involves the use of enhanced surfaces. Many data exist on pool boiling heat transfer from smooth and enhanced surfaces for a wide variety of pure refrigerants (e.g., Thome, 1990; Pais and Webb, 1991). For low integral-fin tubes (748-1575 fpm), typical enhancements of up to four have been obtained by Webb and Pais (1992).

The influence of oil on the heat transfer performance of evaporators has been studied as early as 1955. Researchers have sought to understand the effects of small oil concentration's on pool boiling of refrigerant-oil mixtures on smooth surfaces, and more recently on enhanced surfaces. The literature dealing with the effect of oil concentrations on boiling of refrigerants and refrigerant-oil mixtures in pool boiling is quite limited, especially for proposed alternative refrigerants. A limited range of studies (e.g., Chongrungreong and Sauer, 1980) has shown that the nucleate boiling heat transfer coefficients decrease with increasing oil concentration; however, Dougherty and Sauer (1974) found that at low oil concentration ($\leqq 3$ percent), the heat transfer coefficients actually increased compared to the pure refrigerant data. Recently, Memory and Marto (1992) studied the effect of oil on nucleate boiling using R-114 as the test fluid on six enhanced tubes including a porous coated copper-nickel tube. They also reported a significant degradation with oil contamination. At 100 kW/m^2 a small increase in the performance of all low integral-fin tubes for a 3 percent oil contamination was also reported. Further oil increase led to a decrease in the heat transfer coefficient.

In recent years, environmental concerns over the use of CFCs as working fluids in refrigeration and air-conditioning plants have led to the development of alternative fluids. Among these alternatives, R-134a is seen as a replacement for the commonly used CFC-12. Moreover, considerable recent effort has been made in finding ways to design more compact and efficient evaporators for the process and refrigeration industries based on CFCs.

The objective of this paper is to enlarge the pool boiling data base for alternative refrigerants by providing heat transfer data for distilled water (H_2O) and R-134a/oil mixtures from a variety of smooth and rib-roughened enhanced surfaces and, furthermore, to develop a correlation suitable for the present enhanced geometry and to examine the mechanisms controlling nucleate boiling of refrigerant-oil mixtures.

2 Experimental Setup and Procedure

2.1 Test Facility and Test Section. The experimental apparatus for the study is shown in Fig. 1. It consists of a cylindrical stainless steel pressure vessel volume of $(\pi/4)(21.6)^2 \times (40)$ cm^3, a stainless steel side panel provided with ports for electric wires, pressure gauge and thermocouples, a vacuum pump, a reflux condenser, auxiliary heaters (or thermostat baths), and a test section support. Insulation was peripherally provided on the outside of the tank; the side windows were made of quartz glass placed midway for visualization. The evaporator tube was designed to simulate a portion of a typical tube in refrigerant-flooded evaporator. It was fabricated from a copper tube. The tube specimen is soldered to a flange at one end of the tank. The copper tubes were 27 mm in diameter over the ribs with an inner diameter of 11 mm. Each cartridge heater was 350 mm long (actual heated length is 330 mm) and 10.95

Contributed by the Heat Transfer Division for publication in the Journal of Heat Transfer. Manuscript received by the Heat Transfer Division October 12, 1995; revision received September 13, 1996; Keywords: Augmentation & Enhancement, Boiling, Refrigeration. Associate Technical Editor: V. K. Dhir.

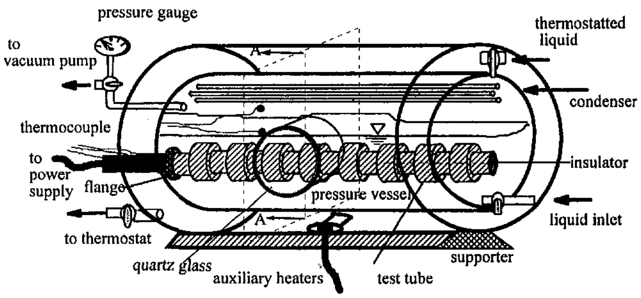

(a) Test section

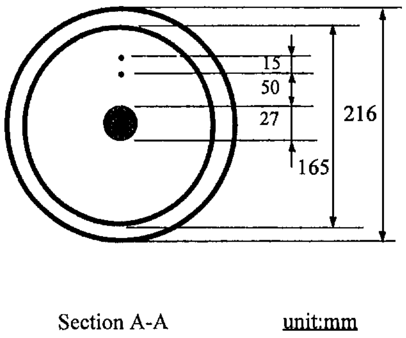

(b) Thermocouple locations

Fig. 1 Pool boiling apparatus setup

mm in diameter with a maximum power output of 2 kW and was inserted in the copper tube. The detailed description of insertion of the cartridge heater can be found from Hsieh and Hsu (1994). The test section included both smooth and rib-roughened surfaces with rib angles of 30 deg, 45 deg, 60 deg, and 90 deg. The dimensional specifics are given in Table 1. Also shown in Table 1 is a detailed sketch of the rib-roughened test section.

Four thermocouples were equally spaced circumferentially at the middle of the test roughened surfaces which have been proved to give a good accuracy of average wall temperature. Calibrated Chromel-Alumel thermocouples (within ±0.3°C) of diameter 0.12 mm were employed to measure the wall temperature. To minimize longitudinal heat conduction, silicon rubber and Devon five minute epoxy glue, mixed with polystyrene foam, was applied to the ends of the thermocouples for use with water and R-134a, respectively. The liquid temperature in the evaporator was measured by two thermocouples placed close to the free surface of the liquid. The temperature difference between these two points was between ±0.1°C at the maximum power input. Another thermocouple was used to measure the vapor temperature and was positioned midway along the evaporator, about 15 mm above the liquid surface.

2.2 Working Fluid Used. The working fluid used in the present experiments was distilled water (H_2O) and R-134a for which up to 10 percent (mass fraction) of ICI EMKARATE RL refrigeration lubricant oil was added. The properties of the oil were measured by ICI, and estimated where appropriate. The oil properties are listed in Table 2. The oil-refrigerant mixtures were prepared on a weight basis by weighing precalculated amounts of each pure component to give the required weight percent for the mixture. The volume fraction was determined from the weight percent by

$$\phi_f = \frac{w_f/\rho_f}{w_f/\rho_f + w_o/\rho_o} \tag{1}$$

The physical properties of the distilled water (H_2O) and R-134a mixtures were estimated using the following interpolation formula obtained from Bell et al. (1987):

$$\frac{1}{\rho} = \frac{w_f}{\rho_f} + \frac{w_o}{\rho_o} \tag{2}$$

$$C_p = w_f C_{pf} + w_o C_{po} \tag{3}$$

$$\frac{1}{\mu} = \frac{\phi_f}{\mu_f} + \frac{\phi_o}{\mu_o} \tag{4}$$

$$\sigma = \sigma_f + (\sigma_o - \sigma_f)\sqrt{w_o} \tag{5}$$

$$k = k_f w_f + k_o w_o - 0.72(k_o - k_f) w_o w_f \tag{6}$$

2.3 Experimental Procedure. Prepared test sections were cleaned with chlorinol and water and finally, with acetone. The tank was cleaned with acetone before each run. Once the evaporator tube was installed, the system was evacuated to a pressure of about 30 Pa. If no leaks were detected over a 24 hour interval the evaporator was charged with the working fluid from the reservoir to a level of 50 mm above the top of the tube. This resulted in a vapor pressure of 101.3 kPa (distilled water) and 343.06 kPa (R-134a), respectively.

The power was given to the pool to degas the test fluid, H_2O and R-134a, at heat flux of 35 kW/m^2 for 3.5 hour and 1.5 hour, respectively. For the pure refrigerant, saturation temperature at the measured pressure was compared to the pool temperature measured by the thermocouple. The power supplied to the test

Nomenclature

A = heat transfer area
b = $[2\sigma/g(\rho_L - \rho_V)]^{1/2}$ Laplace constant
C_p = specific heat
d_1 = outside diameter of test tube
d_2 = base diameter
d_e = equilibrium break off diameter (d_e = $0.146\beta b$), in Fig. 5
H = rib height
h = heat transfer coefficient
h_{LV} = latent heat
h_0 = heat transfer coefficient for W_o = 0 percent
h_s = heat transfer coefficient for smooth tube
k = thermal conductivity
L = length of test tube
N = number of ribs
P = pressure
P_c = critical pressure
P' = boiling pressure in Fig. 5
p = pitch of rib
Q = heat transfer rate
q = heat flux (Q/A)
q_{down} = decreasing heat flux
q_{up} = increasing heat flux
T = temperature
ΔT = temperature difference
W = width of rib
W_o = oil concentration by weight
α = thermal diffusivity
β = contact angle (35 deg)
w = mass fraction
θ = rib angle
μ = viscosity
ν = kinematic viscosity
ρ = density
σ = surface tension
ϕ = volume fraction

Subscripts

avg = average
f = refrigerant
L = liquid
o = oil
sat = saturation
V = vapor
w = wall of tube

Table 1 The dimensions of test tube

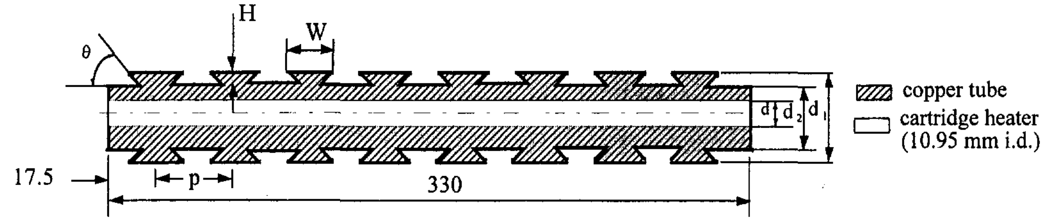

test tube detail

Unit:mm

test tube θ	d_1 (mm)	d_2 (mm)	number of rib	p (mm)	W (mm)	H (mm)	A (mm^2)
smooth	27	—	—	—	—	—	27992
30°	27	19	8	39.4	15	4	38292
45°	27	19	8	39.4	15	4	32787
60°	27	19	8	39.4	15	4	29973
90°	27	19	8	39.4	15	4	27502

Note:"—" means data not applicable

section was gradually, and slowly, reduced zero. The test pool was maintained close to the saturated temperature with an auxiliary heater for about 30 minutes; then it was switched off to minimize convective effects. The heating power supplied to the test section was slowly and gradually increased to nearly 50 kW/m^2. Both increasing and decreasing heat flux data were taken in order to observe boiling hysteresis. For the decreasing data, the heat flux was reduced from 50 kW/m^2 in pre-determined steps by means of a variac. It generally took about 30 minutes to achieve steady conditions after the power level was changed.

Table 2 Typical properties of EMKARATE RL refrigeration lubricants

characteristic	value
ISO viscosity grade	68
viscosity (cSt)	
at 40°C	74.1
at 100°C	10.1
at -20°C	7356
viscosity index	118
pour point (°C)	-35
specific gravity at 15°C	0.979
density at 15°C (g/ml)	0.978
flash point (°C)	246
acid value (mgKOH/g)	<0.05
miscibility	
10% lube in R134a	
>80°C	high
-3°C	low
surface tension at 21°C (N/m)	0.028
specific heat at 21°C (kJ/kgK)	2.008
thermal conductivity (W/mK)	0.1237

During all the tests, the saturation temperature was kept near 99.9°C (water) and 4.4°C (R-134a), respectively. The liquid level was kept approximately 50 mm above the test tube. All the data were obtained and reduced with a computer-controlled data acquisition system. Once the pure refrigerant test was completed, oil was added to establish the required concentration. When the required oil concentration was reached, the power input was increased to the highest flux and the system was again allowed to boil and mix for one hour. The test procedure is described for the pure refrigerant case only. Additional amounts of oil were added in succession to obtain the desired concentration for each run.

2.4 Precautions Taken during Experiments. In measuring boiling heat transfer coefficients, great care must be exercised to ensure good accuracy. The following list are those precautions:

1 The pool temperature was compared to the saturation temperature corresponding to the measured saturation pressure for pure refrigerants. This ensures that there are no noncondensibles in the system. It also verifies that there is no subcooling in the liquid pool within ±0.2°C.
2 The heater was tested for circumferential uniformity of heat flux. To smooth out any nonuniformities in the heat flux caused by the cartridge heater, a copper sleeve with the aforementioned two-walled sink compound was used inside the test tube into which the cartridge heater was inserted with a tight mechanical fit. The outer diameter of the sleeve was machined to the inside diameter of the test tube. Its center was bored out to accommodate the cartridge heater.
3 To ensure that the correct wall temperature was measured, a tightly-pressed thermocouple was put onto the wall of a sleeve insert with thermal jointing compound applied to the tube. The variation of the thermocouple reading was found to be less than 0.1°C.

The average wall temperature was used to define the heat transfer coefficient; it is defined as the average value of the four wall thermocouples. The heat flux is based on the heated area of the tube which was in contact with the liquid.

3 Data Reduction and Uncertainty Analysis

For each power input, the heat transfer coefficient was calculated on the basis of bulk fluid saturation temperature, tube heat flux, and the average of the four tube wall temperatures. The heat transfer coefficient at each power input was then calculated as follows:

$$h = \frac{Q}{[A(T_{\text{avg}} - T_{\text{sat}})]} \tag{7}$$

where A is the heated area of the tube and defined as:

$$\begin{aligned} A = N \times \pi \times \{ & W \times d_1 + (p - W) \times d_2 \\ & + 0.5(d_1 \times d_1 - d_2 \times d_2)/\sin\theta + 2 \times d_2 \times H \times \cot\theta\} \\ & + (17.5 - 0.5W) \times \pi \times d_2 . \end{aligned}$$

One thing that needs special mention is that of T_{sat}. The present T_{sat} is defined as the measured temperature of the saturated fluid/oil mixture. This indicates that the oil-free and mixture heat transfer coefficient are consistent on the same reference, and could be compared at the same refrigerant temperature (e.g., Memory et al., 1993).

The uncertainty in the experimental data was estimated using a propagation of error analysis. The uncertainty in the wall superheat was dominated by the uncertainty in the wall temperature measurements. The values of the four wall temperatures were recorded and compared to examine variations caused either by nonuniformities in the cartridge heater or by the test tube soldering and assembly procedure. The maximum variation of the four measured wall temperatures was ±0.5°C at the maximum heat flux ($\cong$50 kW/m^2) and ±0.1°C at the minimum heat flux ($\cong$0.8 kW/m^2). The uncertainty in the saturation temperature was estimated to be less than ±0.1°C. These caused the uncertainty of the corresponding wall superheat ($T_w - T_{\text{sat}}$) to be within ±14 percent at low heat flux and within ±2 percent at high heat flux. The heat flux accuracy was ±0.01 kW/m^2 at the minimum heat flux of 0.8 kW/m^2. Based on these uncertainties, it indicates the uncertainty of the wall heat transfer coefficient to be about ±16 percent at $q \cong 0.8$ kW/m^2 and ±3 percent at $q \cong 50$ kW/m^2.

4 Results and Discussion

More than 50 test runs were performed on smooth and rib-roughened tubes in saturated distilled water and R-134a with oil concentration. Some of these tests were repeated after several months to verify the reproducibility. The repeated data agreed well and were within the previously mentioned experimental accuracy.

4.1 Boiling Characteristics.

4.1.1 Pure fluids. The present data were all taken at a saturated temperature of 99.9°C for distilled water and 4.4°C for R-134a. Oil concentrations (W_o) of 0 (i.e., pure fluid), 2, 5 and 10 percent by weight were used. Figure 2 shows the data taken for smooth and rib-roughened tubes with rib angles of 30 deg, 45 deg, 60 deg, and 90 deg for distilled water and R-134a. Both increasing and decreasing heat flux modes were conducted. There was hysteresis in the measurements of wall superheat in each case. The incipient boiling condition is indicated by a change in slope when heat flux is plotted versus ΔT and it is given by an arrow shown in Fig. 2. It can be seen that for all conditions of heat flux for various tubes for pure fluid, the data with roughened surfaces showed a significant improvement in heat transfer, especially for a rib angle of 45 deg (in distilled water) and 30 deg (in R-134a). A line representing the correlation developed by Junkhan and Bergles (1976) for distilled water and R-134a for natural convection from a horizontal cylinder is also shown. Generally, at low heat flux, heat transfer was by natural convection with two stray data points that are way to the left in Fig. 2(*a*); it was found that they were due to the pool convection induced by the auxiliary heaters. As the power to the test section was increased, bubble activity was observed within the rib channels or nucleation sites for the smooth tube. At a heat flux of $q \cong 45$ kW/m^2, the rib-roughened enhancement was 1.56, 2.46, 1.39, and 1.25 for 30 deg, 45 deg, 60 deg, and 90 deg rib angles. The present data for pure distilled water were in general agreement with the data for GEWA K tubes of Ayub and Bergles (1987), which is shown in Fig. 2(*a*).

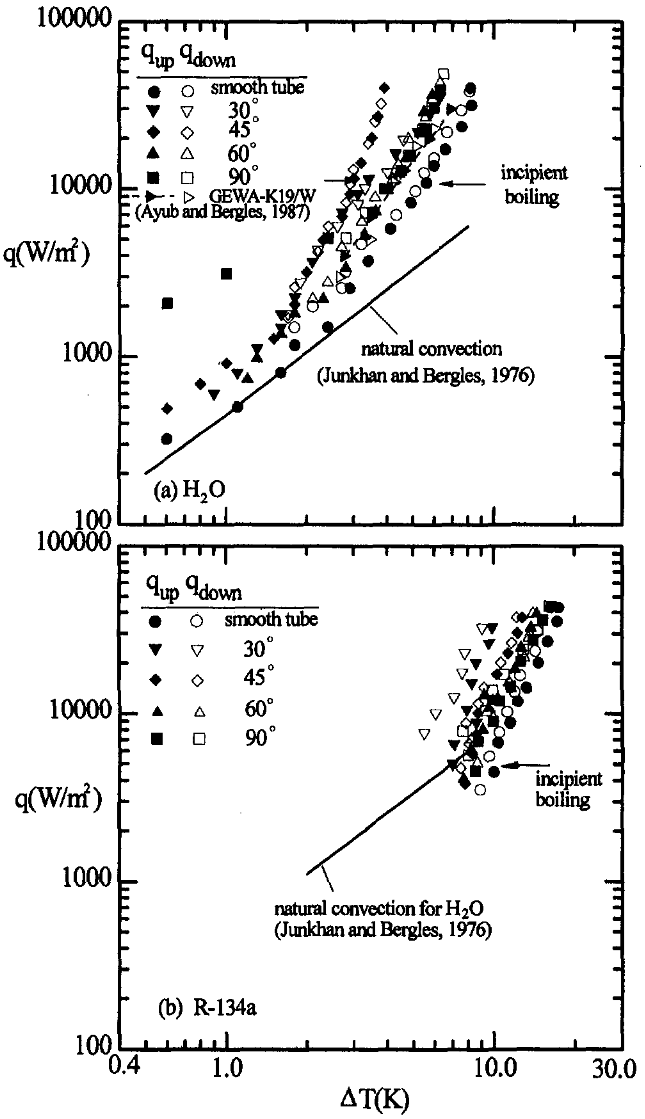

Fig. 2 Comparison of smooth tube/roughened tube for H_2O and R-134a

Taking careful examination, it is found that a larger incipient boiling superheat is required for the smooth tube ($\cong$5 K) and a smaller one for the 45 deg ($\cong$3 K) rib angle; the rest of the rib angles are located in between. However, the R-134a data, shown in Fig. 2(*b*), indicate a larger ΔT ($\cong$6 K for 45 deg rib angle, for instance) in every case. This most likely occurs because of the high wettability of R-134a, compared to the distilled water, on roughened surfaces; the large cavities become flooded with liquid and higher superheats are needed to nucleate smaller cavities. Moreover, in each figure a hysteresis pattern is noted for both distilled water and the R-134a. Furthermore, an usual counter-clockwise path of the hysteresis loop was found for both fluids with increasing, followed by decreasing, heat flux. In fact, boiling hysteresis depends on the fluid/surface combinations. In general, enhancement effect was both found in Figs. 2(*a*) and (*b*) for all the rib-roughened cases studied. Again, the findings stated above are in good agreement with the earlier study from Hsieh and Hsu (1994).

For correlation of $q = C_1 \Delta T^m$ for various refrigerant/oil mixtures, based on 95 percent confidence level, m was found to be 2.853 ± 0.388 for the cases studied. This value is quite close to the traditional value of $m \cong 3$ for pool boiling (Carey, 1992). Using $m = 2.853$ for all cases studied when considering the correlation in the form of $q = C_1 \Delta T^m$, it is found that the present roughened surface exhibits an enhancement of 1.86 and 2.23 (30 deg rib angle), 2.81 and 1.27 (45 deg rib angle), and 1.49 and 1.14 (60 deg rib angle), respectively, for distilled water and R-134a.

4.1.2 Water/Oil and R-134a/Oil Mixtures. Typical boiling curves for distilled water which show the effect of oil concentration on nucleate pool boiling of water/oil mixtures are shown in Fig. 3 for smooth and rib-roughened tubes (rib angles of 30 deg, 45 deg, 60 deg). The qualitative results of these experiments except for 30 deg and 60 deg cases agree well with the results of previous studies (e.g., Jensen and Jackman, 1984). With increasing oil concentration and viscosity, the heat transfer rate decreases. The distilled water seems completely immiscible with oil. Some augmentation of the heat transfer was observed at a low oil concentration (≤2 percent) for smooth and rib roughened (=45 deg) tubes which are shown in Figs. 3(*a*) and (*c*). No such enhancement was found in Figs. 3(*b*) and (*d*). Note that in Fig. 3 the slopes of the nucleate boiling portions of the boiling curves for both distilled water and the distilled water/oil mixtures decrease slightly with an increasing oil concentration. This agrees with papers referenced by Stephan (1982) and Memory et al., (1993). The "knee" of the boiling curve of the distilled water/oil mixtures (refer to Jensen and Jackman, 1984) appears to be shifted upward and to the right compared to the pure distilled water curve.

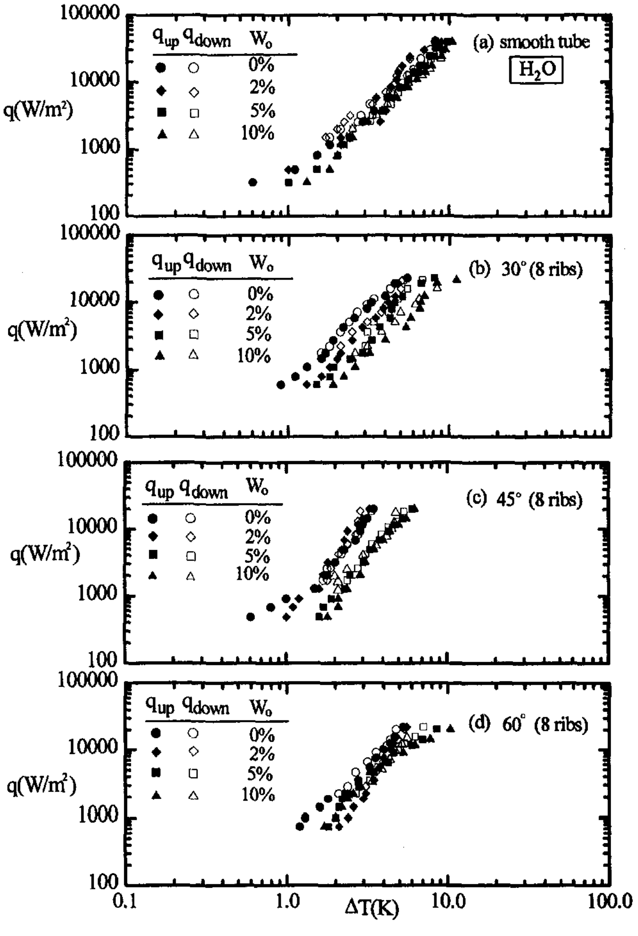

Fig. 3 Boiling data for H₂O/oil mixture for smooth tube/roughened tube

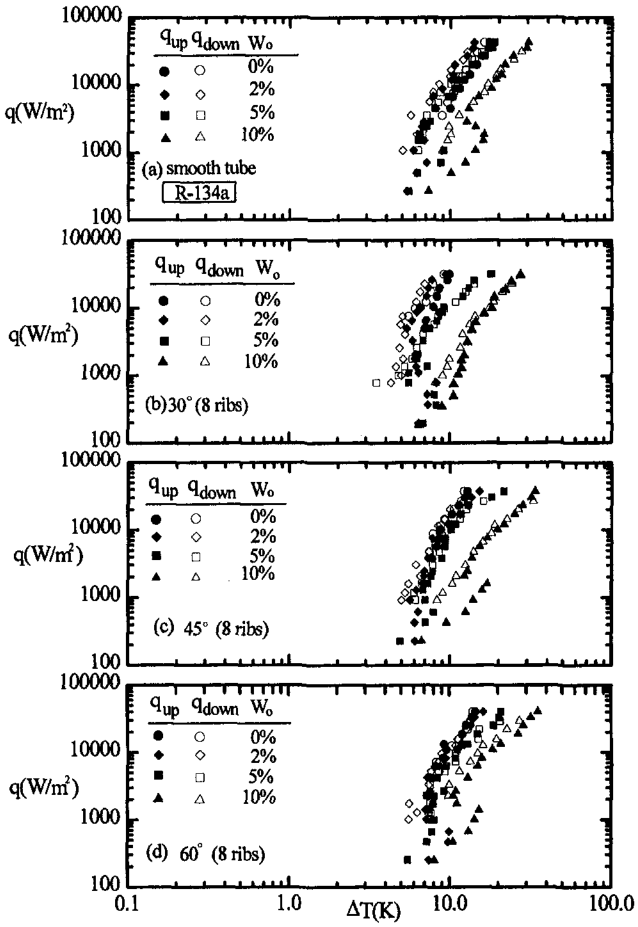

Fig. 4 Boiling data for R-134a/oil mixture for smooth tube/roughened tube

Hysteresis effects appear to be much more pronounced as the oil concentration increases, when compared to the distilled water data. Taking close examination of Figs. 3(*a*) and (*c*), it is found that, as W_o increases, the heat transfer at first increases (for $W_o \leq 2$ percent) before decreasing as W_o approaches 10 percent. This increase (≅94 percent at 25 kW/m²) is similar in magnitude to what has been reported for other refrigerants with small quantities of oil added (e.g., Stephan, 1982 and Memory et al., 1993). The reason for this will be discussed later. As mentioned earlier, this behavior was not found for the remaining figures (Figs. 3(*b*) and (*d*)). This clearly indicates that the rib angle does have an influence on the heat transfer when oil is added to the refrigerant. The same situation also nearly occurred for the R-134a data, as shown in Fig. 4 in which the "knee" of the boiling curve of the R-134a/oil mixture is not clearly observed. The gap between $W_o = 10$ percent and other concentrations seems big compared to the data for distilled water. Additionally, the augmentation of the heat transfer was also observed at low concentration (≤2 percent) for smooth and rib roughened (=30 deg) tubes which are shown in Figs. 4(*a*) and (*b*). The differences, due to the different rib angles, for these two refrigerants may be caused by the higher wettability of R-134a which needs a smaller rib angle to entrap the vapor residue. Also, unlike Fig. 3(*d*), the peculiar trend of the worst heat transfer performance for W_o = 2 percent was not found anymore. The exact reason is not understood at this stage.

4.2 Heat Transfer Coefficient and Enhancement. Figure 5 compares the smooth tube data for distilled water and R-134a with the data for the present roughened surface with oil concentrations of 2, 5, and 10 percent in the decreasing heat flux mode. For small oil addition ($\leq$2 percent), the smooth tube as well as the 45 deg (distilled water)/30 deg (R-134a) rib angle roughened tube data exhibit a heat transfer enhancement (see Figs. 5(*a*), (*b*), and (*c*)). This is perhaps due to the significant foaming established with a small quantity of oil addition. This foam draws the liquid and vapor interface closer to the wall resulting in a thinner liquid film between the foam and heated surface (tube wall). Moreover, this foam also facilitates secondary nucleation (Udomboresuwan and Mesler, 1986) which in turn enhances nucleate boiling. Also, the foam seems to help scour the oil from the surface (Stephan, 1982; Memory et al., 1993). However, this phenomenon was degraded with the present roughened surface evidenced by Fig. 5(*c*) compared to Fig. 5(*a*). As oil concentration is increased beyond a certain amount (>2 percent), the high rate of transport of oil to the surface starts to counterbalance the enhancing effect of the foam and, consequently, results in thermal performance degradation. Except for the case mentioned, the heat transfer decreases as W_o increases as stated earlier. For all the cases studied, the heat transfer data for R-134a are much lower than those for distilled water. The reasons were stated earlier. Again, the effect of oil addition is clearly noted, especially for W_o = 10 percent.

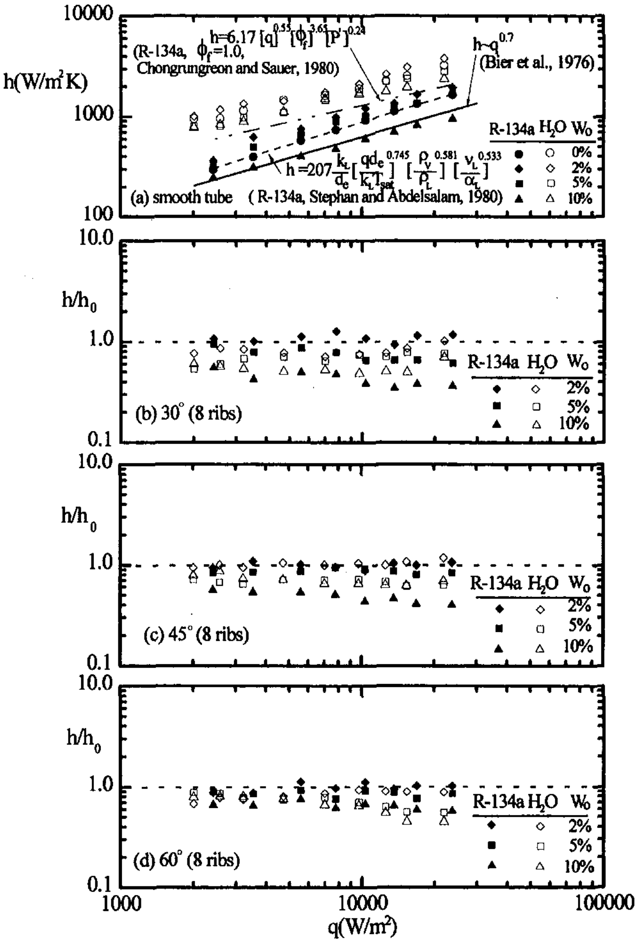

Fig. 5 Comparison of heat transfer oil effects of H_2O and R-134a/oil mixtures for various tubes

The data obtained in this study were correlated in the form of $h = C_2q^n$. For a 95 percent confidence level, the value of n was found to be 0.658 ± 0.031 which agrees quite well with the value of 0.7 reported from Ratiani and Shekriladze (1972). In addition, examination of all the data shows that the slope of the h versus q curve is approximately equal for various refrigerants and even for refrigerant/oil mixtures with different rib angles. This again verifies the previous finding of the exponent n. The results from Bier et al. (1976) and Stephan and Abdelsalam (1980) as well as Chongrungreong and Sauer (1980) with 10 percent oil addition are also plotted in Fig. 5(*a*) for comparison.

Figs. 5(*b*)–(*d*) also illustrate the effects of oil addition for the tubes tested at different heat flux levels for the distilled water and R-134a. The influence due to oil concentration is less noted in the tubes with a rib angle of 60 deg. The roughened tube with a rib angle of 45 deg and smooth tube do show adverse effects of oil addition when W_o = 2 percent. Again, the smooth tube seems to exhibit the most adverse effect of oil. This is in general agreement with the results of Memory et al. (1993). Moreover, the present results show that roughened geometry is inclined to degrade the performance more than a smooth surface when the oil is added. This is perhaps because the cavity existing in the present roughened surface tends to retain more of the oil rich mixture at the heating/boiling surface. Generally speaking, Figs. 5(*b*)–(*d*) show that the heat transfer coefficient ratio (h/h_0) is dependent upon the heat flux level. The influence of oil addition on the heat transfer coefficient is quite clear for all the rib-roughened tubes studied at different heat flux levels. For the smooth tube (not shown here) and the tube with a rib angle of 45 deg, the degradation increases as the heat flux increases. However, a 30 deg roughened tube shows a different trend. The degradation at first increases until the heat flux reaches 6 kW/m² and then decreases as the heat flux increases. The reason for this is not well understood at this stage. Most investigators have observed some foaming as was observed for the tube with a rib angle of 45 deg and the smooth tube from the present study. This is also evidenced by the boiling visualization in a later section. It is believed that the drop in heat transfer performance at high heat flux and high oil concentration may be due to a combination of changes in thermodynamic properties and the roughened geometry. Obviously, the size and present structure of the cavity strongly affects the influx of liquid from the pool drawn into the internal tunnel of the cavity. The oil-refrigerant mixture drawn into the cavities subsequently evaporates and emits bubbles from the active sites. The refrigerant vaporizes faster than the oil and, depending on the heat flux and cavity geometry, the liquid remaining behind will be mostly oil.

Generally speaking, low-finned tubes augment nucleate pool boiling heat transfer in two different ways; by increasing the wetted surface area per unit tube length and by modifying the boiling process.

Figure 6 reports the boiling heat transfer coefficient of the roughened tubes with rib angles of 30 deg, 45 deg, 60 deg compared to those of the corresponding smooth tube for the nucleate boiling region with distilled water and R-134a under different oil additions. In general, the heat transfer enhancement factor increases as the heat flux is increased initially at a lower heat flux (say, 2 kW/m²) and thereafter, it levels off to a nearly constant value except for the case of a rib angle of 60 deg and W_o = 10 percent in which a heat transfer degradation was noted, especially at a higher heat flux (say, 20 kW/m²). This is because as heat flux increases the enhancement deteriorates. This is perhaps because, at lower heat fluxes, the larger tunnels created within the present roughened geometry result in the occurrence of separation of the vapor columns and, consequently, neighboring vapor columns do not coalesce as readily, this gives a higher heat transfer coefficient. On the contrary, at higher heat fluxes, it is speculated that the present geometrical configuration

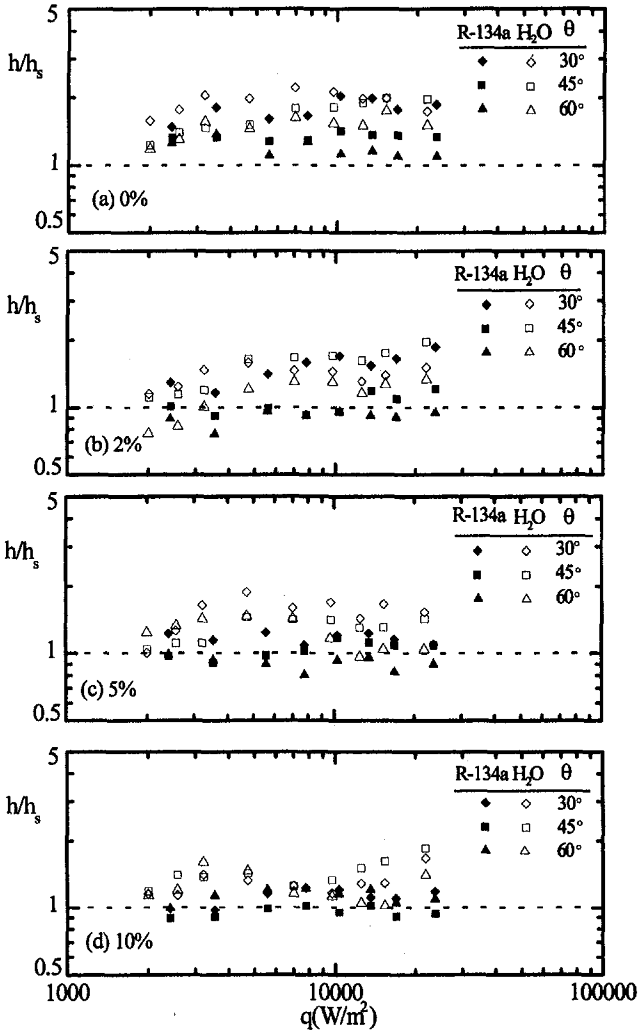

Fig. 6 Comparison of enhanced tube effects of H_2O and R-134a/oil mixtures for various oil concentrations

gives it the characteristic of a smooth tube with fins, rather than a surface with numerous active sites which results in poor heat transfer enhancement. However, this behavior becomes less prolific as the oil addition increases as shown in Figs. 6(*c*)–(*d*). This is perhaps because, as the oil concentration is increased, the high rate of transport of oil to the surface starts to override the effect due to the heat flux increase. For all the cases under study, it clearly shows that roughened tubes with the rib angle of 45 deg (distilled water)/30 deg (R-134a) have the best heat transfer enhancement effect regardless of the oil addition for most heat flux levels. Detailed enhancement ratios (h/h_s) are tabulated in Table 3 at a specified heat flux level (=25 kW/m^2) for R-134a and distilled water. Again, the values illustrated indicate the superiority in heat transfer of rib angles 45 deg and 30 deg for distilled water and R-134a as also evidenced earlier in Fig. 6. Also listed in Table 3 is the previous study of Memory et al. for HCFC-124 for various enhanced tubes for comparison. Despite the superiority in heat transfer of the enhanced tubes used by Memory et al., the present rib geometry does provide an easy fabrication process due to a much lower number of ribs.

4.3 Correlation of Heat Transfer Coefficient with Parameters.

The correlation of all the experimental data can be determined by using the least squares technique. This technique is used for deriving a model that "best fits" a set of experimental data of distilled water and R-134a. The resultant equation shown in Fig. 7(*a*), proposed for use in predicting the boiling heat transfer coefficient of refrigerant-oil mixtures, is given by:

$$Nu = 2114.225\left[\frac{qd_1}{\mu_L h_{LV}}\right]^{0.645}[\Pr]^{4.427} \times [\phi_f]^{3.708}[\theta]^{-0.430}\left[\frac{\sigma_L}{gd_1^2(\rho_L-\rho_V)}\right]^{1.318}$$

$$0.873 \le \phi_f \le 1.000$$

$$0.524\left(=\frac{\pi}{6}\right) \le \theta \le 1.047\left(=\frac{\pi}{3}\right) \qquad (8)$$

95 percent of the experimental data lie within ±20 percent of Eq. (8). The dimensionless group $(qd_1/\mu_L h_{LV})$, known as the boiling Reynolds number, Pr, and $[\sigma_L/gd_1^2(\rho_L-\rho_V)]$ are familiar from other established boiling correlations; the rest of the dimensionless groups, ϕ_f and θ, represent the oil concentration and the present rib geometric configuration, respectively. The comparison between the correlation, Eq. (8), and the data is shown in Fig. 7(*b*) is quite good (within ±30 percent). The regression analysis further confirms that the heat transfer performance is inversely proportional to that of rib angle θ. The above correlation also agrees with the data for pure refrigerant with 0 percent oil addition. However, the dependence on ϕ_f seems stronger than that of θ because the absolute value of the exponent for ϕ_f is much bigger than that of θ. This also confirms that oil addition as well as surface roughness does affect the boiling performance and, consequently, they should be carefully considered and selected.

4.4 Boiling Visualization.

Visual tests with the transparent sight-glass window of the test section showed a particular liquid-vapor exchange occuring during nucleate boiling. Figure 8 shows the boiling phenomenon in certain detail. It was observed that firstly, several nucleation sites are activated right at the tip or edge of the rib when the heat flux is low, as shown in Figs. 8(*a*)–(*d*). As the heat flux is gradually increased, the liquid is "splashed" over the tunnel by the expanding vapor while still staying in the tunnel between two consecutive ribs. Eventually, the vapor pressure within the elongated bubble gets larger than the retentive force and results in vapor escape. This causes a pumping action within the tunnel, and allows the liquid to flow in. The fed liquid is vaporized, the ebullition is complete, and the cycle is repeated (not shown here). As the heat flux is increased, the bubble departure frequency also increases as evidenced by comparing Figs. 8(*a*) and (*b*). It is also seen from Figs. 8(*c*)–(*d*) that boiling for pure refrigerants takes place around the tubes. Boiling for the mixture (see Figs. 8(*e*)–(*f*)) hardly occurs near the lower part of the tubes, and the number of the nucleation sites significantly decreases. This is also because diffusion of oil back to the bulk mixture establishes an equilibrium concentration gradient which inhibits bubble growth and should lead to a drop off in heat transfer performance. Moreover, the miscibility of oil in R-134a as the heat flux increases seems to vary. Overall, the thermal performance under study is strongly influenced by the type of refrigerant, heat flux level, and oil concentration. This is a very complex phenomenon which involves the interactions of all three of these aforementioned factors. In addition, the bubble size and frequency strongly depend on the percentage of oil addition and heat flux levels as shown in Figs. 8(*e*)–(*h*). This is in agreement with the report from Inoue and Monde (1994).

For instance, in R-134a, the frequency of bubble generation becomes higher than that of the distilled water, but the bubble size becomes very small with vapor blanketing the entire enhanced surface. This may have something to do with the reduced pressure P/P_c. As is known, P/P_c would affect bubble diameter,

Table 3 Enhancement ration for various enhanced tubes with distilled water and R-134a as pure refrigerants

relevant studies	refrigerant	heat flux	25 kW/m²				
		oil concentration	0%	2%	3%	5%	10%
present studies (24fpm)	H₂O and R-134a	smooth	1.00 1.00	1.00 1.00	— —	1.00 1.00	1.00 1.00
		30°	1.83 1.87	1.60 1.86	— —	1.62 1.10	1.76 1.18
		45°	2.06 1.34	2.05 1.21	— —	1.52 1.09	1.94 0.94
		60°	1.62 1.10	1.45 0.95	— —	1.15 0.90	1.52 1.10
Memory et al. (1993)	HCFC-124	smooth	1.00	—	1.00	—	1.00
		748 fpm	2.90	—	2.70	—	2.80
		1023 fpm	2.10	—	1.70	—	1.80
		HIGH FLUX	6.20	—	4.90	—	4.80
		TURBO-B	6.00	—	4.30	—	3.70

Note: "—" stands for data not available; underlined "_" indicates R-134a as pure refrigerant

departing frequency, and consequently, the heat transfer coefficient, somehow. Detailed phenomena may be included in a further study. It is interesting to note that the same thing happens for the R-134a/oil mixture, and sometimes, it gets worse when $W_o = 10$ percent and $q = 3.29$ kW/m^2 as evidenced by Fig. 8(h). It is also seen from Figs. 8(e) and (f) that the effect of oil becomes less evident at a lower heat flux because, at this stage, the nucleation sites (and hence foaming effect) die out quickly. However, at a relatively high heat flux $q = 3.29$ kW/m^2, it is found from Figs. 8(g) and (h) that there is a higher number of active nucleation sites (hence foaming) at $W_o = 2$ percent than at $W_o = 10$ percent. Moreover, at $W_o = 10$ percent (as stated earlier), a larger diffusion layer thickness exists, and consequently, results in an increase in bubble point temperature. This gives a poor heat transfer performance. In summary, the major reason that the heat transfer deteriorates for the refrigerant/oil mixture seems due to the decreases in the bubble size and the number of nucleation sites (also reducing the foaming) when $W_o > 2$ percent. While, in some cases for $W_o \leq 2$ percent, the heat transfer is slightly enhanced due to the foaming effect. This discrepancy can be clearly and qualitatively seen in Figs. 8(g) and (h) which again verifies the previous statements.

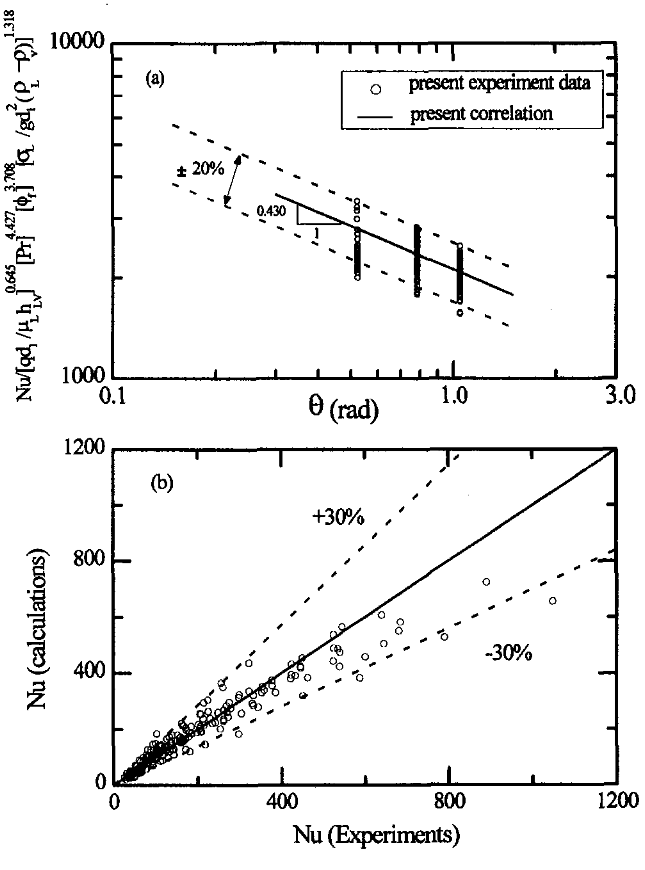

Fig. 7 The present correlation and its deviation with experimental data

5 Conclusions

The study of pool boiling from rib-roughened tubes and a plain tube for two different refrigerants (distilled water and R-134a) with oil mixtures has established that, in addition to boiling curve data and hysteresis identification, heat transfer enhancement is to be expected with moderately wetting liquids such as water and highly wetting liquids such as R-134a. The effect of oil addition on the nucleate boiling heat transfer coefficients of oil-refrigerant mixtures was extensively conducted and the data were presented. These results lead to the following conclusions:

1 The heat transfer for roughened tubes are consistently higher than those for the plain tube for the two refrigerants with and without oil addition. As the weight percent concentration of oil in the refrigerant increases, the boiling heat transfer coefficient (h) decreases except for the cases of a 45 deg rib angle and a smooth tube when $W_o \leq 2$ percent.
2 The hysteresis effect was clearly noted for distilled water for all the cases studied and compared with those for R-134a, especially with oil addition.
3 Diffusion seems to play an important role in the reduction in boiling heat transfer coefficients in refrigerant-oil mixtures when compared to pure refrigerants, and oil foaming seemingly enhances heat transfer slightly when $W_o \leq 2$ percent for a smooth and roughened tube with a 45 deg rib angle.
4 A correlation has been developed which satisfactorily models the heat transfer processes occurring in nucleate

(a) H_2O, $\theta = 45°$, W_o=0%, q=0.92kW/m^2 (b) H_2O, $\theta = 45°$, W_o=0%, q=3.84kW/m^2

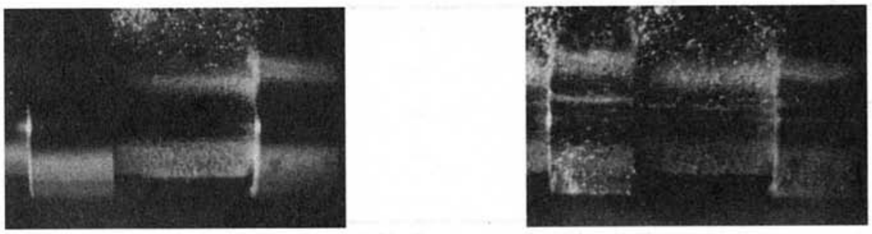

(c) R-134a, $\theta = 45°$, W_o=0%, q=0.92kW/m^2 (d) R-134a, $\theta = 45°$, W_o=0%, q=3.84kW/m^2

(e) R-134a, $\theta = 30°$, W_o=5%, q=0.78kW/m^2 (f) R-134a, $\theta = 30°$, W_o=10%, q=0.78kW/m^2

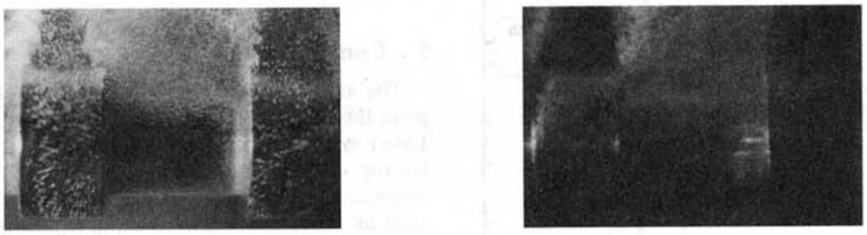

(g) R-134a, $\theta = 30°$, W_o=2%, q=3.29kW/m^2 (h) R-134a, $\theta = 30°$, W_o=10%, q=3.29kW/m^2

Fig. 8 Illustrations of boiling visualization

pool boiling of refrigerant-oil mixtures within an accuracy of about ±20 percent.

5 Through boiling visualization, the photographs qualitatively indicate that the presence of protruding ribs generates more active and stable nucleation sites in the vicinity of the rib, while oil addition generally reduces the size and frequency of bubbles, and consequently, results in a lower boiling heat transfer.

Acknowledgment

This work was supported by a research grant (NSC 82-0401-E110-128) from the National Science Council, Taiwan, R.O.C. Assistance from Mr. Feng-Yu Wu for preparation of the manuscript is sincerely appreciated.

References

Ayub, Z. H., and Bergles, A. E., 1987, "Pool Boiling From GEWA Surfaces in Water and R-113," *Warme- und Stoffubertragung*, Vol. 21, pp. 209–219.

Bell, K. I., and Hewitt, G. F., and Morris, S. D., 1987, "Nucleate Pool Boiling of Refrigerant/Oil Mixture," *Experimental Heat Transfer*, Vol. 1, pp. 71–86.

Bier, K., Engelhorn, H-R., and Gorenflo, D., 1976, "Heat Transfer with Low-Boiling Halogene Refrigerants, Measurements Taken with Single Tubes and Transmission in Tube Nets," *Klima Kaelte Ing.*, Vol. 11, pp. 399–406.

Chongrungreong, S., and Sauer, Jr., H. J., 1980, "Nucleate Boiling Performance of Refrigerants and Refrigerant-Oil Mixture," ASME JOURNAL OF HEAT TRANSFER, Vol. 102, pp. 701–705.

Carey, V. P., 1992, Liquid-Vapor Phase-Change Phenomena, Hemisphere Publishing Corporation, Washington D.C., pp. 233.

Dougherty, R. L., and Sauer, Jr., H. J., 1975, "Nucleate Pool Boiling of Refrigerant-Oil Mixtures from Tubes," *ASHRAE Transactions*, Vol. 95, pp. 175–193.

Hsieh, S. S., and Hsu, P. T., 1994, "Nucleate Boiling Characteristics of R-114, Distilled Water (H_2O) and R-134a on Plain and Rib-Roughened Tube Geometries," *International Journal of Heat Mass Transfer*, Vol. 37, pp. 1424–1432.

Inoue, T., and Monde, M., 1994, "Nucleate Pool Boiling Heat Transfer in Binary Mixture," *Warme- und Stoffubertragung*, Vol. 29, pp. 171–180.

Jensen, M. K., and Jackman, D. L., 1984, "Prediction of Nucleate Pool Boiling Heat Transfer Coefficients of Refrigerant-Oil Mixtures," ASME JOURNAL OF HEAT TRANSFER, Vol. 106, pp. 184–190.

Junkhan, C. H., and Bergles, A. E., 1976, "Heat Transfer Laboratory Data Acquisition System," Heat Transfer Laboratory Report HTL-12, ISU-ERI-Ames-77178, Iowa State University, Ames, Iowa.

Memory, S. B., and Marto, P. J., 1992, ''The Influence of Oil on Boiling Hysteresis of R-114 from Enhanced Surfaces,'' *Pool and External Flow Boiling*, V. Dhir and A. E. Bergles, eds. ASME, New York, pp. 63–71.

Memory, S. B., and Bertsch, G., and Marto, P. J., 1993, ''Pooling Boiling of HCFC-124/Oil Mixtures from Smooth and Enhanced and Enhanced Tubes,'' HTD-Vol. 243, *Heat Transfer with Alternate Refrigerants*, ASME, New York, pp. 9–18.

Pais, C., and Webb, R. L., 1991, ''Literature Survey on Single-Tube Pool Boiling on Enhanced Surfaces,'' *ASHRAE Transactions*, Vol. 97, pp. 79–89.

Ratiani, G. V., and Shekriladze, I. G., 1972, ''Study of the Process of Fully Developed Boiling of Liquid,'' *Heat Transfer-Soviet Research*, Scripta Inc., Vol. 4, pp. 126–141.

Stephan, K., 1982, ''Heat Transfer in Boiling of Mixtures,'' *Proceedings of the 7th Int. Heat Transfer Conference*, Vol. 1, pp. 59–81.

Stephan, K., and Abdelsalam, M., 1980, ''Heat-Transfer Correlation for Natural Convection Boling,'' *International Journal of Heat Mass Transfer*, Vol. 23, pp. 73–87.

Thome, J. R., 1990, *Enhanced Boiling Heat Transfer*, Hemisphere Publishing Corporation, Washington D.C.

Udomboresuwan, A., and Mesler, R., 1986, ''The Enhancement of Nucleate Boiling by Foam,'' *Eight International Heat Transfer Conference*, Vol. 6, pp. 2939–2944.

Webb, R. L., and Paris, C., 1992, ''Nucleate Pool Boiling Data for Five Refrigerants on Plain, Integral-Fin and Enhanced Tube Geometries,'' *International Journal of Heat Mass Transfer*, Vol. 35, pp. 1893–1904.

Point Measurements of Noncondensable Gas Concentration in Condensing Systems

A. Obonai
Tohoku Electric Power Co.,
1-18-6-302 Nishinakata,
Taihaku-Ku, Sendai, Miyagi, 981-11
Japan

Per F. Peterson
Associate Professor

V. E. Schrock
Professor of the Graduate School,

Department of Nuclear Engineering,
University of California,
Berkeley, CA 94720-1730

Condensation in the presence of noncondensable gases continues to receive considerable attention, most recently in the application to containment performance for advanced passive nuclear reactors. In experiments, it is often desired to make point measurements of noncondensable gas concentrations under conditions where the gas concentration can be small and superheat can be significant. This paper presents test results for a novel miniature psychrometer. The tests and analysis presented here show that a wetted cylindrical body will approach closely the local saturation temperature of an air-steam mixture, under a wide range of flow velocities and superheat levels, even when the bulb is allowed to drip water. This permits local gas concentrations to be measured with high accuracy, particularly when the thermopile method introduced here is used to measure the wet-bulb temperature relative to a reference pure steam temperature generated in a small boiler.

I Introduction

Condensation of vapors in the presence of noncondensable gases continues to receive extensive analytical and experimental attention. One of the more significant recent applications is in the design of advanced passive nuclear reactor containments, where steam from the reactor vessel must be condensed on containment walls or in vertical tubes after mixing with nitrogen or air in the containment volume. To study these systems, both separate effect and integral system experiments are underway. In these experiments, local measurements of noncondensable gas concentrations are desirable.

To support ongoing experimental investigations of noncondensable gas effects, this paper presents test and design information for an accurate method of determining the noncondensable gas mole fractions in vapor-gas mixtures. To achieve this goal we employed a novel miniature wet-bulb/dry-bulb probe. These tests also provided important fundamental information on the behavior of wetted bodies in superheated vapor-gas mixtures, showing that such bodies tend to approach closely the local saturation temperature.

Analysis of the wet-bulb/dry-bulb technique for measuring the air humidity is given in several standard textbooks (i.e., Rohsenow and Choi, 1961). A wet-bulb/dry-bulb probe has been designed for noncondensable gas concentration measurements in nuclear reactor systems by Bowman and Griffith (1987), but the probe is too large to make point measurements. In addition, the analysis neglects bulk mass transport, an assumption commonly made for humidity measurement analysis which is not valid at low gas concentrations.

Peterson and Tien (1987) developed a probe which consisted of a liquid-soaked porous sphere as small as 0.5 mm in diameter with a fine-gauge thermocouple embedded at its center. The probe was used to make detailed measurements of the spatial distribution of noncondensable gases in a 5 cm diameter, two phase gas loaded thermosyphon. Measurements of only the total pressure, with a pressure transducer, and point wet-bulb temperature were needed to determine the local gas concentration. However, for this older method, the accuracy of pressure transducers is not sufficient to measure low gas concentrations accurately. Furthermore, at higher superheat levels, the use of liquid, pumped through a capillary tube to the bulb, must be considered for keeping the probe moist.

The key features of the new psychrometer probe discussed here are:

1 High probe precision was achieved by using a thermopile method to measure the difference between the wet-bulb temperature and the saturation temperature at the total pressure, where the reference temperature was generated using an external boiler maintained at the test section pressure by a vent line. This technique achieves a substantial improvement in measurement accuracy, particularly at small gas concentrations.
2 An automatic water makeup system was designed for keeping psychrometer probes moist. Both dripping and nondripping modes were developed and tested. The dripping mode permits the probe to be located at large distances from the supply system.

We examined the effects on the wet-bulb temperature measurements created by liquid supply rates, radiation heat transfer to wall surfaces, the Reynolds number of the flow over the probe, vapor-gas mixture superheat, and total pressure and gas concentration. To provide a wide variation of the probe Reynolds number, two test sections were used: a 2.0 inch IPS pipe for high Reynolds number flows, and a 6.0 inch IPS pipe with a deflector plate for low Reynolds number flows.

II Theory

The temperature of a wet bulb is controlled by the balance between heat transfer to the bulb and mass transfer from the bulb,

$$(h_c + h_r)(T_\infty - T_{wb})A_c = M_v \dot{c}''_L h_{fg} A_D \qquad (1)$$

where h_c and h_r are the convective and radiative heat transfer coefficients, A_c and A_D the areas available for heat transfer and

---

Contributed by the Heat Transfer Division for publication in the JOURNAL OF HEAT TRANSFER. Manuscript received by the Heat Transfer Division April, 4, 1996; revision received October 18, 1996; Keywords: Condensation, Instrumentation, Measurement Techniques. Associate Technical Editor: M. Sohal.

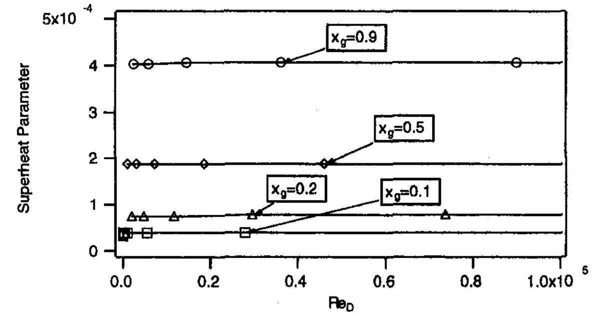

Fig. 1 Superheat parameter S as a function of the Re_D for cylindrical wet-bulbs

mass transfer, M_v the molecular weight, $\dot{c}''_L$ the molar flux of liquid from the surface, and h_{fg} the latent heat of vaporization.

A mass balance at the surface for the vapor and the gas, assuming the gas concentration in the liquid phase is zero, yields

$$\dot{c}''_L = c_{v,wb}v_m - \left(c_T D \frac{\partial x_v}{\partial r}\right)_{wb} \tag{2}$$

$$0 = c_{g,wb}v_m - \left(c_T D \frac{\partial x_g}{\partial r}\right)_{wb} \tag{3}$$

where c is the molar density, v_m the molar average velocity, x the mole fraction, and D the mass diffusivity.

Assuming the pressure and temperature are relatively constant, the total molar density is constant and can be brought inside the derivative, $c_T \partial x_v/\partial r = \partial c_v/\partial r$. Then the convective term can be eliminated from Eq. (2) using Eq. (3), giving

$$\dot{c}''_L = \frac{-D(\partial c_v/\partial r)_{wb}}{(1 - x_{v,wb})} = \frac{h_D(c_{v,wb} - c_{v,\infty})}{x_{g,wb}} \tag{4}$$

where h_D is the mass transfer coefficient, which relates the local concentration gradient at the interface, $(\partial c_v/\partial r)_{wb}$, to the concentration difference $c_{v,wb} - c_{v,\infty} = c_T(x_{v,wb} - x_{v,\infty})$. Thus the fundamental equation for the ambient noncondensable gas mole fraction is derived,

$$x_{g,\infty} = 1 - x_{v,wb} + S\left(1 + \frac{h_r}{h_c}\right)(T_\infty - T_{wb}) \tag{5}$$

The superheat parameter S is defined as

$$S = \frac{A_c}{A_D}\frac{h_c}{h_D}\frac{RT_{wb}}{M_v h_{fg} P_T}\left(1 - \frac{P_{v,wb}}{P_T}\right) \tag{6}$$

For cylinders (Edwards et al., 1979),

$$\frac{h_c}{h_D} = \frac{k}{D}\left(\frac{0.43 + K\,\mathrm{Re}_D^m\,\mathrm{Pr}^{0.31}}{0.43 + K\,\mathrm{Re}_D^m\,\mathrm{Sc}^{0.31}}\right) \tag{7}$$

where $K = 0.53$, $m = 0.5$ for $1000 < \mathrm{Re}_D < 4000$; $K = 0.193$, $m = 0.618$ for $4000 < \mathrm{Re}_D < 40000$; and $K = 0.0265$, $m = 0.8$ for $\mathrm{Re}_D > 40000$.

Figure 1 shows how the superheat parameter S varies with Re_D. We found that the magnitude of S is small (below 10^{-3}) and the variation of S with Re_D is also small. This indicates that in many cases, the effects of superheat can be neglected if the superheat levels are modest (<30°C).

Next we consider the effect of radiation heat transfer. Again for a cylindrical wet-bulb geometry

$$\mathrm{Nu} = 0.43 + K\,\mathrm{Re}_D^m\,\mathrm{Pr}^{0.31} \tag{8}$$

Then,

$$1 + \frac{h_r}{h_c} = 1 + \frac{2r_{wb}\sigma\epsilon(T_w^4 - T_{wb}^4)}{k(0.43 + K\,\mathrm{Re}_D^m\,\mathrm{Pr}^{0.31})(T_\infty - T_{wb})} \tag{9}$$

where T_w is the wall temperature, σ the Stefan-Boltzmann constant, ϵ the emissivity, r_{wb} the radius of the wet-bulb, and k the thermal conductivity of the vapor.

Figure 2 shows how the $(1 + h_r/h_c)$ varies with $(T_w - T_{wb})$. We find that, because S is typically small, the effect of thermal radiation on the measured gas concentration is usually small.

Neglecting superheat and applying Dalton's law, Eq. (5) can be simplified as follows:

$$\begin{aligned} x_{g,\infty} &= 1 - x_{v,wb} = 1 - \frac{P_{v,wb}}{P_T} \\ &= \frac{T_{sat} - T_{wb}}{P_T}\left(\frac{dP}{dT}\right)_{sat} \\ &= \frac{\Delta T_{wb}\left(\dfrac{dP}{dT}\right)_{sat}}{P_T}. \end{aligned} \tag{10}$$

III Psychrometer Description

The key feature of the psychrometer described in this paper is the measurement of the temperature difference between the wet bulb and the pure steam generated in the boiler. Two dual sheathed thermocouples were used to form a thermopile and doubled the potential between the wet bulb and the boiler, as shown by the circuit diagram in Fig. 3. The 1.6 mm (0.062 inch) O.D. dual thermocouples contain two separate, un-

Nomenclature

A = area available to heat or mass transfer
c = molar density
$\dot{c}''$ = mole flux
D = mass diffusivity
h = heat or mass transfer coefficient
h_{fg} = latent heat of vaporization
k = thermal conductivity
$\dot{m}$ = mass flow rate
M = molecular weight
n = number of thermocouple junctions
Nu = Nusselt number
P = pressure
Pr = Prandtl number
r = radial coordinate
R = universal gas constant
Re_D = probe Reynolds number
S = superheat parameter, Eq. (6)
Sc = Schmidt number
S.D. = standard deviation
T = absolute temperature
v = mole average velocity
V = voltage
w = uncertainty
x = mole fraction
ϵ = emissivity
σ = Stefan-Boltzmann constant

Subscripts

c = heat convection, calculated value
D = mass transfer
g = noncondensable gas
L = liquid
m = measured value
r = radiation
sat = saturation
T = total
v = vapor
w = wall
wb = wet-bulb surface
∞ = ambient

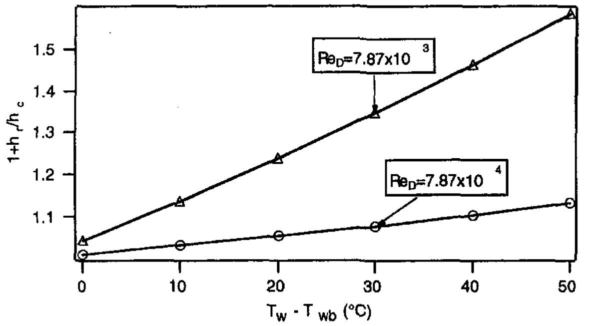

Fig. 2 Variation of $(1 + h_r/h_c)$ with $(T_w - T_{wb})$ for $x_g = 0.2$, for $T_\infty = T_w$

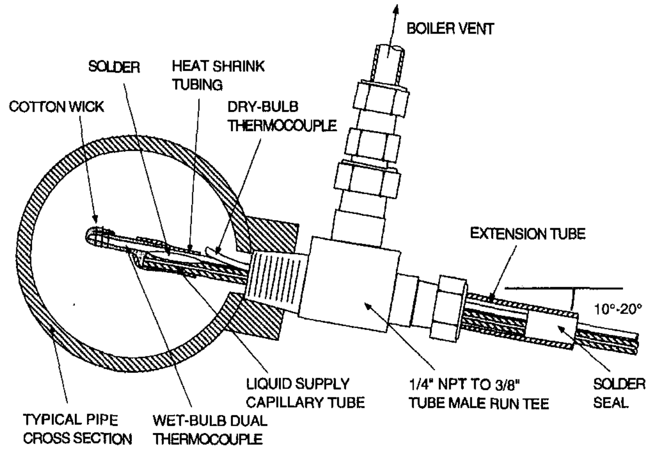

Fig. 4 Detail of miniature probe design (showing wick design)

grounded thermocouple junctions inside a single stainless steel sheath. For the devices studied here, copper constantan (*T*-type) thermocouples were used.

The miniature probe was fabricated using cotton wick material (similar to shoe lace) to provide good wetting. The wick of the probe, shown in Fig. 4 in a pipe-mounted configuration, slides over both the dual thermocouple and a thin 3.2 mm ($\frac{1}{8}$ inch) diameter stainless steel capillary tube. The thermocouple and tube were soldered together. Heat shrink tubing was used to seal the wick to the soldered area of the dual thermocouple and capillary tube. The heat shrink tubing extended past the end of the capillary tube so that when it was shrunk down, it compressed the wick around the wet-bulb thermocouple. This increased the flow resistance from the capillary supply tube to the tip of the wick and aided in wetting the tip of the wick. The end of the cotton wick was doubled back and wrapped into place with fine copper wire. The probe was installed to slope up at a 10 deg to 20 deg angle to insure that drips did not fall from the probe tip.

A separate single-sheathed thermocouple was located close to the wet-bulb to measure the dry-bulb temperature. The probe also provided a vent connection for the boiler to maintain the boiler at the same pressure as the wet-bulb. The vent line must be sloped to prevent accumulation of any condensate, and drain valves provided at any low points.

A rotameter metered water to the capillary tube which supplied the probe wick. The capillary water flow rate was controlled by an integral needle valve to between 0.5 and 1.0 cc/min, as shown in Fig. 5. Alternatively, for nondripping operation, a small positive hydrostatic head between 0 and 1 cm was maintained. The nondripping mode was found to be more challenging to implement.

The boiler, shown schematically in Fig. 5, used a closed-loop thermosyphon to provide a reference saturation temperature measurement at the ambient pressure of the wet-bulb. The condenser prevented steam from entering the test volume, this ensured that the pressure difference between the boiler and test volume was negligible, while maintaining a pure steam environment around the total saturation thermocouple. The sight glass provided visual indication for the presence of sufficient water in the boiler. The boiler could be operated in an overflow mode, supplying a constant water flow from a rotameter to ensure adequate water supply during unmonitored operation. During overflow mode operation, excess water drains down the vent line to the test volume. Two heaters were successfully demonstrated, one, a 50W kapton sheet heater with a pressure sensitive adhesive wrapped around the copper boiler tube, and the second, a 100W cartridge heater. Both heaters showed good durability during continued operation. Fig. *A*1 in the appendix shows a detailed, scaled drawing of the boiler used in these experiments.

The psychrometer was tested using carefully measured flows from the campus steam and building compressed air supplies. The air supply was equipped with a 2 kW heater that permitted a wide range of superheat levels. The entire length of the steam and piping was insulated with 5 cm of fiberglass to minimize heat loss and prevent condensate formation upstream of the test sections. The nominal steam and air supply pressures were 758 kPa (110 psig) and 620 kPa (90 psig), respectively.

A calibrated orifice and differential pressure transducer were used to measure the steam flow rate at higher flow rates. At low flow rates (below 17 kg/hr), the condensate mass flow rate was measured volumetrically. A condenser was used, consisting of coaxial 1.6 m long copper tubes; the outer diameters being 3.2 cm for the jacket tube and 1.6 cm for the condensing tube. Building cooling water was supplied to the heat exchanger annulus. At the outlet of the heat exchanger, a graduated cylinder was used to measure the condensate volume.

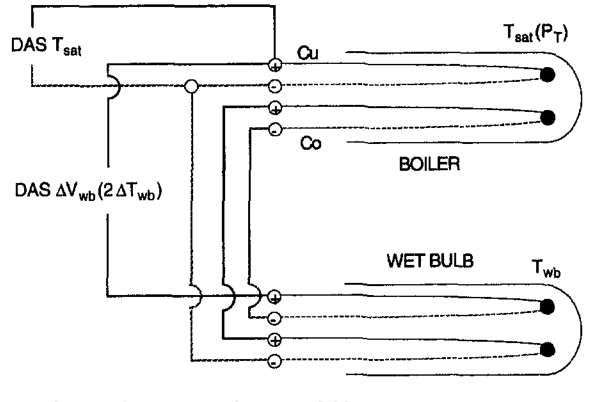

Fig. 3 Circuit diagram for data acquisition system showing measurement scheme using dual sheathed copper-constantan (*T*-type) thermocouples

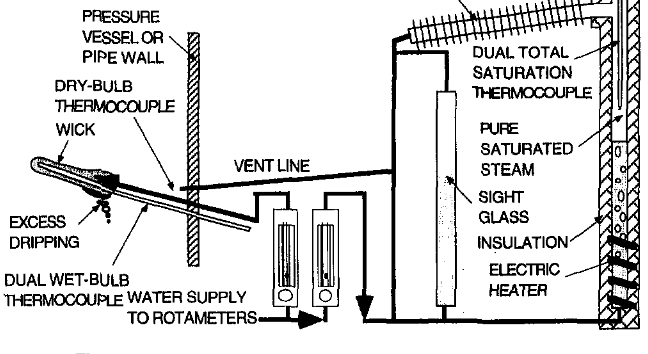

Fig. 5 Piping schematic for probe and boiler assembly

A pipe test section was provided for high-Reynolds number tests, while a larger chamber provided low Reynolds numbers. The pipe test section was constructed from a 5.25 cm ID carbon steel pipe. To study the effect of thermal radiation from the pipe wall, the pipe was wrapped with heater cable and insulated with 5 cm of fiberglass so the pipe wall could be heated to higher temperatures than the mixture bulk temperature. The low-velocity chamber test section was constructed from a 15.8 cm ID stainless steel pipe, and a deflector plate was employed to break up the jet entering the test section. This chamber was also wrapped with the same heater cable and insulated with 5.0 cm of fiberglass.

The data acquisition system consisted of terminal boxes, data acquisition cards, and a Macintosh IIci computer with software to display and log data. Strawberry Tree model T21 terminal panels, with eight channels each, were used to connect all temperature, pressure, and flow analog signals from the instruments. Three Strawberry Tree model ACM2-12-16 cards with sixteen differential analog inputs and sixteen digital input/output lines were used as an analog-to-digital converter. Six input ranges spanned from 25 millivolts to 10 volts full scale to accept data transmitted from the terminal panels. By selecting the signal type, or specifying a conversion formula, the analog output signals from experimental instrumentation were converted to the desired digital data units and displayed directly, including the gas mole fraction calculated using the psychrometer data algorithm discussed later.

The psychrometer test procedure used the following steps: (1) water supply to the wick and boiler was initiated by opening needle valves on the rotameters; (2) water level in the boiler was confirmed, then power was supplied to the boiler and steady-state condition of the saturation temperature achieved; (3) steam flow was supplied to the test section at the desired rate, then compressed air flow; (4) upon reaching steady-state conditions, data was recorded; (5) the steam and air flow rates were varied to obtain the desired gas mole fractions.

An extensive test matrix was examined to determine the effects of pipe wall thermal radiation, Reynolds number, pressure, mixture superheat, and gas concentration. In total, 29 test conditions were studied as summarized by Obonai (1994).

IV Data Reduction

We found that we could simultaneously measure the saturation temperature and the difference between the saturation and wet-bulb temperatures using the circuit shown in Fig. 3. The local mixture gas concentration, temperature, superheat, and total pressure were determined using three thermocouples (one single and two dual) and three data acquisition channels.

The data were reduced directly with the data acquisition software (using the following data reduction algorithm) which allowed the gas concentration to be displayed in real time. Three quantities were measured directly by the data acquisition system: the saturation temperature at the total pressure from the boiler, T_{sat}; the dry-bulb temperature, T_{db}; and the thermopile voltage generated by the difference between the wet-bulb and total saturation temperatures, V_{wb}. The data reduction algorithm was comprised of four steps.

1 The total pressure (bar) was calculated from the measured saturation temperature T_{sat} at the total pressure from the boiler using a curve fit of steam table data in the pressure range of interest. This curve fits well for water vapor in the immediate range of one atm. The maximum error between actual value and curve fitting value is 0.66 percent.

$$P_T = 491700 \exp\left(-\frac{4885.4}{273.14 + T(°\mathrm{C})}\right)(\mathrm{bar}) \tag{11}$$

2 The temperature difference, $\Delta T_{wb} = T_{sat} - T_{wb}$, was determined using the curve fit for the slope of voltage and potential for type T thermocouples. This curve, in °C/Volt, fits well and has a maximum error of 0.49 percent.

$$\left(\frac{dT}{dV}\right) = 24.26 - 0.02908T(°\mathrm{C}) \tag{12}$$

The temperature difference was calculated in two steps to provide a centered difference approximation,

$$\Delta T'_{wb} = \frac{\Delta V_{wb}}{n}(24.26 - 0.02908T_{sat}) \tag{13}$$

$$\Delta T_{wb} = \frac{\Delta V_{wb}}{n}\left[24.26 - 0.02908\left(T_{sat} - \frac{\Delta T'_{wb}}{2}\right)\right] \tag{14}$$

where $n = 2$ because the dual thermocouple thermopile has two thermocouples.

3 The slope of the saturation pressure and temperature curve was evaluated from steam table data. This curve fits well in the immediate range between zero and five atm. The maximum error between the actual and the curve fit values is 0.54 percent.

$$\left(\frac{dP}{dT}\right)_{sat} = (1.674 \times 10^{-5})T(°\mathrm{C})^2 + (-2.357 \times 10^{-3})T(°\mathrm{C}) + 0.1050 \tag{15}$$

with units bar/°C, where $T = T_{sat} - \Delta T_{wb}/2$.

4 The gas concentration measured by the wet-bulb probe was then calculated from Eq. (10). This form does not contain a correction for vapor superheat. Under most conditions the correction is predicted to be small.

All these formulas were automatically calculated by the data acquisition system and the resulting gas concentration was displayed in real time.

The use of the thermopile provides a large reduction in the measurement error compared to previous methods where total pressure is measured with a pressure transducer (Peterson and Tien, 1987), and permits noncondensable gas concentrations to be measured even at low gas mole fractions with relatively small errors. Uncertainty for the thermopile method can be contrasted with the error introduced from traditional methods.

We consider the following example for a analysis of the measurement uncertainty: $P_{tot} = 3.0$ bar; $x_g = 0.05$; superheat $T_\infty - T_{wb} = 25°\mathrm{C}$; thermocouple uncertainty of 1°C, so the uncertainty of $P(T_{sat})$ is $w_{P(Twb)} = 0.09$ bar; and pressure transducer uncertainty of 2 percent, so the uncertainty of P_{tot} is $w_{Pt} = 0.06$ bar.

For the thermopile method introduced in this paper, the gas mole fraction is evaluated using Eq. (10). Uncertainty in the

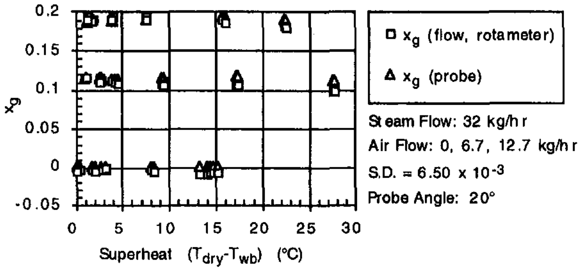

Fig. 6 Effect of superheat on measured gas concentration

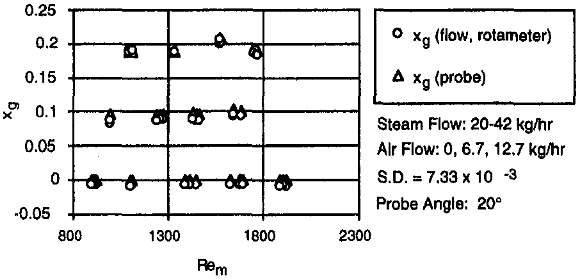

Fig. 7 Effect of flow Reynolds number (based on probe diameter) on measured gas concentration

thermopile temperature difference, total pressure, and super heat contribute to the total uncertainty,

$$w_{x_g} = \left\{ \left(\frac{\partial x_g}{\partial \Delta T_{wb}} w_{\Delta T_{wb}} \right)^2 + \left(\frac{\partial x_g}{\partial P(T_{sat})} w_{P(T_{sat})} \right)^2 + \left(\frac{\partial x_g}{\partial S} w_S \right)^2 \right\}^{(1/2)}$$

$$= \left\{ \left(\frac{w_{\Delta T_{wb}}}{\Delta T_{wb}} \right)^2 + \left(\frac{w_{P(T_{sat})}}{P(T_{sat})} \right)^2 + \left(S\left(1 + \frac{h_r}{h_c}\right)(T_\infty - T_{wb}) \right)^2 \right\}^{(1/2)} \qquad (16)$$

Considering an uncertainty in the thermopile voltage measurement of 4 percent (6 mV), the uncertainty in ΔT_{wb} is then 4 percent/n = 4 percent/2 = 2 percent. Then, from Eq. (16), the measurement uncertainty for the example case is $w_{x_g}/x_g = 0.036$, where the contribution due to the superheat effect is very small.

The conventional psychrometer method evaluates the difference between the total pressure measured with a pressure transducer and the vapor partial pressure calculated from the measured wet-bulb temperature. Measured with conventional technique, uncertainty in the wet-bulb vapor pressure, total pressure, and superheat contribute to the total uncertainty,

$$w_{x_g} = \left\{ \left(\frac{\partial x_g}{\partial P(T_{wb})} w_{P(T_{wb})} \right)^2 + \left(\frac{\partial x_g}{\partial P_t} w_{P_t} \right)^2 + \left(\frac{\partial x_g}{\partial S} w_S \right)^2 \right\}^{(1/2)}$$

$$= \left\{ \left(x_g \frac{w_{P(T_{wb})}}{P_t} \right)^2 + \left(x_g \frac{P(T_{wb})}{P_t} w_{P_t} \right)^2 + \left(S\left(1 + \frac{h_r}{h_c}\right)(T_\infty - T_{wb}) \right)^2 \right\}^{(1/2)}. \qquad (17)$$

For the conventional method, the uncertainty becomes much larger, $w_{x_g}/x_g = 1.28$. At lower gas concentrations particularly, the thermopile technique provides a substantial improvement in measurement accuracy.

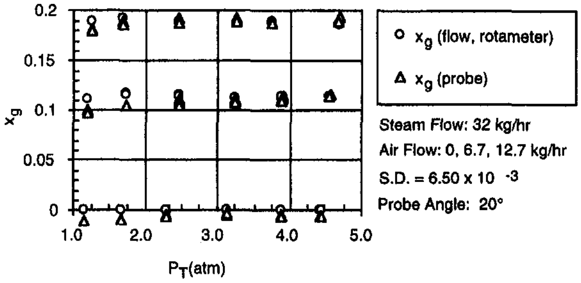

Fig. 8 Effect of total pressure on measured gas concentration

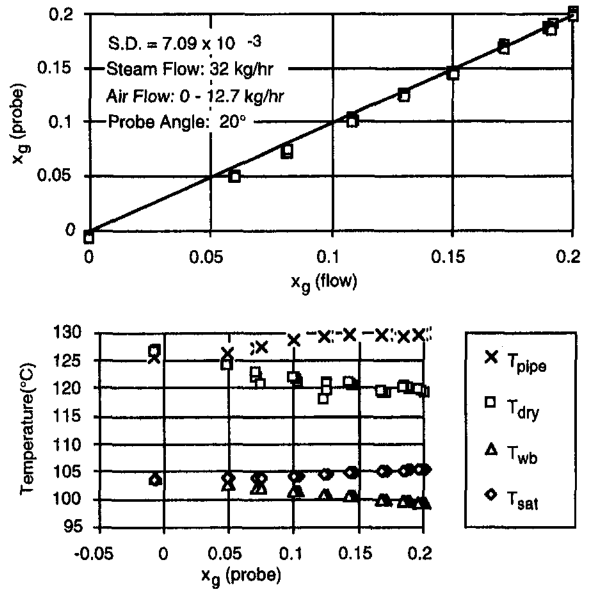

Fig. 9 Comparison of gas mole fractions measured by probe and calculated from gas and steam flow rates showing small effects of pipe wall temperature and superheat

V Experimental Results

We provided a metered flow of steam and air to the test sections and discharged the flow to a pool of water or to a heat exchanger to condense the steam. The gas mole fraction was then calculated using

$$x_{g,m} = \frac{\dot{m}_g/M_g}{\dot{m}_g/M_g + \dot{m}_v/M_v} \qquad (18)$$

With the differential pressure transducer, the uncertainty of the steam flow rate measurement was a function of flow rate, however, the average uncertainty was 3.4 percent for the steam flow rates used here (Obonai, 1994). The uncertainty for the volumetric condensate measurements at low steam flow rates was 2.8 percent based on the uncertainty of the volume measurement in the graduated cylinder (20 cc or 1 percent), the uncertainty of the time measurement (1.0 sec or 0.8 percent), the fluctuation of steam supply pressure (2 percent), and vapor carryover with the 20°C noncondensable gas from the condenser (1.5 percent). The uncertainty of the air flow rate measurement was 2.8 percent based on the accuracy of the rotameter (2 percent) and the fluctuation of air supply pressure (2 percent).

Figure 6 compares the gas mole fraction measured by the miniature psychrometer x_m to that calculated from measured flow rates of air and steam x_c, as the superheat level was varied from 0 to 27°C. The agreement is good, with a standard

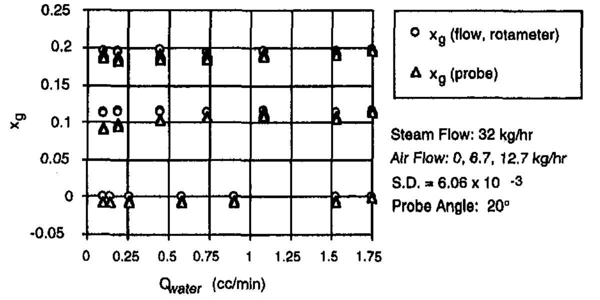

Fig. 10 Effect of capillary water flow rate to wick on measured gas concentration

deviation of 0.0065, where the standard deviation is defined as

$$\text{S.D.} = \left(\frac{1}{n} \sum_{i=1}^{n} (x_c - x_m)^2 \right)^{1/2}. \qquad (19)$$

This standard deviation falls inside the range anticipated due to the combined uncertainties of the probe and the flow rate measurements. As expected from the analysis, superheat has little effect on the probe measurement, even in the limit of zero gas concentration due to the small value of the superheat parameter S.

Figure 7 shows the effect of varying the flow Reynolds number over the probe. It shows that the effect of the flow velocity over the probe was also small, with a standard deviation of 0.0073, within the bounds of the measurement uncertainty. Due to the steam throttling from the higher supply pressure, the air steam mixture was superheated from between 15°C to 25°C. The minimal effect of flow Reynolds number also agrees with the analysis. Experiments performed in the larger stagnant chamber, where the flow velocities were $\frac{1}{5}$ the minimum velocity in Fig. 7, gave similar results, with a standard deviation of 0.0084. Figure 8 shows that the effect of total pressure on the probe performance was also small.

The perturbation of radiation heat transfer from hot surfaces to the probe was also of concern. Figure 9 shows results where the pipe wall was heated between 20 and 30°C above the wet-bulb temperature. Again the effect on the measured gas concentration is small.

Though the probe can be operated in a nondripping mode by providing a small static head of water (0 cm to 1 cm), in many cases dripping is acceptable. Operation in dripping mode, with water supplied from a small rotameter, greatly simplifies the probe installation and operation. The measurements reported above were made at a drip rate of 0.9 cc/min. The concern with the dripping mode is to provide a sufficient flow to prevent dry out and to insure that the sensible cooling from the make-up flow does not perturb the probe measurement. Figure 10 shows a comparison of the gas mole fraction calculated from the flow measurements with the fraction measured using the stationary probe for the dripping mode at a wick angle of 20 deg. From this figure we find that the agreement between the gas mole fractions measured with the probe and calculated from the mass balance was good when the capillary water was controlled between 0.5 and 1.75 cc/min.

Based on these experiment results, the following design and operating guidelines should be adhered to when dripping mode operation is used: (1) Use a rotameter to provide a constant, slow supply of water to the wick at a flow rate of 1.0 cc/min. ± 0.5 cc/min. This flow rate is sufficient to insure wetting all the way to the wick tip and to prevent dry out; (2) Orient the wick such that it points upward at approximately a 10 deg ~ 20 deg angle so that drips run away from the wick tip.

VI Conclusions

The stationary psychometer presented here provides a powerful and accurate tool for measuring local gas mole fractions even in the limit of zero gas concentration. Both nondripping and dripping modes were demonstrated. In particular, the dripping mode option becomes most attractive if the added liquid inventory is acceptable in the system because it simplifies the instrumentation and reduces the cost significantly. The dripping mode also eliminates the requirement for horizontal penetration of the wet-bulb probe, allowing for longer, nonhorizontal runs of capillary tubing to the probe location.

We improved the probe precision using a thermopile method to compare the probe wet-bulb temperature with the saturation temperature at the total pressure (generated in an external boiler maintained at the test section pipe pressure by a vent line). The stationary probe predicted gas mole fractions within ±0.01 in both the nondripping and dripping modes. The effects of radiation heat transfer to surfaces, flow Reynolds number over the probe, mixture superheat, and pressure were shown to negligible, verifying that the fundamental theory for the psychrometer (Peterson and Tien, 1987) is correct.

References

Bowman, J., and Griffith, P., 1987, "Determining Noncondensable Gas Fraction at Elevated Temperatures and Pressures Using Wet and Dry Bulb Temperature Measurements," ASME Journal of Heat Transfer, Vol. 109, pp. 271–272.

Edwards, D. K., Denny, V. E., and Mills, A. F., 1979, *Transfer Processes*, 2nd Ed., p. 142, Hemisphere Publishing Co., Washington.

Obonai, A., 1994, A Stationary Psychrometer for Measuring Gas Mole Fractions, M.S. thesis, Department of Nuclear Engineering, University of California, Berkeley, CA.

Peterson, P. F., and Tien, C. L., 1987, "A Miniature Wet-Bulb Technique for Measuring Gas Concentrations in Condensing or Evaporating Systems," *Experimental Heat Transfer*, Vol. 1, pp. 1–15.

Rohsenow, W. M., and Choi, H., 1961, *Heat, Mass, and Momentum Transfer*, p. 419, Prentice-Hall, Englewood Cliffs, N.J.

APPENDIX

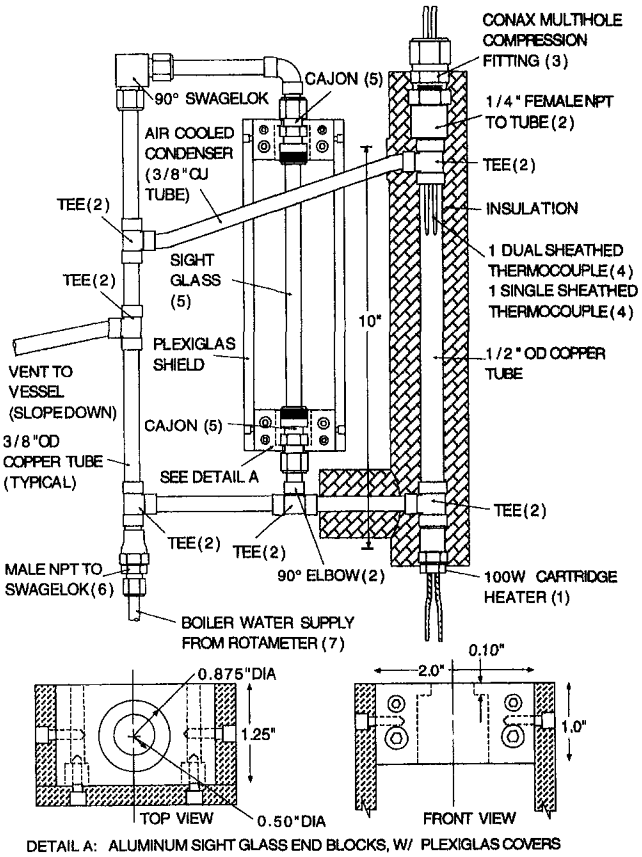

Fig. A1 Detailed scaled drawing of saturation boiler, with: (1) 100W $\frac{3}{8}''$ OD cartridge heater with $\frac{1}{4}''$ Male NPT connector (Omega Co. CIR-2013/120/9C/B); (2) $\frac{3}{8}''$ copper solder fittings; (3) Conax compression fitting for 2 thermocouples; (4) 304L sheathed thermocouples with single and dual elements; (5) $\frac{3}{8}''$ Swagelok to $\frac{3}{8}''$ Cajon (SS-6-UT-6-600) for connection to Pyrex sight-glass tube; (6) $\frac{1}{8}''$ Swagelok to $\frac{1}{4}''$ male NPT (B-200-1-4); and (7) 0 to 1.41 cc/min rotameter with integral flow control valve (Omega Co. FL-3213G).

X. Liu
Carrier Corporation,
United Technologies,
P.O. Box 4803,
6500 Chrysler Drive,
Syracuse, NY 13221
Mem. ASME

Condensing and Evaporating Heat Transfer and Pressure Drop Characteristics of HFC-134a and HCFC-22

Condensing and evaporating heat transfer and pressure drop characteristics of an ozone friendly refrigerant HFC-134a and a HCFC refrigerant R-22, flowing inside a 9.5 mm ($\frac{3}{8}$ in) OD axially grooved tube were investigated experimentally to obtain the quasi-local heat transfer data and the correlations. When compared to R-22 at the same refrigerant flow rate, the condensing heat transfer coefficients for R-134a are 8 percent to 18 percent higher, and the pressure drop is 50 percent higher. The evaporating heat transfer coefficient with R-134a is about the same for mass velocity below 270 kg/m^2-s and decreases above that velocity, relative to R-22. Performance characteristics are compared with data from literature reports.

Introduction

In the transition to ozone-safe refrigerants fundamental heat transfer and fluid flow information is necessary for design and performance simulation of refrigeration and air-conditioning systems. This study will focus on HFC-134a and its comparison to HCFC-22.

Some heat transfer experimental results of R-134a are available in literature (Eckels and Pate, 1991; Torikoshi et al., 1992, 1993; Ebisu and Torikoshi, 1993; Dobson et al., 1993a, b; Wattelet et al., 1993a, b; Christoffersen et al., 1993). The lengths of the tubes that are tested in those studies are relatively short (Tables 3 and 4). Thus, the imposed heat fluxes are much higher than the values actually encountered in practice, and only average heat transfer coefficients are obtained. An average heat transfer coefficient under two-phase flow condition depends on specific operational conditions (Liu, 1996) and is of limited use in design. This study obtains the quasi-local heat transfer coefficient and pressure drop from a test section of 10.8 m in length. The results reveal some special local heat transfer characteristics of R-134a, especially the decrease in heat transfer coefficient for mass velocity above 270 kg/m^2-s. The commonly used evaporating heat transfer correlations do not cover high vapor quality region, and the data for that region are limited too. The present study provides data and correlations up to the vapor quality of unity.

Test Apparatus and Procedure

The refrigerant test facility (Fig. 1) consisted of four closed cycle loops: a refrigerant cycle containing a reciprocating-type compressor to supply a controlled, variable refrigerant flow (via hot gas bypass) for condensing or evaporating tests; a heated, controlled water loop that supplied the load for the evaporator; a cooled, controlled water loop that removed the load for the condenser; and a cooling tower brine circuit that served to remove heat from the system.

In the evaporation tests, the manual expansion valve lowered the refrigerant pressure to the value corresponding to the desired saturation temperature before the refrigerant entered the test section. The refrigerant entered the test section at a vapor quality around 15 percent and left at a vapor quality varying from about saturation to 1 K superheat. The refrigerant was then superheated by an auxiliary evaporator to ensure a liquid-free vapor. It then entered an oil separator to have the injected oil removed before entering the compressor to complete the loop. For the condensation tests, the hot vapor was desuperheated, condensed, and subcooled throughout the test section before it entered the flow meter. The concentration of oil (AB/cs68 oil for R-22 and POE/cs68 for R-134a) was controlled to 1 percent by mass.

Test Section. The test section consisted of six identical horizontal passes, constructed as double tube heat exchangers. Each pass was about 2.2 m long and connected, in order, by 7.6 cm radius U-bends. The heat transfer section of each pass, which had the water path in the annular side, was 1.8 meters long.

The inner (refrigerant) tube of the test section was a 9.5 mm (nominal $\frac{3}{8}$ inch) copper tube of 0.348 mm wall thickness with 72 axial fins of 0.185 mm height on its inner surface. The apex angle of the fins was 15 deg and the helix angle was 0 deg. The refrigerant pressure was measured with a Heise gauge at the entrance to pass one and at the exit of pass six. The refrigerant pressure drop was measured across each of the six passes and return bends using differential pressure transducers. Thermocouples for refrigerant-side measurements were located at the entrance and exit of each pass.

The annulus-side water, providing heating (evaporating mode) or cooling (condensing mode), flowed through the annular space between inner and outer tubes. Two separate water supplies, entering the first and the fourth passes, were used to limit the total water temperature change and improve accuracy. The water temperature was measured at the entrance and exit of each pass using calibrated high precision platinum resistance temperature detectors (RTDs).

Experimental Procedure. The refrigerant flow rate and supply liquid temperature were adjusted so that the refrigerant mass velocity and entering vapor quality were at the desired values. The water flow rate and temperature were then adjusted until the condensation or evaporation process was complete at the appropriate location along the circuit. After steady-state conditions were attained in the system, all measurement channels were scanned three times with a data acquisition system.

Contributed by the Heat Transfer Division for publication in the Journal of Heat Transfer. Manuscript received by the Heat Transfer Division February 10, 1996; revision received October 17, 1996; Keywords: Condensation, Evaporation, Refrigeration. Associate Technical Editor: M. Sohal.

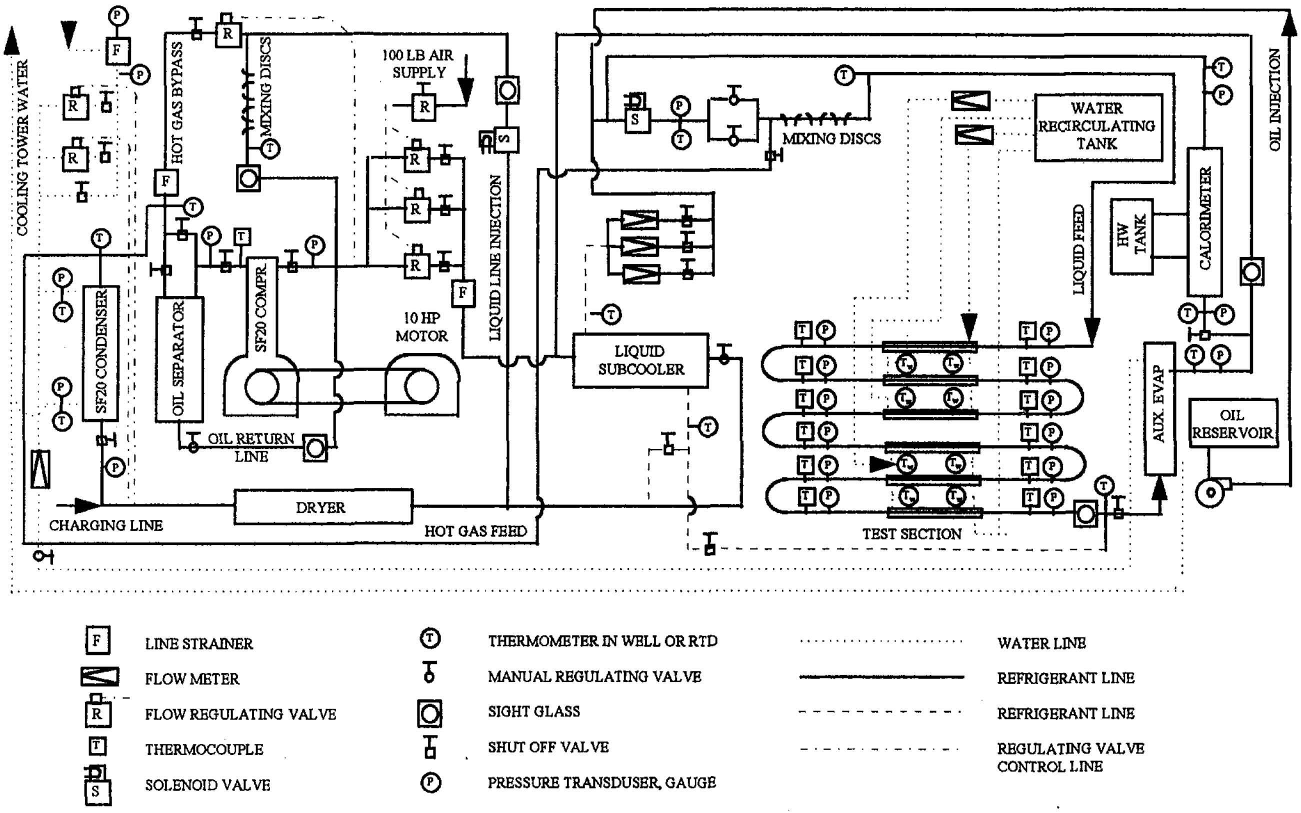

Fig. 1 Experiment apparatus

The results were examined by checking the average and standard deviations before data sets were accepted for subsequent data reduction.

Data Reduction

The amount of heat transferred in each pass, $Q_{w,n}$, was determined from the water side via the water flow rate, $\dot{m}_w$, and the temperature rise in each pass. Minor corrections for ambient heat transfer were made for both the water and refrigerant sides. The amount of heat transferred in the test section for the refrigerant side, the product of measured refrigerant flow rate and specific enthalpy change from the entrance to the exit of the test section, was also determined, in order to check the energy balance between the water and refrigerant sides. The enthalpies of the refrigerant superheated vapor and subcooled liquid entering and leaving the test section, $h_{r,\text{in}}$ and $h_{r,\text{out}}$, were taken from thermodynamic properties at the appropriate saturation conditions and the measured superheat and subcool temperatures. The water-side measurement was the basis for subsequent data treatment due to its reliability.

The flow rate of refrigerant was based on the net heat transferred and the specific enthalpy change across the test section,

$$\dot{m}_r = \frac{\Sigma Q_w}{|h_{r,\text{in}} - h_{r,\text{out}}|} . \tag{1}$$

The specific enthalpy change was apportioned according the fraction of the total heat transferred by each pass,

$$h_{r,n,\text{out}} = h_{r,n,\text{in}} \pm \frac{Q_{w,i}}{\dot{m}_r} . \tag{2}$$

The vapor quality at the entrance and exit of each pass was defined in terms of the specific enthalpy at the chosen points and the enthalpies of saturated vapor and liquid,

$$x = \frac{h - h_{l,\text{sat}}}{h_{v,\text{sat}} - h_{l,\text{sat}}} . \tag{3}$$

Nomenclature

A = area
Bo = boiling number
d = diameter of tube
G = mass flux
h = heat transfer coefficient
k = conductivity
l = length
LMTD = log mean temperature difference
$\dot{m}$ = mass flow rate
Nu = Nusselt number, hd/k
P = pressure
Pr = Prandtl number, $C_p\mu/k$
Q = heat transfer rate
Re = Reynolds number
Re* = modified Reynolds number, $Gxd/\mu_l\sqrt{\rho_l/\rho_v}$
T = temperature
x = vapor quality
X_{tt} = Martinelli parameter, $(x/(1-x))^{0.9}(\rho_l/\rho_v)^{0.5}(\mu_v/\mu_l)^0$
U = overall heat transfer coefficient

Greek Letters

μ = viscosity
ρ = density

Subscript

i = inside
in = inlet
l = liquid
n = pass number
o = outside
out = outlet
r = refrigerant
sat = saturation
w = water
v = vapor

Table 1 Test conditions

	R-22		R-134a	
	Cond.	Evap.	Cond.	Evap.
Nominal T_{sat} ,°C	40.6	7.2	40.6	7.2
Mass flux, kg/m^2-s	140.0-1260.0	132.9-570.0	131.1-868.0	70.5-393.3
Entering quality	super-heat	0.15	super-heat	0.15
Leaving quality	slightly sub-cooled	2.8-5.6 K super-heat	slightly sub-cooled	2.8-5.6 K super-heat
dx/dl, (1/m)	0.0085	0.0073-0.015	0.0085	0.0073-0.015

The overall heat transfer coefficient for the nth pass was

$$U_n = \frac{Q_n}{A_{i,n}\mathrm{LMTD}_n}, \tag{4}$$

where the internal surface area, A_i, was calculated based on the area of a smooth tube having an inside diameter equal to the maximum inside diameter of the micro-fin tube. The ratio of the micro-fin surface area to the smooth surface area was 1.64. The refrigerant temperatures were based on the measured corresponding saturation pressures at the entrance and exit of each pass. The quasi-local refrigerant-side heat transfer coefficient, $h_{r,n}$, for the nth pass were obtained as:

$$\frac{1}{h_{r,n}} = \frac{1}{U_n} - \frac{A_i}{A_o h_{w,n}} - \frac{A_i \ln (D_o/D_i)}{2\pi k L}, \tag{5}$$

where the water-side heat transfer coefficient, $h_{w,n}$, was determined through the use of a modified Wilson plot technique. The uncertainty of the refrigerant-side heat transfer coefficient was about 5 percent, based on the error analysis of the test facility, the uncertainty of the data, and the uncertainty of the water-side heat transfer coefficient.

Test Results and Discussion

The test conditions used in this study are summarized in Table 1. The heat flux varies in evaporating tests by adjusting the annulus water temperature to fully evaporate the refrigerant at the exit of passes 3, 4, and 6.

Heat Transfer Coefficient. The correlation of the nondimensionalized groups collapse the condensing data for both R-22 and R-134a (Fig. 2). For a given mass flux and vapor quality, the lower vapor density of R-134a relative to R-22 results in higher vapor velocity. Thus, R-134a yields a higher local condensing heat transfer coefficient (Fig. 3), based on the correlations developed from the data. The ratio of integrated arithmetic average heat transfer coefficient $\bar{h} = \int_0^1 h(x)dx$ based on the correlations (Fig. 4) shows that R-134a gives a 8 percent to 18 percent higher condensing heat transfer coefficient.

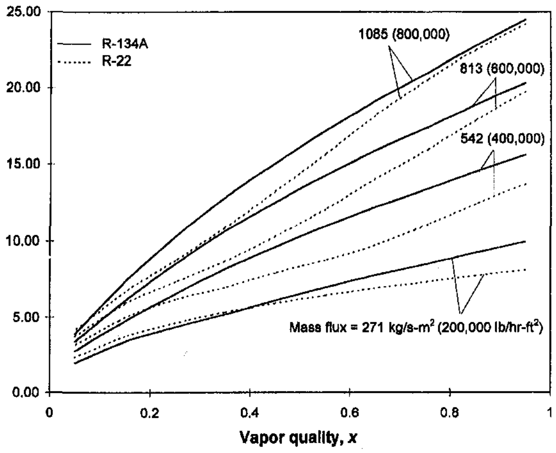

Fig. 3 Local condensing heat transfer coefficient

Both R-134a and R-22 evaporating data demonstrate that the heat transfer coefficient behaves quite differently in a high vapor quality region ($X_{tt} > 14.0$) compared to a low vapor quality region ($X_{tt} < 14.0$). In the low vapor quality region, the heat transfer coefficient increases with vapor quality; in the high vapor quality region it decreases. Most of the commonly used correlations do not cover the high vapor quality region. The sign change of the exponent of X_{tt}, from positive in low vapor quality region to negative in high vapor quality region (Fig. 5–Fig. 8), implies the difference between heat transfer characteristics in the two regions. The primary cause of the change in the heat transfer behavior is vapor velocity, which results in dry-out of the wall at high vapor quality, and therefore decreases the heat transfer rate. In the region of $X_{tt} < 14.0$, the data also suggest that the boiling contribution can not be neglected. In the region of $X_{tt} > 14.0$ the boiling contribution is suppressed and the boiling number can be dropped in the correlation.

R-134a exhibits two major differences in heat transfer characteristics from R-22: (1) the decrease of heat transfer coefficient with mass velocity for mass velocity above 270 kg/m^2-s; and (2) a lower heat transfer coefficient in the low vapor quality region and a higher coefficient in the medium quality region for mass velocity below 270 kg/m^2-s. R-134a has a lower reduced

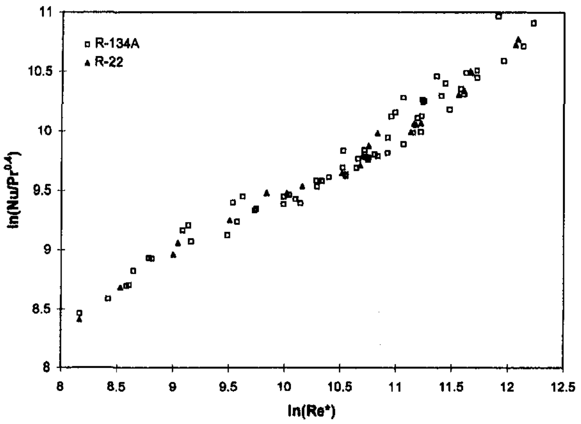

Fig. 2 Condensing heat transfer coefficient for R-22 and R-134a

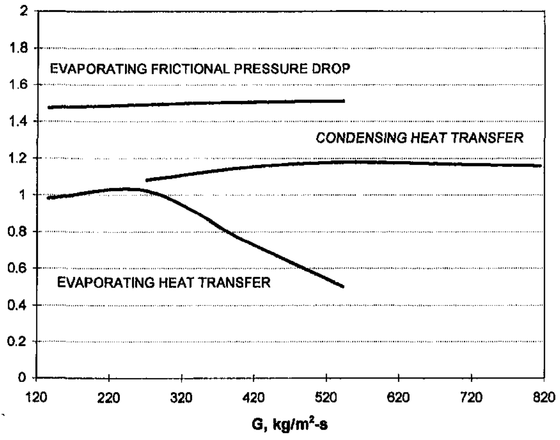

Fig. 4 Ratio of average heat transfer coefficient and pressure drop between R-134a and R-22 as a function of mass flux

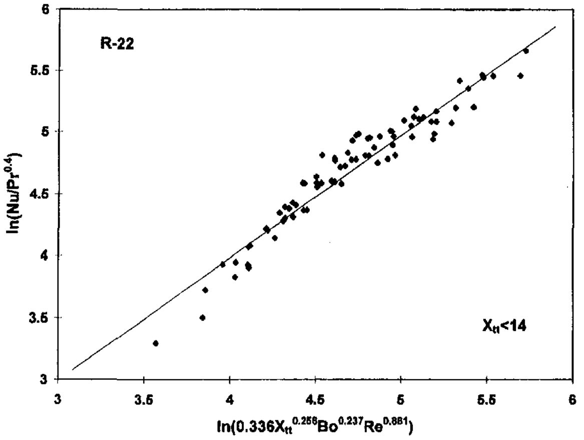

Fig. 5 Evaporating heat transfer coefficient of R-22 for $X_{tt} < 14.0$

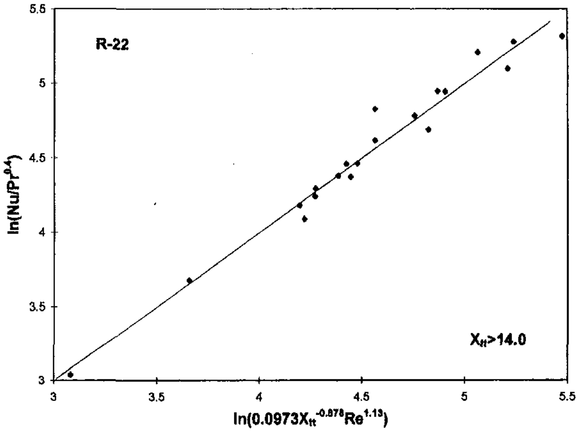

Fig. 6 Evaporating heat transfer coefficient of R-22 for $X_{tt} > 14.0$

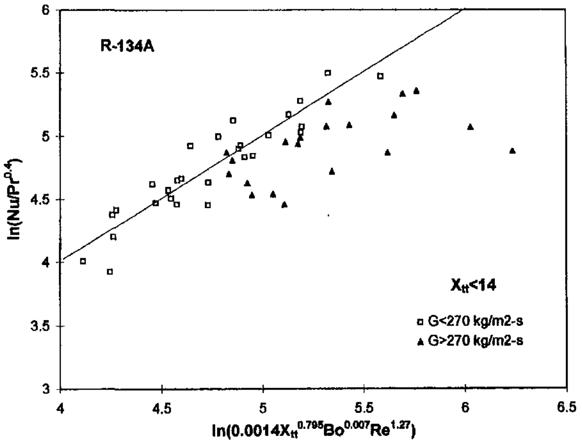

Fig. 7 Evaporating heat transfer coefficient of R-134a for $X_{tt} < 14.0$

pressure than R-22 (0.086 versus 0.117) and its boiling contribution is expected to be lower (Cooper, 1984). This results in a lower heat transfer coefficient for R-134a in comparison to R-22 at low vapor quality (Fig. 9). On the other hand, a higher vapor velocity of R-134a leads to a higher heat transfer coefficient at medium vapor quality region. The heat transfer coefficient of R-134a is correlated in the same form as R-22:

$$\frac{\mathrm{Nu}}{\mathrm{Pr}^{0.4}} = \exp(C_0)\,\mathrm{Re}^{C_1}X_{tt}^{C_2}\mathrm{Bo}^{C_3}$$

and the constants are given in Table 2.

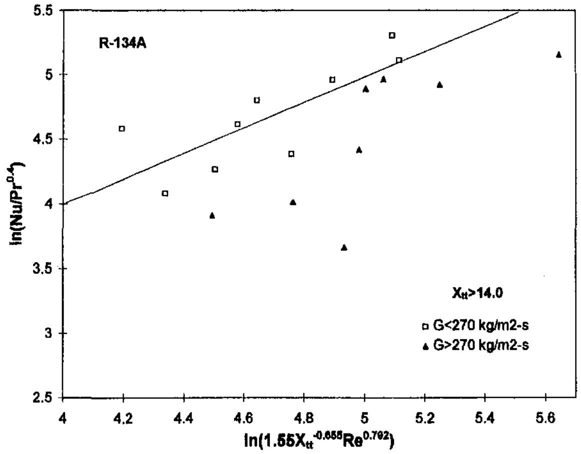

Fig. 8 Evaporating heat transfer coefficient of R-134a for $X_{tt} > 14.0$

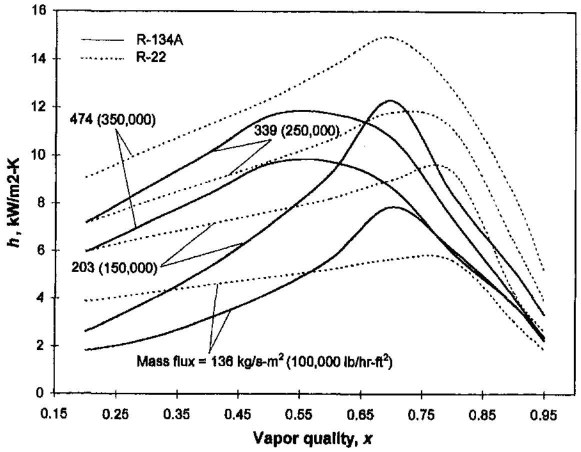

Fig. 9 Local evaporating heat transfer coefficient

Table 2 Constants in R-134a evaporating heat transfer correlation

		C_o	C_1	C_2	C_3
Gr<270 kg/m²-s	Xtt<14	-6.57	1.270	0.795	0.07
	Xtt>14	0.44	0.792	-0.655	0.0
Gr>270 kg/m²-s	Xtt<14	10.11	-0.557	0.387	0.078
	Xtt>14	12.95	-0.641	-0.809	0.0

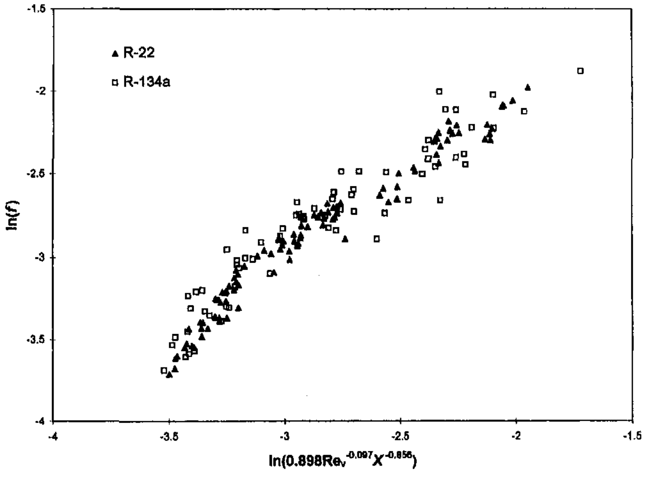

Fig. 10 Evaporating friction coefficient for R-22 and R-134a

Table 3 Experimental results for condensation heat transfer with R-134a

Source	Refrigerant	ID/ Length	Mass flow rate kg/m^2-s	Test/ Inlet/outlet condition	Increase of condensing Heat Transfer
Eckels & Pate (1991)	R-134a/R-12	7.98 mm/ 3.66 m	130-400	Tsat 30-50 ° Inlet: X=0.80-0.88 outlet: X=.05-0.13	25-30%
Torikoshi *et al.* (1993)	R-134a/R-12	8.71 mm/ 4 m smooth	54.3-271.2	Tsat=50 °C Superheat 45°C Subcooling 4 °C	25%
Dobson *et al.* (1993a)	R-134a/R-12	4.57 mm)/ 2.9 m smooth	74.59-495.0	35-60 °C X: 0.10-0.90	10-20%
Dobson *et al.* (1993b)	R-134a/R-22	4.57 mm/ 2.9 m smooth	74.59-495.0	35-60 °C X: 0.10-0.90	Same
Torikoshi *et al.* (1993)	R-134a/R-22	8.7mm/ 4 m smooth	54.25-271.2		10%
Christofferson *et al.* (1993)	R134a/R-22	4.57 mm/ 2.9 m smooth	74.59-495.0	Tsat=45 °C X: 0.0-1.0	Slightly higher at high x
Present studies	R134a/R-22	9.5 mm/ 10.8 m axial grooved tube	128.8-868.0	Tsat=40.6 °C X: 0.0-1.0	8-18%

As vapor velocity goes beyond a certain value, the liquid film in an annular flow can become unstable. The vapor begins to strip the annular liquid film from the inner wall of the tube. As a result, the wall may become partially dry, thus deteriorating the heat transfer. The heat transfer coefficient for R-134a decreases beyond 270 kg/m^2-s mass velocity for the whole vapor quality region (Fig. 9). This behavior is clearly shown in the ratio of the integrated heat transfer coefficient over vapor quality between R-134a and R-22 (Fig. 4).

Frictional Pressure Drop. The evaporating frictional pressure drop data (Fig. 10) suggest that the frictional pressure drop coefficient, based on vapor density,

$$\frac{\Delta P}{\Delta l} = \frac{1}{2d} f \frac{(Gx)^2}{\rho_v}, \qquad (6)$$

can be correlated for different refrigerant data, better than that based on liquid density. At a given mass velocity, the two-phase flow pressure drop is approximately proportional to the inverse of the vapor density. This result agrees with commonly accepted theory. In the Martinelli number, X_{tt}, the density ratio is the dominant factor if the viscosity ratio of the two refrigerants is close to unity. Taking the integrated arithmetic average over vapor quality based on the evaporating pressure drop correlations for R-134a and R-22, Fig. 4 shows that R-134a yields a 50 percent higher frictional pressure drop on average relative to that of R-22.

Table 4 Experimental results for evaporation heat transfer with R-134a

Source	Refrigerant	ID/ Length	Mass flow rate kg/m^2-s	Test/ Inlet/outlet condition	Increase of condensing Heat Transfer (HR) coefficient and Pressure Drop (PD) relative to R-22
Eckels & Pate (1991)	R-134a/R-12	7.98 mm /3.66 m	130.0-398.7	Tsat 5-15 °C Inlet: X=0.05-0.13 outlet: X=.80-0.88	HR:40% for smooth and 20% for Micro-fin PD: up to 50%
Kedzierski & Kaul (1993)	R-134a/R-12	9mm smooth (roughness 0.3μm)	Re: 0-9500	$P_{reduced}$ =0.13 X=0.1	HR:20%
Wattelet, Chato et al. (1993a)	R-134a/R-12	7.0 mm/ 2.44 m smooth	25.77-103.1	-15—5 °C X: 0.10-0.90	HR:25%
Wattelet, Chato et al. (1993b)	R-134a/R-22	7.75 mm/ 2.44 m smooth	25.77-103.1	-15—5 °C X: 0.10-0.90	HR:same
Torikoshi et al. (1993)	R-134a/R-22	8.71mm/ 4 m smooth	54.25-271.2		HR:-15% PD: 63%
Christofferson *et al.* (1993)	R-134a/R-22	7.75 mm/ 2.44 m smooth	50.85-508.6	Tsat=5-15.6 °C X: 0.20-0.90	HR: same PD: 50-70%
Present studies	R-134a/R-22	9.5 mm/ 10.8 m axial grooved tube	89.78-534.4	Tsat=4.4-15.6 °C	HR: similar for mass velocity below critical value PD: 50%

The pressure drop through the return bends is about 25 percent of the total pressure in the six passes. In the data reduction, the return bend pressure drop is excluded from the data. Therefore, the above discussion on pressure drop only applies to straight tubes.

Comparison to Other Results

Considering the uncertainty of the test data, our test results agree reasonably well to some of the data reported in literature (Tables 3 and 4). Besides, there are several factors that may have contributed to the discrepancy between the present data and those from literature:

1 *Shorter test section:* most of the tests in the tables have much shorter test sections and impose much higher heat fluxes (dx/dl) than those in the present study.
2 *Different test conditions:* such as tube diameter, mass velocity, etc.
3 *Local versus average heat transfer coefficient:* most of those investigations obtain average heat transfer data. The average heat transfer coefficient in two-phase flow is dependent on the operational conditions. Thus, special attention should be paid to the test conditions when comparing the test results from different sources.

References

Christoffersen, B. R., Chato, J. C., Wattelet, J. P., and de Souza, A. L., 1993, "Heat Transfer and Flow Characteristics of R-22, R-32/R-125 and R-134a in Smooth and Micro-Fin Tubes," Report of ACRC Project, Refrigerant-Side Evaporation and Condensation Studies, University of Illinois, August.

Cooper, M. G., 1984, "Heat Flow Rates in Saturated Nucleate Pool Boiling—A Wide-Ranging Examination Using Reduced Properties," *Advances in Heat Transfer,* Vol. 16, Academic Press.

Dobson, M. K., Chato, J. C., Hinde, D. K., and Wang, S. P., 1993a, "Experimental Evaluation of Internal Condensation of Refrigerants R-134a and R-12," Report of ACRC Project, Refrigerant-Side Evaporation and Condensation Studies, University of Illinois, May.

Dobson, M. K., Chato, J. C., Hinde, D. K., and Wang, S. P., 1993b, "Initial Condensation Comparison of R-22 with R-134a and R-32/R-125," Report of ACRC Project, Refrigerant-Side Evaporation and Condensation Studies, University of Illinois, June.

Ebisu, T., and Torikoshi, K., 1993, "In-Tube Condensation of Alternative Refrigerants," *Proceedings of Condensation and Condenser Design Conference,* St. Augustine, Florida, pp. 593–600.

Eckels, S. J., and Pate, M., 1991, "In-Tube Evaporation and Condensation of Refrigerant-Lubricant Mixture R-134a and CFC-12—Part 2," *Transactions ASHRAE,* Vol. 97, pp. 71–81.

Liu, X., 1996, "Modified LMTD Method for Two-Phase Heat Transfer and Application in Heat Exchangers," *Proceedings of 1996 International Refrigeration Conference,* Purdue University, West Lafayette, IN, pp. 145–150.

Torikoshi, K., Kawabata, K., and Ebisu, T., 1992, "Heat Transfer and Pressure Drop Characteristics of R-134a in a Horizontal Heat Transfer Tube," *Proceedings of 1992 International Refrigeration Conference,* Vol. 1, pp. 167–176.

Torikoshi, K., and Ebisu, T., 1993a, "Evaporation and Condensation Heat Transfer Characteristics of R-134a, R-32 and a Mixture of R-32/R-134a Inside a Tube—Part I," *Transactions ASHRAE,* Vol. 99, pp. 90–96.

Wattelet, J. P., Chato, J. C., Souza, A. L., and Christoffersen, B. R., 1993a, "Evaporative Characteristics of R-134a, MP-39, and R-12 at Low Mass Fluxes," Report of ACRC Project, Refrigerant-Side Evaporation and Condensation Studies, University of Illinois.

Wattelet, J. P., Chato, J. C., Souza, A. L., and Christoffersen, B. R., 1993b, "Initial Evaporative Comparison of R-22 With Alternative Refrigerants R-134a and R-32/R-125," Report of ACRC Project, Refrigerant-Side Evaporation and Condensation Studies, University of Illinois.

Y. Joshi
Department of Mechanical Engineering,
University of Maryland
College Park, MD 20742

P. Dutta
Department of Mechanical Engineering
Indian Institute of Science
Bangalore, India

P. E. Schupp

D. Espinosa

Department of Mechanical Engineering
Naval Postgraduate School
Monterey, CA 93943

Nonaxisymmetric Convection in Stationary Gas Tungsten Arc Weld Pools

Observations of surface flow patterns of steel and aluminum GTAW pools have been made using a pulsed laser visualization system. The weld pool convection is found to be three-dimensional, with the azimuthal circulation depending on the location of the clamp with respect to the torch. Oscillation of steel pools and undulating motion in aluminum weld pools are also observed even with steady process parameters. Current axisymmetric numerical models are unable to explain such phenomena. A three-dimensional computational study is carried out in this study to explain the rotational flow in aluminum weld pools.

1 Introduction

Fusion welding processes are the most common class of techniques for the joining of metallic materials. Their use spans large structural applications such as the joining of aircraft sections and submarine hulls, to microfabrication steps involving electronic packages. These processes involve the use of an intense energy source such as an electric arc, electron beam, or laser for the localized melting of the two materials to be joined. The pieces are joined upon solidification of the molten region. Additional molten filler material may be introduced using a feed wire. If no filler is employed, the welding process is termed autogenous. Currently, over fifteen different types of fusion welding processes are in common use (*Welding Handbook,* 1991).

The relatively recent interest in understanding the fluid flow characteristics during fusion welding has resulted from an increasing concern for quality improvement and process automation. It is now well established that the weld pool flow and thermal and solidification characteristics have a profound impact on the microstructure of the weld region (Woods and Milner, 1971), and hence, the resulting strength and other mechanical properties of the welded joint. Correlation of process parameters, such as welding power and heat source speeds to the weld pool flow and heat transfer, has resulted in significant current interest. The joining of large structures requires consistent quality control over extended lengths, often difficult to achieve manually. This, coupled with the need for increased process speeds, has resulted in a move towards automated welding. Indeed, the experience and skills of a trained welder must be replicated by such automated systems if they are to be successful. Such process intelligence can be provided by arrays of sensors which may monitor, for example, the thermal or acoustic emissions from the weld pool and the surface flow patterns. By identifying the signatures associated with acceptable and faulty welds, the sensor array can be used to monitor and control weld quality on-line (Doumanidis, 1994).

Due to the potential importance of weld pool flow and heat transfer modeling, a number of investigations into their characteristics have been made. The two most widely modeled welding processes are Gas Tungsten Arc Welding (GTAW) and laser welding. The focus of the present study is on the GTAW process. Indeed, a number of comprehensive studies exist on laser weld pools. However, the physical phenomena found in such pools are considerably different due to the different nature of heat source and absence of electromagnetic forces. As a result, we have not discussed laser welding studies in this paper.

In the GTAW process, the weld pool is created by an arc produced by a stationary electrode placed over it (Fig. 1). Atthey (1980) examined the fluid mechanics of an isothermal weld pool under the influence of electromagnetic or Lorentz forces, set up as a result of the interaction of the current flow and the self-induced magnetic field. Closed form expressions were obtained for the axisymmetric Lorentz force field by solving the Maxwell's equations under the magneto-hydrodynamic assumptions. Fluid flow and temperature variations were examined in a comprehensive study by Oreper and Szekely (1984), who numerically solved the axisymmetric transport equations under the combined influence of buoyancy, surface tension (Marangoni), and electromagnetic forces. The flow patterns were found to be radially inward or outward, depending on the variation of the surface tension with temperature. For pure metallic melts the surface tension decreases with temperature resulting in radially outward surface flows. With the addition of surface-active agents, the nature of surface tension-temperature relationship is altered, and the surface flow pattern may be reversed.

A number of follow-up computational studies of the GTAW process have included the effects of the heat source movement and three-dimensional transport (Kou and Wang, 1986; Zacharia et al., 1988; Ramanan and Korpela, 1990; Kanouff and Greif, 1992). The key aspects of selected computational studies on GTAW are summarized in Table 1. These studies have brought out the effects of surface tension forces and melt Prandtl number. Recent calculations (Dutta et al., 1995) reveal that in most welding applications, the current flow path from the anode to the cathode is nonaxisymmetric. Significant modifications in the flow patterns compared to the axisymmetric formulation were found under these conditions.

Despite the large number of numerical investigations of weld pool fluid flow and heat transfer during GTAW process, only limited experimental corroboration of these exists. The high temperatures and luminosities in the vicinity of weld pools generally make such measurements quite difficult. Only recently have surface temperature measurements, using optical tech-

---

Contributed by the Heat Transfer Division for publication in the Journal of Heat Transfer. Manuscript received by the Heat Transfer Division February 6, 1996; revision received September 30, 1996; Keywords: High-Temperature Phenomena, Mat'ls. Processing & Manufacturing Process, Phase-Change Phenomena. Associate Technical Editor: A. Lavine.

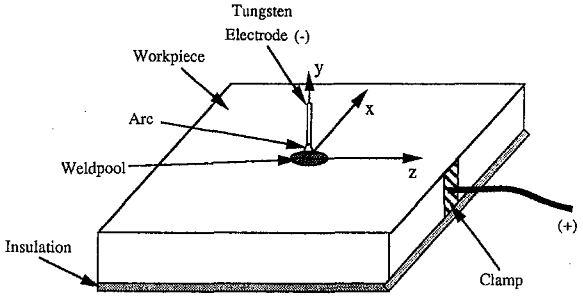

Fig. 1 Schematic sketch of the GTAW process

niques, been reported for weld pools (Kraus, 1989). The availability of pulsed high power lasers have made the visualization of the weld pool free surface possible (Bolstad, 1987), yet no systematic study of these has been reported.

The present investigation is carried out to visualize the free surfaces of steel and aluminum weld pools during autogenous GTAW. A number of new features observed during this investigation reveal the complexities of weld pool motions. These include surface rotations, oscillations, and undulations which have not been predicted by any of the existing computational studies. Computations are next carried out using a three-dimensional, finite volume based approach to explain the observed rotational flow patterns in aluminum weld pools using a nonaxisymmetric Lorentz force formulation. The need for experimental validation of computational models of complex processes, such as welding, is clearly brought out by the present study.

2 Experimental Apparatus and Procedure

The heart of the welding system is the power source (Miller Model SR600/SCMIA, 239/450 Volts) which can be set at different currents ranging from 50 to 500 amps, and voltage ranging from 10 to 35 volts. The uncertainties in the measured current and voltage are ±2 A and ±0.2 V, respectively. The torch, which is designed to hold the tungsten electrode firmly, and to transmit the welding current to the electrode, is water cooled. The electrode is shielded by Argon gas flowing through a ceramic nozzle fitted at the end of the torch.

In arc welding operations, the weld pool and its vicinity are subjected to extreme bright light because of the arc. This makes it very difficult to perform flow visualization using regular video imagery techniques. In the present study, an intense pulsed ultraviolet laser is used to overcome the bright arc light effects. A commercially available laser-augmented welding vision system (manufactured by Control Vision Inc., Idaho) consisting of a pulsed nitrogen laser, an image intensifier tube, a solid state video camera, a video monitor, a time lapse recorder, and a system controller, is used. The camera contains a standard end-viewing optical head which interfaces directly with the image intensifier tube that is integrated with the camera. The camera is located about six to eight inches from the weld site, for the best field-of-view, and can be adjusted by appropriate refocusing of the lens barrel. A schematic diagram of the experimental arrangement is shown in Fig. 2.

The camera and laser light are focused at the region of the workpiece just below the tungsten electrode. For stationary arc welding (as in the present study) both the workpiece and the electrode are held stationary. For moving arc welding operations, the workpiece is moved linearly after the arc is struck. The pulsed laser light reflected from the welding site is instantaneously much brighter than either the direct emission or reflection from the welding arc at the laser wavelength. The video camera is equipped with a CCD video sensor and a very high speed electronic shutter which is synchronized with the laser flash. The laser, in turn, is synchronized with the framing of the video sensor and is fired once for each video frame. Each pulse fired by the laser lasts for about 3 ns (nanoseconds) at a wavelength of 337 nm (nanometers) which corresponds to the near-visible ultraviolet portion of the electromagnetic spectrum. A narrow-band optical filter matching the laser wavelength further suppresses the arc lighting and produces a clean video image for flow visualization at the weld pool free surface.

3 Visualization of Weld Pools in Steel

In most common applications, the electrode in GTA welding has a negative potential. The arc impinges vertically onto the weld pool and the electrons then flow through the weld pool to the ground off-take point (clamp). Position of the clamp relative to the electrode would, therefore, affect the current flow path inside the workpiece which may, in turn, affect the Lorentz force field inside the weld pool. One of the objectives of the present study is to study how a nonaxisymmetric current field alters the flow of molten metal inside the weld pool.

Two kinds of workpiece geometry are used: a circular steel plate with the clamp located at the bottom geometric center of the plate (Fig. 3*a*) for creating an axisymmetric current path; and a rectangular plate with the clamp located at a corner (Fig. 3*b*) for producing an asymmetric current flow. In either case, the electrode is held stationary at the center of the workpiece. The location of the workpiece also remained fixed in space to produce a stationary bead-on-plate welding on steel plates. Although we realize that most practical welding operations are performed by moving the torch relative to the workpiece, the purpose of the present study, which is based on stationary welding, is to investigate the effects of current distribution on the flow patterns in the molten pool. Using the apparatus described in Section 2, we have carried out surface flow visualizations of steel welds by sprinkling alumina particles (which have a higher melting point than steel) and then observing their motion on the weld pool surface. Welding is performed at various current

Nomenclature

$\mathbf{B}$ = magnetic flux density vector
c = specific heat
h = heat transfer coefficient
H = Enthalpy
$\mathbf{J}$ = current density vector
k = thermal conductivity
L = latent heat of fusion
n = direction normal to a surface
q'' = heat flux input
Q = total heat input
r = radial distance from the center of the torch
r_q = radius for heat input distribution
r_j = radius for current outflow distribution (at the electrode end)
S_H = source term in energy equation
S_X, S_Y, S_Z = source terms in momentum equations in x, y, and z directions, respectively
t = time
T = temperature
T_m = melting temperature
T_∞ = Ambient fluid temperature
u, v, w = fluid velocity in x, y, and z direction, respectively
x, y, z = Cartesian coordinate system in a stationary reference frame

Greek Symbols

ϵ = emissivity
μ = dynamic viscosity of the liquid
Φ = transport variables such as u, v, w, or T
ρ = density
σ = Stefan-Boltzman constant

Table 1 Selected computational studies of weldpool convection during GTAW process

Investigators/year	Remarks
Oreper and Szekeley (1984)	First computations of stationary, axisymmetric GTA welding process using finite difference method; included bouyancy, electromagnetic, and surface tension effects.
Kou and Wang (1986)	Moving arc source GTA process, including the driving forces considered in Oreper and Szekeley (1984). Also, assumed axisymmetric Lorentz force field.
Correa and Sundell (1986)	Axisymmetric stationary arc source. Same effects as in Oreper and Szekeley (1984) included. Different grid sizes for computation of flow and electromagnetic fields.
Zacharia et al. (1988)	Three-dimensional calculations with the three driving forces considered in Oreper and Szekeley (1984). Surface curvature effects, turbulence model and filler included. Results for autogenous GTAW show pool free surface depressed at center.
Ramanan and Korpela (1990)	Axisymmetric stationary arc source. Same effects as in Oreper and Szekeley (1984). Pointed out the need for adequate resolution near the free surface. Used multi-grid methods.
Kanouff and Greif (1992)	Axisymmetric stationary arc source. Same driving sources as in Oreper and Szekeley (1984). Evaporation model used at the free surface. Moving grids used to track the phase change boundary.

levels and for different clamp positions. Some noteworthy observations are presented below.

With a circular steel plate (30.5 cm diameter, 2.54 cm thick) clamped at the bottom center, and with a power level of 1.13 kW (100 A and 11.3 V), the surface flow visualizations reveal a smooth laminar weld pool with virtually no circumferential rotation. A radial pulse phenomenon is observed in a number of these runs at this low power level. Previously seeded particles of alumina periodically moved from the outside of the weld pool toward the center along annular rings. Although a complete explanation for this motion does not exist, the inward radial direction of flow suggests partial agreement with the existing models using axisymmetric current distribution (e.g., Zacharia et al., 1989; Ramanan and Korpela, 1988). Kou and Wang (1986) indicate that axisymmetric electromagnetic forces cause an inward radial motion, counteracting an outward motion created by buoyancy. Surface tension forces would normally produce an outward flow but the driving force can be reversed by the presence of surface-active chemicals such as sulfur and manganese (Sahoo et al., 1988). The pulsed inward motion observed in the present experiments may indicate an instability of the flow which is not predicted by the existing models. With a higher current level (198 A), too, there is no observed rotation of pool for the same welding configuration. Flows tend to be more active than at lower currents but particles of alumina on the surface are observed to remain in the same relative position for long periods of time (3 to 4 seconds). In several instances, particles are found to be spinning about a local axis, while rotation about the center of the pool is not observed.

With a rectangular steel plate (30.48 cm × 15.24 cm × 2.54 cm) clamped at a corner (Fig. 3*b*), the surface flow visualizations of the weld pools reveal some interesting features. Alumina particles sprinkled on the pool surface are observed to rotate about the pool axis. With the clamping arrangement as in Fig. 3*b*, a clear clockwise rotation is observed as shown in the picture sequences in Fig. 4. As marked by the arrows in Fig. 4, a visible alumina particle is observed to execute half a revolution (180 degrees) in about two-thirds of a second. The observed speed of rotation is found to fluctuate between slow and rapid circulation but the overall clockwise rotation is, indeed, obvious. Present axisymmetric GTAW models do not predict this circumferential rotation of weld pools. However, similar circulation was observed experimentally by Woods and Milner (1971) in a molten copper pool with a similar location of the anode. Recently, Dutta et al. (1995) showed numerically that a nonaxisymmetric clamp location does, indeed, produce a rotation of a steel weld pool about its axis.

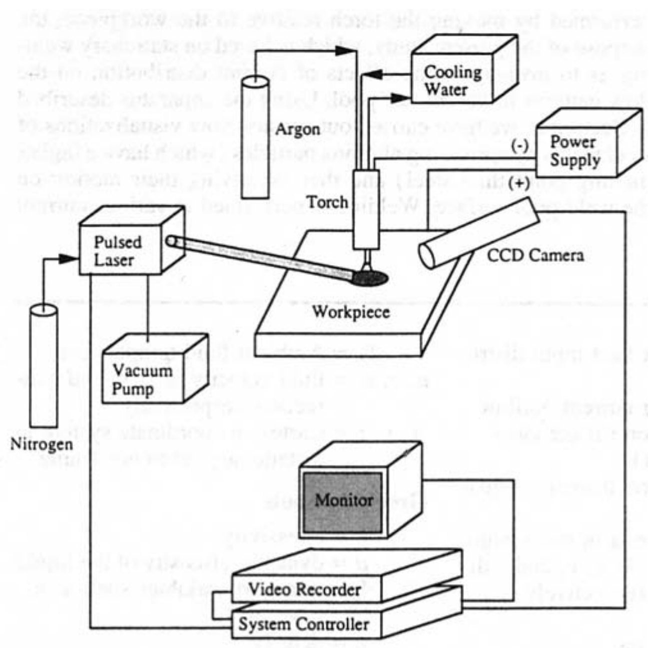

Fig. 2 Schematic diagram of the experimental arrangement

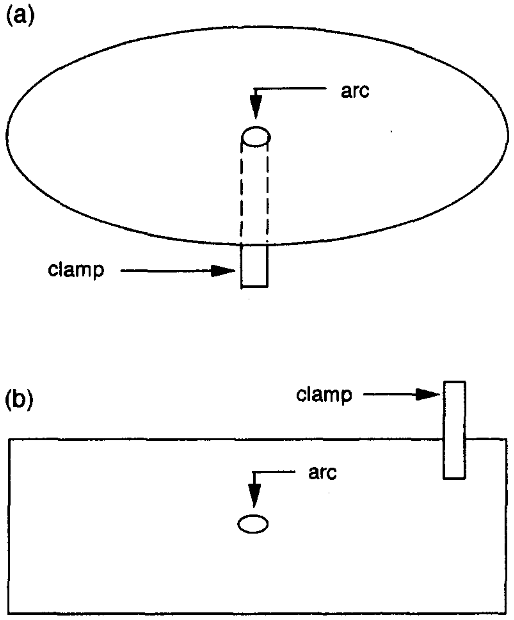

Fig. 3 Two kinds of clamping arrangement: (*a*) a circular steel plate with the clamp located at the bottom geometric center of the plate for creating an axisymmetric current path; and (*b*) a rectangular plate with the clamp located at a corner for producing an asymmetric current flow

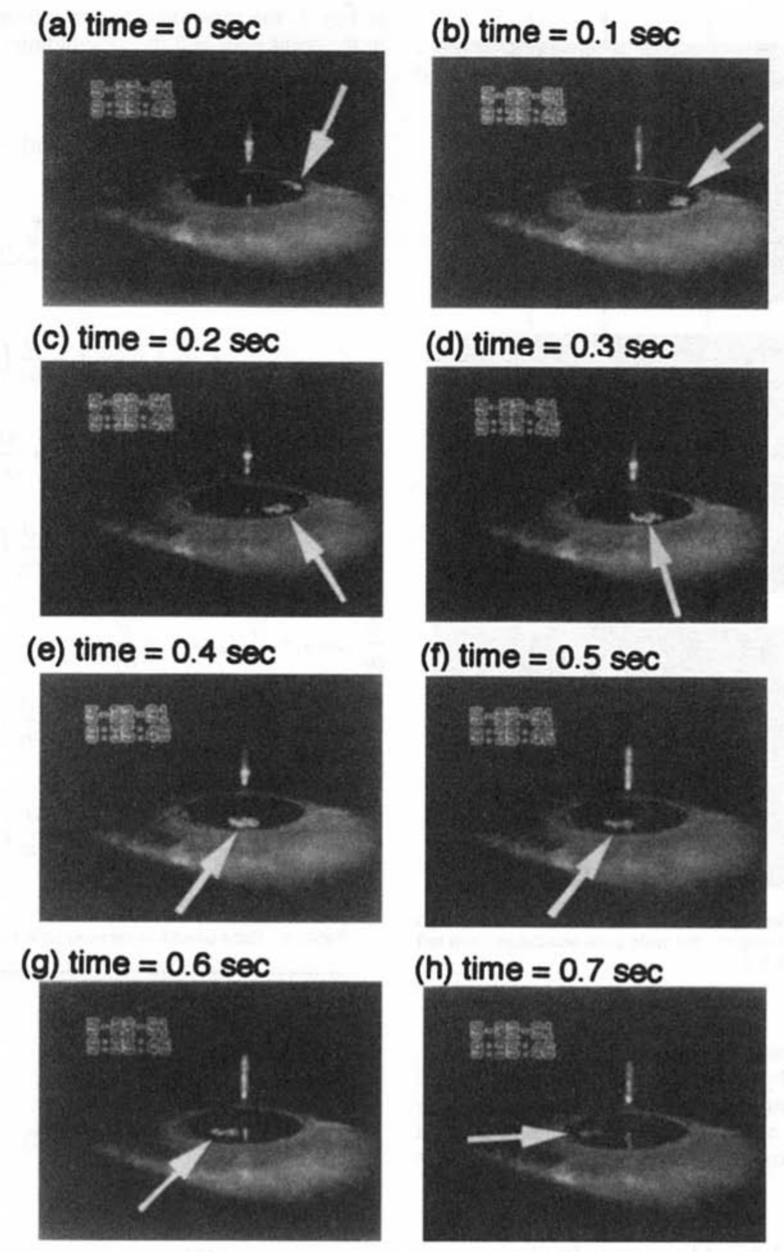
(a) time = 0 sec
(b) time = 0.1 sec
(c) time = 0.2 sec
(d) time = 0.3 sec
(e) time = 0.4 sec
(f) time = 0.5 sec
(g) time = 0.6 sec
(h) time = 0.7 sec

Fig. 4 Weld pool rotation during steel welding (200 A, 14.0 V, 4 mm arc length, 20 deg electrode tip angle) as observed from the movement of the floating alumina particle

Oscillations are observed for several nonsymmetric clamp locations, especially at high currents. Oscillations in shape, size, and centering of the weld pool are clearly observable, usually after the pool becomes fully developed. Selected video frames displaying weld pool oscillations are presented in Fig. 5. Neither the existing computational models (Atthey, 1980; Oreper and Szekely, 1984; Kou and Wang, 1986; Zacharia et al., 1989; Dutta et al., 1995) nor the experimental studies (Kraus, 1989; Bolstad, 1987) have been able to bring out this phenomenon.

4 Visualization of Weld Pools in Aluminum

Similar experiments are also conducted with 1.25 cm thick rectangular aluminum plates with non-symmetric clamp locations as shown in Fig. 3*b*. Weld pool development and surface flow pattern are of primary interest in these experiments. Flow visualization on the free surface is considerably more difficult on the aluminum because of the rapid build up of an oxide layer on the surface. However, several features unique to aluminum are detected. For example, a vertical undulation of the pool surface is noted during the welding process. This undulation is found to rotate in a counterclockwise direction as revealed in Fig. 6 which corresponds to the case in which the clamp is located at the top left corner of the workpiece. Also, a crater-shaped depression is formed in the pool region upon cessation of the welding arc and solidification of the material.

During low power welding (100 A, 11.2 V) the weld pool is virtually impossible to distinguish from the surface oxide layer due to the very small size of the pool (approximately 3.0 mm diameter). For higher power welds (150 A, 11.2 V) the weld pool diameter is found to grow to approximately 7.0 mm. At this power level, vertical undulation of the molten pool and depression in the solidified material are noted. Surface flow visualization revealed a distinct counterclockwise

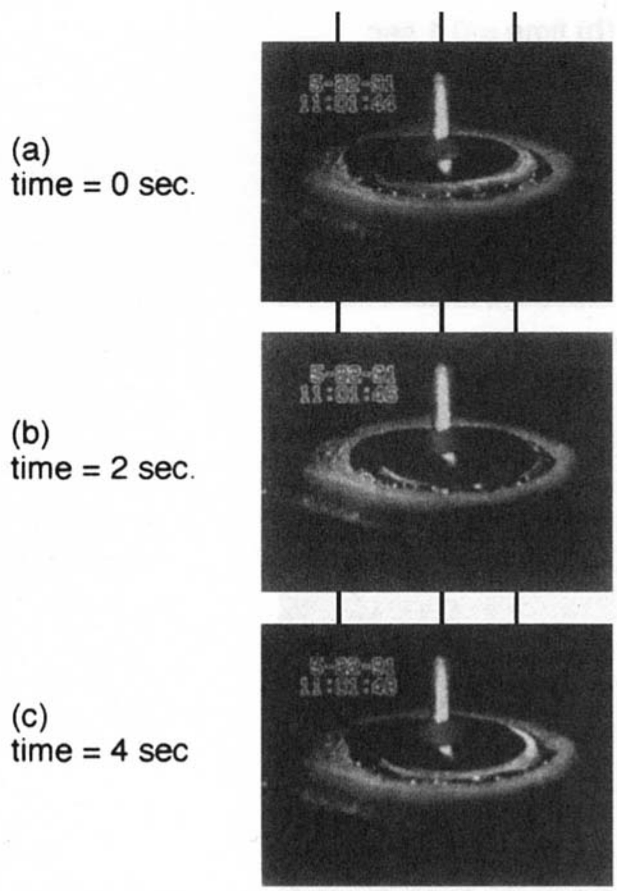

Fig. 5 **Weld pool oscillation during steel welding (200 A, 14.0 V, 4 mm arc length, 20 deg electrode tip angle); the weld pool oscillates from left (*a*) to right (*b*) and back to left (*c*)**

rotation of the molten material underneath the oxide layer. This motion is inferred by the observed undulation of the oxide layer. Figure 6 contains a sequence of pictures showing vertical undulation of the oxide layer making it apparent that the material beneath the oxide layer is moving in a circular pattern.

5 A Numerical Model for Aluminum Pools

The experimental results clearly show that the weld pool dynamics are three-dimensional as well as unsteady. Needless to say, the existing two-dimensional axisymmetric models would not be able to predict such weld pool behavior. Recently, a three-dimensional transient model (Dutta et al., 1995) which included buoyancy, electromagnetic, and surface tension forces predicted a pool rotation of steel welds with an asymmetric clamp location. The direction of azimuthal circulation was found to depend on the current flow path, and hence on the clamp location relative to the torch position.

For the case of aluminum, however, a thick oxide layer develops quickly on the pool surface which then suppresses surface tension effects. Hence, surface tension forces, which proved to be a dominant factor influencing steel weld pools, are now excluded from the present model of aluminum pools. Also, our experimental observations reveal that the oxide layer is relatively stationary while the molten metal beneath it appears to be stirred vigorously. Consequently, the top surface is modeled with a no-slip condition for the velocities. Surface deformation has been ignored for the time being as our primary focus in this study is to examine the effects of asymmetric current path on the dynamics of the pool. With reference to the sketch shown in Fig. 1, the three-dimensional governing transport equations in the weld pool and its surroundings are:

Continuity:

$$\frac{\partial \rho}{\partial t} + \frac{\partial}{\partial x}(\rho u) + \frac{\partial}{\partial y}(\rho v) + \frac{\partial}{\partial z}(\rho w) = 0 \qquad (1)$$

Momentum:

$$\frac{\partial}{\partial t}(\rho u) + \frac{\partial}{\partial x}(\rho u u) + \frac{\partial}{\partial y}(\rho v u) + \frac{\partial}{\partial z}(\rho w u) = \frac{\partial}{\partial x}\left(\mu \frac{\partial u}{\partial x}\right) + \frac{\partial}{\partial y}\left(\mu \frac{\partial u}{\partial y}\right) + \frac{\partial}{\partial z}\left(\mu \frac{\partial u}{\partial z}\right) - \frac{\partial p}{\partial x} + S_x \qquad (2)$$

$$\frac{\partial}{\partial t}(\rho v) + \frac{\partial}{\partial x}(\rho u v) + \frac{\partial}{\partial y}(\rho v v) + \frac{\partial}{\partial z}(\rho w v) = \frac{\partial}{\partial x}\left(\mu \frac{\partial v}{\partial x}\right) + \frac{\partial}{\partial y}\left(\mu \frac{\partial v}{\partial y}\right) + \frac{\partial}{\partial z}\left(\mu \frac{\partial v}{\partial z}\right) - \frac{\partial p}{\partial y} + S_y \qquad (3)$$

$$\frac{\partial}{\partial t}(\rho w) + \frac{\partial}{\partial x}(\rho u w) + \frac{\partial}{\partial y}(\rho v w) + \frac{\partial}{\partial z}(\rho w w) = \frac{\partial}{\partial x}\left(\mu \frac{\partial w}{\partial x}\right) + \frac{\partial}{\partial y}\left(\mu \frac{\partial w}{\partial y}\right) + \frac{\partial}{\partial z}\left(\mu \frac{\partial w}{\partial z}\right) - \frac{\partial p}{\partial z} + S_z \qquad (4)$$

Table 2 **Data used in computations (for aluminum welding)**

density, ρ (kg/m^3)	2300
viscosity, μ (kg/m-s)	0.0005
thermal conductivity, k (W/m-K)	138
specific heat, c (J/kg-K)	1174
current input (A)	150
voltage (V)	12
welding thermal efficiency	0.9
radius for heat input distribution, r_q (m)	0.0035
radius for current density distribution, r_j (m)	0.0032
melting point, T_m (^{o}C)	660
latent heat of fusion, L (J/kg)	3.95E+05
length of workpiece, (m)	0.04
width of workpiece, (m)	0.04
thickness of workpiece, (m)	0.009

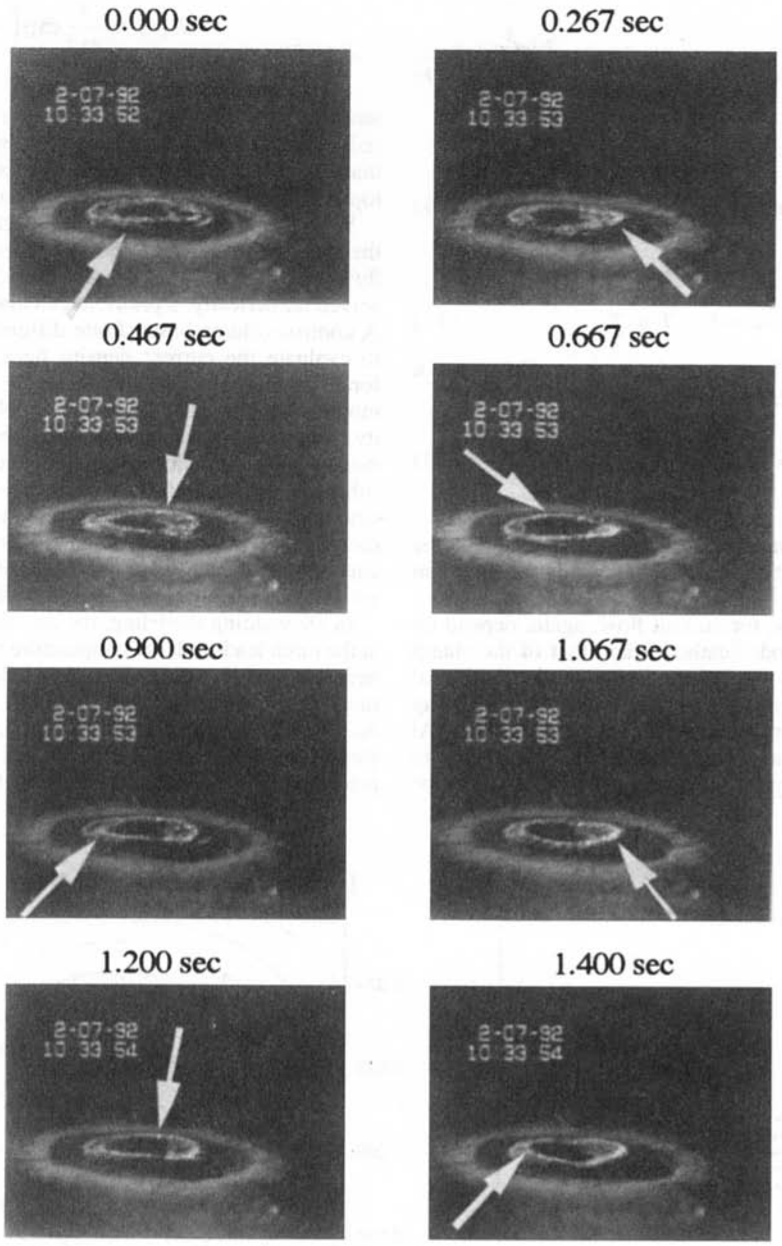
0.000 sec
0.267 sec
0.467 sec
0.667 sec
0.900 sec
1.067 sec
1.200 sec
1.400 sec

Fig. 6 Observed undulating motion and rotation of an aluminum pool (150 A, 11.2 V, 3 mm arc length, 20 deg electrode tip angle); the arrows mark the instantaneous location of a wavefront describing a counterclockwise rotation

Energy:

$$\frac{\partial}{\partial t}(\rho H) + \frac{\partial}{\partial x}(\rho u H) + \frac{\partial}{\partial y}(\rho v H) + \frac{\partial}{\partial z}(\rho w H)$$
$$= \frac{\partial}{\partial x}\left(k\frac{\partial T}{\partial x}\right) + \frac{\partial}{yx}\left(k\frac{\partial T}{\partial y}\right) + \frac{\partial}{zx}\left(k\frac{\partial T}{\partial z}\right) + S_H \quad (5)$$

In this numerical model, a single domain enthalpy-porosity method (Brent et al., 1988) has been used for the phase change process. Phase change is assumed to occur isothermally at T_m. The source terms in the above momentum equations include the porous medium model of the mushy region at the solid/liquid interface, the $(\mathbf{J} \times \mathbf{B})$ Lorentz force components in the respective directions, and the buoyancy force in the vertical direction.

The electromagnetic force terms in the above equations can be obtained by solving a steady state version of Maxwell's equations in the domain of the workpiece. The numerical method for obtaining the nonaxisymmetric Lorentz force field and the implementation of the enthalpy-porosity model for the phase change process are described elaborately in Dutta et al. (1995). The boundary conditions for the flow variables (u, v, w, T), with reference to the workpiece, are as follows:

Top surface: Gaussian heat flux input, radiative and convective heat loss,

$$-q''(r) - h(T - T_\infty) - \sigma\epsilon\{T^4 - T_\infty^4\} = -k\frac{\partial T}{\partial y} \quad (6)$$

$$\text{Flat surface condition,} \quad v = 0 \quad (7)$$

$$\text{No slip condition,} \quad u = w = 0 \quad (8)$$

Sides:

$$\text{Convective heat loss,}\quad h(T - T_\infty) = -k\frac{\partial T}{\partial n} \tag{9}$$

Bottom:

$$\text{Insulated,}\quad k\frac{\partial T}{\partial y} = 0 \tag{10}$$

Solid/Liquid interface:

$$u = v = w = 0, \quad T = T_m \tag{11}$$

In Eq. (6), the heat flux input, $q''(r)$, is assumed to have a Gaussian distribution on the top surface of the workpiece:

$$q''(r) = \frac{Q}{\pi r_q^2}\exp\left(-\frac{r^2}{r_q^2}\right) \tag{12}$$

where Q is the total heat input into the workpiece, and r_q is the radius for heat input distribution. In Eq. (9), n is the direction normal to a surface.

The boundary conditions for current flow, again, depend on the locations of the electrode (cathode) and that of the clamp (anode). In general, there would be a Gaussian distribution of current outflow at the top surface, with all other surfaces being electrically insulated except for the location of the clamp. At the top surface, the incident plasma arc causes a normal current flow with a current density profile assumed to be of the form:

$$J_n(r) = \frac{I}{\pi r_j^2}\exp\left(-\frac{r^2}{r_j^2}\right) \tag{13}$$

where n is the direction normal to the top surface, and r_j is the radius for current outflow. The condition at the clamp is such that, for a steady current flow, the total current outflow at the top surface is equal to the total current inflow at the clamp.

With the assumption that the electric current flow through the workpiece is steady and that there is no coupling between fluid flow and electric current, the Maxwell's equations are solved numerically, a priori, to calculate the Lorentz force field. A control-volume based finite difference method is employed to evaluate the current density field. The calculated Lorentz force field is then used as the body force distribution in the momentum Eqs. (2), (3), and (4). Next, the coupled continuity, momentum, and energy equations are solved numerically using a fully implicit finite volume technique [SIMPLER algorithm (Patankar, 1980)]. In the numerical solution of the energy equation, the latent heat content of each control volume is updated using the temperature field predicted from the energy equation after each iteration. The method followed here is described elaborately in Brent et al. (1988).

In arc welding modeling, the presence of an intense heat flux at the torch leads to large temperature gradients in the workpiece near the torch location. This also induces rapid melting of the metal (typically in less than a second) just after the arc is struck. As a result, choice of grid size and distribution along with time steps for computation are of utmost importance for accurate prediction of heat transfer and fluid flow in the weld pool. In

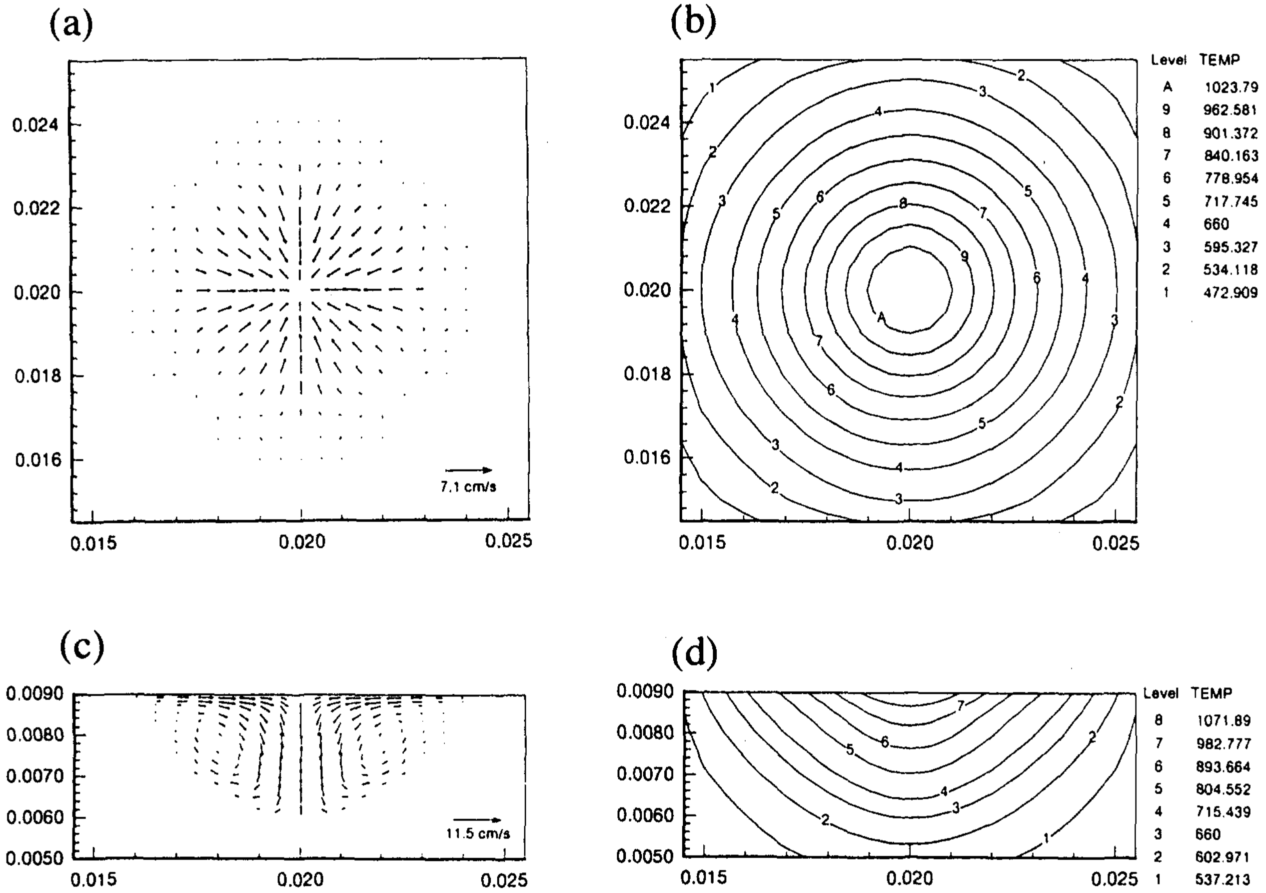

Fig. 7 Velocity and temperature fields for combined buoyancy and electromagnetically driven flow for an axisymmetric current distribution corresponding to a clamp location at center of an aluminum workpiece directly below the torch: (*a*) and (*b*) are the top views of the flow and temperature fields 0.2 mm below the top surface, respectively; (*c*) and (*d*) are the flow and temperature fields, respectively, in a sectional view

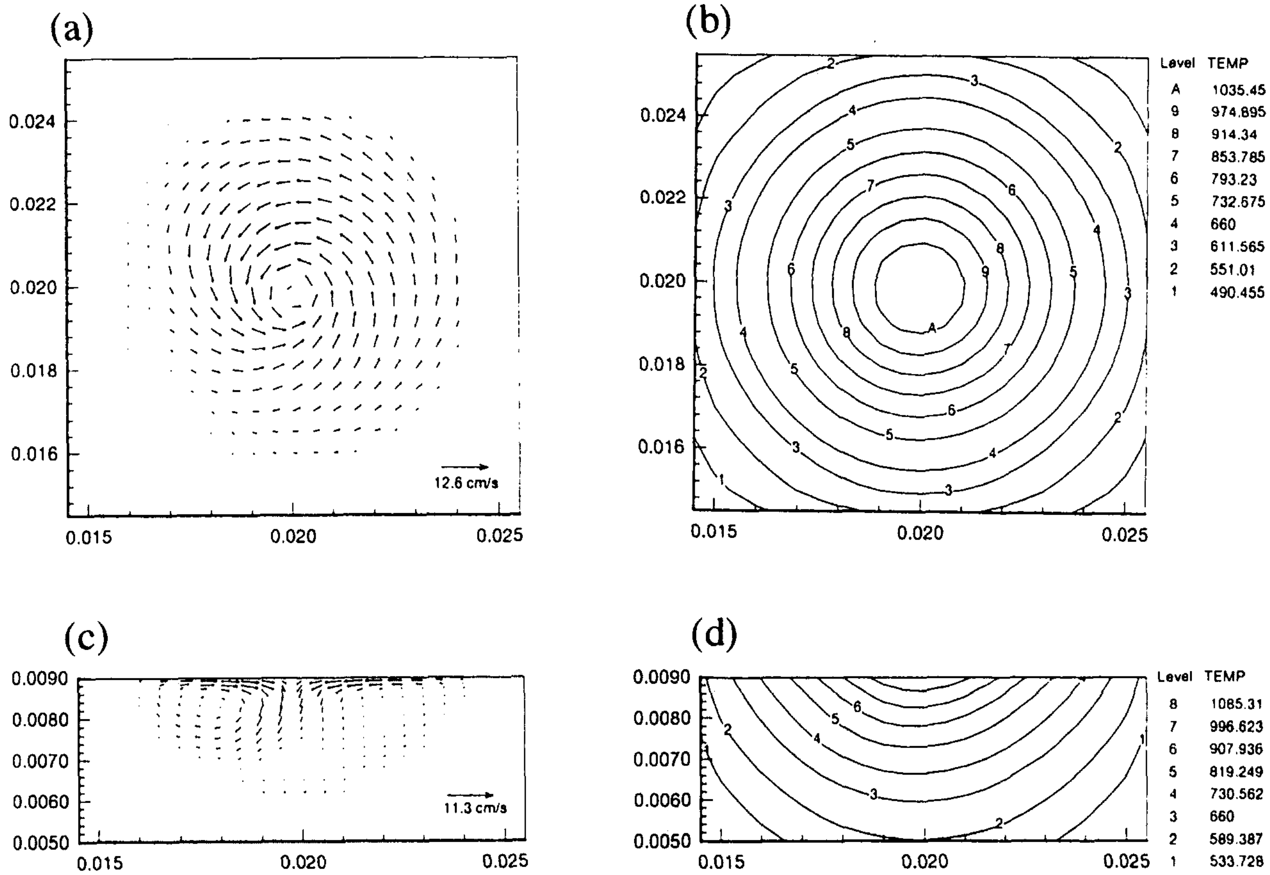

Fig. 8 Velocity and temperature fields for combined buoyancy and electromagnetically driven flow for a nonaxisymmetric current distribution corresponding to a clamp location at the top left hand corner of an aluminum workpiece: (*a*) and (*b*) are the top views of the flow and temperature fields 0.2 mm below the top surface, respectively; (*c*) and (*d*) are the flow and temperature fields, respectively, in a sectional view

the absence of a surface tension driven boundary layer which is commonly found in steel weld pools, a grid size of 0.25 mm in the vertical direction is found to be sufficiently fine to capture the flow details. In the horizontal planes, various grid sizes are tried, ranging from a coarse (0.5 mm × 0.5 mm) to a fine (0.2 mm × 0.2 mm). It is found that a grid size of 0.3 mm × 0.3 mm is optimum for the parameters used in this study because a finer grid system is not found to alter the results appreciably. Outside the weld pool, in the solid region, a nonuniform grid system is used. Overall, a 43 × 43 × 23 grid system is used to discretize a workpiece having dimensions of 4.0 cm × 4.0 cm × 0.9 cm.

The time steps for computations are varied according to the stages of the melting process. During the conduction phase, large time steps (about 0.2 s) may be allowed until melting begins (typically after 0.4 s). Time steps during the initial stages of pool development are, however, chosen to be very small (about 0.05 s) to capture the details of the rapidly developing pool in the presence of vigorous convection by the action of electromagnetic and buoyancy forces. Time steps may be increased after the pool is sufficiently developed. Computations are continued until the weld pool is fully developed (typically 10 s).

The temperature and velocity values of each cell are checked after each iteration to verify convergence within a time step. Convergence is declared after the following conditions are satisfied at each grid point:

$$\left| \frac{\phi - \phi_{\text{old}}}{\phi_{\max}} \right| \leq 10^{-4} \tag{14}$$

where ϕ stands for each variable u, v, w, and T at a grid point at the current iteration level, ϕ_{old} represents the value at the previous iteration level, and $\phi_{\max}$ is the maximum value of the variable at that iteration level in the entire domain. In addition, an overall energy balance is performed during each time step, and iterations are carried out until the absolute value of the energy balance is within 0.1 percent of the total stored energy within the workpiece.

Based on the above model, numerical studies have been made to bring out the effects of clamp location on the aluminum weld pool convection during stationary arc welding operations. The physical properties and other pertinent data used for the computations are listed in Table 2. It may be noted here that an assumption of weld pool efficiency is necessary for modeling weld pool convection. In this case, we select a value of 0.9, which is consistent with the range provided by Giedt (1987) based on water cooled anode experiments.

First, an axially symmetric current distribution is simulated by locating the cathode (electrode) just above the center of the top surface of the workpiece and the anode (clamp) under the workpiece directly beneath the cathode. This arrangement leads to a symmetric current flow and body force distribution. The resulting weld pool (Fig. 7) shows an axisymmetric radially inward flow somewhat similar to those predicted by axially symmetric models of steel weld pools found in the literature. It should be noted that the velocity at the top surface will be zero as a result of our imposition of the no-slip condition, hence the horizontal section chosen in Figs. 7*a* and 7*b* is slightly below the top surface to reveal the nature of velocity and temperature distribution.

However, in actual arc welding operations, the workpiece is usually clamped at an edge or a corner. In such a situation, the current flow through the workpiece will have a preferred direction and will no longer be symmetric, as reported in Dutta et al. (1995). Figure 8 represents such a case where the clamp is located at the top left corner resulting in a counterclockwise circulation of the molten pool (Fig. 8*a*). The flow pattern including the sense of rotation are in agreement with the experimental observation presented above. A flat surface condition has been assumed in our model and it is unable to mimic the undulations of the oxide layer as observed experimentally. Further possible refinements of the present model would include the use of a deformable free surface. Since the objective of the present study was only to demonstrate the existence of a nonaxisymmetric effect, such an effort was not undertaken here.

6 Conclusions

The experimental observations clearly suggest that the GTAW pool is three-dimensional and inherently unsteady. The variety of flow phenomena observed is not predicted by the existing axisymmetric models of weld pool convection. Weld pool dynamics are found to be sensitive to the location of the torch relative to the clamp. Azimuthal circulation of steel and aluminum pools was observed whenever the clamp is located at an edge or a corner. Also, pool undulations and oscillations are observed even if the process parameters are held steady. The present study provides a clear confirmation of nonaxisymmetric convection patterns during the GTAW process. Such asymmetric motions have a profound effect on the temperature distribution and peak temperature inside the weld pool, which, in turn, will have a significant effect on the extent of the heat affected zone, cooling rate, post-weld microstructure, and the mechanical properties of the welded joint.

Computations are presented for the Aluminum pool under a nonaxisymmetric Lorentz force field. The rotational motion observed in the numerical study is in good agreement with the predictions. In case of Aluminum, however, the effect of nonaxisymmetric motions on the temperature distribution is less significant but still present, as seen in Figs. 7 and 8. This phenomenon with a low Prandtl number melt such as aluminum has also been observed in past studies (e.g., Ramanan and Korpela, 1990).

Acknowledgments

The authors acknowledge the support of this effort by National Science Foundation Grant #CBT-8808970. Additionally, P. Dutta acknowledges the National Research Council for the award of a Research Associateship to pursue this work.

References

Atthey, D. R., 1980, "A Mathematical Model for Fluid Flow in a Weld Pool at High Currents," *Journal of Fluid Mechanics*, Vol. 98, pp. 787–801.

Bolstad, J. O., 1987, "Electronic Imaging Technique for Welding and Other High Luminosity Processes," Idaho National Engineering Laboratory Report, EGG-SD-7847.

Brent, A. D., Voller, V. R., and Reid, K. J., 1988, "Enthalpy-Porosity Technique for Modeling Convection-Diffusion Phase Change: Application to the Melting of a Pure Metal," *Numerical Heat Transfer*, Vol. 13, pp. 297–318.

Correa, S. M., and Sundell, R. E., 1986, "A Computational and Experimental Study of the Fluid Flow in Weld Pools," S. Kou and R. Mehrabian, eds., *Modeling and Control of Casting and Welding Processes, Metallurgical Society*, Warrendale, PA, pp. 211–227.

Doumanidis, C. C., 1994, "In-Process Control of Scan Weilding," HTD, Vol. 289, ASME, New York, pp. 99–106.

Dutta, P., and Joshi, Y., and Janaswamy, R., 1995, "Thermal Modeling of Arc Welding Processes with Non-Axisymmetric Boundary Conditions," *Numerical Heat Transfer*, Part A, Vol. 27, pp. 499–518.

Giedt, W. H., 1987, "GTA Weld Penetration and the Effects of Deviations in Machine Variables," Sandia Report No. SAND87-8221.UC-38.

Kanouff, M., and Greif, R., 1992, "The Unsteady Development of a GTA Weld Pool," *International Journal of Heat and Mass Transfer*, Vol. 35 (4), pp. 967–979.

Kou, S., and Wang, Y. H., 1986, "Computer Simulation of Convection in Moving Arc Weld Pools," *Metallurgical Transactions A*, Vol. 17A, pp. 2271–2277.

Kou, S., and Wang, Y. H., (1986) "Weld Pool Convection and its Effect," *Welding Journal*, Vol. 65, pp. 63s–70s.

Kraus, H. G., 1989, "Experimental Measurement of Stationary SS 304, SS 316L and 8630 GTA Weld Pool Surface Temperatures," *Welding Journal*.

Oreper, G. M., and Szekely, J., 1984, "Heat and Fluid-Flow Phenomena in Weld Pools," *Journal of Fluid Mechanics*, Vol. 147(10), pp. 53–79.

Patankar, S. V., 1980, *Numerical Heat Transfer and Fluid Flow*, Hemisphere, Washington, D.C.

Ramanan, N., and Korpela, S. A., 1990, "Fluid Dynamics of a Stationary Weld Pool," *Metallurgical Transaction A*, Vol. 21A, pp. 45.

Sahoo, P., Debroy, T., and McNallan, M. J., 1988, "Surface Tension of Binary Metal-Surface Active Solute Systems Under Conditions Relevant to Welding Metallurgy," *Metallurgical Transaction B*, Vol. 19B, pp. 483–491.

Welding Handbook, 8th ed., 1991, Vol. 1, Chapter 1, Survey of Joining and Cutting Processes, pp. 2–23, American Welding Society, Miami, FL.

Woods, R. A., and Milner, D. R., 1971, "Motion in the Weld Pool in Arc Welding," *Welding Journal Research Supplement*, Vol. 50, pp. 163s.

Zacharia, T., Eraslan, A. H., Aidun, D. K., 1988, "Modeling of Autogenous Welding," *Welding Journal*, Vol. 67, pp. 53s–62s.

Journal of Heat Transfer
Technical Briefs

Velocity and Relative Contact Size Effects on the Thermal Constriction Resistance in Sliding Solids

N. Laraqi[1]

Nomenclature

α = thermal diffusivity
A_r = one cell real contact area ($=2l.2b$)
A_t = one cell apparent contact area ($=(2L)^2$)
b = half-width of the real contact area in y direction
k = thermal conductivity
l = half-width of the real contact area in x direction
L = half-width of the apparent contact area
q = heat flux density
Q = heat flux ($=q(2l.2b)$)
R_{cs} = thermal constriction resistance
T = temperature
$\bar{T}$ = average temperature
u = dimensionless temperature ($=T/(qL/k)$)
$\bar{u}_c$ = dimensionless average temperature of the contact area
$\underset{\sim}{u}$ = u Fourier transform: Eq. (13)
$\tilde{u}$ = $\tilde{u}$ cosine Fourier transform: Eq. (14)
V = sliding velocity
V^* = dimensionless velocity ($=V2L/\alpha$)
x, y, z = space coordinates
ξ, μ, η = dimensionless space coordinates ($\xi = x/L$, $\mu = y/L$, $\eta = z/L$)
ϵ = relative contact size ($= \sqrt{A_r/A_t} = \sqrt{\epsilon_x \epsilon_y}$)
ϵ_x, ϵ_y = ratio l/L and b/L respectively
ψ_c = constriction parameter ($=R_{cs}k\sqrt{A_r}$)

1 Introduction

It is well known that the contact temperatures of two sliding solids are important parameters in tribology (Play and Godet, 1977). A review of research on dry friction is given by Kennedy (1984). The author presents an analysis on thermal and mechanical aspects of sliding contact phenomena. Some analytical models (El-Sherbiny et al., 1977; Floquet et al., 1978; Gecim et al., 1984; Kouans et al., 1972) have been developed in order to calculate the contact temperature and partition of heat between two sliding solids in perfect contact. The experiments of Ling and Simkins (1963) show that there exists an important jump of temperature at the interface. The experiments of Berry and Barber (1984), Mazo et al. (1978), and Vullierme et al. (1979) show that the contact resistance decreases while the velocity increases. The thermal resistance in static contact has been widely studied (Bardon, 1972; Beck, 1979; Cooper et al., 1969; Degiovanni and Moyne, 1989; Fletcher, 1988; Negus et al., 1989; Yovanovich, 1976). In the sliding contact, the constriction phenomenon is modified by the motion and surface evolution effects. Some imperfect sliding contact models (Bardon, 1994; Laraqi, 1992) have been suggested. These models are based on the thermal constriction resistances. The thermal constriction resistance plays an important role in the estimation of the local temperatures arising from dry friction between solids. Not only does it define the temperature jump at the contact area, as in static contact, but it also contributes to the partition of the heat flux generated by the friction between the two solids.

A three-dimensional analytical model is developed in order to calculate the constriction resistance depending on geometrical (ϵ) and dynamical (V^*) parameters. It considers the surfaces to consist of numerous asperities represented by rectangular (or square) shaped heat sources centered in the square shaped apparent contact area (or heat flux tubes) and uniformly distributed over the contact plane. From the practical point of view, the roughnesses have any form and are randomly distributed, the average values of the heat flux tubes and asperities' dimensions of the real surfaces can be calculated using statistical models (Cretegny, 1985; Withehouse and Archard, 1970). Considering equal values of the relative contact size, the dimensionless thermal constriction resistances, for square or circular shaped heat flux tubes and asperities, are nearly identical (Negus et al., 1989).

The geometry investigated using the present model is the same as the one considered in the analytical model of Degiovanni and Moyne (1989) and Negus et al. (1989), in stationary contact, and in the experiments of Vullierme et al. (1979), in sliding contact. The results issued from the present model are compared to those given in these references. The influence of the asperity geometry is also investigated.

2 Schematization of the Local Heat Transfer Between Two Sliding Solids

In this paragraph we consider only the thermal constriction effect. We analyse the local heat transfer between two rough surfaces in sliding contact (Fig. 1). In one contact cell, the heat flux Q_0, generated in the solid/solid contact, is partitioned between the two solids; Q_1 for solid (1) and Q_2 for solid (2). We assume, without limiting the generality of the model, that the interstitial thermal resistance is high. The temperatures at the boundaries of the constriction zone of both solids are T_{cs1}

---

[1] Maître de Conférences Université Paris VI, Laboratoire de Mécanique Physique, URA CNRS 879, BP. 160 4-Place Jussieu, 75252 Paris Cedex 05, France

Contributed by the Heat Transfer Division for publication in the Journal of Heat Transfer. Manuscript received by the Heat Transfer Division February 6, 1996; revision received November 15, 1996; Keyword: Conduction. Associate Technical Editor: T. L. Bergman.

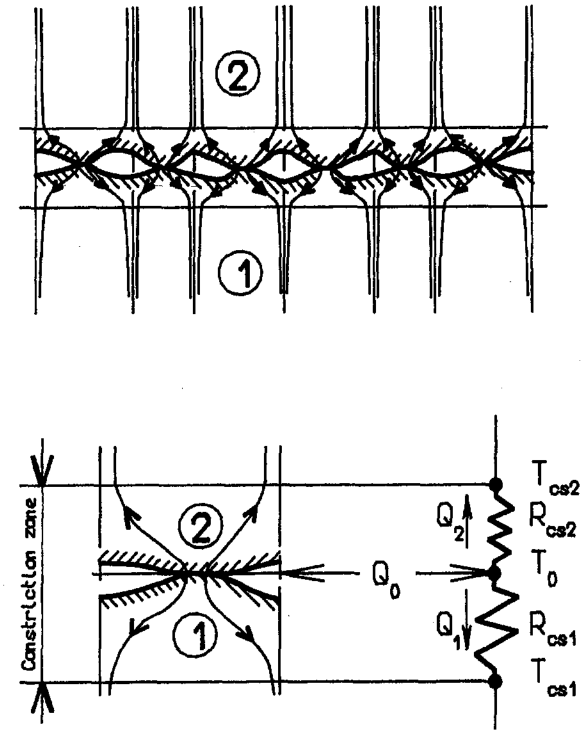

Fig. 1 Structure of a real contact

and T_{cs2}, and T_0 is the contact temperature. The thermal equilibrium is then given by

$$T_0 - T_{cs1} = R_{cs1}Q_1 \tag{1}$$

$$T_0 - T_{cs2} = R_{cs2}Q_2 \tag{2}$$

$$Q_0 = Q_1 + Q_2 \tag{3}$$

and therefore,

$$Q_1 = \frac{R_{cs2}}{R_{cs1} + R_{cs2}} Q_0 + \frac{T_{cs2} - T_{cs1}}{R_{cs1} + R_{cs2}} \tag{4}$$

$$Q_2 = \frac{R_{cs1}}{R_{cs1} + R_{cs2}} Q_0 - \frac{T_{cs2} - T_{cs1}}{R_{cs1} + R_{cs2}}\,. \tag{5}$$

Equations (4–5) consist of a first term that is similar but not equal to the local heat partition coefficient in the current literature, and a second one corresponding to a temperature jump.

3 Development of the Analytical Model

Consider an insulated semi-infinite medium (Fig. 2), in which the plane ($z = 0$) is subjected to a uniform heat flux density q on the rectangular (or square) areas ($2l \times 2b$). The periodicity length of the heat sources, assumed identical in the x and y directions, is $2L$. The solid is moving with the velocity V along the x direction.

Taking into account the periodicity of temperatures, and their gradients along the x-axis and their symmetry along the y-axis, the domain can be reduced by considering only one single cell (Fig. 2).

The steady state heat transfer is given by the solution of the following equation in dimensionless form,

$$\frac{\partial^2 u}{\partial \xi^2} + \frac{\partial^2 u}{\partial \mu^2} + \frac{\partial^2 u}{\partial \eta^2} - \frac{V^*}{2}\frac{\partial u}{\partial \xi} = 0 \quad \begin{cases} -1 \le \xi \le +1 \\ 0 \le \mu \le 1 \\ 0 \le \eta < \infty \end{cases} \tag{6}$$

with the boundary conditions,

$$u(-1, \mu, \eta) = u(+1, \mu, \eta) \quad \begin{cases} 0 \le \mu \le 1 \\ 0 \le \eta < \infty \end{cases} \tag{7}$$

$$\frac{\partial u}{\partial \xi}(-1, \mu, \eta) = \frac{\partial u}{\partial \xi}(+1, \mu, \eta) \quad \begin{cases} 0 \le \mu \le 1 \\ 0 \le \eta < \infty \end{cases} \tag{8}$$

$$\frac{\partial u}{\partial \mu}(\xi, 0, \eta) = 0 \quad \begin{cases} -1 \le \xi \le +1 \\ 0 \le \eta < \infty \end{cases} \tag{9}$$

$$\frac{\partial u}{\partial \mu}(\xi, 1, \eta) = 0 \quad \begin{cases} -1 \le \xi \le +1 \\ 0 \le \eta < \infty \end{cases} \tag{10}$$

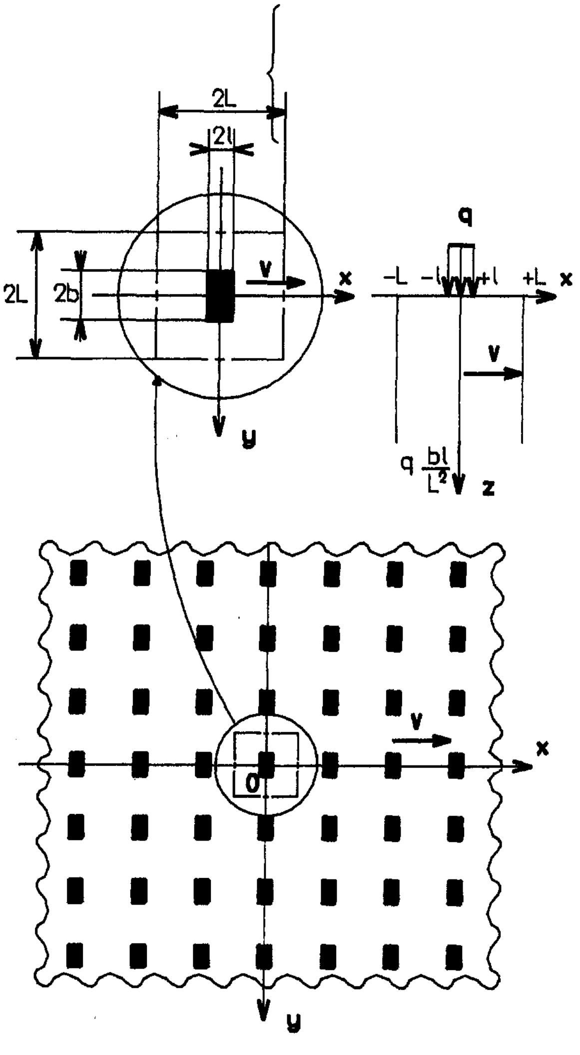

Fig. 2 Geometry of the studied contact surface

$$-\frac{\partial u}{\partial \eta}(\xi, \mu, 0) = \begin{cases} 1 & \begin{cases} -\epsilon_x \le \xi \le +\epsilon_x \\ 0 \le \mu \le \epsilon_y \end{cases} \\ 0 & \text{(elsewhere)} \end{cases} \quad (11)$$

$$-\frac{\partial u}{\partial \eta}(\xi, \mu, \infty) = \epsilon^2 \begin{cases} -1 \le \xi \le +1 \\ 0 \le \mu \le 1. \end{cases} \quad (12)$$

Considering the following finite Fourier transforms,

$$\tilde{u} = \frac{\alpha_p}{2}\int_{-1}^{+1} u \exp(-ip\pi\xi)d\xi$$

$$\begin{cases} \alpha_p = 1 & \text{for} \quad p = 0 \\ \alpha_p = 2 & \text{for} \quad p = 1, 2, \ldots, \infty \end{cases} \quad (13)$$

$$\tilde{\tilde{u}} = \int_0^1 \tilde{u} \cos(n\pi\mu)d\mu \quad (n = 0, 1, \ldots, +\infty) \quad (14)$$

and their corresponding inverse transforms,

$$\tilde{u} = \tilde{\tilde{u}}(n = 0) + 2\sum_{n=1}^{\infty} \tilde{\tilde{u}} \cos(n\pi\mu) \quad (15)$$

$$u = \Re\left[\sum_{p=0}^{\infty} \tilde{u} \exp(ip\pi\xi)\right] \quad (16)$$

the dimensionless surface temperature can be written as,

$$u(\xi, \mu, 0) = B_{00} + \sum_{n=1}^{\infty} \frac{2\epsilon_x \sin(n\pi\epsilon_y)\cos(n\pi\mu)}{(n\pi)^2} + \sum_{p=1}^{\infty} \frac{2\epsilon_y \sin(p\pi\epsilon_x)\cos(p\pi\xi - \gamma_{p0}/2)}{(p\pi)^2 \sqrt[4]{1 + (V^*/2p\pi)^2}}$$
$$+ \sum_{p=1}^{\infty}\sum_{n=1}^{\infty} \frac{4\sin(p\pi\epsilon_x)\sin(n\pi\epsilon_y)\cos(n\pi\mu)\cos(p\pi\xi - \gamma_{pn}/2)}{(p\pi)(n\pi)\sqrt{(p\pi)^2 + (n\pi)^2}\sqrt[4]{1 + [V^*p\pi/2[(p\pi)^2 + (n\pi)^2]]^2}} \quad (17)$$

where

$$B_{00} = Cst, \quad \gamma_{p0} = a\tan(V^*/2p\pi),$$

$$\gamma_{pn} = a\tan(V^*p\pi/2((p\pi)^2 + (n\pi)^2)). \quad (18)$$

The expression of the thermal constriction resistance is defined by

$$\mathcal{R}_{cs} = \frac{\bar{T}_c - \bar{T}_{z=0}}{Q} = \frac{\bar{u}_c - B_{00}}{4Lk\epsilon^2}. \quad (19)$$

The dimensionless average temperature of the contact area $\bar{u}_c$ is obtained by integrating Eq. (17) on the segment $\xi \in [-\epsilon_x, +\epsilon_x]$ and $\mu \in [0, \epsilon_y]$. Then, we deduce the expression of the constriction parameter as follows:

$$\psi_c = \sum_{p=1}^{\infty} \frac{\epsilon_y \sin^2(p\pi\epsilon_x)}{\sqrt{2}\epsilon\epsilon_x(p\pi)^3}\sqrt{\frac{1}{\sqrt{1 + (V^*/2p\pi)^2}} + \frac{1}{1 + (V^*/2p\pi)^2}} + \sum_{n=1}^{\infty} \frac{\epsilon_x \sin^2(n\pi\epsilon_y)}{\epsilon\epsilon_y(n\pi)^3}$$
$$+ \sum_{p=1}^{\infty}\sum_{n=1}^{\infty} \frac{\sqrt{2}\sin^2(p\pi\epsilon_x)\sin^2(n\pi\epsilon_y)}{\epsilon^3(p\pi)^2(n\pi)^2\sqrt{(p\pi)^2 + (n\pi)^2}}$$
$$\times \sqrt{\frac{1}{\sqrt{1 + [V^*p\pi/2[(p\pi)^2 + (n\pi)^2]]^2}} + \frac{1}{1 + [V^*p\pi/2[(p\pi)^2 + (n\pi)^2]]^2}}. \quad (20)$$

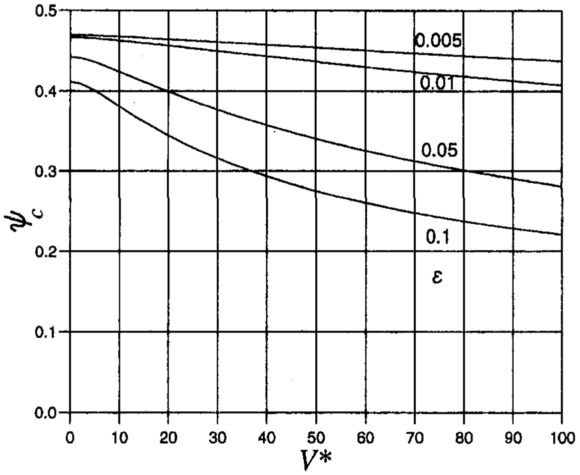

Fig. 3 Constriction parameter evolution as function of ϵ and V^*

4 Results and Discussion

Figure 3 shows that (considering $l = b$) the constriction parameter decreases with the increase of ϵ and V^*. Note that for a static contact ($V^* = 0$), Eq. (20) is identical to that given by Degiovanni and Moyne (1989), and Negus et al. (1989).

The constriction parameter, given by Eq. (20), is composed of three terms showing the influence of the constriction in the x direction, the y direction and the three-dimensional effect, respectively. The constriction in the y direction is independent of the velocity. The effect of the asperity geometry (ϵ_x/ϵ_y), for a constant value of $\epsilon = 0.1$, on the thermal constriction resistance for variable V^* is shown in Fig. 4. In a nonmoving contact, the thermal constriction resistance is smaller in the case of elongated asperities ($\epsilon_x/\epsilon_y \gg$, or, $\ll 1$) than in the cases of the square or circular shaped asperities.

In the sliding contact case, elongated asperities normal to the direction of displacement offer the lower thermal constriction resistance. This result has to be taken into account when machining solids for friction purposes. Negus et al. (1989) proposed the following correlation to calculate the constriction parameter (ψ_c^s) in statical contact for square shaped heat flux tubes and asperities:

$$\psi_c^s = 0.4732 - 0.62075\epsilon + 0.1198\epsilon^3. \quad (21)$$

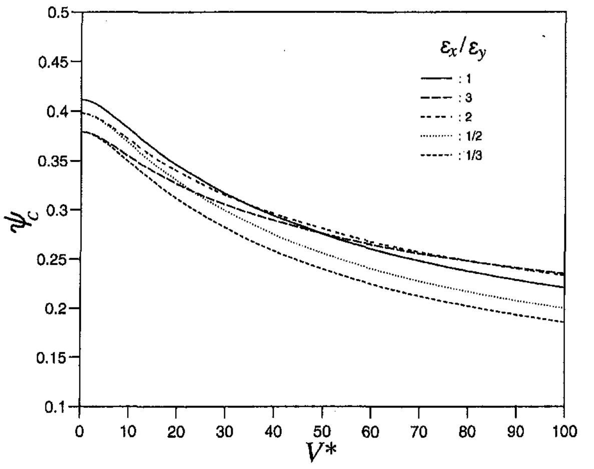

Fig. 4 Geometry of the asperity effect on the thermal constriction parameter (ϵ = 0.1)

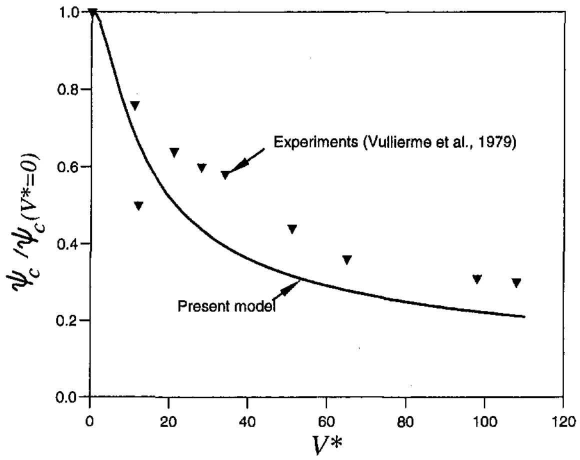

Fig. 6 Comparison of the ratio ψ_c/ψ_c (V^* = 0) evolution between the present model and the experiments (Vullierme et al., 1979)

This equation shows that for $\epsilon \le 0.01$ ($A_r/A_t \le 0.0001$) there is o interaction between asperities. For such small values of ϵ, a great number of terms are necessary to assure the convergence of the series in Eq. (20). In this particular case, it is preferable to use the expression given by Laraqi (1996),

$$\psi_c = \frac{2}{\sqrt{\pi}} \int_0^\infty \sqrt{\sigma} F\left[\frac{1}{2\sqrt{\sigma}}\right] \left\{ F\left[\frac{1 + v^*\sigma}{2\sqrt{\sigma}}\right] + F\left[\frac{1 - v^*\sigma}{2\sqrt{\sigma}}\right] - 2F\left[\frac{v^*\sqrt{\sigma}}{2}\right] \right\} d\sigma \quad (22)$$

where

$$F[X] = \int_0^X \operatorname{erf}(\vartheta)\, d\vartheta, \quad v^* = Vl/\alpha \quad (23)$$

or the correlation,

$$\psi_c = \frac{0.4732(1 - e^{-c})}{c} (1 + 0.6777(1 - e^{-c}) - 0.7257(1 - e^{-c})^2) \quad (24)$$

where

$$c = 0.629\sqrt{v^*}. \quad (25)$$

The proposed model is compared to experimental results obtained by Vullierme et al. (1979) using the experimental setup shown in Fig. 5. It consists of two hollow cylinders. The rotating cylinder is in brass, and its surface has band-shaped macroasperities uniformly distributed in the azimuthal direction. The stationary cylinder is in steel, and its frictional surface is flat. The inner and outer diameters of the cylinders are 60 mm and 80 mm, respectively. In Fig. 6, the ratio ψ_c/ψ_c (V^* = 0) obtained experimentally for $\epsilon_x = 0.2$ and $\epsilon_y = 1$ are compared to the values obtained from Eq. (20). The results are correctly represented by the proposed model.

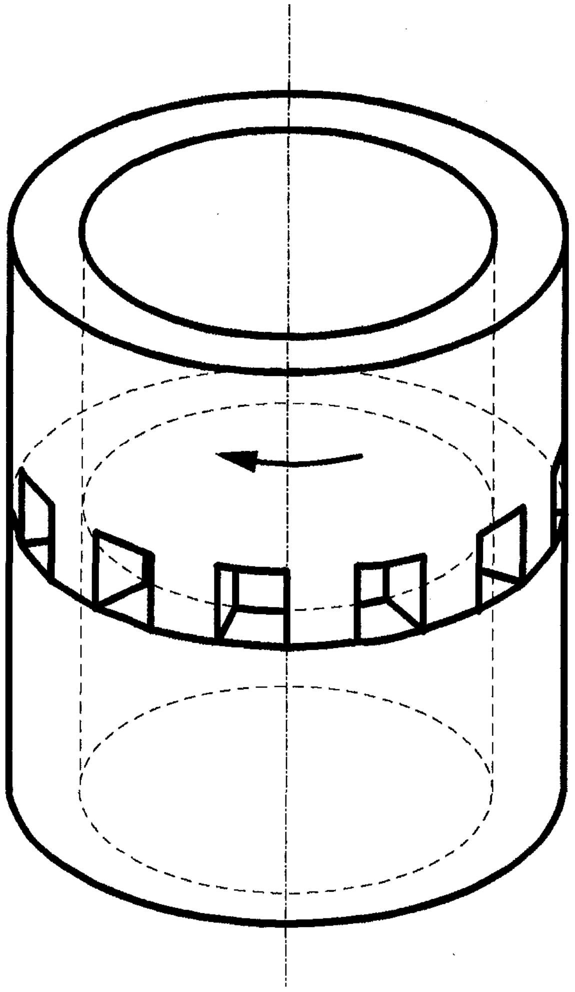

Fig. 5 Experimental set-up (Vullierme et al., 1979)

5 Conclusions

An analytical model giving the constriction parameter as a function of the relative contact size ϵ and the dimensionless slide velocity V^* has been developed. The results show that the constriction parameter decreases when the values of these two parameters increase. This is in agreement with the experimental results given in the pertinent literature. Furthermore, it is shown that the thermal constriction resistance in a sliding contact is the smallest when the moving surface has elongated asperities normal to the direction of displacement.

References

Bardon, J. P., 1972, "Introduction à l'Etude des Résistances Thermiques de Contact," *Revue Générale de Thermique Fr*, No. 125, pp. 429–447.

Bardon, J. P., 1994, ''Bases Physiques des Conditions de Contact Thermique Imparfait entre Milieux en Glissement Relatif,'' *Revue Générale de Thermique Fr*, No. 386, pp. 86–91.

Beck, J. V., 1979, ''Effects of Multiple Sources in the Contact Conductance Theory,'' ASME JOURNAL OF HEAT TRANSFER, Vol. 101, pp. 132–136.

Berry, G. A., and Barber, J. R., 1984, ''The Division of Frictional Heat—A Guide to the Nature of Sliding Contact,'' *ASME Journal of Tribology*, Vol. 106, pp. 405–415.

Cooper, M., Mikic, B. B., and Yovanovich, M. M., 1969, ''Thermal Contact Conductance,'' *Int. J. of Heat and Mass Transfer*, Vol. 12, pp. 279–300.

Cretegny, J. F., 1985, ''Etude Théorique et Expérimentale des Raideurs de Contact,'' *Thèse de Doctorat de l'ISMCM*, Saint-Ouen (93), France.

Degiovanni, A., and Moyne, C., 1989, ''Résistance Thermique de Contact en Régime Permanent. Influence de la Géométrie du Contact,'' *Revue Générale de Thermique Fr*, No. 334, pp. 557–563.

El-Sherbiny, M., and Newcomb, T. P., 1977, ''The Temperature Distribution Due to Frictional Heat Generated Between a Stationary Cylinder and a Rotating Cylinder,'' *Wear*, Vol. 42, pp. 23–42.

Fletcher, L. S., 1988, ''Recent Developments in Contact Conductance Heat Transfer,'' ASME JOURNAL OF HEAT TRANSFER, Vol. 110, pp. 1059–1070.

Floquet, A., Play, D., and Godet, M., 1978, ''Contribution à l'Etude Thermique du Frottement Sec dans les Paliers,'' *J. de Mécanique Appliquée*, 2, No. 4, pp. 499–539.

Gecim, B., and Winer, W. O., 1984, ''Steady Temperature in a Rotating Cylinder Subject to Surface Heating and Convective Cooling,'' *ASME Journal of Tribology*, Vol. 106, pp. 120–127.

Kennedy, F. E., Jr., 1984, ''Thermal and Thermomechanical Effects in Dry Sliding,'' *Wear*, Vol. 100, pp. 453–476.

Kounas, P. S., Dimarogonas, A. D., and Sandor, G. N., 1972, ''The Distribution of Friction Heat Between a Stationary Pin and Rotating Cylinder,'' *Wear*, Vol. 19, pp. 415–424.

Laraqi, N., 1992, ''Température de Contact et Coefficient de Partage de Flux Généré par Frottement Sec entre Deux Solides. Approche Nouvelle de la Génération de Flux,'' *Int. J. of Heat and Mass Transfer*, Vol. 35, No. 11, pp. 3131–3139.

Laraqi, N., 1996, ''Phénomène de Constriction Thermique dans les Contacts Glissants,'' *Int. J. of Heat and Mass Transfer*, Vol. 39, No. 17, pp. 3717–3724.

Ling, F. F., and Simkins, T. E., 1963, ''Measurement of Pointwise Juncture Condition of Temperature at the Interface of Two Bodies in Sliding Contact,'' *J. Basic Engineering*, pp. 481–487.

Mazo, L., Cassagne, B., Badie-Levet, D., and Bardon, J. P., 1978, ''Etude des Conditions de Liaison Thermique dans le Cas de Frottement Sec Métal-Plastique,'' *Revue Générale de Thermique Fr*, No. 204, pp. 921–933.

Negus, K. J., Yovanovich, M. M., and Beck, J. V., 1989, ''On the Nondimensionalization of Constriction Resistance for Semi-Infinite Heat Flux Tubes,'' ASME JOURNAL OF HEAT TRANSFER, Vol. 111, pp. 804–807.

Play, D., and Godet, M., 1977, ''Design on High Performance Dry Bearing,'' *Wear*, Vol. 41, pp. 25–44.

Vullierme, J. J., Lagarde, J. J., and Cordier, H., 1979, ''Etude de la Résistance de Contact Entre Deux Matériaux—Influence de la Vitesse de Glissement,'' *Int. J. of Heat and Mass Transfer*, Vol. 22, pp. 1209–1219.

Whitehouse, D. J., and Archard, J. F., 1970, ''The Proprieties of Random Surfaces of Significance in Their Contact,'' *Proc. Roy. Soc.*, 316, A, pp. 97–121.

Yovanovich, M. M., 1976, ''General Expression for Circular Constriction Resistances for Arbitrary Flux Distribution,'' *AIAA. 13th Aerospace Sciences Meeting*, Pasadena, California, pp. 381–396.

A Note on the Evaluation of Thermal Constriction Resistance for Finite Thickness Gaps

Ashok Kumar Das[1], and Satwindar Singh Sadhal[2]

Nomenclature

A, B = constants, Eqs. (3) and (4)
I = values of integrals, Eqs. (8) and (10)
k = thermal conductivity
q = heat flux
q_0 = heat flux at infinity
$\mathcal{R}_c$ = constriction resistance
T = temperature
T' = temperature disturbance
$\underline{T^\infty}$ = uniform flux temperature solution
$\overline{\Delta T}$ = average interface temperature jump Eqs. (7) and (9)
t = half gap thickness $(t_1 + t_2)/2$, Fig. 1
w = gap half width, Fig. 1
(x, z) = rectangular coordinates

Greek Symbols

δ = inter-gap spacing, Fig. 1
η = bipolar coordinate
κ_g = gap area fraction
ψ = nondimensional resistance
ξ = bipolar coordinate

Subscripts

1, 2, 3 = medium 1, 2, 3
12, 23, 13 = media-interfaces

Superscripts

(a) = definition (a) for $\overline{\Delta T}$
(b) = definition (b) for $\overline{\Delta T}$

1 Introduction

The thermal constriction resistance between two solids in contact is defined as the ratio of average temperature jump across the interface, $\overline{\Delta T}$, to an appropriate heat flux which is the far-field flux or the average flux per unit apparent contact area. In the steady state, both the values are the same. While the evaluation of heat flux has been quite consistent in the literature, in the case of $\overline{\Delta T}$, there is some variation. Broadly speaking, there have been two methodologies used for evaluating this jump: (a) the difference between the average surface temperatures of the contacting interfaces; and (b) difference between the projection of the far field temperatures in the two solids onto the interface.

For cases when the gaps between the contact areas are assumed to be adiabatic and flat (i.e., of zero thickness), $\overline{\Delta T}$ is generally computed as per definition (a), and for such cases it is consistent with definition (b). The former definition has been used for both single-contact or ''cell'' models and multi-contact models in the literature. For the cases of non-zero thickness gaps between the contact areas, in general, definition (b) has been used to evaluate $\overline{\Delta T}$. The exception to this are the gas-gap models employing statistical theories to evaluate the gap-conductance. Fenech & Rohsenow (1963) were the first to study the gaps of finite thickness, and use definition (b) in their ''cell'' model. Later, Veziroglu & Chandra (1968) and Dundurs & Panek (1976) used this temperature jump as seen from the far field. While it is relatively simple to evaluate the temperature jump $\overline{\Delta T}$ for ''cell'' models and for multiple-gap models of zero-thickness gaps, it is not so straightforward for models with ''multiple'' gaps of ''non-zero'' thickness, especially in certain curvilinear coordinate systems such as bipolar. A discussion of such cases is the subject of this paper.

2 Temperature Solution for Two Solids in Contact with Non-zero Thickness Gaps

A model has been developed for two solids in contact with non-zero thickness gaps occupied by an interstitial fluid of finite conductivity (Das and Sadhal, 1991, 1992). The model consists of an array of two-dimensional gaps of width $2w$ and half-thickness t at regular intervals δ at the interface of two

---

[1] Applied Materials, Inc., 4250 Burton Drive, M/S 2402, Santa Clara, CA 95054

[2] Department of Mechanical Engineering, University of Southern California, Los Angeles, CA 90089-1453

Contributed by the Heat Transfer Division for publication in the Journal of Heat Transfer. Manuscript received by the Heat Transfer Division October 4, 1995; revision received October 17, 1996; Keywords: Conduction, Electronic Equipment, Thermal Packaging. Associate Technical Editor: K. Vafai.

Bardon, J. P., 1994, "Bases Physiques des Conditions de Contact Thermique Imparfait entre Milieux en Glissement Relatif," *Revue Générale de Thermique Fr*, No. 386, pp. 86–91.

Beck, J. V., 1979, "Effects of Multiple Sources in the Contact Conductance Theory," ASME JOURNAL OF HEAT TRANSFER, Vol. 101, pp. 132–136.

Berry, G. A., and Barber, J. R., 1984, "The Division of Frictional Heat—A Guide to the Nature of Sliding Contact," *ASME Journal of Tribology*, Vol. 106, pp. 405–415.

Cooper, M., Mikic, B. B., and Yovanovich, M. M., 1969, "Thermal Contact Conductance," *Int. J. of Heat and Mass Transfer*, Vol. 12, pp. 279–300.

Cretegny, J. F., 1985, "Etude Théorique et Expérimentale des Raideurs de Contact," *Thèse de Doctorat de l'ISMCM*, Saint-Ouen (93), France.

Degiovanni, A., and Moyne, C., 1989, "Résistance Thermique de Contact en Régime Permanent. Influence de la Géométrie du Contact," *Revue Générale de Thermique Fr*, No. 334, pp. 557–563.

El-Sherbiny, M., and Newcomb, T. P., 1977, "The Temperature Distribution Due to Frictional Heat Generated Between a Stationary Cylinder and a Rotating Cylinder," *Wear*, Vol. 42, pp. 23–42.

Fletcher, L. S., 1988, "Recent Developments in Contact Conductance Heat Transfer," ASME JOURNAL OF HEAT TRANSFER, Vol. 110, pp. 1059–1070.

Floquet, A., Play, D., and Godet, M., 1978, "Contribution à l'Etude Thermique du Frottement Sec dans les Paliers," *J. de Mécanique Appliquée*, 2, No. 4, pp. 499–539.

Gecim, B., and Winer, W. O., 1984, "Steady Temperature in a Rotating Cylinder Subject to Surface Heating and Convective Cooling," *ASME Journal of Tribology*, Vol. 106, pp. 120–127.

Kennedy, F. E., Jr., 1984, "Thermal and Thermomechanical Effects in Dry Sliding," *Wear*, Vol. 100, pp. 453–476.

Kounas, P. S., Dimarogonas, A. D., and Sandor, G. N., 1972, "The Distribution of Friction Heat Between a Stationary Pin and Rotating Cylinder," *Wear*, Vol. 19, pp. 415–424.

Laraqi, N., 1992, "Température de Contact et Coefficient de Partage de Flux Généré par Frottement Sec entre Deux Solides. Approche Nouvelle de la Génération de Flux," *Int. J. of Heat and Mass Transfer*, Vol. 35, No. 11, pp. 3131–3139.

Laraqi, N., 1996, "Phénomène de Constriction Thermique dans les Contacts Glissants," *Int. J. of Heat and Mass Transfer*, Vol. 39, No. 17, pp. 3717–3724.

Ling, F. F., and Simkins, T. E., 1963, "Measurement of Pointwise Juncture Condition of Temperature at the Interface of Two Bodies in Sliding Contact," *J. Basic Engineering*, pp. 481–487.

Mazo, L., Cassagne, B., Badie-Levet, D., and Bardon, J. P., 1978, "Etude des Conditions de Liaison Thermique dans le Cas de Frottement Sec Métal-Plastique," *Revue Générale de Thermique Fr*, No. 204, pp. 921–933.

Negus, K. J., Yovanovich, M. M., and Beck, J. V., 1989, "On the Nondimensionalization of Constriction Resistance for Semi-Infinite Heat Flux Tubes," ASME JOURNAL OF HEAT TRANSFER, Vol. 111, pp. 804–807.

Play, D., and Godet, M., 1977, "Design on High Performance Dry Bearing," *Wear*, Vol. 41, pp. 25–44.

Vullierme, J. J., Lagarde, J. J., and Cordier, H., 1979, "Etude de la Résistance de Contact Entre Deux Matériaux—Influence de la Vitesse de Glissement," *Int. J. of Heat and Mass Transfer*, Vol. 22, pp. 1209–1219.

Whitehouse, D. J., and Archard, J. F., 1970, "The Proprieties of Random Surfaces of Significance in Their Contact," *Proc. Roy. Soc.*, 316, A, pp. 97–121.

Yovanovich, M. M., 1976, "General Expression for Circular Constriction Resistances for Arbitrary Flux Distribution," *AIAA. 13th Aerospace Sciences Meeting*, Pasadena, California, pp. 381–396.

A Note on the Evaluation of Thermal Constriction Resistance for Finite Thickness Gaps

Ashok Kumar Das[1], **and**
Satwindar Singh Sadhal[2]

Nomenclature

A, B = constants, Eqs. (3) and (4)
I = values of integrals, Eqs. (8) and (10)
k = thermal conductivity
q = heat flux
q_0 = heat flux at infinity
$\mathcal{R}_c$ = constriction resistance
T = temperature
T' = temperature disturbance
$\underline{T^\infty}$ = uniform flux temperature solution
$\overline{\Delta T}$ = average interface temperature jump Eqs. (7) and (9)
t = half gap thickness $(t_1 + t_2)/2$, Fig. 1
w = gap half width, Fig. 1
(x, z) = rectangular coordinates

Greek Symbols

δ = inter-gap spacing, Fig. 1
η = bipolar coordinate
κ_g = gap area fraction
ψ = nondimensional resistance
ξ = bipolar coordinate

Subscripts

1, 2, 3 = medium 1, 2, 3
12, 23, 13 = media-interfaces

Superscripts

(a) = definition (a) for $\overline{\Delta T}$
(b) = definition (b) for $\overline{\Delta T}$

1 Introduction

The thermal constriction resistance between two solids in contact is defined as the ratio of average temperature jump across the interface, $\overline{\Delta T}$, to an appropriate heat flux which is the far-field flux or the average flux per unit apparent contact area. In the steady state, both the values are the same. While the evaluation of heat flux has been quite consistent in the literature, in the case of $\overline{\Delta T}$, there is some variation. Broadly speaking, there have been two methodologies used for evaluating this jump: (a) the difference between the average surface temperatures of the contacting interfaces; and (b) difference between the projection of the far field temperatures in the two solids onto the interface.

For cases when the gaps between the contact areas are assumed to be adiabatic and flat (i.e., of zero thickness), $\overline{\Delta T}$ is generally computed as per definition (a), and for such cases it is consistent with definition (b). The former definition has been used for both single-contact or "cell" models and multi-contact models in the literature. For the cases of non-zero thickness gaps between the contact areas, in general, definition (b) has been used to evaluate $\overline{\Delta T}$. The exception to this are the gas-gap models employing statistical theories to evaluate the gap-conductance. Fenech & Rohsenow (1963) were the first to study the gaps of finite thickness, and use definition (b) in their "cell" model. Later, Veziroglu & Chandra (1968) and Dundurs & Panek (1976) used this temperature jump as seen from the far field. While it is relatively simple to evaluate the temperature jump $\overline{\Delta T}$ for "cell" models and for multiple-gap models of zero-thickness gaps, it is not so straightforward for models with "multiple" gaps of "non-zero" thickness, especially in certain curvilinear coordinate systems such as bipolar. A discussion of such cases is the subject of this paper.

2 Temperature Solution for Two Solids in Contact with Non-zero Thickness Gaps

A model has been developed for two solids in contact with non-zero thickness gaps occupied by an interstitial fluid of finite conductivity (Das and Sadhal, 1991, 1992). The model consists of an array of two-dimensional gaps of width $2w$ and half-thickness t at regular intervals δ at the interface of two

---

[1] Applied Materials, Inc., 4250 Burton Drive, M/S 2402, Santa Clara, CA 95054

[2] Department of Mechanical Engineering, University of Southern California, Los Angeles, CA 90089-1453

Contributed by the Heat Transfer Division for publication in the Journal of Heat Transfer. Manuscript received by the Heat Transfer Division October 4, 1995; revision received October 17, 1996; Keywords: Conduction, Electronic Equipment, Thermal Packaging. Associate Technical Editor: K. Vafai.

solids of conductivity, k_1 and k_2 (Fig. 1). The gap is occupied by a fluid of conductivity k_3 and flanked by contacting "strips". A constant heat flux q_0 is imposed far away from the interface. In all of these analyses, the gaps are assumed to be circular in profile, while the contact strips are flat. In the present development, full interfacial coupling between the gaps and the solids is implemented. The problem is solved in bipolar coordinates (ξ, η) which are related to the rectangular coordinates (x, z) as

$$x = \frac{w \sinh \xi}{\cosh \xi + \cos \eta}, \quad z = \frac{w \sin \eta}{\cosh \xi + \cos \eta}, \tag{1}$$

for $-\pi \leq \eta \leq \pi$ and $-\infty < \xi < \infty$, with metric coefficients $h_\xi = h_\eta = w/(\cosh \xi + \cos \eta)$.

For the case of sparsely distributed gaps at the interface when the interaction between the gaps can be neglected, the problem has been simplified to a single gap at the surface of contact of two semi-infinite conducting solids, the rest of the surface being in perfect contact. For this case, the temperatures in the two solids are given as (Das and Sadhal, 1991, 1992),

$$\begin{aligned} T_1 &= T_1^\infty + T_1' = -\frac{q_0}{k_1} z + T_1' \quad \text{and} \\ T_2 &= T_2^\infty + T_2' = -\frac{q_0}{k_2} z + T_2', \end{aligned} \tag{2}$$

where T_1^∞ and T_2^∞ are the solution for uniform flux problem, and

$$T_1'(\xi, \eta) = \frac{q_0 w}{k_1} \int_0^\infty \left[A_1(\lambda) \frac{\sinh \lambda(\pi - \eta)}{\sinh \lambda(\pi - \eta_{13})} + B_1(\lambda) \frac{\sinh \lambda(\eta - \eta_{13})}{\sinh \lambda(\pi - \eta_{13})} \right] \cos \lambda \xi d\lambda \tag{3}$$

and,

$$T_2'(\xi, \eta) = \frac{q_0 w}{k_2} \int_0^\infty \left[A_2(\lambda) \frac{\sinh \lambda(\pi + \eta)}{\sinh \lambda(\pi + \eta_{23})} + \frac{k_2}{k_1} B_1(\lambda) \frac{\sinh \lambda(\eta_{23} - \eta)}{\sinh \lambda(\pi + \eta_{23})} \right] \cos \lambda \xi d\lambda \tag{4}$$

are temperature "disturbances" introduced due to the presence of the gaps. The expressions for the constants $A_1(\lambda)$, $A_2(\lambda)$, and $B_1(\lambda)$ are given in Das and Sadhal (1991).

3 Evaluation of Thermal Constriction Resistance

The thermal constriction resistance is defined as $\mathcal{R}_c = \overline{\Delta T}/q_0$, where $\overline{\Delta T}$ is the average temperature jump across the interface and q_0 is the far field heat flux. As discussed earlier, $\overline{\Delta T}$ is the temperature jump across the interface as seen from the far field (definition (b)). For noninteracting multiple gaps, the far field due to a single gap does not provide much information towards the evaluation of a meaningful $\overline{\Delta T}$. In that case, the only definition that can be used is definition (a). However, as will be shown later, this definition is meaningless and has no physical significance. One must, for such cases, consider the cumulative effect due to the array of gaps at far field to get any meaningful temperature jump.

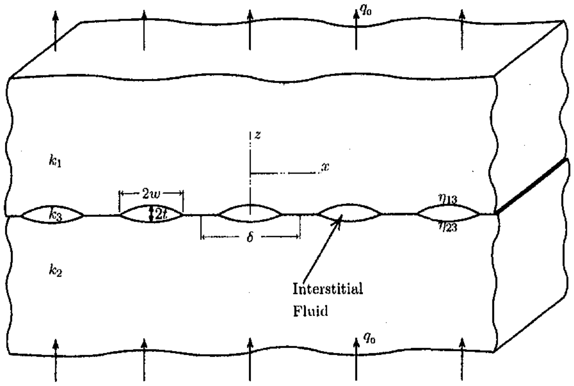

Fig. 1 An array of two-dimensional gaps and contacts at the interface of two semi-infinite solids in contact

According to definition (b), temperature jump $\overline{\Delta T}$ is the difference between the average far field temperatures in the two solids when projected onto the interface. The uniform flux terms T_1^∞ and T_2^∞, in the temperature solution in the two solids (Eq. 2), are linear in z and hence vanish when averaged over x at far field and projected back to the interface $z = 0$. It is, therefore, only the temperature disturbance terms T_1' and T_2' which contribute to the temperature jump.

The individual effects of the temperature disturbances T_1' and T_2' vanish away from the interface ($(x^2 + z^2) \to \infty$ or $\xi \to 0$ and $\eta \to \pm\pi$ simultaneously) when considered completely noninteracting with other gaps in the array. However, the cumulative effect of such disturbances arising out of each gap in an array (even though sparsely distributed) will still be noticeable even far away from the interface. At the far field, this cumulative effect manifests itself in an average temperature jump across the interface (Fig. 2).

In order to compute $\overline{\Delta T}$, we therefore need to evaluate the sum of the effects, far away from the interface, of the temperature disturbance T' due to each of the gaps in the array, and project it back to the interface. However, the far-field linear temperature distribution given by Eq. (2) has been removed in Eqs. (3) and (4). Hence, the values of T_1' and T_2' averaged over any z should be constants, independent of z. We could as well take these averages at $z = z_0 \to \pm\infty$ for convenience. The cumulative effect of $(2N + 1)$ gaps over the region $-l \leq x \leq l$, with $l \to \infty$, amounts to

$$\overline{\Delta T}_\infty = \lim_{l \to \infty} \frac{1}{2l} \int_{-l}^{l} \lim_{z_0 \to -\infty} \sum_{n=-N}^{N} T_2'(x + n\delta, z_0) dx - \lim_{l \to \infty} \frac{1}{2l} \int_{-l}^{l} \lim_{z_0 \to \infty} \sum_{n=-N}^{N} T_1'(x + n\delta, z_0) dx, \tag{5}$$

where $2l = (2N + 1)\delta$. Since the contribution from each of the gaps is identical, by switching the order of integration and summation, and properly taking the limit with $l \to \infty$ (and consequently $N \to \infty$), we obtain

$$\overline{\Delta T}_\infty = \frac{1}{\delta} \lim_{z_0 \to -\infty} \int_{-\infty}^{\infty} T_2' |_{z=z_0} dx - \frac{1}{\delta} \lim_{z_0 \to \infty} \int_{-\infty}^{\infty} T_1' |_{z=z_0} dx, \tag{6}$$

where $1/\delta$ represents the gap number density.

To evaluate the integrals in Eq. (6) we must first express the temperatures in terms of x and z, fix $z = z_0$, integrate with respect to x, and then take the limit as $z_0 \to \pm\infty$. Since the transformation from the rectangular to the bipolar coordinates is highly complicated (Eq. 1), such a simplification of the expression for the temperatures (Eqs. 3, 4) is prohibitive. However, we can utilize the mathematical simplification that the above procedure of averaging and then projecting back to the interface $z = 0$, is identical to first projecting the temperature field onto the interface $z = 0$ and then performing the averaging process. A proof of the same appears in Das and Sadhal (1995) along with an example to illustrate the point. Mathematically,

$$\overline{\Delta T}^{(b)} = \frac{1}{\delta}\left[\int_{-\infty}^{\infty} T_2'|_{z=0}dx - \int_{-\infty}^{\infty} T_1'|_{z=0}dx\right]$$

$$= \frac{1}{\delta}\left[\int_{-x_0}^{x_0} T_2'|_{z=0}dx - \int_{-x_0}^{x_0} T_1'|_{z=0}dx\right]. \quad (7)$$

The superscript (b) refers to the definition (b). The nondimensional resistance is then obtained as

$$\psi^{(b)} = \frac{k_1k_2}{k_1+k_2}\frac{\mathcal{R}_c}{\delta} = \frac{\pi}{2}\kappa_g^2\frac{1}{1+k_2/k_1}\left[I_2^{(b)} - \frac{k_2}{k_1}I_1^{(b)}\right], \quad (8)$$

where $\kappa_g = 2w/\delta$ is the gap area fraction. The details of the expression for $I_1^{(b)}$ and $I_2^{(b)}$ are given in Das and Sadhal (1995).

If we use definition (a) for computing the temperature jump (Das & Sadhal, 1991; 1992), then integration of the surface temperature over one "period" δ gives

$$\overline{\Delta T}^{(a)} = \frac{1}{\delta}\left[\int_{-\infty}^{\infty} T_2\frac{w}{\cosh\xi + \cos\eta}\bigg|_{\eta=\eta_{23}} d\xi - \int_{-\infty}^{\infty} T_1\frac{w}{\cosh\xi + \cos\eta}\bigg|_{\eta=\eta_{13}} d\xi\right]. \quad (9)$$

Once again, the superscript (a) refers to the definition (a). The nondimensional resistance is

$$\psi^{(a)} = \frac{k_1k_2}{k_1+k_2}\frac{\mathcal{R}_c}{\delta} = \frac{\pi}{2}\kappa_g^2\frac{1}{1+k_2/k_1}\left[I_2^{(a)} - \frac{k_2}{k_1}I_1^{(a)}\right], \quad (10)$$

with details of the expression given in Das and Sadhal (1995).

4 Results and Discussion

The nondimensional contact resistance ψ is numerically evaluated and plotted in Fig. 3 for the two definitions (a) and (b) of ψ given by Eqs. (10) and (8), respectively. The resistance has been computed for values of the ratio of interstitial fluid to solid conductivity up to 1.5. The values greater than unity have been included in order to emphasize the importance of the definition. It is expected that if the gaps are occupied by a fluid of conductivity, k_3, greater than that of the solids ($k_1 = k_2$, assumed), the constriction resistance would be negative. This important feature is not manifested by simple addition of gap and constriction conductances. Also, the resistance is zero when k_3 equals $k_1 = k_2$. From the plots in Fig. 3, it can be seen that the resistance obtained by definition (b), $\psi^{(b)}$, indeed shows this behavior for the entire range of gap thicknesses. However, the resistance obtained with definition (a), $\psi^{(a)}$, does not. Thus, it is seen that definition (b) is a better representation of the physical phenomenon than definition (a).

The values of $\psi^{(a)}$ are observed to be always positive. This behavior for $\psi^{(a)}$ is a direct manifestation of the fact that for any value of k_3, the temperature difference between the gap surfaces will always be positive; this results in a positive $\overline{\Delta T}$, and hence, positive $\psi^{(a)}$ over the entire range of k_3 and t. For $k_3/k_1 < 1$, $\psi^{(b)}$ is observed to be lower than $\psi^{(a)}$ for the entire range of gap thickness, except at very small values where the resistance itself is small, and the two values almost overlap. This behavior could be attributed to the fact that $\psi^{(a)}$ is essentially the "gap resistance" rather than the "overall constriction resistance" ($\psi^{(b)}$) of the interface, and hence, would be higher. Song et al. (1992) also reported that the measured joint conductance (or "overall contact conductance") is the sum of contact and gap conductances, which qualitatively conforms to the present analysis. However, there are no published data for the case of $k_3/k_1 > 1$ which gives negative resistance. Based on these discussions, it is recommended that definition (b) should be used as *it is more appropriate and physically consistent with* gap conductivity values relative to the surrounding solids.

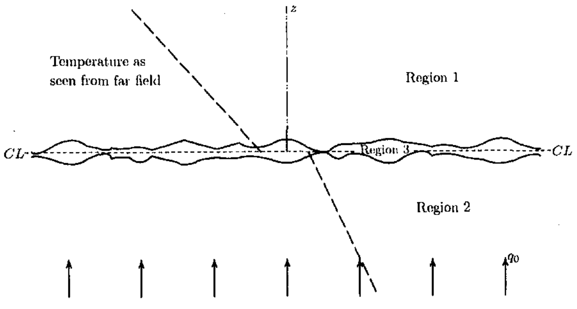

Fig. 2 Far field temperature and flux for two rough surfaces in contact

Here however, it must be noted that the definition of an "interface" is not very straightforward in many real situations, and that the temperature jump depends on the location of the "interface" CL as shown in Fig. 2. In general, $z = 0$ is chosen as the "reference" or "nominal" plane to define the "interface" for the purpose of projecting the far field onto this interface. While this plane is, in many cases, the nominal plane of contact, especially for symmetric gaps flanked by flat strips (Fig. 1), asymmetric roughness of the actual surfaces of the solid may not render $z = 0$ as the "nominal" interface (Fig. 2). In that case, care must be taken to project the temperature fields onto an "appropriate" plane of nominal contact for computing the temperature jump.

5 Conclusions

Thermal constriction resistance has been obtained for an array of finite thickness gaps based on two prevalent definitions in the literature: (a) the difference between the average surface temperatures of the contacting interfaces; and (b) the difference between the projection of the far field temperatures in the two solids onto the interface. In definition (b), it is realized that $\overline{\Delta T}$ arises solely due to the presence of the array of gaps, and hence the average temperature jump is the difference in the cumulative temperatures at infinity in the two solids. However, it is difficult to evaluate the far field temperature due to the complexity of the expression for the temperature in curvilinear coordinates. It is, therefore, proposed that the cumulative effect be computed by integrating the projection of the temperatures in regions 1 and 2, $T_1(\xi, \eta)$ and $T_2(\xi, \eta)$, into the gap at the $z = 0$ plane. This is a meaningful result even though $T_1(\xi, \eta)$ and $T_2(\xi, \eta)$ represent temperatures outside the gap.

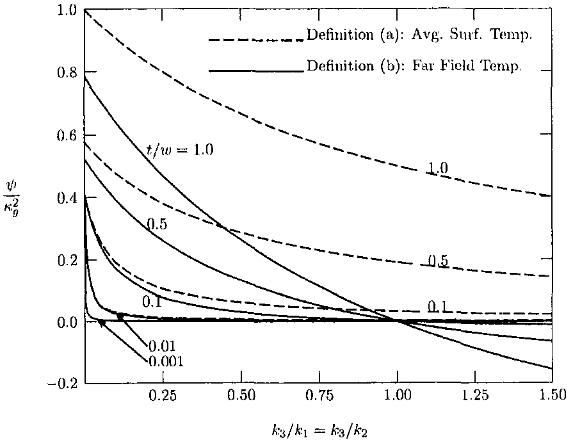

Fig. 3 Comparison of dimensionless resistance as a function of gap-to-solid conductivity ratio for the two definitions (*a*) and (*b*)

The results show that resistance obtained by definition (b) is zero for cases when the gap conductivity equals the solid conductivities which are also assumed to be equal, and that it is negative for gap conductivities greater than that of the solids. The zero and negative resistance values are important features of the result and represent the actual physical phenomenon. It is also observed that the resistance obtained with definition (a) is positive for all gap conductivities. This is a consequence of the fact that the temperature difference between the gap surfaces will always be positive for any value of gap conductivity. It is, therefore, recommended that one must use definition (b) for computation of constriction resistance in such cases.

References

Das, A. K., and Sadhal, S. S., 1991, "Thermal Constriction Resistance: The Effect of Interstitial Fluid," *Fundamentals of Conduction*, ASME HTD Vol. 173, pp. 35–39.

Das, A. K., and Sadhal, S. S., 1992, "Effect of Interstitial Fluid on Thermal Constriction Resistance," ASME JOURNAL OF HEAT TRANSFER, Vol. 114, No. 4, pp. 1045–1048.

Das, A. K., and Sadhal, S. S., 1995, "A Note on the Evaluation of Thermal Contact Resistance for Non-Zero Thickness Gaps," ASME HTD Vol. 310, pp. 131–138.

Dundurs, J., and Panek, C., 1976, "Heat Conduction Between Bodies With Wavy Surfaces," *International Journal of Heat Mass Transfer*, Vol. 19, No. 7, pp. 731–736.

Fenech, H., and Rohsenow, W. M., 1963, "Prediction of Thermal Conductance of Metallic Surfaces in Contact," ASME JOURNAL OF HEAT TRANSFER, February, pp. 15–24.

Song, S., Yovanovich, M. M., and Nho, K., 1992, "Thermal Gap Conductance: Effects of Gas Pressure and Mechanical Load," *Journal of Thermophysical Heat Transfer*, Vol. 6, No. 1, pp. 62–68.

Veziroglu, T. N., and Chandra, S., 1968, "Thermal Conductance of Two-Dimensional Constrictions," *Progress in Astronautics and Aeronautics, Vol. 21: Thermal Design Principles of Spacecraft and Entry Bodies*, pp. 591–615.

Derivation of Rayleigh Number for Nonpenetrative Thermal Convection

A. K. Prasad[1]

Nomenclature

C_p = specific heat
g = acceleration due to gravity
k = thermal conductivity
Nu = Nusselt number
Pr = Prandtl number
Q = heat flux (W/m^2)
Q_o = kinematic heat flux = $Q/\rho C_p$(K-m/s)
Ra = Rayleigh number
ΔT = temperature scale
z_* = depth of fluid layer

Greek Symbols

β = thermal expansion coefficient
α = thermal diffusivity
λ_T = thickness of conduction layer
ν = kinematic viscosity
ρ = density

Subscripts

b = lower boundary (bottom) of fluid layer
t = upper boundary (top) of fluid layer
m = mixed layer
NP = nonpenetrative
RB = Rayleigh-Benard

I Introduction

A common laboratory model used to simulate thermally induced motions in the atmosphere consists of a shallow layer of fluid heated from below and capped from above by a stable stratified layer (for an example, see Deardorff et al., 1969). The stable layer represents the inversion that caps the turbulent motions in the atmosphere. Over the course of the experiment, heating at the lower boundary drives the turbulent motions, in the form of plumes and thermals, to rise through the depth of the mixed or convecting layer and impact the base of the stable layer, gradually eroding it away. This model mimics the gradual erosion of the inversion layer in the atmosphere over the course of the day, due to the action of buoyancy-driven motions arising from solar heating at the earth's surface. This form of convection is called "penetrative convection," alluding to the penetration of turbulent structures from the mixed layer into the stable inversion layer.

An idealization of the penetrative configuration described above is obtained by replacing the stable inversion layer with a rigid insulating boundary, a situation called nonpenetrative convection. Nonpenetrative convection also occurs in lakes or oceans where the surface layer is evaporatively cooled, and the bottom of the fluid layer forms the rigid insulating boundary.

There obviously exists a vast difference in length scale between the atmosphere/ocean and the laboratory experiment. Furthermore, laboratory experiments do not usually consider radiative transfers, or the phase change of water associated with moist convection. In spite of these simplifications, laboratory models continue to provide valuable insight into turbulent mechanisms in the atmosphere and the ocean, e.g., turbulence measurements in nonpenetrative convection by Adrian et al. (1986) and Prasad and Gonuguntla (1996).

In this paper, the chosen nonpenetrative configuration pertains to a horizontal fluid layer heated from below and insulated from above (see Fig. 1). The energy supplied to the fluid at the lower boundary is absorbed by the fluid, resulting in a gradual increase in the bulk temperature of the fluid over time. In contrast, the fluid in Rayleigh-Bénard convection maintains a steady bulk temperature owing to the removal of heat at the upper boundary at the same rate as the heat influx at the lower boundary. However, it is important to note that because all of the fluid in the nonpenetrative case experiences the same (constant) time rate-of-change of temperature, the mean temperature at any location in the fluid $T(z, t)$ may be decomposed as

$$T(z, t) = T'(z) + \frac{Q_o}{z_*} t$$

where T' is purely a function of z, Q_o is the kinematic heat flux at the lower boundary ($=Q/\rho C_P$), and z_* is the height of the fluid layer. Consequently, the temperature T' is a steady-state quantity (in a Reynolds-averaged sense) and the temperature difference between any two vertically separated points, such as the temperature in the mixed layer T_m and the temperature of the bottom boundary T_b, is constant over the duration of the experiment.

II Problem Definition

Unlike Rayleigh-Bénard convection, there does not exist a prescribed temperature scale for nonpenetrative convection

---

[1] Department of Mechanical Engineering, University of Delaware, Newark, DE 19716-3140

Contributed by the Heat Transfer Division of THE AMERICAN SOCIETY OF MECHANICAL ENGINEERS. Manuscript received by the Heat Transfer Division August 2, 1996; revision received September 18, 1996; Keywords: Natural Convection, Transient & Unsteady Heat, Turbulence. Associate Technical Editor: T. Bergman.

The results show that resistance obtained by definition (b) is zero for cases when the gap conductivity equals the solid conductivities which are also assumed to be equal, and that it is negative for gap conductivities greater than that of the solids. The zero and negative resistance values are important features of the result and represent the actual physical phenomenon. It is also observed that the resistance obtained with definition (a) is positive for all gap conductivities. This is a consequence of the fact that the temperature difference between the gap surfaces will always be positive for any value of gap conductivity. It is, therefore, recommended that one must use definition (b) for computation of constriction resistance in such cases.

References

Das, A. K., and Sadhal, S. S., 1991, "Thermal Constriction Resistance: The Effect of Interstitial Fluid," *Fundamentals of Conduction*, ASME HTD Vol. 173, pp. 35–39.

Das, A. K., and Sadhal, S. S., 1992, "Effect of Interstitial Fluid on Thermal Constriction Resistance," ASME JOURNAL OF HEAT TRANSFER, Vol. 114, No. 4, pp. 1045–1048.

Das, A. K., and Sadhal, S. S., 1995, "A Note on the Evaluation of Thermal Contact Resistance for Non-Zero Thickness Gaps," ASME HTD Vol. 310, pp. 131–138.

Dundurs, J., and Panek, C., 1976, "Heat Conduction Between Bodies With Wavy Surfaces," *International Journal of Heat Mass Transfer*, Vol. 19, No. 7, pp. 731–736.

Fenech, H., and Rohsenow, W. M., 1963, "Prediction of Thermal Conductance of Metallic Surfaces in Contact," ASME JOURNAL OF HEAT TRANSFER, February, pp. 15–24.

Song, S., Yovanovich, M. M., and Nho, K., 1992, "Thermal Gap Conductance: Effects of Gas Pressure and Mechanical Load," *Journal of Thermophysical Heat Transfer*, Vol. 6, No. 1, pp. 62–68.

Veziroglu, T. N., and Chandra, S., 1968, "Thermal Conductance of Two-Dimensional Constrictions," *Progress in Astronautics and Aeronautics, Vol. 21: Thermal Design Principles of Spacecraft and Entry Bodies*, pp. 591–615.

Derivation of Rayleigh Number for Nonpenetrative Thermal Convection

A. K. Prasad[1]

Nomenclature

C_p = specific heat
g = acceleration due to gravity
k = thermal conductivity
Nu = Nusselt number
Pr = Prandtl number
Q = heat flux (W/m^2)
Q_o = kinematic heat flux = $Q/\rho C_p$(K-m/s)
Ra = Rayleigh number
ΔT = temperature scale
z_* = depth of fluid layer

Greek Symbols

β = thermal expansion coefficient
α = thermal diffusivity
λ_T = thickness of conduction layer
ν = kinematic viscosity
ρ = density

Subscripts

b = lower boundary (bottom) of fluid layer
t = upper boundary (top) of fluid layer
m = mixed layer
NP = nonpenetrative
RB = Rayleigh-Benard

I Introduction

A common laboratory model used to simulate thermally induced motions in the atmosphere consists of a shallow layer of fluid heated from below and capped from above by a stable stratified layer (for an example, see Deardorff et al., 1969). The stable layer represents the inversion that caps the turbulent motions in the atmosphere. Over the course of the experiment, heating at the lower boundary drives the turbulent motions, in the form of plumes and thermals, to rise through the depth of the mixed or convecting layer and impact the base of the stable layer, gradually eroding it away. This model mimics the gradual erosion of the inversion layer in the atmosphere over the course of the day, due to the action of buoyancy-driven motions arising from solar heating at the earth's surface. This form of convection is called "penetrative convection," alluding to the penetration of turbulent structures from the mixed layer into the stable inversion layer.

An idealization of the penetrative configuration described above is obtained by replacing the stable inversion layer with a rigid insulating boundary, a situation called nonpenetrative convection. Nonpenetrative convection also occurs in lakes or oceans where the surface layer is evaporatively cooled, and the bottom of the fluid layer forms the rigid insulating boundary.

There obviously exists a vast difference in length scale between the atmosphere/ocean and the laboratory experiment. Furthermore, laboratory experiments do not usually consider radiative transfers, or the phase change of water associated with moist convection. In spite of these simplifications, laboratory models continue to provide valuable insight into turbulent mechanisms in the atmosphere and the ocean, e.g., turbulence measurements in nonpenetrative convection by Adrian et al. (1986) and Prasad and Gonuguntla (1996).

In this paper, the chosen nonpenetrative configuration pertains to a horizontal fluid layer heated from below and insulated from above (see Fig. 1). The energy supplied to the fluid at the lower boundary is absorbed by the fluid, resulting in a gradual increase in the bulk temperature of the fluid over time. In contrast, the fluid in Rayleigh-Bénard convection maintains a steady bulk temperature owing to the removal of heat at the upper boundary at the same rate as the heat influx at the lower boundary. However, it is important to note that because all of the fluid in the nonpenetrative case experiences the same (constant) time rate-of-change of temperature, the mean temperature at any location in the fluid $T(z, t)$ may be decomposed as

$$T(z, t) = T'(z) + \frac{Q_o}{z_*} t$$

where T' is purely a function of z, Q_o is the kinematic heat flux at the lower boundary ($=Q/\rho C_P$), and z_* is the height of the fluid layer. Consequently, the temperature T' is a steady-state quantity (in a Reynolds-averaged sense) and the temperature difference between any two vertically separated points, such as the temperature in the mixed layer T_m and the temperature of the bottom boundary T_b, is constant over the duration of the experiment.

II Problem Definition

Unlike Rayleigh-Bénard convection, there does not exist a prescribed temperature scale for nonpenetrative convection

---

[1] Department of Mechanical Engineering, University of Delaware, Newark, DE 19716-3140

Contributed by the Heat Transfer Division of THE AMERICAN SOCIETY OF MECHANICAL ENGINEERS. Manuscript received by the Heat Transfer Division August 2, 1996; revision received September 18, 1996; Keywords: Natural Convection, Transient & Unsteady Heat, Turbulence. Associate Technical Editor: T. Bergman.

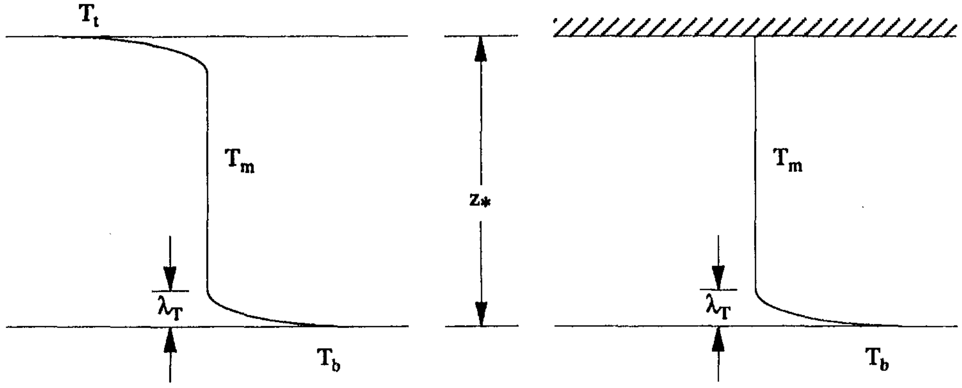

Rayleigh-Benard

Non-Penetrative

Fig. 1 Rayleigh-Bénard versus nonpenetrative thermal convection (adapted from Adrian et al., 1986)

since in the latter it is the heat flux at the lower boundary that is specified. Consequently, it is not possible to calculate directly the Rayleigh number for nonpenetrative convection according to the usual definition,

$$\mathrm{Ra} = \frac{g\beta\Delta T z_*^3}{\nu\alpha} \tag{1}$$

where g is the acceleration due to gravity, β is the thermal expansion coefficient, ΔT is the temperature scale, z_* is the height of the fluid layer, ν is the kinematic viscosity, and α is the thermal diffusivity. In the case of Rayleigh-Bénard convection, $\Delta T = T_b - T_t$, i.e., the prescribed temperature difference between the bottom and top boundaries, respectively.

In order to circumvent the lack of a prescribed temperature scale in nonpenetrative convection, an alternative definition using the heat flux at the lower boundary, Q, could be proposed as follows:

$$\mathrm{Ra}' = \frac{g\beta(Q/k)z_*^4}{\nu\alpha}$$

where k is the thermal conductivity. However, the above definition could be rearranged as the product of two terms:

$$\mathrm{Ra}' = \left[\frac{g\beta\Delta T z_*^3}{\nu\alpha}\right]\left[\frac{Qz_*}{k\Delta T}\right].$$

where the first term is the conventional definition of the Rayleigh number as expressed by Eq. 1, and the second term, $Qz_*/k\Delta T$ is the Nusselt number. And, since the Nusselt number is significantly larger than unity for turbulent convection, Ra′ greatly exceeds Ra even when the two situations are dynamically similar. It should be noted that while the heat flux in Rayleigh-Bénard convection is a constant independent of height z, the same is not true for nonpenetrative convection in which the heat flux decreases linearly from a maximum, at the lower boundary, to zero, at the upper boundary. It might, therefore, be more appropriate to use the average value of $Q/2$ instead of Q in the expression for Ra′ for nonpenetrative convection. However, since Nu can take on values that are in the tens or even hundreds in laboratory experiments, the factor of two will not resolve the stated problem.

How, then, does one obtain an equivalent Rayleigh number for nonpenetrative convection which will convey the same information as in the case of Rayleigh-Bénard convection? It is obvious that the missing piece of information is a suitable temperature scale, viz., the difference in the temperature between the lower boundary T_b and the mixed layer T_m. The following analysis provides a method to derive $T_b - T_m$ and the Rayleigh number.

III Rayleigh Number Derivation

We begin by examining correlations for the Nusselt number obtained from previous studies of Rayleigh-Bénard convection. Goldstein et al. (1990) list a summary of such correlations. A significant fraction of these studies report correlations of the form: $\mathrm{Nu} \sim \mathrm{Ra}^{1/3}$, while other studies report exponents slightly smaller than one-third. Goldstein et al.'s (1990) study of high Rayleigh number convection also yielded an exponent of one-third. Of all the studies summarized in Goldstein et al. (1990), the work of Globe and Dropkin (1959) is perhaps the most comprehensive in terms of the range of Prandtl and Rayleigh numbers. They give

$$\mathrm{Nu} = 0.069\,\mathrm{Pr}^{0.074}\,\mathrm{Ra}^{1/3} \tag{2}$$

which is valid for $0.02 < \mathrm{Pr} < 8750$ and $1.51 \times 10^5 < \mathrm{Ra} < 6.76 \times 10^8$. The one-third exponent on the Rayleigh number in Eq. 2 agrees with the classical argument given by Thomas and Townsend (1957) that when the convection is highly turbulent, the heat-flux at the boundary is independent of the height of the fluid layer. In this case, the mixed layer has a constant temperature T_m, whereas all of the temperature drop occurs adjacent to the boundaries, as shown in Fig. 1.

Consider now a situation wherein the upper boundary condition in Rayleigh-Bénard convection is changed from one of constant temperature to one of zero heat-flux and everything else remains unchanged (such as the fluid properties, the height of the fluid layer, and the heat flux at the lower boundary) in order to obtain nonpenetrative convection. What are the corresponding Nusselt and the Rayleigh numbers?

Again, assuming that the convection is highly turbulent, the upper boundary condition does not significantly influence the lower boundary so it is reasonable to assume that the thickness of the conduction layer, λ_T, is identical in both cases since the heat flux is chosen to be identical. Therefore, the temperature drop across the conduction layer must also be identical in both cases. Of course, there exists an equal temperature drop across the conduction layer adjacent to the upper boundary in the Rayleigh-Bénard case, whereas the nonpenetrative case does not experience this additional drop, giving $T_b - T_t = 2(T_b - T_m)$.

Using the subscripts RB for Rayleigh-Bénard and NP for nonpenetrative, we can write (see Fig. 1)

$$\mathrm{Nu}_{\mathrm{RB}} = \frac{\partial T/\partial z|_{z=0}}{(T_b - T_t)/z_*} = \frac{(T_b - T_t)/2/\lambda_T}{(T_b - T_t)/z_*} = \frac{z_*}{2\lambda_T}.$$

Similarly, we obtain for the nonpenetrative case

$$\mathrm{Nu}_{\mathrm{NP}} = \frac{\partial T/\partial z|_{z=0}}{(T_b - T_m)/z_*} = \frac{(T_b - T_m)/\lambda_T}{(T_b - T_m)/z_*} = \frac{z_*}{\lambda_T}.$$

Since λ_T is identical for both cases as explained earlier,

$$\mathrm{Nu}_{\mathrm{NP}} = 2\,\mathrm{Nu}_{\mathrm{RB}}. \tag{3}$$

For the Rayleigh number

$$\mathrm{Ra}_{\mathrm{RB}} = \frac{g\beta(T_b - T_t)z_*^3}{\nu\alpha}$$

and

$$\mathrm{Ra}_{\mathrm{NP}} = \frac{g\beta(T_b - T_m)z_*^3}{\nu\alpha} = \frac{g\beta(T_b - T_t)z_*^3}{2\nu\alpha}.$$

Therefore,

$$\mathrm{Ra}_{\mathrm{NP}} = \mathrm{Ra}_{\mathrm{RB}}/2 \tag{4}$$

for the same heat flux at the lower boundary. Temporarily absorbing the Prandtl number dependence in Eq. 2 into the constant, we have

$$\mathrm{Nu}_{\mathrm{RB}} = C_{\mathrm{RB}}\mathrm{Ra}_{\mathrm{RB}}^{1/3}.$$

Similarly,

$$\mathrm{Nu}_{\mathrm{NP}} = C_{\mathrm{NP}}\mathrm{Ra}_{\mathrm{NP}}^{1/3}.$$

Taking the ratio of the above two expressions, and using the results from Eq. 3 and 4, we get

$$C_{\mathrm{NP}} = 2^{4/3}C_{\mathrm{RB}}. \tag{5}$$

Substituting Eq. 5 into Eq. 2, we have

$$\mathrm{Nu}_{\mathrm{NP}} = 0.174\,\mathrm{Pr}^{0.074}\,\mathrm{Ra}_{\mathrm{NP}}^{1/3}$$

which may be rewritten as

$$Q = 0.174\,\mathrm{Pr}^{0.074}k\left[\frac{g\beta}{\nu\alpha}\right]^{1/3}(T_b - T_m)^{4/3}. \tag{6}$$

IV Comparison With Previous Experiments

Deardorff et al. (1969) present a version of Eq. 6 which ignores the Pr dependence. They use

$$Q = Ck\left[\frac{g\beta}{\nu\alpha}\right]^{1/3}(T_b - T_m)^{4/3} \tag{7}$$

and state that C is a universal constant. By substituting $\mathrm{Pr} = 5.5$ in Eq. 6 (midway in the range $4 \le \mathrm{Pr} \le 7$ used by Deardorff et al. in their penetrative convection experiment in a water tank), the present analysis yields $C = 0.197$. Deardorff et al. (1969) quote values for C between 0.18 and 0.21, in good agreement with our analysis.

Adrian et al. (1986), using the same expression (Eq. 7) as Deardorff et al. (1969), find $C = 3.49^{-4/3} = 0.189$ for nonpenetrative convection in water with $4.5 < \mathrm{Pr} < 6$, which is also in good agreement with our analysis.

Thomas and Townsend (1957) conducted temperature measurements in turbulent convection of air over a heated horizontal surface. They expressed their results in the form:

$$\log\frac{T_b}{T_m} = A\left[\left(\frac{Q}{\rho C_p T}\right)^3\frac{1}{\alpha g}\right]^{1/4}$$

where T is the absolute mean temperature (in their air-experiment, $T = \beta^{-1}$), and A is a function of the Prandtl number. After rearrangement, the above expression gives:

$$Q = A^{-4/3}k\left[\frac{\beta g}{\alpha^2}\right]^{1/3}(T_b - T_m)^{4/3}.$$

Upon comparison with Eqs. 6 and 7 it is apparent that

$$A^{-4/3}\left(\frac{\nu}{\alpha}\right)^{1/3} = 0.174\,\mathrm{Pr}^{0.074}(= C). \tag{8}$$

Using $\mathrm{Pr} = 0.71$ for air in the range of temperatures given by Thomas and Townsend (1957), our analysis predicts $A = 3.47$; a value consistent with the results of Thomas and Townsend (1957) who give $A = 3.4$. Townsend (1959) describes additional temperature measurements in air over a heated horizontal surface and finds $A = 3.14$, which matches less satisfactorily with our results. Finally, Townsend (1964) provides an expression identical to Eq. 7 with $C = 0.193$ for "fluids with linear expansion." This value of C is ostensibly based on Townsend's (1959) measurements in air over a heated horizontal surface and is obtained by evaluating the left-hand-side of Eq. 8 with $A = 3.14$ and $\mathrm{Pr} = 0.71$, whereas our analysis (right-hand-side of Eq. 8) gives $C = 0.170$.

The value of 0.193 given by Townsend (1964), we believe, is obtained from earlier measurements in air, not water. Confusion has been created owing to the fact that Townsend (1964) states this value of C in a paper describing experiments using water without correcting for the ten-fold difference in Prandtl number. Subsequent researchers have also applied this value to experiments in water without correcting for the different Prandtl number. The present derivation removes this confusion by including the Prandtl number, thus increasing the applicability of the result.

Equation 6 can be solved to obtain $(T_b - T_m)$, the desired temperature scale for nonpenetrative convection. Using this result, the Rayleigh number can be cast in terms of the heat-flux Q, which is the prescribed quantity for nonpenetrative convection where

$$\mathrm{Ra}_{\mathrm{NP}} = 3.71\left[\frac{g\beta z_*^3}{\nu\alpha}\,\frac{Qz_*}{k}\right]^{3/4}\mathrm{Pr}^{-0.056}. \tag{9}$$

Equation 9 is the desired expression for the Rayleigh number which can now be determined directly by knowing the heat-flux Q, and is, therefore, suitable for nonpenetrative convection. Equation 9 accurately conveys the dynamic state of nonpenetrative convection in the same sense that Eq. 2 does for Rayleigh-Bénard convection.

V Conclusions

A derivation is presented for the Rayleigh number in nonpenetrative thermal convection. The derivation assumes that the flow is driven strongly enough by buoyancy to be in the turbulent regime and incorporates the classical position that the heat flux at the boundary is independent of the layer height ($\mathrm{Nu} \sim \mathrm{Ra}^{1/3}$). The analysis first presents a method to derive the temperature difference between the lower boundary and mixed layer. The result is shown to agree well with previous experiments. The temperature difference is then used to obtain an expression for the Rayleigh number.

References

Adrian, R. J., Ferreira, R. T. D. S., and Boberg, T., 1986, "Turbulent Thermal Convection in Wide Horizontal Fluid Layers," *Experiments in Fluids*, Vol. 4, pp. 121–141.

Deardorff, J. W., Willis, G. E., and Lilly, D. K., 1969, "Laboratory Investigation of Non-Steady Penetrative Convection," *Journal of Fluid Mechanics*, Vol. 35, pp. 7–31.

Globe, S., and Dropkin, D., 1959, "Natural-Convection Heat Transfer in Liquids Confined by Two Horizontal Plates and Heated From Below," ASME JOURNAL OF HEAT TRANSFER, Vol. 81, pp. 24–28.

Goldstein, R. J., Chiang, H. D., and See, D. L., 1990, "High-Rayleigh-Number Convection in a Horizontal Enclosure," *Journal of Fluid Mechanics*, Vol. 213, pp. 111–126.

Prasad, A. K., and Gonuguntla, P. V., 1996, "Turbulence Measurements in Nonpenetrative Thermal Convection," *Physics of Fluids*, Vol. 8, pp. 2460–2470.

Thomas, D. B., and Townsend, A. A., 1957, "Turbulent Convection Over a Heated Horizontal Surface," *Journal of Fluid Mechanics*, Vol. 2, pp. 473–492.

Townsend, A. A., 1959, "Turbulent Fluctuations Over a Heated Horizontal Surface," *Journal of Fluid Mechanics*, Vol. 5, pp. 209–241.

Townsend, A. A., 1964, "Convection in Water Over Ice," *Quarterly Journal of the Royal Meteorological Society*, Vol. 90, pp. 248–259.

Similarity Solutions of Natural Convection With Internal Heat Generation

J. C. Crepeau[1], **and R. Clarksean**[2]

Nomenclature

c_p = specific heat at constant pressure
$f(\eta)$ = function defined in Eq. (5)
$f'(\eta)$ = nondimensional velocity
g = gravity constant
Gr_x = Grashof number, $g\beta(T_s - T_\infty)x^3/\nu^2$
k = thermal conductivity
L = length
Nu = Nusselt number
Pr = Prandtl number
q''' = internal heat generation per unit volume
T = temperature
T_s = surface temperature
T_∞ = ambient temperature
u, v = velocity in the x, y direction
x, y = Cartesian coordinates
β = volumetric coefficient of thermal expansion
η = similarity variable defined in Eq. (4)
ν = kinematic viscosity
ρ = density
ψ = similarity variable defined in Eq. (5)
$\theta(\eta)$ = nondimensional temperature, $(T - T_\infty)/(T_s - T_\infty)$

1 Introduction

A large number of physical phenomena involve natural convection driven by internal heat generation. An example includes convection in the earth's mantle (McKenzie, et al., 1974), but perhaps the most widespread application is in the field of nuclear energy. In nuclear reactor cores (Smith and Hammitt, 1966) and in postaccident heat removal (Baker et al., 1976), natural convection driven by internal heat generation plays an important role in the overall heat transfer. Natural convection with internal heat generation also applies to fire and combustion modeling (Delichatsios, 1988), the development of a metal waste form from spent nuclear fuel (Westphal, 1994), and for the storage of spent nuclear fuel.

Theoretical, numerical, and experimental analyses have been completed on natural convection with internal heat generation. Typical examples include Tritton and Zarraga (1967), Roberts (1967), and Jahn and Reineke (1974). In view of the amount of work done on natural convection with internal heat generation, it is worthwhile to determine if similarity solutions exist for this system. Similarity solutions of natural convection along a vertical isothermal plate have been shown by Ostrach (1953). The similarity solution results are useful in understanding the interaction of the flow field and temperature field. The trends exhibited can allow the scientist or engineer to determine over what range of internal heat generation rates and Prandtl numbers the addition of internal heat generation needs to be considered.

A similarity solution for a fluid with an exponentially decaying heat generation term and a constant temperature vertical plate is developed. An exponential form is used for the internal energy generation term. All of the numerical solutions were obtained through the use of *Mathematica* (Wolfram, 1991). The procedure used to solve the resultant differential equations was validated by obtaining the solutions for a constant temperature vertical plate without internal heat generation as shown in Fig. 1.

2 Problem Derivation

Consider a vertical plate in a semi-infinite quiescent fluid. The temperature of the plate is held at constant value T_s, and the fluid has an internal volumetric heat generation, q'''. By taking x to be along the plate in the vertical direction, and y perpendicular to the plate, the governing equations (continuity, momentum, and energy) for the Boussinesq approximation within the boundary layer are given by,

$$\frac{\partial u}{\partial x} + \frac{\partial v}{\partial y} = 0 \tag{1}$$

$$u\frac{\partial u}{\partial x} + v\frac{\partial u}{\partial y} = g\beta(T - T_\infty) + \nu\frac{\partial^2 u}{\partial y^2} \tag{2}$$

$$\rho c_p\left(u\frac{\partial T}{\partial x} + v\frac{\partial T}{\partial y}\right) = k\frac{\partial^2 T}{\partial y^2} + q'''. \tag{3}$$

Similarity variables of the form (Jaluria, 1980),

$$\eta(x, y) = \frac{y}{x}\left(\frac{\mathrm{Gr}_x}{4}\right)^{1/4} \tag{4}$$

$$\psi(x, y) = 4\nu f(\eta)\left(\frac{\mathrm{Gr}_x}{4}\right)^{1/4} \tag{5}$$

are introduced into Eqs. 1–3. In order for a similarity condition to exist, the volumetric heat generation must be of the form

$$q''' = \frac{k(T_s - T_\infty)}{x^2}\left(\frac{\mathrm{Gr}_x}{4}\right)e^{-\eta}.$$

By inserting the similarity variables and the nondimensional temperature into the governing equations, the following similarity equations result:

---

[1] Department of Mechanical Engineering, University of Idaho, P.O. Box 50778, Idaho Falls, ID 83405. Assoc. Mem. ASME.

[2] Clarksean and Associates, Ottertail, MN 56571. Assoc. Mem. ASME.

Contributed by the Heat Transfer Division of THE AMERICAN SOCIETY OF MECHANICAL ENGINEERS. Manuscript received by the Heat Transfer Division January 11, 1996; revision received August 29, 1996; Keywords: Liquid Metals, Mat'ls. Processing & Manufacturing Process, Natural Convection. Associate Technical Editor: K. Vafai.

References

Adrian, R. J., Ferreira, R. T. D. S., and Boberg, T., 1986, "Turbulent Thermal Convection in Wide Horizontal Fluid Layers," *Experiments in Fluids*, Vol. 4, pp. 121–141.

Deardorff, J. W., Willis, G. E., and Lilly, D. K., 1969, "Laboratory Investigation of Non-Steady Penetrative Convection," *Journal of Fluid Mechanics*, Vol. 35, pp. 7–31.

Globe, S., and Dropkin, D., 1959, "Natural-Convection Heat Transfer in Liquids Confined by Two Horizontal Plates and Heated From Below," ASME JOURNAL OF HEAT TRANSFER, Vol. 81, pp. 24–28.

Goldstein, R. J., Chiang, H. D., and See, D. L., 1990, "High-Rayleigh-Number Convection in a Horizontal Enclosure," *Journal of Fluid Mechanics*, Vol. 213, pp. 111–126.

Prasad, A. K., and Gonuguntla, P. V., 1996, "Turbulence Measurements in Nonpenetrative Thermal Convection," *Physics of Fluids*, Vol. 8, pp. 2460–2470.

Thomas, D. B., and Townsend, A. A., 1957, "Turbulent Convection Over a Heated Horizontal Surface," *Journal of Fluid Mechanics*, Vol. 2, pp. 473–492.

Townsend, A. A., 1959, "Turbulent Fluctuations Over a Heated Horizontal Surface," *Journal of Fluid Mechanics*, Vol. 5, pp. 209–241.

Townsend, A. A., 1964, "Convection in Water Over Ice," *Quarterly Journal of the Royal Meteorological Society*, Vol. 90, pp. 248–259.

Similarity Solutions of Natural Convection With Internal Heat Generation

J. C. Crepeau[1], and R. Clarksean[2]

Nomenclature

c_p = specific heat at constant pressure
$f(\eta)$ = function defined in Eq. (5)
$f'(\eta)$ = nondimensional velocity
g = gravity constant
Gr_x = Grashof number, $g\beta(T_s - T_\infty)x^3/\nu^2$
k = thermal conductivity
L = length
Nu = Nusselt number
Pr = Prandtl number
q''' = internal heat generation per unit volume
T = temperature
T_s = surface temperature
T_∞ = ambient temperature
u, v = velocity in the x, y direction
x, y = Cartesian coordinates
β = volumetric coefficient of thermal expansion
η = similarity variable defined in Eq. (4)
ν = kinematic viscosity
ρ = density
ψ = similarity variable defined in Eq. (5)
$\theta(\eta)$ = nondimensional temperature, $(T - T_\infty)/(T_s - T_\infty)$

1 Introduction

A large number of physical phenomena involve natural convection driven by internal heat generation. An example includes convection in the earth's mantle (McKenzie, et al., 1974), but perhaps the most widespread application is in the field of nuclear energy. In nuclear reactor cores (Smith and Hammitt, 1966) and in postaccident heat removal (Baker et al., 1976), natural convection driven by internal heat generation plays an important role in the overall heat transfer. Natural convection with internal heat generation also applies to fire and combustion modeling (Delichatsios, 1988), the development of a metal waste form from spent nuclear fuel (Westphal, 1994), and for the storage of spent nuclear fuel.

Theoretical, numerical, and experimental analyses have been completed on natural convection with internal heat generation. Typical examples include Tritton and Zarraga (1967), Roberts (1967), and Jahn and Reineke (1974). In view of the amount of work done on natural convection with internal heat generation, it is worthwhile to determine if similarity solutions exist for this system. Similarity solutions of natural convection along a vertical isothermal plate have been shown by Ostrach (1953). The similarity solution results are useful in understanding the interaction of the flow field and temperature field. The trends exhibited can allow the scientist or engineer to determine over what range of internal heat generation rates and Prandtl numbers the addition of internal heat generation needs to be considered.

A similarity solution for a fluid with an exponentially decaying heat generation term and a constant temperature vertical plate is developed. An exponential form is used for the internal energy generation term. All of the numerical solutions were obtained through the use of *Mathematica* (Wolfram, 1991). The procedure used to solve the resultant differential equations was validated by obtaining the solutions for a constant temperature vertical plate without internal heat generation as shown in Fig. 1.

2 Problem Derivation

Consider a vertical plate in a semi-infinite quiescent fluid. The temperature of the plate is held at constant value T_s, and the fluid has an internal volumetric heat generation, q'''. By taking x to be along the plate in the vertical direction, and y perpendicular to the plate, the governing equations (continuity, momentum, and energy) for the Boussinesq approximation within the boundary layer are given by,

$$\frac{\partial u}{\partial x} + \frac{\partial v}{\partial y} = 0 \tag{1}$$

$$u\frac{\partial u}{\partial x} + v\frac{\partial u}{\partial y} = g\beta(T - T_\infty) + \nu\frac{\partial^2 u}{\partial y^2} \tag{2}$$

$$\rho c_p\left(u\frac{\partial T}{\partial x} + v\frac{\partial T}{\partial y}\right) = k\frac{\partial^2 T}{\partial y^2} + q'''. \tag{3}$$

Similarity variables of the form (Jaluria, 1980),

$$\eta(x, y) = \frac{y}{x}\left(\frac{\mathrm{Gr}_x}{4}\right)^{1/4} \tag{4}$$

$$\psi(x, y) = 4\nu f(\eta)\left(\frac{\mathrm{Gr}_x}{4}\right)^{1/4} \tag{5}$$

are introduced into Eqs. 1–3. In order for a similarity condition to exist, the volumetric heat generation must be of the form

$$q''' = \frac{k(T_s - T_\infty)}{x^2}\left(\frac{\mathrm{Gr}_x}{4}\right)e^{-\eta}.$$

By inserting the similarity variables and the nondimensional temperature into the governing equations, the following similarity equations result:

---

[1] Department of Mechanical Engineering, University of Idaho, P.O. Box 50778, Idaho Falls, ID 83405. Assoc. Mem. ASME.

[2] Clarksean and Associates, Ottertail, MN 56571. Assoc. Mem. ASME.

Contributed by the Heat Transfer Division of THE AMERICAN SOCIETY OF MECHANICAL ENGINEERS. Manuscript received by the Heat Transfer Division January 11, 1996; revision received August 29, 1996; Keywords: Liquid Metals, Mat'ls. Processing & Manufacturing Process, Natural Convection. Associate Technical Editor: K. Vafai.

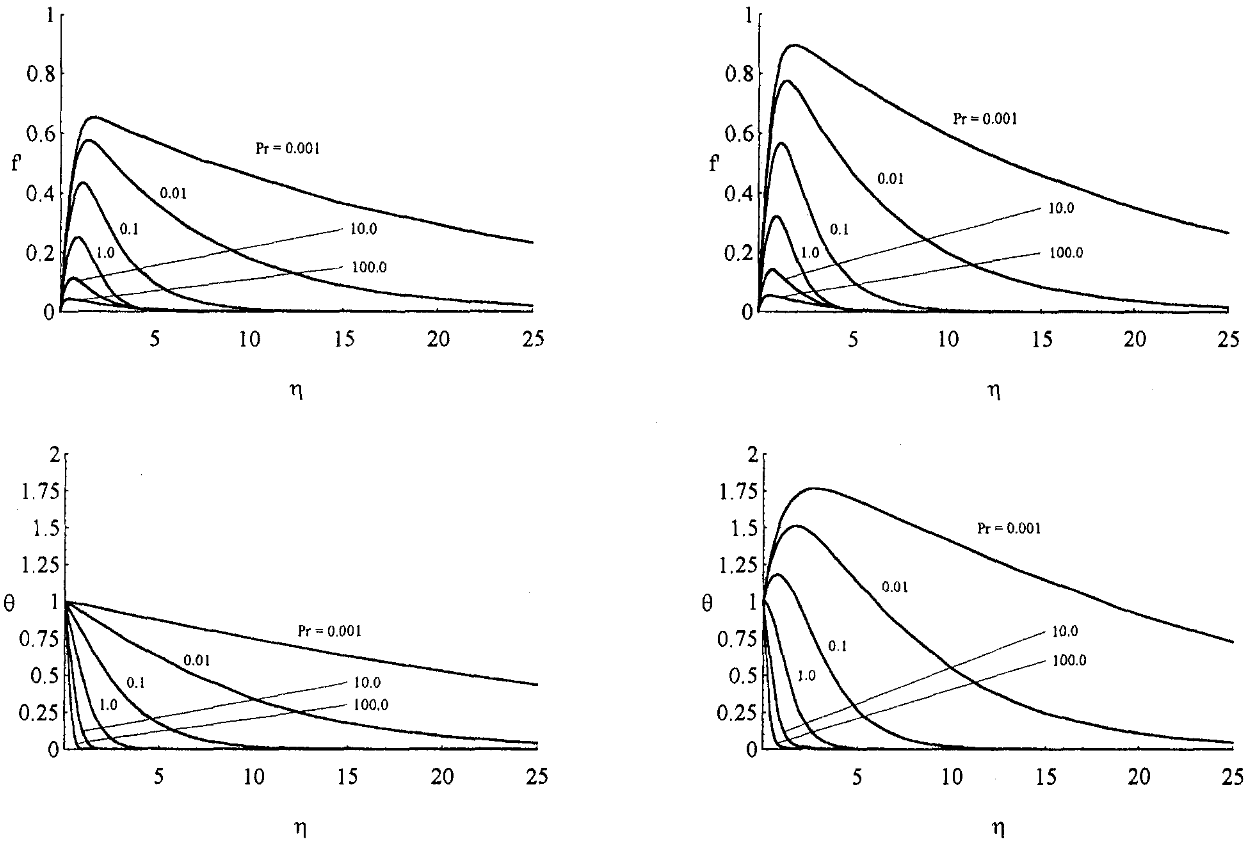

Fig. 1 Solutions of Eqs. 6 and 7 for a constant temperature plate and various Prandtl numbers. Top curves represent velocity profiles, bottom curves temperature profiles. Curves on the left are for fluids without internal heat generation; curves on the right are for fluids with internal heat generation.

$$f''' + 3ff'' - 2f'^2 + \theta(\eta) = 0 \tag{6}$$

$$\theta'' + 3\,\mathrm{Pr} f\theta' + e^{-\eta} = 0 \tag{7}$$

with boundary conditions,

$$f(0) = f'(0) = f'(\infty) = 0$$

$$\theta(0) = 1,\ \theta(\infty) = 0.$$

The exponentially decaying heat generation model can be used in mixtures where a radioactive material is surrounded by inert alloys and has been used to model electromagnetic heating of materials (Şahin, 1992).

3 Results and Discussion

The solutions to Eqs. 6 and 7 over a range of Prandtl numbers are given in Fig. 1. The plots on the left hand side are for a fluid without the exponentially decaying heat generation term, while those on the right include $e^{-\eta}$. The nondimensional velocity f' plots are on the top, and the nondimensional temperature θ curves are shown on the bottom. The effect of the internal heat generation is especially pronounced in the low Prandtl number profiles.

It is interesting to note in Fig. 1 that $d\theta/d\eta|_{\eta=0}$ is zero for a Pr of approximately one. At this point, there is no heat transfer to or from the fluid. The flow develops as a result of the internal energy generation and is not impacted by the constant temperature vertical plate. For Pr < 1, $\theta_{\max} > 1$, which indicates the importance of the thermal properties.

The similarity velocity f' is greater when internal energy generation exists. This is logical because the internal energy generation results in an increase in the buoyancy forces which will induce more flow along the plate. In Fig. 1 the location of the maximum velocity occurs at roughly the same value of η for Pr ≤ 1. For Pr ≥ 1, the location of the maximum velocity occurs at a larger distance from the plate, indicating the influence of the increased viscosity.

From the figure, the average Nusselt number along a plate of length L can be determined (Incropera and DeWitt, 1990) by,

$$\overline{\mathrm{Nu}}_L = -\frac{4}{3}\left(\frac{\mathrm{Gr}_L}{4}\right)^{1/4} \frac{d\theta}{d\eta}\bigg|_{\eta=0}$$

where the gradients are shown in Table 1. In addition to heat transfer applications, determination of the Nusselt number is important in solidification processes since convection is the dominant heat transfer mode by an order of magnitude over conduction (Yao, 1984). Not only does an enhanced Nusselt number cause tremendous changes in the solidification rate (Yao and Prusa, 1989), but it also affects the shape of the solid-liquid interface and the alloy structure of the solid (Viskanta, 1988).

4 Conclusions

Similarity solutions have been developed to analyze the effect of an exponential form for internal heat generation for a constant temperature vertical plate. A range of Pr has been examined. As expected, the presence of internal energy generation leads to increased flow, and in some cases, temperatures that exceed the wall temperature, especially for fluids with Pr < 1.0. The effect of internal heat generation is important in several applications that include reactor safety analyses, metal waste form development for spent nuclear fuel, fire and combustion studies, and the storage of radioactive materials.

Table 1 Computed values of $d\theta/d\eta\vert_{\eta=0}$ for the similarity equations for a constant temperature plate (Equations 6 and 7) with and without internal heat generation (q''')

Pr	$d\theta/d\eta\vert_{\eta=0}$, constant temperature plate	
	without q'''	with q'''
0.001	-0.02640	0.9392
0.01	-0.08059	0.8236
0.1	-0.2302	0.5425
1.0	-0.5671	0.005786
10.0	-1.169	-0.7963
100.0	-2.191	-1.979

5 Acknowledgments

The authors gratefully acknowledge the support of an Associated Western Universities Summer Faculty Fellowship at Argonne National Laboratory-West. We would also like to thank Dr. Charles Solbrig of ANL-W for his help and insight.

References

Baker, L., Faw, R. E., and Kulacki, F. A., 1976, "Postaccident Heat Removal–Part I: Heat Transfer Within an Internally Heated, Nonboiling Liquid Layer," *Nucl. Sci. Eng.*, Vol. 61, pp. 222–230.

Delichatsios, M. A., 1988, "Air Entrainment Into Buoyant Jet Flames and Pool Fires," *The SFPA Handbook of Fire Protection Engineering*, P. J. DiNenno et al., eds., NFPA Publications, Quincy, MA, pp. 306-314.

Incropera, F. P., and DeWitt, D. P., 1990, *Introduction to Heat Transfer*, Wiley, New York, pp. 496–497.

Jahn, M., and Reineke, H. H., 1974, "Free Convection Heat Transfer with Internal Energy Sources; Calculations and Measurements," Paper NC 2.8, *Proceedings, 5th International Heat Transfer Conference*, Tokyo, Japan, pp. 74–78.

Jaluria, Y., 1980, *Natural Convection Heat and Mass Transfer*, Pergamon, New York, pp. 10–73.

McKenzie, D. P., Roberts, J. M., and Weiss, N. O., 1974, "Convection in the Earth's Mantle: Towards a Numerical Simulation," *Journal of Fluid Mech.*, Vol. 62, pp. 465–538.

Ostrach, S., 1953, "An Analysis of Laminar Free Convection Flow and Heat Transfer About a Flat Plate Parallel to the Direction of the Generating Body Force," NACA Technical Report 1111.

Roberts, P. H., 1967, "Convection in Horizontal Layers With Internal Heat Generation. Theory," *Journal of Fluid Mech.*, Vol. 30, pp. 33–49.

Şahin, A. Z., 1992, "Transient Heat Conduction in Semi-Infinite Solid with Spatially Decaying Exponential Heat Generation," *Int. Comm. Heat Mass Transfer*, Vol. 19, pp. 349–358.

Smith, W., and Hammitt, F. G., 1966, "Natural Convection in a Rectangular Cavity with Internal Heat Generation," *Nucl. Sci. Eng.*, Vol. 25, pp. 328–342.

Tritton, D. J., and Zarraga, M. N., 1967, "Convection in Horizontal Layers With Internal Heat Generation. Experiments," *Journal of Fluid Mech.*, Vol. 30, pp. 21–31.

Viskanta, R., 1988, "Heat Transfer During Melting and Solidification of Metals," ASME JOURNAL OF HEAT TRANSFER, Vol. 110, pp. 1205–1219.

Westphal, B. R., Keiser, D. D., Rigg, R. H., and Laug, D. V., 1994, "Production of Metal Waste Forms From Spent Nuclear Fuel Treatment," DOE Spent Nuclear Fuel Conference, Salt Lake City, UT, pp. 288–294.

Wolfram, S., 1991, *Mathematica*, Addison–Wesley, Reading, MA.

Yao, L. S., 1984, "Natural Convection Effects in the Continuous Casting of a Horizontal Cylinder," *Int. J. Heat Mass Transfer*, Vol. 114, pp. 773–777.

Yao, L. S., and Prusa, J., 1989, "Melting and Freezing," *Advances Heat Transfer*, J. P. Hartnett and T. F. Irvine, eds., Vol. 19, Academic, San Diego, pp. 1–95.

Benchmark Solutions of Radiative Heat Transfer Within Nonhomogeneous Participating Media Using the Monte Carlo and YIX Method

Pei-feng Hsu,[1] J. T. Farmer[2]

Introduction

Solutions of radiative heat transfer in fire and combustion systems have been an important and active research subject in recent years. Most of the applications encountered in actual systems contain nonhomogeneous participating media. It is important that the flames and combustion systems are treated as such due to the non-uniform distributions of temperature and absorbing gaseous species, and participating particle concentrations. While several methods (Siegel and Howell, 1992) have treated some benchmarks successfully, the lack of the direct comparisons of any nonhomogeneous medium benchmark solution using different methods motivated the current study. In this study, we use two different methods (one stochastic—the Monte Carlo, and one deterministic—the YIX) to solve radiative transfer within the three-dimensional, nonhomogeneous, absorbing, emitting, scattering media and compare the solution differences between the two methods. The results are tabulated for future comparisons with other solution techniques.

In the first Symposium on Solution Methods for Radiative Heat Transfer in Participating Media at the 1992 National Heat Transfer Conference (Tong and Skocypec, 1992), the YIX (Hsu et al., 1993) and the Monte Carlo (M.C.) methods (Farmer and Howell, 1994) were shown to be able to solve complicated radiative heat transfer problems that have nonhomogeneous and nongray participating media. It was later shown that the differences between the two methods are within five percent (Hsu, 1994). Our experience leads us to suspect that the difference in spectral integration techniques is major cause of discrepancy. One of the purposes of this study is to confirm the agreement of the two methods for a series of gray nonhomogeneous media with and without anisotropic scattering as a first step.

Benchmark Problems

The geometry of the problem is a unit cube with black walls. Several different cases are treated. All cases have similarly shaped optical thickness (τ = extinction coefficient times the side length) distribution given by Eq. (1), i.e.,

---

[1] Mechanical & Aerospace Engineering Programs, Florida Institute of Technology, Melbourne, FL

[2] Thermal and Life Support Division, NASA Marshall Space Flight Center, Huntsville, AL

Contributed by the Heat Transfer Division for publication in the JOURNAL OF HEAT TRANSFER. Manuscript received by the Heat Transfer Division February 6, 1996; revision received September 30, 1996; Keywords: Combustion, Numerical Methods, Radiation. Associate Technical Editor: M. Modest.

Table 1 Computed values of $d\theta/d\eta|_{\eta=0}$ for the similarity equations for a constant temperature plate (Equations 6 and 7) with and without internal heat generation (q''')

Pr	$d\theta/d\eta\|_{\eta=0}$, constant temperature plate	
	without q'''	with q'''
0.001	-0.02640	0.9392
0.01	-0.08059	0.8236
0.1	-0.2302	0.5425
1.0	-0.5671	0.005786
10.0	-1.169	-0.7963
100.0	-2.191	-1.979

5 Acknowledgments

The authors gratefully acknowledge the support of an Associated Western Universities Summer Faculty Fellowship at Argonne National Laboratory-West. We would also like to thank Dr. Charles Solbrig of ANL-W for his help and insight.

References

Baker, L., Faw, R. E., and Kulacki, F. A., 1976, "Postaccident Heat Removal-Part I: Heat Transfer Within an Internally Heated, Nonboiling Liquid Layer," *Nucl. Sci. Eng.*, Vol. 61, pp. 222–230.

Delichatsios, M. A., 1988, "Air Entrainment Into Buoyant Jet Flames and Pool Fires," *The SFPA Handbook of Fire Protection Engineering*, P. J. DiNenno et al., eds., NFPA Publications, Quincy, MA, pp. 306-314.

Incropera, F. P., and DeWitt, D. P., 1990, *Introduction to Heat Transfer*, Wiley, New York, pp. 496–497.

Jahn, M., and Reineke, H. H., 1974, "Free Convection Heat Transfer with Internal Energy Sources; Calculations and Measurements," Paper NC 2.8, *Proceedings, 5th International Heat Transfer Conference*, Tokyo, Japan, pp. 74–78.

Jaluria, Y., 1980, *Natural Convection Heat and Mass Transfer*, Pergamon, New York, pp. 10–73.

McKenzie, D. P., Roberts, J. M., and Weiss, N. O., 1974, "Convection in the Earth's Mantle: Towards a Numerical Simulation," *Journal of Fluid Mech.*, Vol. 62, pp. 465–538.

Ostrach, S., 1953, "An Analysis of Laminar Free Convection Flow and Heat Transfer About a Flat Plate Parallel to the Direction of the Generating Body Force," NACA Technical Report 1111.

Roberts, P. H., 1967, "Convection in Horizontal Layers With Internal Heat Generation. Theory," *Journal of Fluid Mech.*, Vol. 30, pp. 33–49.

Şahin, A. Z., 1992, "Transient Heat Conduction in Semi-Infinite Solid with Spatially Decaying Exponential Heat Generation," *Int. Comm. Heat Mass Transfer*, Vol. 19, pp. 349–358.

Smith, W., and Hammitt, F. G., 1966, "Natural Convection in a Rectangular Cavity with Internal Heat Generation," *Nucl. Sci. Eng.*, Vol. 25, pp. 328–342.

Tritton, D. J., and Zarraga, M. N., 1967, "Convection in Horizontal Layers With Internal Heat Generation. Experiments," *Journal of Fluid Mech.*, Vol. 30, pp. 21–31.

Viskanta, R., 1988, "Heat Transfer During Melting and Solidification of Metals," ASME JOURNAL OF HEAT TRANSFER, Vol. 110, pp. 1205–1219.

Westphal, B. R., Keiser, D. D., Rigg, R. H., and Laug, D. V., 1994, "Production of Metal Waste Forms From Spent Nuclear Fuel Treatment," DOE Spent Nuclear Fuel Conference, Salt Lake City, UT, pp. 288–294.

Wolfram, S., 1991, *Mathematica*, Addison-Wesley, Reading, MA.

Yao, L. S., 1984, "Natural Convection Effects in the Continuous Casting of a Horizontal Cylinder," *Int. J. Heat Mass Transfer*, Vol. 114, pp. 773–777.

Yao, L. S., and Prusa, J., 1989, "Melting and Freezing," *Advances Heat Transfer*, J. P. Hartnett and T. F. Irvine, eds., Vol. 19, Academic, San Diego, pp. 1–95.

Benchmark Solutions of Radiative Heat Transfer Within Nonhomogeneous Participating Media Using the Monte Carlo and YIX Method

Pei-feng Hsu,[1] J. T. Farmer[2]

Introduction

Solutions of radiative heat transfer in fire and combustion systems have been an important and active research subject in recent years. Most of the applications encountered in actual systems contain nonhomogeneous participating media. It is important that the flames and combustion systems are treated as such due to the non-uniform distributions of temperature and absorbing gaseous species, and participating particle concentrations. While several methods (Siegel and Howell, 1992) have treated some benchmarks successfully, the lack of the direct comparisons of any nonhomogeneous medium benchmark solution using different methods motivated the current study. In this study, we use two different methods (one stochastic—the Monte Carlo, and one deterministic—the YIX) to solve radiative transfer within the three-dimensional, nonhomogeneous, absorbing, emitting, scattering media and compare the solution differences between the two methods. The results are tabulated for future comparisons with other solution techniques.

In the first Symposium on Solution Methods for Radiative Heat Transfer in Participating Media at the 1992 National Heat Transfer Conference (Tong and Skocypec, 1992), the YIX (Hsu et al., 1993) and the Monte Carlo (M.C.) methods (Farmer and Howell, 1994) were shown to be able to solve complicated radiative heat transfer problems that have nonhomogeneous and nongray participating media. It was later shown that the differences between the two methods are within five percent (Hsu, 1994). Our experience leads us to suspect that the difference in spectral integration techniques is major cause of discrepancy. One of the purposes of this study is to confirm the agreement of the two methods for a series of gray nonhomogeneous media with and without anisotropic scattering as a first step.

Benchmark Problems

The geometry of the problem is a unit cube with black walls. Several different cases are treated. All cases have similarly shaped optical thickness (τ = extinction coefficient times the side length) distribution given by Eq. (1), i.e.,

---

[1] Mechanical & Aerospace Engineering Programs, Florida Institute of Technology, Melbourne, FL

[2] Thermal and Life Support Division, NASA Marshall Space Flight Center, Huntsville, AL

Contributed by the Heat Transfer Division for publication in the JOURNAL OF HEAT TRANSFER. Manuscript received by the Heat Transfer Division February 6, 1996; revision received September 30, 1996; Keywords: Combustion, Numerical Methods, Radiation. Associate Technical Editor: M. Modest.

Table 1 Conditions of different benchmark cases

CASE	Scattering albedo	LAS coefficient, β in Eq. (2)	Constants in Eq. (1)	Boundary conditions
E1	0.	n/a	$a = 0.9, b = 0.1$	6 cold walls
E2	0.9	0.	$a = 0.9, b = 0.1$	6 cold walls
E3	0.9	1.	$a = 0.9, b = 0.1$	1 hot/5 cold walls
E4	0.9	-1.	$a = 0.9, b = 0.1$	1 hot/5 cold walls
E7	0.9	1.	$a = 5.0, b = 5.0$	1 hot/5 cold walls

$$\tau(x, y, z) = a\left(1. - \frac{|x|}{0.5}\right)\left(1. - \frac{|y|}{0.5}\right)\left(1. - \frac{|z|}{0.5}\right) + b \quad (1)$$

The constants a and b in Eq. (1) for each case are listed in Table 1. The coordinate origin lies at the center of the cube and $-0.5 \leq (x, y, z) \leq 0.5$ is the domain of computation. The optical thickness distribution depends on a and b. For all cases studied, the media have higher optical thickness at the center than near the walls. For cases with scattering albedo not equal to zero, a linear anisotropic scattering (LAS) phase function, Eq. (2), is employed.

$$\Phi(\omega, \omega') = 1 + \beta P_1(\omega \cdot \omega') \quad (2)$$

where the P_1 is the Legendre function and $\omega \cdot \omega'$ represents the inner product of the in-scattering direction and incident intensity direction unit vectors. β is the coefficient of the LAS phase function. The walls are black and diffuse. Both methods can handle non-black surfaces and higher order anisotropic scattering phase function. Nonetheless, these are not considered in this study. The conditions for different cases are listed in Table 1. For cases E1 and E2, unity blackbody emissive power in the medium is given and the surface heat flux and divergence of radiative heat flux are to be solved. For cases E3, E4, and E7, the radiative equilibrium is assumed and one of the black walls ($x = -0.5$) has unity emissive power. The medium emissive power is to be found along with the surface heat flux. The set of cases was selected with several objectives in mind.

(1) The cases provide a variety of computational goals including computation of emissive power and surface flux, or radiative flux divergence and surface flux.

(2) The distribution in extinction coefficient provides a medium which under certain conditions can accentuate the "ray effects" (Lathrop, 1971) which can reduce the accuracy of solution in methods like the discrete ordinates (S-N), discrete transfer, and YIX methods.

(3) The optical thickness is varied from case to case to evaluate the sensitivity in accuracy and computation time to increased optical thickness, which can slow both methods.

(4) The asymmetry in the wall heating conditions (one hot wall) provides a means to judge the accuracy in applying the selected anisotropic phase function.

Results and Discussion

The solution algorithm of Monte Carlo method can be found in Farmer and Howell (1994) and Farmer (1995) and that of YIX is described in Hsu et al. (1993). Both numerical schemes are similar to those discussed in the above mentioned references with the exception of the techniques to compute emissive power. Particularly in the case of the Monte Carlo, the numerical scheme discussed in the earlier Monte Carlo references is used to find the exchange factor from each element to all other elements ensuring a proper energy balance, then a simple iterative solver is used to compute the emissive power using the exchange factor matrix and applied zero flux divergence condition. The YIX code applies energy balance check on each volume and surface elements to reduce the errors caused by the quadratures. In all computations except case E7, the same grid is used, i.e., $9 \times 9 \times 9$ cubic grid with side length of 1/9. In case E7, an additional solution is obtained for $27 \times 27 \times 27$ cubic grid to improve the accuracy. The YIX method uses S16 angular quadrature set and 0.001 (in optical thickness unit) as the first integration point for the distance quadrature in all cases except the case E7, where the first integration point is 0.01. For opti-

Table 2 Comparison of YIX and Monte Carlo for cases E1 and E2; (a) divergence of radiative heat fluxes at $y = z = 0$; surface heat fluxes at $x = -0.5$ and $y = 0$.

CASE	E1	E1		E2	E2	
x	YIX	M.C.	Uncertainty	YIX	M.C.	Uncertainty
-4/9	0.72219	0.72910	0.00020	0.07912	0.07974	0.00001
-3/9	1.37209	1.38739	0.00034	0.15739	0.15866	0.00002
-2/9	1.95658	1.98360	0.00073	0.23482	0.23673	0.00003
-1/9	2.49628	2.53635	0.00120	0.31163	0.31433	0.00003
0	3.03664	3.09813	0.00165	0.38842	0.39192	0.00005

CASE	E1	E1		E2	E2	
z	YIX	M.C.	Uncertainty	YIX	M.C.	Uncertainty
-4/9	0.10872	0.10959	0.00054	0.01214	0.01219	0.00020
-3/9	0.14171	0.14125	0.00052	0.01589	0.01564	0.00017
-2/9	0.16619	0.16729	0.00056	0.01877	0.01892	0.00028
-1/9	0.18569	0.18552	0.00067	0.02107	0.02103	0.00024
0	0.19291	0.19260	0.00049	0.02192	0.02202	0.00022

Table 3 Comparison of YIX and Monte Carlo for cases E3 and E4; (a) emissive power at $y = z = 0$; (b) surface heat fluxes at $x = -0.5$ and $y = 0$.

CASE	E3	E3		E4	E4	
x	YIX	M.C.	Uncertainty	YIX	M.C.	Uncertainty
-4/9	0.50679	0.46100	0.00053	0.52294	0.47660	0.00045
-3/9	0.36282	0.36640	0.00038	0.37710	0.37990	0.00051
-2/9	0.28177	0.28420	0.00042	0.29267	0.29450	0.00060
-1/9	0.22135	0.21830	0.00047	0.22730	0.22430	0.00046
0	0.17049	0.16650	0.00042	0.17050	0.16640	0.00029
1/9	0.11959	0.12580	0.00024	0.11505	0.12120	0.00026
2/9	0.09547	0.09642	0.00027	0.08914	0.08987	0.00023
3/9	0.06832	0.07516	0.00020	0.06159	0.06820	0.00021
4/9	0.06417	0.05986	0.00020	0.05795	0.05326	0.00021

CASE	E3	E3		E4	E4	
z	YIX	M.C.	Uncertainty	YIX	M.C.	Uncertainty
-4/9	0.98586	0.98490	0.00016	0.96680	0.96560	0.00039
-3/9	0.98112	0.98010	0.00024	0.95218	0.95100	0.00037
-2/9	0.97706	0.97620	0.00025	0.93944	0.93870	0.00043
-1/9	0.97360	0.97310	0.00036	0.92947	0.92950	0.00038
0	0.97170	0.97170	0.00027	0.92465	0.92530	0.00058

cally thick medium as in E7, the larger first integration point can be used to reduce computation time without loss of accuracy.

The results for E1 and E2 agree quite well (Table 2), having less than one percent average deviation in both surface flux and flux divergence. The total number of rays used in Monte Carlo simulations range from about $9.3 \cdot 10^6$ for case E2 to $3.5 \cdot 10^8$ for case E7. It is interesting to note, for the Monte Carlo solutions of E1 and E2, the numbers of rays used were driven by the need to reduce uncertainty in the surface flux results. The uncertainty values listed in Tables 2–4 are the statistical uncertainties in the Monte Carlo results. These uncertainties were derived using a 95% confidence interval and the standard deviations in results computed from 30 independent Monte Carlo simulations performed for each set of conditions. The extinction coefficient distribution in these problems is such that most of the radiation is emitted from the higher thickness region in the center of media away from the walls. In the current Monte Carlo algorithm the number of rays launched is proportional to the absorption coefficient and the emissive power in the media. Therefore, most of the rays are launched from the fairly small center region. In case E1 these rays travel straight toward the walls in their initially emitted directions. If the number of rays is small enough the emission may not be uniformly distributed leading to shortages of rays striking some of the surfaces which decreases the precision from run to run. In E2, the high scattering tends to spread out the ray paths improving the uniformity such that fewer rays are needed to guarantee enough rays strike on each surface. This is somewhat serendipitous since using the same proportionality between emissive power and absorption coefficient as applied in E1 produces an order of magnitude less rays because the absorption coefficient for E2 are an order of magnitude lower. The average run time for each ray, however, increases for rays in E2 because the decreased absorption and increased scattering lengthen the distance traveled and increase the number of elements entered by each ray.

Cases E3 and E4 (Table 3) have the same distribution of extinction coefficient and albedo as the case E2 but with strong forward and backward LAS phase functions, respectively. In addition, there is a hot wall at $x = -0.5$. The average differences of emissive power (e_g) at the volume elements are six percent and those of q_s are slightly higher than six percent. These are larger than the $\nabla \cdot q_r$ and q_s differences in the cases E1 and E2. It can be attributed to the ray effects occurring in YIX solutions. The ray effects cause anomalous emissive powers distributions at some regions. The anomalies are not caused by scattering since a case (not presented here) which uses the same conditions as E3 but with zero scattering albedo also shows similar irregular emissive power distributions.

The ray effects only appear on the volume and wall elements far away from the hot wall. At the elements near the hot wall, the e_g differences of both methods are much smaller. This is expected because the far away elements are easier to miss the hot wall due to the limited number of rays in angular quadrature (Lathrop, 1971). At volume nodes with $x \gtrsim 1/9$ and $y = z \approx 0$, the ray effects are mitigated due to the larger optical thickness in the center region of the cube. In other words, whatever the

Table 4 Comparison of YIX and Monte Carlo for case E7. The YIX solution is based on the 27 × 27 × 27 grid; (a) emissive power at $y = z = 0$; (b) surface heat fluxes at $x = -0.5$ and $y = 0$.

CASE	E7b	E7	
x	YIX	M.C.	Uncertainty
-4/9	0.64099	0.64420	0.00047
-3/9	0.47755	0.48220	0.00060
-2/9	0.34883	0.35100	0.00042
-1/9	0.24702	0.24700	0.00030
0	0.16740	0.16640	0.00021
1/9	0.10854	0.10760	0.00015
2/9	0.06940	0.06878	0.00014
3/9	0.04358	0.04310	0.00010
4/9	0.02548	0.02484	0.00006

CASE	E7b	E7	
z	YIX	M.C.	Uncertainty
-4/9	0.72862	0.73260	0.00076
-3/9	0.62774	0.62550	0.00071
-2/9	0.57357	0.56670	0.00101
-1/9	0.54266	0.53450	0.00063
0	0.53151	0.52340	0.00110

boundary condition at $x = -0.5$, its effects will not propagate deep enough into the region behind the optically thicker core.

Cases E3 and E4 are the extreme tests of ray effects for methods using the distance-angular quadrature for radiative transfer equation. The effective remedy of ray effects in YIX method will be to increase the order of discrete ordinate set used in the angular quadrature. The YIX computational time is directly proportional to the number of directions (n). However, the increase in computational time can be much less than n, if the higher order S-N set is applied only to those regions where ray effects can be properly identified. In comparison, the computational expense by the discrete ordinates method for higher order S-N set is proportional to $O(n^2)$ (see Lathrop, 1971) and consistent order of the S-N set has to be used throughout the whole computational domain.

The results of case E7 (similar to E3, but with higher optical thickness) reveal that the YIX ray effects are completely mitigated by this higher optical thickness. In Table 4, the E7b is case E7 run with a 27 × 27 × 27 grid by the YIX method. A Monte Carlo solution for this larger grid was not run due to memory problems on the M.C. machine, and the excessive run times expected. In the YIX solution of E7b, smaller grid size is required for this optically dense medium, which has optical thickness of ten in the center and five at the walls. Ideally, adaptive grid with equal optical depth in grid size will ensure same order of local error within the medium. However, this is currently not adopted in either the YIX or M.C. schemes. Although the e_g distributions agree very well at the core region (overall averaged difference is 2.2 percent), the q_s distributions have larger differences (overall averaged is 2.7 percent), especially at the hot wall center.

References

Farmer, J. T., and Howell, J. R., 1994, "Monte Carlo Prediction of Radiative Heat Transfer in Inhomogeneous, Anisotropic, Nongray Media," AIAA *Journal of Thermophysics and Heat Transfer,* Vol. 8, No. 1, pp. 133–139.

Farmer, J. T., 1995, *Improved Algorithms for Monte Carlo Analysis of Radiative Heat Transfer in Complex Participating Media,* Ph.D. Dissertation, The University of Texas at Austin.

Hsu, P.-F., Tan, Z., and Howell, J. R., 1993, "Radiative Transfer by the YIX Method in Nonhomogeneous, Scattering and Non-Gray Medium," AIAA *Journal of Thermophysics and Heat Transfer,* Vol. 7, No. 3, pp. 487–495.

Hsu, P.-F., 1994, private communication with Jeff T. Farmer (3/94).

Lathrop, K. D., 1971, "Remedies for Ray Effects," *Nuclear Science and Engineering,* Vol. 45, pp. 255–268.

Siegel, R., and Howell, J. R., 1992, *Thermal Radiation Heat Transfer,* 3rd ed., Hemisphere, New York.

Tong, T. W., and Skocypec, R. D., 1992, "Summary on Comparison of Radiative Heat Transfer Solutions for a Specified Problem," ASME HTD, Vol. 203, pp. 253–258.

Nonequilibrium Laser Heating of Metal Films

M. A. Al-Nimr and S. A. Masoud[1]

Nomenclature

C = heat capacity, $\mathrm{Jm^{-3}\,K^{-1}}$
G = electron-phonon coupling factor, $\mathrm{Wm^{-3}\,K^{-1}}$
I = laser intensity, $\mathrm{Wm^{-2}}$
K = thermal conductivity, $\mathrm{Wm^{-1}\,K^{-1}}$
L = film thickness, m
P = dimensionless source term
Q = source term, $\mathrm{Wm^{-3}}$
R = metal surface reflectivity
t = time, s
t_p = laser pulse duration, s
T = temperature, K
T_i = initial temperature of both lattice and electron gas, K
T_D = Debye temperature, K
x = spatial coordinate, m

Greek Symbols

α = radiation absorption coefficient, $\mathrm{m^{-1}}$
Δ = difference function
ϵ = dimensionless small parameter
ξ = dimensionless spatial coordinate, x/L
θ = dimensionless temperature, $(T - T_i)/T_i$
τ = dimensionless time, $tK_e/(L^2C_e)$
τ_p = dimensionless laser pulse duration time, $t_pK_e/(L^2C_e)$

Subscripts

e = electron
i = initial
l = lattice

1 Introduction

There exist basically four different models describing the mechanism of energy transport during short-pulse laser heating. The first is the parabolic one-step model which is based on the classical Fourier conduction law. The second is the hyperbolic one-step model (Kim et al., 1990; Chen and Lin, 1994) which was first postulated for gases by Maxwell (1867). The third and forth models are the parabolic two-step and the hyperbolic two-step models (Qiu and Tien, 1993; Tzou et al., 1994; Tzou, 1995).

The microscopic two-step model was pioneered by Anisimov et al. (1974) and was advanced later by Fujimoto et al. (1984). The two-step model involves two coupled energy equations governing the heat transfer in the electron gas and the metal lattice. The electron-phonon coupling factor varies within a wide range of limits. Many metals have a very low coupling factor. As an example, the coupling factor of gold is about $2.6 \times 10^{16}\ \mathrm{Wm^{-3}\,K^{-1}}$. However, many other metals have a very high coupling factor. As an example, the coupling factor of Vanadium (V) is about $648 \times 10^{16}\ \mathrm{Wm^{-3}\,K^{-1}}$. As the value of the coupling factor increases, the thermalization time, which is the time required for the electron and lattice to reach the thermal equilibrium state, decreases. This implies that the normalized temperature difference between the electron gas and the lattice becomes small but not negligible. This small temperature difference between the electron gas and the lattice is observed especially in materials having large coupling factors and when the laser duration time is long enough to enable the electron gas to give part of its energy to the solid lattice. When the temperature difference between the electron gas and the lattice becomes small enough, this difference may be normalized in the form of a perturbed quantity. As a result, perturbation technique may be used to eliminate the coupling between the two energy equations. The elimination of this coupling produces two uncoupled partial differential equations which have the same order as the original coupled partial differential equations and which do not contain any mixed derivative terms.

2 Analysis

Consider applications involving short-pulse laser heating of metals. When the laser pulse duration is much shorter than the electron-phonon thermal relaxation time, the hot electrons do

---

[1] Mechanical Engineering Department, Jordan University of Science and Technology, Irbid, Jordan.

Contributed by the Heat Transfer Division for publication in the Journal of Heat Transfer. Manuscript received by the Heat Transfer Division January 3, 1996; revision received July 25, 1996; Keywords: Conduction, Laser Processing, Transient & Unsteady Heat Transfer. Associate Technical Editor: Dr. Tong.

boundary condition at $x = -0.5$, its effects will not propagate deep enough into the region behind the optically thicker core.

Cases E3 and E4 are the extreme tests of ray effects for methods using the distance-angular quadrature for radiative transfer equation. The effective remedy of ray effects in YIX method will be to increase the order of discrete ordinate set used in the angular quadrature. The YIX computational time is directly proportional to the number of directions (n). However, the increase in computational time can be much less than n, if the higher order S-N set is applied only to those regions where ray effects can be properly identified. In comparison, the computational expense by the discrete ordinates method for higher order S-N set is proportional to $O(n^2)$ (see Lathrop, 1971) and consistent order of the S-N set has to be used throughout the whole computational domain.

The results of case E7 (similar to E3, but with higher optical thickness) reveal that the YIX ray effects are completely mitigated by this higher optical thickness. In Table 4, the E7b is case E7 run with a 27 × 27 × 27 grid by the YIX method. A Monte Carlo solution for this larger grid was not run due to memory problems on the M.C. machine, and the excessive run times expected. In the YIX solution of E7b, smaller grid size is required for this optically dense medium, which has optical thickness of ten in the center and five at the walls. Ideally, adaptive grid with equal optical depth in grid size will ensure same order of local error within the medium. However, this is currently not adopted in either the YIX or M.C. schemes. Although the e_g distributions agree very well at the core region (overall averaged difference is 2.2 percent), the q_s distributions have larger differences (overall averaged is 2.7 percent), especially at the hot wall center.

References

Farmer, J. T., and Howell, J. R., 1994, "Monte Carlo Prediction of Radiative Heat Transfer in Inhomogeneous, Anisotropic, Nongray Media," AIAA *Journal of Thermophysics and Heat Transfer,* Vol. 8, No. 1, pp. 133–139.

Farmer, J. T., 1995, *Improved Algorithms for Monte Carlo Analysis of Radiative Heat Transfer in Complex Participating Media,* Ph.D. Dissertation, The University of Texas at Austin.

Hsu, P.-F., Tan, Z., and Howell, J. R., 1993, "Radiative Transfer by the YIX Method in Nonhomogeneous, Scattering and Non-Gray Medium," AIAA *Journal of Thermophysics and Heat Transfer,* Vol. 7, No. 3, pp. 487–495.

Hsu, P.-F., 1994, private communication with Jeff T. Farmer (3/94).

Lathrop, K. D., 1971, "Remedies for Ray Effects," *Nuclear Science and Engineering,* Vol. 45, pp. 255–268.

Siegel, R., and Howell, J. R., 1992, *Thermal Radiation Heat Transfer,* 3rd ed., Hemisphere, New York.

Tong, T. W., and Skocypec, R. D., 1992, "Summary on Comparison of Radiative Heat Transfer Solutions for a Specified Problem," ASME HTD, Vol. 203, pp. 253–258.

Nonequilibrium Laser Heating of Metal Films

M. A. Al-Nimr and S. A. Masoud[1]

Nomenclature

C = heat capacity, $\mathrm{Jm^{-3}\,K^{-1}}$
G = electron-phonon coupling factor, $\mathrm{Wm^{-3}\,K^{-1}}$
I = laser intensity, $\mathrm{Wm^{-2}}$
K = thermal conductivity, $\mathrm{Wm^{-1}\,K^{-1}}$
L = film thickness, m
P = dimensionless source term
Q = source term, $\mathrm{Wm^{-3}}$
R = metal surface reflectivity
t = time, s
t_p = laser pulse duration, s
T = temperature, K
T_i = initial temperature of both lattice and electron gas, K
T_D = Debye temperature, K
x = spatial coordinate, m

Greek Symbols

α = radiation absorption coefficient, $\mathrm{m^{-1}}$
Δ = difference function
ϵ = dimensionless small parameter
ξ = dimensionless spatial coordinate, x/L
θ = dimensionless temperature, $(T - T_i)/T_i$
τ = dimensionless time, $tK_e/(L^2C_e)$
τ_p = dimensionless laser pulse duration time, $t_pK_e/(L^2C_e)$

Subscripts

e = electron
i = initial
l = lattice

1 Introduction

There exist basically four different models describing the mechanism of energy transport during short-pulse laser heating. The first is the parabolic one-step model which is based on the classical Fourier conduction law. The second is the hyperbolic one-step model (Kim et al., 1990; Chen and Lin, 1994) which was first postulated for gases by Maxwell (1867). The third and forth models are the parabolic two-step and the hyperbolic two-step models (Qiu and Tien, 1993; Tzou et al., 1994; Tzou, 1995).

The microscopic two-step model was pioneered by Anisimov et al. (1974) and was advanced later by Fujimoto et al. (1984). The two-step model involves two coupled energy equations governing the heat transfer in the electron gas and the metal lattice. The electron-phonon coupling factor varies within a wide range of limits. Many metals have a very low coupling factor. As an example, the coupling factor of gold is about $2.6 \times 10^{16}\ \mathrm{Wm^{-3}\,K^{-1}}$. However, many other metals have a very high coupling factor. As an example, the coupling factor of Vanadium (V) is about $648 \times 10^{16}\ \mathrm{Wm^{-3}\,K^{-1}}$. As the value of the coupling factor increases, the thermalization time, which is the time required for the electron and lattice to reach the thermal equilibrium state, decreases. This implies that the normalized temperature difference between the electron gas and the lattice becomes small but not negligible. This small temperature difference between the electron gas and the lattice is observed especially in materials having large coupling factors and when the laser duration time is long enough to enable the electron gas to give part of its energy to the solid lattice. When the temperature difference between the electron gas and the lattice becomes small enough, this difference may be normalized in the form of a perturbed quantity. As a result, perturbation technique may be used to eliminate the coupling between the two energy equations. The elimination of this coupling produces two uncoupled partial differential equations which have the same order as the original coupled partial differential equations and which do not contain any mixed derivative terms.

2 Analysis

Consider applications involving short-pulse laser heating of metals. When the laser pulse duration is much shorter than the electron-phonon thermal relaxation time, the hot electrons do

---

[1] Mechanical Engineering Department, Jordan University of Science and Technology, Irbid, Jordan.

Contributed by the Heat Transfer Division for publication in the Journal of Heat Transfer. Manuscript received by the Heat Transfer Division January 3, 1996; revision received July 25, 1996; Keywords: Conduction, Laser Processing, Transient & Unsteady Heat Transfer. Associate Technical Editor: Dr. Tong.

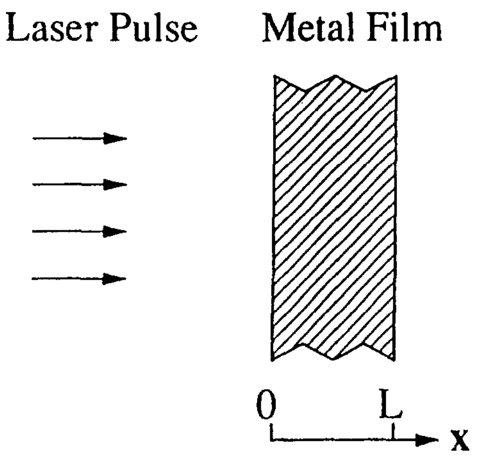

Fig. 1 Schematic diagram for laser heating of a metal film

not have enough time to establish local thermal equilibrium with the lattice. Consequently, the electrons and the lattice have two different temperatures θ_e and θ_l. This non-equilibrium heating process can be modeled phenomenologically using the two-step model as:

$$\frac{\partial\theta_e}{\partial\tau} = \frac{\partial^2\theta_e}{\partial\xi^2} - H_1(\theta_e - \theta_l) + P_e(\tau, \xi) \tag{1}$$

$$\frac{\partial\theta_l}{\partial\tau} = H_2\frac{\partial^2\theta_l}{\partial\xi^2} + H_3(\theta_e - \theta_l) \tag{2}$$

where

$$H_1 = \frac{GL^2}{K_e}, \quad H_2 = \frac{K_lC_e}{K_eC_l},$$

$$H_3 = \frac{GL^2C_e}{K_eC_l}, \quad P_e = P_l = \frac{L^2Q(\tau, \xi)}{K_eT_i}.$$

Equations (1) and (2) are two coupled partial differential equations which are second order in space and first order in time. Elimination of the coupling between these equations yields a mixed derivative partial differential equation which is fourth order in space and second order in time. The higher order and mixed derivative terms which appear in the resulting equation increases the difficulty of solving such problems. However, in many applications, the coupling between the two energy Eqs. (1) and (2) may be eliminated without raising the order of the resulted partial differential equations and without the appearing of mixed derivative terms. These applications involve situations in which the incident thermal radiation interacts with materials having a very large coupling factor or situations in which the laser pulse duration is not too short. In these situations, the difference between the electron and lattice temperature may be normalized in the form of a very small perturbed quantity. This difference may be written as:

$$\theta_e(\tau, \xi) = \theta_l(\tau, \xi) + \epsilon\Delta(\tau, \xi) \tag{3}$$

where $\Delta(\tau, \xi)$ is a function of space and time, and $\epsilon = 1/H_1$ is a dimensionless small parameter. Now, Eqs. (1) and (2) can be written as:

$$\frac{\partial\theta_e}{\partial\tau} = H_4\frac{\partial^2\theta_e}{\partial\xi^2} + C_RP_e(\tau, \xi) + O(\epsilon) \tag{4}$$

$$\Delta(\tau, \xi) = -\frac{\partial\theta_e}{\partial\tau} + \frac{\partial^2\theta_e}{\partial\xi^2} + P_e(\tau, \xi) \tag{5}$$

where

$$H_4 = \frac{C_e}{C_e + C_l}\frac{K_e + K_l}{K_e}, \quad C_R = \frac{C_e}{C_e + C_l}.$$

Equation (4) is obtained by combining Eqs. (1) and (2); Equation (5) is Eq. (1) with regard to Eq. (3). It is clear that Eq. (4) is a simple partial differential equation which has the same order as that of the original governing Eqs. (1) and (2) and which has no mixed derivative terms.

3 Study Case

Consider the interaction of a short-pulse laser beam with a pure metal film having a high coupling factor G. The metal film, which is of thickness L, is analyzed on the basis of a one-dimensional model, since the beam diameter is typically much larger than the heat diffusion penetration depth in a very short time. By neglecting the temperature dependence of thermal properties, the governing equations are Eqs. (4) and (5). The heating source term that appears in these equations is given in a dimensionless form as (Qiu and Tien, 1993; Tzou et al., 1994; Tzou, 1995):

$$P_e(\tau, \xi) = \frac{L^2}{K_eT_i}(1 - R)I\alpha \exp^{-\alpha L\xi} \times \exp^{-11.08} \exp^{-2.77(\tau^2/\tau_p^2)} \exp^{11.08(\tau/\tau_p)} \tag{6}$$

where τ_p is the dimensionless pulse duration time. In Eq. (6) we have made a phase shift in time in the form $\tau = \hat{\tau} + 2$. This shift is done to enable us to take the initial conditions at zero time. As a result of this phase shift, the initial and boundary conditions of the problem are given as:

$$\theta_e(0, \xi) = \theta_l(0, \xi) = 0 \tag{7}$$

$$\frac{\partial\theta_l(\tau, 0)}{\partial\xi} = \frac{\partial\theta_l(\tau, 1)}{\partial\xi} = \frac{\partial\theta_e(\tau, 0)}{\partial\xi} = \frac{\partial\theta_e(\tau, 1)}{\partial\xi} = 0. \tag{8}$$

Solution for Eq. (4) is obtained using Green's function method. This solution assumes the form (Ozisik, 1993):

$$\theta_e(\tau, \xi) = A\sum_{m=0}^{\infty}\frac{1}{N(\beta_m)}\exp^{-H_4\beta_m^2\tau}\cos(\beta_m\xi)D_m\sqrt{\pi\delta} \times \exp^{\gamma^2\delta}\left[erf\left(\gamma\sqrt{\delta} + \frac{\tau}{2\sqrt{\delta}}\right) - erf(\gamma\sqrt{\delta})\right] \tag{9}$$

where

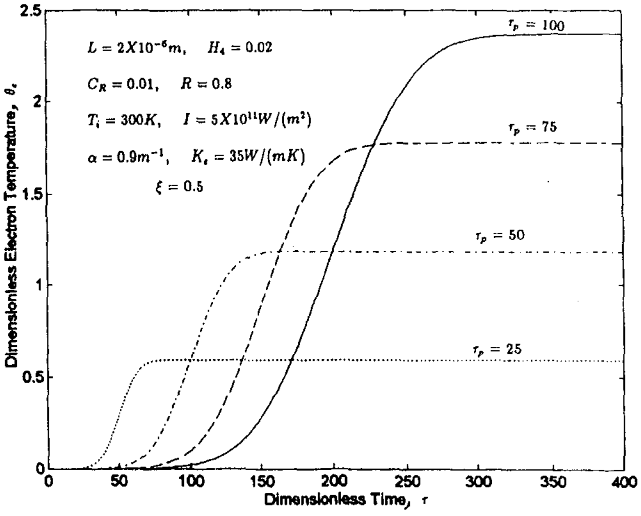

Fig. 2 The dynamic response of the electron temperature θ_e at different duration times

$$D_m = \frac{L\alpha[1 - \exp^{-\alpha L}\cos(m\pi)]}{\alpha^2L^2 + m^2\pi^2}, \quad A = \frac{C_RL^2}{K_eT_i}(1 - R)I\alpha$$

$$\gamma = -H_4m^2\pi^2 - \frac{11.08}{\tau_p}, \quad \delta = \frac{\tau_p^2}{11.08},$$

$$\beta_m = m\pi, \quad N(\beta_m) = 0.5, \quad N(0) = 1$$

Expression for $\theta_l(\tau, \xi)$ is obtained from Eq. (3) where $\Delta(\tau, \xi)$ is obtained from Eqs. (5) and (9) as:

$$\begin{aligned}\Delta(\tau, \xi) = {} & A(H_4 - 1)\sum_{m=0}^{\infty}\frac{1}{N(\beta_m)} \\ & \times (m^2\pi^2)\exp^{-H_4\beta_m^2\tau}\cos(\beta_m\xi)D_m\sqrt{\pi\delta} \\ & \times \exp^{\gamma^2\delta}\left[erf\left(\gamma\sqrt{\delta} + \frac{\tau}{2\sqrt{\delta}}\right) - erf(\gamma\sqrt{\delta})\right] \\ & - A\sum_{m=0}^{\infty}\frac{1}{N(\beta_m)}\exp^{-H_4\beta_m^2\tau}\cos(\beta_m\xi)D_m\exp^{\gamma^2\delta} \\ & \times \exp^{-[\gamma\sqrt{\delta}+\tau/2\sqrt{\delta}]^2} + P_e(\tau, \xi). \quad (10)\end{aligned}$$

A sample of the results is plotted in Fig. 2 which shows the dynamic response of the dimensionless electron temperature at a given location (where $\xi = 0.5$) of the metal film.

References

Anisimov, S. L., Kapeliovich, B. L., and Perelman, T. L., 1974, "Electron Emission From Metal Surfaces Exposed to Ultra-Short Laser Pulses," *Soviet Physics JETP*, Vol. 39, pp. 375–377.

Chen, Han-Taw, and Lin, Jae-Yuh, 1994, "Analysis of Two-Dimensional Hyperbolic Heat Conduction Problems," *Int. J. Heat and Mass Transfer*, Vol. 37(1), pp. 153–164.

Fujimoto, J. G., Liu, J. M., and Ippen, E. P., 1984, "Femtosecond Laser Interaction With Metallic Tungsten and Non-Equilibrium Electron and Lattice Temperature," *Physical Review Letters*, Vol. 53, pp. 1837–1840.

Kim, W. S., Hector, L. G., and Ozisik, M. N., 1990, "Hyperbolic Heat Conduction Due to Axisymmetric Continuous or Pulsed Surface Heat Sources," *J. Applied Phys.*, Vol. 68, pp. 5478–5485.

Maxwell, J. C., 1867, "On the Dynamic Theory of Gases," *Philos. Trans. Soc. London*, Vol. 157, pp. 49–88.

Qiu, T. Q., and Tien, C. L., 1993, "Heat Transfer Mechanism During Short-Pulse Laser Heating of Metals," ASME JOURNAL OF HEAT TRANSFER, Vol. 115, pp. 835–841.

Tzou, D. Y., Ozisik, M. N., and Chiffelle, R. J., 1994, "The Lattice Temperature in the Microscopic Two-Step Model," Vol. 116, pp. 1034–1038.

Tzou, D. Y., 1995, "A Unified Field Approach for Heat Conduction From Macro- to Micro-Scales," ASME JOURNAL OF HEAT TRANSFER, Vol. 117, pp. 8–16.

Ozisik, M. N., 1993, *Heat Conduction*, 2nd Edition, John Wiley, chap. 6, pp. 214–256.

Determination of Flow Properties in Non-Darcian Flow

H.-I. You, C.-H. Chang[1]

Introduction

Channel flow filled with porous medium is an efficient way to enhance the heat transfer of a compact heat exchanger. Since, in most cases, high velocity flow prevails in the porous medium flow, non-Darcian effects, consisting of boundary, viscous and inertial resistance, had been considered by many investigators in their heat transfer analysis (e.g., Vafai and Kim, 1990). Flow properties of permeability and inertial constant pertaining to a porous medium structure, need to be determined before the thermal analysis of forced convection heat transfer is performed.

For non-Darcian flow through a porous medium, the pressure drop was generally expressed as the sum of two terms as follows (Ergun, 1952):

$$-\frac{dp}{dx} = a\mu U + b\rho U^2 \tag{1}$$

Reformulating Eq. (1) and using 640 experimental data representing different gas through various-sized spheres, sand etc., Ergun obtained permeability K and inertial constant F belonging to the associated porous medium flow. Beavers and Sparrow (1969) conducted experimental work by using distilled water through a latticework of metallic fibers. Following a similar procedure of data analysis, they obtained both flow properties. Sparrow and Grannis (1991) determined the pressure-drop characteristics as a function of Reynolds number, based on pore characteristic length, for air flow through arrays of diamond-shaped pin fins. A bundle of series connected capillaries, in which the flow path may branch and, later on, join together, is considered to be a theoretical model of porous structure (Scheidegger, 1974). Microstructure composed of a large number of short pin fins is considered to be a porous structure and is designed for use in forced convection heat transfer. Flow properties of permeability and inertial constant, belonging to this microstructure, need to be experimentally determined, as done by other investigators. A modified procedure on the determination of such flow properties is proposed in the present investigation.

Equation of Fully Developed Flow

The momentum equation in x-direction is (Vafai and Kim, 1990):

$$-\frac{dp_f}{dx} = -\mu\frac{d^2u}{dy^2} + \frac{\mu}{K}u + \frac{F}{\sqrt{K}}\rho u^2 \tag{2}$$

The volume flow rate passing through each channel section is constant, i.e.,

$$\int_0^\delta u dy = U\delta \tag{3}$$

In Eq. (2), p_f represents the actual fluid pressure which can be measured by a pressure gauge. Due to inertial resistance in the porous structure, a flat velocity profile was found prevailing in the utmost part of the porous flow channel. Applying Eq. (2) on the center line of the porous flow channel, and noting that d^2u/dy^2 can be absolutely set equal to zero, Eq. (2) reduces to:

$$-\frac{dp_f}{dx} = \frac{\mu}{K}U_c + \frac{F}{\sqrt{K}}\rho U_c^2 \tag{4}$$

Clearly, Eq. (4) is comparable with Eq. (1) in which the Darcian velocity U is replaced by the maximum centerline velocity U_c.

Experimental Preparation

An experimental apparatus of air flow system, similar to that used by Sparrow and Grannis (1991), was constructed in the present study. The flow test section was composed of uniformly distributed square pin-fins on a metal substrate. The test section

---

[1] Department of Mechanical Engineering, National Chung-Hsing University, Taichung, Taiwan, R.O.C.

Contributed by the Heat Transfer Division for publication in the JOURNAL OF HEAT TRANSFER. Manuscript received by the Heat Transfer Division January 11, 1996; revision received September 5, 1996; Keywords: Forced Convection, Porous Media, Thermophysical Properties. Associate Technical Editor: K. Vafai.

$$D_m = \frac{L\alpha[1 - \exp^{-\alpha L}\cos(m\pi)]}{\alpha^2 L^2 + m^2\pi^2}, \quad A = \frac{C_R L^2}{K_e T_i}(1 - R)I\alpha$$

$$\gamma = -H_4 m^2\pi^2 - \frac{11.08}{\tau_p}, \quad \delta = \frac{\tau_p^2}{11.08},$$

$$\beta_m = m\pi, \quad N(\beta_m) = 0.5, \quad N(0) = 1$$

Expression for $\theta_l(\tau, \xi)$ is obtained from Eq. (3) where $\Delta(\tau, \xi)$ is obtained from Eqs. (5) and (9) as:

$$\begin{aligned}\Delta(\tau, \xi) = {} & A(H_4 - 1)\sum_{m=0}^{\infty}\frac{1}{N(\beta_m)} \\ & \times (m^2\pi^2)\exp^{-H_4\beta_m^2\tau}\cos(\beta_m\xi)D_m\sqrt{\pi\delta} \\ & \times \exp^{\gamma^2\delta}\left[erf\left(\gamma\sqrt{\delta} + \frac{\tau}{2\sqrt{\delta}}\right) - erf(\gamma\sqrt{\delta})\right] \\ & - A\sum_{m=0}^{\infty}\frac{1}{N(\beta_m)}\exp^{-H_4\beta_m^2\tau}\cos(\beta_m\xi)D_m\exp^{\gamma^2\delta} \\ & \times \exp^{-[\gamma\sqrt{\delta}+\tau/2\sqrt{\delta}]^2} + P_e(\tau, \xi). \quad (10)\end{aligned}$$

A sample of the results is plotted in Fig. 2 which shows the dynamic response of the dimensionless electron temperature at a given location (where $\xi = 0.5$) of the metal film.

References

Anisimov, S. L., Kapeliovich, B. L., and Perelman, T. L., 1974, "Electron Emission From Metal Surfaces Exposed to Ultra-Short Laser Pulses," *Soviet Physics JETP*, Vol. 39, pp. 375–377.

Chen, Han-Taw, and Lin, Jae-Yuh, 1994, "Analysis of Two-Dimensional Hyperbolic Heat Conduction Problems," *Int. J. Heat and Mass Transfer*, Vol. 37(1), pp. 153–164.

Fujimoto, J. G., Liu, J. M., and Ippen, E. P., 1984, "Femtosecond Laser Interaction With Metallic Tungsten and Non-Equilibrium Electron and Lattice Temperature," *Physical Review Letters*, Vol. 53, pp. 1837–1840.

Kim, W. S., Hector, L. G., and Ozisik, M. N., 1990, "Hyperbolic Heat Conduction Due to Axisymmetric Continuous or Pulsed Surface Heat Sources," *J. Applied Phys.*, Vol. 68, pp. 5478–5485.

Maxwell, J. C., 1867, "On the Dynamic Theory of Gases," *Philos. Trans. Soc. London*, Vol. 157, pp. 49–88.

Qiu, T. Q., and Tien, C. L., 1993, "Heat Transfer Mechanism During Short-Pulse Laser Heating of Metals," ASME JOURNAL OF HEAT TRANSFER, Vol. 115, pp. 835–841.

Tzou, D. Y., Ozisik, M. N., and Chiffelle, R. J., 1994, "The Lattice Temperature in the Microscopic Two-Step Model," Vol. 116, pp. 1034–1038.

Tzou, D. Y., 1995, "A Unified Field Approach for Heat Conduction From Macro- to Micro-Scales," ASME JOURNAL OF HEAT TRANSFER, Vol. 117, pp. 8–16.

Ozisik, M. N., 1993, *Heat Conduction*, 2nd Edition, John Wiley, chap. 6, pp. 214–256.

Determination of Flow Properties in Non-Darcian Flow

H.-I. You, C.-H. Chang[1]

Introduction

Channel flow filled with porous medium is an efficient way to enhance the heat transfer of a compact heat exchanger. Since, in most cases, high velocity flow prevails in the porous medium flow, non-Darcian effects, consisting of boundary, viscous and inertial resistance, had been considered by many investigators in their heat transfer analysis (e.g., Vafai and Kim, 1990). Flow properties of permeability and inertial constant pertaining to a porous medium structure, need to be determined before the thermal analysis of forced convection heat transfer is performed.

For non-Darcian flow through a porous medium, the pressure drop was generally expressed as the sum of two terms as follows (Ergun, 1952):

$$-\frac{dp}{dx} = a\mu U + b\rho U^2 \quad (1)$$

Reformulating Eq. (1) and using 640 experimental data representing different gas through various-sized spheres, sand etc., Ergun obtained permeability K and inertial constant F belonging to the associated porous medium flow. Beavers and Sparrow (1969) conducted experimental work by using distilled water through a latticework of metallic fibers. Following a similar procedure of data analysis, they obtained both flow properties. Sparrow and Grannis (1991) determined the pressure-drop characteristics as a function of Reynolds number, based on pore characteristic length, for air flow through arrays of diamond-shaped pin fins. A bundle of series connected capillaries, in which the flow path may branch and, later on, join together, is considered to be a theoretical model of porous structure (Scheidegger, 1974). Microstructure composed of a large number of short pin fins is considered to be a porous structure and is designed for use in forced convection heat transfer. Flow properties of permeability and inertial constant, belonging to this microstructure, need to be experimentally determined, as done by other investigators. A modified procedure on the determination of such flow properties is proposed in the present investigation.

Equation of Fully Developed Flow

The momentum equation in x-direction is (Vafai and Kim, 1990):

$$-\frac{dp_f}{dx} = -\mu\frac{d^2u}{dy^2} + \frac{\mu}{K}u + \frac{F}{\sqrt{K}}\rho u^2 \quad (2)$$

The volume flow rate passing through each channel section is constant, i.e.,

$$\int_0^\delta u\,dy = U\delta \quad (3)$$

In Eq. (2), p_f represents the actual fluid pressure which can be measured by a pressure gauge. Due to inertial resistance in the porous structure, a flat velocity profile was found prevailing in the utmost part of the porous flow channel. Applying Eq. (2) on the center line of the porous flow channel, and noting that d^2u/dy^2 can be absolutely set equal to zero, Eq. (2) reduces to:

$$-\frac{dp_f}{dx} = \frac{\mu}{K}U_c + \frac{F}{\sqrt{K}}\rho U_c^2 \quad (4)$$

Clearly, Eq. (4) is comparable with Eq. (1) in which the Darcian velocity U is replaced by the maximum centerline velocity U_c.

Experimental Preparation

An experimental apparatus of air flow system, similar to that used by Sparrow and Grannis (1991), was constructed in the present study. The flow test section was composed of uniformly distributed square pin-fins on a metal substrate. The test section

---

[1] Department of Mechanical Engineering, National Chung-Hsing University, Taichung, Taiwan, R.O.C.

Contributed by the Heat Transfer Division for publication in the JOURNAL OF HEAT TRANSFER. Manuscript received by the Heat Transfer Division January 11, 1996; revision received September 5, 1996; Keywords: Forced Convection, Porous Media, Thermophysical Properties. Associate Technical Editor: K. Vafai.

had a narrow flow path with an inlet cross section of 120 (width) × 15 (height) mm and length (L) 120 mm. Five units of the flow test section with porosity, ϵ, equal to 0.865, 0.782, 0.679, 0.599, and 0.462 were prepared. The pressure drop Δp across the test section is measured using a manometer filled with water or mercury, chosen depending on the magnitude of the pressure drop. The constant pressure gradient dp_f/dx across the test section is calculated by $\Delta p/L$. The minimum water height reading of the U-type manometer in the measurement of pressure drop for the case of the least air flow rate is about 80 ± 1 mm. The accuracy on measurement of channel length is also within ± 1 mm. The maximum uncertainty of $\Delta p/L$ is therefore within three percent.

Analysis

To determine the permeability K and the inertial constant F associated with a specified porous structure, a number of test runs on flow experiment should be done. These experiments are generally conducted over a wide range of air flow rates. To each test, the pressure drop, denoted by $\Delta p_{\text{mea.}}$, is measured, and all of the data pairs ($\Delta p_{\text{mea.}}$, U) are then collected for data analysis. Rewrite Eq. (4) (as done by Beavers and Sparrow, 1969) in the following form:

$$\frac{1}{\mu U_c}\left(-\frac{\Delta p}{L}\right) = a + b\,\frac{\rho U_c}{\mu} \tag{5}$$

where $a = 1/K$ and $b = F/\sqrt{K}$.

If all of the maximum centerline velocities, U_c's, corresponding to the associated air flow rates, are known, then in conjunction with the measured pressure drops $\Delta p_{\text{mea.}}$, the values of a and b (then K and F) can be obtained from Eq. (5) by using the numerical method of least square. In the present paper, this calculation is completed by using the subroutine RLINE called from IMSL (1989). However, since U_c's are not known beforehand, first trial solutions of a and b are obtained by using the data pairs of ($\Delta p_{\text{mea.}}$, U). The values of K and F obtained in this first solution are, essentially, obtained by Beavers and Sparrow (1969). Numerical solution of u (and also U_c) is solved from Eq. (2), in which K and F use the foregoing trial solutions.

Equation (2) is an ordinary differential equation of velocity, $u(y)$, with the no-slip boundary conditions specified at the walls. A computing subroutine, named BVPFD called from IMSL (1989), is used to solve for $u(y)$. The unknown pressure gradient, dp_f/dx, across the porous structure, is also iteratively determined if the flow continuity, Eq. (3) satisfies the following criterion of the convergence, i.e.,

$$\left|\left(\int_0^\delta u dy - U\delta\right)/U\delta\right| \leq 10^{-3} \tag{6}$$

When the calculated value of dp_f/dx is equal to $\Delta p/L$ within the following prescribed accuracy:

$$|(dp_f/dx - \Delta p/L)/\Delta p/L| \leq 10^{-3} \tag{7}$$

then the final values of K and F are the desired solution. Otherwise, modified values of K and F are iteratively obtained by using the new data pairs of ($\Delta p_{\text{mea.}}$, U_c) in the least-square computation. The convergence was rapidly attained within three to four iterative cycles in the present calculation.

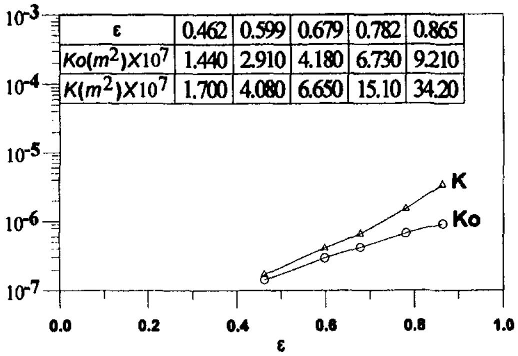

ε	0.462	0.599	0.679	0.782	0.865
$Ko(m^2)X10^7$	1.440	2.910	4.180	6.730	9.210
$K(m^2)X10^7$	1.700	4.080	6.650	15.10	34.20

Fig. 1 Computational results of permeability K versus porosity ϵ

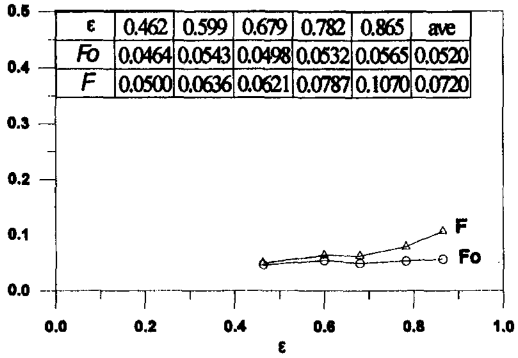

ε	0.462	0.599	0.679	0.782	0.865	ave
Fo	0.0464	0.0543	0.0498	0.0532	0.0565	0.0520
F	0.0500	0.0636	0.0621	0.0787	0.1070	0.0720

Fig. 2 Computational results of the inertial constant F versus porosity ϵ

Results and Discussion

Figure 1 shows the computational results of permeability K associated with each porous matrix of porosity ϵ. The first trial solutions of permeability, K_0, equivalent to Beavers and Sparrow's solution, are also shown in the figure for reference. It is found that the typical value of K associated with the practical microstructure is of the order of 10^{-7} to 10^{-6} m^2 in the present investigation. In Fig. 1, the logarithmic scale for the permeability K is used and a steadily increasing rate of K is observed. Equation (2) reduces to the momentum equation applied for the channel flow without a porous medium as $K \rightarrow \infty$. However, it is found from Fig. 1 that K seems to approach a finite value, roughly 10^{-4}, instead of ∞, as ϵ tends to 1. Figure 2 shows the computational results of the inertial constant F associated with the corresponding porosity ϵ. The Beavers and Sparrow's solutions, F_0, are also listed in the figure for reference. It is seen from Fig. 2 that variation of F with ϵ is moderate, which indicate that the flow resistance due to the presence of a porous matrix is not a strong function of porosity. An average value of 0.072 can be assessed in the present paper. It should be noted that a reasonable value of $F = 0.074$ was proposed by Beavers and Sparrow (1969).

Conclusions

The non-Darcian flow is assumed passing through the pin-fins porous matrix. The permeability K associated with the practical porous matrix is of the order of 10^{-7} to 10^{-6} m^2. A rapidly increasing rate of K is obtained as porosity becomes large. Variation of inertial constant F with ϵ is considered to be moderate and an average value of 0.072 is proposed.

Acknowledgment

This work was supported by National Science Council, Taiwan, R. O. C. under grant number NSC 83-0401-E005-068.

References

Beavers, G. S., and Sparrow, E. M., 1969, "Non-Darcy Flow Through Fibrous Porous Media," JOURNAL OF APPLIED MECHANICS, pp. 711–714.

Ergun, S., 1952, "Fluid Flow Through Packed Columns," Chemical Engineering Process, Vol. 48, pp. 89–94.

IMSL MATH/LIBRARY, version 1.1, MALB-USM-UNBND-EN8912-1.1, December 1989.

Scheidegger, A. E., 1974, *The Physics of Flow Through Porous Media,* University of Toronto Press, ISBN 0-8020-1849-1.

Sparrow, E. M., and Grannis, V. B., 1991, "Pressure Drop Characteristics of Heat Exchangers Consisting of Arrays of Diamond-Shaped Pin Fins," *Int. J. Heat Mass Transfer,* Vol. 34, No. 3, pp. 589–600.

Vafai, K., and Kim, S. J., 1990, "Analysis of Surface Enhancement by a Porous Substrate," JOURNAL OF HEAT TRANSFER, Vol. 112, pp. 700–706.

Journal of Heat Transfer

Discussion

Discussion of a Discussion by F. Chen, and C. F. Chen[1]

D. A. Nield.[2] The closures by Vafai and Kim (1995b, 1996) have been helpful in clarifying some matters, but they have raised some other issues which invite comment.

Vafai and Kim (1990) in their equation (10b) wrote two expressions ''which together imply the matching of the total normal stress at the interface,'' and only later mentioned that they were adopting the approximation of setting the effective viscosity equal to the fluid viscosity. They did not then point out the implications of this. Vafai and Kim (1995a, b) presented an argument aimed at showing that the total normal stress boundary condition reduced to the continuity of pressure at the interface without any mention of the value of the effective viscosity, leading the reader to infer that the argument is meant to hold for all choices of the effective viscosity. It seems to me that this argument (for the general viscosity ratio) breaks down at the crucial point where they referred to Chen and Chen (1992) and that the basic conclusion of Chen and Chen (1996) is correct: the two expressions are equivalent when the effective viscosity is equal to the fluid viscosity (and the fluid is incompressible), but there is inconsistency for other choices of the effective viscosity. In order to remove possible confusion, it is necessary that Vafai and Kim now clarify their position regarding the situation where the effective viscosity is not equal to the fluid viscosity.

It is fortunate that Vafai and his colleagues have not implemented two expressions for the normal stress in their numerical work. Rather, they used a one-domain approach in terms ot the vorticity-stream function-temperature formulation. They believed that in this formulation, the normal stress condition was satisfied indirectly. For example, Vafai and Huang (1994) said nothing about how their normal stress boundary conditions (10b) were implemented, and the reader was left to guess that they probably implicitly assumed that the stream function and vorticity are continuous across the interface. It is true that the continuity of velocity and tangential stress (and viscosity) do imply the continuity of stream function and vorticity, but that is independent of the form of the normal stress condition.

It is interesting that Poulikakos et al. (1986) did not explicitly impose any normal stress boundary condition at the interface in their work, which also involved a vorticity-stream function formulation. It seems that in this formulation there is some sort of implicit numerical matching condition which replaces the physical boundary condition. Professor J. L. Lage has pointed out to me that there is a fundamental difficulty in translating from a two-media formulation (with interface boundary conditions) to a single medium, in the way in which Vafai and Huang (1994) have done. What defines the interface conditions is no longer the analytical model but rather the numerical scheme used to solve the equations. One or more general differential equations are taken to apply for the whole domain. What distinguishes one subdomain from the other are the physical properties of each subdomain (permeability, porosity, inertia coefficient, etc.); what happens at the interface depends on how the code is structured. A detailed investigation will be required in order to learn how the numerical solution, based on a particular code, relates to the physical boundary conditions which should be satisfied at the interface between a porous medium and a fluid. I would expect the numerical solution from a vorticity-streamfunction approach to overestimate the heat transfer as a result of the constraining effect of the physical normal stress condition not being fully taken into account.

There is one further feature of the Vafai and Huang (1994) paper which requires comment. It is not immediately clear if the symbol **v** in their Eq. (5) denotes the Darcy velocity or the intrinsic velocity; the reader is left to deduce that if the effective conductivity is defined in the usual manner, then their Eq. (6) implies that **v** must denote the Darcy velocity. If that is correct then the left hand side of Eq. (5) should be divided by a factor ϵ (the porosity). It is fortunate that Vafai and Huang have performed calculations for the case of small Darcy numbers only, so the effect on the numerical results is expected to be small. It is important to note that their results are limited to this case. It would have been less confusing if they had omitted the convective term completely, as recommended by Nield (1991). Incidentally, it also appears that eq. (6) of Vafai and Huang (1994) differs from eq. (16) of Vafai and Tien (1981) in that the symbol α_e is defined differently in the two papers (the porosity is explicitly involved in one expression but not in the other). An explanation for this difference would help the reader.

Vafai and Kim (1996) conclude a long paragraph with ''it becomes clear in their Eqs. (16) and (17), Chen and Chen (1992) have failed to set these viscosity coefficients equal. This mistake affects the results of the analysis of Chen and Chen (1992).'' It is not clear to me that Chen and Chen have made any mistake. Their Eqs. (16) and (17) are simply the nondimensional component forms of their Eq. (5), which indicates that they have taken the effective (dynamic) viscosity μ_{eff} equal to the fluid μ/ϕ, where μ denotes the fluid viscosity and ϕ the porosity. This is in agreement with the result obtained by local volume averaging by Vafai and Tien (1981) and several other authors. This appears to be the best choice of effective viscosity to model flow near the solid boundaries. The solid boundaries are more restrictive to the flow and are thus expected to have a greater effect on heat transfer than the interface, so it is important to deal accurately with the effect of the solid boundaries.

---

[1] Published in the February 1996 issue of the ASME JOURNAL OF HEAT TRANSFER, Vol. 118, pp. 266–268.

[2] Department of Engineering Science, University of Auckland, Private Bag 92019, Auckland, New Zealand.

At the interface, the stress is somewhat indeterminant so it is not too important which value of the effective viscosity is taken in modelling the interface. Chen and Chen chose to take μ (the simplest expression) as the effective viscosity at the interface and in my view that is a reasonable choice.

Caution is needed in referring to the work of Brinkman (1947), Lundgren (1972), and Neale and Nader (1974). Brinkman used the equation which now bears his name for a purpose different from that of modern authors, and a similar remark applies to Lundgren's work. Neale and Nader were concerned with relating the Brinkman equation to the well known semi-empirical equation of Beavers and Joseph, and their work is restricted to unidirectional flows parallel to the interface. Thus, their work should not be expected to extend automatically to the more general flow treated by Chen and Chen (1992), so Chen and Chen were under no obligation to follow Brinkman, Lundgren, Neale, and Nader in their choice of effective viscosity.

For the case of media of small or moderate permeability, it probably does not matter much, from a purely empirical as distinct from a scientific viewpoint, whether or not one takes the effective viscosity to be equal to the fluid viscosity, or that divided by the porosity, in the differential equation or the boundary conditions. In that case, the Brinkman term plays a minor role in comparison with the Darcy term. Also, in the determination of the temperature field, the stress boundary conditions play a minor role (because higher derivatives are involved) in comparison with the conditions of continuous temperature, heat flux, and normal velocity. Consequently, the published heat transfer results of Chen and Chen, Vafai and coworkers, and other authors should all be satisfactory. However, for media of high permeability further investigation is necessary in order to determine the range of validity of the published results (the ratio of effective viscosity to fluid viscosity can be of order 10; for example, Givler and Altobelli (1994) reported the fact that one material yielded an experimental value of about 7.5 for this ratio).

References

Brinkman, H. C., 1947, "A Calculation of the Viscous Force Exerted by a Flowing Fluid on a Dense Swarm of Particles," *Applied Scientific Research,* Vol. A1, pp. 27–34.

Chen, F., and Chen, C. F., 1992, "Convection in Superposed Fluid and Porous Layers," *Journal of Fluid Mechanics,* Vol. 234, pp. 97–119.

Chen, F., and Chen, C. F., 1996, discussion, ASME JOURNAL OF HEAT TRANSFER, Vol. 118, pp. 266–267.

Givler, R. C., and Altobelli, S. A., 1994, *Journal of Fluid Mechanics,* Vol. 258, pp. 355–370.

Lundgren, T. S., 1972, "Slow Flow Through Stationary Random Beds and Suspensions of Spheres," *Journal of Fluid Mechanics,* Vol. 51, pp. 273–299.

Neale, G., and Nader, W., 1974, "Practical Significance of Brinkman's Extension of Darcy's Law: Coupled Parallel Flows Within a Channel and a Bounding Porous Medium," *Canadian Journal of Chemical Engineering,* Vol. 52, pp. 475–478.

Nield, D. A., 1991, "The Limitations of the Brinkman-Forchheimer Equation in Modeling Flow in a Saturated Porous Medium and at an Interface," *International Journal of Heat Fluid Flow,* Vol. 12, pp. 269–272.

Nield, D. A., 1995, discussion, ASME JOURNAL OF HEAT TRANSFER, Vol. 117, p. 554.

Poulikakos, D., Bejan, A., Selimos, B., and Blake, K. R., 1986, "High Rayleigh Number Convection in a Fluid Layer Overlying a Porous Bed," *International Journal of Heat and Fluid Flow,* Vol. 7, pp. 109–116.

Vafai, K., and Huang, P. C., 1994, "Analysis of Heat Transfer Regulation and Modification Employing Intermittently Emplaced Porous Cavities," ASME JOURNAL OF HEAT TRANSFER, Vol. 116, pp. 604–613.

Vafai, K., and Kim, S. J., 1995a, "On the Limitations of the Brinkman-Forchheimer Extended Equation," *International Journal of Heat and Fluid Flow,* Vol. 16, pp. 11–16.

Vafai, K., and Kim, S. J., 1995b, author's closure, ASME JOURNAL OF HEAT TRANSFER, Vol. 117, pp. 554–555.

Vafai, K., and Kim, S. J., 1996, authors' closure, ASME JOURNAL OF HEAT TRANSFER, Vol. 118, pp. 267–268.

Vafai, K., and Tien, C. L., 1981, "Boundary and Inertia Effects on Flow and Heat Transfer in Porous Media," *International Journal of Heat and Mass Transfer,* Vol. 24, pp. 195–203.

Closure[3]

K. Vafai[4] and S. J. Kim[5]. We would like to thank Professor Nield for his comments and further discussion on this topic. However, it would have been quite beneficial if the author had read our statements, or even his, as related to this topic more carefully. Perhaps we can just quote Professor Nield here as we believe his own previous statements and our responses will further clarify what has already been a very clear description by us all along. First, it should be noted that in Nield (1995) the main subject of the discussion was about the fact that Vafai and Huang (1994) and Huang and Vafai (1994) are setting the fluid viscosity and the effective viscosity equal, i.e., they are using the same viscosity in front of both terms in both papers. In fact, Nield (1995) starts out his discussion about the works of Vafai and Huang (1994) and Huang and Vafai (1994) by saying, "In each of these papers the authors have modeled flow in a porous medium by a Brinkman-Forchheimer-extended Darcy equation (Eq. (5) of the first paper, Eq. (2) of the second) in which the coefficient of the Darcy term v/K is the same as the coefficient of the Brinkman term $\nabla^2 v$, and each is denoted by ν_{eff}." Therefore, the primary subject of the discussion and the closure (Vafai and Kim, 1995b) is centered around the fact that our coefficient for the Darcy term v/K is the same as our coefficient for the Brinkman term $\nabla^2 v$. We use different symbols for the fluid viscosity and the effective viscosity so as to make it clear that they are usually different (also to avoid another discussion on the same point), but then we make it clear that due to lack of definitive data we always use the same value of viscosity for both when dealing with porous-fluid interfaces.

These points were reiterated in our response in Vafai and Kim (1995b) which is reproduced here: "In general the coefficient of the Darcy term v/K is μ_f, and the coefficient of the Brinkman term, $\nabla^2 v$, is μ_{eff}, as shown in Eq. (5) of Vafai and Kim (1990). We are well aware that there are some situations where it is important to make a distinction as shown and discussed (for example, Vafai and Kim, 1990; Ettefagh, Vafai, and Kim, 1991; Huang and Vafai, 1994). But Lundgren (1972) and Neal and Nader (1974) have shown that setting the effective viscosity of the fluid-saturated porous medium equal to the fluid viscosity provides good agreement with experimental data. Hence, lacking definitive information on μ_{eff}, it has become a common practice to set the effective viscosity equal to the fluid viscosity." This effective viscosity as explained by Vafai and Kim (1995a, 1995b) is taken to be the fluid viscosity. This has always been our de facto approach for problems dealing with the porous-fluid interface.

In addition, it would be instructive if our interactive joint discussion in Nield et al. (1996) is read more carefully. In this discussion, once again, Nield states that, "The effective viscosity . . . may differ substantially from the fluid viscosity," and also that, "Vafai and Kim's argument on the normal stress condition collapses because they . . . have confused tangential and normal coordinates." In the same interactive discussion we once again have responded to these statements by stating, "The reason we always set the effective viscosity equal to the fluid viscosity is, as we had mentioned at various times, due to the lack of rigorous data and that it provides good agreement with past experimental data (Lundgren, 1972; Neale and Nader, 1974)," and, "With respect to the porous/fluid interface, the arguments stand. The confusion appears to be Nield's as we have not "confused tangential and normal coordinates." In Vafai and Kim (1995) and our other porous/fluid interface works, always a two-dimensional, incompressible, and isotropic porous medium, in which the effective and the fluid viscosities are

---

[3] Only references which are not given, if any, in the discussion are cited.

[4] Department of Mechanical Engineering, The Ohio State University, Columbus, Ohio 43210.

[5] Storage Systems Division, IBM Corporation, Tucson, AZ 85744.

At the interface, the stress is somewhat indeterminant so it is not too important which value of the effective viscosity is taken in modelling the interface. Chen and Chen chose to take μ (the simplest expression) as the effective viscosity at the interface and in my view that is a reasonable choice.

Caution is needed in referring to the work of Brinkman (1947), Lundgren (1972), and Neale and Nader (1974). Brinkman used the equation which now bears his name for a purpose different from that of modern authors, and a similar remark applies to Lundgren's work. Neale and Nader were concerned with relating the Brinkman equation to the well known semi-empirical equation of Beavers and Joseph, and their work is restricted to unidirectional flows parallel to the interface. Thus, their work should not be expected to extend automatically to the more general flow treated by Chen and Chen (1992), so Chen and Chen were under no obligation to follow Brinkman, Lundgren, Neale, and Nader in their choice of effective viscosity.

For the case of media of small or moderate permeability, it probably does not matter much, from a purely empirical as distinct from a scientific viewpoint, whether or not one takes the effective viscosity to be equal to the fluid viscosity, or that divided by the porosity, in the differential equation or the boundary conditions. In that case, the Brinkman term plays a minor role in comparison with the Darcy term. Also, in the determination of the temperature field, the stress boundary conditions play a minor role (because higher derivatives are involved) in comparison with the conditions of continuous temperature, heat flux, and normal velocity. Consequently, the published heat transfer results of Chen and Chen, Vafai and coworkers, and other authors should all be satisfactory. However, for media of high permeability further investigation is necessary in order to determine the range of validity of the published results (the ratio of effective viscosity to fluid viscosity can be of order 10; for example, Givler and Altobelli (1994) reported the fact that one material yielded an experimental value of about 7.5 for this ratio).

References

Brinkman, H. C., 1947, "A Calculation of the Viscous Force Exerted by a Flowing Fluid on a Dense Swarm of Particles," *Applied Scientific Research,* Vol. A1, pp. 27–34.

Chen, F., and Chen, C. F., 1992, "Convection in Superposed Fluid and Porous Layers," *Journal of Fluid Mechanics,* Vol. 234, pp. 97–119.

Chen, F., and Chen, C. F., 1996, discussion, ASME JOURNAL OF HEAT TRANSFER, Vol. 118, pp. 266–267.

Givler, R. C., and Altobelli, S. A., 1994, *Journal of Fluid Mechanics,* Vol. 258, pp. 355–370.

Lundgren, T. S., 1972, "Slow Flow Through Stationary Random Beds and Suspensions of Spheres," *Journal of Fluid Mechanics,* Vol. 51, pp. 273–299.

Neale, G., and Nader, W., 1974, "Practical Significance of Brinkman's Extension of Darcy's Law: Coupled Parallel Flows Within a Channel and a Bounding Porous Medium," *Canadian Journal of Chemical Engineering,* Vol. 52, pp. 475–478.

Nield, D. A., 1991, "The Limitations of the Brinkman-Forchheimer Equation in Modeling Flow in a Saturated Porous Medium and at an Interface," *International Journal of Heat Fluid Flow,* Vol. 12, pp. 269–272.

Nield, D. A., 1995, discussion, ASME JOURNAL OF HEAT TRANSFER, Vol. 117, p. 554.

Poulikakos, D., Bejan, A., Selimos, B., and Blake, K. R., 1986, "High Rayleigh Number Convection in a Fluid Layer Overlying a Porous Bed," *International Journal of Heat and Fluid Flow,* Vol. 7, pp. 109–116.

Vafai, K., and Huang, P. C., 1994, "Analysis of Heat Transfer Regulation and Modification Employing Intermittently Emplaced Porous Cavities," ASME JOURNAL OF HEAT TRANSFER, Vol. 116, pp. 604–613.

Vafai, K., and Kim, S. J., 1995a, "On the Limitations of the Brinkman-Forchheimer Extended Equation," *International Journal of Heat and Fluid Flow,* Vol. 16, pp. 11–16.

Vafai, K., and Kim, S. J., 1995b, author's closure, ASME JOURNAL OF HEAT TRANSFER, Vol. 117, pp. 554–555.

Vafai, K., and Kim, S. J., 1996, authors' closure, ASME JOURNAL OF HEAT TRANSFER, Vol. 118, pp. 267–268.

Vafai, K., and Tien, C. L., 1981, "Boundary and Inertia Effects on Flow and Heat Transfer in Porous Media," *International Journal of Heat and Mass Transfer,* Vol. 24, pp. 195–203.

Closure[3]

K. Vafai[4] and S. J. Kim[5]. We would like to thank Professor Nield for his comments and further discussion on this topic. However, it would have been quite beneficial if the author had read our statements, or even his, as related to this topic more carefully. Perhaps we can just quote Professor Nield here as we believe his own previous statements and our responses will further clarify what has already been a very clear description by us all along. First, it should be noted that in Nield (1995) the main subject of the discussion was about the fact that Vafai and Huang (1994) and Huang and Vafai (1994) are setting the fluid viscosity and the effective viscosity equal, i.e., they are using the same viscosity in front of both terms in both papers. In fact, Nield (1995) starts out his discussion about the works of Vafai and Huang (1994) and Huang and Vafai (1994) by saying, "In each of these papers the authors have modeled flow in a porous medium by a Brinkman-Forchheimer-extended Darcy equation (Eq. (5) of the first paper, Eq. (2) of the second) in which the coefficient of the Darcy term v/K is the same as the coefficient of the Brinkman term $\nabla^2 v$, and each is denoted by ν_{eff}." Therefore, the primary subject of the discussion and the closure (Vafai and Kim, 1995b) is centered around the fact that our coefficient for the Darcy term v/K is the same as our coefficient for the Brinkman term $\nabla^2 v$. We use different symbols for the fluid viscosity and the effective viscosity so as to make it clear that they are usually different (also to avoid another discussion on the same point), but then we make it clear that due to lack of definitive data we always use the same value of viscosity for both when dealing with porous-fluid interfaces.

These points were reiterated in our response in Vafai and Kim (1995b) which is reproduced here: "In general the coefficient of the Darcy term v/K is μ_f, and the coefficient of the Brinkman term, $\nabla^2 v$, is μ_{eff}, as shown in Eq. (5) of Vafai and Kim (1990). We are well aware that there are some situations where it is important to make a distinction as shown and discussed (for example, Vafai and Kim, 1990; Ettefagh, Vafai, and Kim, 1991; Huang and Vafai, 1994). But Lundgren (1972) and Neal and Nader (1974) have shown that setting the effective viscosity of the fluid-saturated porous medium equal to the fluid viscosity provides good agreement with experimental data. Hence, lacking definitive information on μ_{eff}, it has become a common practice to set the effective viscosity equal to the fluid viscosity." This effective viscosity as explained by Vafai and Kim (1995a, 1995b) is taken to be the fluid viscosity. This has always been our de facto approach for problems dealing with the porous-fluid interface.

In addition, it would be instructive if our interactive joint discussion in Nield et al. (1996) is read more carefully. In this discussion, once again, Nield states that, "The effective viscosity . . . may differ substantially from the fluid viscosity," and also that, "Vafai and Kim's argument on the normal stress condition collapses because they . . . have confused tangential and normal coordinates." In the same interactive discussion we once again have responded to these statements by stating, "The reason we always set the effective viscosity equal to the fluid viscosity is, as we had mentioned at various times, due to the lack of rigorous data and that it provides good agreement with past experimental data (Lundgren, 1972; Neale and Nader, 1974)," and, "With respect to the porous/fluid interface, the arguments stand. The confusion appears to be Nield's as we have not "confused tangential and normal coordinates." In Vafai and Kim (1995) and our other porous/fluid interface works, always a two-dimensional, incompressible, and isotropic porous medium, in which the effective and the fluid viscosities are

---

[3] Only references which are not given, if any, in the discussion are cited.

[4] Department of Mechanical Engineering, The Ohio State University, Columbus, Ohio 43210.

[5] Storage Systems Division, IBM Corporation, Tucson, AZ 85744.

equal, is considered. The equations are correct as they are for the cited conditions. We cannot emphasize this point any stronger. Once again, it would be good if our previous discussions are read more carefully.

With respect to, "There is one further feature of the Vafai and Huang (1994) paper which requires comment . . . ," we are thankful for Professor Nield for clarifying the positions that we have always invariably held. However, it is ironic that he is now basing his discussion on a term that he has been stating all along should not even be there. This is a term that we have clearly shown to be negligible "for most practical situations", Vafai and Tien, (1981), and various other works have also shown it to be negligible except for rare cases discussed in Vafai and Tien (1981). In the work presented in Vafai and Huang (1994), once again we have found that the convective term has essentially no effect on the results. We had found early that it makes no difference in our runs whether the epsilon-related coefficient in front of the convective term is present or not. This is because this term itself has no impact on the results. Therefore, in lieu of the fact that it has literally no impact, we had decided to just leave it out. This has no effect on any of the results. It is good, however, to see that Nield is moving ever more closely to the position that we have invariably held from the very beginning of proposing the generalized formulation. With respect to the thermal conductivity, we are thankful to Professor Nield for raising the question. However, it should be noted that the porosity in Eq. (6) of Vafai and Huang (1994) is embedded in the effective thermal conductivity. It should be noted that the effective thermal conductivity is already a function of the porosity. Therefore, the effective thermal conductivity is just presented in a different form. In essence, this is like representing $f_1(x)/x$ by $f_2(x)$. Conceptually, there is no difference between the two formulations. We are also thankful for Professor Nield's attention to this paper which is quite rich in physical and phenomenological descriptions that set a very innovative approach for heat transfer regulation and modification.

With respect to the comments on the vorticity-stream function formulation, here, once again, it appears that there is misunderstanding of the numerical procedure for handling a porous/fluid composite layer. As pointed out in Vafai and Kim (1990), one can use separate calculation schemes for the porous and fluid regions which would require an involved iterative procedure for matching the interface conditions. A more efficient approach is to combine the two sets of governing equations for the fluid region and the porous region into one set of conservation equations. In other words, the porous substrate and the fluid region can be modeled as a single domain governed by one set of equations, the solution of which satisfies the continuity of the velocities, stresses, temperature, and the heat fluxes across the porous/fluid interface. Hence, the inclusion of derivatives of the Darcy number and inertial coefficient in Eq. (17) of the first paper plays a role only across the interface. The same approach has been used by other investigators. It is good to hear about Professor Lage's personal feelings about this approach and we are thankful for his extra attention to our works. However, it should be noted that the one domain approach used by us is based on physical principles and it is not at all dependent on how our code is structured, as long as it is written correctly.

As for our statements regarding Chen and Chen's failure to set these coefficients equal, our statements and position stand as they are. Unfortunately, the statements by Professor Nield regarding the work of Brinkman (1947) stem from a confusion of the very issue that he is trying to discuss. Therefore, to clarify this issue once again we will briefly go through the explanation of the factors that must be considered and the clarifications regarding the effective viscosity and the fluid viscosity coefficients. For these coefficients to be equal, the coefficient for the Darcy term v/K and the coefficient for the Brinkman term $\nabla^2 v$ need to be set equal. This means that the effective viscosity, which refers to the coefficient in front of the Laplacian of the velocity of the fluid-saturated porous medium, should be equal to the fluid-viscosity. This point is directly and exactly consistent with the original formulation by Brinkman (1947) as displayed in his Eq. (5), Neale and Nader (1974) as displayed in their Eq. (1.7), as well as various other investigators. This is precisely what Vafai and Huang (1994) and Huang and Vafai (1994) have done. This is not a matter of style.

Finally, it is quite interesting to read after all these discussions that Nield is stating, "For the case of media of small or moderate permeability, it probably does not matter much, from a purely empirical as distinct from a scientific viewpoint, whether or not one takes the effective viscosity to be equal to the fluid viscosity, or that divided by the porosity, in the differential equation or the boundary conditions." We cannot help but think why we had to spend so much time on this issue.

In summary, we would like to thank Professor Nield for an extension of an extension of this discussion. However, we have already discussed these issues at length and with clarity with respect to several inapplicable points. As such, we believe any further discussion on what has already been presented at length would not serve any technical need.

Additional Reference

Nield, D. A., Vafai, K., and Kim, S. J., 1996, "Closure Statements on the Brinkman-Forchheimer Extended Darcy Model," *International Journal of Heat and Fluid Flow*, Vol. 17, pp. 34–35.

Discussion of a Discussion by K. Vafai and S. J. Kim[1]

D. A. Nield[2] and J. L. Lage.[3] In their discussion of a recent paper, Vafai and Kim (1995, p. 1097) stated that they had shown that, "the solution of Vafai and Kim (1989) . . . is valid for Da < 1, which covers the entire range of all porous media." In making this statement they have overlooked the fact that there is a class of materials of practical importance which are appropriately modeled by the Brinkman-Forchhiemer equation and for which the Darcy number can exceed unity. For example, Weinert and Lage (1994) reported permeabilities of compressed aluminum-alloy foams as high as 8×10^{-6} m^2, and for a 1.0 mm thick layer of such material the Darcy number is equal to about eight. Materials in this class have a connected solid matrix and a connected void space.

For this type of porous medium that we propose be called a "hyperporous medium," the Brinkman term has order of magnitude comparable with that of the Darcy term throughout the medium (rather than just in boundary layers near solid walls). The "permeability" K which appears in the Darcy term of the general momentum equation is no longer determined, in a Darcy type experiment, as simply the fluid viscosity times the mean Darcy velocity divided by the pressure gradient. Rather, one has to allow for the contribution of the Brinkman term to the pressure gradient. As the porosity becomes closer to unity, the Brinkman term dominates over the Darcy term, and the value of K (and hence the Darcy number) can increase without limit (other than that imposed by the strength of the solid material from which the matrix is constructed).

---

[1] Published in the November 1995 issue of the ASME Journal of Heat Transfer, Vol. 117, pp. 1097–1098.

[2] Department of Engineering Science, University of Auckland, Private Bag 92019, Auckland, New Zealand.

[3] Department of Mechanical Engineering, Southern Methodist University, Dallas, TX 75275-0337.

equal, is considered. The equations are correct as they are for the cited conditions. We cannot emphasize this point any stronger. Once again, it would be good if our previous discussions are read more carefully.

With respect to, "There is one further feature of the Vafai and Huang (1994) paper which requires comment . . . ," we are thankful for Professor Nield for clarifying the positions that we have always invariably held. However, it is ironic that he is now basing his discussion on a term that he has been stating all along should not even be there. This is a term that we have clearly shown to be negligible "for most practical situations", Vafai and Tien, (1981), and various other works have also shown it to be negligible except for rare cases discussed in Vafai and Tien (1981). In the work presented in Vafai and Huang (1994), once again we have found that the convective term has essentially no effect on the results. We had found early that it makes no difference in our runs whether the epsilon-related coefficient in front of the convective term is present or not. This is because this term itself has no impact on the results. Therefore, in lieu of the fact that it has literally no impact, we had decided to just leave it out. This has no effect on any of the results. It is good, however, to see that Nield is moving ever more closely to the position that we have invariably held from the very beginning of proposing the generalized formulation. With respect to the thermal conductivity, we are thankful to Professor Nield for raising the question. However, it should be noted that the porosity in Eq. (6) of Vafai and Huang (1994) is embedded in the effective thermal conductivity. It should be noted that the effective thermal conductivity is already a function of the porosity. Therefore, the effective thermal conductivity is just presented in a different form. In essence, this is like representing $f_1(x)/x$ by $f_2(x)$. Conceptually, there is no difference between the two formulations. We are also thankful for Professor Nield's attention to this paper which is quite rich in physical and phenomenological descriptions that set a very innovative approach for heat transfer regulation and modification.

With respect to the comments on the vorticity-stream function formulation, here, once again, it appears that there is misunderstanding of the numerical procedure for handling a porous/fluid composite layer. As pointed out in Vafai and Kim (1990), one can use separate calculation schemes for the porous and fluid regions which would require an involved iterative procedure for matching the interface conditions. A more efficient approach is to combine the two sets of governing equations for the fluid region and the porous region into one set of conservation equations. In other words, the porous substrate and the fluid region can be modeled as a single domain governed by one set of equations, the solution of which satisfies the continuity of the velocities, stresses, temperature, and the heat fluxes across the porous/fluid interface. Hence, the inclusion of derivatives of the Darcy number and inertial coefficient in Eq. (17) of the first paper plays a role only across the interface. The same approach has been used by other investigators. It is good to hear about Professor Lage's personal feelings about this approach and we are thankful for his extra attention to our works. However, it should be noted that the one domain approach used by us is based on physical principles and it is not at all dependent on how our code is structured, as long as it is written correctly.

As for our statements regarding Chen and Chen's failure to set these coefficients equal, our statements and position stand as they are. Unfortunately, the statements by Professor Nield regarding the work of Brinkman (1947) stem from a confusion of the very issue that he is trying to discuss. Therefore, to clarify this issue once again we will briefly go through the explanation of the factors that must be considered and the clarifications regarding the effective viscosity and the fluid viscosity coefficients. For these coefficients to be equal, the coefficient for the Darcy term v/K and the coefficient for the Brinkman term $\nabla^2 v$ need to be set equal. This means that the effective viscosity, which refers to the coefficient in front of the Laplacian of the velocity of the fluid-saturated porous medium, should be equal to the fluid-viscosity. This point is directly and exactly consistent with the original formulation by Brinkman (1947) as displayed in his Eq. (5), Neale and Nader (1974) as displayed in their Eq. (1.7), as well as various other investigators. This is precisely what Vafai and Huang (1994) and Huang and Vafai (1994) have done. This is not a matter of style.

Finally, it is quite interesting to read after all these discussions that Nield is stating, "For the case of media of small or moderate permeability, it probably does not matter much, from a purely empirical as distinct from a scientific viewpoint, whether or not one takes the effective viscosity to be equal to the fluid viscosity, or that divided by the porosity, in the differential equation or the boundary conditions." We cannot help but think why we had to spend so much time on this issue.

In summary, we would like to thank Professor Nield for an extension of an extension of this discussion. However, we have already discussed these issues at length and with clarity with respect to several inapplicable points. As such, we believe any further discussion on what has already been presented at length would not serve any technical need.

Additional Reference

Nield, D. A., Vafai, K., and Kim, S. J., 1996, "Closure Statements on the Brinkman-Forchheimer Extended Darcy Model," *International Journal of Heat and Fluid Flow*, Vol. 17, pp. 34–35.

Discussion of a Discussion by K. Vafai and S. J. Kim[1]

D. A. Nield[2] and J. L. Lage.[3] In their discussion of a recent paper, Vafai and Kim (1995, p. 1097) stated that they had shown that, "the solution of Vafai and Kim (1989) . . . is valid for Da < 1, which covers the entire range of all porous media." In making this statement they have overlooked the fact that there is a class of materials of practical importance which are appropriately modeled by the Brinkman-Forchhiemer equation and for which the Darcy number can exceed unity. For example, Weinert and Lage (1994) reported permeabilities of compressed aluminum-alloy foams as high as 8×10^{-6} m^2, and for a 1.0 mm thick layer of such material the Darcy number is equal to about eight. Materials in this class have a connected solid matrix and a connected void space.

For this type of porous medium that we propose be called a "hyperporous medium," the Brinkman term has order of magnitude comparable with that of the Darcy term throughout the medium (rather than just in boundary layers near solid walls). The "permeability" K which appears in the Darcy term of the general momentum equation is no longer determined, in a Darcy type experiment, as simply the fluid viscosity times the mean Darcy velocity divided by the pressure gradient. Rather, one has to allow for the contribution of the Brinkman term to the pressure gradient. As the porosity becomes closer to unity, the Brinkman term dominates over the Darcy term, and the value of K (and hence the Darcy number) can increase without limit (other than that imposed by the strength of the solid material from which the matrix is constructed).

---

[1] Published in the November 1995 issue of the ASME JOURNAL OF HEAT TRANSFER, Vol. 117, pp. 1097–1098.

[2] Department of Engineering Science, University of Auckland, Private Bag 92019, Auckland, New Zealand.

[3] Department of Mechanical Engineering, Southern Methodist University, Dallas, TX 75275-0337.

We suggest that in future work concerned with hyperporous media, one should distinguish between: (i) K_D, the usual ''Darcy permeability'' obtained experimentally using Darcy's law only; and (ii) K_h, the ''hyperporous permeability,'' i.e., the parameter that appears in the momentum equation and represents a coefficient for viscous drag caused by the solid matrix only.

Vafai and Kim (1995) have also overlooked the fact that their Fig. 2, which presents plots of Nusselt number and centerline velocity versus Darcy number Da, for an unstated value of their inertia parameter Λ_I, shows a small but significant systematic discrepancy between their new numerical results and the results of Vafai and Kim (1989) as soon as Da is greater than about 0.01. Furthermore, the velocity profile displayed in their Fig. 1 reveals that for $\Lambda_I = 10$ and $\mathrm{Da} = 1$ there is a significant discrepancy between the two sets of results. If they had performed calculations for smaller values of Λ_I they would have found a larger discrepancy. Although Vafai and Kim (1995) describe the solution of Vafai and Kim (1989) as an ''exact solution,'' it in fact involves a boundary-layer approximation, and they have now merely shown that their approximate solution is accurate in those cases in which boundary layers occur (which is true for most, but not all, practical situations).

We note that Vafai and Kim (1995) have corrected a ''typo'' in Eq. (9) of their 1989 paper and that this conforms with the correct solution of the differential equation for the case $\Lambda_I = 0$, a solution originally obtained (essentially) by Kaviany (1985) and presented in rearranged form by Lauriat and Vafai (1991). However, Eq. (8) of Vafai and Kim (1989) actually leads to the asymptotic expression

$$u = 1 - \exp[\mathrm{Da}^{-1/2}(y - 1)]. \qquad (1)$$

This result has been supplied to us by Professor Vafai (1996), and we have confirmed its correctness. The discrepancy in the predicted centerline velocity is thus of magnitude $\exp(-\mathrm{Da}^{-1/2})$, and this becomes significant as soon as Da is of order unity. For example, when $\Lambda_I = 0.1$, values of the discrepancy are 11 percent for $\mathrm{Da} = 0.2$ and 37 percent for $\mathrm{Da} = 1$.

In order to deal with a hyperporous medium an analytical solution of the momentum equation of Vafai and Kim (1989) valid for all values of Da is essential. Such a solution, including the effect of the Forchheimer term, has been reported by Nield, Junqueira, and Lage (1996). When the Forchhheimer term is negligible, the simple formula given by Kaviany (1985) is appropriate.

References

Nield, D. A., Junqueira, S. L. M., and Lage, J. L., 1996, ''Forced Convection in a Fluid Saturated Porous Medium Channel With Isothermal or Isoflux Boundaries,'' *Journal of Fluid Mechanics,* Vol. 322, pp. 201–214.

Kaviany, M., 1985, ''Laminar Flow Through a Porous Channel Bounded by Isothermal Parallel Plates,'' *International Journal of Heat Mass Transfer,* Vol. 28, pp. 851–858.

Lauriat, G., and Vafai, K., 1991, ''Forced Convection Flow and Heat Transfer Through a Porous Medium Exposed to a Flat Plate or Channel,'' *Convective Heat and Mass Transfer in Porous Media,* S. Kakac et al., eds., Kluwer Academic, Dordrecht, pp. 289–327.

Vafai, K., 1996, personal communication.

Vafai, K., and Kim, S. J., 1989, ''Forced Convection in a Channel Filled With a Porous Medium: An Exact Solution,'' ASME JOURNAL OF HEAT TRANSFER, Vol. 111, pp. 1103–1106.

Vafai, K., and Kim, S. J., 1995, discussion, ASME JOURNAL OF HEAT TRANSFER, Vol. 117, pp. 1097–1098.

Weinert, A., and Lage, J. L., 1994, ''Porous Aluminum-Alloy Based Cooling Devices for Electronics,'' SMU-MED-CPMA Inter. Rep., 1.01/94.

Closure[4]

K. Vafai[5] and S. J. Kim[6]. We appreciate the comments by Nield and Lage on our discussion with Hadim (Vafai and Kim, 1995). We are thankful to the attention they have given to our original work (Vafai and Kim, 1989). Nield et al. (1996) have come up with a different perspective of the exact solution given by Vafai and Kim (1989). They have obtained an interesting mathematical representation of a numerical integration procedure which is a useful counterpart to the full numerical solution of the momentum equation.

The interesting porous medium (a layer which is one mm thick as cited by the authors) which resides in Professor Lage's laboratory, while being novel and obviously quite useful, is similar to a thin screen. Furthermore, the types of porous media Nield and Lage are considering do not satisfy the basic characteristics of what constitutes a porous medium. For example, their porous medium does not have a persistent solid phase, nor does it satisfy the Representative Elementary Volume (REV) requirement mentioned in various places, including Nield and Bejan (1992). In reality, what the authors should mention is that they like to extend the use of the porous medium formulation for situations other than those represented by a real porous medium. In fact, an approach using the porous medium formulation for situations in which there is, in essence, no real porous media has been used by our group in the past. We prefer to refer to all these cases as ''pseudo porous medium.'' This, in our opinion, is a more accurate and representative term as it covers an entire class of materials which are not really porous media but for which the porous medium formulation is utilized to represent the transport processes. Therefore, we support the authors to follow up on the utilization of the porous medium formulation for the ''pseudo porous medium'' as we and a few other researchers have done in the past.

Vafai and Kim's (1989) solution is based on the free stream velocity, u_∞, which is equal to the center line velocity after the flow is fully developed, as long as the two boundary layers along the walls (top and bottom) don't interact with each other. This is because: (1) the thickness of the momentum boundary layer does not grow as the streamwise coordinate increases; and (2) the thickness of the momentum boundary layer is of the order of $\sqrt{K/\delta}/H$ or $\mathrm{Da}^{1/2}$. These two facts were shown by Vafai and Tien (1981) and later further substantiated by various other researchers (e.g., Kaviany, 1985) and were well addressed in Vafai and Kim (1989). The main difference between the interesting numerical solution presented by Nield et al. (1996) and the exact closed form solution presented by Vafai and Kim (1989) is in the use of the second derivative of the velocity with respect to y. Vafai and Kim (1989) assumed that outside the momentum boundary layer, in the core region,

$$\frac{d^2u}{dy^2} = 0.$$

The validity of this assumption, which can be shown by scaling analysis, was also rigorously proven and established by comparing the exact solution from Vafai and Kim (1989) with the ''Full Numerical Solution'' of the momentum Eq. (4) and boundary conditions (5a) and (5b) (using no slip boundary conditions on both walls of the channel) of Vafai and Kim (1989). As established by Hadim, the exact solution obtained by Vafai and Kim (1989) precisely matches (the curves corresponding to the numerical solution and the exact solution are inseparable for a vast range of parameters which covers, to the best of our knowledge, the entire range of known bona fide porous media) the numerical solution of the momentum equation given by Eq. (4) and boundary conditions (5a) and (5b) of Vafai and Kim (1989). The exact solution starts deviating from the numerical solution for $\mathrm{Da} > 1$.

Nield et al. (1996) used Romberg's numerical integration to solve the integrals in their Eqs. (10) and (11). This is an interesting counterpart to the full numerical solution of the momentum equation which is an ODE. Even though they have presented a different numerical procedure, their solution cannot

---

[4] Only references which are not given, if any, in the discussion are cited.

[5] Department of Mechanical Engineering, The Ohio State University, Columbus, Ohio 43210.

[6] Storage Systems Division, IBM Corporation, Tucson, AZ 85744.

We suggest that in future work concerned with hyperporous media, one should distinguish between: (i) K_D, the usual "Darcy permeability" obtained experimentally using Darcy's law only; and (ii) K_h, the "hyperporous permeability," i.e., the parameter that appears in the momentum equation and represents a coefficient for viscous drag caused by the solid matrix only.

Vafai and Kim (1995) have also overlooked the fact that their Fig. 2, which presents plots of Nusselt number and centerline velocity versus Darcy number Da, for an unstated value of their inertia parameter Λ_l, shows a small but significant systematic discrepancy between their new numerical results and the results of Vafai and Kim (1989) as soon as Da is greater than about 0.01. Furthermore, the velocity profile displayed in their Fig. 1 reveals that for $\Lambda_l = 10$ and $\mathrm{Da} = 1$ there is a significant discrepancy between the two sets of results. If they had performed calculations for smaller values of Λ_l they would have found a larger discrepancy. Although Vafai and Kim (1995) describe the solution of Vafai and Kim (1989) as an "exact solution," it in fact involves a boundary-layer approximation, and they have now merely shown that their approximate solution is accurate in those cases in which boundary layers occur (which is true for most, but not all, practical situations).

We note that Vafai and Kim (1995) have corrected a "typo" in Eq. (9) of their 1989 paper and that this conforms with the correct solution of the differential equation for the case $\Lambda_l = 0$, a solution originally obtained (essentially) by Kaviany (1985) and presented in rearranged form by Lauriat and Vafai (1991). However, Eq. (8) of Vafai and Kim (1989) actually leads to the asymptotic expression

$$u = 1 - \exp[\mathrm{Da}^{-1/2}(y - 1)]. \tag{1}$$

This result has been supplied to us by Professor Vafai (1996), and we have confirmed its correctness. The discrepancy in the predicted centerline velocity is thus of magnitude $\exp(-\mathrm{Da}^{-1/2})$, and this becomes significant as soon as Da is of order unity. For example, when $\Lambda_l = 0.1$, values of the discrepancy are 11 percent for $\mathrm{Da} = 0.2$ and 37 percent for $\mathrm{Da} = 1$.

In order to deal with a hyperporous medium an analytical solution of the momentum equation of Vafai and Kim (1989) valid for all values of Da is essential. Such a solution, including the effect of the Forchheimer term, has been reported by Nield, Junqueira, and Lage (1996). When the Forchhheimer term is negligible, the simple formula given by Kaviany (1985) is appropriate.

References

Nield, D. A., Junqueira, S. L. M., and Lage, J. L., 1996, "Forced Convection in a Fluid Saturated Porous Medium Channel With Isothermal or Isoflux Boundaries," *Journal of Fluid Mechanics,* Vol. 322, pp. 201–214.

Kaviany, M., 1985, "Laminar Flow Through a Porous Channel Bounded by Isothermal Parallel Plates," *International Journal of Heat Mass Transfer,* Vol. 28, pp. 851–858.

Lauriat, G., and Vafai, K., 1991, "Forced Convection Flow and Heat Transfer Through a Porous Medium Exposed to a Flat Plate or Channel," *Convective Heat and Mass Transfer in Porous Media,* S. Kakac et al., eds., Kluwer Academic, Dordrecht, pp. 289–327.

Vafai, K., 1996, personal communication.

Vafai, K., and Kim, S. J., 1989, "Forced Convection in a Channel Filled With a Porous Medium: An Exact Solution," ASME JOURNAL OF HEAT TRANSFER, Vol. 111, pp. 1103–1106.

Vafai, K., and Kim, S. J., 1995, discussion, ASME JOURNAL OF HEAT TRANSFER, Vol. 117, pp. 1097–1098.

Weinert, A., and Lage, J. L., 1994, "Porous Aluminum-Alloy Based Cooling Devices for Electronics," SMU-MED-CPMA Inter. Rep., 1.01/94.

Closure[4]

K. Vafai[5] and S. J. Kim[6]. We appreciate the comments by Nield and Lage on our discussion with Hadim (Vafai and Kim, 1995). We are thankful to the attention they have given to our original work (Vafai and Kim, 1989). Nield et al. (1996) have come up with a different perspective of the exact solution given by Vafai and Kim (1989). They have obtained an interesting mathematical representation of a numerical integration procedure which is a useful counterpart to the full numerical solution of the momentum equation.

The interesting porous medium (a layer which is one mm thick as cited by the authors) which resides in Professor Lage's laboratory, while being novel and obviously quite useful, is similar to a thin screen. Furthermore, the types of porous media Nield and Lage are considering do not satisfy the basic characteristics of what constitutes a porous medium. For example, their porous medium does not have a persistent solid phase, nor does it satisfy the Representative Elementary Volume (REV) requirement mentioned in various places, including Nield and Bejan (1992). In reality, what the authors should mention is that they like to extend the use of the porous medium formulation for situations other than those represented by a real porous medium. In fact, an approach using the porous medium formulation for situations in which there is, in essence, no real porous media has been used by our group in the past. We prefer to refer to all these cases as "pseudo porous medium." This, in our opinion, is a more accurate and representative term as it covers an entire class of materials which are not really porous media but for which the porous medium formulation is utilized to represent the transport processes. Therefore, we support the authors to follow up on the utilization of the porous medium formulation for the "pseudo porous medium" as we and a few other researchers have done in the past.

Vafai and Kim's (1989) solution is based on the free stream velocity, u_∞, which is equal to the center line velocity after the flow is fully developed, as long as the two boundary layers along the walls (top and bottom) don't interact with each other. This is because: (1) the thickness of the momentum boundary layer does not grow as the streamwise coordinate increases; and (2) the thickness of the momentum boundary layer is of the order of $\sqrt{K/\delta}/H$ or $\mathrm{Da}^{1/2}$. These two facts were shown by Vafai and Tien (1981) and later further substantiated by various other researchers (e.g., Kaviany, 1985) and were well addressed in Vafai and Kim (1989). The main difference between the interesting numerical solution presented by Nield et al. (1996) and the exact closed form solution presented by Vafai and Kim (1989) is in the use of the second derivative of the velocity with respect to y. Vafai and Kim (1989) assumed that outside the momentum boundary layer, in the core region,

$$\frac{d^2u}{dy^2} = 0.$$

The validity of this assumption, which can be shown by scaling analysis, was also rigorously proven and established by comparing the exact solution from Vafai and Kim (1989) with the "Full Numerical Solution" of the momentum Eq. (4) and boundary conditions (5a) and (5b) (using no slip boundary conditions on both walls of the channel) of Vafai and Kim (1989). As established by Hadim, the exact solution obtained by Vafai and Kim (1989) precisely matches (the curves corresponding to the numerical solution and the exact solution are inseparable for a vast range of parameters which covers, to the best of our knowledge, the entire range of known bona fide porous media) the numerical solution of the momentum equation given by Eq. (4) and boundary conditions (5a) and (5b) of Vafai and Kim (1989). The exact solution starts deviating from the numerical solution for $\mathrm{Da} > 1$.

Nield et al. (1996) used Romberg's numerical integration to solve the integrals in their Eqs. (10) and (11). This is an interesting counterpart to the full numerical solution of the momentum equation which is an ODE. Even though they have presented a different numerical procedure, their solution cannot

---

[4] Only references which are not given, if any, in the discussion are cited.

[5] Department of Mechanical Engineering, The Ohio State University, Columbus, Ohio 43210.

[6] Storage Systems Division, IBM Corporation, Tucson, AZ 85744.

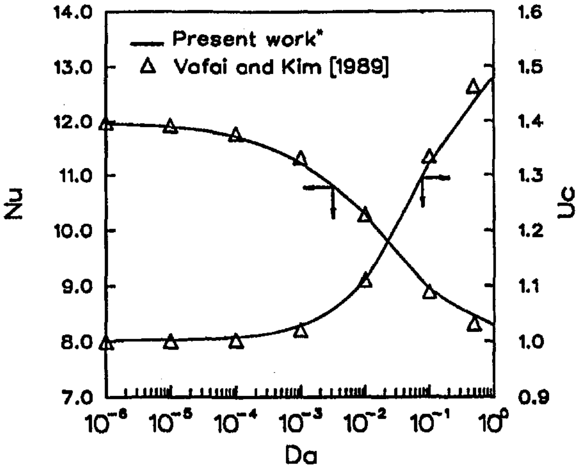

Fig. 2 Comparison of results with Vafai and Kim (1989) *Hadim, A, 1995, "Closure of 'Forced Convection in a Porous Channel with Localized Sources'," ASME Journal of Heat Transfer, Vol. 117, p. 1098.

be easily used for benchmarking the numerical solutions. However, as always, a full numerical solution can be compared with the numerical solution obtained by their Romberg's integration method and this can be a useful addition.

Vafai and Kim (1989) use $du/dy = 0$ when $u = 1$ (instead of $y = 0$) to satisfy $du/dy = 0$ as well as $d^2u/dy^2 = 0$ at $y = 0$. This strategy, which is based on the physics of the problem, as explained in Vafai and Kim (1989), is exact for known porous media. Essentially, this is exact for all practical porous media that we know of other than the interesting and unique set residing in Professor Lage's laboratory. It is important to note that Nield et al. (1996) satisfy the boundary condition $du/dy = 0$, when $y = 0$, implicitly, as was done (i.e., implicitly) in Vafai and Kim (1989). It should also be noted that the left hand side of their Eq. (8) is zero when $u = b_2$. It can then be seen that their numerical solution does not explicitly satisfy the boundary condition $du/dy = 0$ when $y = 0$, either. Their solution satisfies the boundary condition $du/dy = 0$ when $y = 0$, implicitly, which is the same way (i.e., implicitly) that Vafai and Kim (1989) arrived at their solution.

Another point that needs to be noted in Nield et al.'s (1996) work is with respect to recovering a previously obtained analytical solution from their numerical approach for the case $F = 0$. This recovery does not occur as their solution does not approach the known analytical solution as $F = 0$. They had solved the equation analytically for this new case. They did not use Eq. (11) to asymptotically get Eq. (21). When $F = 0$ their Eq. (11) takes the following form:

$$\frac{1}{\sqrt{MDa}}\, y = \int_u^{b_2} \frac{dt}{\sqrt{[t - (2\mathrm{Da} - b_2)](t - b_2)}},$$

which can be integrated to give

$$u = \mathrm{Da} - \Delta \cosh(\lambda y).$$

In our opinion, their Eq. (11) is not the final closed form solution but a mathematical representation of a numerical integration to solve an ordinary differential equation. In essence, this is equivalent to presenting

$$\int \frac{dt}{f(t)} = \int dy$$

as a solution to

$$\frac{du}{dy} = f(u)$$

which is a good representation for a numerical solution of the problem but in our opinion does not constitute an analytical solution.

Comparisons between the full numerical solution based on the momentum equation given by Eq. (4) and boundary conditions (5a) and (5b) of Vafai and Kim (1989) and the exact solution given in the same paper were shown in Figs. 1 and 2 of Vafai and Kim (1995). The exact solution starts deviating from the numerical solution for Da ~ 1. For a reasonably sized porous medium this translates to a permeability, K, of about 10^{-4} or 10^{-3} m^2 at most, and probably smaller. It should be noted that real porous media have permeabilities of at least 10^{-5} m^2 and smaller. Even for the extreme nonrealistic case of $K \sim 10^{-2}$ m^2 and $\Lambda_l = 30$, the agreement is still within 0.7 percent. It should also be noted that Fig. 2 of the discussion given in Vafai and Kim (1995) was not presented by us (as Nield and Lage have incorrectly attributed to us) but rather it was produced independently using a full numerical solution by Professor Hadim. That figure, indeed, does show an excellent agreement up to Da = 1. For the benefit of the readers, Fig. 2 of that discussion, which was obtained by Professor Hadim, is reproduced here. We believe that the readers can easily see the differences between the numerical results of Hadim and the exact solution of Vafai and Kim (1989) in that uncomplicated figure and that there is no need for a guided tour. Furthermore, the cited numbers by Nield and Lage do not correspond to a real porous medium and as such do not relate to our exact solution which was for real porous media. However, we agree that the novel and interesting porous medium (a thin screen which is one mm thick) which resides in Professor Lage's laboratory falls under a different category which we refer to as a pseudo porous medium. Even though we appreciate the opportunity for the additional discussion on this subject with the authors, we believe any further discussion on what had already been presented at length would not serve any technical need.

Reference

Nield, D. A., and Bejan, A., 1992, *Convection in Porous Media*, Springer-Verlag.

Editorial Correction. The authors of the closure that appeared in the ASME JOURNAL OF HEAT TRANSFER, Vol. 118, pp. 267–268 were K. Vafai and S. J. Kim. Our apologies for this inadvertent omission.

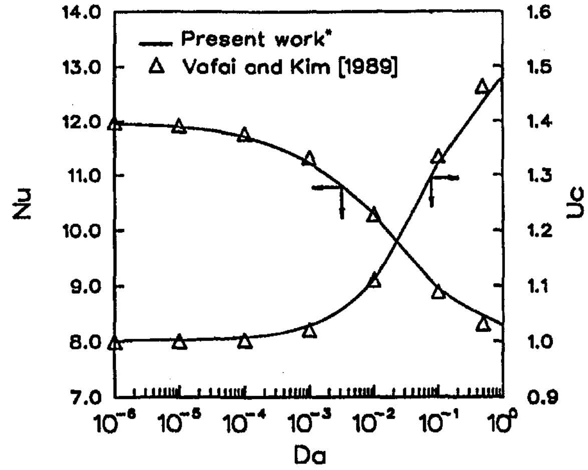

Fig. 2 Comparison of results with Vafai and Kim (1989) *Hadim, A, 1995, "Closure of 'Forced Convection in a Porous Channel with Localized Sources'," ASME Journal of Heat Transfer, Vol. 117, p. 1098.

be easily used for benchmarking the numerical solutions. However, as always, a full numerical solution can be compared with the numerical solution obtained by their Romberg's integration method and this can be a useful addition.

Vafai and Kim (1989) use $du/dy = 0$ when $u = 1$ (instead of $y = 0$) to satisfy $du/dy = 0$ as well as $d^2u/dy^2 = 0$ at $y = 0$. This strategy, which is based on the physics of the problem, as explained in Vafai and Kim (1989), is exact for known porous media. Essentially, this is exact for all practical porous media that we know of other than the interesting and unique set residing in Professor Lage's laboratory. It is important to note that Nield et al. (1996) satisfy the boundary condition $du/dy = 0$, when $y = 0$, implicitly, as was done (i.e., implicitly) in Vafai and Kim (1989). It should also be noted that the left hand side of their Eq. (8) is zero when $u = b_2$. It can then be seen that their numerical solution does not explicitly satisfy the boundary condition $du/dy = 0$ when $y = 0$, either. Their solution satisfies the boundary condition $du/dy = 0$ when $y = 0$, implicitly, which is the same way (i.e., implicitly) that Vafai and Kim (1989) arrived at their solution.

Another point that needs to be noted in Nield et al.'s (1996) work is with respect to recovering a previously obtained analytical solution from their numerical approach for the case $F = 0$. This recovery does not occur as their solution does not approach the known analytical solution as $F = 0$. They had solved the equation analytically for this new case. They did not use Eq. (11) to asymptotically get Eq. (21). When $F = 0$ their Eq. (11) takes the following form:

$$\frac{1}{\sqrt{MDa}}\, y = \int_{u}^{b_2} \frac{dt}{\sqrt{[t - (2\mathrm{Da} - b_2)](t - b_2)}},$$

which can be integrated to give

$$u = \mathrm{Da} - \Delta \cosh(\lambda y).$$

In our opinion, their Eq. (11) is not the final closed form solution but a mathematical representation of a numerical integration to solve an ordinary differential equation. In essence, this is equivalent to presenting

$$\int \frac{dt}{f(t)} = \int dy$$

as a solution to

$$\frac{du}{dy} = f(u)$$

which is a good representation for a numerical solution of the problem but in our opinion does not constitute an analytical solution.

Comparisons between the full numerical solution based on the momentum equation given by Eq. (4) and boundary conditions (5a) and (5b) of Vafai and Kim (1989) and the exact solution given in the same paper were shown in Figs. 1 and 2 of Vafai and Kim (1995). The exact solution starts deviating from the numerical solution for Da ~ 1. For a reasonably sized porous medium this translates to a permeability, K, of about 10^{-4} or 10^{-3} m^2 at most, and probably smaller. It should be noted that real porous media have permeabilities of at least 10^{-5} m^2 and smaller. Even for the extreme nonrealistic case of K ~ 10^{-2} m^2 and $\Lambda_l = 30$, the agreement is still within 0.7 percent. It should also be noted that Fig. 2 of the discussion given in Vafai and Kim (1995) was not presented by us (as Nield and Lage have incorrectly attributed to us) but rather it was produced independently using a full numerical solution by Professor Hadim. That figure, indeed, does show an excellent agreement up to Da = 1. For the benefit of the readers, Fig. 2 of that discussion, which was obtained by Professor Hadim, is reproduced here. We believe that the readers can easily see the differences between the numerical results of Hadim and the exact solution of Vafai and Kim (1989) in that uncomplicated figure and that there is no need for a guided tour. Furthermore, the cited numbers by Nield and Lage do not correspond to a real porous medium and as such do not relate to our exact solution which was for real porous media. However, we agree that the novel and interesting porous medium (a thin screen which is one mm thick) which resides in Professor Lage's laboratory falls under a different category which we refer to as a pseudo porous medium. Even though we appreciate the opportunity for the additional discussion on this subject with the authors, we believe any further discussion on what had already been presented at length would not serve any technical need.

Reference

Nield, D. A., and Bejan, A., 1992, *Convection in Porous Media*, Springer-Verlag.

Editorial Correction. The authors of the closure that appeared in the ASME JOURNAL OF HEAT TRANSFER, Vol. 118, pp. 267–268 were K. Vafai and S. J. Kim. Our apologies for this inadvertent omission.
